Annual Research Briefs – 1998

Center for Turbulence Research

December 1998

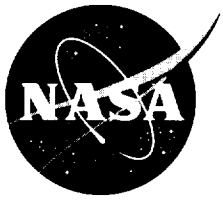

CONTENTS

Preface

This report contains the 1998 annual progress reports of the postdoctoral Fellows and visiting scholars of the Center for Turbulence Research. It summarizes the research efforts undertaken under the core CTR program. In addition, earlier this year a report containing the proceedings of the 1998 CTR Summer Program was distributed. These reports and other CTR publications are available on the World Wide Web (http://www-fpc.stanford.edu/CTR). Last year, CTR sponsored eighteen resident Postdoctoral Fellows, seven Research Associates, one Research Engineer, three Senior Research Fellows, hosted fifteen short term visitors, and supported two doctoral students.

For over a decade CTR's core funding has been provided by NASA Ames Research Center; last year NASA Langley Research Center and NASA Lewis Research Center joined Ames in supporting CTR. We view this as a positive development and hope for it to continue in the future, and as a result expect to have more direct interactions with the technical staff at Langley and Lewis. Turbulence is a major problem for all of NASA; CTR provides the critical mass needed to address different aspects of this important problem for aerospace technology by attracting researchers worldwide. CTR also provides technical and infrastructure support for an extensive array of programs supported by the U.S. Department of Defense and Department of Energy at Stanford University. The combination of all these activities has provided a unique environment for turbulence research at CTR.

The reports in this volume are collected into four groups. The first group deals with turbulent combustion where modeling efforts in the Reynolds Averaged Navier Stokes (RANS) and large eddy simulation (LES) techniques are described. New efforts in numerical methodology for turbulent flows with combustion and a new experimental activity for validation of the numerical studies are described. The second group begins with a technical report on CTR's new efforts in simulation and understanding of Hall thrusters, a propulsion engine used for satellite maneuvering. This is part of a new research activity for CTR where the tools developed for prediction of turbulent flows are applied to other areas such as plasma simulations. The remaining reports in this group include an account of progress in using LES for prediction of flow generated noise and new efforts for prediction of transition with application to turbomachinery. The RANS activity, presented in the third group, continues to play a major role in CTR's core program. The list of flows where CTR's V2F model has been successfully applied was extended to transonic flows with shocks. In addition, our renewed interest in turbomachinery flows has motivated our investigation and development of RANS for heat transfer prediction. The V2F model has now been incorporated in several major NASA codes as well as other widely used CFD codes. Finally, CTR's effort in LES has focused on the problem of wall layer modeling for more efficient LES computations and on the development of high order conservative numerical methods for flows in complex geometries. These studies are described in the final group of reports in this volume.

We are grateful to Debra Spinks for her skillful compilation of this report and for her efficient day-to-day management of the Center operations.

Parviz Moin
William C. Reynolds
Nagi N. Mansour

Direct numerical simulation of turbulent non-premixed combustion with realistic chemistry

By W. K. Bushe AND R. W. Bilger[1]

1. Motivation and objectives

Combustion is an important phenomenon in many engineering applications; combustion of hydrocarbons is still by far the most common source of energy in the world. In virtually every application of combustion processes, the flow in which the chemical reactions are taking place is turbulent. Furthermore, the combustion process itself is usually described by a very large system of elementary chemical reactions. These chemical kinetic mechanisms are usually extremely stiff and involve, for long-chain hydrocarbon species, perhaps hundreds of chemical species (which, if the combustion process is to be completely simulated, implies a need to solve hundreds of partial differential equations simultaneously). The governing equations describing the chemical composition are closely coupled to those describing the turbulent transport. Also, the chemical reaction rates are non-linear and strongly depend on the instantaneous composition and temperature. For these reasons, a full understanding of the many processes at work in devices such as furnaces, diesel engines, and gas turbines has been lacking.

In many devices of interest such as those mentioned above, the combustion takes place in what is known as the "non-premixed" regime. The fuel and oxidizer are initially unmixed, and in order for chemical reaction to take place, they must first mix together. In this regime, the rate at which fuel and oxidizer are consumed and at which heat and product species are produced is, therefore, to a large extent controlled by mixing. The nature of such flows lends itself to a particular variety of models which attempt to take advantage of this. These models describe mixing based on what is called the "mixture fraction", or the fraction of fluid which originated in the fuel stream; they attempt to either describe a steady state flame by a simple mapping operation—as in fast chemistry models (Bilger, 1980) and laminar flamelet models (Peters, 1984)—or incorporate reaction rates by expressing them as functions of the mixture fraction—as in the unsteady laminar flamelet model of Pitch and Peters (1998), the Conditional Moment Closure (CMC) model proposed independently by Klimenko (1990) and Bilger (1993a,b), and the Conditional Source-term Estimation (CSE) model of Bushe and Steiner (1998).

Work attempting to improve and validate models for turbulent combustion has been hampered by a lack of adequate experimental results. Experimental methods which might provide the necessary insight are also extremely expensive, difficult to perform, and still quite limited in the information they provide. Direct Numerical

1 The University of Sydney, Australia

Simulation (DNS) of the governing equations offers an alternative to experiments; however, such simulations are limited by available computer resources. Previous simulations have either been limited to extremely simple chemical kinetic mechanisms (Vervisch, 1992; Chen, *et al.*, 1992) or to two-dimensional flows (Smith, 1996; Chen & Echekki, 1996).

With the advent of new techniques for the systematic reduction of chemical kinetic mechanisms, new reduced kinetic mechanisms are now available which are still relatively simple but which retain sufficient complexity from the original mechanism to provide good predictions of flame structure and reaction rates. In a previous study which implements such a reduced mechanism in DNS (Swaminathan & Bilger, 1997 & 1998a), the flow was assumed to be incompressible so that effects of heat release on the flow were neglected. While the results of this study have been encouraging, validation of the CMC method against this constant property DNS data is not completely convincing. There is clearly a need to obtain DNS data using realistic chemical kinetics in turbulence where effects of the heat release on the flow are included.

In the present study, a reduced kinetic mechanism has been incorporated into a fully compressible DNS code. The results of the simulations will be used for the validation and, hopefully, improvement of current combustion models such as those mentioned above.

2. Accomplishments

2.1 Chemistry

The chemical kinetic mechanism that was used in the simulations is one representative of the oxidation of a methane/nitrogen mixture by an oxygen/nitrogen mixture. There are three reactions in the mechanism; the first two represent the oxidation of the methane (Williams, 1991), and the third represents the formation of nitric oxide and was obtained by putting the Oxygen free radical in the simple Zel'dovich into partial equilibrium. The reactions are:

$$Fuel + Oxi \rightarrow Int + Prod \qquad \text{(I)}$$

$$Int + Oxi \rightarrow 2Prod \qquad \text{(II)}$$

$$N_2 + Oxi \rightarrow 2NO \qquad \text{(III)}$$

where *Fuel* is CH_4, *Oxi* is O_2, *Int* is $\left(\frac{4}{3}H_2 + \frac{2}{3}CO\right)$, and *Prod* is $\left(\frac{2}{3}H_2O + \frac{1}{3}CO_2\right)$.

In order to reduce computational costs and to make the mechanism more tractable for modeling purposes, the reaction rate expressions were simplified. The chemical kinetic mechanism was incorporated into a DNS code which solves the governing equations for fully compressible turbulent flow (Ruetsch *et al.*, 1995), based on the algorithms of Lele (1992) and Poinsot and Lele (1992). The implementation of the mechanism was thoroughly tested in one- and two-dimensional simulations; this work was described previously (Bushe *et al.*, 1997) and will not be discussed here.

2.2 Three-dimensional simulations

Having tested the implementation of the chemical kinetic mechanism and having established that simulation with turbulence was possible, a series of three-dimensional simulations were undertaken. Several limitations on initial and boundary conditions had been established in the two-dimensional tests.

For the simulation results to be useful for the purpose of model validation, it was clear that the bulk pressure in the domain would have to remain constant. In order to ensure this, fluid had to be allowed to leave the domain; therefore, it was necessary to use partially non-reflecting outflow boundary conditions (Poinsot & Lele, 1992) for at least one boundary. An additional constraint was then that the reaction rates at any such a boundary was required to be zero; otherwise, these boundary conditions become ill-posed. Also, because the chemical kinetic rates depend on the hydrogen free radical concentration, the mechanism cannot auto-ignite; therefore, the fields had to be initialized such that at least some chemical reaction is already underway.

The species mass fractions were initialized in the one-dimensional simulations by first defining the mixture fraction as a linear combination of mass fractions such that the chemical source term in its transport equation is zero:

$$Z = \frac{60Y_{Fuel} - 60Y_{Oxi} - 36Y_{Prod} - 32Y_{\mathrm{NO}} + 18}{27}. \tag{1}$$

The mixture fraction was initialized with the analytical solution to the diffusion equation for a semi-infinite slab of fuel mixing with a semi-infinite slab of oxidizer,

$$Z(x,t) = \mathrm{erf}\left(\frac{x}{\sqrt{4\mathcal{D}t}}\right), \tag{2}$$

at an arbitrary time, chosen such that the reaction zone would be sufficiently resolved with the available number of grid points. Mass fractions for each species were then calculated by assuming that an arbitrary fraction of moles for each of reaction I and II had reacted to completion. This assumption also allowed for the calculation of the heat released as a function of mixture fraction, from which the temperature field can be calculated. The initial velocity was zero, and both boundaries in the one-dimensional simulations allowed for partially reflecting out-flow.

The mass fraction, temperature, density, and velocity fields for the three-dimensional simulations were then initialized by using a stabilized one-dimensional flame solution. By placing a stable flame in the middle of the three-dimensional domain, the time until the reaction zone (the region of the flow in which chemical reaction takes place) reached a boundary could hopefully be maximized. The placement of the flame is depicted in Fig. 1.

Initial turbulent velocity fluctuations were obtained by using a pseudo-spectral code (Ruetsch & Maxey, 1991) to solve the governing equations for incompressible flow and forcing a periodic, three-dimensional flow field on a 120^3 grid from quiescence until its statistics became stationary. Two identical 120^3 boxes were placed

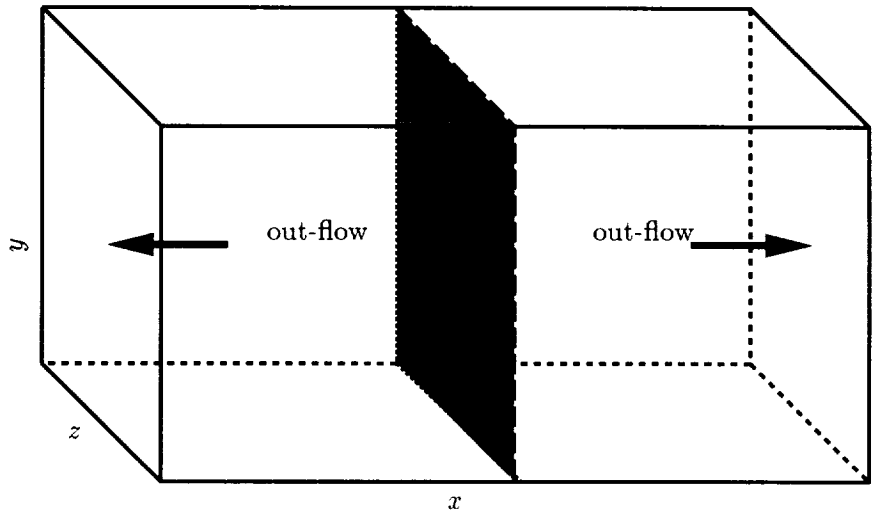

FIGURE 1. Depiction of initial flame placement.

next to each other to fill out the 120 × 120 × 240 domain; periodic boundary conditions were retained for the y and z directions and out-flow boundaries used in the x direction as shown in Fig. 1. The turbulent fluctuations near the out-flow boundaries were filtered to zero to avoid potential generation of unphysical vorticity. The incompressible turbulent fluctuations were taken to be fluctuations in the momentum; thus, the turbulent velocity was divided by the density so as to satisfy

$$\frac{\partial(\rho u_i)}{\partial x_i} = 0,$$

in the initial field. The resulting turbulent velocity field was added to the velocity field induced by dilatation in the one-dimensional flame.

2.3 Results

Six sets of data have been produced. Two simulations were run for 90 time units, and the remainder were run only for 20 time units. These additional simulations were run to provide a larger ensemble of points from which to extract statistics. In each simulation the same initial flame was used, but the initial velocity field was either shifted or rotated such that the flame saw the same velocity field in a statistical sense but underwent a very different evolution. In all cases, data was stored for every 2.5 non-dimensional time units so that the evolution of the flow and scalar fields could be studied. The data stored included the density, the temperature, the mass fractions of Fuel, Oxidizer, Intermediate, Product and NO, and the velocity in each direction for every point in the domain.

2.3.1 Visualization of slices

In Figs. 2–4, eight different properties are visualized for a single plane oriented normal to the flame brush. These figures show the properties taken from one simulation at three different times (7.5, 15.0, and 30.0 time units). The properties

shown are summarized in Table 1, along with a legend to the colors in Figs. 2-4. The minima and maxima of the properties are kept the same for all three figures to allow direct comparison between them. Superimposed on these plots are isopleths of mixture fraction. The black lines are spaced at intervals of mixture fraction of 0.1, and the white line is the isopleth of the stoichiometric mixture fraction of 1/3. The gas at the right-hand edge of the figures is pure fuel (where the mixture fraction has a value of unity), and the gas at the left-hand edge of the figures is pure oxidizer (where the mixture fraction has a value of zero).

sub-figure	Property	Minimum (white)	Maximum (black)
a	χ	0	0.0125
b	T	300K	2000K
c	Y_{Int}	0	0.032
d	Y_{H}	0	0.0024
e	$\dot{\omega}_{\mathrm{I}}$	0	6.5×10^{-5}
f	$\dot{\omega}_{\mathrm{II}}$	0	6.0×10^{-5}
g	Y_{NO}	0	1.4×10^{-8}
h	$\dot{\omega}_{\mathrm{III}}$	0	2.3×10^{-5}

Table 1. Legend for Figs. 2, 3, and 4.

In Fig. 2, there is a peak in scalar dissipation evident, which coincides with a saddle point in the temperature. There is considerable fine-scale structure in the scalar dissipation. In the middle of the slice, there is a fairly large region in which the scalar dissipation along the stoichiometric isopleth is very low; it is in this region where the temperature is a maximum. This region also coincides with the maximum production rate of Nitric Oxide. Furthermore, the Intermediate and Nitric Oxide mass fractions also peak here. The Hydrogen radical, however, peaks in a region of moderately high scalar dissipation. Neither of reactions I or II show any sign of local extinction at this early time in the simulation; however, there are in both reaction rates double peaks, which may indicate turbulent structure within the reaction zone, although it is more likely a consequence of out-of-plane folding. Regardless, it would be difficult to describe the flame shown in this figure as being locally one-dimensional.

In Fig. 3, the peak in scalar dissipation which was apparent in Fig. 2 has become larger in magnitude and has been transported by the flow. The scalar dissipation still exhibits fine-scale structure. The saddle point in the temperature still coincides with the peak in scalar dissipation and has become deeper. The region of low scalar dissipation where the temperature is high has become larger, and the maximum temperature is slightly higher here. The Intermediate and Nitric Oxide mass fractions as well as the Nitric Oxide production rate all peak in this region. Interestingly, the Intermediate species mass fraction nearly vanishes at the location of the peak in scalar dissipation, as does the mass fraction of the Hydrogen radical,

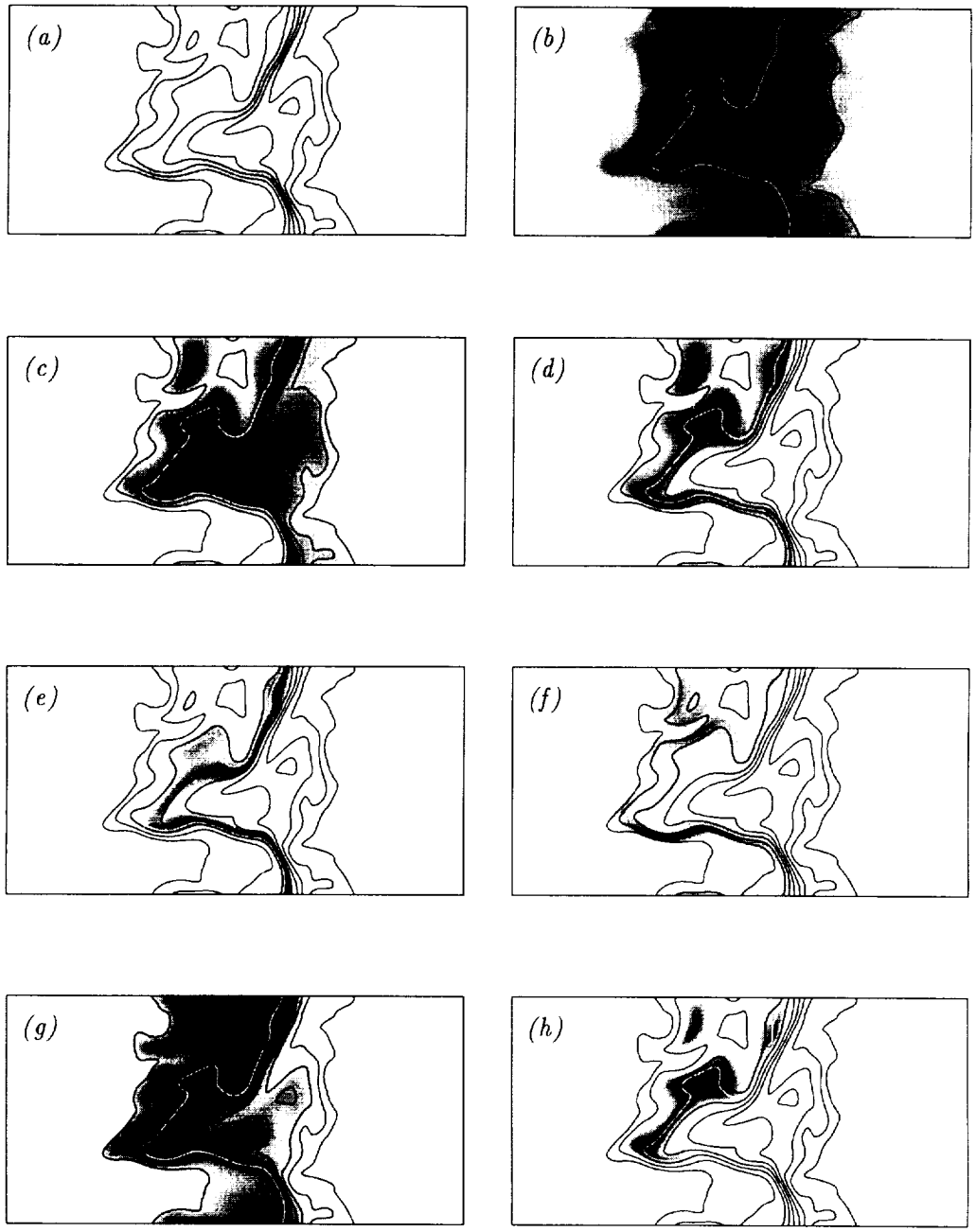

FIGURE 2. Visualization of properties on a slice through the three-dimensional domain after 7.5 acoustic time units: a) Scalar dissipation, b) Temperature, c) Mass fraction of Intermediate, d) Mass fraction of Hydrogen radical, d) Reaction rate I, e) Reaction rate II, f) Mass fraction of Nitric Oxide, g) Reaction rate III. See Table 1 for legend.

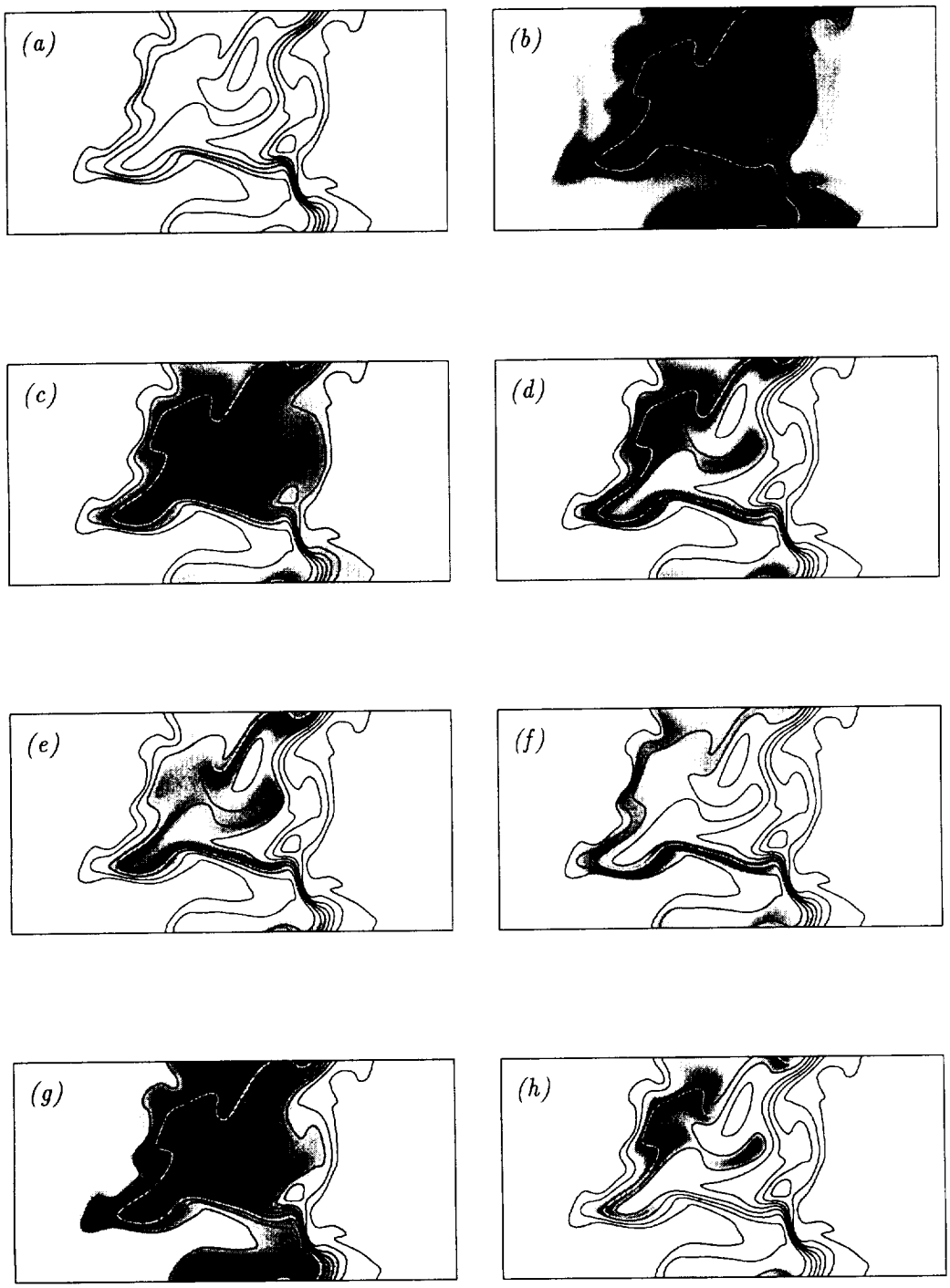

FIGURE 3. Visualization of same properties shown in Fig. 2 after 15.0 acoustic time units. See Table 1 for legend.

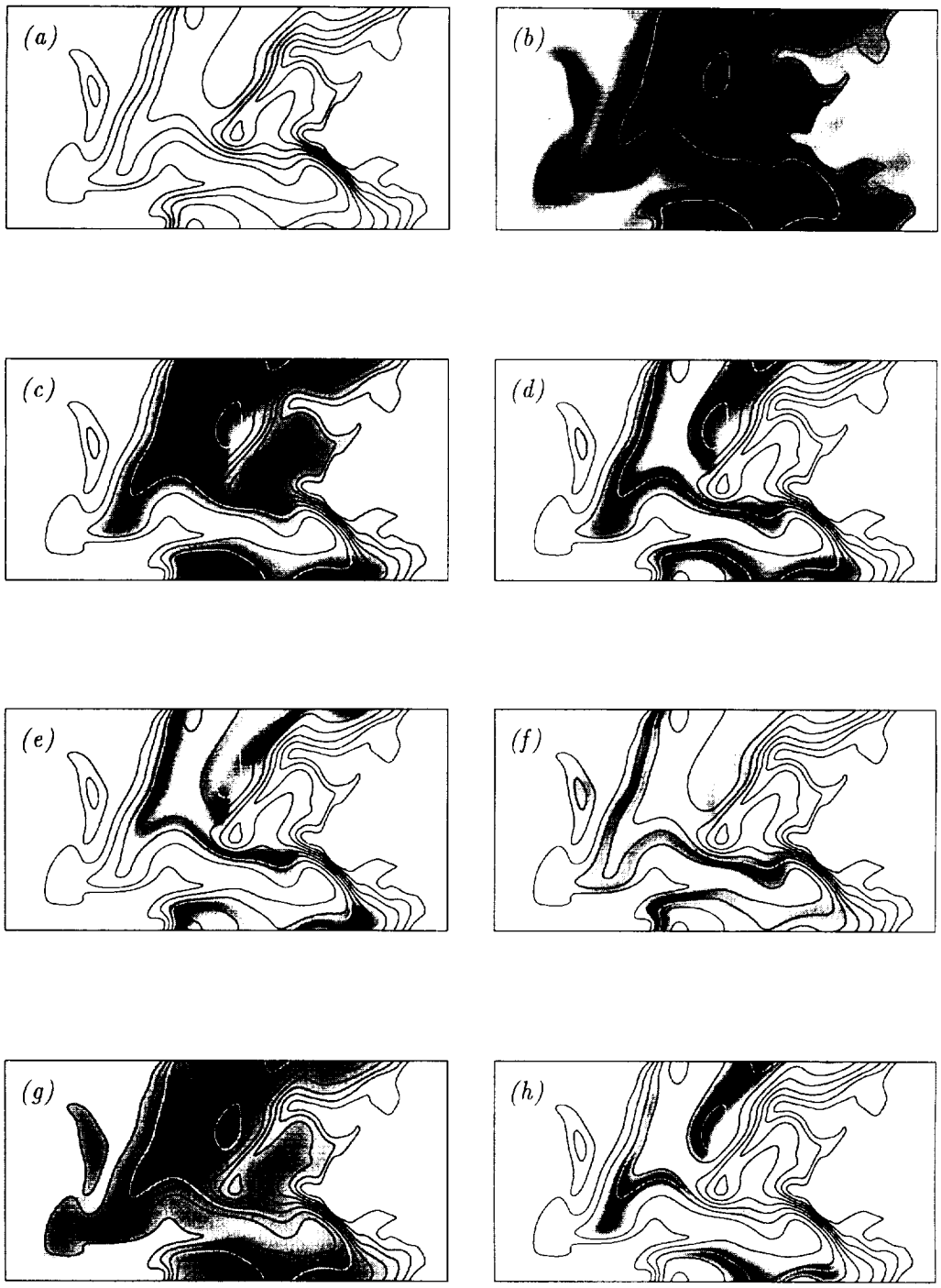

FIGURE 4. Visualization of same properties shown in Fig. 2 after 30.0 acoustic time units. See Table 1 for legend.

even along the stoichiometric isopleth of mixture fraction. This, coupled with the low temperature at this spot, has the effect of extinguishing the rates of reactions I and II; that is, the local reaction rates are more than an order of magnitude lower than they are at other locations with the same stoichiometry; this is what is known as local extinction. At this later time, reaction I is significant in a very broad region in space where the scalar dissipation is low (that the scalar dissipation is low here indicates that this is not merely a consequence of out-of-plane folding); furthermore, there is also a pocket of unreacting gas surrounded by reacting gas.

In Fig. 4, the peak in the scalar dissipation has been convected further to the right, but the peak is lower in magnitude. The structure in the scalar dissipation field is starting to exhibit somewhat larger scales than was seen at the earlier times. The temperature field still peaks in a region of very low scalar dissipation, and the saddle point in temperature associated with the peak in scalar dissipation has become even lower. The Intermediate mass fraction and the rate of reaction II are both very low in this region, and the Hydrogen radical mass fraction and rates of reactions I and III are all negligibly small. Peaks in the Nitric Oxide mass fraction are at the same locations as peaks in the rate of reaction III; these coincide with peaks in the temperature.

2.3.2 Scatter plots

Figure 5 gives scatter plots of the scalar dissipation, temperature, and mass fractions of Oxidizer, Fuel, Intermediate, and Hydrogen radical as functions of the mixture fraction for the simulation discussed above at a time of 15.0 time units. The scalar dissipation shows considerable scatter with a peak at a mixture fraction around 0.5. The peak scalar dissipation in the turbulent flow at this time is over 200 times the peak in the original laminar flow. In the plots of the temperature and the Fuel, Oxidizer, Intermediate, and Hydrogen radical mass fractions, the laminar flame with which the simulation was initialized is superimposed on the scatter plots. Most of the points in the temperature scatter plot lie below the initial flame, which is an effect of the increased scalar dissipation caused by turbulent mixing. Almost all of the points in the oxidizer and fuel mass fractions are higher above the curves of the initial flame, as are most of the points in the Hydrogen radical mass fraction plot. In this last plot, however, there are still a few points below the laminar flame curve; these are points that lie in regions of local extinction such as that discussed above. The Intermediate species mass fraction exhibits the most scatter of the mass fraction plots; however, the bulk of the points lie close to the laminar flame curve.

2.3.3 Turbulence statistics

While the field used to initialize the velocity in the turbulent simulations came from an isotropic simulation, the mixture fraction was initialized with an anisotropic field, and the turbulent velocity fluctuations were adjusted using the initial laminar flame density. Also, the viscosity was taken to be a function of the temperature, and the temperature had, as seen in the previous section, substantial variation even as a function of mixture fraction. Therefore, the initial velocity field was strongly anisotropic in the direction across the layer. As such it is difficult to describe the

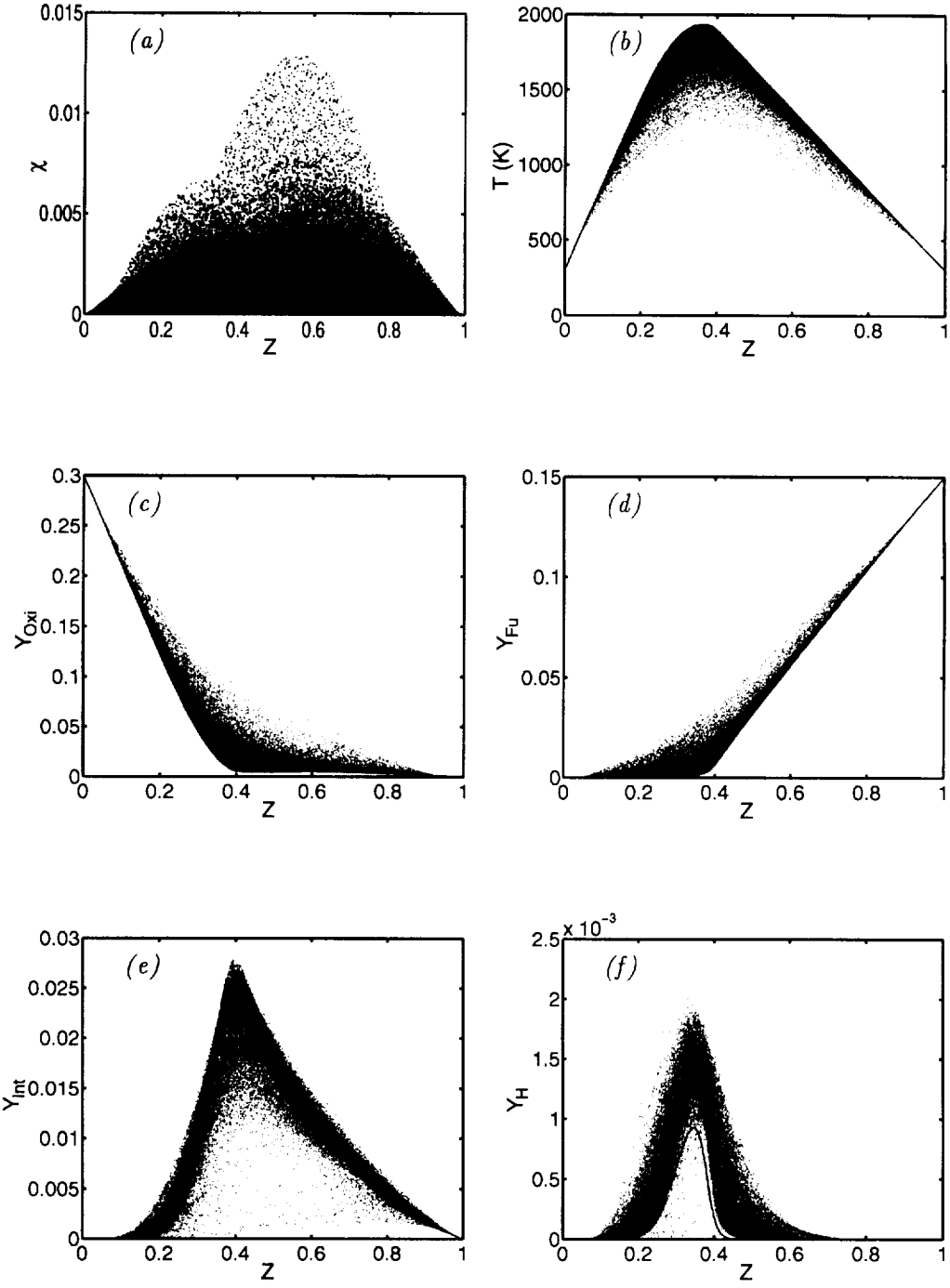

FIGURE 5. Scatter plots of a) Scalar dissipation, b) Temperature, c) Mass fraction of Oxidizer, d) Mass fraction of Fuel, e) Mass fraction of Intermediate and f) Mass fraction of hydrogen radical. Solid lines are initial laminar flame profiles.

characteristics of the flow using statistics. In order to examine the characteristics of the flow field, statistics were taken on planes normal to the direction of anisotropy in the mixture fraction field; that is, properties were averaged together on planes normal to the x direction. One unfortunate consequence of this is that there are only 120^2 points on each plane, which may mean that the statistics on these planes are not properly converged.

The Taylor microscale is defined by Tennekes and Lumley (1992) as

$$\lambda = \sqrt{\frac{10 \cdot \widetilde{\nu} \cdot \widetilde{k}}{\widetilde{\epsilon}}}$$

where $\nu = \frac{\overline{\rho\nu}}{\overline{\rho}}$ is the Favre averaged kinematic viscosity,

$$\widetilde{k} = \frac{\overline{\rho(u_i - \widetilde{u}_i)(u_i - \widetilde{u}_i)}}{2\overline{\rho}}$$

is the Favre averaged turbulent kinetic energy, and

$$\widetilde{\epsilon} = \frac{\overline{\rho\nu\left(\frac{\partial u_i}{\partial x_j} + \frac{\partial u_j}{\partial x_i}\right)\frac{\partial u_j}{\partial x_i}}}{\overline{\rho}}$$

is the Favre averaged dissipation rate of turbulent kinetic energy (Hinze, 1975). The Reynolds number based on the Taylor microscale is

$$\mathrm{Re}_\lambda = \frac{\sqrt{\frac{2}{3}\widetilde{k}}\lambda}{\widetilde{\nu}}.$$

This is shown as a function of x in Fig. 6 for several times: the initial condition is shown, as are those times for which visualizations were given in section 2.3.1 (7.5, 15 and 30 acoustic time units) along with the last time for which data is available at 90.0 acoustic time units.

The Taylor scale Reynolds number was initially around 60 in the cold fluid; however, the higher viscosity reduced this to only 20 in the flame. The effect of filtering the velocity fluctuations to zero at the outflow boundaries is apparent in that the Reynolds number drops dramatically to zero at the boundaries in the initial field. The diffusive nature of turbulence and the dilatation caused by heat release in the middle of the domain change this very quickly—by 7.5 time units; the Reynolds number at the boundaries rose to around 20. While a Taylor scale Reynolds number of 20 is very low, it can still be taken as an indication that there is turbulent motion present; this is roughly the Reynolds number of the turbulence in the reaction zone for all but the latest time shown.

The Kolmogorov length scale, which is

$$l_k = \left(\frac{\widetilde{\nu}^3}{\widetilde{\epsilon}}\right)^{1/4},$$

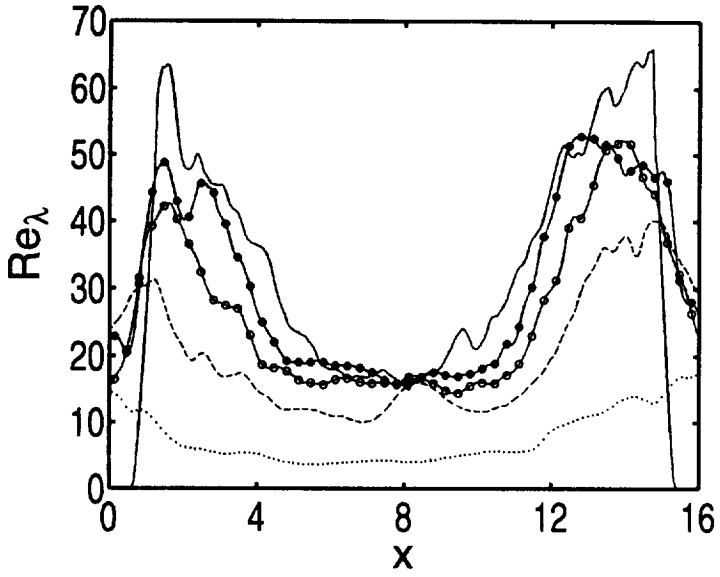

FIGURE 6. Favre averaged Taylor Reynolds number on planes of constant x through the mixing layer: —— $t = 0.0$; —●— $t = 7.5$; —○— $t = 15.0$; ---- $t = 30.0$; ····· $t = 90.0$.

is shown in Fig. 7. This is initially almost constant in the domain except at the edges, where the dissipation is zero because the velocity fluctuations have been filtered out (this is why the Kolmogorov length shoots up to infinity at the edges). The Kolmogorov length in the middle of the domain, where the heat is released, rises with time much faster than it does at the edges of the domain. Initially the Kolmogorov length is somewhat smaller than the grid spacing (0.067) and this gets larger with time; this indicates that the turbulence was adequately resolved on the grid throughout the simulation.

The initial turbulent flow field did not exhibit any inertial range in its spectrum so it would be inappropriate to consider the integral length scale of the flow field. Instead, the dissipation length and time scales were examined. The dissipation length is

$$l_{\text{diss}} = \frac{u''^3}{\widetilde{\epsilon}}$$

and the dissipation time is

$$t_{\text{diss}} = \frac{l_{\text{diss}}}{u''},$$

where $u'' = \sqrt{\frac{2\widetilde{k}}{3}}$. These are shown in Fig. 8. The dissipation length is initially around $0.8L$ in the middle of the domain and just over $2.5L$ in the cold fluid near the edges; it is zero at the boundaries, but this is again due to the filtering of the fluctuations there. In time, the dissipation length appears to decay to around

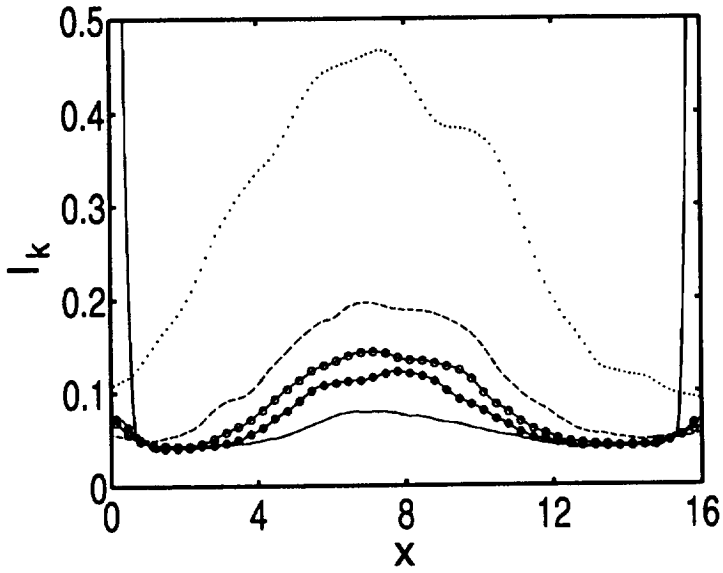

FIGURE 7. Favre averaged Kolmogorov length on planes of constant x through the mixing layer: —— $t = 0.0$; —●— $t = 7.5$; —○— $t = 15.0$; ---- $t = 30.0$; ····· $t = 90.0$.

$0.7L$ throughout the domain. The dissipation time is initially very low—around 2 acoustic time units—in the middle of the domain, but exceeds 50 in the cold fluid. In time, the dissipation time increases to around 25 acoustic time units in the middle of the domain but remains around 45 at the edges. The dissipation length in the middle of the domain is initially about one order of magnitude larger than the Kolmogorov length. Only at 90 time units do these lengths become comparable. This is further evidence that the flow is turbulent albeit not very vigorous given the fairly long dissipation times.

The Favre averaged scalar dissipation is shown in Fig. 9a. Clearly, in the presence of turbulence the mean scalar dissipation is considerably larger in magnitude than the initial, laminar profile. The peak in scalar dissipation is at 7.5 time units and this decays slowly. Only when the turbulence has effectively decayed away, evidenced by the low Reynolds number, does the mean scalar dissipation return to near the initial laminar curve.

The Favre average of the temperature is shown in Fig. 9b. The peak mean temperature drops abruptly in the presence of turbulence; this is likely due more to the variance of mixture fraction that results from large scale mixing than to local changes in the flame. The peak mean temperature never approaches that of the initial curve although the increase in the area under the mean temperature curve with time indicates that the reactions are still clearly proceeding in earnest throughout the run.

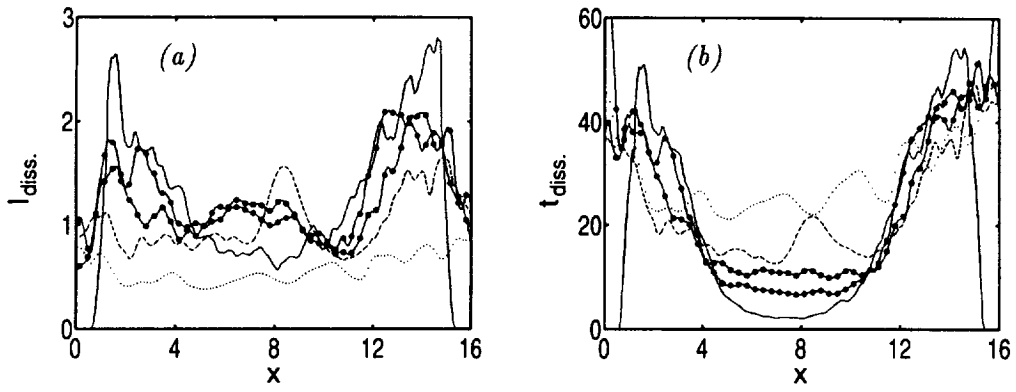

FIGURE 8. Favre averaged dissipation length (a) and time (b) on planes of constant x through the mixing layer: —— $t = 0.0$; —●— $t = 7.5$; —○— $t = 15.0$; ---- $t = 30.0$; ····· $t = 90.0$.

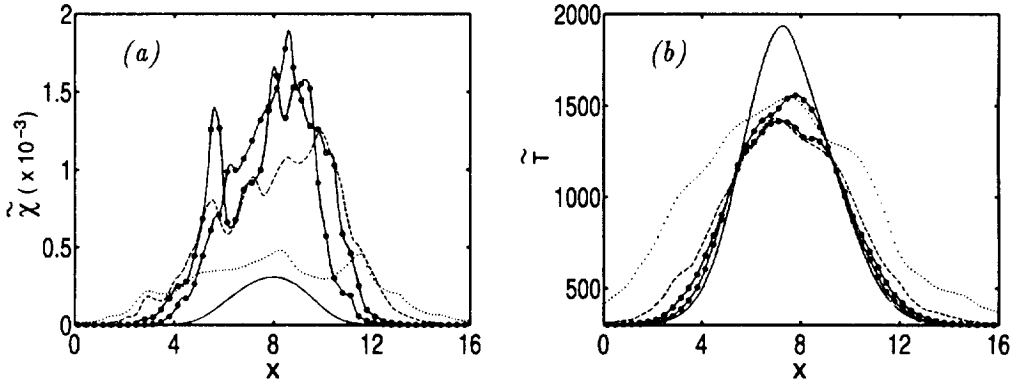

FIGURE 9. Favre averaged scalar dissipation rate (a) and temperature (b) on planes of constant x through the mixing layer: —— $t = 0.0$; —●— $t = 7.5$; —○— $t = 15.0$; ---- $t = 30.0$; ····· $t = 90.0$.

2.3.4 Conditional reaction rates

In Fig. 10, the conditional averages of the reaction rates are compared to those predicted by evaluating the reaction rates with the conditionally averaged mass fractions, temperature, and density in the entire domain at 15 acoustic time units. This is a test of the validity of the first order CMC hypothesis, which is used to obtain closure for the chemical source terms in both the CMC and CSE approaches. The reaction rates for reactions I and II are predicted to within 5%. However, the under-prediction of reaction III is substantial—over 25%.

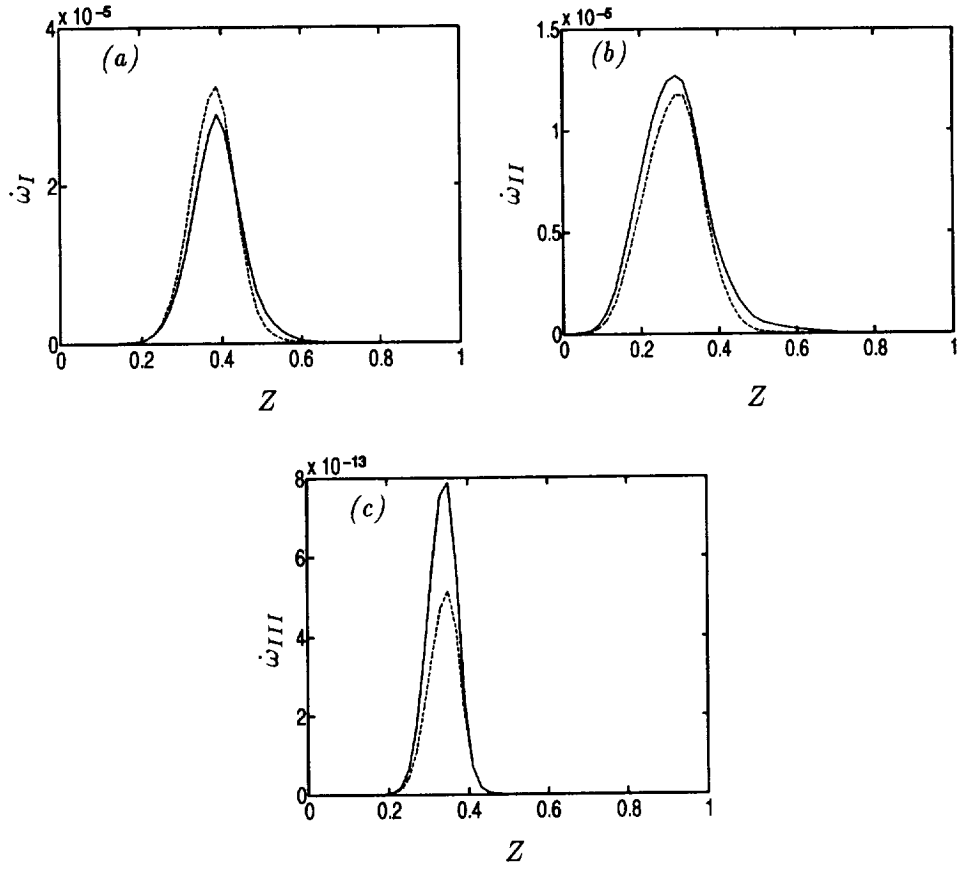

FIGURE 10. Comparison of conditionally averaged reaction rates to reaction rates predicted using the first order CMC approximation at 15 time units:
(a) ——— , $\langle\dot{\omega}_I(Y_J,T)|Z=\eta\rangle$; ····· , $\dot{\omega}_I(Q_J,\langle T|Z=\eta\rangle)$;
(b) ——— , $\langle\dot{\omega}_{II}(Y_J,T)|Z=\eta\rangle$; ····· , $\dot{\omega}_{II}(Q_J,\langle T|Z=\eta\rangle)$;
(c) ——— , $\langle\dot{\omega}_{III}(Y_J,T)|Z=\eta\rangle$; ····· , $\dot{\omega}_{III}(Q_J,\langle T|Z=\eta\rangle)$.

2.4 Discussion

Several interesting findings are seen in the previous section. These will now be discussed in greater detail.

2.4.1 Extinction effect

Non-premixed flames can be thought of as a competition between local chemical reaction and local mixing. At low values of local scalar dissipation (which is a direct measure for the rate of mixing), the reactions which consume fuel and oxidizer are limited by the mixing rate. As the local scalar dissipation increases, these chemical reaction rates will increase. When the local scalar dissipation rate becomes very large, the rate of diffusion of heat away from the reaction zone, the region of space in which chemical reaction is taking place, becomes large and can exceed the

rate at which chemical reaction replenishes that heat; the local temperature goes down. Since virtually all chemical reaction rates in flames are strongly temperature dependent, the reaction rates are slowed. If the high scalar dissipation persists for a sufficiently long time, these reactions can become quenched. Once this has occurred, even if the scalar dissipation subsides, the reaction rates will not recover, and re-ignition occurs either by a premixed front originating from non-extinguished gas adjacent to the region of local extinction or by auto-ignition.

This local extinction phenomenon is clearly evident in the sequence of Figs. 2-4. At 7.5 time units, the scalar dissipation peaks at a location where the temperature reaches a local saddle point, and yet reaction rates I and II are significant at the same location. It is only at 15.0 time units that these reaction rates appear to be quenched.

At this time, however, it is not yet clear whether the extinction events seen in the database are genuinely a result of low-temperature quenching of the reaction rates or an effect of the form of the steady-state expression for the Hydrogen radical. The form used contains an exponential term which is a surrogate for a sharp cut-off function of $Y_{\mathrm{Fu}}/Y_{\mathrm{Oxi}}$. It is conceivable that the extinction events were caused by depletion of the Hydrogen radical and that the low local temperatures are a consequence of extinction rather than the cause. This shall remain a question for future work.

2.4.2 Edge-flames

It is interesting to note that the flames at the edges of the extinction event seen in Figs. 3 and 4 do not exhibit triple flame structure. This was investigated carefully—where colormaps for the plots were manipulated so as to highlight even very low reaction rates—and found to be true for all of the times at which data was analyzed. It has not yet been possible to search through the fields at later times to establish if this is a persistent phenomenon. Furthermore, given the possibility that the extinction events may be caused by Hydrogen radical depletion rather than low-temperature quenching, it is possible that the lack of premixed branches is a consequence of the form of the reaction rates. In earlier simulations using different initial conditions (with the same chemical kinetic mechanism), premixed branches of triple flames were clearly evident; thus this seems an unlikely explanation. Alternatively, the lack of premixed branches on the edges of the reaction zones may be an indicator that the edge-flames are receding or that the local scalar dissipation is still so high that the premixed branches ordinarily associated with triple-flames have merged with the diffusion branch (Vervisch & Trouvé, 1998). This, too, will remain a question for future work.

2.4.3 NO production

It is also interesting to note the correlation between production of Nitric Oxide and peak temperature. Given the very large activation energy of this reaction, it would be expected that it would be sensitive to temperature. It also appears to be sensitive to the mass fraction of the Hydrogen radical.

2.4.4 Scatter plots

One important effect of the local extinction phenomenon is to cause considerable scatter in the scalar fields. This could pose considerable difficulty to moment closure methods such as CMC or CSE; conditional averages of most of the properties shown in Fig. 5 would fail to represent the wide scatter, and the mean reaction rates, which are highly sensitive non-linear functions of the scalar fields, would not be well represented by the first moment CMC closure hypothesis. Thus, local extinction phenomena, in particular their effect on scatter in the scalar fields, would likely necessitate either adding an additional conditioning variable to account for the physical process at the root of the scatter—such as the scalar dissipation—or the use of a second moment closure.

2.4.5 Favre averaged statistics

The Favre averages make clear the fact that the turbulent flow field is substantially influenced by the presence of the flame. This is true in the initial field as evidenced by the strong spatial dependence of the Taylor scale Reynolds number. It is also clear in the Kolmogorov length scale, which is almost constant across the layer in the initial field, but is almost five times greater in the middle of the layer, where the temperature peaks, than at the edges of the simulation after 90 time units. While the Kolmogorov length varies more across the layer as time progresses, the Reynolds number, dissipation length, and time all tend to become more evenly distributed.

The scalar dissipation and temperature plots (Figs. 9a and 9b) show how misleading mere Favre averages can be. In the scalar dissipation plot, the maximum mean scalar dissipation is almost one order of magnitude lower than the peak scalar dissipation seen in the visualizations (Figs. 2-4). If one were using a model that incorporated scalar dissipation into the prediction of reaction rates, such as CMC or laminar flamelets, one could conceivably under-predict the significance of extinction phenomena (which are clearly strongly dependent on scalar dissipation) by using only the mean scalar dissipation and neglecting fluctuations around that mean. The temperature plot shows an abrupt drop to around a 1500 K peak temperature, which is not evident in the visualizations. The drop in the Favre average of temperature appears to be primarily due to the out-of-plane folding across the layer. This highlights the difficulty in providing closure for the chemical source terms. One would grossly under-predict the reaction rates if one were to attempt to estimate these using the Favre averaged values directly.

2.4.6 Implications for modeling

The test of the validity of Conditional Moment Closure for the chemical source terms is encouraging. It would not be expected that single moment closure using only mixture fraction as a conditioning variable would give such agreement even in the presence of the extinction phenomena described above. Indeed, several modifications to the method have been proposed in order to improve closure for cases where extinction might occur. These include the addition of other conditioning variables (as in Bilger, 1991 and Bushe & Steiner, 1998) or the use of conditional

variances (as in Li & Bilger, 1993; Kronenburg *et al.*, 1998; Swaminathan & Bilger, 1998b).

While the closure appears to work well for two of the reactions, it appears to break down for the slower pollutant formation step. Since the activation energy of the Nitric Oxide formation reaction is very large, it is quite sensitive to variations in temperature. The considerable scatter in the temperature evident in Fig. 5b has a significant impact on this reaction. This indicates that a higher moment closure might be necessary although the potential to use scalar dissipation, with which variations in temperature appear to correlate strongly, as a second conditioning variable might improve closure as well.

3. Future work

Several issues remain to be addressed. A more detailed analysis of the affect of heat release on the flow field is needed so as to better describe the interaction of the flow with the chemical reactions. Further research into the edge flames present after extinction events will also be needed to attempt to establish the parameters which control whether or not triple flames form.

Ultimately, however, the purpose of the database was originally intended to be the validation of modeling, and it is this direction that attention will be focused in the near future. Already, the database has been used in *a priori* tests of models. Beyond the comparisons shown herewith, Cook and Bushe (1998) have used the database to test a new model for scalar dissipation for use in LES. The data is also being used to test the CSE approach in a RANS context. Model validation work is going to continue; in particular, *a priori* tests of the CSE approach for LES will be conducted and statistics relevant to second moment CMC closure will be extracted.

Acknowledgments

The authors wish to thank G. R. Ruetsch for providing the codes used in the development of this database. R. W. B. gratefully acknowledges the financial support of the Australian Research Council. The simulations were performed at the NAS facility of the NASA Ames Research Center.

REFERENCES

BILGER, R. W. 1980 Nonpremixed turbulent reacting flows. *Topics in Applied Physics.* **44,** Springer-Verlag, 65.

BILGER, R. W. 1991 Conditional moment methods for turbulent reacting flow using Crocco variable conditions. *Charles Kolling Laboratory Report,* Department of Mechanical Engineering, The University of Sydney, TN F-99

BILGER, R. W. 1993a Conditional moment closure for turbulent reacting flow. *Phys. Fluids A.* **5**(2), 436.

BILGER, R. W. 1993b Conditional moment closure modeling and advanced laser measurements. In *Turbulence and Molecular Processes in Combustion,* T. Takeno (Ed), Elsevier, 267.

BUSHE, W. K., BILGER, R. W. AND RUETSCH, G. R. 1997 Incorporating realistic chemistry into direct numerical simulations of turbulent non-premixed combustion. *Annual Research Briefs,* Center for Turbulence Research, NASA Ames/Stanford Univ., 195.

BUSHE, W. K. AND STEINER, H. 1998 Conditional Moment Closure for Large Eddy Simulation of non-premixed turbulent reacting flows. *CTR Manuscript 170,* Center for Turbulence Research, NASA Ames/Stanford Univ.

CHEN, J. H., MAHALINGAM, S., PURI, I. K. AND VERVISCH, L. 1992 Effect of finite-rate chemistry and unequal Schmidt numbers on turbulent non-premixed flames modeled with single-step chemistry. *Proceedings of the 1992 Summer Program,* Center for Turbulence Research, NASA Ames/Stanford University, 367.

CHEN, J. H. AND ECHEKKI, T. 1996 Unsteady strain rate and curvature effects in turbulent premixed methane-air flames. *Combust. & Flame.* **106,** 184.

COOK, A. AND BUSHE, W. K. 1998 A subgrid-scale model for the scalar dissipation rate in nonpremixed combustion. *Proceedings of the 1998 Summer Program,* Center for Turbulence Research, NASA Ames/Stanford University, *to appear.*

HINZE, J. O. 1975 *Turbulence,* McGraw-Hill.

KLIMENKO, A. Y. 1990 Multicomponent diffusion of various admixtures in turbulent flow. *Fluid Dynamics.* **25,** 327.

KRONENBURG, A., BILGER, R. W. AND KENT, J. H. 1998 Second order Conditional Moment Closure for turbulent jet diffusion flames. *Twenty-seventh Symposium (International) on Combustion, The Combustion Institute, Pittsburgh, PA (to appear).*

LELE, S. 1992 Compact finite difference schemes with spectral-like resolution. *J. Comp. Phys.* **103,** 16.

LI, J. D. AND BILGER, R. W. 1993 Measurement and prediction of the conditional variance in a turbulent reactive-scalar mixing layer. *Phys. Fluids A.* **5,** 12, 3255.

PETERS, N. 1984 Laminar diffusion flamelet models. *Prog. Energy Combust. Sci.* **10,** 319.

PITSCH, H., AND PETERS, N. 1998 A Consistent Flamelet Formulation for Non-Premixed Combustion Considering Differential Diffusion Effects. *Combust. & Flame.* **114,** 26.

POINSOT, T., AND LELE, S. 1992 Boundary conditions for direct simulations of compressible viscous flows. *J. Comp. Phys.* **101,** 104.

RUETSCH, G. R., AND MAXEY, M. R. 1991 Small-scale features of the vorticity and passive scalar fields in homogeneous isotropic turbulence. *Phys. Fluids.* **3,** 1587.

RUETSCH, G. R., VERVISCH, L., AND LIÑÁN, A. 1995 Effects of heat release on triple flames. *Phys. Fluids.* **7,** 1447.

SMITH, N. A. S. 1996 Conditional moment closure of mixing and reaction in turbulent nonpremixed combustion. *Annual Research Briefs,* Center for Turbulence Research, NASA Ames/Stanford Univ., 85.

SWAMINATHAN, N. AND BILGER, R. W. 1997 Direct numerical simulation of turbulent nonpremixed hydrocarbon reaction zones using a two-step reduced mechanism. *Comb. Sci. & Tech.* **127,** 167.

SWAMINATHAN, N. AND BILGER, R. W. 1998a Assessment of combustion submodels for turbulent nonpremixed hydrocarbon flames. *Combust. & Flame.* In press).

SWAMINATHAN, N. AND BILGER R. W. 1998b Conditional variance equation and its analysis. *Twenty-seventh Symposium (International) on Combustion, The Combustion Institute, Pittsburgh, PA (to appear).*

TENNEKES, H. AND LUMLEY, J. L. 1992 *A First Course in Turbulence,* MIT Press.

VERVISCH, L. 1992 Study and modeling of finite rate chemistry effects in turbulent non-premixed flames. *Annual Research Briefs,* Center for Turbulence Research, NASA Ames/Stanford Univ., 411.

VERVISCH, L. AND TROUVÉ, A. 1998 LES modeling for lifted turbulent jet flames. *Proceedings of the 1998 Summer Program,* Center for Turbulence Research, NASA Ames/Stanford Univ., (to appear).

WILLIAMS, F. A. 1991 Overview of asymptotics for methane flames, in *Reduced Kinetic Mechanism and Asymptotic Approximations for Methane-Air Flames,* Springer-Verlag, New York, 68.

LES of non-premixed turbulent reacting flows with Conditional Source term Estimation

By H. Steiner AND W. K. Bushe

1. Motivation and objectives

In the foreseeable future, Direct Numerical Simulation (DNS), a technique in which all flow scales are resolved, will remain computationally unaffordable for turbulent reacting flows at technically relevant high Reynolds numbers Thus, Large Eddy Simulation (LES), which resolves only the large scale motion of the flow while modeling the contribution of the small (subgrid) scales, has been recognized as a powerful alternative approach. The LES set of equations is obtained by applying a spatial filter to the governing transport equations of mass, momentum, and energy. Several subgrid-scale models for the filtered means of the unresolved turbulent transport of momentum and species have been developed. They range from the widely used constant-coefficient model of Smagorinsky (1963) to dynamic models where the model coefficients are computed as functions of the instantaneous flow field (Moin *et al.*, 1991; Germano *et al.*, 1991). These dynamic models, which have proven to be successful in many types of non-reacting flows, are well established tools in LES. In combusting flows, however, the subgrid-scale modeling of the chemistry is still a major challenge; our present study is focused on this issue.

In an LES of turbulent reactive flows, a spatial filter is applied to the governing set of differential conservation equations. Let

$$\widetilde{f} = \frac{\overline{\rho f}}{\overline{\rho}}$$

be the density weighted (or Favre) filtered representation of some quantity f. Then, the filtered transport equations for the mass fraction Y_I of some species I and enthalpy $\widetilde{h} = \overline{c}_p \widetilde{T}$ read

$$\frac{\partial \overline{\rho}\widetilde{Y}_I}{\partial t} + \frac{\partial \overline{\rho}\widetilde{u}_i\widetilde{Y}_I}{\partial x_i} = \frac{\partial}{\partial x_i}\left[\overline{\rho}\left(\widetilde{\mathcal{D}_l} + \widetilde{\mathcal{D}_t}\right)_I \frac{\partial \widetilde{Y}_I}{\partial x_i}\right] + \overline{\dot{\omega}}_I, \tag{1}$$

$$\frac{\partial \overline{\rho}\widetilde{h}}{\partial t} + \frac{\partial \overline{\rho}\widetilde{u}_i\widetilde{h}}{\partial x_i} = \frac{\partial}{\partial x_i}\left[\overline{\rho}\left(\widetilde{\kappa_l} + \widetilde{\kappa_t}\right)\frac{\partial \widetilde{T}}{\partial x_i}\right] + \sum_I (\overline{\dot{\omega}}_I h_{0_I}), \tag{2}$$

where $\overline{\rho}$ is the spatially filtered density and $\overline{\dot{\omega}}_I$ and h_{0_I} are the reactive source term and the enthalpy of formation of species I, respectively. The turbulent subgrid-scale fluxes

$$\overline{\rho}\left(\widetilde{u_i Y_I} - \widetilde{u_i}\widetilde{Y_I}\right) = \overline{\rho}\widetilde{\mathcal{D}_t}_I \frac{\partial \widetilde{Y}_I}{\partial x_i}$$

$$\overline{\rho}\left(\widetilde{u_i}\widetilde{h} - \widetilde{u_i h}\right) = \overline{\rho}\widetilde{\kappa}_t \frac{\partial \widetilde{T}}{\partial x_i}$$

have been modeled in terms of diffusive fluxes involving the corresponding eddy diffusivities $\widetilde{\mathcal{D}}_{tI}$ and $\widetilde{\kappa}_t$. Subgrid-scale models providing these quantities have already been mentioned above.

The main challenge faced in modeling combustion is that chemical reaction rates are usually highly non-linear functions of temperature, density, and species mass fractions. For a system with N possible species, the K-th chemical reaction can be written as

$$\sum_{J=1}^{N} \eta'_{JK} A_J \rightleftharpoons \sum_{J=1}^{N} \eta''_{JK} A_J,$$

where A_J is the chemical symbol for species J and η'_{JK} and η''_{JK} are the stoichiometric coefficients for species J in reaction K. If M chemical reactions are to be considered, then the chemical source term for species I becomes (Williams, 1985)

$$\dot{\omega}_I = W_I \sum_{K=1}^{M} (\eta''_{IK} - \eta'_{IK}) B_K T^{\gamma_K} e^{-\frac{E_K}{RT}} \prod_{J=1}^{N} \left(\frac{\rho Y_J}{W_J}\right)^{\eta'_{JK}}, \tag{3}$$

where W_I is the molecular mass of species I, T is the temperature, R is the universal ideal gas constant, E_K is the activation energy, and B_K is the frequency factor. The power of the pre-exponential term γ_K for reaction K accounts for non-exponential temperature dependence of the reaction rate. Due to the strong non-linearity of (3), substituting the filtered temperature, density, and mass fractions into (3), yielding

$$\overline{\dot{\omega}_I} \approx \dot{\omega}_I(\overline{\rho}, \widetilde{T}, \widetilde{Y_J}),$$

will generally provide a very poor estimate for the filtered reaction rates. It is evident that closure for the filtered chemical reaction rates has to be provided. In non-premixed combustion, where fuel and oxidizer are initially separated and must mix together before they react, several different approaches have been suggested:

Assuming Fast Chemistry circumvents the estimation of the chemical source terms. Under this assumption the thermodynamical state is completely determined as a function of the mixture fraction (Cook & Riley, 1994). However, effects like ignition and extinction, which may crucially affect many real flames, cannot be accounted for. Fast Chemistry also poorly predicts pollutants whose rates of formation are kinetically limited.

The Laminar Flamelet model (Peters, 1984; Cook *et al.*, 1997) assumes the flame structures to be thin in comparison to the turbulent eddies. Within the "laminar flamelet regime" the flame is considered to be comprised of an ensemble of strained laminar flames, which themselves merely depend on mixture fraction and scalar dissipation. Given the filtered means of these two quantities and assuming the shape of their joint probability density function, the filtered means of the mass fractions and temperature can be computed. There is still considerable argument on the

applicability of this method to flames outside the "flamelet regime". Furthermore, the chemistry is assumed to be in steady-state; for LES, this implies a quasi-steady-state assumption neglecting important transient effects on phenomena like ignition and extinction. In order to overcome this drawback, an unsteady Laminar Flamelet model has been devised for RANS of combusting flows (Peters, 1997). Thereby, an unsteady flamelet code is running simultaneously with the CFD code. Receiving the time dependent thermodynamic state and the scalar dissipation from the CFD code as inputs, the unsteady flamelet solution yields the actual chemical composition as a function of mixture fraction. Assuming the shape of the probability density function for the mixture fraction, the updated chemical composition vector in physical space can be computed and fed into the CFD code. Whether or not the unsteady Laminar Flamelet model can also be employed in LES has yet to be investigated. Unlike unsteady RANS, LES provides a time-accurate solution without periodicity in time. Thus, the number of unsteady flamelets to be tracked might increase continuously; in the long run, this could make the LES prohibitively expensive.

The PDF-Transport methods solve a transport equation for the Filtered Joint Probability Density Function of mass fractions, energy, etc. (Pope 1985; Givi, 1989; Colucci *et al.*, 1998). In the transport equation of the PDF, the chemical source terms occur in closed form; however, the dimensionality increases with the number of species, and the unclosed molecular mixing term has to be modeled. The closure problem for the chemical reaction term has apparently been commuted to the closure for the molecular mixing.

Recently, Bilger (1993a,1993b) and Klimenko (1990) independently proposed a new approach for modeling turbulent reacting flows, called Conditional Moment Closure (CMC). The CMC method solves for the transport equations of conditionally averaged quantities instead of their spatially filtered counterparts. Variables on which the chemical reactions are known to depend on are chosen to be the conditioning variables. Solving the transport equations also in conditioning space adds a further dimension to the problem which inhibits the application of CMC to three-dimensional flow simulations due to its high computational cost.

In the present study the Conditional Source term Estimation (CSE) method (Bushe & Steiner, 1998) has been proposed as an alternative to the aforementioned methods for closing the chemical source terms. CSE is based on the CMC hypothesis. However, unlike in traditional CMC methods, it is not necessary to solve the transport equations in the conditioning space; this makes the method computationally affordable. In its present form the proposed model is devised to provide the filtered means of the chemical source terms needed to close the LES set of equations in reacting flows. CSE has proven its predictive capability in an *a priori* test using DNS data of turbulent reacting mixing layer, and it is currently being tested in an LES of a turbulent jet diffusion flame.

2. Accomplishments

2.1 Conditional Source term Estimation (CSE)

CSE is based on the CMC closure hypothesis. In the CMC method proposed

by Klimenko (1990) and Bilger (1993a, 1993b), the transport equations are conditionally averaged, with the condition being some variable on which the chemical reaction rates are known to depend.

2.2.1 One condition

In non-premixed combustion far from extinction, the reaction rates mainly depend on mixture fraction. Thus, the mixture fraction is clearly an appropriate conditioning variable. In the context of non-premixed combustion, the mixture fraction represents the local fraction of mass originating from the feeding fuel stream. Thus, it is zero in pure oxidizer and one in pure fuel. In the following the conditional average of some quantity f, conditional on the mixture fraction Z having some value ζ, will be denoted by an overline:

$$\overline{f \mid Z} = \langle f \mid Z = \zeta \rangle.$$

The conditionally averaged reaction term occurring in the conditionally averaged transport equation for the mass fraction Y_I is closed with the first order CMC hypothesis: the conditional average of the chemical source term of some species I can be modeled by evaluating the chemical reaction rates using the conditional averages of the composition vector $\overline{Y_K \mid Z}$, temperature $\overline{T \mid Z}$, and density $\overline{\rho \mid Z}$. Thus,

$$\overline{\dot{\omega}_I(Y_K, T, \rho) \mid Z} \approx \dot{\omega}_I \left(\overline{Y_K \mid Z}, \overline{T \mid Z}, \overline{\rho \mid Z} \right). \tag{4}$$

It has been established that the CMC hypothesis, based on a single conditioning variable, provides adequate predictions of reaction rates for flames far from extinction (Bilger, 1993a; Smith 1994). The CSE method makes use of the CMC hypothesis (4); however, it suggests an alternative way to obtain the conditional averages. Rather than solving the conditionally averaged transport equations, which would be computationally expensive having the mixture fraction Z as additional dimension, it takes advantage of the spatial homogeneity of the conditional averages on particular surfaces in the reacting flow field. For example, in case of a reacting mixing layer, the conditionally averaged quantities show only small variation on planes normal to the reacting interface. Based on this spatial homogeneity the "extraction" process of the conditional averages might work as follows: For some set of $m = 1, ..., M$ cells in an LES domain which lie on the surface of homogeneity, the conditional average of the temperature is invariant in all m cells:

$$\left(\overline{T \mid Z} \right)_m = \overline{T \mid Z}. \tag{5}$$

The density weighted, filtered temperature in each cell m can be expressed as

$$\overline{T}_m = \int_0^1 P_m(Z)\, \overline{T \mid Z}\, dZ, \tag{6}$$

where $P_m(Z)$ is the probability density function of the mixture fraction within the filtered cell m. Eq. (6) is an integral equation—a Fredholm equation of the first

kind—which, for discrete intervals in Z, can be inverted to yield $\overline{T \mid Z}$. Similar equations can be written for the density and the mass fractions to obtain $\overline{\rho \mid Z}$ and $\overline{Y_K \mid Z}$, respectively . Even in the case of non-homogeneity, where (5) does not hold, the inversion of (6) would still yield an approximation for the conditional average of the temperature on the surface constituted by the ensemble of $m = 1, ..., M$ LES cells. The conditional average of the chemical source terms $\overline{\dot{\omega}_I \mid Z}$ can now be obtained using the CMC hypothesis (4), and the unconditional mean chemical source term is then

$$\overline{\dot{\omega}}_{I,m} = \int_0^1 P_m(Z)\ \overline{\dot{\omega}_I \mid Z}\ dZ. \tag{7}$$

In this manner, it should be possible to obtain closure for the sub-grid scale mean reaction rate for any chemical kinetic mechanism. No assumptions have been made regarding the thickness of the regions in which chemical reactions are significant relative to the turbulent length scales. Only the assumption of statistical homogeneity of the conditional averages of temperature, density, and pressure on some surface must be made. As for the probability density function $P_m(Z)$, a $\beta - PDF$ with the same mean $\overline{Z}_m$ and variance $\overline{Z_m''^2}$ of the mixture fraction has proven to approximate the real PDF appropriately (Bushe & Steiner, 1998). The mean of the mixture fraction $\overline{Z}_m$ is obtained as a resolved quantity of the LES. The filtered variance $\overline{Z_m''^2}$ can be estimated either through a subgrid-scale model, e.g., a Dynamic Model or using a similarity approach (Jiménez *et al.*, 1996), or by solving a transport equation for $\overline{Z_m''^2}$. The latter, however, requires modeling of the filtered scalar dissipation

$$\overline{\chi} = \overline{2\rho \nabla Z \nabla Z}. \tag{8}$$

2.2.1 Two conditions

It is known that conditioning only on mixture fraction is insufficient to account for phenomena such as extinction or ignition. Since the occurrence of these phenomena depends strongly on the scalar dissipation χ, defined in (8), it seems sensible to introduce scalar dissipation—or some closely related quantity—as the additional conditioning variable (Bushe, 1995). Assuming for the functional dependence of scalar dissipation on mixture fraction the shape of the laminar counter-flow solution (Peters, 1984), the scalar dissipation can be written as

$$\chi = \chi^* \cdot \exp\left(-2\left[\mathrm{erf}^{-1}(Z)\right]^2\right). \tag{9}$$

The sufficiently weak dependence of the new random variable χ^* on the mixture fraction Z allows expression of the joint probability density function $P(Z, \chi^*)$ as

$$P(Z, \chi^*) = P(Z)\, P(\chi^*),$$

where $P(Z)$ again can be approximated as a $\beta - PDF$. Analogously to the assumptions made for PDF of the scalar dissipation χ (Monin & Yaglom, 1975; Eswaran

& Pope, 1988; Yeung & Pope 1989), the probability density function of χ^* is taken to be approximately log-normal as well. In every LES cell m, $P_m(\chi^*)$ is determined in terms of the filtered mean $\overline{\chi^*}_m$ and the standard deviation. The first is provided by the relation

$$\overline{\chi}_m = \int_0^1 P_m(Z)\,\overline{\chi \mid Z} dZ = \overline{\chi^*}_m \int_0^1 P_m(Z) \cdot \exp\left(-2\left[\mathrm{erf}^{-1}(Z)\right]^2\right) dZ, \qquad (10)$$

and the latter is taken to be unity. The rhs of (10) involves again a $\beta - PDF$ for $P_m(Z)$ and the laminar counter-flow solution. The filtered mean of the scalar dissipation $\overline{\chi}_m$ has to be modeled.

The "extraction" process of the conditional averages is then straightforward. It is virtually the same as already described for one condition in the previous section. Inverting the expression

$$\overline{T}_m = \int_0^\infty \int_0^1 P_m(Z,\chi^*)\,\overline{T \mid Z,\chi^*}\; dZ\; d\chi^*, \qquad (11)$$

which is equivalent to (6) in the one-condition case, yields the conditionally averaged quantities needed for the CMC hypothesis now with two conditions:

$$\overline{\dot{\omega}_I \mid Z,\chi^*} \approx \dot{\omega}\left(\overline{Y_K \mid Z,\chi^*}, \overline{T \mid Z,\chi^*}, \overline{\rho \mid Z,\chi^*}\right). \qquad (12)$$

The mean chemical source term becomes

$$\overline{\dot{\omega}}_{I,m} = \int_0^\infty \int_0^1 P_m(Z,\chi^*)\;\overline{\dot{\omega}_I \mid Z,\chi^*}\; dZ\; d\chi^*. \qquad (13)$$

2.2.3 Effects of density weighted filtering

Dealing with non-constant density flows the LES set of transport equations (1)-(2) are solved for the Favre filtered averages of mass fractions and temperature. In this case the CSE equations have only to be adjusted to the density weighted LES inputs into the model, the closure hypothesis and the extraction process remain the same. In terms of density weighted averages (6) and (7) read

$$\widetilde{T}_m = \int_0^1 \widetilde{P}_m(Z)\,\overline{T \mid Z}\; dZ,$$

$$\overline{\dot{\omega}}_m = \overline{\rho}_m \int_0^1 \widetilde{P}_m(Z)\,\overline{\dot{\omega} \mid Z}\left(\overline{\rho \mid Z}\right)^{-1} dZ,$$

respectively, where $\widetilde{P}_m(Z) = P(Z;\widetilde{Z}_m,\widetilde{Z''^2_m})$ is the Favre PDF of the mixture fraction, which will again be approximated using the β-PDF. Its shape is now determined by the Favre filtered mean and variance of the mixture fraction $\widetilde{Z}_m$ and $\widetilde{Z''^2_m}$, respectively.

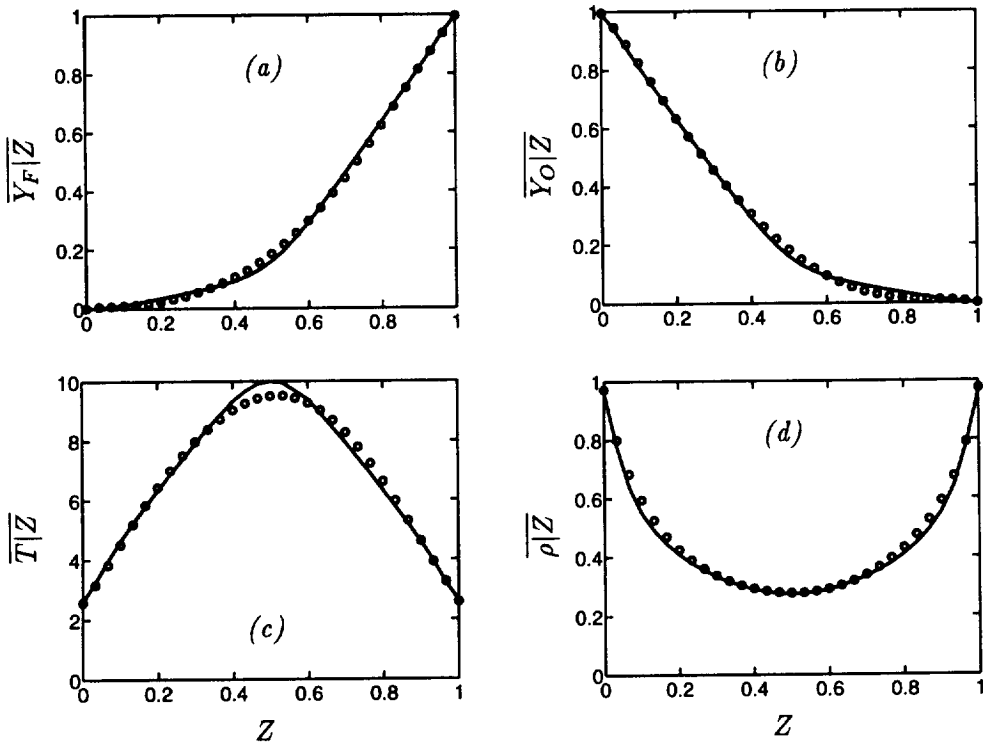

FIGURE 1. Result of *a priori* test of integral inversion process to obtain the conditional averages of: *(a)* mass fraction of fuel, *(b)* mass fraction of oxidizer, *(c)* non-dimensional temperature, *(d)* non-dimensional density; —— : result of inversion process, o : DNS value.

2.3 A priori test of the model

In order to test the method described above, the output from several different time steps in the DNS database of Vervisch (1992) was filtered. The simulation is of a shear-free, temporal mixing layer with fuel and oxidizer mixing in the presence of turbulence. The domain was rectangular with 128 points across the layer and 64 points in each direction tangential to the layer. A $(16 \times 8 \times 8)$−top-hat filter was used to compute the spatially filtered means on the LES grid.

The chemical kinetic mechanism used in creating the DNS database was a single step,

$$F + O \rightarrow P,$$

with F, O, and P being Fuel, Oxidizer, and Product, respectively. The reaction rate was

$$\dot{\omega} = Da\,\rho^2\,Y_F\,Y_O\,\exp\left(\frac{-\beta(1-\theta)}{1-\alpha(1-\theta)}\right),$$

with

$$\alpha = \frac{T_{\rm ad} - T_0}{T_{\rm ad}} = 0.8, \quad \beta = 8 \quad \text{and} \quad \theta = \frac{T - T_0}{T_0 - T_{\rm ad}}.$$

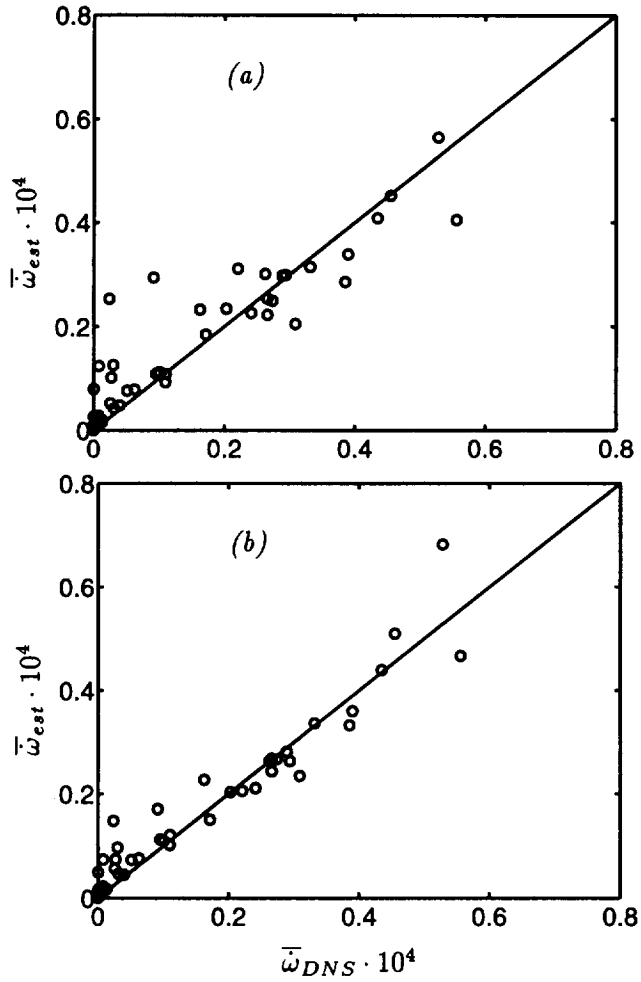

FIGURE 2. Comparison of reaction rate $\overline{\dot{\omega}}_{est}$ estimated using CSE closure to filtered reaction rate from DNS data $\overline{\dot{\omega}}_{DNS}$: *(a)* CSE with one conditioning variable Z, *(b)* CSE with two conditioning variables Z and χ^*.

All temperatures—including T_0 (the initial temperature) and $T_{\rm ad}$ (the adiabatic flame temperature at stoichiometric conditions)—were non-dimensionalized with the reference temperature $T_{\rm ref} = (\gamma - 1)T_0$, and γ, the ratio of specific heats, was taken to be 1.4. The Damköhler number Da was unity.

The first test was to try to use the quantities $\overline{Z}_m$ and $\overline{Z_m''^2}$ at each point to predict $P_m(Z)$ using the β–PDF as described above and then to substitute $\overline{\rho}_m$, $\overline{Y_F}_m$, $\overline{Y_O}_m$, and $\overline{T}_m$ and $P_m(Z)$ into (6) to predict the conditional averages. The results of this *a priori* test for one time in the simulation (a fairly late time, approximately 1.6 eddy turnover times in the simulation) are shown in Fig. 1, where the results of the inversion of the integral equation using a simple linear regularization method is compared to the actual conditional average from the entire flow field. With the

exception of a slight over-prediction of the maximum temperature, the prediction of the conditional averages appears to be very good. Similar results have been found for all other times at which data is available.

The next test is to invoke the CMC hypothesis (4) and use these conditional averages to predict the conditional mean reaction rate $\overline{\dot{\omega} \mid Z}$. Then, the unconditional mean reaction rate is predicted from the prediction of the conditional mean reaction rate using (7). The estimate $\overline{\dot{\omega}}_{est}$ obtained by this process is compared to the actual average of the reaction rate $\overline{\dot{\omega}}_{DNS}$ in every cell in Fig. 2a. The standard error in the prediction of the cells where $\overline{\dot{\omega}}_{DNS}$ is significant (greater than 1×10^{-5}) is about 15%. It should be noted that there is some extinction in the DNS database which cannot be predicted by the single condition version of this method. This is made evident by the presence of several points where $\overline{\dot{\omega}}_{DNS}$ is very small but $\overline{\dot{\omega}}_{est}$ is still significant. These are cells which contain local extinction events. Nevertheless, that the method is capable of predicting the reaction rates with such accuracy even in the presence of heat release and extinction seems to be very encouraging.

As was discussed above, adding a second condition to the inversion process is expected to make the method capable of modeling extinction and ignition phenomena. This was tested by simply adding the second condition and inverting the two-dimensional problem described by (11), using the conditional averages to estimate the conditional average of the reaction rate (12) and integrating (13). The result of this process is shown in Fig. 2b. The standard error in the prediction of the cells where $\overline{\dot{\omega}}_{DNS}$ is significant (again, greater than 1×10^{-5}) is about 10%. Not only is the error in the prediction somewhat smaller than was found with only one condition, the evidence of over-prediction of the reaction rate in cells containing extinction events is no longer apparent. It seems that the extinction phenomenon is captured at least to some extent by the inclusion of the second conditioning variable. Thus, even though the overall improvement of the prediction for the reaction rate at first sight seems to be rather small, the additional effort of carrying a second condition variable is still justified: it makes it possible to account for extinction and ignition phenomena.

Future plans

The CSE model is at present being tested in an LES of turbulent reacting jets. The code into which the subgrid-scale models have been introduced originally was written for DNS of non-reacting jets by Boersma (1998a). The first test considers a piloted jet diffusion flame at $Re = 4000$; for this basic test case one-step chemistry is assumed. Preliminary results of this LES showing temperature and fuel mass fraction contours when looking at the vertical jet from the side are presented in Fig. 3. Planes of equal distance downstream from the nozzle exit have been assumed as statistically homogeneous surfaces. The conditional averages have been computed using the LES filtered means gathered on these planes. The LES results obtained so far are going to be compared with the corresponding DNS data. These DNS data will be provided by a DNS performed by Boersma (1998b) for exactly the same test case. Further test cases will then consider experimentally investigated methane-air flames with high Reynolds numbers. The first case will deal with a piloted

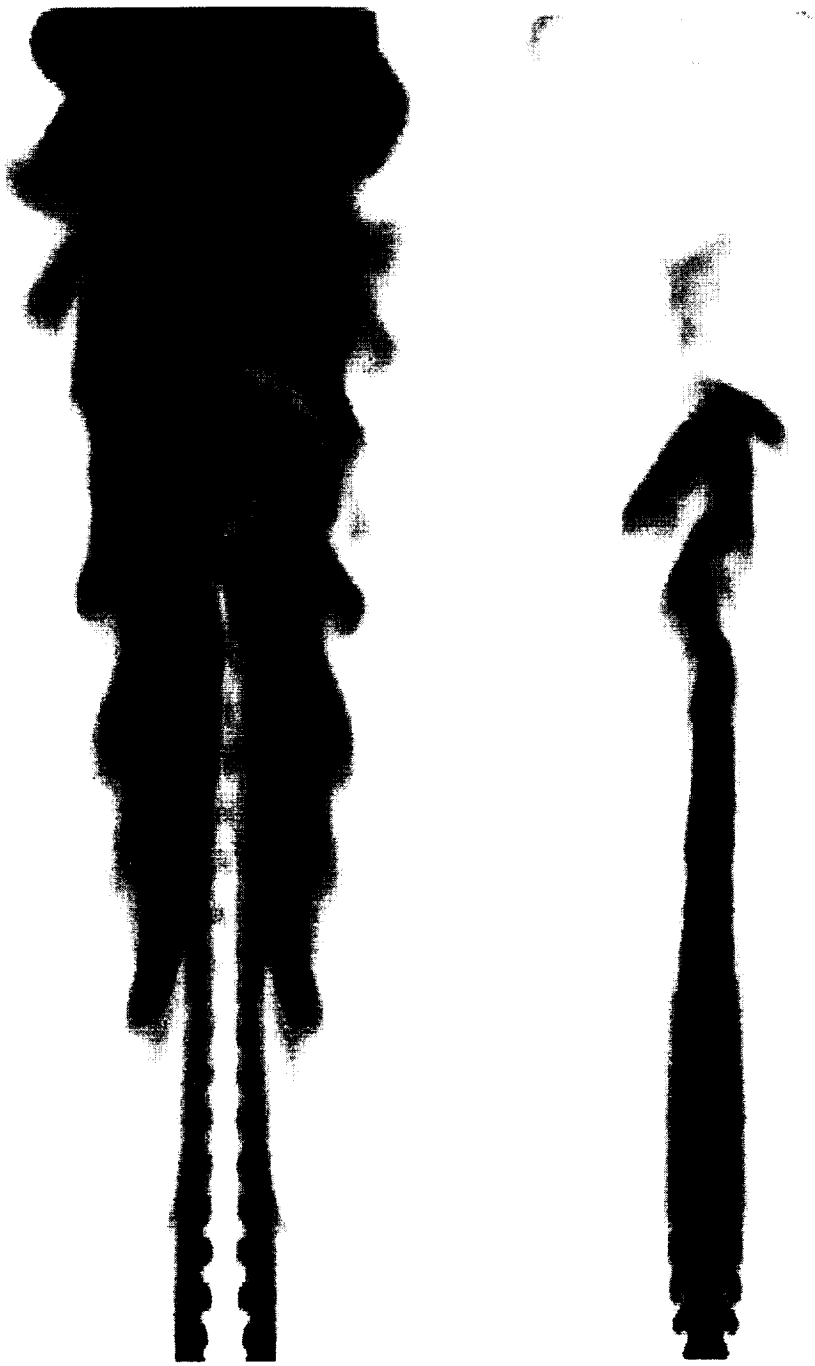

(a) (b)

FIGURE 3. Results of LES of piloted jet flame: *(a)* non-dimensional temperature: white-black, $T/T_0 = 1$ to 5; *(b)* mass fraction of fuel: white-black, $Y_F = 0$ to 1.

jet flame experiment performed in the Sandia Turbulent Diffusion Flame Facility (Masri *et al.*, 1988a,1988b). From these measurements extensive data on chemical composition and temperature fields are available. Then LES of a lifted methane-air jet (Muñiz & Mungal, 1997) will be attempted. There, the main challenge will be to capture ignition effects. Using a second conditioning variable, it is hoped that it will be possible to obtain a realistic prediction for the flame liftoff heights.

Acknowledgments

The authors wish to thank G. Kośaly, A. Kerstein, N. Peters, R. W. Bilger, and the staff at the Center for Turbulence Research for useful suggestions and discussions. H. S. gratefully acknowledges the financial support of the Fonds zur Förderung der Wissenschaftlichen Forschung of Austria.

REFERENCES

BOERSMA, B. J., BRETHOUWER, G. & NIEUWSTADT, F. T. M. 1998a A numerical investigation on the effect of the inflow conditions on the self-similar region of a round jet. *Phys. Fluids.* **10,** 899-909.

BOERSMA, B. J. 1998b Direct simulation of a jet diffusion flame. *Annual Research Briefs*, Center for Turbulence Research, NASA Ames/Stanford University.

BILGER, R. W. 1993 Conditional moment closure for turbulent reacting flow. *Phys. Fluids A.* **5,** 436-444.

BILGER, R. W. 1993 Conditional moment closure modeling and advanced laser measurements. in T. Tekeno, *Turbulence and Molecular Processes in Combustion.* Elsevier Science Publishers BV.

BUSHE, K. 1995 *Conditional Moment Closure Methods for Autoignition Problems. PhD thesis, Cambridge University, U.K.*

BUSHE, K. & STEINER, H. 1998 Conditional moment closure for large eddy simulation of non-premixed turbulent reacting flows. Submitted to *Phys. Fluids.*

COLUCCI, P. J., JABERI, F. A., GIVI, P. & POPE, S. B. 1998 Filtered density functions for large eddy simulation of turbulent reacting flows. *Phys. Fluids.* **10,** 499-515.

COOK, A. W. & RILEY, J. J. 1994 A subgrid model for equilibrium chemistry in turbulent flows. *Phys. Fluids.* **6,** 2868-2870.

COOK, A. W., RILEY, J. J. & KOSÁLY, G. 1997 A laminar flamelet approach to subgrid-scale chemistry in turbulent flows. *Combust. Flame.* **109,** 332-341.

ESWARAN, V. & POPE, S. B. 1988 Direct numerical simulations of turbulent mixing of a passive scalar. *Phys. Fluids.* **31,** 506-520.

GERMANO, M., PIOMELLI, U., MOIN, P. & CABOT, W. B. 1991 A dynamic subgrid-scale eddy viscosity model. *Phys. Fluids A.* **3,** 1760-1765.

GIVI, P. 1989 Model free simulations of turbulent reacting flows. *Prog. Energy Comb. Sci.* **15,** 1-107.

JIMÉNEZ, J., LIÑÁN, A., ROGERS, M. M. & HIGUERA, F. J. 1996 *A-priori* testing of subgrid-scale models for chemical reacting non-premixed turbulent shear flows. *Proceedings of the 1996 Summer Program.* Center for Turbulence Research, NASA Ames/Stanford University, 89-110.

KLIMENKO, A. YU. 1990 Multicomponent diffusion of various admixtures in turbulent flow. *Fluid Dynamics.* **25,** 327-334.

MASRI, A. R., BILGER, R. W. & DIBBLE, R. W. 1988a Turbulent nonpremixed flames of methane near extinction: mean structure from Raman measurements. *Combust. Flame.* **71,** 245-266.

MASRI, A. R., BILGER, R. W. & DIBBLE, R. W. 1988b Turbulent nonpremixed flames of methane near extinction: Probability Density Functions. *Combust. Flame.* **73,** 261-285.

MOIN, P., SQUIRES, K., CABOT, W. B. & LEE, S. 1991 A dynamic subgrid-scale model for compressible turbulence and scalar transport. *Phys. Fluids A.* **3,** 2746-2757.

MONIN, A. S. & YAGLOM, A. M. 1975 *Statistical Fluid Mechanics*, MIT Press, Cambridge.

MUÑIZ, L. & MUNGAL, M. G. 1997 Instantaneous flame-stabilization velocities in lifted jet diffusion flames. *Comb. Flame.* **111,** 16-31.

PETERS, N. 1984 Laminar diffusion flamelet models. *Prog. Energy Comb. Sci.* **10,** 319-339.

PETERS, N. 1997 Four lectures on turbulent combustion. ERCOFTAG Summer School, Institut für Technische Mechanik, RTWH Aachen, Germany.

POPE, S. B. 1985 PDF methods for turbulent reactive flows. *Prog. Energy Comb. Sci.* **11,** 119-192.

SMAGORINSKY, J. 1963 General circulation experiments with the primitive equations, I. The basic experiment. *Mon. Weather Rev.* **91,** 99-164.

SMITH, N. S. A. 1994 *Development of Conditional Moment Closure Method for Modelling Turbulent Combustion*, PhD thesis, Department of Mechanical & Mechatronic Engineering, University of Sydney, Sydney, Australia

VERVISCH, L. 1992 Study and modeling of finite rate chemistry effects in turbulent non-premixed flames. *Annual Research Briefs*, Center for Turbulence Research, NASA Ames/Stanford University, 411-429.

WILLIAMS, F. A. 1985 *Combustion Theory.* Benjamin Cummings, Menlo Park.

YEUNG, P. K., POPE, S. B. 1989 Lagrangian statistics from direct numerical simulations of isotropic turbulence. *J. Fluid Mech.* **207,** 531-586.

Measurements of the three-dimensional scalar dissipation rate in gas-phase planar turbulent jets

By L. K. Su

1. Motivation and objectives

The scalar dissipation rate, $\chi \equiv D\nabla C \cdot \nabla C$, where C is a conserved scalar and D is the scalar diffusivity, is a quantity which is of great interest to models of turbulent non-premixed combustion. Mathematically, it represents the loss term in the evolution equation for $\frac{1}{2}C^2$, the scalar energy:

$$\left(\frac{\partial}{\partial t} + \mathbf{u}\cdot\nabla - D\nabla^2\right)\frac{1}{2}C^2 = -D\nabla C\cdot\nabla C \equiv -\chi.$$

Physically, χ can be interpreted as a mixing rate, or equivalently as a rate at which scalar fluctuations are destroyed. More specifically for combustion applications, Peters (1983) identified χ as a characteristic diffusion time scale, imposed by the mixing field. Then, local flame extinction could be explained by the scalar dissipation rate exceeding a critical value, thus making the diffusion time smaller than the chemical time of the local flame structure. Accurate representation of flame quenching and stabilization poses notable difficulties for diffusion flame computations, because the scalar dissipation can occur at the finest mixing length scales of the flow. This means that modeling is required for the scalar dissipation in, for example, large-eddy simulations (LES) of turbulent combustion, where the filtered mixture fraction is used as a starting point to describe the combustion.

This study will address two issues regarding the properties of the scalar dissipation which are of particular significance in the context of combustion. The first concerns the length scales at which dissipation occurs, in particular their magnitude and their dependence on Reynolds number. The second issue concerns the scaling of the mean dissipation values with downstream distance in jet flows. Defining the thicknesses of the dissipation layers will be of use in determining the resolution requirements of both DNS and LES computations of turbulent diffusion flames. Meanwhile, experimental assessment of existing models for the downstream decay of mean dissipation will provide a fundamental test of our understanding of the properties of the dissipation rate.

The experimental data used in this study are the planar measurements of the complete, three-dimensional scalar dissipation rate by Su & Clemens (1998a,b) in the self-similar region of a gas-phase planar turbulent jet. The data are unique in providing scalar field information simultaneously in two parallel spatial planes, with sufficient resolution to permit differentiation in all three spatial dimensions. Determining the three spatial components explicitly obviates the need to invoke Taylor's hypothesis, while the planar nature of the measurement volume allows direct determination of structural properties of the dissipation field.

Previous planar measurements of the three-dimensional scalar dissipation at the smallest scales have been demonstrated in water flows (Southerland & Dahm (1994)). Some difficulties may arise, however, in applying scalar mixing results in the liquid phase to the gas phase, which is of particular interest in combustion applications. The Schmidt number ($Sc \equiv \nu/D$, where ν is the kinematic viscosity and D the molecular diffusivity) of water is approximately 2000, while in gas-phase flows $Sc \approx 1$. From Batchelor (1952), the ratio of the smallest length scales in the velocity and scalar gradient fields in turbulent mixing scales as $Sc^{-1/2}$. Thus, while in water flows scalar gradients can be sustained on scales roughly 45 times smaller than the smallest velocity gradient scales, in the gas phase these scales are expected to be of the same order. It is reasonable to expect that the details of scalar mixing in the high and low Schmidt number regimes will differ as a result. Results from analysis of the present gas-phase scalar dissipation data are expected to be directly applicable to mixing in combustion systems.

1.1 Expressions for the dissipation length scale

Some confusion arises in defining the dissipation length scale in turbulent flows because different expressions are used. Here we will define the scalar dissipation length scale as

$$\lambda_D = \Lambda \delta Re_\delta^{-3/4} Sc^{-1/2}, \tag{1}$$

where δ is the flow width, Re_δ is the Reynolds number based on δ and a measure of large-scale velocity, Sc is the Schmidt number, and the constant Λ is to be determined. More commonly, this dissipation scale is expressed in the form due to Kolmogorov and Batchelor. From dimensional arguments, Kolmogorov showed that the finest turbulence length scale, λ_K, should depend on the kinematic viscosity, ν, and mean kinetic energy dissipation rate, ϵ, as

$$\lambda_K \equiv (\nu^3/\epsilon)^{1/4}. \tag{2}$$

Subsequently, Batchelor introduced the equivalent expression for the scalar dissipation length scale,

$$\lambda_B \equiv \lambda_K \cdot Sc^{-1/2}.$$

The expressions for λ_D and λ_B are equivalent to within a constant factor. To show this, begin by expressing the mean kinetic energy dissipation as $\epsilon \propto U^3/\delta$, were U and δ respectively are measures of the large-scale velocity and flow width. In the self-similar region of a round jet, Friehe *et al.* (1971) found

$$\epsilon = 48 \frac{U_0^3}{d} \left(\frac{y}{d}\right)^{-4},$$

where y is the downstream coordinate, U_0 the initial jet velocity, and d the jet nozzle diameter. To convert to the large-scale variables U and δ, we use the relations $U/U_0 = 6.2\,(y/d)^{-1}$ and $\delta = 0.37\,y$ (e.g. Chen & Rodi (1980)), defining U as the jet

mean centerline velocity and δ as the jet full-width at the 5% points of the velocity profile. Then, Friehe's result becomes

$$\epsilon = 0.075 \left(\frac{U^3}{\delta} \right).$$

Though derived from results for the round jet, this result should be general to all turbulent shear flows, under the assumption that the small-scale behavior of fully developed turbulence is universal and is described by the parameters U and δ.

Inserting this result for ϵ into the definition for λ_B, and using $Re_\delta \equiv U\delta/\nu$, we obtain

$$\lambda_B = 0.075^{-1/4}\delta \left(\frac{\nu^3}{U^3\delta^3} \right)^{1/4} Sc^{-1/2} = 1.9\,\delta \cdot Re_\delta^{-3/4} Sc^{-1/2}. \tag{3}$$

Thus the Batchelor scale λ_B is equivalent to λ_D with a coefficient $\Lambda = 1.9$. The coefficient 1.9 appearing in these relations results from assuming a proportionality constant of 1 in the Kolmogorov/Batchelor scale definition. Since that definition is purely dimensional, there is no reason to expect that the proper proportionality constant should be 1. Empirical determination of the true value for Λ is discussed below (Section 2.2.1).

2. Accomplishments

2.1 Experimental conditions

This section presents a brief discussion of the experimental method. A comprehensive description can be found in Su & Clemens (1998a,b).

2.1.1 Flow field

The flow considered in these experiments is a planar, turbulent jet of propane issuing into a slow co-flow of air. The nozzle exit has a slot width $h = 1$ mm and spans 150 mm. This aspect ratio is sufficiently high that three-dimensional effects in the mean flow should be negligible in the flow region of interest, which extends to $127\,h$ downstream of the exit. The nozzle itself has a contraction ratio of 75 : 1 to provide a uniform exit velocity profile. Jet exit velocities ranged from 5.9 to 10.7 m/s, while the co-flow velocity was 0.3 m/s. For the planar jet, the jet exit Reynolds number is insufficient to describe the local turbulence because the centerline velocity decays as $y^{-1/2}$ (y is the downstream coordinate) while the jet grows linearly in y, so the local outer scale Reynolds number, Re_δ, grows as $y^{1/2}$. Here, Re_δ was determined using the scalings of Bradbury (1965) and Everitt & Robins (1978), namely

$$\delta_{0.05} = 0.39\,y \tag{4}$$

and

$$U/U_0 = 2.4\,(\rho_J/\rho_\infty)^{1/2}(y/h)^{-1/2},$$

and using the kinematic viscosity of air, $\nu = 0.155\,\mathrm{cm}^2/\mathrm{s}$. For the present measurements, consisting of a total of 906 image pairs, y ranged from 65 to $127\,h$, and Re_δ ranged from 3200 to 8400. The binary diffusivity of propane and air is $D = 0.114\,\mathrm{cm}^2/\mathrm{s}$, giving a Schmidt number of 1.36.

2.1.2 Laser diagnostics

Previous efforts at three-dimensional scalar field imaging in gas-phase flows have used either simultaneous two-plane Rayleigh scattering (Yip & Long (1986)), or multi-plane scattering or laser-induced fluorescence (LIF), in which a single laser sheet is swept through a three-dimensional volume (Yip *et al.* (1988)). The former measurements, however, showed somewhat weak signal levels, while the latter technique suffers from temporal resolution limitations introduced by the laser sheet scanning.

The current measurements were performed by simultaneous Rayleigh scattering and LIF in two planes. This approach eliminates temporal skewing effects, while the high efficiency of LIF yields much higher signal levels for a given amount of laser energy than two-plane Rayleigh scattering. In fact, only a single, frequency-doubled Nd:YAG laser was required. Propane was chosen for the jet fluid because its high index of refraction results in a Rayleigh scattering cross-section over 13 times that of air. For the LIF, acetone was seeded into the jet fluid to approximately 5% by volume. The 532 nm output of the laser was split so that 75% was used for the Rayleigh scattering, while the remainder was further doubled to 266 nm to excite the LIF. The resulting laser sheet energies were typically 240 mJ/pulse at 532 nm and 30 mJ/pulse at 266 nm. To capture the signals, two slow-scan, thermoelectrically cooled CCD cameras, with 500 × 500 pixel resolution, were used. Optical filters ensured separation of the LIF signal (which peaks in the range 400-500 nm) from the 532 nm Rayleigh scattering signal. To obtain the scalar concentrations from the raw imaging signals, standard background and sheet intensity profile corrections were performed. For additional accuracy, however, the intensity profiles for the two sheets were captured for individual pulses rather than on an average basis.

In computing the three components $\partial C/\partial x_i$ of the scalar gradient vector, the out-of-plane component (here, $\partial C/\partial z$) will be subject to the highest uncertainties, owing to the need to perform the difference calculation across distinct planes, which were obtained by different techniques and processed independently. To quantify the errors incurred, Su & Clemens (1998a,b) applied the two-plane technique to a single spatial plane, for which the scalar fields measured in the two imaging planes should be equal. Deviations from this were used to estimate the errors in the three-dimensional measurements. It was found that errors in the $\partial C/\partial z$ term were substantially smaller than the magnitudes of $\partial C/\partial z$ corresponding to significant events in the dissipation fields.

2.1.3 Spatial resolution

To increase signal levels, the scalar field images were binned 2 × 2; in the data reduction process it was also necessary to match the fields of view of the two cameras geometrically, with the resulting pixel resolution being 220 × 220. This measurement area spanned 34 jet widths, h, per side, giving a grid resolution $\Delta x = \Delta y$ of roughly 150 μm. The 266 nm laser sheet showed a Gaussian cross-sectional profile, with a full width at the 5% points of 200 μm at its waist, while the 532 nm laser sheet showed a roughly uniform profile with a full width of 180 μm. The laser sheet spacing Δz was 200 μm. These parameters are to be compared with the estimated finest

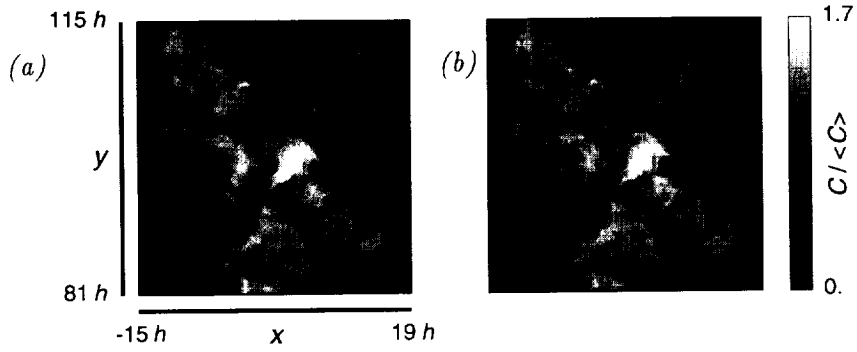

FIGURE 1. Scalar fields measured by *(a)* PLIF and *(b)* Rayleigh scattering, with a laser sheet separation of 200 μm. The mean flow direction is upward in the images. The Reynolds number, Re_δ, evolves from 5100 to 6200 in the measurement area.

dissipation length scale λ_D (Eq. 1), here computed using $\Lambda = 11.2$ as suggested by Buch & Dahm (1991). For these measurements the downstream coordinate y spanned from 65 to 127 h, and the Reynolds number Re_δ ranged from 3200 to 8400. The resulting λ_D ranged from 370 μm to 720 μm. Therefore $0.21 < \Delta x/\lambda_D < 0.41$ and $0.28 < \Delta z/\lambda_D < 0.54$, where these non-dimensional grid spacings should be 0.5 or less to satisfy the Nyquist resolution criterion.

2.2 Results

A scalar field image pair obtained by this simultaneous Rayleigh/LIF technique is shown in Fig. 1. The mean flow is upward in the images, so the positive y direction is streamwise, while the x direction is cross-span and the z (out-of-plane) direction is spanwise relative to the mean flow. In these fields C is normalized by $< C >$, the mean centerline concentration value for the full set of 906 image pairs.

Figure 2a shows the scalar dissipation for the scalar field of Fig. 1. The in-plane derivative components were determined from the LIF image (Fig. 1a) by two-point central differencing, and the out-of-plane component was found by simple differencing between the LIF and Rayleigh images. The dissipation shown in the figure is non-dimensional, with the scalar values being normalized by $< C >$, and the Δx_i used in the differencing being normalized by λ_D (Eq. 1), with $\Lambda = 11.2$. Figure 2*b* shows the dissipation layer centers for dissipation field of Fig. 2a. The layer center field was compiled by first identifying peaks in the dissipation field. A given point was determined to be a 'peak' if it both exceeded a given threshold, and represented the local maximum of dissipation in both its positive and negative in-plane scalar gradient directions. A connectivity condition was then imposed on the peak field to remove noise effects. For Fig. 2a, the threshold value was that which captures 50% of the total dissipation for the full data set (non-dimensional $\chi = 0.058$), and the connectivity condition required that the dissipation structures span a minimum length of twice λ_D.

The probability distribution of the logarithm of the dissipation is shown in Fig. 3. Also shown is a Gaussian distribution having the same first two moments. The

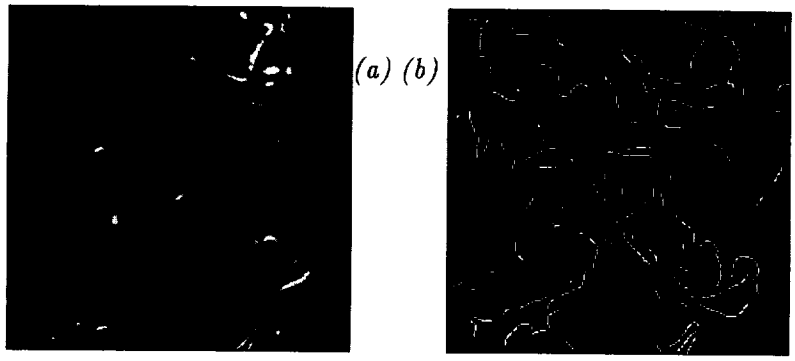

FIGURE 2. *(a)* The non-dimensional scalar dissipation for the scalar fields of Fig. 1. *(b)* The layer centers.

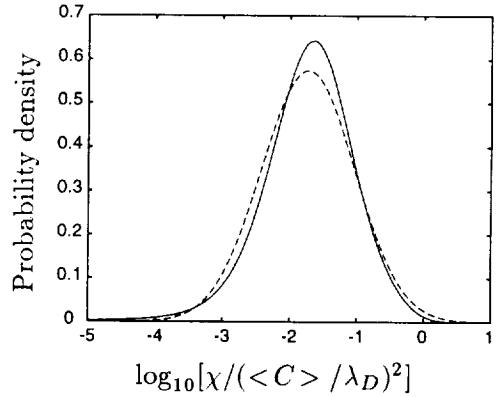

FIGURE 3. Distribution of the logarithm of the non-dimensional scalar dissipation. Current data, ——— ; Gaussian (with same first two moments), ---- .

measured distribution follows the Gaussian quite closely, except for a slight negative skewness. Similar asymmetry has been observed in both experiments (Feikema et al. (1996)) and direct numerical simulations (Eswaran & Pope (1988)) of scalar mixing, and has also been seen in the kinetic energy dissipation in DNS (Vincent & Meneguzzi (1991)).

2.2.1 Length scales

It is generally accepted that the scalar dissipation field is organized into layers; the thickness of these layers will scale with the local outer scale Reynolds number, Re_δ, in a manner dependent on the strain field on the layers. Where the strain field is the inner scale strain the normalized layer thickness, λ_D/δ, scales as $Re_\delta^{-3/4}$ (Batchelor/Kolmogorov scaling), while if the strain field were the outer scale strain the thickness would scale as $Re_\delta^{-1/2}$ (Taylor scaling). The traditional view (e.g. Tennekes & Lumley (1972)) holds that the bulk of the scalar dissipation occurs at the Batchelor scale, though Dowling (1991), based on time-resolved single point scalar

field measurements, has suggested that the regions of highest dissipation observe Taylor scaling. Nevertheless, Dowling (1991) found that the smallest dissipation scales observe Batchelor scaling.

Numerous studies have attempted to find the value of the constant Λ in Eq. 1 which accurately defines the size of the smallest dissipation scales. These efforts have generally proceeded by analysis of single-point scalar or velocity time series data. The difficulties of this approach can be seen by noting that Dowling & Dimotakis (1990) found $\Lambda \approx 25$ from spectra of scalar concentration fluctuations, while, using the same scalar time series data set, Dowling (1991) subsequently obtained $\Lambda \approx 5$ from scalar dissipation rate estimates. In contrast, Buch & Dahm (1991) determined $\Lambda = 11.2$ from explicit measurement of the average thicknesses of dissipation structures in two-dimensional scalar field images. This latter approach is taken here.

Consistent with Buch & Dahm (1991), we define λ_D from Eq. 1 as the average of the full widths of the dissipation layers, where this width is computed as the distance across a layer between those points where the dissipation is 20% of the maximum. As a first step in computing the layer thicknesses, the layer center fields for the images were found, as described in Sec. 2.2 and shown in Fig. 2b. For each of the points on these layer centers, a search was then performed in the scalar gradient direction (both positive and negative) until the dissipation value dropped to 20% of the maximum. The resulting layer half width values were then doubled to give a measure of the full width. Statistics were not compiled for those layers where the dissipation failed to drop monotonically, indicating a possible intersection of layers. Finally, because the dissipation images, and thus the thickness computations, are strictly two-dimensional, the resulting thicknesses were adjusted by a factor of $\cos\phi$, where ϕ is the out-of-plane angle of ∇C.

Figure 4 shows the distribution of layer thicknesses, expressed in terms of Λ, as determined from Eq. 1. The threshold and connectivity conditions used for the layer center determination were the same as those used to compute the layer center field of Fig. 2b. To minimize the effect of the $\cos\phi$ correction, only dissipation maxima where $\phi \leq 60°$ were considered. The mean of the distribution is $\Lambda = 14.8$, indicating the the layers in these data are somewhat thicker than predicted by Buch & Dahm (1991), and are over seven times larger than the Batchelor scale determined using a proportionality constant of 1 in the Kolmogorov scale definition (Eqs. 2, 3).

In Fig. 5, the dependence of λ_D on the local outer scale Reynolds number Re_δ is shown. The curve was compiled by dividing the Reynolds number range 3200 to 8400 into 26 bins, then computing the thicknesses for each bin as above, with the same threshold and connectivity conditions. The curve thus represents the average layer thickness for the given Re_δ. The dashed line in the plot is the curve $14.5 \cdot Re_\delta^{-3/4}$. The actual least-squares fit gives a Reynolds number dependence of $Re_\delta^{-.74}$. From this plot it is quite evident that the *average* layer thicknesses observe the $Re_\delta^{-3/4}$ Batchelor scaling. (The constant $\Lambda = 14.5$ differs slightly from that found from the curve of Fig. 4 because the data are not evenly distributed in Re_δ space.)

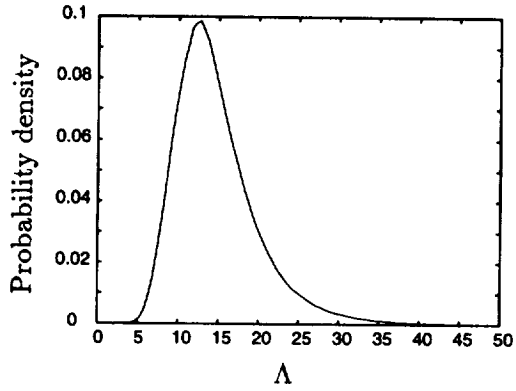

FIGURE 4. Distribution of dissipation layer thicknesses, expressed in terms of Λ.

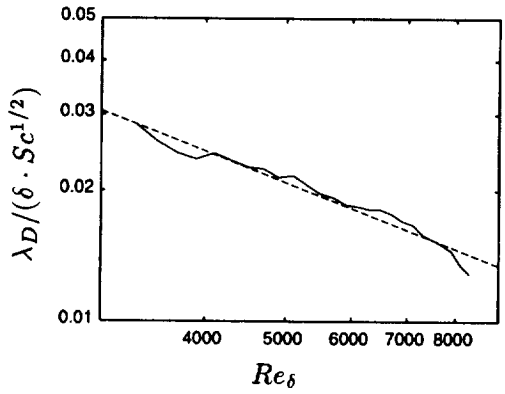

FIGURE 5. Average layer thickness conditioned on local outer scale Reynolds number. Current data, ——— ; $14.5 \cdot Re_\delta^{-3/4}$, - - - - .

However, Dowling (1991) concluded that while the majority of the dissipation occurred at scales which followed Batchelor scaling, a substantial portion of the dissipation, in particular the highest local dissipation values, occurred at the larger Taylor scales. With the present data this can be assessed by considering the Reynolds number dependence of the extremes of the thickness distribution. Figure 6 shows the Re_δ dependence of the average thickness of the thickest and thinnest 25% of layers, together with the overall average as shown in Fig. 5. There is no evidence of Taylor scaling of the thickest layers. The least-squares fit to the thickness curve for the thickest 25% of the layers has dependence $Re_\delta^{-.73}$, while the curve for the thinnest 25% has dependence $Re_\delta^{-.75}$. The trend of weaker Re_δ dependence for thicker layers is consistent with Dowling's hypothesis, but this very slight difference of $Re_\delta^{-.73}$ versus $Re_\delta^{-.75}$ is likely within experimental tolerances, and certainly gives no indication of $Re_\delta^{-1/2}$ scaling.

Figure 7 shows the dependence of Λ on the threshold value of the dissipation rate. Again, in contradiction to the idea that high dissipation values take place on length

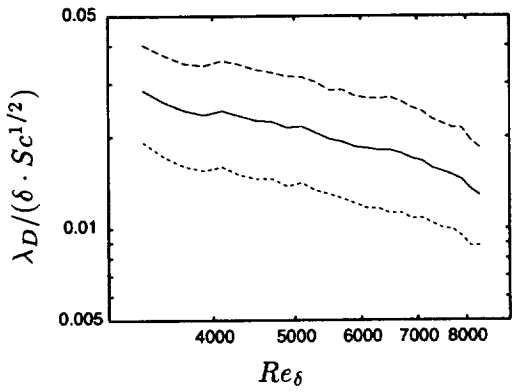

FIGURE 6. Layer thickness conditioned on Re_δ. Average thickness of all layers, ——— ; average of thickest 25% of layers, ---- ; average of thinnest 25%, ····· .

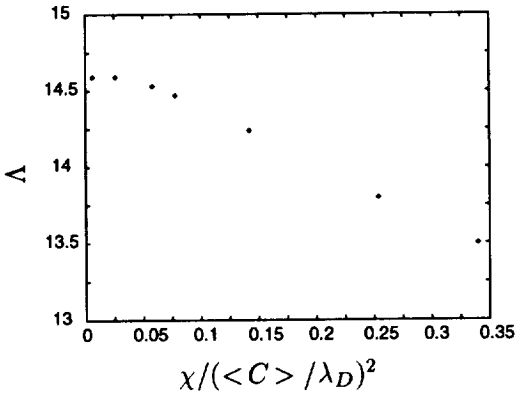

FIGURE 7. Dependence of the coefficient Λ on the threshold value of the dissipation rate.

scales observing Taylor scaling, it can be seen that higher values of χ are associated with *thinner* layers.

2.2.2 Dissipation rate scaling

The scaling of mean scalar dissipation rates with downstream distance in turbulent jets is of interest in certain models of the stabilization properties of turbulent jet diffusion flames. Peters & Williams (1983) suggest that the mean scalar dissipation rate should scale linearly with the global strain rate, with the square of the local mean centerline scalar concentration, and with the inverse square of the local jet width. For the planar turbulent jet, we thus expect $\chi \propto (U_0/h)(y/h)^{-3}$. The few existing measurements for the downstream dependence of the mean dissipation fail to observe the expected scalings, however. In round jets, both Lockwood & Moneib (1980) and Effelsberg & Peters (1988) found that the decay of χ in the self-similar region was significantly weaker than the predicted $(y/d)^{-4}$ dependence.

The present measurements span from 65 to 127 jet widths downstream, and

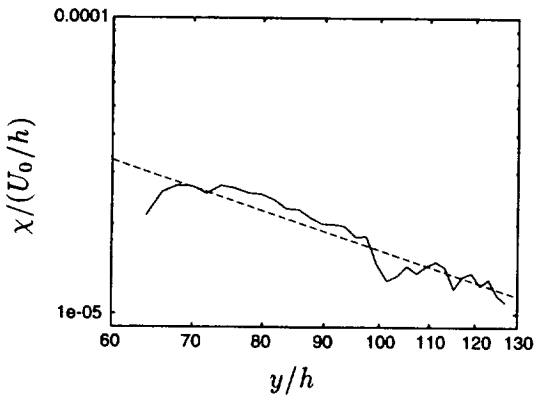

FIGURE 8. Downstream decay of scalar dissipation rate, normalized by global strain rate. Current data, ——— ; best fit, $y^{-1.4}$, ---- .

so can provide useful information on the decay of the dissipation rate. However, because the present measurements were intended primarily for investigation of the structure of the scalar dissipation rate field, no direct effort was made to correlate the measured scalar concentrations to the initial jet value. We account for the scalar decay here by assuming that the recommended scaling from Chen & Rodi (1980) applies, namely

$$< C(y) > /C_0 = 2.46\,(y/h)^{-1/2},$$

where $< C(y) >$ and C_0 are the local mean centerline concentration and initial jet concentration, respectively, and the effect of the jet and ambient fluid density difference has been included. For each data set of 15 or 30 image pairs, the centerline average is found, the effective C_0 value is computed from the above formula, and this C_0 is then used to normalize the scalar field values for the purpose of compiling the dimensional dissipation rate χ.

Figure 8 shows the conditional average of $\chi/(U_0/h)$ with downstream distance, for off-center positions $|x|/\delta \leq 0.05$, i.e. near the centerline. The dissipation rate χ is computed here as $\chi = D\,(\partial C/\partial x_i)(\partial C/\partial x_i)$, where D is the propane-air diffusivity, 0.114 cm^2/s, C is the scalar concentration normalized by C_0, and the x_i are dimensional. The global strain rate U_0/h has been divided from χ to isolate the dependence of the decay on (y/h). The dotted line is the best linear fit to the data, which has a slope of -1.4. Consistent with previous results, the data predict a much slower decay than anticipated by the theory of Peters & Williams (1983). It should be pointed out that for both planar and round jets, the fine scales increase in size with downstream distance, and thus resolution requirements are relaxed as the measurement area moves away from the nozzle. It is therefore possible that the decay rates are underestimated because high dissipation rates are more accurately measured further downstream. For the present measurements, however, the relative resolution differs at most by a factor of two between the $y = 65\,h$ and $y = 127\,h$ locations. Considering only these two locations, a dependence of χ on y^{-3} would require that χ decay by a factor of 7.5 from $y = 65\,h$ to $127\,h$, while the measured

$y^{-1.4}$ dependence corresponds to a χ decay factor of 2.5. From the evidence of existing measurements which assess the effects of varying resolution (e.g. Dowling (1991), Antonia & Mi (1993)), this factor of three discrepancy cannot be accounted for by the resolution difference between near and far downstream positions. Rather it appears, based on these limited results, that the current understanding of the scaling of dissipation rates is quite incomplete.

3. Future plans

While this paper has focused on the fine scales of the mixing field, the data are also well suited to analysis of larger scale properties and, perhaps more significantly, to analysis of the interactions of the large and small scales. At the upstream limit of the measurement domain, $y = 65\,h$, the jet width (Eq. 4) is $\delta \approx 25\,h$, while at the downstream limit, $y = 127\,h$, we find that the jet width is $\delta \approx 50\,h$. Since each imaging plane spans $34\,h$, each scalar field image covers a range of scales from the finest mixing scale to in excess of $0.68\,\delta$. It is therefore possible, for example, to investigate scale similarity over the full range of flow length scales. As pointed out by Frederiksen *et al.* (1996), information on the full three-dimensional dissipation rate is necessary to assess the true scale similarity of the mixing process. Direct, *a priori* assessments of subgrid models for LES can also be performed, by filtering the scalar and scalar dissipation results and comparing the model predictions based on these filtered quantities with the actual values on the original, resolved measurement grid. Similar tests have been demonstrated both on DNS data for $Sc = 1$ mixing, and on experimental liquid-phase mixing results (Cook & Riley (1994)).

REFERENCES

ANTONIA, R. A. & MI, J. 1993 Temperature dissipation in a turbulent round jet. *J. Fluid Mech.* **280,** 179-197.

BATCHELOR, G. K. 1952 The effect of homogeneous turbulence on material lines and surfaces. *Proc. Roy. Sci. London A.* **213,** 349-366.

BRADBURY, L. J. S. 1965 The structure of a self-preserving turbulent plane jet. *J. Fluid Mech.* **23,** 31-64.

BUCH, K. A. & DAHM, W. J. A. 1991 Fine scale structure of conserved scalar mixing in turbulent shear flows: $Sc \gg 1$, $Sc \approx 1$ and implications for reacting flows. *Report 026779-5,* University of Michigan.

CHEN, C. J. & RODI, W. 1980 *Vertical Turbulent Buoyant Jets: A Review of Experimental Data.* Pergamon.

COOK, A. W. & RILEY, J. J. 1994 A subgrid model for equilibrium chemistry in turbulent flows. *Phys. Fluids* **6**, 2868-2870.

DOWLING, D. R. 1991 The estimated scalar dissipation rate in gas-phase turbulent jets. *Phys. Fluids A* **3**, 2229-2246.

DOWLING, D. R. & DIMOTAKIS, P. E. 1990 Similarity of the concentration field of gas-phase turbulent jets. *J. Fluid Mech.* **218,** 109-141.

EFFELSBERG, E. & PETERS, N. 1988 Scalar dissipation rates in turbulent jets and jet diffusion flames. In *Proc. Twenty-Second Symp. (Int'l) on Combustion*, 693-700.

ESWARAN, V. & POPE, S. B. 1988 Direct numerical simulations of the turbulent mixing of a passive scalar. *Phys. Fluids* **31**, 506-520.

EVERITT, K. W. & ROBINS, A. G. 1978 The development and structure of turbulent plane jets. *J. Fluid Mech.* **88**, 563-583.

FEIKEMA, D. A., EVEREST, D. & DRISCOLL, J. F. 1996 Images of dissipation layers to quantify mixing within a turbulent jet. *AIAA J.* **34**, 2531-2538.

FREDERIKSEN, R. D., DAHM, W. J. A. & DOWLING, D. R. 1996 Experimental assessment of fractal scale similarity in turbulent flows. Part I: One-dimensional intersections. *J. Fluid Mech.* **327**, 35-72.

FRIEHE, C. A., VAN ATTA, C. W. & GIBSON, C. H. 1971 Jet turbulence: dissipation rate measurements and correlations. In *AGARD Turbulent Shear Flows*, **CP-93**, 18-1-18-7.

LOCKWOOD, F. & MONEIB, H. 1980 Fluctuating temperature measurements in a heated round free jet. *Comb. Sci. Tech.* **22**, 63-81.

NAMAZIAN, M., SCHEFER, R. W. & KELLY, J. 1988 Scalar dissipation measurements in the developing region of a jet. *Comb. Flame* **74**, 147-160.

PAUL, P., VAN CRUYNINGEN, I., HANSON, R. K. & KYCHAKOFF, G. 1990 High resolution digital flowfield imaging of jets. *Exp. Fluids* **9**, 241-250.

PETERS, N. 1983 Local quenching due to flame stretch and non-premixed turbulent combustion. *Comb. Sci. Tech.* **30**, 1-17.

PETERS, N. & WILLIAMS, F. A. 1983 Liftoff characteristics of turbulent jet diffusion flames. *AIAA J.* **21**, 423-429.

SOUTHERLAND, K. B. & DAHM, W. J. A. 1994 A four-dimensional experimental study of conserved scalar mixing in turbulent flows. *Report 026779-12,* University of Michigan.

SU, L. K. & CLEMENS, N. T. 1998a The structure of the three-dimensional scalar gradient in gas-phase turbulent jets. *AIAA Paper 98-0429.*

SU, L. K. & CLEMENS, N. T. 1998b Planar measurements of the full three-dimensional scalar dissipation rate in gas-phase turbulent flows. Submitted to *Exp. Fluids.*

TENNEKES, H. & LUMLEY, J. L. 1972 *A First Course in Turbulence.* MIT Press.

VINCENT, A. & MENEGUZZI, M. 1991 The spatial structure and statistical properties of homogeneous turbulence. *J. Fluid Mech.* **225**, 1-20.

YIP, B. & LONG, M. B. 1986 Instantaneous planar measurement of the complete three-dimensional scalar gradient in a turbulent jet. *Opt. Lett.* **11**, 64-66.

YIP, B., SCHMITT, R. L. & LONG, M. B. 1988 Instantaneous three-dimensional concentration measurements in turbulent jets and flames. *Opt. Lett.* **13**, 96-98.

Direct simulation of a jet diffusion flame

By B. J. Boersma

1. Motivation and objective

The main energy source in the Western world is the combustion of fossil fuels, and it will remain to be the major energy source for at least several decades to come. Everybody is aware of the problems connected to the combustion of these fuels. First, their supply is finite, and this means that they should be used economically. Second, during combustion of fossil fuels, air pollution is generated, e.g., in the form of toxic gases such as NO_x or SO_2 but also in the form of gases harmless for man such as CO_2, which are nevertheless considered harmful because they may influence our climate by processes such as the greenhouse effect. In view of these problems, it will be clear that combustion of fossil fuels with an optimal fuel efficiency and with a minimal production of pollutants must have a high priority.

The process of combustion is highly complex. It involves fluid mechanical processes such as turbulent mixing and heat transfer but also other processes such as radiation and chemistry. The fact that the combustion involves these very different processes makes it not only a highly multidisciplinary topic for research, but also a highly challenging one. For this reason the scientific problem of combustion has been nominated as one of the "Grand Challenges"to be solved when a Tera-flops computer becomes available, and this is the background of the project that we propose here.

In this project we aim to perform a numerical simulation of a non-premixed turbulent diffusion flame. The objective is to shed light on one of the important processes in combustion that have been mentioned above, namely turbulent mixing, which is an essential link in the modeling of combustion. In the past researchers and designers have used so-called Reynolds-averaged turbulence models to predict the combustion in various appliances. However, these models have their weaknesses, especially in the complicated environment of a flame, and they have, in general, failed to produce acceptable results. A factor contributing to this failure has been the fact that it is very difficult to perform measurements in the hostile environment of a combustion flame, and such measurements are needed for validating and developing turbulence models. Therefore, the problem of turbulent mixing within the combustion process is to be considered as unsolved.

Recently, new methods have become available for combustion research as a result of increasing computer power (especially due to the appearance of parallel computers). Two very powerful new methods are direct numerical simulation (DNS) and large eddy simulation (LES). The first technique (DNS) solves the governing equations for the combustion without any model. In the second method, a model is used for the small scales of motion. The first method is computationally very expensive but gives in general very reliable results. The second method (LES) is

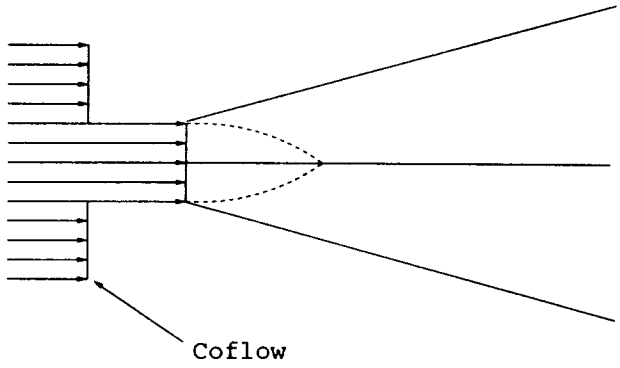

FIGURE 1. The geometry of the coflowing jet.

much cheaper, but the modeling of the small scales introduces an error. In this paper we will use DNS; there is also LES and experimental work going on for the same problem (see e.g. Steiner, and Su this volume).

1.2 The geometry

In Fig. 1 we show the geometry of the problem. The jet fluid (in general fuel) is injected in a slower flowing air (oxidizer) stream. In the experiment the Reynolds number based on the jet fluid is approximately between 5,000 and 50,000. The coflow velocity is typically 1 to 5% of the jet velocity.

For the DNS we will use a very simple binary reaction:

$$[Fuel] + [Oxidizer] \rightarrow 2[Prod]$$

The factor 2 is included to conserve mole fractions. The reaction rate of this reaction is given by

$$\dot{\omega} = Da\rho Y_f \rho Y_o \exp[-\hat{\Theta}]. \tag{1}$$

In which Da is the Dahmköhler number, ρ is the density, Y_f the fuel mass fraction, Y_o the oxidizer mass fraction, and

$$\hat{\Theta} = \beta \frac{1-\theta}{1-\alpha(1-\theta)}. \tag{2}$$

In which α is the heat release parameter and β the Zeldovich number. The non dimensional temperature θ is defined as $\theta = (T - T_o)/(T_a - T_o)$ with T_a as adiabatic flame temperature and T_o as room temperature.

2. Low Mach number approximation

There are basically two ways to compute chemically reacting flows with significant heat-release. The first option is to use a fully compressible flow solver (including acoustic waves). The second one is to use an incompressible solver with variable

density. The second method is very attractive for flows with low Mach numbers because numerical time steps are not related to the speed of sound. Furthermore, the formulation of the boundary conditions is much simpler than in the fully compressible case.

The low Mach number approximation of the equations of motion can be found in the literature (see e.g. Williams 1985) For completeness we will give the non-dimensional governing equations here. Conservation of mass reads

$$\frac{\partial \rho}{\partial t} + \nabla \cdot (\rho \mathbf{u}) = 0, \tag{3}$$

where $\mathbf{u}$ is the fluids velocity vector. Conservation of momentum

$$\frac{\partial \rho \mathbf{u}}{\partial t} + \nabla \cdot (\rho \mathbf{u}\mathbf{u}) = -\nabla P + \frac{1}{Re} \nabla \cdot \frac{\mu}{\mu_0} (\nabla \mathbf{u} + (\nabla \mathbf{u})^T) \tag{4}$$

In which P is the pressure, Re the Reynolds number, and μ the dynamic viscosity. The energy or temperature equation reads:

$$\frac{\partial \rho T}{\partial t} + \nabla \cdot \rho \mathbf{u} T = \frac{1}{RePr} \nabla \cdot \frac{\mu}{\mu_0} \nabla T + 2\dot{\omega} \tag{5}$$

with Pr the Prandtl number. Furthermore, we have two equations for the chemical species, i.e. one for the fuel and oxidizer.

$$\frac{\partial \rho Y_i}{\partial t} + \nabla \cdot \rho \mathbf{u} Y_i = \frac{1}{ReSc} \nabla \cdot \frac{\mu}{\mu_0} \nabla Y_i - \dot{\omega} \tag{6}$$

with Sc the Schmidt number. The equation of state gives a relation between density and temperature:

$$P = \rho T \tag{7}$$

For the temperature dependent viscosity μ we will use the following relation

$$\frac{\mu}{\mu_0} = \left(\frac{T}{T_0} \right)^{3/4} \tag{8}$$

The main assumption in the low Mach number approximation is that the pressure P can be written as:

$$P = P_0(t) + \gamma Ma^2 P_1 \tag{9}$$

In which $P_0(t)$ is the total pressure, which is only a function of time. For an open domain like our jet, the pressure $P_0(t)$ is a constant with an arbitrary value, say 1. This means that in the Navier-Stokes equations (4) P_1, which will be further on denoted by p, plays only a role and that $\rho T = 1$ at the lowest order.

3. Numerical method and parallel implementation

In this section we will give an outline of the numerical method which will be used to solve the governing equations. The spatial terms in the continuity and momentum equations are discretized with help of a second-order finite volume method on a staggered three-dimensional spherical grid (see e.g. Boersma *et al.* 1998). The convective term in the transport equations are treated with a TVD scheme (see e.g. Vreugdenhil and Koren 1993) to keep the scalar concentrations between the specified minimum and maximum, say 0 and 1. For this, we had to recast the transport equations in the following form:

$$\frac{\partial T}{\partial t} + \nabla \cdot \mathbf{u}T - T\nabla \cdot \mathbf{u} = \frac{1}{\rho}\frac{1}{PrRe}\nabla \cdot \frac{\mu}{\mu_0}\nabla T + \frac{2}{\rho}\dot{\omega} \tag{10}$$

The diffusive part of the transport equations is treated in a similar way as in the momentum equations.

The time advancement is accomplished with a predictor-corrector method similar to the one used by Najm, Wyckoff and Knio (1998). First the transport equations are integrated from time level n with an explicit Adams-Bashforth step to an intermediate level, i.e.

$$T^* - T^n = \Delta t[\frac{3}{2}(-A_t + D_t)^n - \frac{1}{2}(-A_t + D_t)^{n-1}] \tag{11}$$

where A_t and D_t stand for the advective and diffusive terms in the transport equations (equations for Y_i are similar). The equation of state, $P = \rho T$, is then used to find the density at the intermediate level. Also the momentum equations are integrated to the intermediate level,

$$\frac{\rho^* u^* - \rho^n u^n}{\Delta t} = [\frac{3}{2}(-A_m + D_m)^n - \frac{1}{2}(-A_m + D_m)^{n-1}] \tag{12}$$

In which A_m and D_m stand for the advective and diffusive terms in the momentum equations. The intermediate hydrodynamic pressure is determined from the pressure Poisson equation

$$\nabla^2 p^* = \frac{1}{\Delta t}[\nabla \cdot (\rho^* \mathbf{u}^*) + \frac{\partial \rho^*}{\partial t}] \tag{13}$$

The derivative $\partial\rho^*/\partial t$ is calculated with help of a backward difference formula using ρ^*, ρ^n and ρ^{n-1}. Once the Poisson equation is solved, $\rho^*\mathbf{u}^*$ can be corrected in the following way

$$\rho^*\mathbf{u}^* := \rho^*\mathbf{u}^* - \Delta t \nabla p^* \tag{14}$$

The next step is to use the Adams-Moulton corrector for the transport equations:

$$T^{n+1} - T^n = \frac{1}{2}[(-A_t + D_t)^n + (-A_t + D_t)^*]. \tag{15}$$

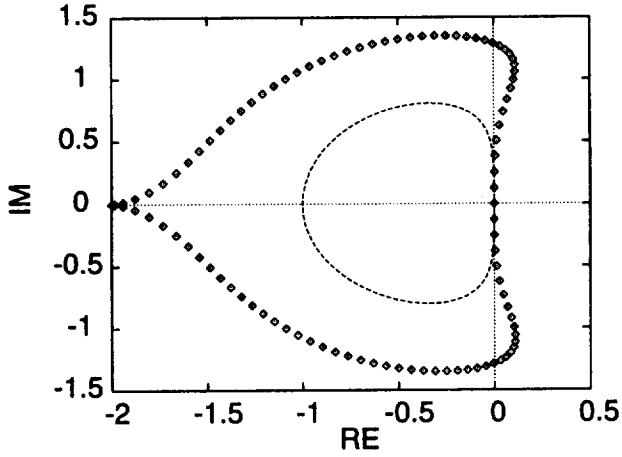

FIGURE 2. The stability regions of the Adams-Bashforth (AB2) and the predictor corrector (P-C) method. AB2: ---- ; P-C: $\diamond$.

The equation of state again gives the density, but now at time level $n+1$ Again the momentum equations are integrated:

$$\frac{\rho' \mathbf{u}' - \rho^n \mathbf{u}^n}{\Delta t} = \frac{1}{2}[(-A_m + D_m)^n + (-A_m + D_m)^*] \tag{16}$$

The Poisson equation is used to obtain the pressure at $n+1$, and the velocity correction gives the final velocity (or flux) at $n+1$.

The scheme above is quite similar to the one used by Rutland (1989) and the one used by Najm *et al.* (1998). In Rutland's work the predictor corrector method is replaced by a fully implicit method using Crank-Nicolson. The advantage of this method is that there is no restriction on the time step. However, for a full three-dimensional calculation, the solution of the matrix vector equation is very expensive. Najm *et al.* (1998) use the predictor-corrector strategy only for the transport equations (5), (6) and not for the full system of equations (4), (5) and (6). In Fig. 2 we show the stability regions of the method proposed by Najm *et al.* (1998) and of our method. It is clear that the full predictor corrector method has a considerably bigger time step without much extra work. Furthermore, the predictor-corrector scheme does not have the weak instability for advection which the second-order Adams-Bashforth method has.

3.1 Boundary conditions

In this section we will describe the boundary conditions for the coflowing jet calculations. At the inflow all components of the velocity are prescribed on the staggered grid:

$$u_r = U \cos\theta \tag{17}$$

$$u_\theta = -U \sin\theta \tag{18}$$

$$u_\phi = 0 \tag{19}$$

$$T = 1,\ Y_f = 1,\ Y_o = 0, \quad \text{In the orifice}$$

$$T = 1,\ Y_f = 0,\ Y_o = 1, \quad \text{In the coflow}$$

where U is the velocity (jet or coflow) in a Cartesian system. This boundary condition will be used for both the velocity and predicted velocity ($\mathbf{u}^*$).

At the lateral boundary of the jet, several boundary conditions can be used, for instance, the frequently used free-slip conditions (Gresho 1991) which read:

$$u_\theta = \frac{\partial u_r}{\partial \theta} = \frac{\partial u_\phi}{\partial \theta} = 0. \tag{20}$$

With this boundary condition no entrainment of fluid into the jet is possible because u_θ is set equal to zero. Another possible boundary condition is the so-called traction free boundary condition, i.e. the traction of the stress tensor with the unit normal on the boundary, Gresho (1991)

$$(-p\delta_{ij} + \tau_{ij}) \cdot n_\theta = 0, \tag{21}$$

For simplicity we will assume that the pressure p at the lateral boundary is constant. Without loss of generality we can also assume that the pressure at this boundary is zero. In the computational domain the pressure is calculated by the model, and the pressure difference between the pressure at the border and the pressure in the computational domain will determine the entrainment of fluid in or out of the jet.

At the outflow boundary we apply a convective boundary condition (see e.g. Akselvoll and Moin 1996).

$$\frac{\partial \rho \mathbf{u}}{\partial t} = -U \frac{\partial \rho \mathbf{u}}{\partial r} \tag{22}$$

where $U = U(\theta)$ is the mean velocity at the outflow boundary. This boundary condition is applied to the predicted velocity $\mathbf{u}^*$. The convective boundary conditions are discretized using a first-order upwind method in space and a first order discretization in time.

From numerical experiments, we found that the flow is rather sensitive to the convective outflow velocity U. It turns out that errors in the outflow boundary condition generate rather high pressure gradients near this boundary, and this influences the entrainment over the lateral boundary, which changes the total behavior of the jet. These large pressure gradients can be avoided by enforcing that the integral,

$$\int\int\int (\frac{\partial \rho^*}{\partial t} + \nabla \cdot \rho \mathbf{u}^*) dVol = \int\int\int \frac{\partial \rho^*}{\partial t} dVol + \int\int \rho \mathbf{u}^* dS, \tag{23}$$

is exactly zero. We enforce this by chancing $\rho \mathbf{u}_*$ at the outflow boundary.

3.2 Parallel implementation

The numerical method outlined above has been implemented on parallel machines using the message passing interface (MPI). Let N_r, N_θ and N_ϕ be the number of grid points in the coordinate directions and N_p the number of processors. It is clear that from a physical point of view N_r will be larger than N_θ and N_ϕ. Therefore, we have decided to distribute the radial direction over the CPU's. Thus on every CPU there are $N_r/N_p \times N_\theta \times N_\phi$ points. To minimize the communication we have added two ghost points in the radial direction, so actually there are $(N_r/Np+2) \times N_\theta \times N_\phi$ point on every CPU. With these ghost points all the explicit updates can be carried out without communication.

The Poisson equation is solved with a combination of Fast Fourier and Cyclic-reduction methods (see e.g. Boersma *et al. 1998*). The Fast Fourier transform of the right-hand side of the Poisson equation in the ϕ direction is local (no communication). The results of Fourier Transform are then redistributed to a distribution $N_r \times N_\theta \times N_\phi/N_p$. The two-dimensional (Helmholtz) problems in r and θ can be solved efficiently with the **BLKTRI** routine from the public domain package **FISHPAK**. The solutions of the Helmholtz problems are again redistributed to the $N_r/N_p \times N_\theta \times N_\phi$ distribution, and another local Fast Fourier Transformation gives the pressure in physical space.

The parallel strategy outlined above scales very well as can be seen from Table 1.

Table 1. Scalability of the parallel code

N_p	Grid	CPU/Δt
4	128^3	62.1 sec
8	128^3	31.2 sec
16	128^3	16.1 sec
32	128^3	8.6 sec
64	128^3	5.1 sec

4. Results

To validate the parallel code we performed a calculation of a cold coflowing jet with a Reynolds number based on the diameter of 4,000 and a velocity excess of 10. The important parameters for this simulation are listed in Table 2.

Table 2. Some important parameters for the cold jet.

$N_r \times N_\theta \times N_\phi$	$768 \times 128 \times 96$
L_r	45 D
N_p	48
Re_d	4,000
λ	10

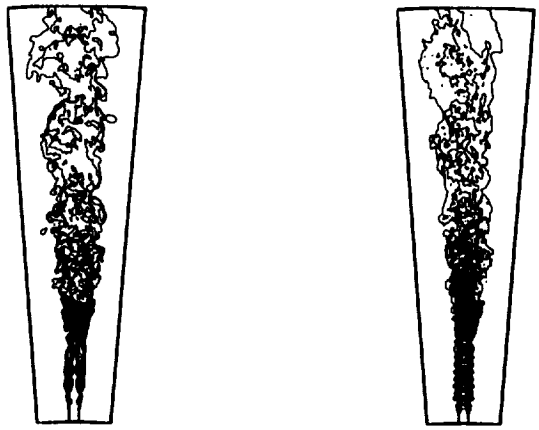

FIGURE 3. Contour plots of the fuel concentration (left) and the axial velocity (right) in the cold jet.

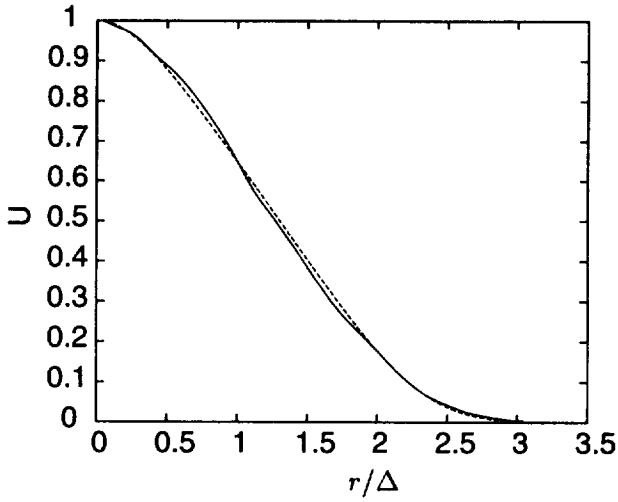

FIGURE 4. The mean velocity profiles obtained from the DNS (———) and from the experiment of Nickels and Perry, 1996 (----).

In Fig. 3 we show a contour plot of the distribution of the scalar field in the cold jet. Close to the jet orifice an axisymmetric Kelvin-Helmholtz instability is present. Further downstream these structures break up in fully three-dimensional ones. In Fig. 4. we show that the mean self-similar velocity profile obtained from the DNS and also the curve fit through the experimental data of Nickels and Perry (1996). It should be noted that the profiles are scaled with the width Δ and not with the

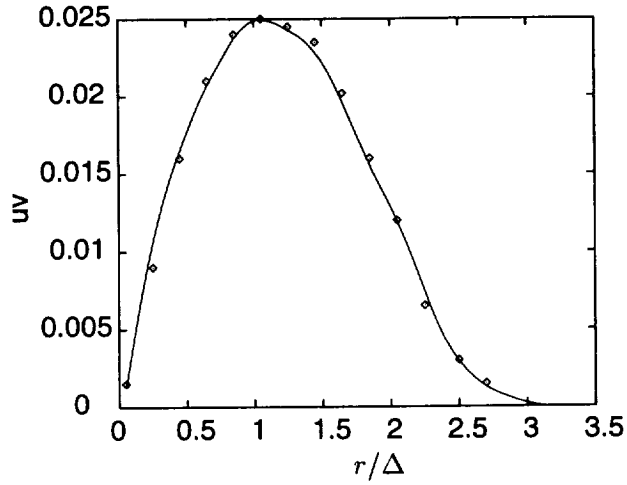

FIGURE 5. The Reynolds shear stress profiles obtained from the DNS (———) and from the experiment of Nickels and Perry, 1996 (----).

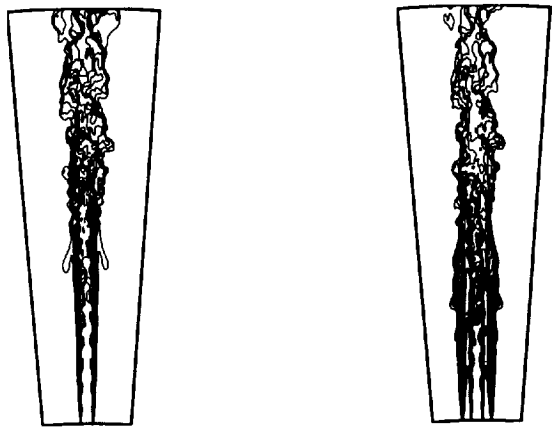

FIGURE 6. The distribution of the fuel (left) and the temperature (right) in the hot jet.

distance to the virtual origin. The agreement between experiment and simulation is rather good. This can also be seen from Fig. 5 in which we compare the computed Reynolds stress (DNS) with the experimental data of Nickels and Perry (1996).

Finally, we show some qualitative pictures of a heated jet. The jet geometry shown in Fig. 1 together with the assumed chemistry might lead to a lifted flame, which requires a very long domain. At this stage we do not want to do a calculation for such a flame because it requires a huge amount of CPU time. Therefore, we have chosen a jet with a pilot, which keeps the flame attached to the orifice. The fluid

leaving the pilot has a temperature of $0.99T_a$ and corresponding fuel and oxidizer concentrations. The effect of the pilot on the flow itself will be small because it has a very small momentum flux compared to the jet (approximately 5%). Figure 6 shows a contour plot of the concentration of fuel. It is clear that the combined effect of temperature/density variation plus increased viscosity due to higher temperature strongly suppresses the Kelvin-Helmholtz instability, leading to an almost laminar flow close to the jet orifice. (The high temperature in the initial shear layer increases the viscosity by more than a factor of three.) Further downstream there is still a clear transition to a fully turbulent state. Figure 6 (right) shows the density in the jet. Here we see more or less the same behavior as in Fig. 6 (left).

5. Conclusions and future work

We have shown that the developed numerical method is capable of simulating cold coflowing jets quite accurately. This gives us confidence for the heated case in which there is hardly any reliable experimental data available. From the preliminary results for the heated jet, it is clear that the combined effect of density variation and increased viscosity has a strong damping influence on the Kelvin-Helmholtz instability, leading to a delayed transition and a flow with considerably less small scales. Therefore, in future calculations it is probably possible to increase the Reynolds number and still resolve all scales of motion for the hot jet. In the near future the results of the DNS will be compared with the LES data obtained for the same geometry by Steiner (this volume) and with the experimental data obtained by Su (this volume).

REFERENCES

AKSELVOLL, K., & MOIN, P. 1996 Large-eddy simulation of turbulent confined coannular jets. *J. Fluid Mech.* **315,** 387.

BOERSMA, B. J., BRETHOUWER, G., & NIEUWSTADT, F. T. M. 1998 A numerical investigation on the effect of the inflow conditions on the self-similar region of a round jet. *Phys. Fluids.* **10,** 899-909.

GRESHO, P. M. 1991 Incompressible fluid dynamics: Some fundamental formulation issues. *Ann. Rev. Fluid Mech.* **23,** 413-454.

NAJM, H. N., WYCKOFF, P. S., & KNIO, O. M. 1998 A semi-implicit numerical scheme for reacting flow. *J. Comp. Phys.* **143,** 381-402.

NICKELS, T. B. & PERRY, A. E. 1996 An experimental and theoretical study of the turbulent coflowing jet. *J. Fluid Mech..* **309,** 157-183.

RUTLAND, C. J. 1989 Effects of strain, vorticity, and turbulence on premixed flames. *Report TF-44,* Stanford CA.

WILLIAMS, F.A. 1985 Combustion Theory,Addison-Wesley, New-York.

VREUGENHIL, C. B., & KOREN, B., 1993 Numerical Methods for Advection-Diffusion Problems. *Notes on Numerical Fluid Mechanics.* **45,** Vieweg, Braunschweig.

On the use of interpolating wavelets in the direct numerical simulation of combustion

By R. Prosser AND W. K. Bushe

1. Motivation

Direct Numerical Simulation (DNS) of turbulent flows is an activity severely limited by presently available computer power. It has long been known (e.g. Corrsin 1961) that in order to resolve accurately the governing Navier-Stokes equations, the number of computational cells required scales as a super-linear power of the Reynolds number. Reacting systems add additional complexity to this already bleak picture. In many flows of industrial interest, the length and time scales associated with the reaction mechanism are much smaller than those of the fluid turbulence, and the resolution requirements for chemically active flow simulations are thereby considerably increased. When this is added to the computational expense incurred by the stiffness of highly non-linear reaction rate source terms, it appears that reacting flow simulations of significant complexity will remain firmly out of reach for the foreseeable future. Nonetheless, the same spatial and temporal stiffness that gives rise to such demanding computations may paradoxically provide a foothold for efficient numerical methods. Many industrial processes involving combustion occupy the *laminar flamelet regime* (Libby & Bray 1980, Bray, Libby & Moss 1985) where the turbulent flame can be regarded as a highly localized sheet of chemical activity, either side of which the fluid composition remains relatively constant.

The ability of wavelet based methods to analyze functions in terms of their *local* rates of change appears eminently suited to the numerical investigation of non-linear partial differential equations, the solutions to which often contain a large number of disparate length scales. In particular, the efficient discretization of fluid flow problems have been the focus of a number of recent investigations, both with chemical reaction (Bockhorn, Frölich & Schneider 1995, Frölich & Schneider 1996, Frölich & Schneider 1997,) and without (Bacry, Mallat & Papanicolaou 1992, Frölich & Schneider 1995, Bihari 1996). Many of the discretizations proposed to date have been limited to periodic domains although recent efforts have led to advances in non-periodic discretizations (Vasilyev, Paolucci & Sen 1995, Vasilyev & Paolucci 1996, Vasilyev & Paolucci 1997).

In this paper, we discuss the generalization to two spatial dimensions of an existing wavelet based scheme intended for combustion problems (Prosser & Cant 1998a). The approach adopts a collocation strategy but, unlike traditional collocation methods, the solution to the set of governing equations is obtained on a grid of collocation points located in a hierarchy of *wavelet* subspaces. The solution is only returned to the physical space in order to evaluate non-linear inertial and chemical reaction rate terms. The key advantage of this approach, and the motivation for its derivation, is that while the solution is expressed in terms of the wavelet spaces, it

is possible to develop an elegant algorithm to exploit the sparsity of the representation in order to reduce both the amount of storage required and the computational effort expended in resolving the chemistry fields.

2. Accomplishments

As a preliminary step towards a fully adaptive wavelet based scheme, a 2-D code has been developed. The governing equations for density, momentum, stagnation internal energy, and species mass fractions are solved using a collocation strategy. Unlike traditional collocation methods, the governing equations are satisfied at collocation points *within* the hierarchy of wavelet spaces. Due to the ability of the wavelets to identify regions of changing continuity properties, an adaption strategy based on the wavelet coefficients' absolute magnitude will automatically track the flame front during the course of a simulation.

The wavelet discretization is based on a tensor decomposition of the two dimensional computational domain and takes the form

$$\begin{aligned}\mathbf{V}_J^{(2)} &= \mathbf{V}_J^x \otimes \mathbf{V}_J^y \\ \mathbf{W}_J^{(2)} &= (\mathbf{V}_J^x \otimes \mathbf{W}_J^y) \oplus (\mathbf{W}_J^x \otimes \mathbf{V}_J^y) \oplus (\mathbf{W}_J^x \otimes \mathbf{W}_J^y) \\ &= \mathbf{W}_J^{(\alpha)} \oplus \mathbf{W}_J^{(\beta)} \oplus \mathbf{W}_J^{(\gamma)}.\end{aligned}$$

$\mathbf{V}_J^{(2)}$ and $\mathbf{W}_J^{(2)}$ are used to denote the two-dimensional scaling function and wavelet spaces, respectively. We observe that the definition of $\mathbf{W}_J^{(2)}$ involves a set of 'cross correlation' spaces, denoted here by $\mathbf{W}_J^{(i)}$, which arise via the definition of the 2-D vector space $\mathbf{V}_J^{(2)}$ and by the causal property of the multiresolution analysis: $\mathbf{V}_J^{(2)} = \mathbf{V}_{J-1}^{(2)} \oplus \mathbf{W}_{J-1}^{(2)}$. The dimensionality of the subspaces are

$$\begin{aligned}\dim(\mathbf{V}_J^x \otimes \mathbf{V}_J^y) &= (2^J + 1) \times 2^J = \dim(\mathbf{V}_J^x \otimes \mathbf{W}_J^y) \\ \dim(\mathbf{W}_J^x \otimes \mathbf{V}_J^y) &= (2^J) \times 2^J = \dim(\mathbf{W}_J^x \otimes \mathbf{W}_J^y),\end{aligned}$$

The disparity between (say) $\mathbf{V}_J^x$ and $\mathbf{V}_J^y$ arises through the span-wise periodicity in the computational domain and is discussed further in Prosser & Cant (1998a).

For this investigation, we have chosen an initial finest resolution for the computational domain of 257×64 grid points. In the language of the previous equations, this implies $\mathbf{V}_J^{(2)} = \mathbf{V}_8^x \otimes \mathbf{V}_6^y$. The reorganization of the domain under the action of the bi-dimensional wavelet transform is depicted in the lower half of Fig. 1. Note that the spanwise decomposition of the domain only occupies two subspaces while the streamwise direction employs four subspaces. This reflects the fact that the principal structure in the domain, the planar flame, is oriented with its normal initially pointing in the streamwise direction.

Figures 2 and 3 show the u-velocity surface through the flame structure and its corresponding decomposition onto a set of wavelet spaces. We see that, due to the considerable irregularity in the physical space representation of the velocity,

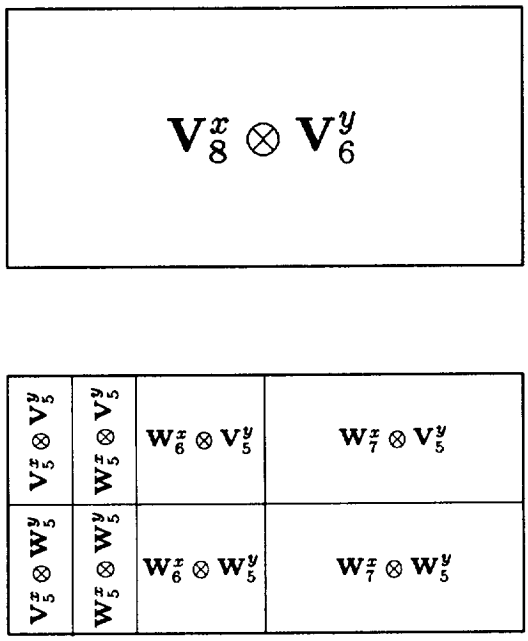

FIGURE 1. 2D tensor decomposition of initial computational domain into wavelet subspaces.

the transform domain is not sparse. This is demonstrated in Table 1 by the large number of wavelet coefficients greater than the prescribed thresholds.

Figure 4 shows a contour plot of the progress variable profile. We note that, due to the comparatively short simulation time, the degree of flame wrinkling is not great. The wrinkling that has taken place, however, is confined mainly to the preheat zone, which places the flame in the *thin reaction zones regime* discussed by Peters (1998). The considerable length scale separation between the flame structure and that of the computational domain leads to a non-trivial sparsity in the wavelet representation of the progress variable profile. Table 2 presents this sparsity in terms of the number of non-trivial wavelet coefficients measured with reference to a given datum. The table shows that, for a threshold of 10^{-5}, 85.4% of the original wavelets used to discretize the profile are redundant. The reduction in accuracy incurred by this surgery is expressed in terms of the normalized l_2 reconstruction error shown in the rightmost column of Table 2. From the small values of these errors, it is apparent that the approximation introduced by thresholding is very small.

3. Future plans

3.1 Discretization of operators

In the present formulation, the discretization of the differential operators $\frac{\partial^n}{\partial x_i^n}$ is

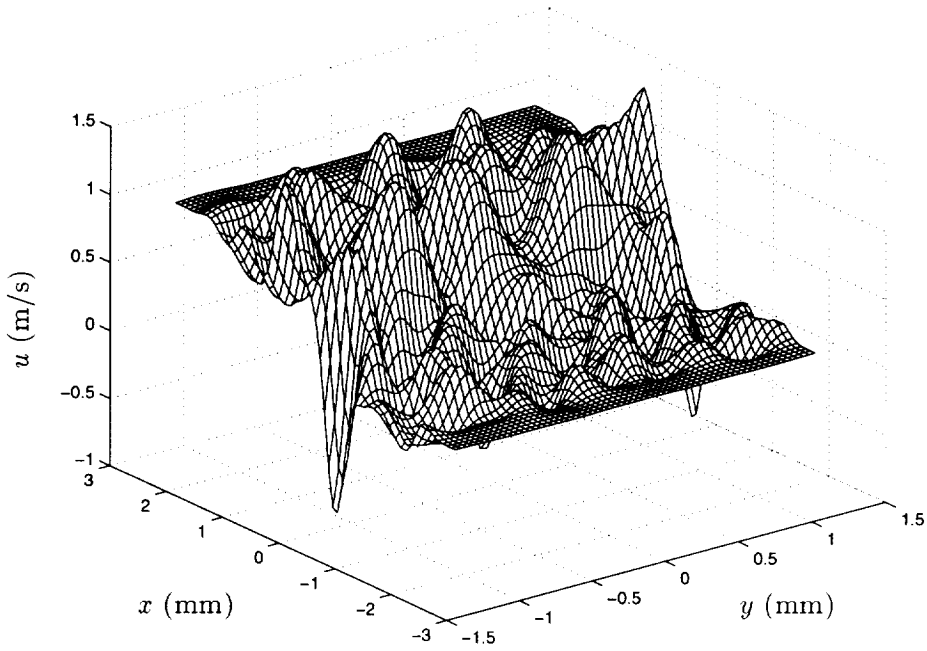

FIGURE 2. Mesh plot of u velocity in real space.

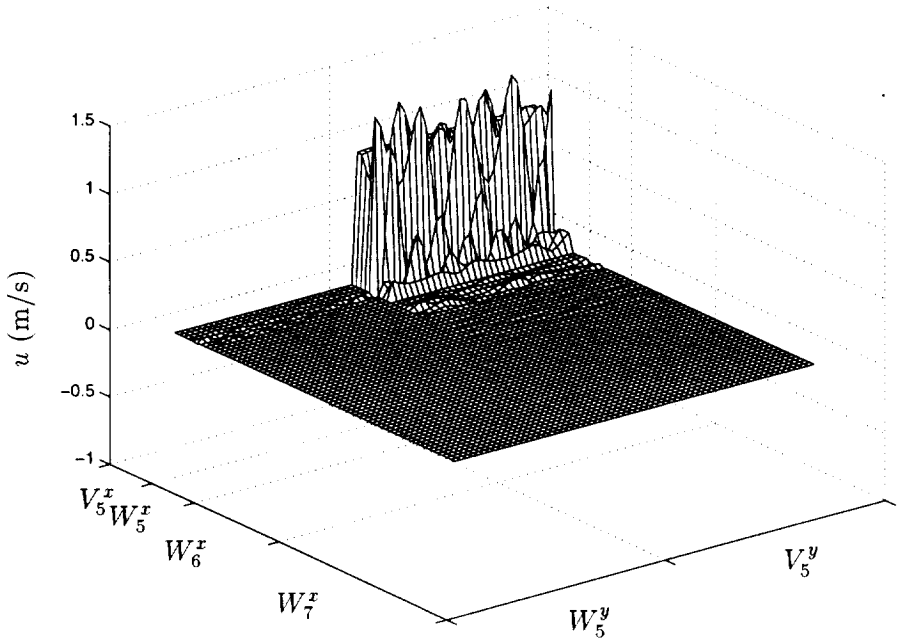

FIGURE 3. Mesh plot of u velocity in wavelet space.

ϵ	$\#\lvert d_{i,k}\rvert \geq \epsilon$	possible compression
10^{-8}	16401	1.0029
10^{-7}	15979	1.0294
10^{-6}	12734	1.2917
10^{-5}	10010	1.6432
10^{-4}	5477	3.0031

Table 1. Number of u-velocity wavelet coefficients with absolute magnitude greater than a prescribed threshold $\epsilon > 0$. Third column shows the possible compression obtainable through thresholding.

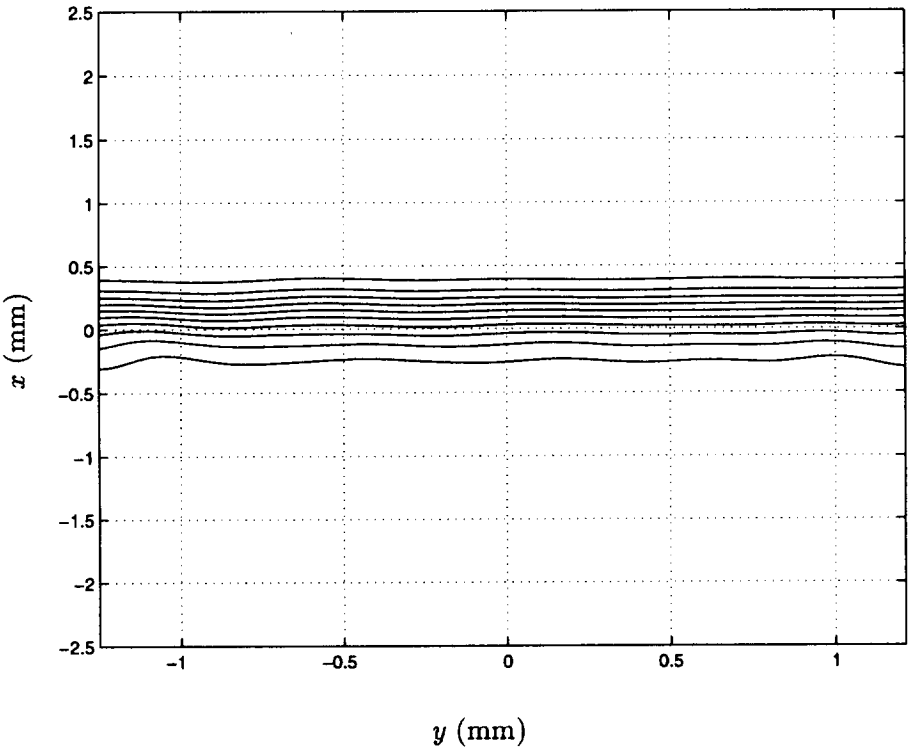

FIGURE 4. Contour plot of progress variable. Products are at the top of the plot, and reactants are at the bottom.

via the *standard decomposition*;

$$\partial_j^n = \left\{ P_{V_{J-p}} + \sum_{i=J-p}^{J-1} P_{W_i} \right\} \frac{\partial^n}{\partial x_i^n} \left\{ P_{V_{J-p}} + \sum_{i=J-p}^{J-1} P_{W_i} \right\}.$$

While this approach is the simplest to implement, it suffers from two drawbacks:

ϵ	$\#\lvert d_{i,k}\rvert \geq \epsilon$	possible compression	$\frac{\lVert c-c_\epsilon\rVert_2}{\lVert c\rVert_2}$
10^{-8}	8625	1.9070	2.3690×10^{-9}
10^{-7}	5877	2.7987	2.7555×10^{-8}
10^{-6}	4032	4.0794	2.7105×10^{-7}
10^{-5}	2407	6.8334	2.4788×10^{-6}
10^{-4}	1349	12.1297	2.8931×10^{-5}

Table 2. Number of progress variable wavelet coefficients with absolute magnitude greater than a prescribed threshold $\epsilon > 0$ and corresponding reconstruction accuracy. Third column shows the possible compression obtainable through thresholding.

- The number of non-zero coefficients in the ∂_j^n operators scale asymptotically as $\mathcal{O}(N \log_2 N)$ (Beylkin, Coifman & Rokhlin 1991).
- The structure of the operator is not readily amenable to an unbounded adaption strategy, in which an arbitrary number of discretizing nodes are introduced. Using the standard decomposition, ∂_j^n needs to be recalculated every time a new set of wavelet subspaces $\mathbf{W}_\mathbf{J}^{(\mathbf{2})}$ are added or removed.

An alternate, more sophisticated approach is to represent the differential operators in terms of the *non-standard* decomposition (Beylkin, Coifman & Rokhlin 1991). In this latter technique, an arbitrary operator T can be represented as an integral kernel;

$$Tf(x) = \int k(x,y)f(y)dy.$$

The integral kernel is then expanded over a set of square wavelet subspaces (i.e. of the form $\mathbf{W}_\mathbf{J}^\mathbf{x} \otimes \mathbf{W}_\mathbf{J}^\mathbf{y}$). The advantages of this approach are twofold:

- The number of entries in the non-standard decomposition is $\mathcal{O}(N)$.
- The decomposition is self-similar across resolutions and can be implemented as a finite difference like scheme. Such an approach is much more readily amenable to truly adaptive calculations.

3.2 Evaluation of non-linear terms

The principal expense incurred using this algorithm is during the evaluation of non-linear terms. Presently, non-linearities are evaluated by first inverting the terms to physical space where, after evaluation, they are re-projected onto the hierarchy of wavelet spaces. While reasonably quick to execute, such a technique does not provide insight into the interactions between scales in the wavelet domain nor into the generation of aliasing errors.

Some preliminary work has been carried out in the evaluation of arbitrary non-linearities for one dimensional wavelet expansions (Prosser & Cant 1998b). As may be expected, the interactions produced by (say) a quadratic non-linearity introduces mixing between the subspaces occupied by the multiplicands. More importantly,

a new term is created, which cannot be represented on a fixed resolution grid and which represents the generation of un-resolvable wavelet coefficients. This term arises as a result of the increasing departure of the non-linear term from the set of polynomials spanned by the scaling function bases alone.

From a practical point of view, the new method of evaluation is approximately twice as fast in execution as the earlier method, and there are grounds for cautious optimism that this increased execution speed may scale geometrically with the spatial dimension of the problem.

REFERENCES

BACRY, E., MALLAT, S. G. & PAPANICOLAOU, G. 1992 A Wavelet Based Space-Time Adaptive Numerical Method for Partial Differential Equations. *Math. Modelling and Num. Anal.* **26,** 793-834.

BEYLKIN, G. AND COIFMAN, R. AND ROKHLIN, V. 1991 Fast Wavelet Transforms and Numerical Algorithms I. *Commun. Pure Appl. Math.* **44,** 141-183.

BIHARI, B. L 1996 Multiresolution Schemes for Conservation Laws with Viscosity. *J. Comp. Phys.* **123,** 207-225.

BOCKHORN, H., FRÖLICH, J. & SCHNEIDER, K. 1995 An Adaptive Two Dimensional Wavelet-Vaguelette Algorithm for the Computation of Flame Balls. *Universität Kaiserslautern (Preprint).*

BRAY, K. N. C., LIBBY, P. A. & MOSS, J. B. 1985 Unified Modeling Approach for Premixed Turbulent Combustion - Part 1: General Formulation . *Combust. Flame.* **61,** 87-102.

CORRSIN, S. 1961 Turbulent Flow. *Am. Sci.* **49,** 300-325.

FRÖLICH, J. & SCHNEIDER, K. 1997 An Adaptive Wavelet-Vaguelette Algorithm for the Solution of PDEs . *J. Comp. Phys.* **130,** 174-190.

FRÖLICH, J. & SCHNEIDER, K. 1995 Numerical Simulation of Decaying Turbulence in an Adapted Wavelet Basis. *Appl. Comput. Harm. Anal.* **2,** 393-397.

FRÖLICH, J. & SCHNEIDER, K. 1996 A Fast Algorithm for Lacunary Wavelet Bases related to the Solution of PDE's. *C. R. Math. Rep. Acad. Sci. Canada.* **16,** 83-86.

LIBBY, P. A. & BRAY, K. N. C. 1980 Implications of the Laminar Flamelet Model in Premixed Turbulent Combustion. *Combust. Flame.* **39,** 33-41.

PETERS, N. 1998 Propagating Thin Reaction Zones in Premixed Turbulent Combustion Part I: Theory and Modelling Aspects. *J. Fluid Mech. (submitted).*

PROSSER, R. & CANT, R. S. 1998(a) A Wavelet-Based Method For the Efficient Simulation of Combustion. *J. Comp. Phys. (to appear).*

PROSSER, R. AND CANT, R. S. 1998(b) Evaluation of Non-linear terms using Interpolating Wavelets. *SIAM J. Num. Anal. (submitted).*

VASILYEV, O. V., PAOLUCCI, S. & SEN, M. 1995 A Multilevel Wavelet Collocation Method for Solving Partial Differential Equations in a Finite Domain. *J. Comp. Phys.* **120,** 33-47.

VASILYEV, O. V. & PAOLUCCI, S. 1996 A Dynamically Adaptive Multilevel Wavelet Collocation Method for Solving Partial Differential Equations in a Finite Domain. *J. Comp. Phys.* **125,** 498-512.

VASILYEV, O. V. & PAOLUCCI, S. 1997 A Fast Adaptive Wavelet Collocation Algorithm for Multidimensional PDEs. *J. Comp. Phys.* **138,** 16-56.

On the use of a dynamically adaptive wavelet collocation algorithm in DNS of non-premixed turbulent combustion

By Oleg V. Vasilyev[1] AND W. Kendal Bushe

1. Motivation and objectives

The ability to model non-premixed combustion is very important; many practical combustion devices operate with non-premixed flames in the presence of turbulent flows (Vervisch & Poinsot, 1998). Non-premixed turbulent flames are characterized by a large spectrum of temporal and length scales. Additional complexity is added by the large number of unknowns and by the stiffness of highly nonlinear chemical source terms associated with realistic kinetic mechanisms. Conventional numerical algorithms are not able to resolve all the characteristic scales affordably. As a consequence, most of the current efforts are focused on developing model equations using either RANS or LES methodologies.

The ability of wavelet based numerical algorithms to locally resolve the structures appearing in the solution without drastic increase in the number of the unknowns enables us to pursue a different avenue of research. Since most flames occupy a relatively small volume within the domain of interest, dynamically adaptive wavelet collocation algorithms are ideally suited for direct numerical simulations of non-premixed turbulent flames with realistic chemistry.

Wavelet analysis is a new numerical concept which allows one to represent a function in terms of basis functions, called wavelets, which are localized in both location and scale (Meyer, 1990; Daubechies, 1992). Good wavelet localization properties in *physical* and *wavenumber* (spectral) spaces can be contrasted with the spectral approach, which employs infinitely differentiable functions but with global support and small discrete changes in the resolution. On the other hand, finite-difference, finite-volume and finite-element methods have small compact support but poor continuity properties. Wavelets appear to combine the advantages of both spectral and finite-difference bases. One can expect that numerical methods based on wavelets will attain both good spatial and spectral resolution.

Recently Vasilyev and Paolucci (1996, 1997) have developed a dynamically adaptive multilevel wavelet collocation algorithm for partial differential equations in multiple dimensions. The basic idea behind the multilevel wavelet approximation is that a function can be approximated as a linear combination of wavelets having different scales and locations. Adaptation is achieved by retaining only those wavelets whose coefficients are greater than a given threshold. This property of the

1 Present address: Department of Mechanical and Aerospace Engineering, University of Missouri, Columbia, MO 65211

multilevel wavelet approximation allows local grid refinement up to an arbitrary small scale without a drastic increase in the number of collocation points; thus, high resolution computations can be carried out only in those regions where sharp transitions occur.

The dynamically adaptive wavelet collocation algorithm is ideally suited to handling problems with localized structures, which might occur intermittently anywhere in the computational domain or change their locations and scales in space and time. Conventional adaptive algorithms are costly because grids can change drastically within a short time interval, thus the use of conventional algorithms on a uniform grid is impractical. Thus, the main advantage of the dynamically adaptive wavelet collocation algorithm is that it will use far fewer grid points than the other algorithms when applied to problems with a great diversity of spatial-temporal scales. In addition, the computational grid can be refined locally to an arbitrary small size grid. We emphasize here that the adaptation of the computational grid does not require additional effort and consists merely in turning on and off wavelets at different locations and scales. Other robust properties of this algorithm are that it can handle general boundary conditions and the relative error can be actively controlled by prescribing a threshold parameter. All of these features make this algorithm an attractive candidate for direct numerical simulation of combustion.

The objective of this report is to present initial results which demonstrate the potential benefits of the use of the dynamically adaptive wavelet collocation algorithm in turbulent combustion simulations. The use of wavelets in modeling complex physical phenomena is something of a novelty, and as a first step to achieve the ambitious goal of efficient numerical simulations of non-premixed turbulent flames, we consider a simple model of laminar flame-vortex interaction.

2. Accomplishments

2.1 Wavelet approximation

The most important property of wavelet analysis is that a function is decomposed in terms of basis functions having different discrete scales and locations. These basis functions are constructed by the discrete (typically dyadic) dilation and translation of a single function, which has good localization properties in physical as well as wave-number spaces. In other words, wavelet analysis can be viewed as a multilevel or multiresolution representation of a function where each level of resolution consists of basis functions having the same scale but located at different positions. In this report we will only describe the main points necessary to introduce the dynamically adaptive wavelet collocation method. A more detailed description is given by Vasilyev (1996) and Vasilyev and Paolucci (1997).

In one-dimensional space the wavelet basis consists of a doubly indexed function set $\{\psi_k^j(x) : j,k \in Z, x \in R\}$ given by

$$\psi_k^j(x) = a_j^{-1/2}\psi\left(\frac{x - b_k^j}{a_j}\right), \tag{1}$$

where $\psi(x)$ is a one-dimensional wavelet and $\psi_k^j(x)$ is a wavelet of scale $a_j = a_0 2^{-j}$ located at position $b_k^j = a_j k$. Superscripts denote the level of resolution and subscripts denote the location in physical space (with the exception of a_j). Wavelet bases can be introduced the same way in multiple dimensions, provided that one uses an n-dimensional wavelet function $\psi(\mathbf{x})$ ($\mathbf{x} \in R^n$). We will use bold symbols to denote n-dimensional vectors, *e.g.* $\mathbf{x} \equiv (x_1, \ldots, x_n)$, $\mathbf{k} \equiv (k_1, \ldots, k_n)$, $\mathbf{b_k} \equiv (b_{k_1}, \ldots, b_{k_n})$. Following this notation, an n-dimensional wavelet basis is given by

$$\psi_{\mathbf{k}}^j(\mathbf{x}) = \left(\prod_{i=1}^{n} a_{x_i j} \right)^{-1/2} \psi \left(\frac{x_1 - b_{k_1}^j}{a_{x_1 j}}, \ldots, \frac{x_n - b_{k_n}^j}{a_{x_n j}} \right), \tag{2}$$

where $a_{x_i j}$ and $b_{k_i}^j$ ($i = 1, \ldots, n, \quad j \in Z, \quad \mathbf{k} \in Z^n$) are wavelet scales and locations at the j^{th} level of resolution.

Let us consider a function $u(\mathbf{x})$ defined on a closed n-dimensional domain Ω. Let $j = 0$ and $j = J$ be the coarsest and finest levels of resolution respectively. Due to the compact or effectively compact wavelet support, at each level of resolution $j = 0, \ldots, J$ there exists a finite n-dimensional integer set Z_Ω^j such that function $u(\mathbf{x})$ can be approximated as

$$u^J(\mathbf{x}) = \sum_{j=0}^{J} \mathbf{C}^j \odot \Psi^j(\mathbf{x}), \tag{3}$$

where $\mathbf{C}^j$ and $\Psi^j(\mathbf{x})$ are n-dimensional arrays of wavelet coefficients and basis functions correspondingly. Operator $\odot$ denotes the summation over the n-dimensional array of indices Z_Ω^j and is given implicitly by

$$\mathbf{C}^j \odot \Psi^j(\mathbf{x}) = \sum_{\mathbf{k} \in Z_\Omega^j} c_{\mathbf{k}}^j \psi_{\mathbf{k}}^j(\mathbf{x}). \tag{4}$$

Equation (4) applies to wavelets of any dimensionality.

The next issue is how to compute wavelet coefficients for a given function $u(\mathbf{x})$. Following the standard collocation approach, wavelet coefficients are found based on the values of a function at certain locations called collocation points. In a wavelet-collocation algorithm a set of collocation points $\{\mathbf{x}_\mathbf{k}^j : \mathbf{k} \in Z_\Omega^j\}$ is defined such that the collocation points of the coarser level of resolution are a subset of the collocation points of the finer level of resolution. In other words, for any j ($0 \le j \le J-1$) the following relation between the collocation points at different levels of resolution is satisfied:

$$\left\{ \mathbf{x}_\mathbf{k}^j \right\} \subset \left\{ \mathbf{x}_\mathbf{k}^{j+1} \right\}. \tag{5}$$

Every wavelet is characterized by its location $\mathbf{b}_\mathbf{k}^j$. Wavelets whose centers are located within the domain will be called "internal" wavelets; those whose centers are located outside the domain will be called "external" wavelets. The choice of

collocation points for wavelets is not unique. For internal wavelets, the location of the center seems to be the most natural choice for the collocation point, provided that the wavelets are non-zero at $\mathbf{b}_\mathbf{k}^j$. We choose the collocation points of external wavelets to correspond to the locations of internal wavelets at finer levels of resolution. This ensures that relation (5) preserved.

Wavelet coefficients are found in a recursive manner. We start from the coarsest level of resolution and progressively move to the finest level. On each level of resolution the coefficients of the lower levels are fixed so that we only obtain the coefficients corresponding to that level. The procedure of finding wavelet coefficients can be described as a consecutive recursive application of two steps. For each level of resolution j $(0 \leq j \leq J)$, we first find the residual between the approximation $u^J(\mathbf{x})$ and the contributions of lower levels of resolution given by $\Delta^j(\mathbf{x}) = u^J(\mathbf{x}) - \sum_{l=0}^{j-1} \mathbf{C}^l \odot \Psi^l(\mathbf{x})$ $(\Delta^0(\mathbf{x}^J) = u^J(\mathbf{x}))$. We then obtain wavelet coefficients by evaluating $\Delta^j(\mathbf{x})$ at $\mathbf{x}_\mathbf{k}^j$ collocation points and requiring the values of the residual $\Delta^j(\mathbf{x}_\mathbf{k}^j)$ to be the same as the wavelet contribution at that level of resolution. This requirement yields the equation:

$$\Delta^j(\mathbf{x}_\mathbf{k}^j) = \mathbf{C}^j \odot \Psi^j(\mathbf{x}_\mathbf{k}^j). \tag{6}$$

Solving this equation gives us the values of wavelet coefficients at the j level of resolution. We repeat this two-step recursive procedure until we reach the finest level of resolution.

The absolute value of the wavelet coefficient $c_\mathbf{k}^j$ depends upon the local regularity of $u(\mathbf{x})$ in the neighborhood of the wavelet location. The wavelet approximation (3) can be written as a sum of two terms composed respectively of wavelets whose amplitudes are above $(u_\geq^J(\mathbf{x}))$ and below $(u_<^J(\mathbf{x}))$ a threshold ϵ:

$$u^J(\mathbf{x}) = u_\geq^J(\mathbf{x}) + u_<^J(\mathbf{x}), \tag{7}$$

where $u_\geq^J(\mathbf{x})$ is given by

$$u_\geq^J(\mathbf{x}) = \sum_{j=0}^{J} \mathbf{C}^j \odot_\geq \Psi^j(\mathbf{x}) = \sum_{j=0}^{J} \sum_{\substack{\mathbf{k} \in Z_\Omega \\ |c_\mathbf{k}^j| \geq \epsilon}} c_\mathbf{k}^j \psi_\mathbf{k}^j(\mathbf{x}), \tag{8}$$

and $u_<^J(\mathbf{x})$ is calculated analogously with the exception that the sum includes only wavelets whose coefficients are below the threshold, *i.e.* $|c_\mathbf{k}^j| < \epsilon$. It is easy to show that

$$\left\| u^J(\mathbf{x}) - u_\geq^J(\mathbf{x}) \right\|_{L^2(R^n)} \leq C\epsilon \left\| u^J(\mathbf{x}) \right\|_{L^2(R^n)}, \tag{9}$$

where C is a constant of order unity. Thus, a good approximation is maintained even when wavelets whose coefficients are below a certain threshold are omitted, and only those wavelets whose coefficients are above the threshold are kept.

2.2 Dynamically adaptive wavelet collocation algorithm

In order for the algorithm to resolve all the structures appearing in the solution and yet be efficient in terms of minimizing the number of unknowns, the basis of active wavelets and, consequently, the computational grid should adapt dynamically in time to reflect local changes in the solution. The adaptation of the computational grid is based on the analysis of wavelet coefficients. The contribution of a wavelet into the approximation is significant if and only if the nearby structures of the solution have comparable size with the wavelet scale. Thus, we may drop a large number of fine scale wavelets with small coefficients in regions where the solution is smooth. Every wavelet is uniquely associated with a collocation point and, consequently, the collocation point should be omitted from the computational grid if the associated wavelet is omitted from the approximation. This property of the multilevel wavelet approximation allows local grid refinement up to an arbitrary small scale without a drastic increase in the number of collocation points.

To ensure accuracy, the basis should also consist of wavelets whose coefficients can possibly become significant during the period of time when the basis and, consequently, the computational grid remain unchanged. Thus, at any instant in time, the basis should not only include wavelets whose coefficients are above a prescribed threshold parameter ϵ, but also the surrounding wavelets. In other words, at any instant in time, the basis should include wavelets belonging to an *adjacent zone* of wavelets for which the magnitude of their coefficients is within an *a priori* prescribed threshold. We say that the wavelet $\psi^l_{\mathbf{m}}(\mathbf{x})$ belongs to the adjacent zone of wavelet $\psi^j_{\mathbf{k}}(\mathbf{x})$ if the following relations are satisfied:

$$|j-l| \le L, \quad |b^j_{k_i} - b^l_{m_i}| \le M_i a_{x_i,l}, \tag{10}$$

where L determines the extent to which coarser and finer scales are included into the adjacent zone and M_i defines the width of the adjacent zone in physical space.

Let us denote by $\mathcal{G}^t_{\geq}$ the irregular grid of collocation points that are retained to approximate the solution at time t. Following the classical collocation approach and evaluating partial differential equations describing flow evolution at collocation points, we obtain a system of nonlinear ordinary differential equations. Functional derivatives appearing in the equations are found by differentiating the wavelet approximation and evaluating the result at collocation points.

The present numerical algorithm consists of three steps:

1. Knowing the values of the solution $\mathbf{u}^J_{\mathbf{k}}(t)$, we compute the values of wavelet coefficients at all levels of resolution. For a given threshold ϵ we adjust $\mathcal{G}^{t+\Delta t}_{\geq}$ based on the magnitude of the wavelet coefficients.
2. If there is no change between computational grids $\mathcal{G}^t_{\geq}$ and $\mathcal{G}^{t+\Delta t}_{\geq}$ at time t and $t+\Delta t$, we go directly to step 3. Otherwise, we compute the values of the solution at the collocation points $\mathcal{G}^{t+\Delta t}_{\geq}$, which are not included in $\mathcal{G}^t_{\geq}$.
3. We integrate the resulting system of ordinary differential equations to obtain new values $\mathbf{u}^J_{\mathbf{k}}(t+\Delta t)$ at positions on the irregular grid $\mathcal{G}^{t+\Delta t}_{\geq}$ and go back to step 1.

The basic hypothesis motivating the algorithm is that, during a time interval Δt, the domain of wavelets with significant coefficients does not move in phase space beyond the adjacent zone. With such an algorithm the grid of collocation points is dynamically adapted in time and follows the local structures that appear in the solution. Note that by omitting wavelets with coefficients below a threshold parameter ϵ we automatically control the error of approximation. Thus the wavelet collocation method has another important feature: active control of the accuracy of the solution. The smaller ϵ is chosen to be, the smaller the error of the solution is. In typical applications the value of ϵ varies between 10^{-2} and 10^{-5}, assuming that the unknown dependent variables have been properly normalized. As the value of ϵ increases, fewer grid points are used in the solution.

2.3 Model problem formulation

The model problem involves a diffusion flame interacting with a vortex pair in a rectangular two-dimensional domain containing fuel and oxidizer on either side of the flame. The chemical mechanism we consider is represented by single reaction between fuel and oxidizer:

$$F + O = P,$$

where unity stoichiometric coefficients were assumed for simplicity. The reaction rate behaves according to the Arrhenius form:

$$\dot{w} = K \rho Y_F \rho Y_O \exp\left(-\frac{T_{\rm ac}}{T}\right), \tag{11}$$

where ρ is the density, $T_{\rm ac}$ is the activation temperature, K is the pre-exponential factor, and Y_F and Y_O are the fuel and oxidizer mass fraction.

The characteristic scales are the length scale L^*, the speed of sound c_0^*, and the density ρ_0^*. The subscript 0 refers to the reference value at some location, and superscript "*" denotes dimensional quantities. The reference state is that of the unburned gas; the reference temperature $T^*_{\rm ref} = (\gamma - 1)T_0^*$ is obtained from the equation of state, where γ is the ratio of specific heats $\gamma = c_p/c_v$. With this normalization, the non-dimensional governing equations are given by (Ruetsch, 1998):

$$\frac{\partial \rho}{\partial t} + \frac{\partial}{\partial x_i}(\rho u_i) = 0, \tag{12a}$$

$$\frac{\partial \rho u_i}{\partial t} + \frac{\partial}{\partial x_j}(\rho u_i u_j) = -\frac{\partial P}{\partial x_i} + \frac{\partial \tau_{ij}}{\partial x_j}, \quad i = 1, 2 \tag{12b}$$

$$\frac{\partial e}{\partial t} + \frac{\partial}{\partial x_j}\left[(e + P)\, u_j\right] = \frac{1}{Re}\frac{\partial}{\partial x_j}(u_i \tau_{ij}) + \frac{1}{RePr}\frac{\partial}{\partial x_j}\left(\mu \frac{\partial T}{\partial x_j}\right) + \dot{w}_e, \tag{12c}$$

$$\frac{\partial \rho Y_F}{\partial t} + \frac{\partial}{\partial x_j}(\rho Y_F u_j) = +\frac{1}{ReSc_F}\frac{\partial}{\partial x_j}\left(\mu \frac{\partial Y_F}{\partial x_j}\right) - \xi \dot{w}_e, \tag{12d}$$

$$\frac{\partial \rho Y_O}{\partial t} + \frac{\partial}{\partial x_j}(\rho Y_O u_j) = \frac{1}{ReSc_O}\frac{\partial}{\partial x_j}\left(\mu \frac{\partial Y_O}{\partial x_j}\right) - \xi \Phi \dot{w}_e, \tag{12e}$$

$$P = \frac{\gamma - 1}{\gamma}\rho T, \tag{12f}$$

where

$$\tau_{ij} = \mu\left(\frac{\partial u_i}{\partial x_j} + \frac{\partial u_j}{\partial x_i} - \frac{2}{3}\frac{\partial u_k}{\partial x_k}\delta_{ij}\right), \tag{13a}$$

$$\mu = \left[(\gamma-1)T\right]^a, \tag{13b}$$

$$e = \frac{1}{2}\rho u_i u_i + \frac{P}{\gamma-1}, \tag{13c}$$

$$\dot{w}_e = \Xi\rho^2 Y_F Y_O \exp\left(-\frac{\beta(1-\theta)}{1-\alpha(1-\theta)}\right), \tag{13d}$$

$$\theta = \frac{1-\alpha}{\alpha}\left((\gamma-1)T-1\right), \tag{13e}$$

$$\alpha = \frac{T_f - T_0}{T_f}, \tag{13f}$$

$$\beta = \alpha\frac{T_{ac}}{T_f}, \tag{13i}$$

$$\xi = \frac{1}{1+\Phi}\frac{1-\alpha}{\alpha}(\gamma-1), \tag{13j},$$

$a = 0.76$, Ξ is the pre-exponential factor, T_f is the adiabatic flame temperature, and Φ is the equivalence ratio. Note that Eq. (13d) is the non-dimensional version of the Eq. (11), rewritten in a form suggested by Williams (1986). The independent non-dimensional parameters appearing in the equations are

$$Re = \frac{\rho_0^* c_0^* L^*}{\mu_0^*}, \qquad Pr = \frac{\mu^* c_P^*}{\lambda^*}, \qquad Sc_F = \frac{\mu^*}{\rho^* D_F^*}, \qquad Sc_O = \frac{\mu^*}{\rho^* D_O^*},$$

where μ^* is dynamic viscosity, λ^* is thermal conductivity, and D_F^* and D_O^* are fuel and oxidizer diffusivities respectively. It is assumed that the Prandtl number Pr and the Schmidt numbers Sc_F and Sc_O are constant throughout the flow.

The initial conditions are given by

$$\rho(x_1, x_2, 0) = 1, \tag{14a}$$

$$u_1(x_1, x_2, 0) = -\sum_{i=1}^{2}\frac{\Lambda_i}{\sigma_i^2}(x_2 - x_{2,i})\exp\left(-\frac{(x_1-x_{1,i})^2 + (x_2-x_{2,i})^2}{\sigma_i^2}\right), \tag{14b}$$

$$u_2(x_1, x_2, 0) = \sum_{i=1}^{2}\frac{\Lambda_i}{\sigma_i^2}(x_1 - x_{1,i})\exp\left(-\frac{(x_1-x_{1,i})^2 + (x_2-x_{2,i})^2}{\sigma_i^2}\right), \tag{14c}$$

$$T(x_1, x_2, 0) = \frac{1}{\gamma-1} \tag{14d}$$

$$Y_F(x_1, x_2, 0) = Y_{F,\infty}\left(\frac{1}{2} - \frac{1}{2}\mathrm{erf}\left(\frac{x_1}{\Delta}\right)\right), \tag{14e}$$

$$Y_O(x_1, x_2, 0) = Y_{O,\infty}\left(\frac{1}{2} + \frac{1}{2}\mathrm{erf}\left(\frac{x_1}{\Delta}\right)\right), \tag{14e}$$

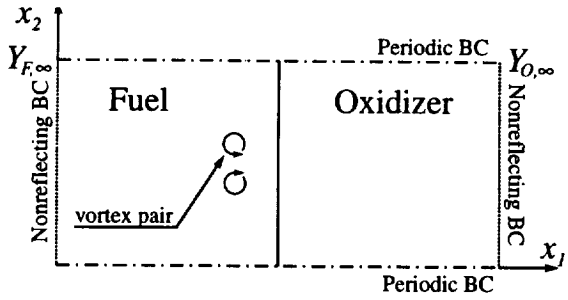

FIGURE 1. Schematic of the model problem and the computational boundary conditions.

where Λ_i $(i = 1,2)$ are vortex intensities, $(x_{1,i}, x_{2,i})$ $(i = 1,2)$ are initial vortex locations, and $\mathrm{erf}(x) = 2\pi^{-1/2} \int_0^x e^{-\xi^2} d\xi$. The domain is chosen to be $[-L_{x_1}, L_{x_1}] \times [-L_{x_2}, L_{x_2}]$, and that the initial flame is located at $x_1 = 0$. The boundary conditions are non-reflecting outflow boundary conditions of Poinsot and Lele (1992) in x_1 direction and periodic boundary conditions in x_2 direction. A schematic of the model problem with initial and boundary conditions is shown in Fig. 1.

2.4 Results

The model problem is solved using the dynamically adaptive wavelet collocation algorithm described in Section 2.2. The tensor product of two one-dimensional correlation functions of Daubechies scaling function of order five (Beylkin & Saito, 1993) was used to construct $\psi(\mathbf{x})$. The threshold parameter is set to $\epsilon = 5 \times 10^{-3}$. The adaptation of the computational grid is based on the analysis of coefficients associated with all six dependent variables of Eqs. (12) and the chemical source term $\dot{w}_e$. The irregular grid $\mathcal{G}^t_{\geq}$ of wavelet collocation points is constructed as a union of irregular grids corresponding to each dependent variable and the chemical source term. In the present work we use the 5th order Gear implicit time integration algorithm implemented in the IMSL routine IVPAG. The time integration step is chosen so that the truncation error associated with the time integration algorithm is less than ϵ.

The problem is solved for the following set of parameters:

$$
\begin{aligned}
&Re = 10^2, \quad Pr = 1, \quad Sc_F = Sc_O = 1, \quad \gamma = 1.4, \\
&\alpha = 0.6, \quad \beta = 4, \quad \Xi = 10^3, \quad \Phi = 1, \quad Y_{F,\infty} = Y_{O,\infty} = 1, \\
&L_{x_1} = 4, \quad L_{x_2} = 1, \quad \Delta = 5 \times 10^{-2}, \quad \Lambda_1 = -\Lambda_2 = 5 \times 10^{-2}, \quad \sigma_1 = \sigma_2 = 0.15, \\
&(x_{1,1}, x_{2,1}) = (-0.25, 0.2), \quad (x_{1,2}, x_{2,2}) = (-0.25, -0.2).
\end{aligned}
$$

These parameters were chosen such that the mixing layer was initially cold; the diffusion thickness Δ was initially very thin so that the reaction zone would have been difficult to resolve with a conventional numerical method. The vortex intensities and locations were chosen to mimic turbulent eddies. The chemical parameters were chosen such that the ignition delay time would be relatively short, but the layer would still be affected by the strain induced by the vortices prior to ignition.

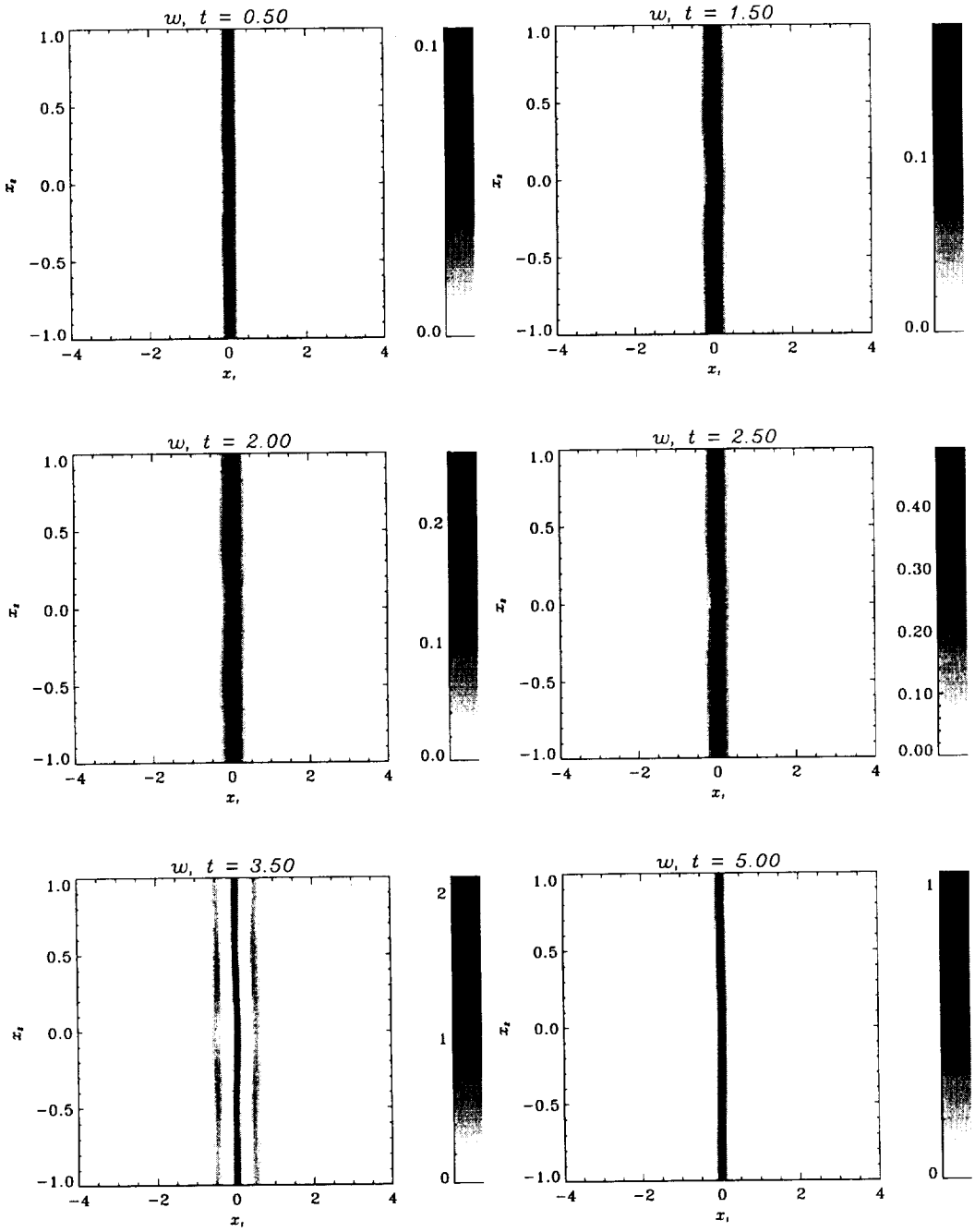

FIGURE 2. Reaction rate $\dot{w}_e$ evolution.

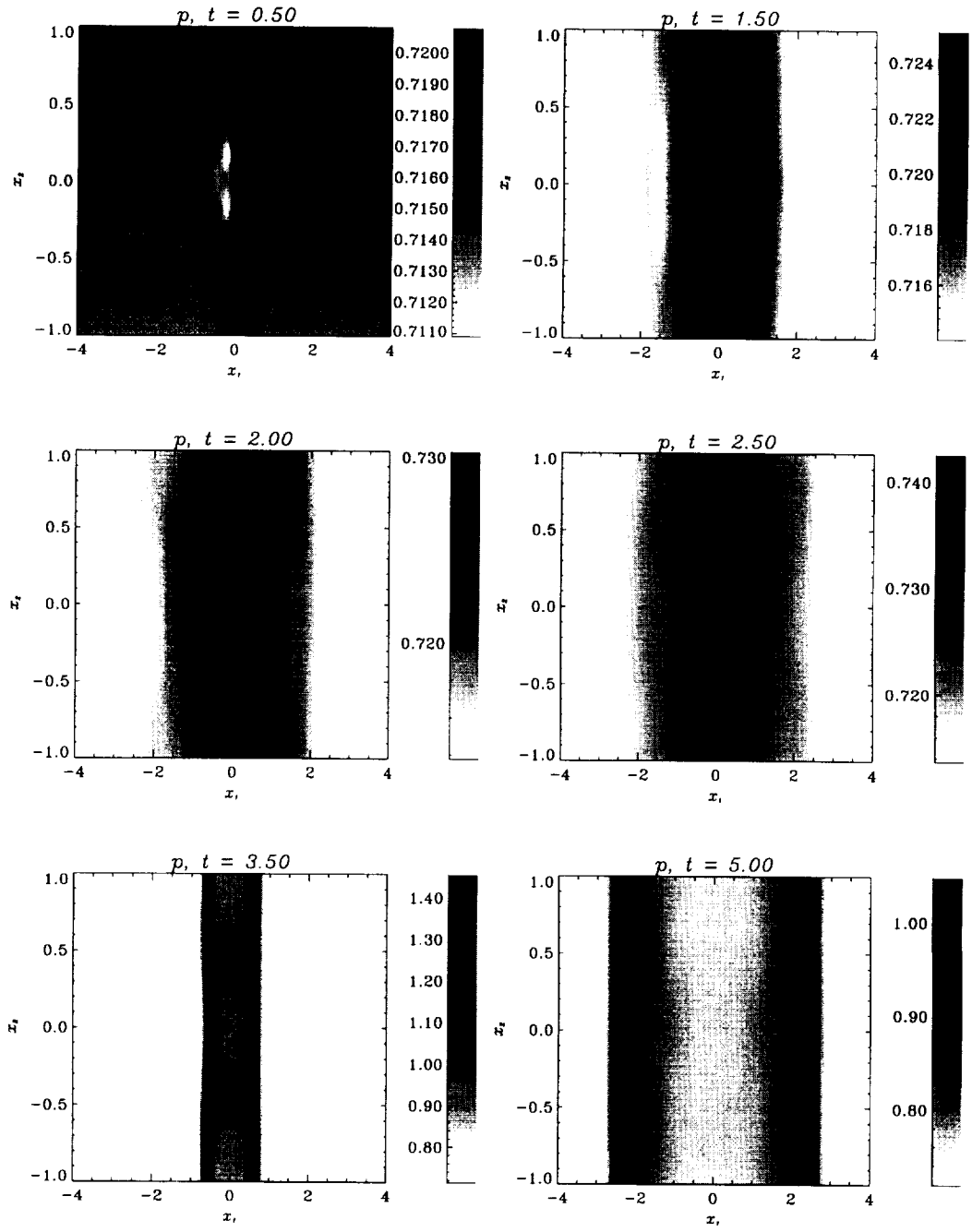

FIGURE 3. Pressure evolution.

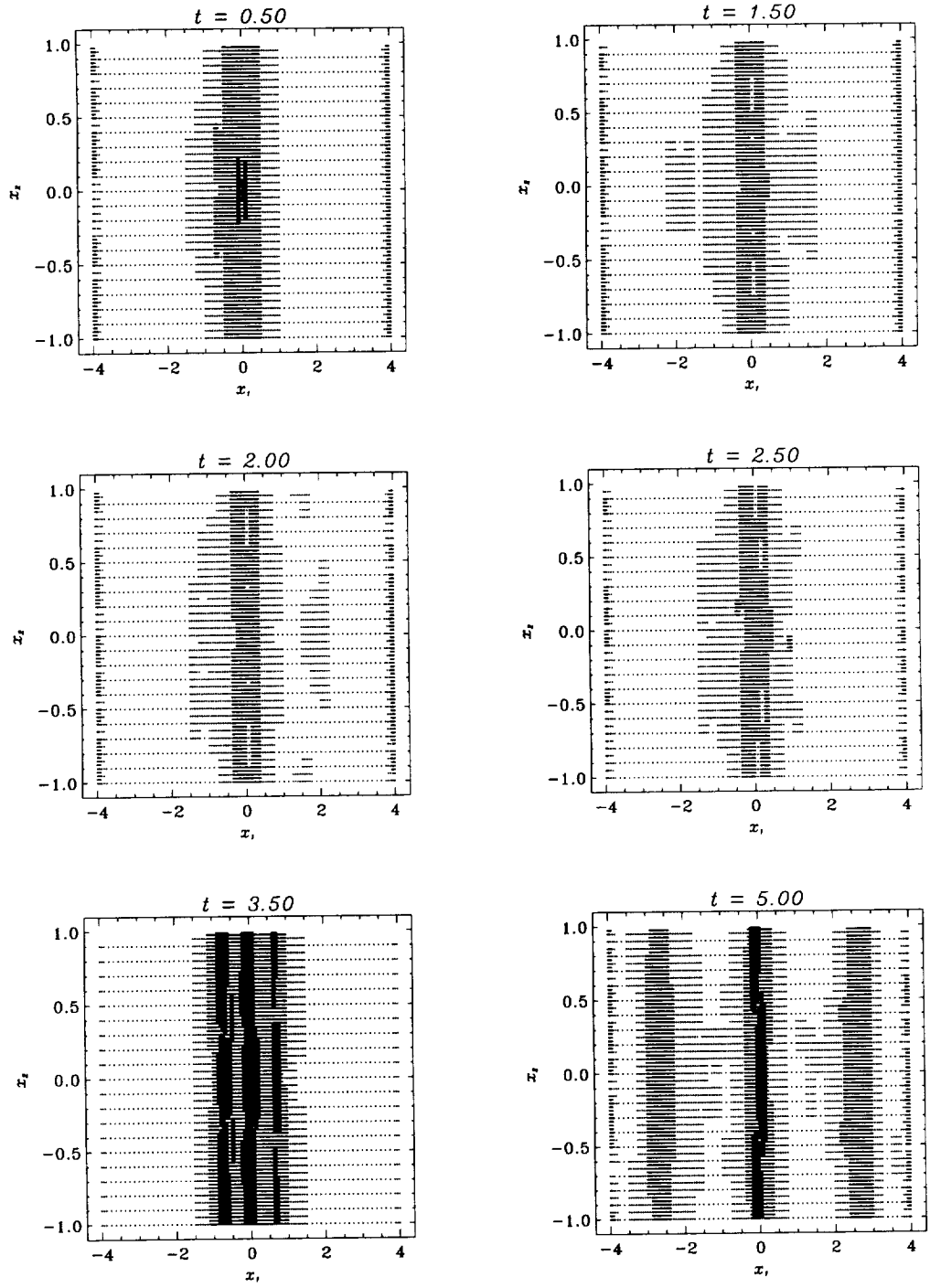

FIGURE 4. Evolution of computational grid.

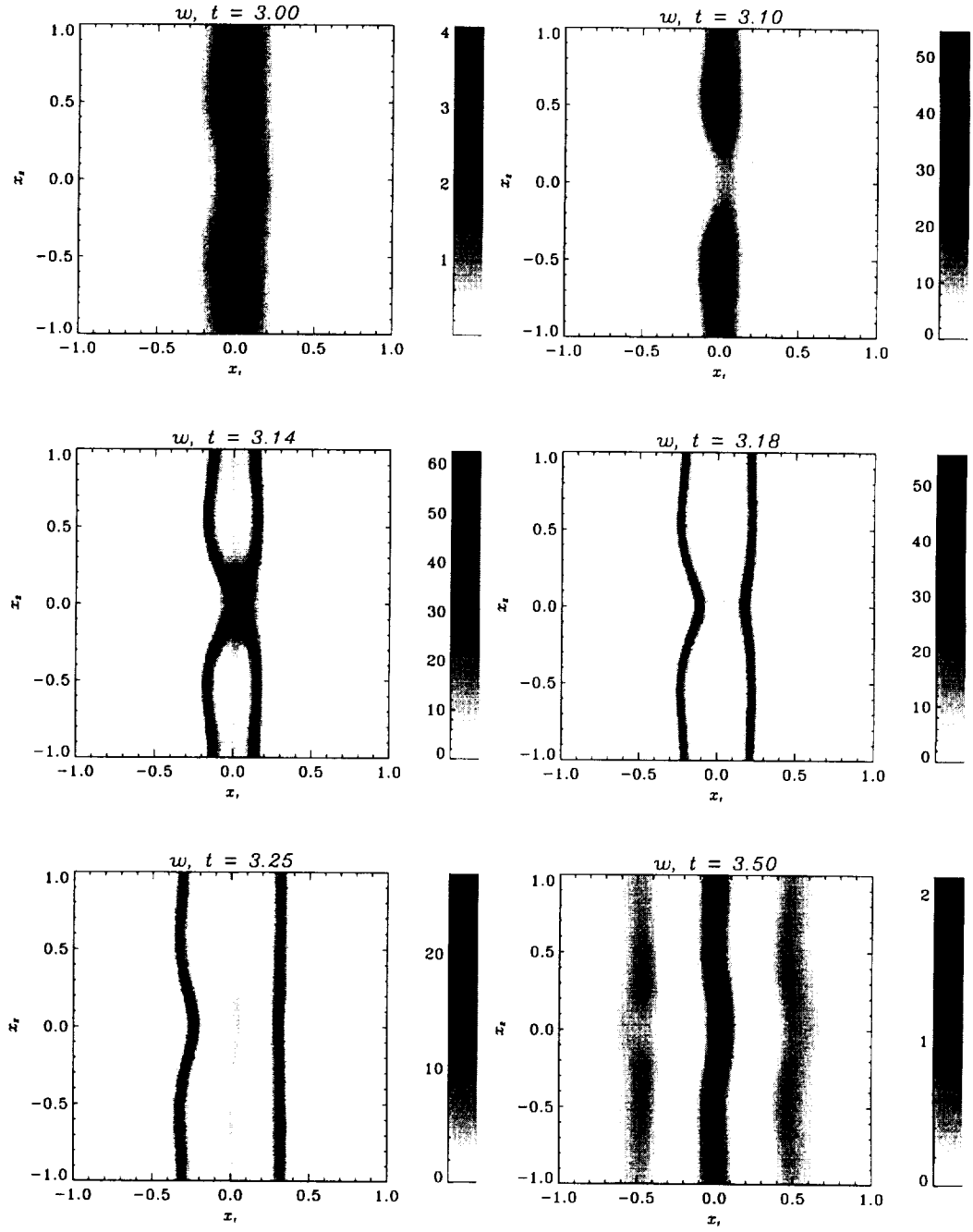

FIGURE 5. Zoomed-in view of the reaction rate $\dot{w}_e$ during ignition.

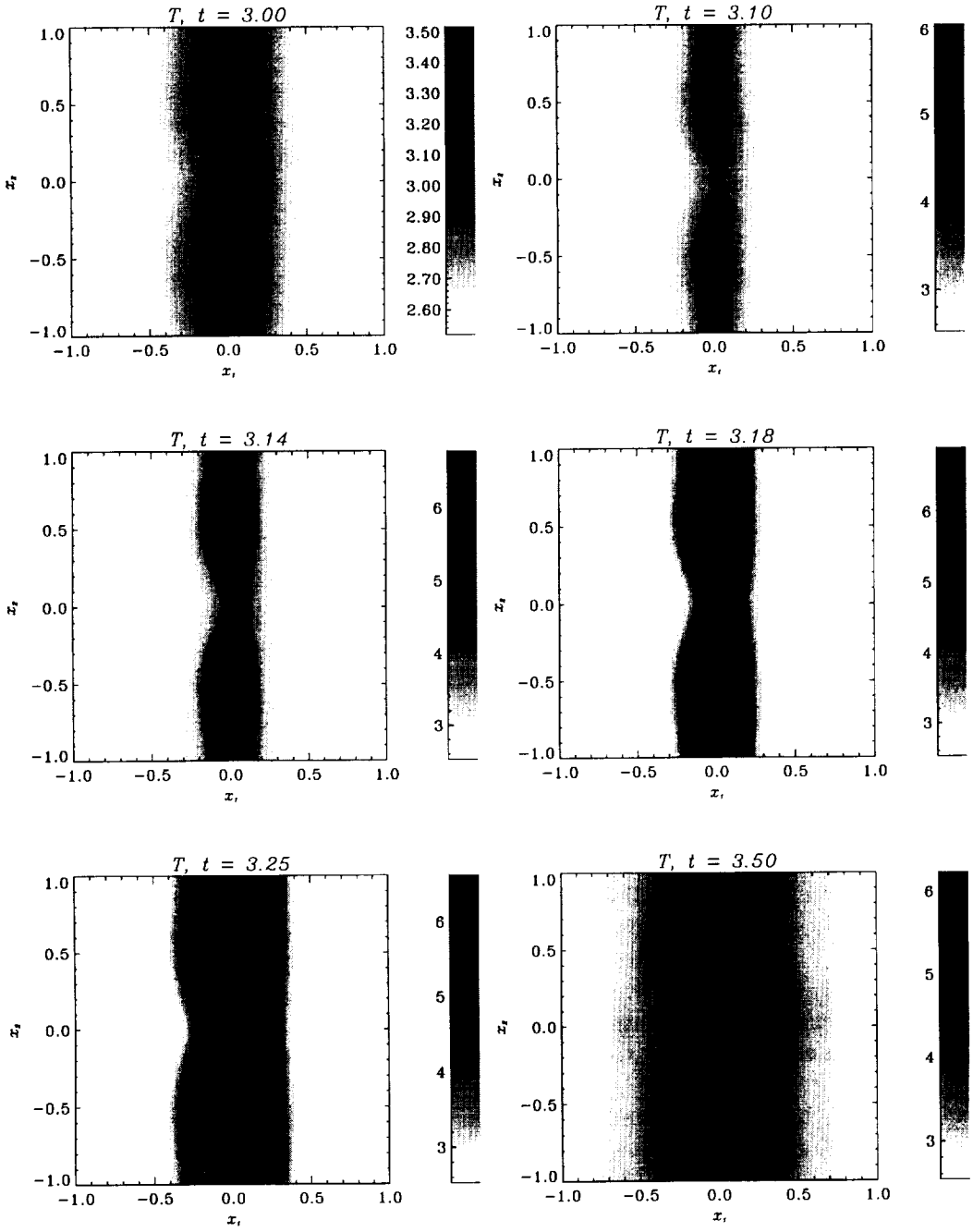

FIGURE 6. Zoomed-in view of the temperature during ignition.

In Fig. 2, the reaction rate in the entire domain is shown at several times. The autoignition of the mixing layer occurs between $t = 2.50$ and $t = 3.50$ acoustic time units. At $t = 3.50$, the ignited diffusion flame at $x = 0$ is clear, as are two premixed flames propagating away from the diffusion flame. It is clear that the reaction zone associated with the diffusion flame is very narrow and requires a very fine grid for adequate resolution. The reaction zones associated with the two premixed flames are quite narrow, and to adequately resolve these would also require a fine grid; the additional challenge here is that the reacting fronts are propagating, so refining the mesh adaptively provides an enormous computational savings. In these figures the affect of the vortex pair appears to be almost negligible; the mixing layer still appears to be effectively one-dimensional.

The pressure associated with the autoignition process is shown in Fig. 3. At $t = 0.50$, the hydrodynamic pressure field induced by the vortex pair is still apparent. This is overwhelmed by the enormous pressure wave associated with the autoignition process by $t = 1.50$ and thereafter. At the later times, two shock waves associated with the premixed flames are clearly evident, indicating that these premixed fronts are weak detonations—weak because, while they are initiated in nearly stoichiometric gas, they rapidly burn into the extremes of flammability on either side of the diffusion flame such that the heat release decreases as the flames propagate and the strength of the associated shock wave goes down. The steep gradients in the pressure field also pose a challenge in terms of grid resolution.

Fig. 4 shows the computational grid for each of the times shown in Figs. 2 and 3. At $t = 3.50$ and $t = 5.00$, it is clear that the grid has adapted to resolve the steep gradients in the reaction rate and pressure fields.

Fig. 5 shows a zoomed-in view of the reaction rate during the autoignition event, and Fig. 6 shows a zoomed-in view of the temperature. During autoignition, the peak reaction rate is more than an order of magnitude greater than either before or after autoignition. The affect of the vortex pair on the mixing layer is apparent. The vortex pair drifts towards the interface, causing strain in the middle of the mixing layer; this in turn results in a non-uniform reaction rate along the interface. In particular, the vortex-flame interaction results in the appearance of two hot spots which eventually lead to autoignition. Since the reaction rate increases with the temperature, the flame ignites locally at these spots. This process is similar to that seen by Mastorakos et al. (1997) in two-dimensional turbulent simulations of autoignition. The ignition process creates two triple-flame structures, similar in character to those studied by Ruetsch *et al.* (1995), which propagate rapidly towards each other and meet at $t \approx 3.14$. After that time the triple-flames form into the diffusion flame and two premixed detonation waves traveling away from it.

Figure 7 shows the time evolution of the total number of collocation points or, effectively, active wavelets as a function of time. We see that the number of grid points increased at $t \approx 3$ when the autoignition event occurred. As the detonation waves traveled away from the diffusion flame, their intensity diminished; this resulted in a decrease of the number of grid points.

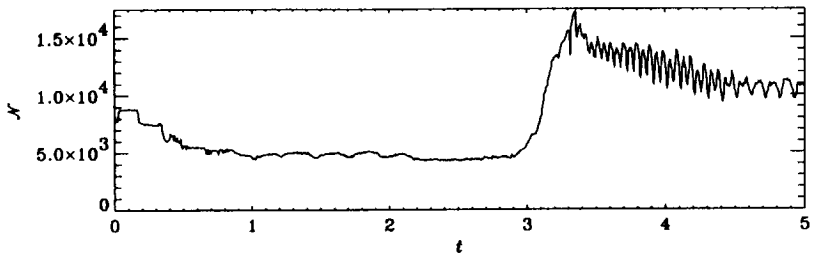

FIGURE 7. Total number of active wavelets (collocation points) as a function of time.

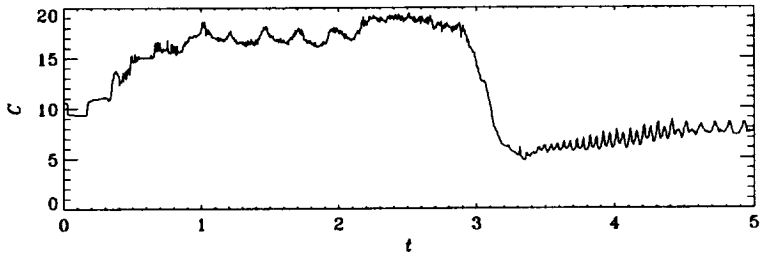

FIGURE 8. Time evolution of the compression ratio $C = N^J/\mathcal{N}$.

The efficiency of the grid adaptation can be demonstrated by studying the compression coefficient $C = N^J/\mathcal{N}$ which measures the ratio of the number of grid points needed in non-adaptive computations N^J (J is the maximum level of resolution used in the computations) and the actual number of grid points used in the calculations $\mathcal{N}$. In the present calculations we used up to 5 levels of resolution with an effective resolution (the resolution of the non-adaptive computational grid needed to perform the same calculation) of 513×160 grid points. The time evolution of the compression coefficient is shown in Fig. 8. We see a drop in the compression coefficient at $t \approx 3$; the compression coefficient decreases approximately three times, which is explained by the appearance of the triple flame structure.

3. Future plans

In spite of the progress made thus far, there are still features of the algorithm which can be improved upon. In the future we plan to improve algorithm in the following areas:

1. To extend the existing code to three dimensions.
2. To develop an efficient implicit time integration algorithm which takes advantage of the multilevel character of the wavelet approximation.
3. To extend the method to complex geometries, which needs to be done if one wants to attack problems of more general relevance.
4. To adapt the algorithm for efficient use on parallel computers.

In the short term, we plan to incorporate turbulence into the problem. The ability to resolve local flame structures and pressure waves without a drastic increase in

the number of grid points should enable us to study turbulent flames at a Reynolds number higher than currently possible using conventional numerical algorithms such as those used by Bushe *et al.* (1997, 1998). As the numerical algorithm becomes more computationally efficient, we will increase the complexity of the problem in terms of incorporating a more realistic chemical kinetic mechanism and increasing the Reynolds number.

REFERENCES

BEYLKIN, G. & N. SAITO 1993 Wavelets, their autocorrelation function and multidimensional representation of signals. in *Proceedings of SPIE - The International Society of Optical Engineering.* **LB26,** Int. Soc. for Optical Engineering, Bellingham.

BUSHE, W. K., BILGER, R. W. AND RUETSCH, G. R. 1997 Incorporating realistic chemistry into direct numerical simulations of turbulent non-premixed combustion. *Annual Research Briefs,* Center for Turbulence Research, NASA Ames/Stanford Univ., 195-211.

BUSHE, W. K., BILGER, R. W. AND RUETSCH, G. R. 1998 Direct Numerical Simulation of turbulent non-premixed combustion with realistic chemistry. *Annual Research Briefs,* Center for Turbulence Research, NASA Ames/Stanford Univ., (in this volume).

DAUBECHIES, I. 1992 *Ten Lectures on Wavelets*, CBMS-NSF Series in Applied Mathematics, SIAM, Philadelphia.

MASTORAKOS, E., BARITAUD, T. A. & POINSOT, T. J. 1997 Numerical simulations of autoignition in turbulent mixing flows. *Combust. Flame.* **109,** 198-223.

MEYER, Y. 1990 *Ondelettes et opérateurs*, Hermann, Paris.

POINSOT, T. & LELE, S. 1992 Boundary conditions for direct simulations of compressible viscous flows. *J. Comp. Phys.* **101,** 104-129.

RUETSCH, G. R., VERVISCH, L., AND LIÑÁN, A. 1995 Effects of heat release on triple flames. *Phys. Fluids.* **7,** 1447-1454.

RUETSCH, G. R. 1998 *Private Communication.*

VASILYEV, O. V. 1996 Multilevel Wavelet Collocation Methods for Solving Partial Differential Equations. *Ph.D. Thesis,* University of Notre Dame.

VASILYEV, O. V. & PAOLUCCI, S. 1996 A Dynamically Adaptive Multilevel Wavelet Collocation Method for Solving Partial Differential Equations in a Finite Domain. *J. Comp. Phys.* **125,** 498-512.

VASILYEV, O. V. & PAOLUCCI, S. 1997 A Fast Adaptive Wavelet Collocation Algorithm for Multidimensional PDEs. *J. Comp. Phys.* **138,** 16-56.

VERVISCH, L. & POINSOT, T. 1998 Direct Numerical-Simulation of Non-Premixed Turbulent Flames. *Ann. Rev. Fluid Mech.* **30,** 655-691.

WILLIAMS, F. A. 1986 *Combustion Theory*, Addison-Wesley, NY.

2D simulations of Hall thrusters

By Eduardo Fernandez, Mark Cappelli, AND Krishnan Mahesh

1. Motivation and objectives

Closed-Drift (Hall) thrusters constitute an important electric propulsion technology for certain applications requiring low thrust levels, e.g. satellite station keeping and orbit transfer (Gulczinski and Spores, 1996). The thrust in Hall thrusters is generated by ions being accelerated through an annular plasma by the electric field set up between an anode and a cathode. This electric field is strongly coupled to an externally applied radial magnetic field which typically localizes the electric field near the channel exit. The ions are generated through electron-impact ionization of Xenon neutrals. Due to their large inertia, the ions are not magnetized, and stream out of the device without experiencing very many collisions. The electrons, on the other hand, collide with the background neutrals as they migrate to the anode across the magnetic field. The cathode is located a few centimeters downstream of the channel exit and provides enough electrons to supply much of the discharge current, ionize the incoming neutrals, and neutralize the beam of exiting ions.

While the overall operational characteristics of Hall thrusters are understood, some key issues remain to be resolved. In particular, the relationship between the various types of fluctuations in these devices and the overall engine efficiency needs to be determined. Electron conductivity is critical in the operation of Hall thrusters since it impacts the ionization of neutrals and the potential drop which accelerates the resulting ions. However, it's expected (classical) value, arising from electron-neutral and Coulomb collisions, is far too low to account for the measured electron current (Morozov *et al.* 1972). Two mechanisms have been proposed to account for the enhanced electron transport (often termed 'anomalous' in the plasma physics literature): electron wall interactions and azimuthal fluctuations in electron density (Morozov *et al.* 1972).

It is important that electron diffusion be accurately modeled if the essential physics of the thruster are to be represented by one- or two-dimensional computations. State of the art approaches (e.g. Fife *et al.* 1997) assume that the electron mobility is given by the 'Bohm model':

$$\mu = \frac{1}{16B} \tag{1}$$

where μ is the electron mobility and B is the magnetic field. It is known from experimental work that this coefficient is only approximate. 'Bohm diffusion' is commonly used to refer to diffusion which *scales* as $\frac{1}{B}$ where the scaling coefficient is arbitrary within a factor of 2 or 3. Early experimental (Janes and Lowder, 1960) and theoretical (Yoshikawa and Rose, 1962) work has shown that this diffusion arises from the correlation between fluctuations in the azimuthal electric potential

and electron density. Given a certain phase between potential and density, the diffusion coefficient can be cast in terms of the ratio of the rms level of electron density to the mean electron density. One of the objectives of this work are to evaluate the modeling of electron diffusion using Eq. (1) and develop alternative approaches.

Another issue of interest is the experimentally observed emergence of a virulent ionization instability in the current saturation part of the I-V curve for these engines (Meezan *et al.*, 1998). Unlike the azimuthal drift wave fluctuations associated with axial electron transport, the ionization instability is believed to be deleterious to engine performance. The more one pushes the engine into the saturation region, the larger the amplitudes of these modes (rms levels on the order of the mean are not uncommon). This instability appears to be caused by the non-uniform ionization of the neutral Xenon atoms. These atoms, emerging from the back of the thruster, enter a region (ionization zone) in which they are ionized upon colliding with the electrons. Once ionized, the resulting ions are quickly accelerated, thus creating a void of both neutral and charged particles. As neutrals replenish the empty region, ionization takes place and the sequence repeats itself. Since the ion velocity is so much greater than that of the neutrals, the relevant timescale of the instability should be proportional to the velocity of the incoming neutral atoms. However, theoretical work (Fife *et al.*, 1997) suggests that the mode frequency is, in fact, proportional to the geometric mean of the neutral and ion velocity. That theory implies that as the ion velocity increases, it actually dominates the mode frequency. The heuristic picture above, however, suggests that as the ion velocity increases it progressively decouples from the mode frequency. One of the objectives of this work is to test the scaling of mode frequency with neutral velocity.

2. Accomplishments

2.1 Approach

Our first step has been to perform two-dimensional hybrid simulations where the electron mobility is modeled assuming Bohm diffusion (Fife 1995). The governing equations are those used by Fife, however, details such as the computational grid, integration scheme, treatment of nonlinear terms, and tracking of heavy PIC particles in non-uniform grids are different.

The thruster modeled in our work is the SPT 100 Russian thruster for which a lot of experimental data exists. The computational geometry is as that used by Fife: it covers the channel and part of the plume.

Figure 1 shows a schematic of the computational geometry. A non-uniform orthogonal grid is used to span the thruster annular channel and part of the plume. The externally imposed magnetic field is obtained by solving a Laplace equation for the magnetic potential, having specified the geometry of the magnetic poles and assumed infinite permeability for the pole pieces. The algorithm is a mixture of particle and fluid approaches. The electrons are treated as a fluid since their effective mean-free-path is their gyro-radius. The ions, however, typically leave the channel without colliding with other particles. Also, experiments show that the ion velocity

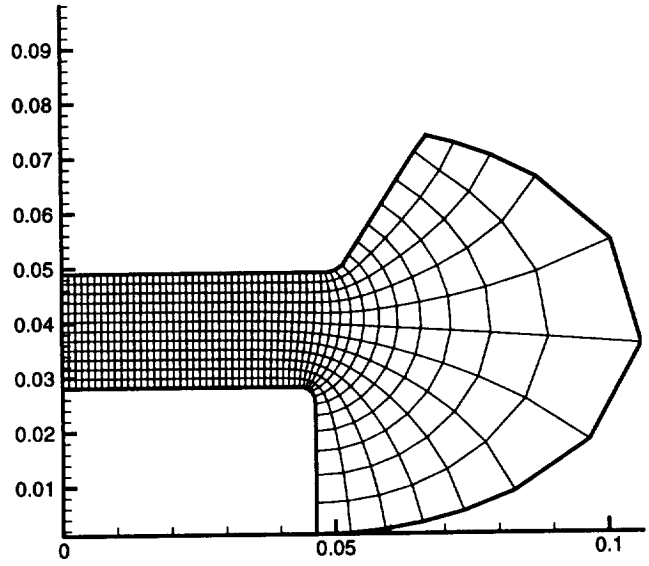

FIGURE 1. Schematic of the computational geometry.

distributions vary markedly from Maxwellian. Therefore, the ions are treated as particles. The neutrals are also treated as particles since they, like the ions, have mean-free-paths longer than the length of the thruster. The details of the governing equations are given in Fife (1995); only a short summary is provided here.

The electron momentum equation perpendicular to the magnetic field (mostly in the axial direction since B is mostly in the radial direction) is given in terms of a drift-diffusion equation, representing a balance between electric, pressure, and drag forces. This form neglects inertial terms which are small in the Hall thruster. The equation can be cast in terms of an electron mobility and diffusion coefficient, representing the electron momentum response to electric and pressure forces applied in the axial direction in the presence of collisions; i.e.,

$$n_e(u_{e\hat{n}} - u_{i\hat{n}}) = -n_e\mu(E_{\hat{n}} + \frac{kT_e}{en_e}\frac{\partial n_e}{\partial \hat{n}} + \frac{k}{e}\frac{\partial T_e}{\partial \hat{n}}) \tag{2}$$

However, there is an added contribution to the axial flux which does not arise from axial electric or pressure forces, but rather from an $E \times B$ drift (azimuthal electric field crossed with radial magnetic field). This component is thus given by nE_θ/B. Although there is no mean E_θ, this term is not zero if there are correlated n and E_θ fluctuations. A two-dimensional approach has no azimuthal direction and, therefore, cannot capture this component. The effect of this term is, therefore, included through an effective mobility and diffusion. So far, a $1/B$ diffusion coefficient has

been used. Work is underway to incorporate a more realistic, axially dependent coefficient. Parallel to the magnetic field, the electric and pressure forces balance each other, yielding a Boltzman relation.

$$\phi = \frac{kT_e}{e} ln(n_e) + \phi^* \cdot \tag{3}$$

with the electric field given by $E = -\nabla\phi$.

An electron temperature equation is also solved. Ionization of neutrals is a strong function of electron temperature, which makes the electron temperature equation an important part of the model. The equation is given by:

$$\frac{\partial}{\partial t}(\frac{3}{2} n_e k T_e) + \frac{\partial}{\partial \hat{n}} \left(\frac{5}{2} n_e u_{e\hat{n}} k T_e - K \frac{\partial T_e}{\partial \hat{n}} \right) = -n_e n_n \zeta(T_e) \varphi(T_e) E_i + j_{e\hat{n}} E_{\hat{n}} \tag{4}$$

where $\zeta(T_e)$, $\varphi(T_e)$, and K are the ionization rate parameter, the ion production cost, and the thermal diffusivity respectively. The functions $\zeta(T_e)$ and $\varphi(T_e)$ have exponential terms and thus are highly nonlinear. These terms are evolved in their original forms and are not linearized, unlike Fife (1995). As in the momentum equation, the diffusivity can be expected to be anomalous. Presently, a simple (constant) value is taken as described by Lentz (1992). The terms on the right-hand side of Eq. (4) are the ohmic heating source term and the ionization-induced sink term. Since thermal conductivity parallel along field lines is much higher than across field lines, magnetic streamlines are assumed to be isothermal. We use this assumption and solve the temperature equation along magnetic stream lines as done by Fife (1995).

Electron continuity is enforced via a total discharge current conservation constraint. Since the plasma is assumed to be quasineutral, charge cannot build up anywhere in the device. Combining electron and ion continuity equations and integrating (along magnetic field lines) yields an equation stating discharge current conservation. This is given by:

$$I_a = \int_A n_e (u_{i\hat{n}} - u_{e\hat{n}}) dS \tag{5}$$

A fourth order Runge-Kutta scheme is used to time advance the temperature equation – other variables such as electron velocity and electric potential are given by algebraic expressions once the temperature has been obtained. The boundary conditions on the temperature are Dirichlet at the cathode and Neumann at the anode. For the electric potential Dirichlet boundary conditions are specified at the cathode and anode.

The boundary condition at the anode can pose problems. Several magnetic streamlines intersect the anode. The issue arises as to what streamline to choose to impose the boundary condition. As far as the physics is concerned, this region is clearly not being accurately modeled since the sheath is not being resolved. The

model equations already imply this: Poisson's equation is not solved, but rather quasineutrality is imposed. The concern is, therefore, not whether the the region close to the anode is accurately modeled, but whether the boundary condition causes numerical problems. The situation is most problematic in the transient period of the simulation when the particles and fields have not yet established an equilibrium. Large oscillations at the anode in temperature and potential, which turn into large oscillations in ion velocity and plasma density, develop and are convected downstream. If severe enough, these oscillations can terminate the simulation. These anode oscillations are also very problematic when one changes the diffusion coefficient.

As stated before, the ions and neutrals are evolved with a PIC approach. Since quasineutrality is enforced, determining the ion density by interpolating to the grid points also determines the electron density. Ion-neutral elastic, and charge exchange collisions are ignored since their cross sections are small. Therefore, a neutral changes its velocity only when it encounters a wall, in which case it is repelled back in a random direction. The only force acting on the ions is the electric field (the magnetic force is ignored due to the large ion inertia). When an ion strikes the wall, it recombines to form a neutral which is injected back in the domain at a random angle. Since the thruster has regions with sharp contrast of plasma and neutral density, the ion or neutral superparticle masses are not identical. Also, the algorithm uses a fractional time-advance step method. The fast time scale in the system is tied to electron dynamics whereas neutral and ion motion is much slower. In view of this fact, the neutrals and ions are time advanced every so many electron time steps. A standard leap frog scheme is used for the time advancement in the PIC approach.

2.2 Results

2.2.1 Evaluation of Bohm diffusion

The Bohm diffusion model for electron transport (Fife 1995) is evaluated in this section. Our simulations show that for the SPT configuration, the use of Bohm diffusion, as given by Eq. (1), yields electron density and ionization profiles that peaks too far upstream as compared to experimental data, while the temperature and electric field actually peaks downstream of the channel exit. Experimentally it is observed that all the above profiles tend to peak roughly at the same axial location, at the exhaust of the channel (Bishaev and Kim 1972).

This discrepancy is interpreted as being due to a diffusion coefficient which is too large: the larger electron current produces too much ionization upstream, thereby quickly depleting the neutral density. This results in ionization-induced temperature losses downstream that are low while the temperature source term is still high through the large electric field. Consequently, the electron temperature peaks too far downstream.

It is instructive to note that that a 1D version of the numerical model which used a $\frac{1}{16B}$ diffusion coefficient was previously used by Lentz (1992) to simulate a short

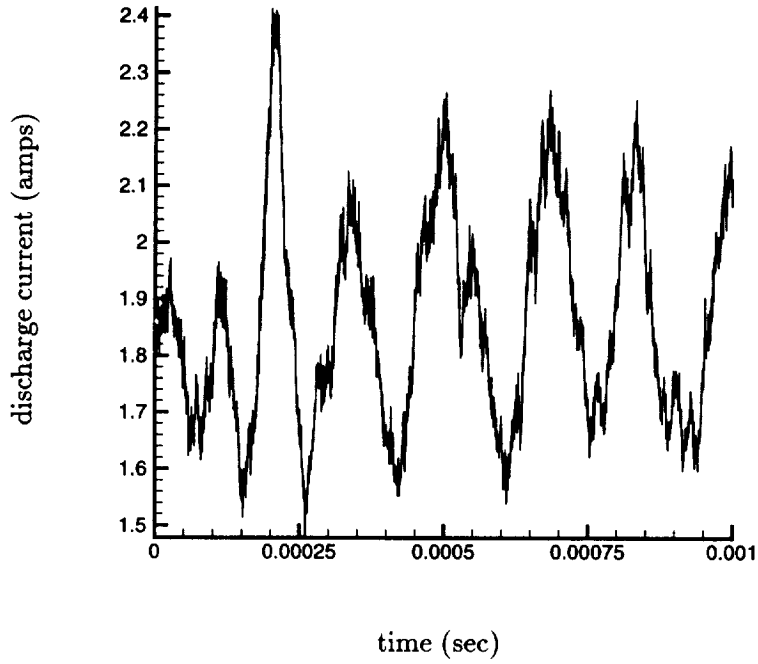

FIGURE 2. Time history of the discharge current in a simulation with discharge voltage of 200 volts and mass flow rate of 3mg/s.

channel, high magnetic field Japanese thruster. In that case, the simulated and experimental profiles were in better agreement. This suggests that different thrusters are likely to have different fluctuation characteristics and electron transport, and that the often quoted $\frac{1}{16B}$ is not likely to apply to every thruster. In fact, a recent study aimed at modeling an American-designed thruster showed that the model reproduces the overall characteristics with a mobility of $\frac{.25}{16B}$ (Szabo, *et al.* 1998). Even if it applies to a given thruster, it's not likely that a fixed $\frac{1}{16B}$ value would be successful as one varied the operational parameters since the fluctuations themselves are a strong function of the current-voltage operational point. The relative importance of fluctuation-induced electron transport versus collisional transport depends on the relative value of the gyro-frequency and collisional frequency. While in the Japanese thruster the electron gyro-frequency was much larger than the collision frequency throughout the channel (due to the broad, large magnetic field), in the SPT these frequencies are not disparate close to the anode. However, at the channel exit the electron gyro-frequency is more than two orders of magnitude larger than the collision frequency. Therefore, one expects the diffusion to be a function of axial position.

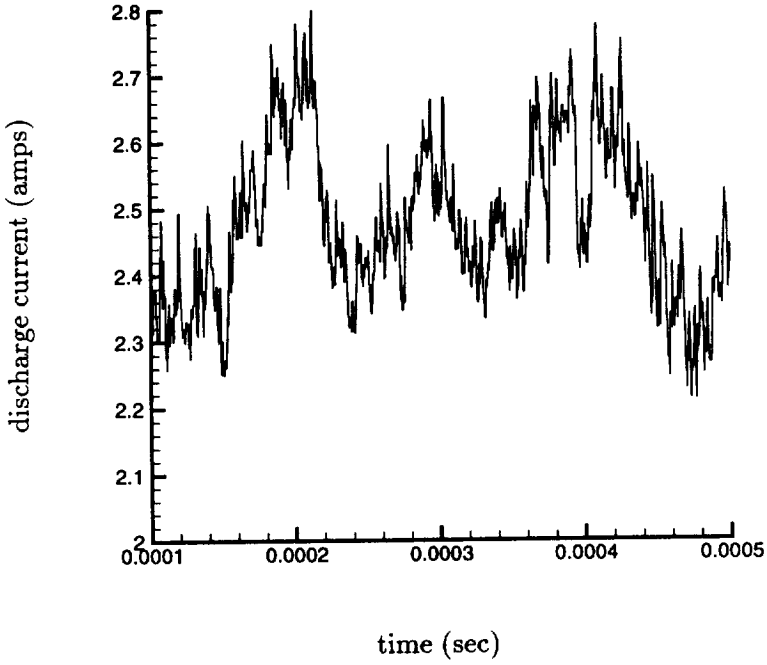

FIGURE 3. Time history of the discharge current in a simulation with discharge voltage of 200 volts and mass flow rate of 3mg/s. The difference from Fig. 2 is the wall ion-neutral recombination mechanism.

2.2.2 Importance of heavy particle-wall interactions

The importance of electron-wall interactions has been discussed in the literature. Our simulations indicate that wall interactions involving heavy particle collisions also have a large influence on overall discharge dynamics. When ions strike the walls, they recombine to form neutrals. If the recombined neutrals have large kinetic energy they have a greater chance of leaving the channel before being ionized. This will tend to lower the discharge current for a given discharge voltage. The converse hold as well.

Figure 3 shows the time history of the discharge current for the same parameters as those of Fig. 2, but with different heavy particle-wall interaction. In Fig. 2, ions that strike the walls recombine to form neutrals which emerge at random direction with the ion's velocity. In Fig. 3, the recombined neutrals are injected back with random directions with the inflow neutral velocity. We see that the effect on discharge current is significant. The average discharge current is 2.5 amps as compared to the experimentally measured 3.1 amps. Given the strong sensitivity of the results to the chosen diffusion coefficient, it is not that meaningful at this point to comment on the quantitative difference between simulation and experimental results. The effect of the heavy particle wall interaction is also seen on plasma

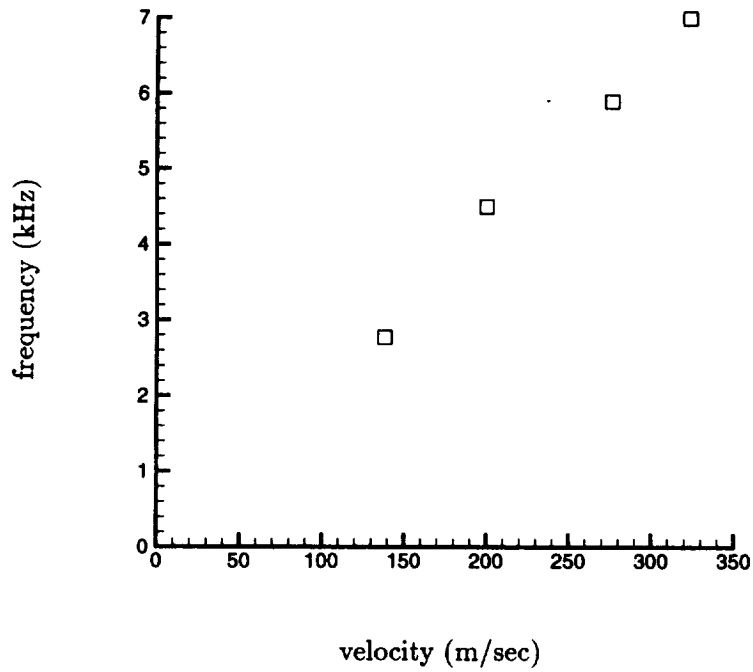

FIGURE 4. Scaling of mode frequency with neutral velocity.

density: Fig. 3 corresponds to a higher plasma density than Fig. 2. The reason for the rise in discharge current (or plasma density) in the second case is that the neutrals coming off collisions with the walls, having lower speed, have a larger chance of being ionized. In reality, the speed of the neutrals after the collision will depend on the wall temperature as well.

2.2.3 Scaling of low frequency oscillations

Recall that characterizing the strong, ionization instability is of special interest for Hall thrusters as it sets limits to the operation of these engines. Figure 2 shows the time history of the discharge current for a simulation with discharge voltage of 200 volts, mass flow rate of 3mg/s, and peak magnetic field of 180 gauss. One observes that the steady state achieved is non-stationary, with large 7 kHz oscillations. This mode corresponds to the ionization instability described above. Superimposed on the dominant mode lie higher frequency components. The discharge current oscillations are about 20 per cent of their mean values. A simulation run with a flow rate of 5mg/s but with otherwise same parameters (including the same neutral velocity at the inflow) gives oscillations of about 60 per cent. Similarly, as one increases the voltage in the current saturation portion of the current-voltage curve, the rms oscillations are expected to increase. While high mass flow rates and high voltages are desirable, the ionization instability becomes very virulent and can extinguish the discharge, thus setting a limit on the operation of these engines.

Fife's *et al.* (1997) analysis of the ionization instability shows that the mode frequency scales as the geometric mean on the neutral and ion velocities. However, the theory is based on a small perturbation analysis which may not apply given the large rms levels of the instability. Intuitively, one rather expects the frequency to scale linearly with the neutral velocity, especially as the ion velocity tends to be much larger than the neutral velocity. The linear relationship is, in fact, observed in Fig. 4. The parameters for the simulation are the same as those in Fig. 2. We only changed the velocity of the neutrals at the inflow, while keeping the mass flow rate constant. The inverse of the slope of the linear fit through the data points yields a length of 4.3 cm. This length should reflect the extent of the ionization region. In fact, this region in the simulation is probably only 3 cm. The characterization of the mode frequency as the neutral velocity divided by the ionization region thus appears to be only qualitatively valid in view of the simulation results. Similar simulations with other voltages and mass flow rates should be performed to better characterize this mode. In particular, the notion that this mode is non-propagating (in the axial direction) and thus acts more as a standing wave needs to be reexamined. Present simulations suggest that the peak of the ionization rate profile moves back and forth about .75 centimeters axially, which would imply that the mode in fact propagates. Further simulations are warranted in view of the fact that previous simulations have not reported or seen this effect.

3. Conclusions and future plans

Two-dimensional simulations of the Hall thruster have been performed as a first step in an ongoing computational effort at CTR. The simulations reproduce some of the overall features observed in experiments such as the strong ionization instability. A linear relationship between the frequency of the instability and the neutral velocity at the inflow is predicted.

Modeling electron transport assuming Bohm diffusion is found to be problematic. The model results strongly depend upon the Bohm diffusion coefficient and can disagree strongly with experiments if appropriate values are not chosen. The thruster dynamics are also strongly influenced by heavy particle-wall interactions. We believe that improving the form of the diffusion coefficient will greatly improve the results. The theory of Yoshikawa and Rose serves as an excellent starting point in this task: the diffusion coefficient will no longer be a fixed value, but will rather depend on fluctuation amplitudes, becoming an axially-dependent 'eddy diffusivity'. Alternatively, work is underway to extract a diffusion coefficient by fixing the location of the ionization region, which can also be obtained from the magnetic field profiles.

Preliminary numerical experiments in which a magnetic field perturbation has been superposed to the equilibrium were performed. The results (not shown) suggest that the strong discharge current oscillation can be affected by applying a perturbation of the same frequency as the natural mode. By adjusting the phase of the applied perturbation, we were able to suppress the mode for about one and one half periods before it developed again. We must caution, however, that the form of the diffusion coefficient could greatly affect these results.

Another numerical experiment to be attempted in the near future consists of injecting a small amount of xenon neutrals from the exit computational boundary. This is meant to model the experimental situation in the laboratory in which a vacuum is never completely achieved. The neutrals can potentially affect ionization rates, electron temperature, and maybe even more importantly, the ionization instability. A quantitative prediction on the effect of these neutrals on engine performance would prove to be quite useful.

REFERENCES

BISHAEV, A., & KIM, V. 1978 Local plasma properties in a Hall-current accelerator with an extended acceleration zone. *Soviet Phys.-Tech. Phys.* **23,** 1055-57.

FIFE, J. 1995 Two-dimensional hybrid particle-in-cell modeling of Hall thrusters. *S.M. thesis,* MIT.

FIFE, J., MARTINEZ-SANCHEZ, M., & SZABO, J. 1997 A numerical study of low-frequency discharge oscillations in Hall thrusters. 33rd AIAA/ASME/SAE/ASEE Joint Prop. Conf. and Exhibit.

GULCZINSKI, P., & SPORES, R. 1996 Analysis of Hall-effect thrusters and ion engines for orbit transfer missions. *AIAA-96-2973.* 32nd Joint Prop. Conf., July 1-3, Lake Buena Vista, FL.

JANES, G., & LOWDER, R. 1966 Anomalous Electron diffusion and ion acceleration in a low-density plasma. *Phys. Fluids.* **9,** 1115-1123.

LENTZ, C. 1993 Transient One dimensional numerical simulation of Hall thrusters. *S.M. thesis,* MIT.

MEEZAN, N., HARGUS, W., & CAPPELLI, M. 1998 Optical and electrostatic characterization of Hall discharge behavior. *AIAA-98-3502.* 34th AIAA/ASME/SAE/ASEE Joint Prop. Conf. and Exhibit. July 13-15, Cleveland, OH.

MOROZOV, A., ESIPCHUK, Y., TILININ, G., TROFIMOV A., SHAROV Y., & SHCHEPKIN G. 1972 Plasma accelerator with closed electron drift and extended acceleration zone. *Soviet Phys.-Techn. Phys.* **17,** 38-45.

SZABO, J., MARTINEZ-SANCHEZ, M., & MONHEISER, J. 1998 Application of 2-d hybrid PIC code to alternative Hall thruster geometries. *AIAA-98-3795.* 34th AIAA/ASME/SAE/ASEE Joint Prop. Conf. and Exhibit. July 13-15, Cleveland, OH.

YOSHIKAWA, S., & ROSE, D. J. 1962 Anomalous Diffusion of a plasma across a magnetic field. *Phys. Fluids.* **3,** 334-340.

Computation of trailing-edge noise at low Mach number using LES and acoustic analogy

By Meng Wang

1. Motivation and objectives

The present work is a continuation of the work described in the previous annual research briefs (Wang 1996, 1997). The objectives of the project are twofold: (1) to develop numerical prediction methods for trailing-edge noise, using a combination of large-eddy simulation (LES) and Lighthill's theory; and (2) to generate a reliable numerical database for the study of noise source mechanisms.

Trailing-edge aeroacoustics is of importance in both aeronautical and naval applications. It is, for example, related to airframe noise, rotor and propeller noise, and noise from underwater vehicles. When turbulent boundary layer eddies are convected past the trailing edge of a large (relative to acoustic wavelength) body, their aeroacoustic source characteristics are modified by the edge, and a more efficient source results (Ffowcs Williams & Hall 1970; Crighton & Leppington 1971). This scattering mechanism produces strong, broadband radiation to the far-field. If there is coherent vortex shedding, typically associated with blunt trailing edges and/or high angles of attack, tonal or narrowband noise is also present. In addition, the highly unsteady edge flow may cause low frequency vibration of an elastic strut and hence noise radiation. To determine the structural vibration modes, the space-time characteristics of surface-pressure fluctuations are frequently required as a forcing-function input.

The case under study corresponds to the experiment conducted by Blake (1975). The flow configuration is shown in Fig. 1. A flat strut with a circular leading edge and an asymmetrically beveled trailing-edge of 25 degrees is placed in a uniform stream at zero-degree angle of attack. The strut's chord is $C = 21.125h$ and span is $L = 23.5h$, where h is the thickness. The Reynolds number based on free-stream velocity U_∞ and the chord is 2.15×10^6. The free-stream Mach number $M = U_\infty/c_\infty \approx 0.088$. Statistical measurements of velocity and fluctuating surface pressure fields in the trailing-edge region are available for comparison with computational results. Acoustic measurements were not made in this experiment although they were made in a separate experiment (Blake & Gershfeld 1988) under different flow conditions, using trailing-edges similar but not identical to the one in Fig. 1.

In the next section we first summarize the LES of the near-field, which provides the acoustic source functions (the fluctuating Reynolds stress) as well as the space-time characteristics of surface pressure fluctuations. The statistics are fully converged and should supersede the preliminary results presented in Wang (1997). Next, we discuss the computation of the radiated far-field noise. The calculations are based on an integral-form solution to the Lighthill equation with a hard-wall Green's function (Ffowcs Williams & Hall 1970).

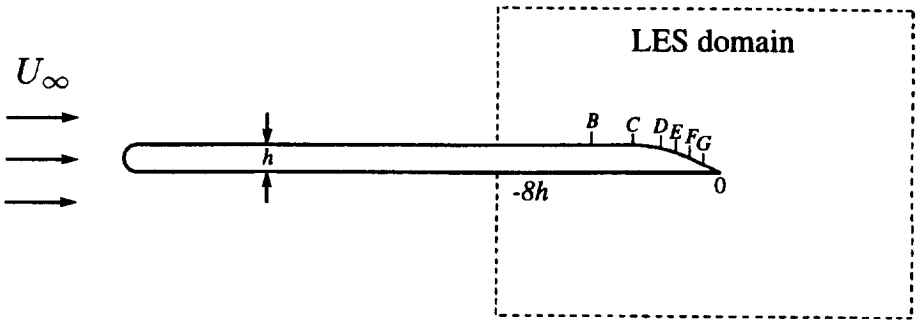

FIGURE 1. Flow configuration and computational domain. The experimental measurement stations B-G are located at $x/h = -4.625$, -3.125, -2.125, -1.625, -1.125, and -0.625, respectively.

2. Accomplishments

2.1 Update on near-field LES

2.1.1 Methodology

A detailed description of the numerical algorithm and procedure can be found in Wang (1997). The spatially filtered, unsteady, incompressible Navier-Stokes equations are solved in conjunction with the dynamic subgrid-scale model (Germano *et al.* 1991; Lilly 1992). The numerical scheme employs second-order central differences in the streamwise and wall-normal directions and Fourier collocation in the spanwise direction. A semi-implicit (Crank-Nicolson for viscous terms and third order Runge-Kutta for convective terms), fractional-step scheme is used for time advancement. The pressure Poisson equation is solved at each Runge-Kutta substep using a multi-grid iterative procedure.

Simulations are conducted in a computational domain containing the aft section of the strut and the near wake, as illustrated schematically in Fig. 1. Except for the inlet, the other three sides of the domain have been truncated for clarity. The actual domain size is approximately $16.5h$, $41h$, and $0.5h$, in the streamwise (x_1), wall normal (x_2), and spanwise (x_3) directions, respectively. The computational grid, defined in curvilinear coordinates in the x_1-x_2 plane and Cartesian coordinate in x_3, uses a total of $1536 \times 96 \times 48$ points, with appropriate clustering in the near-wall and trailing-edge regions. Of the 1536 streamwise grid points, 640 are distributed along the upper surface, 512 along the lower surface, and 2×192 along the wake line (branch cut). The maximum grid-spacing along the strut surface, measured in wall units, is $\Delta x_1^+ \approx 62$, $\Delta x_3^+ \approx 55$, and $\Delta x_2^+ \approx 2$. The simulation,

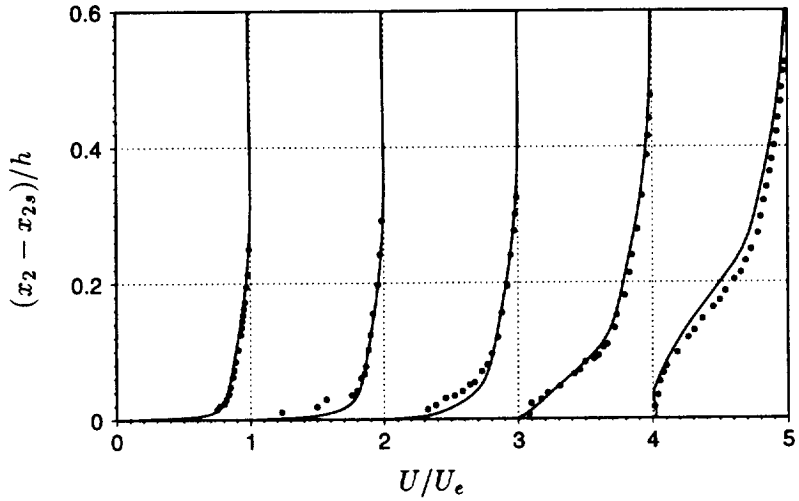

FIGURE 2. Profiles of the normalized mean velocity magnitude as a function of vertical distance from the upper surface, at stations (from left to right) C, D, E, F, and G. —— LES; • Blake's experiment. Individual profiles are separated by a horizontal offset of 1 with the corresponding zero lines located at 0, 1, ..., 4.

running at a maximum CFL number of 1.5, requires 200 single processor CPU hours on a CRAY C90 to advance one flow time across the streamwise domain length, and over 1000 CPU hours for the complete simulation. The velocity and pressure statistics presented below are collected over a period $T_s U_\infty/h \approx 60.62$, or 3.67 flow-through times based on free-stream velocity.

The inflow velocity profiles outside the boundary layers are provided by an auxiliary RANS calculation in a C-grid domain enclosing the entire strut, using Menter's (1993) SST k-ω model. Within the turbulent boundary layers, the time-dependent inflow velocities are generated from two separate LES's of flat-plate boundary layers with zero pressure gradient, using the method described by Lund, Wu & Squires (1998). The local momentum thickness and Reynolds number are matched with those from the RANS simulation. At the downstream boundary the convective outflow condition (Pauley, Moin & Reynolds 1988) is applied. The top and bottom boundaries are placed far away from the strut to minimize the impact of the imposed velocities obtained from RANS calculations. A no-slip condition is applied on the surface of the strut.

The letters B, C, D, E, F, and G in Fig. 1 indicate measurement stations in Blake's experiment. They are located at $x_1/h = -4.625$, -3.125, -2.125, -1.625, -1.125, and -0.625, respectively (the Cartesian coordinate system originates from the trailing edge). In Section 2.1.2 representative results are presented at these stations, and comparisons made with experimental values.

2.1.2 Simulation results

In Fig. 2, the magnitude of the mean velocity $U = (U_1^2 + U_2^2)^{1/2}$ normalized by its

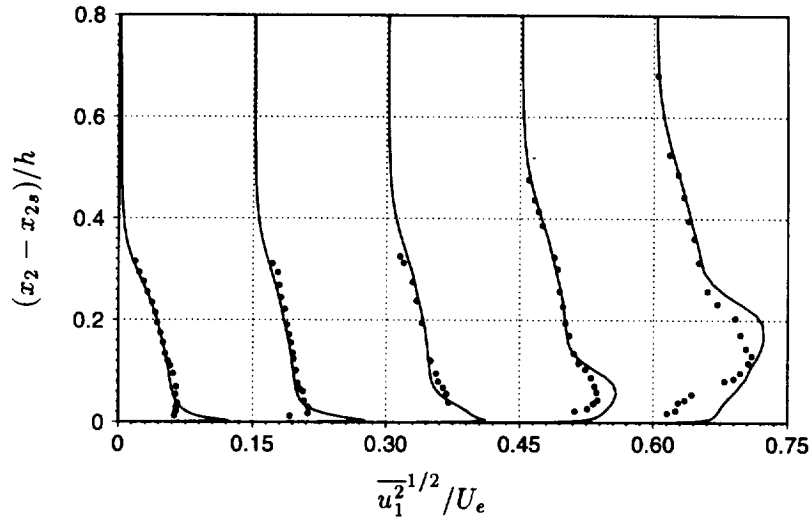

FIGURE 3. Profiles of the rms streamwise velocity fluctuations as a function of vertical distance from the upper surface, at stations (from left to right) B, D, E, F, and G. —— LES; • Blake's experiment. Individual profiles are separated by a horizontal offset of 0.15 with the corresponding zero lines located at 0, 0.15, ..., 0.60.

value at the boundary-layer edge U_e is plotted as a function of vertical distance from the upper surface at streamwise stations (from left to right) C-G. The solid lines are from LES, and the symbols represent Blake's experimental data. Good agreement with the experimental results is obtained at station C and all the upstream locations. At stations D and E, where the boundary layer is subject to strong adverse pressure gradient (cf. Fig. 4) but remains attached to the wall, the LES profiles are more full in the near-wall region than those from the experiment. Further downstream, as an unsteady separated region develops, the discrepancy diminishes, and the computed profiles compare well again with the experimental results at stations F and G.

Figure 3 compares the computational and experimental profiles of the rms streamwise velocity fluctuations at stations (from left to right) B, D, E, F, and G. The agreement between the LES and the experimental results is quite good except in the near-wall region and at the last two stations. The experimental profiles are seen to consistently miss the near-wall peaks known to exist in turbulent boundary layers, suggesting a possible lack of spatial resolution or high-frequency response as the probe approaches the wall. The large discrepancy observed in the separated region (stations F and G) may be caused by both simulation and measurement errors. In general, hot-wire readings become increasingly difficult to interpret if the rms turbulence intensity exceeds 30% of the local mean velocity (Bradshaw 1971), which is the case in the separation bubble where the mean velocity is very small (cf. Fig. 2).

The dimensionless mean pressure ($= C_p/2$) is depicted in Fig. 4 as a function of

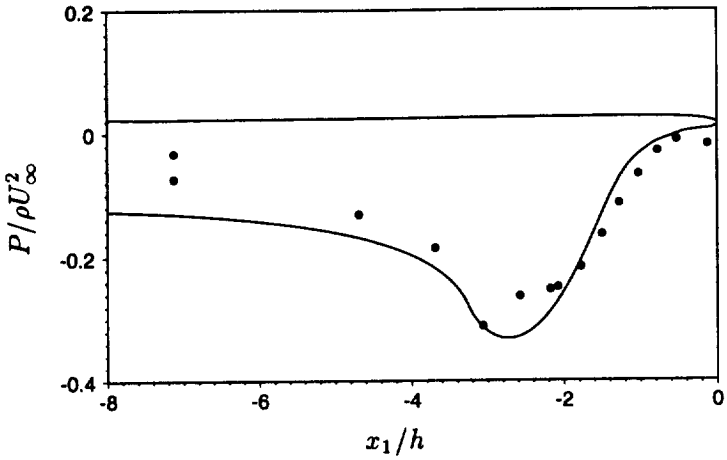

FIGURE 4. Mean surface pressure distribution near the trailing edge. —— LES; • Blake's experiment.

x_1/h. The comparison between the LES and experimental results is reasonable in the trailing-edge region but unsatisfactory upstream of it. The experimental data plotted here differ from those documented by Blake (1975) and referenced by Wang (1997) earlier. The new data set, based on the original record of his 1975 experiment, was provided by Blake (1998, private communication) after the completion of the present LES. Of particular interest is the additional data point measured on the lower surface (the upper point at $x_1/h = -7.125$ in Fig. 4), which sheds some light on the fidelity of inflow velocity conditions used in the simulation. Based on this point and assuming that the mean pressure is approximately constant on the lower surface as suggested by the LES prediction, it is evident that the lift and hence circulation in the experiment are much smaller than those in the LES. Since the circulation in the LES is imposed through the unequal mean velocity profiles on the two sides of the strut at the inlet boundary (cf. Fig. 2 in Wang 1997), one concludes that the inflow velocity difference has been exaggerated. Indeed, an estimate using C_p and the Bernoulli equation indicates that in the experiment the inflow velocities at the boundary layer edges are $U_e^{upper} \approx 1.071U_\infty$ and $U_e^{lower} \approx 1.032U_\infty$, compared with $U_e^{upper} \approx 1.093U_\infty$ and $U_e^{lower} \approx 0.979U_\infty$ used in the LES. Unfortunately, the several RANS calculations conducted earlier using different turbulence models all predict circulations much larger than the experimental value. The one chosen to provide the LES inflow profiles actually has the smallest circulation.

Figure 5 shows the space-time correlations of the upper-surface pressure fluctuations as a function of temporal and spanwise separations at stations C-G and the trailing edge (actually, one half grid spacing from the edge on the staggered mesh). The iso-correlation contours show relatively small variations of the spanwise spatial and temporal scales from stations C to E underneath the attached boundary layer with adverse pressure gradient. A dramatic increase of spatial and temporal scales occurs, however, after the turbulent boundary layer becomes separated (stations

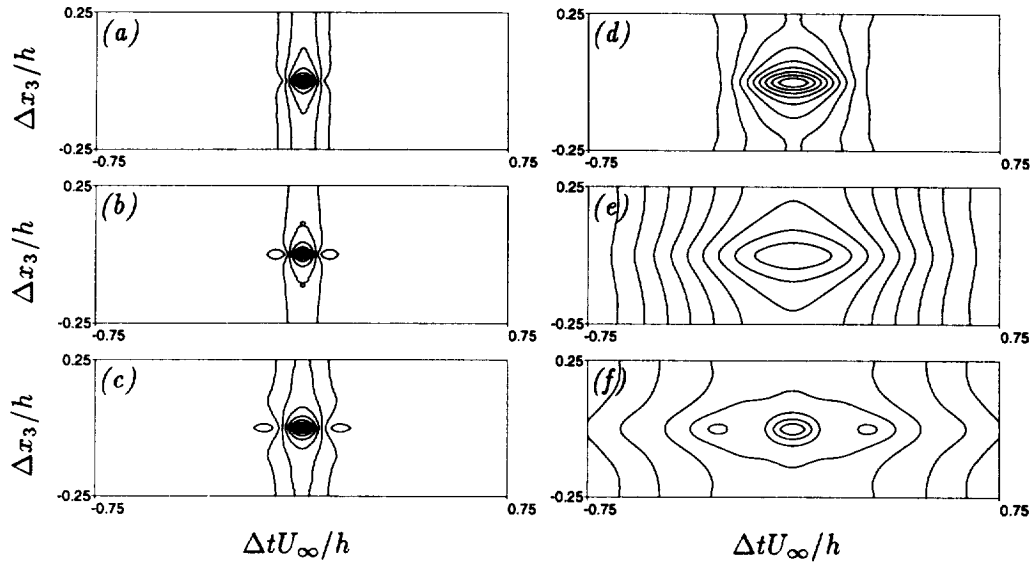

FIGURE 5. Contours of space-time correlation of the upper-surface pressure fluctuations as a function of spanwise and temporal separations, at stations (a) C; (b) D; (c) E; (d) F; (e) G; and (f) trailing-edge. Contour values are from 0.1 to 0.9, with increment 0.1.

F, G, and the trailing edge). The wall pressure fluctuations inside the separated zone are dominated by the effect of large scale fluid motion. The small scale eddies from the upstream boundary layer are lifted away from the wall and hence their contribution to the wall pressure is diminished. At the trailing edge, the correlation contours exhibit some features of small-scale correlation superimposed on the extremely large overall scales, because of the contribution from the attached boundary layer on the lower side of the edge.

It is noted that the correlation contours in Fig. 5 show insufficient drop at maximum spanwise separations inside the separated region, particularly at station G and the trailing edge. This suggests that the computational domain is too restrictive in the spanwise direction to allow the development of fully three-dimensional large-scale flow structures. The effect of the small spanwise domain size on the low-order flow statistics described above has not been investigated. In addition, it has important implications to the acoustic prediction, as will be discussed in Section 2.2.

Figure 6 depicts the frequency spectra of wall pressure fluctuations calculated from LES and compares them with those from Blake's experiment. The variables used for normalization are U_∞, h, and the dynamic pressure $q_\infty = \rho U_\infty^2/2$. The calculated spectra agree relatively well with the experimental data at most stations except station G, where the spectrum is significantly overpredicted. One notices that before the boundary layer separation (stations C-E), the LES spectra drop off more quickly than the experimental spectra at the high frequency end due to limited grid resolution and finite difference errors. The high frequency content

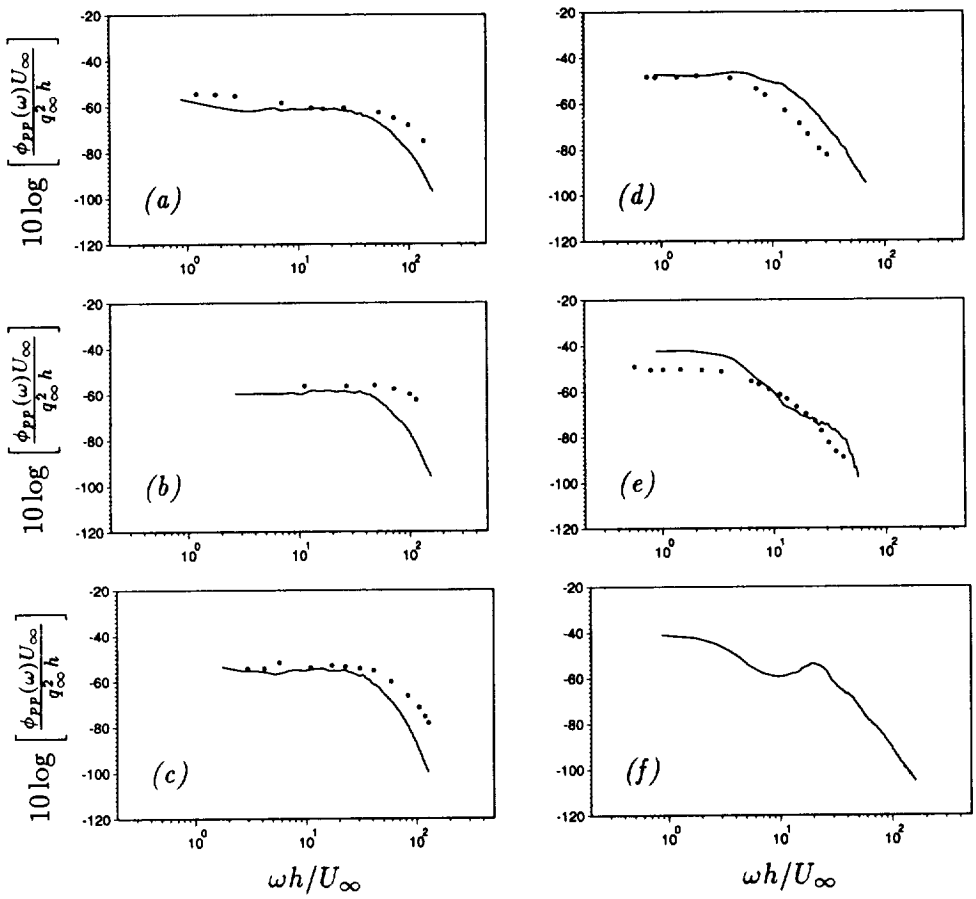

FIGURE 6. Frequency spectra of wall pressure fluctuations at stations (a) C; (b) D; (c) E; (d) F; (e) G; and (f) trailing-edge. —— LES; • experiment.

corresponds to fine spatial structures not resolved on the simulation grid. After the separation, however, the small scale effect is diminished, and the LES is capable of capturing the entire frequency range measured by the experiment. The spectrum at the trailing edge, where no experimental data are available, again consists of contributions from the upper (separated) and lower (attached) boundary layers. The latter is responsible for the high frequency peak shown in the figure.

2.2 Noise computation

2.2.1 Formulation

The noise radiation to the far-field is calculated in the framework of Lighthill's theory (Lighthill 1952). Crighton & Leppington (1971) show that the trailing-edge noise field has a non-multipole character, which is caused by the fact that the scattering surface is noncompact relative to the acoustic wavelength. To account for the surface reflection effect, a hard-wall Green's function, whose normal derivative

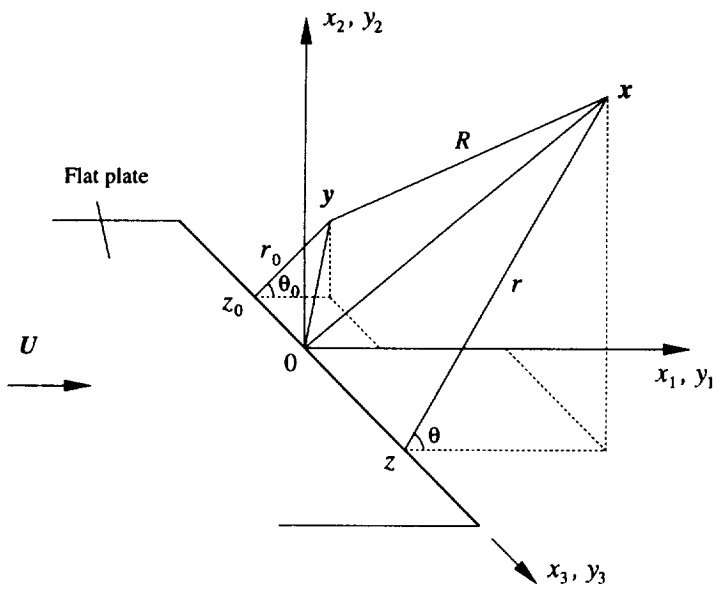

FIGURE 7. Coordinate system for calculating the radiated noise of flow past the trailing-edge of a semi-infinite flat plate.

vanishes on the surface, must be employed in an integral solution to the Lighthill equation.

When the acoustic wavelength is much longer than the thickness of the strut but much shorter than the chord ($h \ll \lambda_a \ll C$), the strut is reasonably approximated by a semi-infinite plane with zero thickness, for which the far-field Green's function is known analytically. The far-field pressure perturbation in the frequency domain can be written in the form (Ffowcs Williams & Hall 1970)

$$\hat{p}_a(\boldsymbol{x},\omega) \approx \frac{2e^{-i\frac{\pi}{4}}}{\pi^{\frac{1}{2}}} k^2 \sin\frac{\theta}{2} \int_V \frac{e^{ikR}}{4\pi R} \frac{(\sin\phi)^{\frac{1}{2}}}{(2kr_0)^{\frac{3}{2}}} \left\{ \rho_\infty \left(\widehat{u_\theta^2 - u_r^2} \right) \sin\frac{\theta_0}{2} \right.$$
$$\left. -2\rho_\infty \widehat{u_r u_\theta} \cos\frac{\theta_0}{2} \right\} d^3\boldsymbol{y}. \qquad (1)$$

where the caret denotes temporal Fourier transform, ω is the circular frequency, and $k = \omega/c_\infty$ the acoustic wavenumber. The velocity components u_r and u_θ are defined in a cylindrical-polar coordinate system shown in Fig. 7. Position vectors $\boldsymbol{x}$ (r, θ, z) and $\boldsymbol{y}$ (r_0, θ_0, z_0) represent far-field and source-field points, respectively, with $R = |\boldsymbol{x} - \boldsymbol{y}|$ and $\sin\phi = r/[r^2 + (z - z_0)^2]^{\frac{1}{2}}$.

In addition to the approximate Green's function, several assumptions are implied in (1). The viscous stress is assumed unimportant as a noise source at high Reynold numbers. The convection, refraction, and scattering of acoustic waves by the turbulent flow are ignored, which is justifiable in the low Mach number limit except at very high frequencies and/or at θ values close to zero or π. Furthermore, the

integrand in (1) is derived for a source region well within one acoustic wavelength ($kr_0 \ll 1$ or $r_0 \ll \lambda_a$). Although only eddies within this distance contribute to the amplified scattering noise, from a computational point of view it may be desirable to integrate further out for better convergence (boundary-independence of the volume integral), given the $(kr_0)^{-3/2}$ decay of the Green's function factor. A more general integral expression valid for all r_0 values is given in Wang (1996). However, noise calculations using both integrals show only a small difference, and hence the simpler expression (1) will be used here.

2.2.2 Evaluation of source terms

In the context of LES, the Lighthill stress is formally expressed as $\overline{T}_{ij} = \rho\overline{u}_i\overline{u}_j + \rho\tau_{ij}$, where the overline indicates spatial filtering and the entropy and viscous terms are ignored. It consists of nonlinear interactions among resolved scales (first term) and the subgrid scale contribution to the resolved scales (second term). Piomelli, Streett, & Sarkar (1997) examined the effect of small scales on sound generation using a channel flow DNS database. In the present computation, the Lighthill stress terms are evaluated using the resolved velocity components only, assuming that the subgrid scale contribution is relatively small. It is noted that the dynamic SGS model used in the source-field simulation gives only the anisotropic part of the SGS stress tensor, $\tau_{ij} - \delta_{ij}\tau_{kk}/3$, and thus the normal stress components cannot be determined. If one desires to include $\rho\tau_{ij}$ in the noise calculation, an alternative formulation of the SGS model such as the dynamic localization model (Ghosal et al. 1995), which solves an additional equation for the subgrid-scale kinetic energy $\tau_{kk}/2$, should be used.

To compute the source terms $\widehat{u_\theta^2 - u_r^2}$ and $-2\widehat{u_r u_\theta}$ in (1), the Cartesian velocity components u_1 and u_2 on the entire computational grid are saved every 10 time steps during the source-field LES. The sampling resolution $\Delta t_s U_\infty/h \approx 0.029$. The total record of $N = 1152$ time samples, covering a period $T_s U_\infty/h \approx 33.47$, is divided into 8 segments with a 50% overlap. For each segment, which contains 256 samples, the source quantities $u_\theta^2 - u_r^2$ and $-2u_r u_\theta$ are computed. The aperiodic time series are multiplied by the Hanning window function, and discrete Fourier transforms are performed. To compensate for the energy loss due to the Hanning window tapering, the resulting Fourier coefficients are renormalized such that the power spectrum computed from them, when integrated over all positive frequencies, gives the mean-square fluctuations of the original function.

As a result of the above procedure, 8 sets of the source terms as a function of frequency ω and spatial coordinates $\boldsymbol{y}$ are available. Each set can be used in (1) to give a sample noise field. The noise power spectra are obtained as the ensemble average of the spectra from all sample fields.

Figure 8 depicts the magnitude of the Reynolds shear-stress source term (normalized), $|-2\widehat{u_r u_\theta}|/U_\infty^2$, in the trailing-edge region at 4 selected frequencies. The other source term representing the normal stress behaves in a qualitatively similar manner. The source magnitudes are averaged over the 8 samples and the spanwise direction. The contour lines show that the spatial distribution of the acoustic source varies significantly with frequency. The low frequency source, associated with the

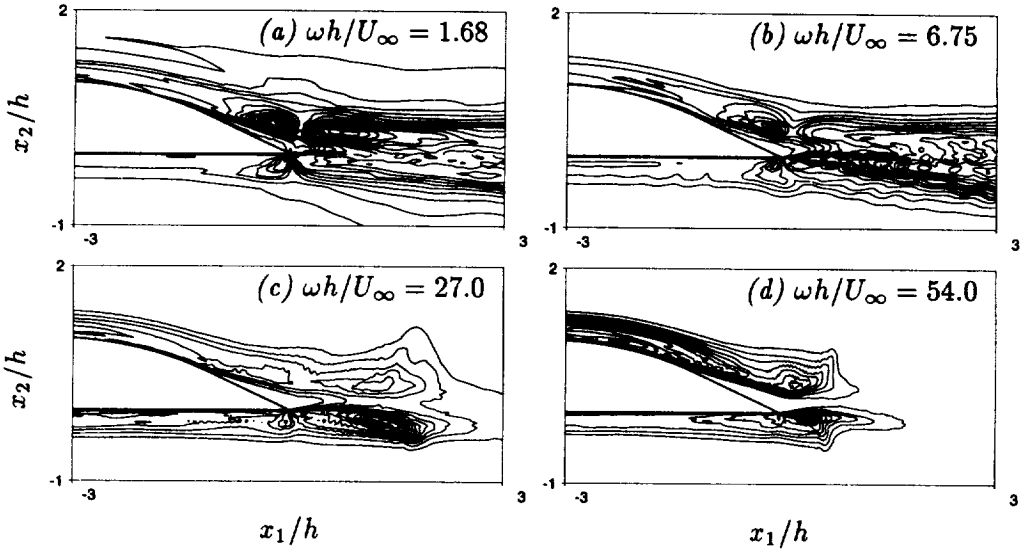

FIGURE 8. Contours of the magnitude of the acoustic source term $-2\widehat{u_r u_\theta}/U_\infty^2$ at four different frequencies. Contour levels ($\times 10^2$): (a) 0.20 to 3.40, with increment 0.20; (b) 0.20 to 3.00, with increment 0.20; (c) 0.10 to 1.40, with increment 0.10; (d) 0.03 to 0.42, with increment 0.03.

large scale unsteady flow structures, exhibits strength in a large region including the wake (cf. Figs. 8a and 8b). The largest values are found in the shear layers emanating from the upper (separated) and lower (attached) boundary layers. As the frequency increases (Figs. 8c and 8d), the source distribution becomes more concentrated, particularly in the lower shear layer close to the trailing edge. The wake region farther from the edge contributes little to the high-frequency source terms due to a lack of the corresponding small-scale flow structures. In the convolution integral (1), the source terms shown in Fig. 8 are weighted by a $(kr_0)^{-3/2}$ factor, and thus the effective noise source is much more concentrated in the trailing-eddy region.

2.2.3 Radiated field

Trailing-edge noise from a source region consisting of the computational domain can be readily obtained by evaluating the volume integral (1) numerically. As an example, Fig. 9 shows the contours of the real part of the acoustic pressure $\widehat{p}_a/P_\infty$ in the x_1-x_2 plane crossing the mid-span, for $\omega h/U_\infty = 1.68$ and 6.75. The trailing edge is located at $x_1 = x_2 = 0$, and the Mach number used in this example is $M = 0.1$. In the figure the frequency dependence of the wavelength and amplitude is evident, as is the distinct edge-noise directivity pattern dictated by the $\sin\frac{\theta}{2}$ factor in (1). The noise spectra can be obtained from the product of $\widehat{p}_a$ and its complex conjugate. It should be mentioned that Fig. 9 is based on a single sample of source functions. Statistical averaging can be done after the noise spectra from multiple source samples have been obtained.

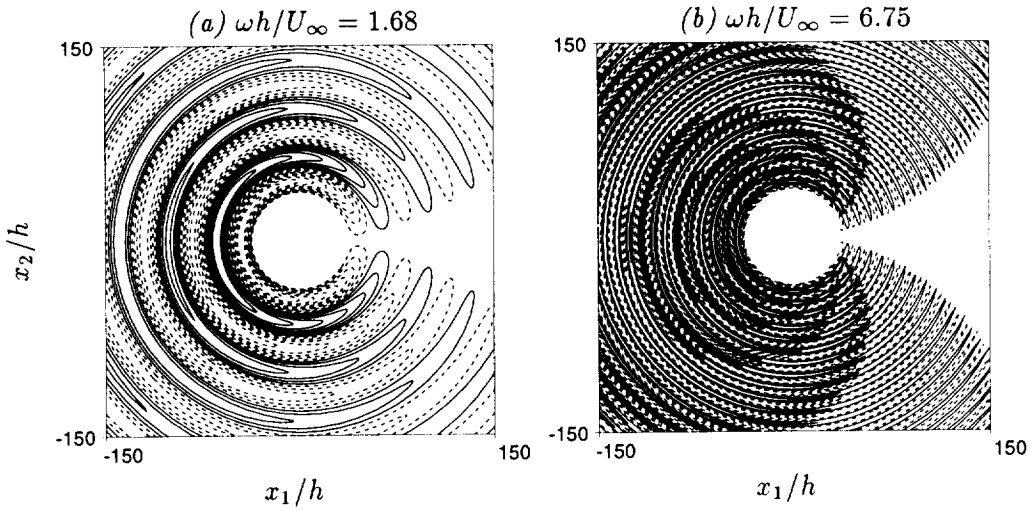

FIGURE 9. Contours of the real part of the acoustic pressure $\widehat{p}_a(\mathbf{x},\omega)/P_\infty$ from sources within the LES Domain at $M = 0.1$, at two different frequencies. Contour levels ($\times 10^6$): (a) -5.70 to 3.90, with increment 0.60; (b) -0.255 to 0.255, with increment 0.03.

In a typical LES, the spanwise width L_z of the computational domain is only a small fraction of the actual span L. For example, $L/L_z = 47$ for the present LES of Blake's experiment. To predict the frequency spectrum of the sound pressure radiated from the entire span, one requires knowledge about the spanwise coherence of the source field. Kato et al. (1993) discussed this issue in their calculation of noise from a cylinder wake. Let $\Lambda_z = \Lambda_z(\omega)$ denote the coherence length for a given frequency, two limiting cases can be found for which the total noise is well defined.

(a) If $L_z \geq \Lambda_z$, source regions separated by the computational box size radiate in a statistically independently manner. Hence, the total noise spectrum is the sum of contributions from L/L_z independent source regions along the span: $\Phi_{pa}^{total} \approx (L/L_z)\,\Phi_{pa}$.

(b) If $L \leq \Lambda_z$, the source is coherent along the entire span (2-d source). Based on (1), if the spanwise variation of the retarded time is ignored, $\widehat{p}_a^{total} \approx (L/L_z)\,\widehat{p}_a$, and hence $\Phi_{pa}^{total} \approx (L/L_z)^2\,\Phi_{pa}$.

In the intermediate regime $L_z < \Lambda_z < L$, an accurate prediction of the total sound pressure is difficult to achieve. The computational domain is too small to accommodate the spanwise flow scales, and thus the acoustic source functions are not computed reliably. The rigorous remedy is to increase the computational box size L_z so that case *a* or *b* described above applies. This is, however, often prohibitively expensive. Kato et al. (1993) resorted to an *ad hoc* approach in which Λ_z is approximated by extrapolating from the slowly-decaying coherence function, and a hybrid formula based on cases *a* and *b* is used to estimate the total noise radiation.

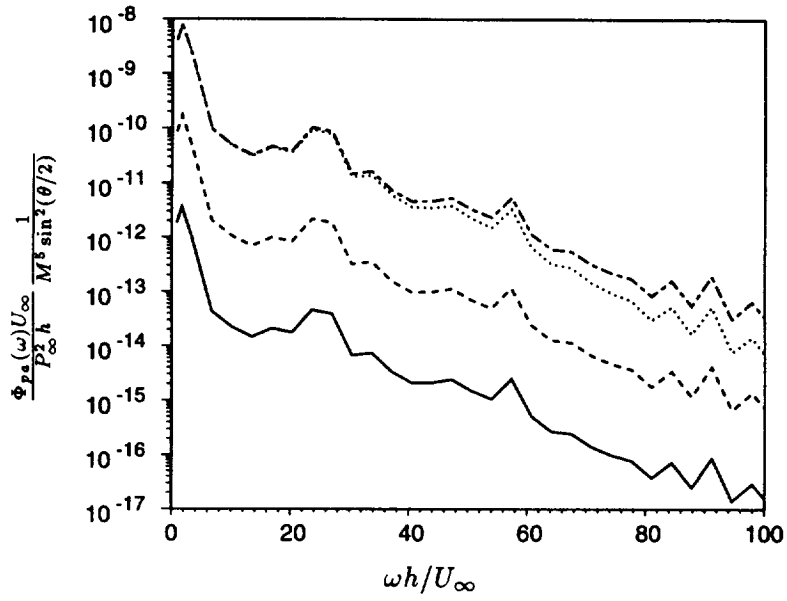

FIGURE 10. Frequency spectra of the far-field noise at $r/h = 150$ and $M = 0.088$. ——— Spectrum calculated from a partial source field (the LES domain); - - - - total spectrum assuming $L_z \geq \Lambda_z$; — — — total spectrum assuming $L \leq \Lambda_z$; ····· total spectrum using periodic source extension in span.

Another *ad hoc* approach employed by previous investigators is the periodic extension of the computed source field to the entire span. The volume integral (1) is then taken over the expanded domain. This approach is essentially equivalent to the approach used in case *b* described above except that the integration takes into account retarded-time variations along the span. Manoha, Troff & Sagaut (1998) used this method in their calculation of the noise from a blunt trailing edge of a flat plate.

In Fig. 10 several noise spectra are plotted as a function of frequency at $r/h = 150$ and $M = 0.088$. Note that the normalization factor for the spectra includes Mach number dependence and directivity. The solid line is computed from the thin slab of the source field within the LES domain. The total noise spectrum under the incoherent source assumption (case *a*) is given by the dashed line, whereas the coherence source calculation (case *b*) gives the chain-dashed line (the top curve). These two curves serve as the lower and upper bounds of the true noise spectrum. The spectrum calculated using periodic source extension in x_3, shown as the dotted curve, coincides with that from the coherence-source calculation at low frequencies but drifts to lower values at higher frequencies due to the increasing importance of retarded time variations.

The frequencies corresponding to $\lambda_a = C$ and h are given by $\omega h/U_\infty \approx 3.38$ and 71.4, respectively. They define the frequency range in which the half-plane Green's

function is approximately valid. Outside this range other appropriate Green's functions should be used. In particular, when $\lambda_a \gg C$, the strut is acoustically compact and thus the free-space Green's function is applicable. Curle's (1955) integral solution to the Lighthill equation provides a useful tool for noise computation (Wang, Lele, & Moin 1996). At high frequencies ($\lambda_a \leq h$), the Green's function must in principle be tailored to the specific trailing-edge shape. However, the potential accuracy improvement is limited, given the relatively small tip-angle of the edge and the competing high-frequency errors caused by the neglect of flow-acoustic interaction and subgrid-scale contribution to the acoustic source functions. The local spectrum peak in Fig. 10 near $\omega h/U_\infty = 23.6$ is caused by the diffraction of boundary layer eddies from the lower side.

As pointed out previously, Blake's (1975) experiment does not include acoustic measurements, and thus a direct comparison with the numerical predictions cannot be made. As a qualitative assessment, the acoustic pressure spectra from a different experiment (Blake & Gershfeld 1988) have been used to compare with the spectra shown in Fig. 10. The experimental data (not shown) are found to be concentrated at the low frequency end and lie between the coherent-source and incoherent-source predictions.

A complete determination of the far-field noise requires the spanwise coherence of the source-field to be computed. For a given field quantity q, the coherence is defined as

$$\gamma^2(\boldsymbol{x}, r, \omega) = \frac{|\Phi_{qq}(\boldsymbol{x}, r, \omega)|^2}{|\Phi_{qq}(\boldsymbol{x}, 0, \omega)||\Phi_{qq}(\boldsymbol{x}+r, 0, \omega)|}, \tag{2}$$

where the cross spectrum function Φ_{qq} is the Fourier transform of the space-time cross correlation function

$$\Phi_{qq}(\boldsymbol{x}, r, \omega) = \int_{-\infty}^{\infty} \langle q(\boldsymbol{x}, t) q(\boldsymbol{x}+r, t+\tau) \rangle e^{-i\omega\tau} d\tau. \tag{3}$$

An estimate of γ^2 is made based on the fluctuating surface pressure ($q \equiv p$) in the vicinity of the trailing edge under the premise that it is representative of the overall coherence of the volume distribution of source terms in (1). Figure 11 shows the spanwise pressure coherence on the upper surface, one half grid spacing from the trailing edge. The left plot shows the iso-coherence contours as a function of frequency and spanwise separation. The coherence is seen to drop rapidly with spanwise separation except at the low frequency end. The coherence at selected low frequencies is depicted in the right plot as a function of spanwise separation. It is observed that for $\omega h/U_\infty \geq 5.26$, the coherence exhibits sufficient drop within the computational domain, and thus $\Phi_{pa}^{total} \approx (L/L_z)\,\Phi_{pa}$ applies. The dashed curve in Fig. 10 gives the total noise spectrum. Below this frequency, however, the coherence length is larger than the spanwise dimension of the computational box, and the total noise cannot be determined with certainty. Given the flat shape of γ^2 at large separations shown in Fig. 11 (the solid and dashed lines), it is not possible to obtain the coherence lengths by extrapolation as in the case of Kato et al. (1993).

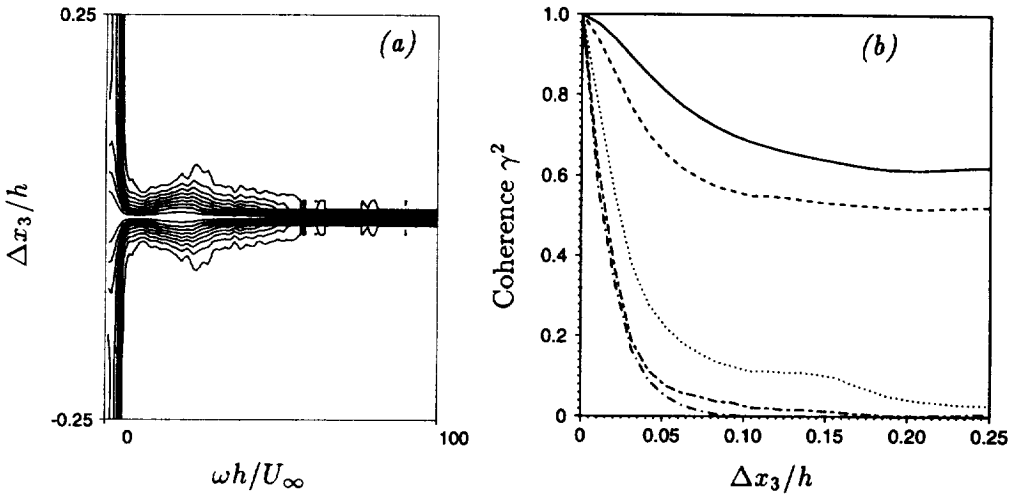

FIGURE 11. Spanwise coherence of the fluctuating surface pressure on the upper surface near the trailing edge. (a) Contour plot (contour levels from 0.1 to 0.9, with increment 0.10). (b) Coherence at frequencies $\omega h/U_\infty \approx 1.75$ (———), 3.51 (- - - -), 5.26 (·····), 7.01 (— - —), and 8.76 (— · —).

3. Summary and future work

A large-eddy simulation has been carried out for turbulent boundary layer flows past an asymmetrically beveled trailing-edge of a flat strut at a chord Reynolds number of 2.15×10^6. The asymmetric edge of 25 degree tip-angle produces a separated boundary layer on one side and an attached boundary layer on the other. The computed mean and fluctuating velocity profiles compare reasonably well with the experimental measurements of Blake (1975). The discrepancies observed at some stations (D, E for mean velocity and F, G for fluctuating velocity) may have been caused by inadequate inflow velocity conditions and small computational domain size as well as possible experimental errors near the wall and inside the separated region.

The inflow velocity profiles constitute a major uncertainty for the LES since they are not available from Blake's experiment. Based on the additional mean surface pressure data provided recently by Blake, it appears that the RANS calculations used to provide the inflow mean velocities have exaggerated the difference between velocities on the two sides of the strut, and hence the circulation. This is evidenced by the significant discrepancy between the mean surface pressure distributions from LES and the experiment.

Thus, future simulations should use more accurate inflow velocity profiles associated with a smaller circulation. The exact profiles are, however, difficult to obtain without additional experimental measurements. While it is possible to deduce from the experimental C_p data the approximate velocity magnitudes at the boundary layer edges near the inflow boundary, this approach does not give the detailed profiles extending to the outer computational boundary.

The objectives of the trailing-edge flow LES are to predict the space-time characteristics of surface pressure fluctuations and to provide the acoustic source functions for the far-field noise calculation. The frequency spectra of surface pressure fluctuations obtained from LES agree well with experimental measurements at most stations. The cause for the significant overprediction at station G needs to be further investigated. The space-time correlations of the fluctuating surface pressure demonstrate a dramatic increase in temporal and spanwise spatial scales beneath the unsteady separation region. The correlation functions near the trailing-edge show insufficient drop at maximum spanwise separations, suggesting the need for a wider computational domain.

The far-field acoustics is computed from an integral-form solution to the Lighthill equation using a hard-wall Green's function (Ffowcs Williams & Hall 1970). The Green's function is approximated by that for an infinitely thin half-plane, given the thin foil (relative to acoustic wavelength) and the small included angle of the trailing-edge. The acoustic evaluation is performed in the Fourier frequency domain and requires the storage and processing of large amount of time-dependent, three-dimensional source field data obtained from LES. Computations have been carried out to determine the source-term characteristics and the far-field noise spectra. To accurately predict the noise radiation from the entire span using a partial source field included in the LES domain, it is required that the spanwise domain size be larger than the coherence length of the source field in that direction. The present LES is found to be adequate for predicting noise radiation over a wide frequency range. At low frequencies, however, the spanwise source coherence estimated based on surface pressure fluctuations does not decay sufficiently. This issue will be addressed in future simulations using an expanded computational domain.

Acknowledgments

We gratefully acknowledge Dr. William K. Blake and Prof. Peter Bradshaw for valuable discussions during the course of this work. This work was supported by the Office of Naval Research under Grant No. N00014-95-1-0221. Computations were carried out on facilities at the DoD Major Shared Resource Center/Aeronautical Systems Center.

REFERENCES

BLAKE, W. K. 1975 *A Statistical Description of Pressure and Velocity Fields at the Trailing Edge of a Flat Strut*, DTNSRDC Report 4241, David Taylor Naval Ship R & D Center, Bethesda, Maryland.

BLAKE, W. K. & GERSHFELD, J. L. 1988 The aeroacoustics of trailing edges. In *Frontiers in Experimental Fluid Mechanics,* Chapt. 10, (Gad-el-Hak, M. Eds.), Springer-Verlag.

BRADSHAW, P. 1971 *An Introduction to Turbulence and Its Measurements*, Pergamon Press, Oxford.

CRIGHTON, D. G. & LEPPINGTON, F. G. 1971 On the scattering of aerodynamic noise. *J. Fluid Mech.* **46,** 577-597.

CURLE, N. 1955 The influence of solid boundaries upon aerodynamic sound. *Proc. Royal Soc. Lond.* A. **231,** 505-514.

FFOWCS WILLIAMS, J. E. & HALL, L. H. 1970 Aerodynamic sound generation by turbulent flow in the vicinity of a scattering half plane. *J. Fluid Mech.* **40,** 657-670.

GERMANO, M., PIOMELLI, U., MOIN, P. & CABOT, W. H. 1991 A dynamic subgrid-scale eddy viscosity model. *Phys. Fluids A.* **3,** 1760-1765.

GHOSAL, S., LUND, T. S., MOIN, P., & AKSELVOLL, K. 1995 A dynamic localization model for large-eddy simulation of turbulent flows. *J. Fluid Mech.* **286,** 229-255.

KATO, C., IIDA, A., TAKANO, Y., FUJITA, H., & IKEGAWA, M. 1993 Numerical prediction of aerodynamic noise radiated from low Mach number turbulent wake, *AIAA Paper 93-0145.*

LIGHTHILL, M. J. 1952 On sound generated aerodynamically; I. General theory. *Proc. R. Soc. Lond.* A. **211,** 564-587.

LILLY, D. K. 1992 A proposed modification of the Germano subgrid scale closure method. *Phys. Fluids A.* **3,** 2746-2757.

LUND, T. S., WU, X. & SQUIRES K. D. 1998 Generation of turbulent inflow data for spatially-developing boundary layer simulations. *J. Comp. Phys.* **140,** 233-258.

MANOHA, E., TROFF, B., & SAGAUT, P. 1998 Trailing edge noise prediction using large eddy simulation and acoustic analogy, *AIAA Paper 98-1066.*

MENTER, F. R. 1993 Zonal two-equation k-ω turbulence models for aerodynamic flows, *AIAA Paper 93-2906.*

PAULEY, L. L., MOIN, P. & REYNOLDS, W. C. 1988 *Numerical Study of Unsteady Laminar Boundary Layer Separation,* Report No. TF-34, Dept. of Mech. Engr., Stanford Univ.

PIOMELLI, U., STREETT, C. L., & SARKAR, S. 1997 On the computation of sound by large-eddy simulation. *J. Eng. Math.* **32,** 217-236.

WANG, M. 1996 Towards numerical simulations of trailing-edge aeroacoustics. *Annual Research Briefs-1996,* Center for Turbulence Research, Stanford University/NASA Ames, 133-142.

WANG, M. 1997 Progress in large-eddy simulation of trailing-edge turbulence and aeroacoustics. *Annual Research Briefs-1997,* Center for Turbulence Research, Stanford University/NASA Ames, 37-49.

WANG, M., LELE, S. K., & MOIN, P 1996 Computation of quadrupole noise using acoustic analogy. *AIAA J.* **34,** 2247-2254.

Weakly nonlinear modeling of the early stages of bypass transition

By S. A. Maslowe

1. Motivation and objectives

Under ideal conditions, boundary layer transition occurs in a six-stage process described, for example, by Stuart (1965). The first stage is that of linear instability, and its onset is predicted accurately by two-dimensional normal mode solutions of the Orr-Sommerfeld equation. In the Blasius case, the critical Reynolds number based on displacement thickness is approximately $Re_{\delta^*} = 520$ and the exponentially growing modes observed at slightly larger values of Re_{δ^*} are known as Tollmien-Schlichting instabilities.

In many important engineering applications, however, transition to turbulence is known to occur at sub-critical Reynolds numbers, and in extreme cases the Tollmien-Schlichting stage may be entirely bypassed. Responsibility for this bypass phenomenon may be linked, for example, to surface roughness or structural vibrations, but in this report we shall be concerned with free-stream turbulence as the source. The reason is that the application of primary concern here is to turbomachinery, where a high level of free-stream turbulence is often produced by upstream stages.

We also wish to investigate the effect of streamwise pressure gradients on bypass transition. The adverse pressure gradient case is of most concern because transition on compressor blades, as well as flow over airplane wings, usually takes place in a region of adverse pressure gradient. However, transitional flows in the presence of a favorable pressure gradient are also of interest. This is particularly true in low-pressure turbines and occurs occasionally in compressors as well.

Experimental studies of the influence of free-stream turbulence on transition reveal the presence of longitudinal vortices with a quasi-periodic structure in the spanwise direction; these are sometimes termed Klebanoff modes. At some point, what may loosely be termed secondary instabilities are observed, and these cause a breakdown of the organized structures into turbulence. The secondary instabilities are usually attributed in the Blasius case to a distortion of the velocity profile such that it develops inflection points (see, *e.g.*, Wundrow & Goldstein (1998)).

Nonlinearity is an essential feature of bypass transition, and the process is clearly of such complexity that only a numerical simulation could describe all the stages. However, DNS simulations are time consuming, and there are many parameters in the problem that can be varied. Analytical methods are needed to suggest optimal initial conditions and also to provide insights that can be helpful in interpreting the results of both experiments and numerical simulations.

An idealization that has proved useful in numerical simulations of bypass transition is to consider an initial disturbance comprised of a pair of oblique modes

inclined at equal and opposite angles to the primary flow direction. This has been done in studies of the Blasius boundary layer by Joslin, Streett & Chang (1993) and also by Berlin, Lundbladh & Henningson (1994). In both studies, Orr-Sommerfeld modes were used as initial conditions. However, they were superimposed in the latter paper in such a way that the vorticity component normal to the wall was zero and a smaller Reynolds number was used in the simulations. Experiments on "oblique transition" were reported recently by Elofsson (1998), and comparisons with the numerical simulations were encouraging.

The objective of the research reported here is to formulate nonlinear analyses to be employed in conjunction with numerical simulations of boundary layer transition influenced by free-stream turbulence. Following discussions with Professors Sanjiva Lele and Paul Durbin, it was decided to represent the perturbations at lowest order by modes belonging to the continuous spectrum of the Orr-Sommerfeld equation. Grosch & Salwen (1978) noted that a patch of vorticity in the free stream can be expanded in terms of these eigenfunctions. Their speed of propagation is close to the free-stream value, and their amplitude is largest around the edge of the boundary layer and very small within the boundary layer. These features are exhibited clearly by the computations of some spatially damped eigenfunctions for a Blasius boundary layer reported by Jacobs & Durbin (1998). The weakly nonlinear approach involves a perturbation about a superposition of modes belonging to the continuous spectrum of the Orr-Sommerfeld equation, so the following section consists of an outline and preliminary results for that problem.

2. Accomplishments

We wish to investigate the evolution of free-stream disturbances to boundary layers with velocity profiles belonging to the Falkner-Skan family of similarity solutions. These solutions are obtained for flows in which the free-stream velocity varies with distance along the surface according to

$$U_e^*(x^*) = U_0^*\, x^{\beta_H/(2-\beta_H)}, \tag{1}$$

where an asterisk denotes a dimensional variable. The Hartree form of the governing equation yielding the velocity profile is

$$f''' + ff'' + \beta_H(1 - f'^2) = 0, \tag{2}$$

where $f'(\eta) = u/U_e^*$ and η is a similarity variable.

In linear stability calculations, it is usual (but not universal) to use the boundary layer displacement thickness in non-dimensionalizing the Orr-Sommerfeld equation, which then takes the form

$$\left(\bar{u} - \frac{\omega}{\alpha}\right)(\phi'' - \alpha^2\phi) - \bar{u}''\phi = \frac{1}{i\alpha Re_{\delta^*}}(\phi'''' - 2\alpha^2\phi'' + \alpha^4\phi), \tag{3}$$

where the perturbation stream function is given by $\hat{\psi} = \phi(y)\exp\{i(\alpha x - \omega t)\}$ and, for spatially evolving waves, ω is real and α is complex. Some care is required in

employing the velocity profiles obtained from similarity solutions in (3) because the derivatives in $\bar{u}''$ are with respect to y, which is non-dimensionalized with respect to δ^*, whereas η is the independent variable in (2). The required relationship is

$$\bar{u}''(y) = \Delta^2 f'''(\eta), \text{ where } \Delta \equiv \int_0^\infty (1 - f')\, d\eta. \tag{4}$$

Equation (4) is analogous to (12b) of Obremski, Morkovin & Landahl (1969) who have presented in some detail the linear stability characteristics of Falkner-Skan profiles for different values of β_H. Their non-dimensionalization utilizes δ, the boundary layer thickness, as the length scale in the Orr-Sommerfeld equation rather than δ^*. This accounts for the different factors in treating the $\bar{u}''$ term.

What differentiates the continuous spectrum from the normal mode solutions of (3) is the asymptotic form of the free-stream boundary conditions. Whereas the Tollmien-Schlichting modes decay exponentially as $y \to \infty$, those of the continuous spectrum are required only to be bounded. Outside the boundary layer, $\bar{u} = 1$; as a result, (3) has constant coefficients, and four linearly independent solutions are readily obtained. One grows exponentially with increasing y and must be rejected. The eigenfunction is then a linear combination of the remaining three, two of which are oscillatory while the third decays exponentially. In the spatial case, it can be shown that all modes are damped (*i.e.*, $\alpha_i > 0$), and the details for the boundary conditions can be found in §2.3 of Grosch & Salwen (1978).

A collocation method has been used to obtain solutions of (3) for values of β_H, the pressure gradient parameter, ranging from zero to $\beta_H = -0.1988$, which corresponds to separation. Only two cases are shown here because of the preliminary nature of our work. Specifically, the sensitivity of the eigenfunctions to pressure gradient was found to depend on which feature is plotted. Whereas previous articles have shown separately the real and imaginary parts of ϕ, in this study examining the variation of $|\phi|$ turned out to be more informative.

In Fig. 1, the modulus of the spatial eigenfunction for a Blasius boundary layer is shown. The magnitude is seen to be very small for the roughly 1/3 of the boundary layer adjacent to the wall. The "penetration depth" is, nonetheless, noticeably greater than in the cases illustrated in Figs. 3 and 4 of the article by Jacobs & Durbin (1998). Our result is consistent with their prediction, based on an analysis of the two-layer Tietjens model, that at lower Reynolds numbers the penetration depth will be greater.

The computations reported here were done at $Re_{\delta^*} = 500$ to agree with the experiments of Boiko *et al.* (1994), whereas those of Jacobs & Durbin were at a considerably higher Reynolds number. However, our frequency is smaller than theirs, so further comparisons would be desirable to confirm these trends.

As shown in Fig. 2, when there is a moderate adverse pressure gradient, $\beta_H = -0.12$, the penetration depth is slightly less than in the Blasius case. However, near the edge of the boundary layer the magnitude of the oscillations around the far field value of $|\phi|$ is seen to be much greater. This suggests that the details of transition

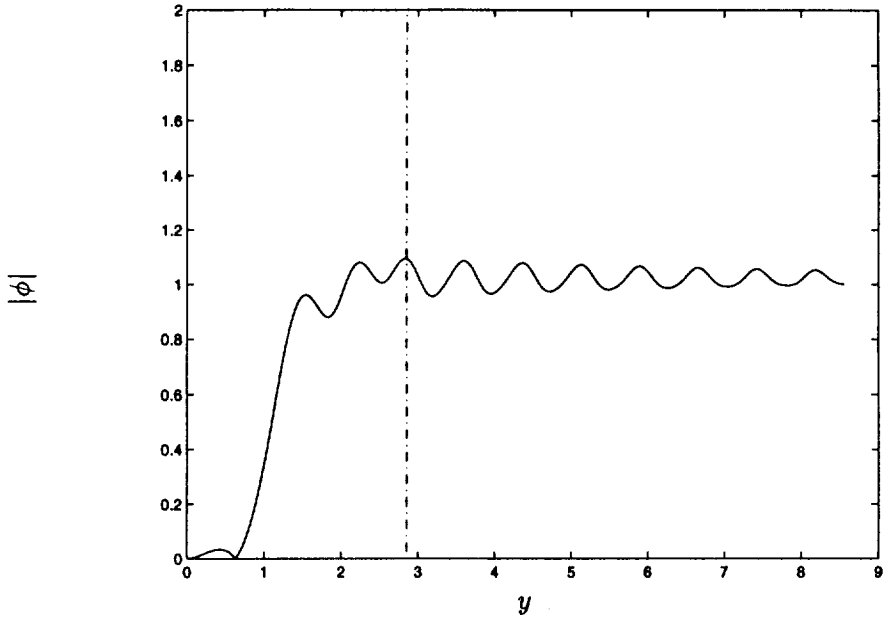

FIGURE 1. Modulus of the spatial eigenfunction for a Blasius boundary layer at $Re_{\delta^*} = 500$, $\omega = 0.18$, and $\alpha_r = 0.1799$.

induced by free-stream disturbances might be significantly different for boundary layers developing in an adverse pressure gradient.

3. Future plans

As discussed near the end of the introductory section, the longer term goal of this research is to formulate an amplitude expansion involving a perturbation about a linear state whose eigenfunction is derived from the continuous spectrum. The streamwise vortices and streaks observed in experiments can be modeled most simply by starting with a pair of oblique waves. A number of new features would be present in such a formulation, and certain mathematical difficulties must be addressed.

To simplify the discussion, let us consider first the simpler problem of formulating a weakly nonlinear analysis for a single plane wave. We expect the amplitude in the spatially evolving case to satisfy a Stuart-Landau equation having the form

$$\frac{dA}{dx} = -\alpha_i A + a_2 A \mid A \mid^2, \tag{5}$$

where a_2 is the Landau constant. When the basic disturbance is a Tollmien-Schlichting wave, the Landau constant is given by the ratio of two definite integrals. These integrals are obtained from imposing an orthogonality condition and the homogeneous boundary conditions. However, because the eigenfunctions of the continuous spectrum do not vanish as $y \to \infty$, the corresponding integrals do not exist, and an alternative solvability condition must be employed.

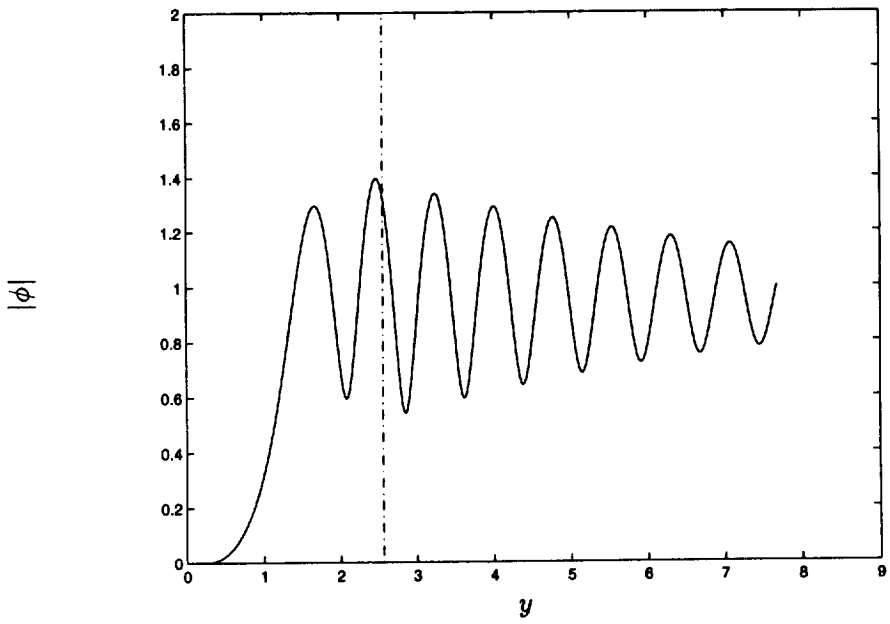

FIGURE 2. Spatial eigenfunction for an adverse pressure gradient boundary layer with $\beta_H = -0.12, Re_{\delta^*} = 500$, $\omega = 0.18$, and $\alpha_r = 0.1799$.

A second difficulty is that in the usual Stuart-Watson theory the perturbation is about a neutral mode. However, the modes of the continuous spectrum are weakly damped. The consequences of this may be minor, perhaps a slower rate of convergence of the amplitude expansion. A possible solution may be to include nonlinearity at the lowest order to obtain a neutral mode. In any case, the matter is one that must be considered.

Returning now to the pair of oblique modes as an initial perturbation, some aspects of the development can be anticipated from the paper by Benney (1961) which provides the most detailed description of the analysis leading to the Benney-Lin vortices. A plane wave in addition to a pair of oblique waves is considered in Benney (1961); however, setting the parameter $\mu = 0$ in §3 of his paper yields equations analogous to those anticipated in our analysis. Of particular significance is a sort of resonance that occurs between the waves and the mean flow at the first order beyond the linear problem. In the nearly-neutral case, this resonance was shown to produce a secondary flow whose u-component velocity grows like t^2 while the mean longitudinal vorticity has a growth proportional to t.

In the formulation under consideration here, the perturbation at lowest order is of the form

$$\begin{aligned} u^{(1)} &= \{A(X)\,\hat{u}(y)\,e^{i(\alpha x-\omega t)} + c.c.\}\cos\beta z \\ v^{(1)} &= \{A(X)\,\hat{v}(y)\,e^{i(\alpha x-\omega t)} + c.c.\}\cos\beta z \\ w^{(1)} &= \{A(X)\,\hat{w}(y)\,e^{i(\alpha x-\omega t)} + c.c.\}\sin\beta z \\ p^{(1)} &= \{A(X)\,\hat{p}(y)\,e^{i(\alpha x-\omega t)} + c.c.\}\cos\beta z\,, \end{aligned} \tag{6}$$

where α is now real and X is a slow variable in the streamwise direction. The quantity $\hat{v}(y)$ satisfies the Orr-Sommerfeld equation (3) with α^2 replaced everywhere by $\alpha^2 + \beta^2$. Once $\hat{v}$ has been determined, the continuity and vertical vorticity equations can be used to obtain the other velocity components, and the pressure perturbation is obtained from the $x-$component momentum equation.

It can be expected based on the considerations discussed above that at the next order a large mean flow response will occur. The amplitude equations will not arise until the following order in the amplitude expansion. One result that is hoped to be obtained after deriving and solving these equations is the obliqueness angle leading to the largest amplification rate. Because we are dealing with the sub-critical case here, an estimate of the amplitude of turbulence in the free stream required to promote instability will also come out of the analysis.

REFERENCES

BENNEY, D. J. 1961 A non-linear theory for oscillations in a parallel flow. *J. Fluid Mech.* **10,** 209-236.

BERLIN, S., LUNDBLADH, A. & HENNINGSON, D. 1994 Spatial simulations of oblique transition in a boundary layer. *Phys. Fluids A.* **6,** 1949-1951.

BOIKO, A. V., WESTIN, K. J. A., KLINGMANN, B. G. B., KOZLOV, V. V. & ALFREDSSON, P. H. 1994 Experiments in a boundary layer subjected to free stream turbulence. Part 2. The role of TS waves in the transition process. *J. Fluid Mech.* **281,** 219-245.

ELOFSSON, P. A. 1998 An experimental study of oblique transition in a Blasius boundary layer flow. Paper 2 in *Ph. D. thesis,* Dept. of Mechanics, Royal Inst. of Technology, Stockholm.

GROSCH, C. E. & SALWEN, H. 1978 The continuous spectrum of the Orr-Sommerfeld equation. Part 1. the spectrum and the eigenfunctions. *J. Fluid Mech.* **87,** 33-54.

JACOBS, R. G. & DURBIN, P. A. 1998 Shear sheltering and the continuous spectrum of the Orr-Sommerfeld equation. *Phys. Fluids A.* **10,** 2006-2011.

JOSLIN, R. D., STREETT, C. L. & CHANG, C.-L 1993 Spatial direct numerical simulation of boundary layer transition mechanisms: validation of PSE theory. *Theor. Comput. Fluid Dyn.* **4,** 271-288.

OBREMSKI, H. J., MORKOVIN, M. V. & LANDAHL, M. T. 1969 A portfolio of stability characteristics of incompressible boundary layers. *AGARDograph 134.* NATO, Paris.

STUART, J. T. 1965 Hydrodynamic stability. *Appl. Mech. Rev.* **18,** 523-531.

WUNDROW, D. W. & GOLDSTEIN, M. E. 1998 Effect on a laminar boundary layer of small-amplitude streamwise vorticity in the upstream flow. *J. Fluid Mech.,* (submitted).

Interactions between freestream turbulence and boundary layers

By J. C. R. Hunt[1], P. A. Durbin AND X. Wu[2]

1. Motivation and objectives

The interaction between free-stream turbulence and boundary layers is one example out of many that involve different types of fluid motion in overlapping or adjacent regions of flow. We are concerned here with flows at high Reynolds and Peclet numbers, so that the effects on the interactions between these flows of molecular diffusion are small except close to the boundary [B] between them. In these complex configurations the overall flow is not generally dominated by a single mechanism; for example, perturbations do not grow everywhere at the same rate (Hunt & Carruthers, 1990), but in zones of limited extent with characteristic flow pattern such as thin shear layers, and on certain ranges of time and/or length scales, the flow can be dominated by specific mechanisms. These tend to be defined by only a few parameters. Interactions between the flow regions, say [F1] and [F2], are often dominated by such mechanisms in layers lying along the interface [B]. Some effects propagate into the interior of the regions by advection or wave motion (Fig. 1), while others act upon the boundary.

A large class of such flow problems that are of fundamental and practical interest are characterized by interactions between two distinct and weakly correlated turbulent velocity fields in adjacent regions. The turbulence in each region may have been generated by different kinds of instability, or they may simply differ in their statistics such as their integral length scales. Such interactions occur continually and randomly within turbulent flows and ionized fluids, for example, where small eddies impinge on large coherent structures or where the outer and inner parts of a turbulent boundary layer meet (Terry, Newman & Mattor 1992). In engineering these problems occur in the design of turbomachines. There, the flow approaching the rotating airfoil blade or centrifugal impeller contains turbulent eddies that are much larger than the small scale turbulence in the boundary layers on the solid moving parts. In order to determine the effects of this external turbulence on heat transfer or on the pressure distribution, it is necessary to understand how the intense small scale turbulence grows in the boundary layers that are initially laminar. This can occur at lower values of the Reynolds number than without external turbulence – the mechanism of 'bypass' transition. Is it caused by the external turbulence being simply advected into the growing boundary layers (an advected interaction AI), or, alternatively, does the external turbulence directly induce pressure and velocity

1 Permanent address: Cambridge University, DAMTP, Silver Street, Cambridge, UK

2 Center for Integrated Turbulence Simulation, Stanford University

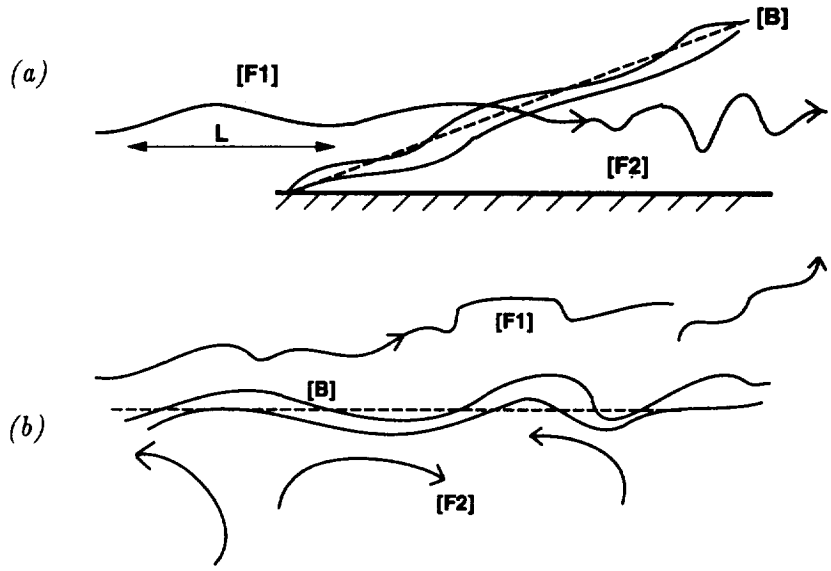

FIGURE 1. Schematic diagram of interactions between external region [F1], containing disturbances, and vortical region [F2], that may be turbulent. Regions separated by interface [B] of finite thickness whose mean position is indicated by a dashed line.

fluctuations in the shear profile of the boundary layer, which may be unstable? This external interaction (EI) mechanism may be very weak because of the tendency of a shear profile to be sheltered from external fluctuations. Experiments and numerical simulations for weak and moderate levels of freestream turbulence (e.g. Goldstein & Windrow 1998, Liu & Rodi 1991) cannot really discriminate between these competing mechanisms without a better theoretical framework, to which we are contributing in this study. Recent measurements by Thole & Bogard (1996) show quite different interactions when the external turbulence is strong relative to the turbulence in the boundary layer.

Similar problems arise on a range of larger scales in meteorology (e.g. Collier *et al.* 1994). For these types of complex flow, practical models are needed; one approach is to make simplifying assumptions about the nature of the interactions and broadly classify them as: (i) superposition (S) of flows in overlapping regions so that interactions can be ignored, (ii) exclusion of flows, or flow processes, in certain regions because a particular mechanism is dominant, especially near the boundary [B]; or (iii) significant interactions (AI and EI) between the flows in the adjoining regions, in which new phenomena or mechanisms may arise.

Theoretical analysis of the appropriate vorticity dynamics and some new direct numerical simulations is the method we use to study these interactions. The theoretical approach is different from but complementary to that based on the hydrodynamic stability theory for small disturbances (Jacobs & Durbin 1998). Both

approaches demonstrate how a shear layer can block certain kinds of external disturbances so that the flow inside the layer is 'sheltered' from them. If the boundaries of the shear layer are highly contorted, then the interactions are different, and it is possible for the weak mean vorticity of the outer part of the shear layer to be distorted and dispersed into the freestream – the process of 'vortex stripping' (Legras & Dritschel, 1993).

2. Analysis of external perturbations to boundary layers

2.1 Long length scale, low amplitude perturbations, and shear sheltering

Our object here is to analyze the external interactions (EI) between perturbations $\mathbf{u}^{[\infty]}(\mathbf{x}, t)$ in the freestream, where the streamwise mean velocity is $\overline{u} = U_\infty$ and the mean velocity profile $U(y)$ in the adjacent boundary layer over a rigid surface at $y = 0$. We are not considering the advected interactions (AI) of the perturbations as they enter the growing layer; in fact, we assume here that the layer has constant thickness h. Thus

$$U(y) = U_\infty \widetilde{U}(\widetilde{y}), \text{ where } \widetilde{y} = y/h$$

and

$$\widetilde{U} \to 1 \text{ as } \widetilde{y} \to \infty, \ \widetilde{U} = 0 \text{ at } \widetilde{y} = 0. \tag{2.1}$$

We consider a relatively weak 2-dimensional fluctuation with magnitude $u_0 << U_\infty$, with a length scale L, and that moves with a velocity c in the freestream. In order to obtain analytic solutions and demonstrate the key processes, we assume that $L >> h$; this approximation is relevant to many experiments and practical configurations (see Fig. 2). Because of their long length scale, any of these external perturbations interacting with a turbulent boundary layer effectively interact only with the smoothly varying mean profile. So any initial boundary layer fluctuations are ignored here but not in §2.2.

Thus in the freestream, as $y/L \to \infty$, the total velocity field $\mathbf{u}^*$ is given by $\mathbf{u}^* = \mathbf{u} + \overline{\mathbf{u}}$, where the perturbation field is expressed in moving coordinates as $\mathbf{u} = \mathbf{u}^{[\infty]} = u_0 \mathbf{f}(\widehat{x}, \widehat{y})$, where

$$\widehat{x} = \frac{(x - ct)}{L}, \ \widehat{y} = \frac{y}{L}, \text{ and } \mathbf{f} = (f_x, f_y, 0). \tag{2.2}$$

Either the maximum value $f_x \approx 1$, or if it is random its rms value $f_x' \approx 1$, so that u_0 indicates the magnitude of the freestream disturbance. We assume that

$$u_o << U_\infty. \tag{2.3}$$

We now consider how $\mathbf{u}$ changes above and within the layer as it is advected downwind. Previous studies by Grosch & Salwen (1978) and Jacobs & Durbin (1998) have considered small disturbances, where $\mathbf{f}$ is periodic in x and y, that travel at the same speed as the mean flow, i.e. $c = U_\infty$. They showed that as $Re(= hU_\infty/\nu) \to \infty$,

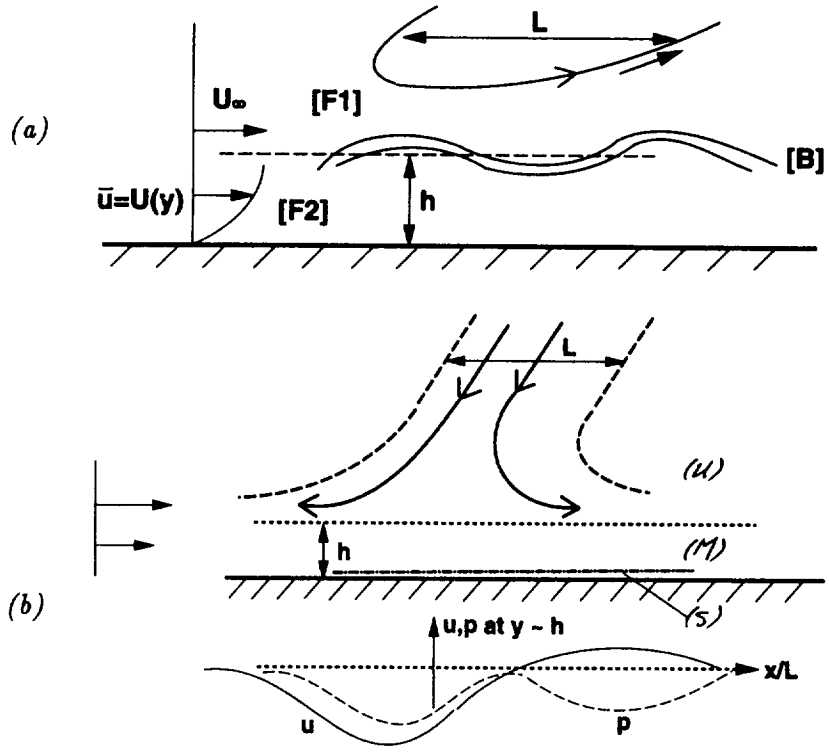

FIGURE 2. External interactions between a boundary layer flow in [F2] and small amplitude disturbances traveling with the freestream speed U_∞ in [F1]; *(a)* schematic diagram with scales showing the flow zones $\{\mathcal{U}\}$ in [F1] and $\{\mathcal{M}\}$, $\{\mathcal{S}\}$ in [F2]; *(b)* the perturbation streamlines in a moving wake traveling outside the boundary layer (after Hodson 1985) and profiles in the streamwise direction of the perturbation velocity u and pressure p at the top of the middle $\{\mathcal{M}\}$ zone.

external disturbances are damped within the boundary layer. If only linear disturbances are considered, they are exponentially small, below a penetration distance δ of order

$$h(hRe/L)^{-1/3}$$

so that as h/L decreases, δ/h increases. In the rest of this study we assume Re is very large, and we ignore such viscous effects except where they are very large in a thin zone, denoted as S, at the surface. These results demonstrate the principle of shear sheltering for linear disturbances when $c = U_\infty$. What happens if these constraints are relaxed? The experimental and numerical evidence is that some penetration can occur.

Consider the problem of a mathematically 'compact' moving disturbance such that $|\mathbf{f}| \to 0$ as $|\widehat{x}| \to \infty$. This could be the wake of a body moving across the stream ahead of the plate (Hodson 1985, Liu & Rodi 1991); in that case $f_x, f_y < 0$. Since $f_y \neq 0$ on $y = 0$, the external disturbances impact on the boundary layer and the plate. This creates a perturbation velocity $\Delta\mathbf{u}$, which is analyzed in different zones

corresponding to different mechanisms, namely: upper $\{\mathcal{U}\}$, where $y > h$; middle $\{\mathcal{M}\}$, where $h < y < h_s$; and surface $\{\mathcal{S}\}$ with depth h_s, where $h_s > y > 0$. As in other rapid distortion problems, the changes to the initial or freestream disturbances are linear over a travel time $T = x/U_\infty$ less than T_d, provided that T_d is much less than the time scale of the disturbance $T_L \sim L/u_0$. In the zone $\{\mathcal{U}\}$ above the boundary layer where the only vorticity is that of the disturbance, this vorticity field is simply advected by the mean flow and is not distorted by the changes to the perturbation velocity near the plate (Hunt & Graham 1978). This implies that the perturbation velocity field is the sum of the initial freestream field and an irrotational field, i.e.,

$$\mathbf{u} = \mathbf{u}^{[\infty]} + \Delta\mathbf{u}, \text{ where } \mathbf{u} = (u, v), \text{ and } (\Delta u, \Delta v) = \nabla\phi. \tag{2.4a}$$

To satisfy continuity

$$\nabla^2\phi = 0. \tag{2.4b}$$

Since the scale of the freestream perturbation $\mathbf{u}^{[\infty]}$ is large compared to the boundary layer depth h, the boundary condition on $\Delta\mathbf{u}$ near the plate is that

$$\text{as } y/L \to 0, \qquad \Delta v = \frac{\partial\phi}{\partial y} = -u_0 f_y. \tag{2.4c}$$

In the free stream as $y/L \to \infty$, $\Delta\mathbf{u} = |\nabla\phi| \to 0$. This linear calculation implies that $\Delta\mathbf{u}$ and ϕ are also functions of $\hat{x}$ and $\hat{y}$ and are not varying in time as they move downstream.

Note that further downstream where $T > T_L$, the impingement of the free stream perturbations onto the plate leads to significant distortion of their vorticity, typically rolling up into vortex tubes near the surface (Hodson 1985, Perot & Moin 1995)

In the middle layer $\{\mathcal{M}\}$, the equation for the vertical velocity perturbation v is essentially the long wave Rayleigh equation for small perturbations to a shear flow (Drazin & Reid 1980). It can be expressed in coordinates moving at the speed of the disturbance c as

$$\frac{\partial^2\hat{v}}{\partial\hat{y}^2} - \hat{v}\left(\frac{d^2U}{d\hat{y}^2}/(U-c)\right) = 0, \tag{2.5}$$

where $\hat{v}(\hat{x},\hat{y}) = v(x,y,t)$, and, for consistency, $\hat{u}(\hat{x},\hat{y}) = u(x,y,t) = -\int \frac{\partial v}{\partial y} dx$. To solve (2.5) it is convenient to write $\overline{U} = U(\hat{y}) - c$, noting that $\hat{y} = \tilde{y}h/L$ and that $d^2U/d\hat{y}^2 = d^2\overline{U}/d\hat{y}^2 \sim U_\infty L^2/h^2$. If $c = U_\infty$, then $\tilde{U} \approx 0$ at the top of the layer, and $\overline{U} \approx -c$ at the plate ($\hat{y} = 0$).

The solution for $(\hat{u},\hat{v})$ can be expressed as a separated variable (Lighthill-Stewartson) solution so that

$$\hat{u}(\hat{x},\hat{y}) = A(\hat{x})\frac{d\overline{U}}{d\hat{y}} + \frac{B(\hat{x})Z(\hat{y})}{U_\infty}, \tag{2.6}$$

where

$$\hat{Z}(\hat{y}) = \left[(d\overline{U}/d\hat{y})\int_{\hat{y}_1}^{\hat{y}} \overline{U}^{-2}(\hat{y}^+)d\hat{y}^+ + \overline{U}^{-1}(\hat{y})\right] U_\infty$$

and $A(\widehat{x})$, $B(\widehat{x})$ and $\widehat{y}_1$ are determined by satisfying the velocity and pressure conditions. In order that $v = 0$ on $y = 0$, and since $\overline{U}(0) \neq 0$, it follows that, $A(\widehat{x}) = 0$, and $\widehat{y}_1 = 0$.

To leading order $p^{[\mathcal{M}]}$ does not vary with y in $\{\mathcal{M}\}$ and is, therefore, equal to its value $p^{[\mathcal{U}]}(x)$ at the bottom of the upper layer $\{\mathcal{U}\}$ above the boundary layer. Thus

$$B(\widehat{x}) = -p^{[\mathcal{M}]}(\widehat{x}) = -p^{[\mathcal{U}]}(\widehat{x}, \widehat{y} \to 0) \tag{2.10}$$

Note that v and p at these two levels at the bottom of $\{\mathcal{U}\}$ and the top of part of $\{\mathcal{M}\}$ match each other.

$$\widehat{v} \sim (h/L)^2 u_0^2 / U_\infty. \tag{2.11}$$

Thus in $\{\mathcal{M}\}$, $\hat{v}$ becomes very much less than u_0. Therefore the blocking boundary condition for v in the upper zone $\{\mathcal{U}\}$ is applicable at the level $y \sim h$. For $y \leq h_\ell$, the streamwise velocity is given in terms of $p^{[\mathcal{M}]}$ by

$$u = p^{[\mathcal{M}]}(\widehat{x}) Z(\widehat{y}) / U_\infty \tag{2.12}$$

Thus in $\{\mathcal{M}\}$ $\hat{u} \sim (u_0^2/U_\infty)$ and is much less than in $\{\mathcal{U}\}$. But $\hat{u} >> \hat{v}$ if $h/L << 1$. At the top of $\{\mathcal{M}\}$, non-linear or viscous processes determine the smooth transition between these layers. An approximate form for u that is finite and continuous across the critical layer at $y \sim h$ and is asymptotically correct when $L >> y > h$ and when $y << h$ is

$$u(\widehat{x}, \widehat{y}) = \frac{-p^{[\mathcal{M}]}(\widehat{x})}{U_\infty / Z(\widehat{y}) + \lambda(\widehat{x})} \quad \text{where } \lambda = -p^{[\mathcal{M}]}/(u(\widehat{x}, \widehat{y} \to 0)) \text{ in } \{\mathcal{U}\}. \tag{2.13}$$

To illustrate these effects of the blocking of the external normal velocity $v^{[\infty]}$ by the vorticity in the boundary layer, when $c = U_\infty$, and the sheltering of the flow within the layer, we consider an example of a small but finite amplitude freestream perturbation that moves with the freestream and is of such a form that the pressure perturbation far above the plate is exactly zero. We take the practical example of a weak jet or wake such that $u = -(\cos\alpha, \sin\alpha) u_0 \widehat{f}$ where $\widehat{f} = 1/(1 + \widehat{x}^2)$. This corresponds to a traveling wake impacting on the boundary layer (Hodson 1985) if $\pi/2 > \alpha > 0$ or an atmospheric downburst if $\pi > \alpha > \pi/2$.

Then for $T < T_d$, at the bottom of the zone $\{\mathcal{U}\}$ just above the boundary layer the solution to (2.4) shows that $\Delta u(\widehat{x}, \widehat{y} = 0) = \lambda_u(\widehat{x}) u_0$, where

$$\lambda_u = \widehat{x} \sin\alpha / (1 + \widehat{x}^2), \tag{2.14}$$

so that for the wake the streamwise velocity perturbation just above the boundary layer consists of the negative freestream perturbation and a forward jet on the leading side of the perturbation and a negative one on the trailing edge. See Fig. 2b.

The results (2.10) and (2.12) show that to first order the velocity fluctuations in the boundary layer ($y < h$) are zero, but to second order are finite and depend on the pressure perturbation p_s in $\{\mathcal{U}\}$, where

$$p^{[\mathcal{M}]} = -(1/2)(u_\infty + \Delta u(y/L \to 0))^2. \tag{2.15a}$$

In this example

$$p^{[\mathcal{M}]}(x) = -\frac{1}{2}u_0^2\left[(-\cos\alpha + \hat{x}\sin\alpha)/(1+\hat{x}^2)\right]^2. \qquad (2.15b)$$

Note that the form of $u(x)$ in $\{\mathcal{M}\}$, derived from (2.12) differs from that in $\{\mathcal{U}\}$, being negative and having two minima. In the surface zone $\{\mathcal{S}\}$, viscous effects induce velocity profiles with inflexion points and may trigger instability there.

These results change as the travel time T increases so as to become comparable with T_L, when the vorticity of the impacting disturbance is significantly distorted. In addition, if the boundary layer is laminar, instabilities tend to be stimulated and modulated by the traveling disturbance above the layer, as recent direct numerical simulations demonstrate (Wu *et al.* 1998). The experimental flow studied by Liu & Rodi (1991) corresponds to that of our example, and the results in the early stages of the interaction are very similar to these theoretical results. Both the DNS and experiments demonstrate the sharp difference between the form and magnitude of the fluctuations in the zones $\{\mathcal{U}\}$ and $\{\mathcal{M}\}$, and both show that the instabilities are initiated very near the surface.

If the disturbances travel at speeds c significantly different from the freestream speed, as occurs in atmospheric downbursts, shear sheltering does not occur. Indeed the surface may be quite large, and their form may be strikingly different from those generated in normal conditions (Collier et al. 1994).

In terms of the concepts of interacting flows proposed in the introduction, these flows demonstrate the phenomena of exclusion (X) in some circumstances and essentially superposition (S) in others, depending largely on the parameter c/U and to a lesser extent on the amplitude u_0/U.

2.2 Finite amplitude perturbations and vortex stripping

In our previous analysis it was assumed that across the bounding interface [B] between the external region [F1] and the vortical region [F2], the vorticity $\vec{\omega}^{[2]}$ in the latter decreases abruptly to a much lower level in [F1]. However, in many vortical regions there is a gradual decrease in the magnitude of $\vec{\omega}^{[2]}$ from characteristic value ω_C in the core to a significantly lower value ω_B near the interface [B] where it is comparable with or smaller than the strain rate in the external region [F1]. Following Legras & Dritschel (1993), we review here the mechanisms for how in these flows external perturbations in [F1] cause large distortions and displacements of the interface [B] over distances of order h, the length scale of [F2]. These are associated with changes to the vorticity field in [F2] that are overwhelming in the outer part and small though significant in the core. Such interactions, involving a different type of inhomogeneity in [F2], plays a critical role in the formation and persistence of large scale vortical motions in the atmosphere and oceans and in the structure of shear flows with high levels of external turbulence.

We consider the interaction between a compact vortical region and a coplanar straining motion $U(x)$ in the external region [F1], having a length scale L that is large compared with h and a characteristic strain rate U_∞/L, see Fig. 3. We make the following assumptions for simplicity: in the core part of [F2], whose length scale

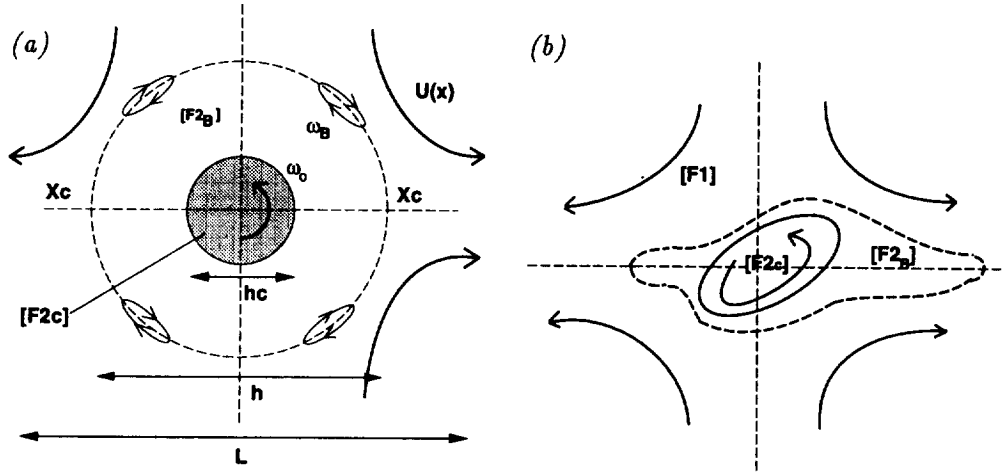

FIGURE 3. Schematic diagram of the mechanism for how external straining motion in [F1] remove, by 'vortex stripping', the low vorticity flow in the outer part $[F2_o]$ of the vortical region, while the inner core [F2c] is only slightly distorted; *(a)* showing the vortex sheet surrounding [F2] when the straining motion is initiated and the convergence points X_c where viscous diffusion leads to detrainment of vorticity.

is $h_C(<< h)$ and is denoted by $[F2_C]$, the initial vorticity is assumed to be much greater than the external strain rate so that $\omega_C >> U_\infty/L$, and in the larger outer part of the region, $[F2_B]$, the initial vorticity is much smaller and is of order ω_B where $\omega_B \leq U_\infty/L$.

The evolution of this flow can be analyzed by inviscid vortex dynamics following G. I. Taylor (See Batchelor 1970) and the theoretical and experimental methods of Rottman *et al.* (1987).

Imagine that the boundary [B] is rigid up to the time $t = 0$ (which means that the external flow passes round the vortex) and is then dissolved (or consider the flow to be generated by a rapidly growing instability); then a vortex sheet is generated around [B]. This vorticity distribution induces the fluid in the interface to follow the direction of the streamlines of the flow in [F1] but does not travel at the same speed. (This is analogous to how, when a cylinder of fluid is suddenly introduced into a cross flow, it distorts itself into a vortex pair and moves downstream at about half the speed of the flow).

The form of [B] as it moves depends on the relative strengths in the outer part of [F2] of the strain rates induced by the external flow and by the core vorticity, indicated by the parameter

$$\Sigma_B = (U_0/L)/(\omega_C h/h_C) \sim (U_0/L)/\omega_B.$$

If $\Sigma_B > 1$, much of the fluid and the vorticity in $[F2_0]$ is swept away in two vortices, leaving a trail behind them back to the core vortex. But if $\Sigma_B < 1$, the fluid and outer vorticity are carried round the core vortex in the form of an elliptical ring.

There is a sharp transition between these two outcomes as Σ_B increases as a result of the formation of singular (zero velocity) position on [B].

Note that, although the core vortex is strong enough that it is only slightly deformed, it is rotated by a finite angle until it reaches a position of equilibrium where it induces a velocity field that is opposite to that of the strain field.

This simple example demonstrates how weaker vorticity can be 'stripped' from the outer region of a vortical region by an external straining flow. Legras & Dritschel (1993) have quantified this process for different types of rotational and irrotational straining motion, and shapes, and orientations of the vortical regions. They find results that are consistent with observations of the changing shape of the the polar vortex and its accompanying 'ozone hole'.

The effect of finite amplitude external perturbations 'stripping' away the weak vorticity at the outer edge of shear layers has been demonstrated in two earlier laboratory studies. Hancock & Bradshaw (1990) measured the interactions between large scale freestream turbulence with rms velocity u_o and length scale L_x and the outer, low vorticity ($\sim \omega_B$) part (or 'wake') of a turbulent boundary layer whose depth is h. Their results show that when $u_0/L_x > \omega_B \sim u_*/h$ (or $u_0 > u_*$ the friction velocity or rms turbulence in the boundary layer), the mean vorticity ω_o in the outer part is stripped away and the thickness and structure of the boundary layer is reduced to that of the higher shear logarithmic region. For lower values of the external turbulence, there was no structural change. Rottman *et al.* (1987) obtained similar results when they measured how the the outer shear region of a gravity current was stripped away by external turbulence when $u_0/L_x > \omega_0$.

This model problem also shows how when vorticity is 'shed' from the boundary of a vortical region, it tends to develop into coherent patches of vorticity even in flows where the two regions are not coplanar as in jets in cross flow Coelho & Hunt 1989). These may have significant dynamical back effects on the region [F2] it 'left behind' and may transport matter and heat away from [F2].

In real rather than model complex flows, the vortical regions have finite gradients of vorticity, evolve on finite time scales, and, at their interface with the external flow, viscous diffusion of vorticity is part of the process of detrainment or shedding of vorticity. We have considered the first two of these idealizations; what about the third?

Vorticity tends to diffuse from a fluid interface around 'convergence' points, denoted by X_c in Fig. 3a, where the flow parallel to the surface converges and streamlines move into the exterior region [F1] from near the surface. Once a vortical region [F2] has developed into a steady form, if it is located in a unidirectional external flow U, the vorticity that diffuses from X_c can be advected away from [B]. Because of the converging flow, this detrained vorticity tends to be confined to 'wakes' whose width is small compared with h, as is observed below rising vortex rings (Turner 1963). Therefore, in such a flow over most of the exterior side of the interface [B], there is little shed vorticity so that the large scale interactions and the dynamics determining the response of [F2] to external perturbations is essentially inviscid, as we have assumed. In support of this hypothesis, one notes that in the above

example of a deformed vortical region, the detrainment of vorticity by unsteady vortex induced motions is very similar to that produced in a slowly changing flow with viscous diffusion, as is also found in many other flows (e.g. Dritschel 1990).

3. DNS study

A direct simulation of transition induced by turbulent wakes incident on a laminar boundary layer has been performed as part of the ASCI/CITS program at Stanford. The ideas discussed in the previous section have been applied to that study. Details can be found in Wu *et al.* (1998).

4. Implications and future work

The analysis in §2 of external fluctuations, with long streamwise length scale, traveling with the flow has shown how they are distorted by the mean shear of the boundary layer so as to be blocked above the layer and to be diminished within the layer. This interaction is not covered by the receptivity theory of Goldstein & Wundrow (1998), which is relevant to the disturbances advected into the layer and inducing long wave Klebanoff mode instabilities there. The transition phenomena simulated here do not have a ready theoretical explanation – this requires a more detailed look at the simulated flow fields (for example, the form and the effective Reynolds number of the inflected profile induced below the traveling disturbance) and perhaps more simulations with different initial conditions. Nevertheless, it became clear that the even the reduced level of velocity perturbations induced by the external unsteady wakes was sufficient to trigger transition, depending on the amplitude of the free stream fluctuations caused by the wake eddies. For low amplitudes the types of instability induced by infinitesimal disturbances were simulated; but as their amplitude became large enough, the instabilities could grow to the non-linear stage within the time of passing of the finite length external disturbance – a quantitative estimate of this threshold is desirable. Once this threshold was reached, the transition process did not change when the frequency of the external disturbances (i.e., its average level but not its peak) was increased. This suggests a saturation level was reached that is consistent with non-linear, dynamical systems concepts (Reddy *et al.* 1998).

To discuss the continuing effect in our simulations of the external disturbances once the boundary layer had become fully turbulent, it is helpful to relate them to previous studies of the interactions between external turbulence and turbulent boundary layers. These can be categorized into three groups. When 'weak' external turbulent eddies have a scale L that is of the order of the thickness h of the boundary layer and are less energetic than those of the boundary layer (i.e., $u_o < u_*$), they are swept round by the swirling movements of the large eddies at the edge of the boundary layer and entrained; their energy adds slightly to that of the turbulence in the boundary layer. But if their scale is large, they are essentially blocked by the mean shear.

When the eddies are of moderate strength (i.e., $u_o > u_*$), where $L \sim h$, the vortex stripping process can operate, and, although this disperses the vorticity upwards,

this effectively means that the outer vorticity is negligible, and the thickness of the boundary layer is reduced to a new level h/t where the mean shear is comparable to the external strain i.e., $du/dy \sim u_o/L$. This implies that the structure of the layer is changed to one where there is no outer 'wake' element, and only a 'log' law profile extends to the outer edge of the layer. As explained in §2.2, this is consistent with previous turbulence experiments. The simulations show that as the average vale of u_o is raised by increasing the frequency of the wake passing, the same trend in the profile is observed. This explanation needs to be tested in studies of the eddy structure in the outer region, for example, using interface sampling methods.

When the external eddies are much stronger than those of the undisturbed layer, (i.e. $u_* << u_o \sim U_\infty$), then its structure becomes more like that of a shear free turbulent boundary layer with the downdrafts and updrafts of the external eddies dominating the structure of the turbulence near the plate, including the surface shear. Thole & Bogard (1995) suggest that theoretical models and simulations (Perot & Moin 1995) for this limiting case are appropriate approximations when $u_o/U_\infty \sim 0.25$.

The next challenge is to investigate which of these results can be modeled with Reynolds averaged statistical equations. Some of the first attempts were reviewed by Pironneau *et al.* (1992).

REFERENCES

BATCHELOR, G. K., 1970 *An Introduction to Fluid Dynamics.* Cambridge University Press.

COELHO, S. L. V. & HUNT, J. C. R. 1989 The dynamics of the near field of strong jets in crossflows. *J. Fluid Mech.* **200,** 95-120.

COLLIER, C. G., DIXON, J., HARRISON, M. S. J., HUNT, J. C. R., MITCHELL, J. F. B. & RICHARDSON, D. S. 1994 Extreme surface winds in mid-latitude storms: forecasting and changes in climatology. *J. Wind Eng. Ind. Aero.* **52,** 1-27.

DRITSCHEL, D. G. 1990 The stability of elliptical vortices in an external straining flow. *J. Fluid Mech.* **210,** 223-261.

GOLDSTEIN, M. E. & WUNDROW, D. W. 1998 On the environmental realizability of algebraically growing disturbances and their relation to Klebanoff modes. *Theor. Comp. Fluid Dyn.* **10,** 171.

GROSCH, C. E. & SALWEN, H. 1978 The continuous spectrum of the Orr-Sommerfeld equation. Part I. The spectrum and the eigenfunctions. *J. Fluid Mech.* **87,** 33-54.

HANCOCK, P. E. & BRADSHAW, P. 1989 Turbulence structure of a boundary layer beneath a turbulent freestream. *J. Fluid Mech.* **205,** 45-76.

HODSON, H. P. 1985 Measurements of wake-generated unsteadiness in the rotor passages of axial flow turbines. *J. Eng. Gas Turbine Power.* **107,** 467-476.

HUNT, J. C .R. & CARRUTHERS, D. J. 1990 Rapid distortion theory and the 'problems' of turbulence. *J. Fluid Mech.* **212,** 497-532.

HUNT, J. C. R. & GRAHAM, J. M. R. 1978 Freestream turbulence near plane boundaries. *J. Fluid Mech.* **84,** 209-235.

JACOBS, R. G. & DURBIN, P. A. 1998 Shear sheltering and the continuous spectrum of the Orr-Sommerfeld equation. *Phys. Fluids.* **10,** 2006-2011.

LEGRAS, B. & DRITSCHEL, D. 1993 Vortex stripping and the generation of high vorticity gradients in two-dimensional flows. *Appl. Sci. Res.* **51,** 445-455.

LIU, X. & RODI, W. 1991 Experiments on transitional boundary layers with wake-induced unsteadiness. *J. Fluid Mech.* **231,** 229-256.

PEROT, B. & MOIN, P. 1995 Shear-free turbulent boundary layers. Part 1. Physical insights into near-wall turbulence. *J. Fluid Mech.* **295,** 199-227.

PIRONNEAU, O., RODI, W., RYHMING, I. L., SAVILL, A. M. & TRUONG, T. V. 1992 *Numerical Simulation of Unsteady Flows and Transition to Turbulence*, Cambridge University Press.

REDDY, S. C., SCHMIDT, P. J., BAGGETT, J. S. & HENNINGSON, D. S. 1998 On the stability of streamwise streaks and transition thresholds in plane channel flows. *J. Fluid Mech.* **365,** 269-303.

ROTTMAN, J. W., SIMPSON, J. E. & STANSBY, P. K. 1987 The motion of a cylinder of fluid released from rest in a cross-flow. *J. Fluid Mech.* **177,** 307-337.

SPALART, P. R. 1988 Direct simulation of a turbulent boundary layer up to $Re_\theta = 1410$. *J. Fluid Mech.* **187,** 61-98.

TERRY, P. W., NEWMAN, D. E. & MATTOR, N. 1992 Coherence of intense localized vorticity in decaying two-dimensional Navier-Stokes turbulence. *Phys. Fluids.* **4,** 927.

THOLE, K. A. & BOGARD, D. G. 1996 High freestream turbulence effects on turbulent boundary layers. *J. Fluid Eng.* **118,** 276-284.

TURNER, J. S. 1963 The motion of buoyant elements in turbulent surroundings. *J. Fluid Mech.* **16,** 1-16.

WU, X., JACOBS, R. G., HUNT, J. C. R. & DURBIN, P. A. 1998 Simulation of boundary layer transition induced by periodically passing wakes. Submitted to *J. Fluid Mech.*

Interfaces at the outer boundaries of turbulent motions

By D. K. Bisset, J. C. R. Hunt[1], X. Cai AND M. M. Rogers

1. Motivation and objectives

Most fully developed turbulent flows are inhomogeneous as a result of being blocked by rigid surfaces or by being in contact with regions of very low turbulence or even no motion at all. Inhomogeneity is a pronounced feature of all the canonical shear flows of engineering interest, e.g. wakes, jets, shear layers, and boundary layers. It is observed that the properties of the turbulent motions vary very rapidly at a bounding surface, either approaching a wall or across a highly contorted, moving interface separating the turbulent from the non-turbulent motions.

In relation to the eddy dynamics and statistical properties of the turbulence, the interface

1. delineates the largest scales of the turbulent velocity field L_x;
2. defines the rate of growth of the turbulent velocity field via the mean velocity of the bounding interface normal to itself (E_b);
3. defines, by its convoluted shape, the statistics of intermittency;
4. contains regions of intense local diffusion of vorticity, and of heat and matter; and
5. embodies a vorticity discontinuity where the normal component has to turn itself into a direction parallel to the interface since vortex lines cannot end within the fluid.

The interface is contorted over a range of length scales at least as great as that of the turbulent velocity field, which implies that the local diffusion is very intense (point 4 above); but this does not necessarily imply that the interface becomes diffuse because the eddy motions continuously rebuild the diffusion front. The usual presence of mean velocity E normal to the interface also plays a part. Even when there is no ambient flow, the turbulence generates such mean flows itself through the gradients of the Reynolds stresses provided that it is developing or is non-symmetrical. This motion E induced by the turbulence is also termed an entrainment velocity, but its magnitude and direction are invariably different from those of E_b (Turner 1986).

Components of velocity parallel to the interface might be increased by a vorticity discontinuity (point 5 above), but on the other hand they might decrease because they have no contribution from induction by the vortex lines that would have been

1 Permanent address: Cambridge University, DAMTP, Silver Street, Cambridge, UK

there in the absence of the interface (Carruthers & Hunt 1986). The fact that the vorticity is parallel while there is some component of fluctuating velocity normal to the interface suggests that the local helicity ($h \equiv \vec{\omega} \cdot \vec{u}$) is small; in fact, normalized h may become smaller as E_b becomes greater (Hunt & Hussain 1991).

Knowing more about the kinematic features of these interfaces will be useful for examining the implications of concepts and models that make simplifying assumptions about their large- and small-scale shape [which range from being flat (Phillips 1955) to fractal (Sreenivasan & Meneveau 1986)] and about their intermittency (Townsend 1976). The dynamics will be better understood when the rapid changes in the vorticity and velocity components are measured and studied in local frames to see if they are locally determined or whether they are essentially determined by the largest scales of the flow (Gartshore 1966). Additionally, the movement of fluid particles relative to the interface is the essential quantity to simulate, measure, and analyze in order to calculate how the interface affects the mixing of scalar quantities and thence how it controls chemical reactions and combustion. The *turbulent* interface considered here is not the viscous superlayer (Corrsin & Kistler 1955) that has a thickness of the order of the Kolmogorov lengthscale, though the superlayer could fall within it.

Some of the specific questions we are examining are the following.

1. What determines the interface propagation velocity E_b? In other words, for an unbounded turbulent shear flow, how does non-turbulent fluid become turbulent? We know that, in the limit, it happens through molecular diffusion across local regions of large velocity gradient and that such regions occur because of:
   - engulfment of irrotational fluid, which is then mixed deep within the flow, and
   - straining (stretching) motions in the vicinity of the turbulent/non-turbulent interface.
   - Are there other possibilities?

   Consider also detrainment, where isolated regions of rotational fluid detach and drift outwards. (See also the studies of Hunt, Durbin & Wu in this volume.)
2. What are the essential features of the interface (whether defined in terms of velocity, vorticity, and combinations such as helicity or scalar quantities and/or their derivatives) and are they distinct enough to define the interface?
3. (a) How can such an interface be defined unambiguously, especially since it may be multiply connected? (b) How can its 3D position and orientation (outward normal) be determined as $f(x, y, z, t)$ in the DNS data? [The answer depends on how distinct it is.]
4. What are the values of various properties in the vicinity of the interface (vector and scalar variances, correlations, ...)?
   - Are there systematic variations, e.g. differences between the outer face and inner face of a protrusion?
   - Are there any interesting changes in properties over time or changes in the interface shape (e.g. during engulfment)?

5. What are the characteristics of irrotational fluid that has moved away from its free-stream state? [Such fluid may contribute to mass flux, for example.]
6. Is there a dependence on Reynolds number, spreading rate, flow type, the nature of the DNS simulation, or other parameters (for example forcing, which clearly increases intermittency and the depth of the convolutions) for any of the above?

2. Accomplishments

The project is still in its early stages, and only a few of the above questions have been addressed so far. All of the work mentioned here utilizes the simulations of a temporally growing, self-preserving turbulent far-wake reported by Moser, Rogers & Ewing (1998). The data set stored at $\tau = 43$ was used for scalar detection work, and the data from $\tau = 91$ were used for vorticity-based detection.

2.1 Interface detection through scalar level

A preliminary investigation of interface properties was carried out by X. Cai using the level of a passive scalar as the interface detection criterion. Under some conditions the scalar can mark vortical regions quite accurately, and unlike vorticity, the scalar has exact, constant bounds to its range of values. Two main advantages result from this. First, detection threshold levels are likely to remain constant over time, and second, the level of numerical noise relative to thresholds can be assessed through examination of out-of-range values of the scalar. However, the way in which the scalar was initialized within the present DNS was aimed at a study of the transfer of fluid from one side of the wake to the other, and therefore the correspondence between scalar-marked regions and vortical regions is not always close, even at later times. The scalar was initialized with value 0.0 in the free-stream *below* the starting field of the turbulent wake and at 1.0 *above* it, with a smooth gradation of values within the turbulence. Nevertheless, these initial results suggest that the interface is very sharp, but that results may depend on the details of the detection procedure and threshold values used. A summary of this work is attached as an appendix.

2.2 Interface detection through vorticity

For current work we are using ω, the magnitude of the vorticity vector, for detection of the turbulent/non-turbulent interface, which should be more reliable than the passive scalar for the present DNS data. At very low levels, however, ω is affected by numerical noise. The magnitude of the noise problem depends on the intrinsic sharpness of the interface; if the interface is sharp, its detection should be relatively independent of the level of ω over some range, and a level slightly above any background noise can be used. Noise particularly affects the calculation of the direction of the normal to the interface.

Conditional averaging outside and inside the interface should be carried out along a line normal to the interface, which involves careful interpolation of data. Stored data in spectral form were projected onto a relatively fine, uniform physical grid of $385 \times 400 \times 97$ points so that linear interpolation between gridpoints would be accurate. For simplicity, the present results are confined to a subset of the data for

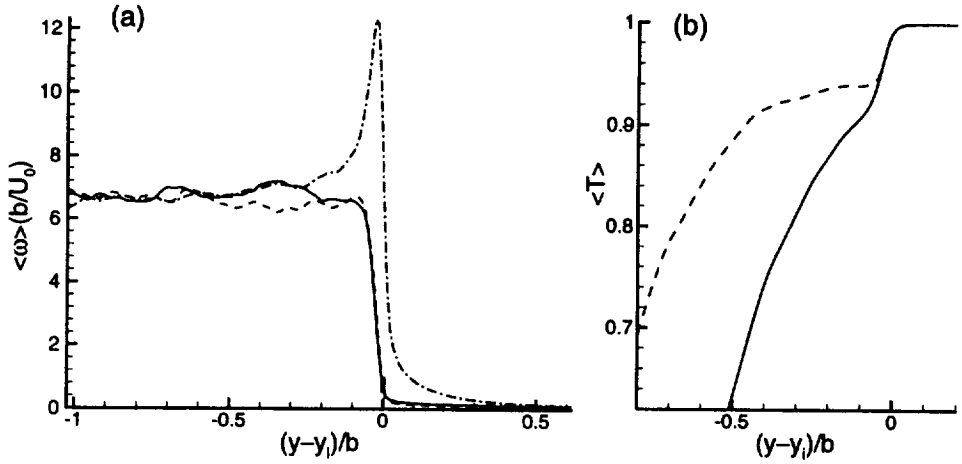

FIGURE 1. Effects of detection parameters on (a) vorticity magnitude, and (b) level of passive scalar, relative to the turbulent/non-turbulent interface. ——— inner group for $C_\omega = 0.7U_0/b$; ---- outer group for $C_\omega = 0.7U_0/b$; —·— $C_\omega = 7U_0/b$

which the surface normal is within 25° of the y-axis (normal to the wake centerplane), and conditional averaging is carried out in the y-direction only (with linear interpolation). Both sides of the wake are used, with sign reversal as appropriate. Only the outermost crossing of the vorticity threshold for any (x, z) position is considered in each case. Further interface positions resulting from irrotational fluid intruding below the detected vortical fluid (which certainly happens here and there) are ignored.

The lowest level of the detection threshold C_ω that seemed to give reliable interface detections was $0.7U_0/b$ (U_0 is the centerline velocity defect and b the wake width across the half-mean-velocity points); this level is used below unless stated otherwise. The interface indeed appears to be quite sharp in that substantial increases in C_ω had only small effects on detected positions, and conditional averages show little vorticity outside the interface. After application of the 25° angle criterion, about 26% of the surface area projected onto the centerplane was accepted.

The direction of the normal may in itself be significant for the properties of the interface, as may be its position on a protrusion or at the depths of an irrotational intrusion, and therefore other criteria may be used in conjunction with ω level. In particular, the main set of interface positions was split into three equal-size subsets according to whether the interface was roughly its average distance from the centerplane, or significantly closer, or further away (the last two being the 'inner' and 'outer' subsets for the following results).

The effects of threshold level and the inner/outer split on $\langle\omega\rangle$ are shown in Fig 1a. Angle brackets indicate conditional averaging relative to the detected interface at y_i while an overbar indicates a conventional average. For the main set of detections,

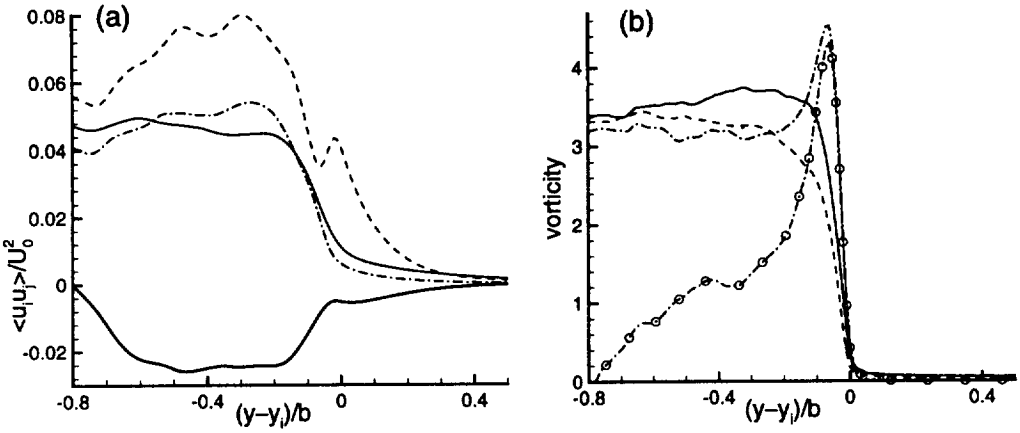

FIGURE 2. Normalized Reynolds stresses and vorticity components for $C_\omega = 0.7U_0/b$. (a) ---- $\langle u^2 \rangle$; —— $\langle v^2 \rangle$; —·— $\langle w^2 \rangle$; lowest curve is $\langle uv \rangle$. (b) —— $\langle |\omega_x| \rangle$; ---- $\langle |\omega_y| \rangle$; —·— $\langle |\Omega_z| \rangle$; ··· o ··· $-\langle \Omega_z \rangle$.

the distribution of $\langle \omega \rangle$ (not shown) is very similar to the inner and outer curves. Increasing C_ω by a factor of ten results in the appearance of a thin layer of very high $\langle \omega \rangle$, but there is a significant 'leakage' of vorticity into the irrotational region (Fig 1a). Also there is a reduction in the number of accepted points from 26% to 17% of the projected surface area here, leaving only the strongest regions for averaging. It turns out that there is very little difference for $\langle \omega \rangle$ between the inner and outer subsets (other quantities behave differently, as will be demonstrated).

The turbulent zone of the wake has almost uniform vorticity (Fig 1a), and the gradient at the interface is quite sharp. This gradient is not an artifact of the detection process: the tiny rectangle near $y = y_i$ shows a typical separation between adjacent data levels/gridpoints that confine the detected interface, and the threshold-based detection merely requires that the $\langle \omega \rangle$ curve should pass down through that rectangle.

Corresponding to the region of high gradient in $\langle \omega \rangle$, there is a large gradient of the scalar $\langle T \rangle$ (Fig 1b) that is almost identical for the inner and outer subsets. In terms of conditional averages, agreement between the interface and the edge of the scalar-marked zones seems remarkably good given the reservations expressed earlier, but it could be worse for surfaces not roughly parallel to the centerplane. Within turbulent zones there is a divergence between the inner and outer subsets, presumably related to the greater distance from the source of 'cold' scalar in this case, but it is not clear why there should then be such similarity within the interface.

Reynolds stresses relative to the interface and a breakdown of the components of ω are shown in Fig. 2 (all subsets combined). As expected, Reynolds stress levels for the interior of the wake are much the same as for the conventionally averaged case (Moser, Rogers & Ewing 1998) with some flattening of the peaks in $\overline{w^2}$ and

$\overline{uv}$. The levels of fluctuations induced in the irrotational zone are not negligible and decrease only slowly outside the interface — these are potential fluctuations, not 'leakage'. Gradients within turbulent zones near the interface (i.e. the slopes of the curves shown) are not as steep as for $\langle\omega\rangle$, which is presumably because of the greater contribution from large-scale structures to Reynolds stresses than to vorticity. It is conceivable that large increases in Reynolds number would steepen these gradients and eventually cause local maxima in $\langle u^2\rangle$ and $\langle w^2\rangle$, as suggested by Carruthers & Hunt (1986). The moderate-sized peak in $\langle u^2\rangle$ presently existing just inside the interface, which continues into the irrotational zone, is a result of the conventional (i.e. Reynolds averaging) definition of u^2 as $(U - \overline{U}(y))^2$, to be discussed shortly. Results for the inner and outer subsets taken separately (not shown) differ a little quantitatively but not qualitatively.

By symmetry $\langle\omega_x\rangle$ and $\langle\omega_y\rangle$ should be zero for surfaces parallel to the centerplane, so their magnitudes $\langle|\omega_x|\rangle$ and $\langle|\omega_y|\rangle$ are presented along with $-\langle\Omega_z\rangle$ and $\langle|\Omega_z|\rangle$ in Fig. 2b (Ω_z includes the non-zero mean spanwise vorticity). As noted earlier, the normal component ω_y is expected to decrease first as the interface is approached, which is verified by the results, while the parallel components exhibit sharper cutoffs. The peak in $-\langle\Omega_z\rangle$ is a result of the direct contribution from mean shear $d\overline{U}/dy$ for surfaces in the present orientation, and it appears that almost all ω_z has the same sign close to the interface. Spanwise vorticity $\langle\Omega_z\rangle$ changes sign across the midplane while its magnitude $\langle|\Omega_z|\rangle$ is nearly constant and similar to the other two magnitudes. Results for surfaces in other orientations may turn out differently.

The conventional mean velocity $\overline{U}(y)$ is compared to $\langle U\rangle$ in Fig. 3a, with the latter curve offset along the x-axis by the average height of interface detections. The gradient in $\langle U\rangle$ is quite sharp, and it is clear that the gentle rolloff in $\overline{U}$ is a result of a statistical distribution of superimposed instantaneously sharp dU/dy events. The larger difference between the two curves in the vicinity of the interface is the explanation for the extra peak in $\langle u^2\rangle$ seen in Fig. 2a, given the conventional definition of fluctuation u.

Conditional mean velocities for the inner and outer subsets show considerable differences (Fig. 3b). Both groups show a large gradient and sharp cutoff in $\langle U\rangle$, but just outside the interface the level of $\langle U\rangle$ is quite different: it is well below its free-stream value for the inner subset and significantly above free-stream for the outer subset. Presumably these are potential-flow effects caused by large protrusions of turbulent fluid either blocking or 'squeezing' the free-stream flow. Transverse velocity $\langle V\rangle$ for the outer group is dominated by a strong outwards flow ($\langle V\rangle$ reaches more than 12% of U_0) in the region inside the interface, suggesting quite active growth of the outer regions of the interface. The dominant feature for the inner group is an inwards flow in the region outside the interface; it is tempting to call this an entrainment flow although we don't know how the interface is moving relative to the fluid at this stage.

2.3 Tentative conclusions

The picture emerging so far, largely in agreement with the concepts of Townsend

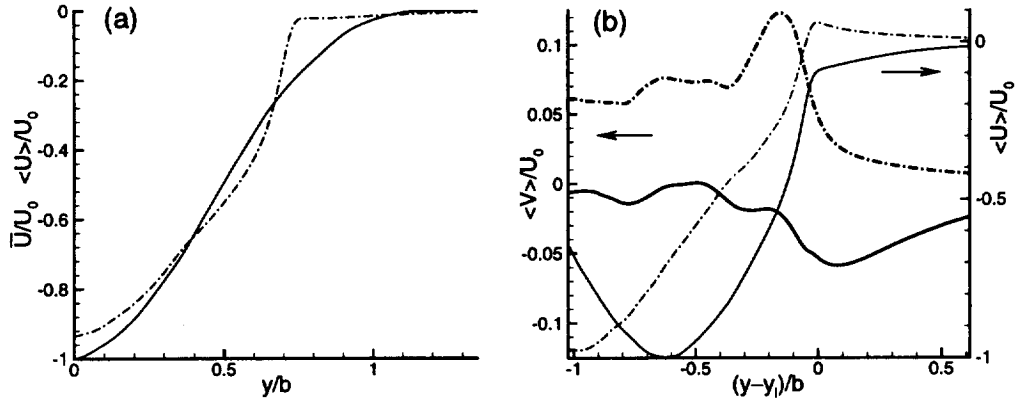

FIGURE 3. Mean velocity distributions. (a) —— $\overline{U}$; —·— $\langle U \rangle$ offset by $y = 0.75b$ (all detections). (b) —— inner subset; —·— outer subset.

(1976) and others, is that the far-wake consists of relatively uniform zones of well-developed turbulence bounded by a convoluted, rather sharp interface. Gradients of velocities, vorticity, and passive scalar are very steep through the interface until they suddenly flatten out at the free-stream. Both velocity fluctuations and systematic deviations in mean velocities $\langle U \rangle$ and $\langle V \rangle$ are quite significant within the irrotational regions near the interface. It will be very important to investigate and describe quantitatively the shape and movement of the interface, which is likely to be a function of the large-scale organized motion of turbulent flow. Additionally, there is at least the possibility of differences at much higher Reynolds numbers than that of the present simulation.

3. Future plans

Because this project is at an early stage, the quickest summary of future plans is to say that we will continue to study the six questions posed in Section 1. To begin with, we will extend the current procedures to regions where the interface is *not* roughly parallel to the wake centerplane.

In addition to the above, we plan to

- examine locally interesting regions including topological features both on and just inside the interface
- develop a means of describing concisely the shape of the interface
- use the unique time-dependent DNS results to determine how the interface moves and changes shape and to determine where and how it moves into irrotational fluid.

Data from the wake simulations with large-scale forcing (Moser, Rogers & Ewing 1998), which show a large increase in the sizes and heights of protrusions and intrusions, may be very useful for these purposes.

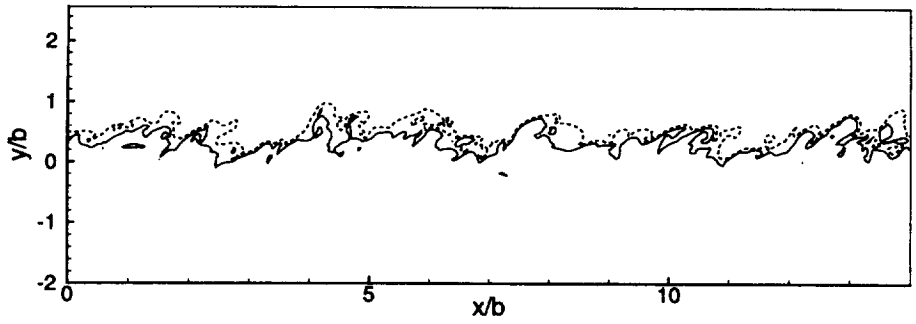

FIGURE A1. Typical interfaces at $C_s = 0.90$ (———) and $C_s = 0.99$ (----).

Appendix: Passive scalar detection of turbulent/non-turbulent interfaces

by Xiaodan Cai

A passive scalar has been used to outline the boundary of turbulent and non-turbulent flow in experimental works, e.g. Weir, Wood and Bradshaw (1981). A traditional reason for this is that the passive scalar obeys the same advective-diffusive equations as the vorticity for two-dimensional flow (given a Prandtl/Schmidt number of order 1). In some flows, such as wakes and mixing layers, the interface between turbulent and non-turbulent flow is dominated by two-dimensional vortical structure. Hence, it is expected that the passive scalar can give a good description of the interface. Based on such observations, an interface-detector is developed in this study. The algorithm for it is to search through the whole scalar field, which is constructed by a linear-interpolation from the calculated discrete values, for the surface with a specific scalar concentration (C_s). This technique is applied to a DNS database of a three-dimensional time-evolving plane wake (Moser, Rogers & Ewing 1998). The wake has reached an approximately self-similar state with a mass-flux Reynolds number (equal to the momentum thickness Reynolds number in spatially developing wakes) of 2000, which is high enough for a short $k^{-5/3}$ range to be evident in the streamwise one-dimensional velocity spectra. A passive scalar is advected within the wake and has a value of one (or zero) in the upper (or lower) external nonturbulent region. Here only the upper interface is analyzed. Fig. A1 shows the scalar contours for typical configurations of the interfaces at the threshold levels of 0.90 and 0.99. The interfaces are almost continuous, and there exist only very few islets.

Five threshold values have been tried for the passive scalar to define the upper interface in this study. Fig. A2 shows the probability density functions for the interface locations. All of the pdf's are approximately Gaussian with a skewness around zero and a flatness around 3.0, as shown in the Table. It is noted that the mean locations of the interface increase with the threshold values and that the interface can even cross the centerline to the lower part of the wake when $C_s \leq 0.9$.

Based on these observations, two sampling methods were investigated to calculate

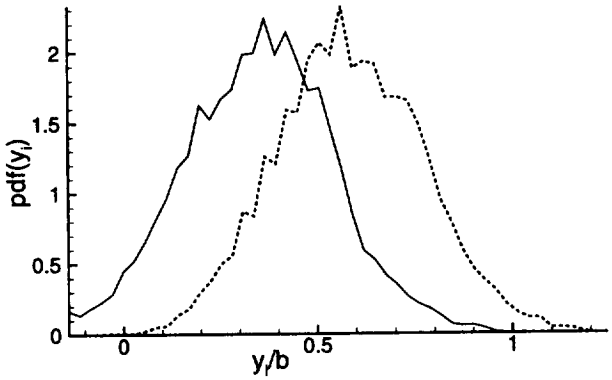

FIGURE A2. Probability density functions of interface positions for thresholds 0.9 (———) and 0.99 (----).

TABLE. Statistics of the interface positions

C_s	$\overline{y_i}/b$	y_i'/b	S_i	F_i
0.85	0.27	0.18	0.34	3.05
0.90	0.36	0.19	− 0.016	2.96
0.95	0.46	0.19	0.025	2.93
0.98	0.55	0.19	0.072	2.89
0.99	0.59	0.21	− 0.69	2.92

the conditional ensemble averages along y relative to the interface. Method I is to select the lowest y points as the locations of the interface whenever islets or multi-folded regions appear. Method II is to leave off the regions from the sampling space whenever islets or multi-folded regions appear. The sampling space is limited to the upper half of the wake. In order to increase the sampling points and reduce the statistical errors, a bar with 0.2 length-unit (based on the momentum thickness) wide is used to collect the samples and labeled according to the distance of its center from the interface. The conditional velocity intensities from the two sampling methods displayed very similar characteristics; Method II is used for the following results. Distributions of u^2, v^2, and w^2 (longitudinal, transverse, and spanwise components respectively) relative to the interface are shown in Fig. A3. Inside the turbulent region, $\langle v^2 \rangle$ is relatively uniform while $\langle u^2 \rangle$ and $\langle w^2 \rangle$ increase to a peak value when approaching the interface, which is consistent with the linear theory prediction by Carruthers and Hunt (1986). In the non-turbulent region, it can be seen that all of the velocity intensities decay towards zero sufficiently far from the interface, and there exists a region where $\langle u^2 \rangle \approx \langle v^2 \rangle + \langle w^2 \rangle$ and $\langle v^2 \rangle \approx \langle w^2 \rangle$, as predicted by the Phillips (1955) theory on the irrotational motion induced by the turbulent boundary flow. These phenomena prevail even when the threshold values are changed (Fig. A3).

Fig. A4 presents the distributions, for different threshold values, of conditional

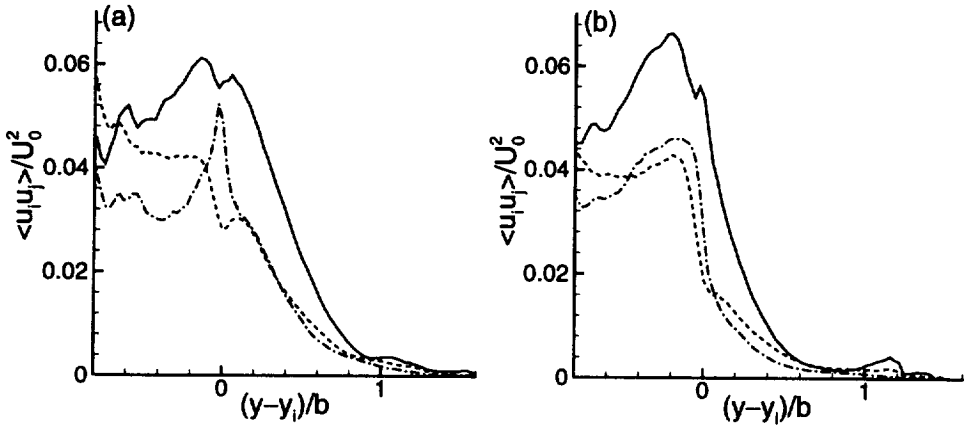

FIGURE A3. Distributions of —— $\langle u^2 \rangle$, ---- $\langle v^2 \rangle$ and —·— $\langle w^2 \rangle$ relative to the interface for threshold values (a) 0.90 and (b) 0.99

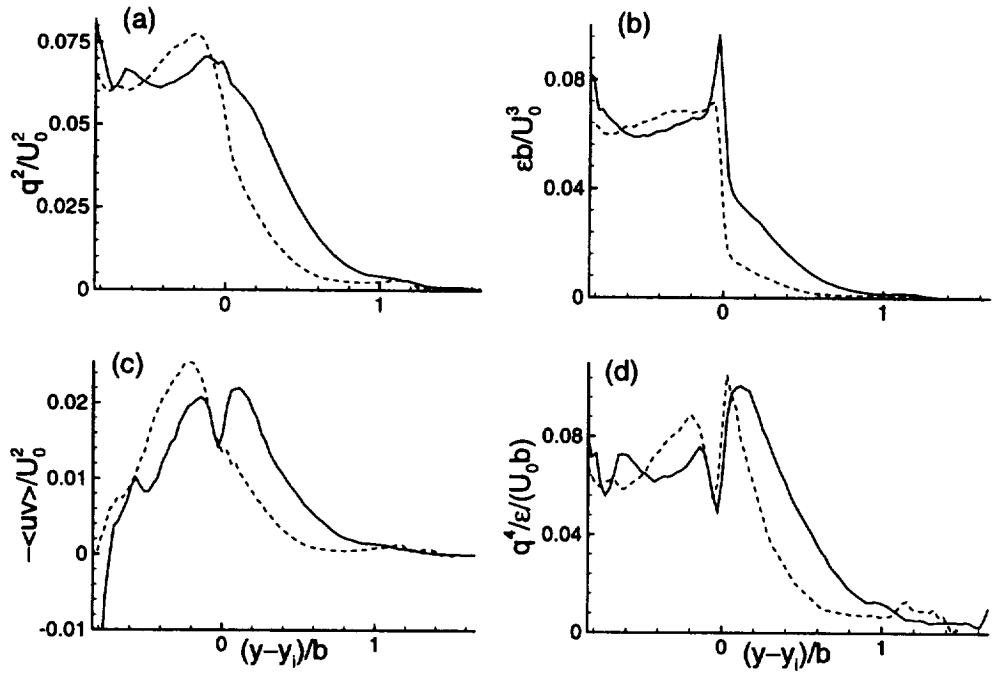

FIGURE A4. Distributions of various conditionally-averaged quantities for threshold values 0.9 (———) and 0.99 (----): a) q^2; b) ε; c) $-\langle uv \rangle$ and d) q^4/ε.

averages of turbulent energy q^2, dissipation rate ε, turbulent shear stress $-\langle uv \rangle$, and turbulent viscosity q^4/ε. Vorticity, and hence dissipation rate, should drop sharply across the turbulent/nonturbulent interface, which is demonstrated in Fig. A4(b). Furthermore, it is noted that the larger the threshold values, the sharper the edge between the turbulent and nonturbulent region, which is a good indication that the above-proposed interface detector works well in this wake flow. It also can be seen that the larger the threshold values, the more physical the results appear to be. As the threshold value increases, the peaks around the interface in Fig. A4(b) are weakened and finally disappear, and the peaks of turbulent shear stress in Fig. A4(c) shift from the nonturbulent side to the turbulent side. Physically, it can be argued that the turbulent shear stress cannot be generated by mean shear rate in irrotational flow, and therefore the peak values in the nonturbulent flow are unphysical. Meanwhile, it can be argued that there may exist different fluctuating kinetic energy-generation mechanisms inside and outside the interface. Inside the interface, the velocity fluctuations are generated by the mean shear rate, which results in a quite uniform value for q^4/ε in Fig. A4(d), while outside the interface, the velocity fluctuations are generated by the turbulent interface, which is the topic studied by Phillips (1955). This argument may explain why there is a big dip around the turbulent/nonturbulent interface in Fig. A4(d).

REFERENCES

CARRUTHERS, D. J. & HUNT, J. C. R. 1986 Velocity fluctuations near an interface between a turbulent region and a stably stratified layer. *J. Fluid Mech.* **165,** 475-501.

CORRSIN, S. & KISTLER, A. L. 1954 *NACA Tech Note 3133.*

GARTSHORE, I. S. 1966 An experimental examination of the large-eddy equilibrium hypothesis. *J. Fluid Mech.* **24,** 89-98.

HUNT, J. C. R. & HUSSAIN, F. 1991 A note on velocity, vorticity and helicity of inviscid fluid elements. *J. Fluid Mech.* **229,** 569-587

MOSER, R. D., ROGERS, M. M. & EWING, D. W. 1998 Self-similarity of time-evolving plane wakes. *J. Fluid Mech.* **367,** 255-289.

PHILLIPS, O. M. 1955 The irrotational motion outside a free boundary layer. *Proc. Camb. Phil. Soc.* **51,** 220.

SREENIVASAN, K. R. & MENEVEAU, C. 1986 The fractal facets of turbulence. *J. Fluid Mech.* **173,** 357-386.

TOWNSEND, A. A. 1976 *The Structure of Turbulent Shear Flow,* 2nd ed. Cambridge University Press.

TURNER, J. S. 1986 Turbulent entrainment: the development of the entrainment assumption and its application to geophysical flows. *J. Fluid Mech.* **173,** 431-471

WEIR, A. D., WOOD, D. H. & BRADSHAW, P. 1981 Interacting turbulent shear layers in a plane jet. *J. Fluid Mech.* **107,** 237.

The largest scales of turbulent wall flows

By Javier Jiménez[1]

1. Introduction

The small scales of wall-bounded turbulent flows have received a lot of attention in recent years, especially in the near-wall region, in part because of the availability of direct numerical simulations that made their detailed study possible (Kim, Moin & Moser 1987). Since those simulations had necessarily moderate Reynolds numbers and little or no separation between their largest and smallest scales, the study of the former independently of the latter in them was difficult. The purpose of this paper is to study the flow scales which are of the order of or larger than the channel width or the boundary layer thickness. We will see that their contribution to the integral flow quantities is not negligible.

The resolution of experiments and simulations is usually adjusted so that the discretized variables are smooth while the size of the numerical box, or of the experimental record, is chosen so that the correlation functions at distances comparable to the box size decay to a negligible level. The latter is intended to guarantee that there is little energy at scales larger than the box size, but it has to be interpreted with care. The energy in a flow that has been low-passed filtered at scales of order λ is proportional to the integral of the correlation function over separations longer than λ and decays slower than the function itself. Since singular spectra such as those in turbulent flows give rise to algebraically decaying correlation tails, it is possible to have correlations which appear to have decayed but which still have a substantial fraction of the energy in their tails.

The peak of the one-dimensional spectrum is moreover typically at $k = 0$. This becomes important if the filtered signals are the interesting ones such as in acoustics, where sound attenuation decreases with wavelength and only long waves survive at long distances.

Large structures are also physically interesting because long wavelengths imply long lifetimes and large volumes, and their integrated coherent effect can be comparable to those of the smaller ones even when their power per unit volume is not. Thus if the one-dimensional power spectrum of a signal tends to a constant E_0 as $k \to 0$, the power is contained in wavelengths longer than λ is $O(E_0/\lambda)$, but since the lifetime of each structure is proportional to λ, the total energy per structure is independent of the wavelength. As an example, even a small transverse velocity acting for a long time would lead to substantial modifications of the velocity profile. For a flow to be well represented in this sense implies that its resolved spectrum should decay at the lowest wavenumbers as well as at the highest ones, which may never be true in turbulent flows.

1 Also with the School of Aeronautics, U. Politécnica Madrid.

A less restrictive spectral criterion, involving only considerations of power per unit volume and, therefore, roughly equivalent to the condition on the correlation function, is that the product

$$\phi = kE(k), \tag{1}$$

should decay for the lowest observed wavenumbers since that pre-multiplied spectrum is proportional to the power in a logarithmic band centered at k (Bullock, Cooper and Abernathy, 1978). Note that the same is true if the wavelength, $\lambda = 2\pi/k$, is used in the abscissae instead of the wavenumber since $\mathrm{d}\log\lambda = -\mathrm{d}\log k$ and the integral is the same in both cases. In this paper we will generally use $\phi(\lambda)$.

There is another reason for studying these largest scales of wall turbulence. We have already mentioned that in some parts of the flow they carry a substantial fraction of the kinetic energy and are, therefore, important by themselves. They may also be simpler to study than regular turbulent structures in the inertial range. Since they are large but their velocity fluctuations are still small compared to the velocity differences in the mean flow, their velocity gradients are weak compared to the mean shear and can be approximately described as quasi-linear. We will in fact see that they share some of the characteristics of rapidly distorted turbulence.

This suggests the appealing possibility that wall flows could be described, as in the case of many free-shear ones, in terms of large-scale quasi-linear structures modulated by essentially isotropic small scales. This would contribute to the unification of an area of turbulence research, the study of the large scales, which has usually been considered non-universal.

2. Experimental evidence

2.1 Spanwise scales

Almost all the available information on the energy-containing spanwise scales in wall turbulence comes from direct numerical simulations. Spectra from two channels at $Re_\tau = 180$ (Kim, Moin & Moser, 1987) and $Re_\tau = 590$ (Mansour, Moser & Kim, 1996) are given in Fig. 1. The spectra of u and w near the wall show the well-known peak at $\lambda_z^+ \approx 100$ corresponding to the spanwise periodicity of the streaks. It is interesting that the wall-normal v spectrum peaks at a wavelength which is twice shorter than the other two. This was already observed in the transverse correlation functions by Kim *et al.* (1987), who explained it as corresponding to the diameter of the streamwise vortices. That explanation is only partly convincing since it is not clear why it would not apply as well to the spanwise velocity, which is also presumably associated with the vortices. The same effect is, moreover, observed at all distances from the wall, where coherent vortices are not necessarily present, and the effect should probably still be considered unexplained.

As we move away from the wall, the spectral peaks move to longer wavelengths and, near the center of the channel, show signs of being constrained by the periodicity of the numerical box. This is specially noticeable in the u spectrum of the high-Reynolds number channel, but all the u and w pre-multiplied spectra above $y/h \approx 0.5$ have their maxima at the second numerical wavelength, making it impossible to predict which their behavior would be in a wider box. It is clear, on the

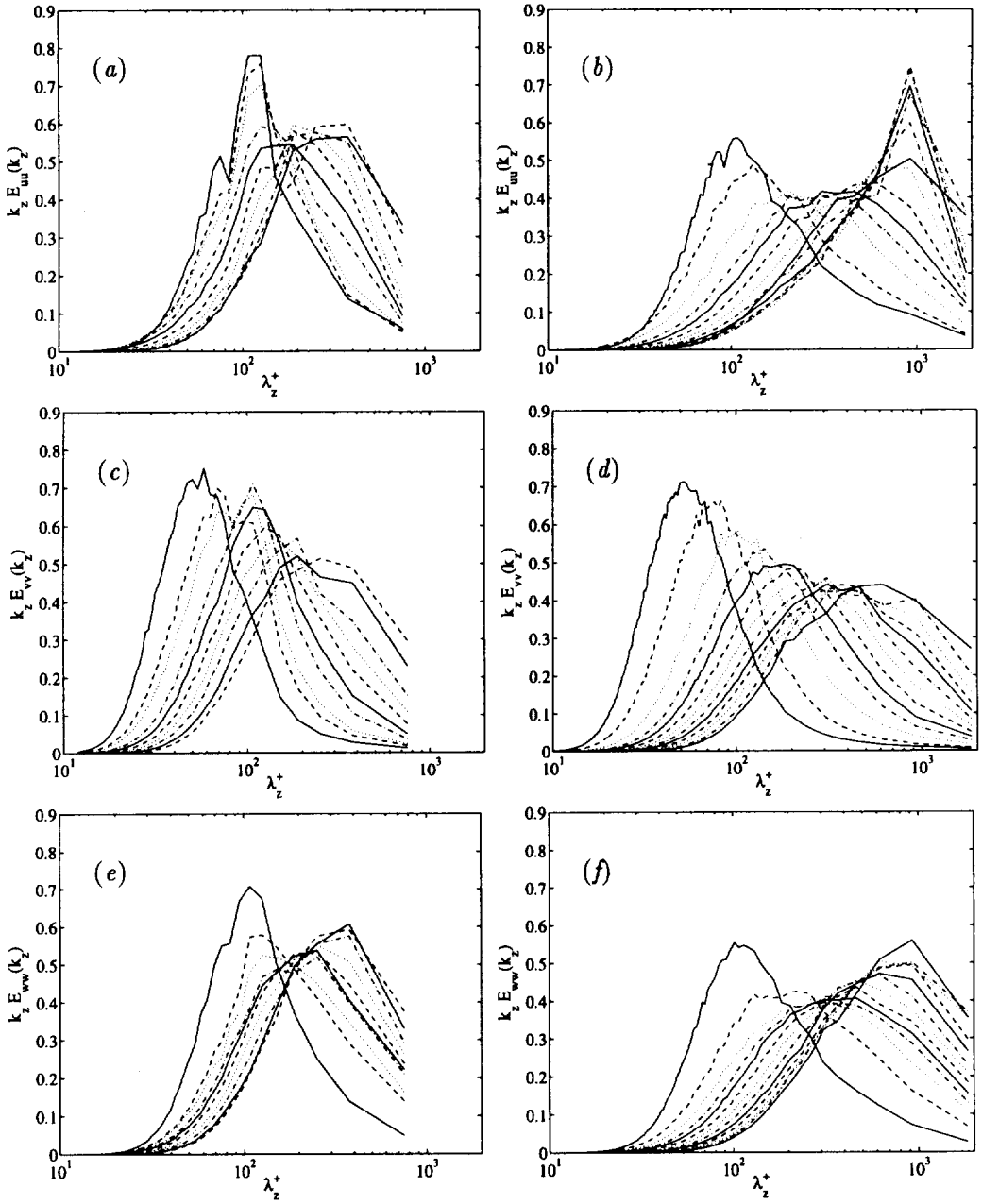

FIGURE 1. Pre-multiplied power spectrum $k_z E(k_z)$, as a function of λ_z^+. (*a*) and (*b*), E_{uu}; (*c*) and (*d*), E_{vv}; (*e*) and (*f*), E_{ww}. (*a*), (*c*) and (*e*), $Re_\tau = 180$ channel from Kim *et al.* (1987): $y^+ = 4$, 17, 23, 38, 50, 66, 84, 107, 141, 180. (*b*), (*d*) and (*f*), $Re_\tau = 590$ channel from Mansour *et al.* (1996): $y^+ = 5$, 19, 39, 60, 77, 99, 129, 167, 215, 274, 357, 461, 590. In both cases increasing y^+ corresponds to a rightward shift of the short-wavelength end of the spectrum, and lines rotate between solid, dashed, dotted and chaindotted. All the spectra are normalized to unit area, to emphasize their frequency content.

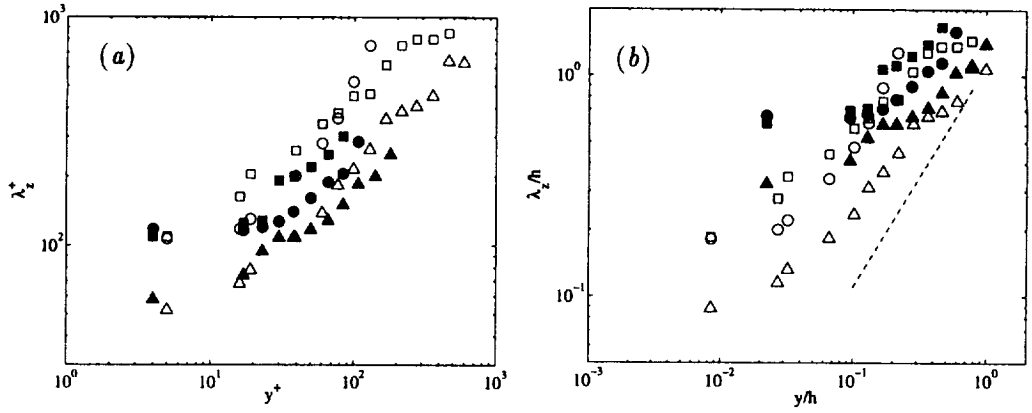

FIGURE 2. Spanwise wavelength of the maxima of the pre-multiplied spectra. ○ , E_{uu}; △ , E_{vv}; □ , E_{ww}. Open symbols, $Re_\tau = 590$; closed symbols, $Re_\tau = 180$. The dashed line has slope 1. (*a*) Wall units. (*b*) Outer units.

other hand, that the range of scales at $Re_\tau = 590$ is wider than at $Re_\tau = 180$, suggesting that, since the wavelengths near the wall clearly scale in wall (Kolmogorov) units, those near the center-line probably scale in outer units and are proportional to the channel width.

The spanwise wavelengths of the energy maxima for the different pre-multiplied spectra are given in Fig. 2. They were extracted manually from the data in Fig. 1 and should, therefore, be only taken as rough approximations. Only spectra whose maxima are not in one of the two rightmost points have been used in the figure. It is apparent that the data from both Reynolds numbers collapse very near the wall to approximately 100 wall units for E_{uu} and E_{ww} and grow approximately linearly as fractions of the channel height beyond $y^+ \approx 50$. The maxima of E_{vv} follow the same trend but are shorter by roughly a factor of two.

The data from v have a somewhat longer useful range near the center of the channel although it is clear from the inspection of Fig. 1 that even they should be treated with care. If we take them at face value and assume that their relation with the other two scales holds all the way to the center-line, the maximum size of of the v structures would be $\lambda_{zv}/h \approx 1$, and those of u and w would be $\lambda_z/h \approx 2$. This agrees with the result of Kim *et al.* (1987) that the velocity correlations decays beyond $z/h \approx 2$.

Note that the scales given by these maxima represent the size of the energy-containing structures and are different from the integral scale

$$\lambda_0 = \frac{\pi}{2} \frac{E(0)}{\int_0^\infty E(k)\,\mathrm{d}k}, \tag{2}$$

which can be shown to be roughly proportional to the width of the graph of ϕ, when plotted against $\log\lambda$, rather than to its maximum. It is actually easy to construct families of spectra such as

$$E(k) = [1 + a(a-1)k]\mathrm{e}^{-ak}, \tag{3}$$

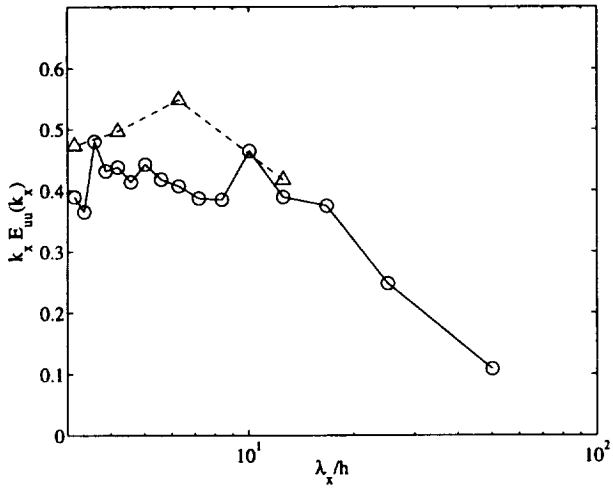

FIGURE 3. Pre-multiplied long-wavelength power spectrum $k_x E_{uu}(k_x)$ for the pipe in Priymak and Miyazaki (1994) at $y^+ = 3$. The dashed line is the spectrum in Kim *et al.* (1987) at $y^+ = 6$, included for comparison. Symbols in both cases are the numerical wave numbers.

which have a fixed integral length and an arbitrary location of the energy-containing peak. In this example λ_0 is always $\pi/2$, while the location λ_{max} of the maximum of ϕ varies from approximately 2π for $a = 1$ to πa for $a \gg 1$.

We will later find cases in which the position of the peak is not enough to characterize the energy-containing scales since the spectrum is dominated by an $E \sim k^{-1}$ range, which appears as a broad plateau in $\phi(\lambda)$, but that is not the case here.

2.2 Streamwise scales

There is evidence of very long streamwise wavelengths in pipes and channels even if the numerical simulations of Kim *et al.* (1987) show that the correlations decay beyond $x/h \approx 4$ in the streamwise direction. In this section we will use h to represent either the half-width of a channel or the radius of a pipe, while δ will be reserved for the boundary layer thickness.

Priymak and Miyazaki (1994), using coarse numerical simulations of a low Reynolds number pipe ($Re_\tau \approx 150$), find that their pre-multiplied streamwise spectra have an $E \sim k^{-1}$ range that only decays beyond $\lambda_x/h \approx 5\pi$ (Fig. 3). This low-wavenumber behavior was found below $y^+ \approx 60$ ($y/h = 0.4$). Note that as mentioned above a substantial part of the pre-multiplied spectrum extending beyond the longest resolved wavelength implies that part of the energy is not properly represented.

Bullock *et al.* (1978) found a similar low-wavenumber behavior in their experimental investigation of a turbulent pipe at $Re_\tau = 2600$. Their pre-multiplied longitudinal velocity spectra contain two 'peaks'. The one at the shortest wavelength is at $\lambda_x^+ \approx 600$ and is the only one present near the wall. Above $y^+ \approx 60$ another peak appears, or rather a k^{-1} range develops between the near-wall peak and a mild maximum at low wavenumbers which vary from $\lambda_x/h \approx 3$ at $y^+ = 60$ to

$\lambda_x/h \approx 20$ at $y/h \approx 0.6$. Beyond this point, the long-wavenumber peak disappears and is replaced by a shorter one at $\lambda_x \approx h$, which can be traced to the migration to longer wavelengths of a weakened version of the near-wall peak.

Both wavelength ranges are different. Radial correlations of the streamwise velocity show that the low wavenumbers are correlated across a wide radial range while the high ones are local in the radius.

Perry, Henbest and Chong (1986) made a detailed study of the streamwise u and v spectra in smooth pipes with $Re_\tau = 1,600 - 3,900$, with a special emphasis on the extent and scaling of the $E \sim k^{-1}$ range. They find that, in the region $y^+ > 140$ and $y/h < 0.3$, E_{uu} has a k^{-1} range which extends between a short-wavelength limit at $\lambda_x/y \approx 5$ and a longer one at $\lambda_x/h \approx 15$. They present no measurements within the near-wall region, but if their short-wavelength limit were extrapolated to the inner edge of the logarithmic layer at $y^+ \approx 100$, it would fall in the same range as the near-wall peak mentioned above. Beyond $y/h \approx 0.3$ the short-wavelength end of the k^{-1} range is no longer proportional to y and settles around $\lambda_x/h \approx 3$. Although the uncertainties from reading printed spectra are large, the order of magnitude of these wavelengths is comparable to the two 'peaks' found by Bullock *et al.* (1978). The marching short-wavelength limit would originate from the near-wall peak and eventually connect with the $\lambda_x \approx h$ outer peak observed in the center of the pipe by Bullock *et al.*, while the long-wavelength peak would be the same in both experiments. It is interesting that in both cases the k^{-1} range is only found in what is usually considered the logarithmic region and disappears towards the center of the pipe.

In a previous paper Perry and Chong (1982) had presented results for rough pipes at comparable Reynolds number, although only for E_{uu} in a narrow range of y stations within the logarithmic region. The k^{-1} is very apparent and appears to be longer than in the smooth case. Its long-wavelength limit is at the same location as in the latter, but it extends to shorter wavelengths of the order of $\lambda_x \approx y$.

The streamwise spectra for the two numerical channels discussed in the previous section are shown in Fig. 4. There is a clear difference between the spectra of the streamwise fluctuations and those of the other two components. While the latter show only a mild drift to longer scales as they get farther from the wall, the former have most of their energy at very long wavelengths, in agreement with the previous discussion, and are clearly constrained by the numerical box. Note that in the $Re_\tau = 180$ channel the short end of the k^{-1} range at the edge of the similarity region would be $5y^+ \approx 300$, shorter than the expected viscous length near the wall. As a consequence the position of the spectral peak moves towards shorter wavelengths as it moves away from the wall.

The short-wavelength peak found near the wall in all these cases is probably related to previous observations in experiments and numerical simulations. Clark and Markland (1971) report that the mean streamwise spacing between near-wall vortices is $\lambda_x^+ = 440$, while various investigators have reported that the mean distance between substructures within turbulent boundary layer spots is $\lambda_x^+ \approx 200 - 500$ (see Sankaran *et al.* 1988, and references therein). Jiménez & Moin (1991) observed that

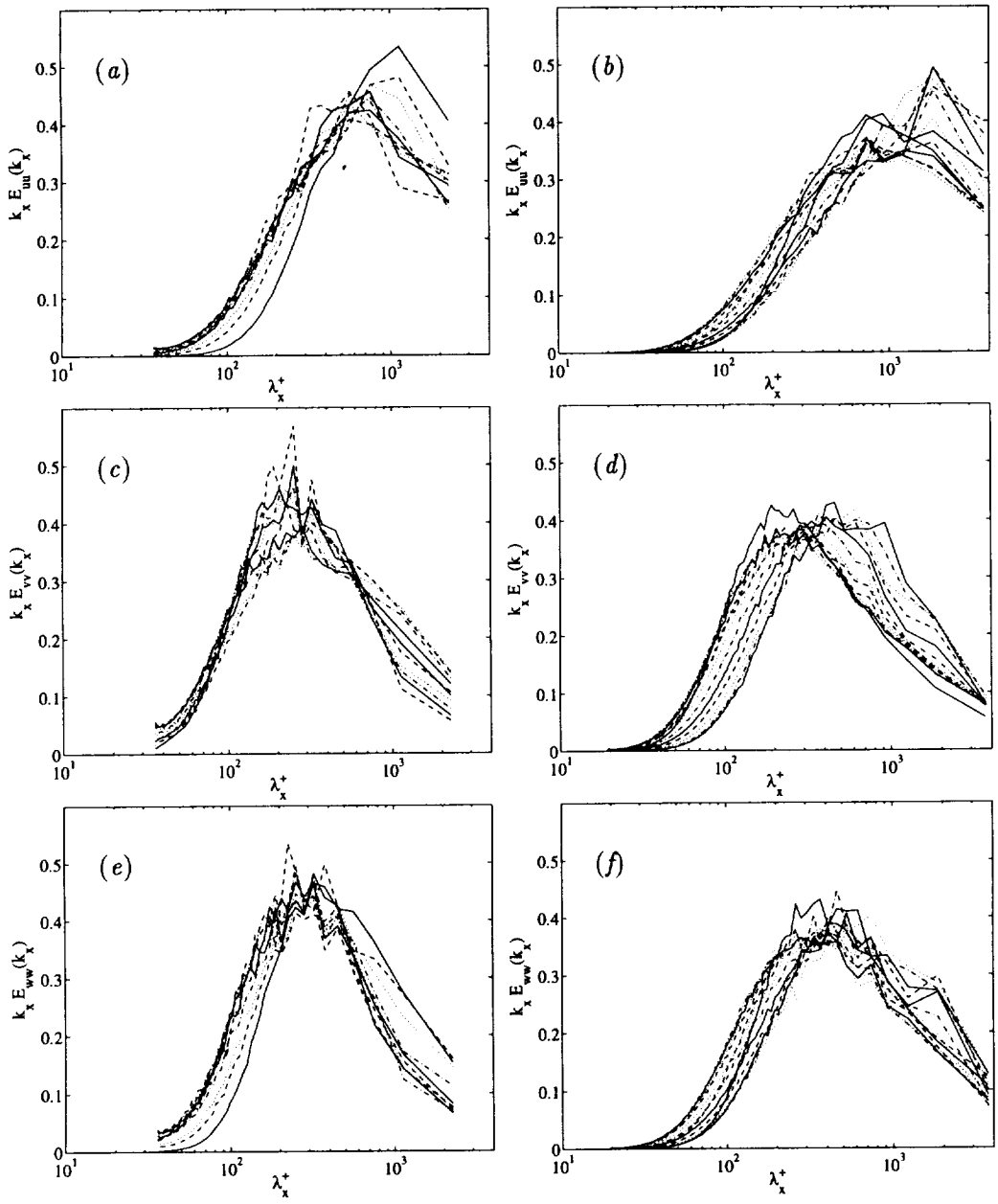

FIGURE 4. Pre-multiplied power spectra $\phi(\lambda_x)$. Symbols as in Fig. 1, but in this case the spectra for $Re_\tau = 180$ move to shorter wavelengths with increasing distance from the wall.

turbulence could not be maintained in numerical boxes with a streamwise periodicity shorter than $\lambda_x^+ \approx 350$, while Jiménez & Pinelli (1998) showed that turbulence decays if the streamwise coherence of the velocity streaks near the wall is disturbed

below $\lambda_x^+ \approx 400$. In both cases the minimum streamwise period corresponds to boxes containing a single pair of streamwise vortices flanking each sublayer velocity streak.

The long wavenumber range has been reported less often, probably in most cases because of insufficient extent of the numerical or experimental records. Choi and Moin (1990), for example, while studying the wall pressure spectra in the channel of Kim *et al.* (1987), noticed a spurious peak at their lowest wavenumber, $k_x h = 0.5$ ($\lambda_x/h = 4\pi$), which they attributed to the periodicity of the box, suggesting that the long wavelengths were poorly resolved.

In boundary layers, whose low-wavenumber characteristics need not be identical to those of internal flows, Farabee and Casarella (1991) measured spectra of the wall pressure fluctuations down to very low frequencies. They found that the low-wavenumber end of their pre-multiplied spectra collapses well in outer flow variables and only decreases beyond $k_x\delta \approx 0.25$ ($\lambda/\delta \approx 8\pi$), where δ is a boundary layer thickness roughly equivalent to the pipe radius. Their Reynolds numbers are $Re_\tau \approx 1,000 - 2,000$.

Nagib and Hites (1995) and Hites (1997) measured longitudinal velocity spectra in boundary layers with $Re_\theta = 4 - 20 \times 10^3$, corresponding to $Re_\tau \approx 1.5 - 6 \times 10^3$. They report a k^{-1} range above $y^+ = 50$, extending from a short-wavelength limit at $\lambda_x^+ \approx 600$ to a longest wavelength of $\lambda_x/\delta \approx 4$. The latter is substantially shorter than the long-wavelength limit observed in pipes and channels and also shorter than the wavelength implied by the pressure spectra of Farabee and Casarella (1991). This might be due to a procedural artifact. Their spectra are computed digitally from records which limit them to wavelengths shorter than about $\lambda_x^+ \approx 10^5$, which at their highest Reynolds numbers corresponds to $\lambda_x/\delta \approx 20$. Since the last few points in the spectrum are generally corrupted by the windowing algorithm, this implies that the location of their low frequency peak is uncertain. It is interesting that their k^{-1} range is only present below $y^+ \approx 200$ and that above that range their pre-multiplied spectra contain a single peak at long wavelengths, suggesting again, when compared to other results, that their longest wavelengths may have been missed by the experimental procedure. In fact, in a different analysis of the same data, Hites (1997) measured the fraction of the streamwise kinetic energy in a low-pass filtered version of his velocity signals and found that about 30–50% of the energy was associated with wavelengths longer than the long-wavenumber peak in his spectra and that this fraction increased with the Reynolds number. About 15% was associated with wavelengths longer than $\lambda_x/\delta = 10$. This was observed at the only two locations studied in this way, $y^+ = 100$ and 300.

The experimental results for the longitudinal extent of the streamwise velocity fluctuations are summarized in Fig. 5. Figure 5*a* gives the location of the short-wavenumber end of the energy-containing range. This is the only longitudinal scale which exists at all positions across the flow. Near the wall it corresponds to an isolated energy peak in the pre-multiplied spectrum near $\lambda_x^+ \approx 600$. It grows away from the wall until $y/h \approx 0.3$, and it remains constant or decreases slightly above that level. The few data available do not collapse well in either wall or outer units,

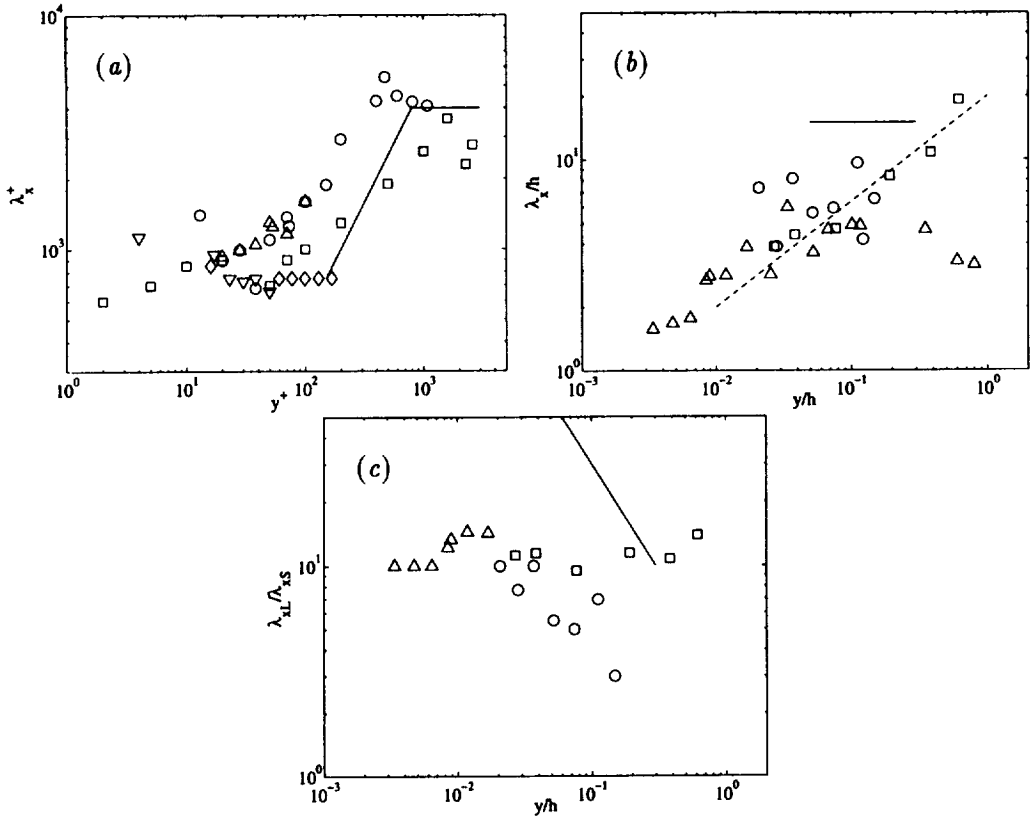

FIGURE 5. Wavelength of the two limits of the k^{-1} range in $E_{uu}(k_x)$, as a function of the distance from the wall. o , Hites (1997), $Re_\tau = 1350$; $\triangle$, Hites(1997), $Re_\tau = 5900$; $\square$, Bullock *et al.* (1978), $Re_\tau = 2600$; ∇ , Kim *et al.* (1987), $Re_\tau = 180$; $\diamond$, Mansour *et al.* (1996), $Re_\tau = 590$; ——— , Perry *et al.* (1986), $Re_\tau \approx 3000$. (*a*) Short-wavelength limit in wall units. (*b*) Long-wavelength limit, in outer units. The dashed line has slope 1/2. (*c*) Ratio between the two limits of the energy-containing range.

and the support for a linear growth with wall distance is only moderate. The range of useful experimental Reynolds available is not large, $Re_\tau = 1,000 - 6,000$, but in that range the maximum wavelength of this peak near the center of the channel is $\lambda_x/h = 1 - 2$. We have seen in the previous section that the spanwise extent of the structures containing the streamwise kinetic energy varies from $\lambda_z^+ = 100$ near the wall to $\lambda_z \approx 2h$ at the center. Assuming that the structures involved are the same in both cases, this would imply that the large scales vary smoothly from a streamwise aspect ratio of about 6 near the wall to approximate isotropy near the center.

The real picture is more complicated. Between $y^+ \approx 100$ and $y/h \approx 0.3 - 0.5$ a second limit appears, which is given in Fig. 5*b*. It scales well in outer units within the present range of Reynolds numbers and constitutes the long-wavelength limit

of an $E \sim k^{-1}$ spectral range which contains essentially all the streamwise kinetic energy. The available data, except for those in Perry *et al.* (1986), suggest that the ratio between those two limits is always approximately equal to 10 (Fig. 5*c*) and that both scales grow as $y^{1/2}$. The long-wavelength limit disappears in the center of the channel, and the k^{-1} range again collapses to a single spectral peak. The existence of the k^{-1} range approximately coincides in these experiments with the logarithmic region of the mean velocity profile.

The square-root dependence on wall distance is surprising and would imply that the length scale is determined by some viscous mechanism, probably based on an eddy viscosity which stays constant across the flow. This would be difficult to understand, and there is enough scatter in the data to leave open the possibility of a linear dependence, but this is one of the many points in these data that call for urgent clarification.

The data on the other velocity components are scantier. The wall-normal component v has been measured in several occasions, and there is general agreement that it does not contain a k^{-1} range (Perry *et al.*, 1986). The $k^{-5/3}$ inertial range in its one-dimensional streamwise spectrum connects directly with a low-frequency range which is essentially flat. The corner between the two regimes is at about the same scale as the short-wavelength end of the k^{-1} range in E_{uu}, and it is at those scales that most of its energy is concentrated. The data in Fig. 4 support this interpretation.

There are even less data on the spanwise component w. The numerical data in Fig. 4 suggest that there is no k^{-1} spectrum for this component and that its characteristic wavelengths are those of v rather than u. The same can be deduced from the spectra given by Lawn (1971), in a pipe at $Re_\tau \approx 2,000$. Although his spectra are noisy and clearly truncated at low frequency, they fall in two groups: long ones for E_{uu}, which continue growing at his lowest measured frequencies, and short ones for E_{vv} and E_{ww}, which flatten beyond $\lambda_x/h \approx 2$.

Perry, Lim and Henbest (1987) suggest that E_{ww} has a short k^{-1} range in contrast to E_{vv}, but inspection of their data reveals that if this range exists it is much narrower than that of E_{uu} and is located at wavelengths which are an order of magnitude shorter than those of u.

Saddoughi & Veeravalli (1994) and Saddoughi (1997) made measurements in rough perturbed boundary layers at $Re_\tau = 30,000 - 160,000$. Although their analysis is centered on the isotropy of the inertial range, the long-wavelength behavior of their spectra can be used as a check of the Reynolds number independence of the previous conclusions since their Re_τ are at least an order of magnitude larger than those discussed up to now. Their spectra also fall clearly in a short group for v and w and a long one for u.

2.3 Reynolds stresses

Perry *et al.* (1987) suggest, mostly on theoretical grounds, that no k^{-1} range should be found in the E_{uv} cospectrum. The basic argument, which goes back to Townsend (1976) and which is implicit in the classical distinction between 'active' and 'inactive' motions, is that, since Reynolds stresses depend on the presence of v,

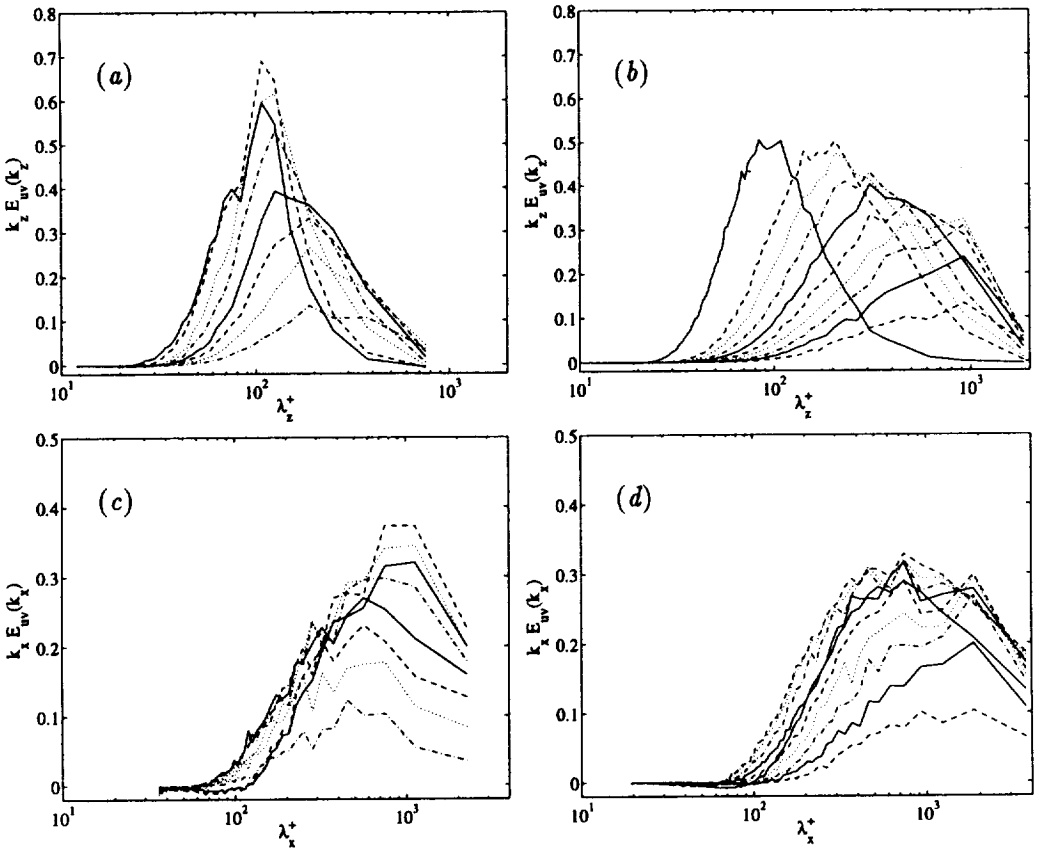

FIGURE 6. Pre-multiplied power co-spectra. (*a*) and (*b*) $k_z E_{uv}(k_z)$, as a function of λ_z^+. (*c*) and (*d*) $k_x E_{uv}(k_x)$, as a function of λ_x^+. (*a*) and (*c*) $Re_\tau = 180$ channel from Kim *et al.* (1987): $y^+ = 17, 23, 38, 50, 66, 84, 107, 141$. (*b*) and (*d*), $Re_\tau = 590$ channel from Mansour *et al.* (1996): $y^+ = 16, 60, 77, 99, 129, 167, 215, 274, 357, 461$. In both cases lines rotate between solid, dashed, dotted, and chaindotted. The spectra are not normalized to unit area, and decreasing amplitudes generally correspond to larger distances from the wall. Note that, as for the velocity spectra in Fig. 4*a*, the scale of the $Re_\tau = 180$ cospectrum in (*c*) decreases away from the wall.

they can not be present at scales at which the latter is not active. A little thought reveal that this is not necessarily so. Consider the low-frequency spectral range in which $E_{uu} \sim k^{-1}$ and $E_{vv} \sim 1$. The only limitation for the cospectrum is that $E_{uv}^2 \leq E_{uu}E_{vv}$, and it is possible to have substantial Reynolds stresses even at wavenumbers at which the v spectrum is already constant.

The streamwise and spanwise cospectra from the two numerical channel simulations are given in Fig. 6. The drift in λ_z away from the wall is similar to that of u and w in Fig. 1, and there is a clear suggestion of a k_x^{-1} range in the streamwise cospectrum of the higher Reynolds number case. A comparison with Fig. 4 shows

that the characteristic wavelengths of the cospectra are those of u rather than those of v.

Krogstad, Antonia and Browne (1992) give spectra for E_{uu}, E_{vv}, and E_{uv} in a boundary layer at $Re_\tau \approx 2,000$. The pre-multiplied E_{uu} and E_{uv} have broad maxima, both of which only decay beyond $\lambda_x/\delta \approx 6$, while E_{vv} has a narrower peak at wavelengths which are an order of magnitude shorter.

Saddoughi & Veeravalli (1994) measured E_{uv} at $y/\delta = 0.1$ and 0.4. The cospectra at the near-wall station have a well-developed k_x^{-1} range that extends from $\lambda/\delta \approx 0.5$ to $\lambda/\delta \approx 7$. Note that these values are very close to the limits of the k_x^{-1} range for E_{uu} given in Fig. 5 at this distance from the wall. Their cospectra at the mid-layer location have essentially no k^{-1} range.

Lawn (1971) measured some cospectra. They are generally short, like v and w, but it is interesting that the two cospectra for which $y^+ > 200$ and $y/h < 0.5$ are 'long' and continue to increase beyond their lowest wavenumber $\lambda_x/h = 50$.

3. Discussion

The general picture suggested by the data discussed above is that there exist in the region of the flow generally associated with a logarithmic velocity profile very long structures with longitudinal aspect ratios of the order of 10, which essentially consist of streamwise velocity fluctuations. They contain most of the streamwise kinetic energy. Spanwise and wall-normal velocities have shorter wavelengths, roughly coincident with the shorter end of the scales of the u structures, and are only slightly elongated in the streamwise direction.

Long streamwise structures which contain predominantly streamwise velocity can best be described as a system of longitudinal jets and are reminiscent of the sublayer low- and high-velocity streaks, although in this case they would clearly be turbulent themselves. In the sublayer streaks, for example, the quasi-streamwise vortices responsible for the v and w fluctuations are also shorter than the streaks, and the latter are the result of the action of several vortex pairs (Jeong, Hussain, Schoppa & Kim 1997).

In Fig. 7 we give an instantaneous picture of the u and v contours for a wall-parallel plane of the numerical $Re_\tau = 590$ numerical channel from Mansour, Moser and Kim (1996), even if we have seen that their box is too short to represent these structures correctly. There is clearly a large low-velocity streak on the upper half of the u-plane which is not present in v. The transverse section in the lower frame of the figure shows that this is not an isolated case and that there are several jets at roughly the same scale. They are distinct from the sublayer streaks, being much larger, but they seem to form from the joint effect of several of them.

Komminaho, Lundbladh, and Johansson (1996), who have observed streamwise structures of the order of $40h$ in low-Reynolds-number Couette flow, publish snapshots of their simulations which look strikingly similar to Fig. 7.

Very large streaky features with widths and heights of several hundred meters are known to occur in the atmospheric boundary layer, apparently associated with storms having a large geostrophic shear (J. C. R. Hunt, private communication), and

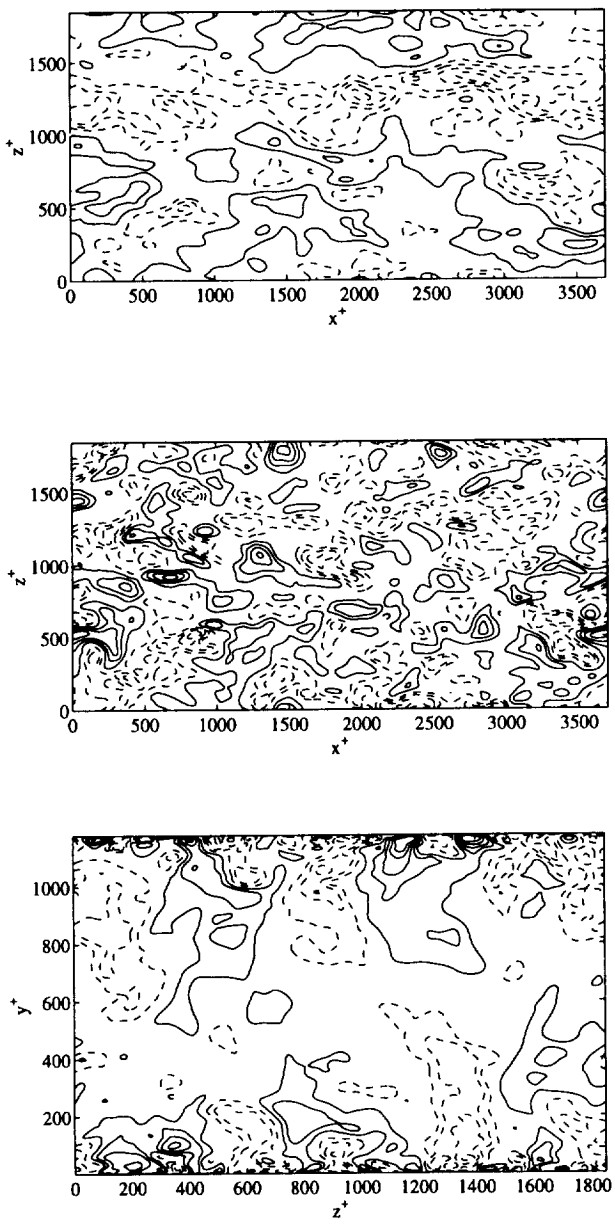

FIGURE 7. Instantaneous filtered velocities in the channel of Mansour *et al.* (1996), $Re_\tau = 590$. (*a*) and (*b*): $y^+ \approx 300$ from the lower wall. Flow is from left to right. Velocities are filtered by averaging on a 13^3 stencil ($\Delta x^+ \times \Delta y^+ \times \Delta z^+ \approx 130 \times 75 \times 60$). (*a*) Streamwise velocity fluctuations; contours are $u' = \pm 0.75(1)$. Negative contours are dashed, and the fluctuations are computed with respect to the instantaneous mean velocity on the x-z plane. (*b*) Wall-normal velocity; contours are $v' = \pm 0.375(0.5)$. (*c*) Transverse section of u' at $x^+ \approx 2500$. Fluctuations, filter and contours as in (*a*), but there is no filtering in y.

have been observed underneath tropical hurricanes (Wuman and Winslow, 1998). Smaller scale features, although still much larger than sublayer streaks, are observed in wind-blown sand in beaches (Jiménez, personal observation), and in blowing snow in snow fields (Adrian, private communication).

Perry *et al.* (1986) describe their results in terms of an 'attached eddy' model which is an elaboration of an earlier one proposed by Townsend (1976). Briefly, in the logarithmic region, the v structures are blocked by the presence of the wall and are constrained to sizes at most of order y. This argument has been extended by Hunt (1984) to any turbulent flow in the presence of a wall, independently of the presence of shear, and to wall-normal correlations lengths. These blocked eddies would form the 'short' $\lambda_x \sim y$ peak in both v and u. A similar peak would also be expected to appear in λ_z, and we saw evidence for it in Fig. 2. For the tangential components there is no blocking effect, and much larger structures are possible. The peak at $\lambda \sim y$ would only constitute a short-wavelength limit for them, and one could expect a range of eddies, large in the tangential directions but attached to the wall in the wall-normal one. Perry *et al.* (1986) give a very specific model for these eddies as attached hairpin vortices and use it to derive the k^{-1} form of the spectrum. The latter behavior is, however, more general than the hairpin model and can be derived from simple dimensional considerations for near-wall structures that are so large that their distance to the wall should not be important (Perry and Abell, 1977).

We have mentioned in the introduction that the internal velocity gradients associated with these large structures are so low that their dynamics should be dominated by the shear in the mean velocity profile. They can, to a first approximation, be considered linear and described by rapid distortion theory. The blocking of v mentioned above is one such linear effect, but it is independent of the mean shear and depends only on the presence of an impermeable wall. It is easy to see that the effect of a mean shear is that any initial turbulence gets deformed into a series of streamwise jets. In essence, any spectral component with a non-trivial dependence on x gets damped by the shear, and only the x-independent motion in the cross-plane is left. This transverse motion depends on the initial conditions and is uncoupled from the streamwise velocity. Except for viscosity, which would be negligible at these large scales, it is undamped and will last for long times. The u component is transported by this transverse velocity as a passive scalar (Orlandi and Jiménez 1994). Wherever v moves towards the wall, u increases, and vice versa. Even if the transverse flow is weak, the modulation of u increases linearly in time and will grow to form large amplitude longitudinal jets until either viscosity or nonlinear effects halt the growth. It was shown by Orlandi & Jiménez (1994) in the context of 'laminar' near-wall streaks that this processes changes the mean velocity profile and, therefore, carries Reynolds stresses.

4. Conclusions and open questions

We have shown that eddies with streamwise lengths of the order of $10-20$ boundary layer thicknesses are present in the logarithmic region of wall-bounded flows.

They contain a substantial fraction of the streamwise kinetic energy and, probably, also of the Reynolds stresses. They can be approximately visualized as a system of streamwise turbulent jets, roughly comparable to the sublayer velocity streaks at a much larger scale.

We have given arguments that they should be describable to a first approximation by the combined linear effects of the blocking by the wall and of the mean shear. The first effect has been treated, for example, by Hunt (1984), who showed that it explains the difference between v and the two tangential spectra. In the absence of a mean shear, there should be no difference in the behavior of the u and w spectra, both of which should be 'large'. We have shown that shear breaks that symmetry and leads directly to longitudinal jets and to a u spectrum which is much longer than the one for w.

The appeal of this argument is that it provides some unification to the arguments on the largest scales of turbulent flows. It has been understood for some time that the large structures of *free* shear flows correspond closely to the most unstable eigenfunctions of their mean velocity profiles (Cimbala, Nagib and Roshko, 1988; Gaster, Kit and Wygnanski, 1985). This explanation does not work for wall-bounded flows, whose profiles are typically stable, but it is easy to convince oneself that the linear mechanism described at the end of the last section is nothing but the result of the neutrally-stable Squire's modes of the inviscid Rayleigh stability equation for the mean profile (Betchov and Criminale 1967).

A unified theory for all these largest structures would treat them as solutions of the linear, inviscid stability equations. If an unstable eigenvalue exists, it dominates the initial value problem. Otherwise, the linearly growing Squire's modes prevail.

As satisfying as that conclusion might be, it is clear that it should only be considered a preliminary step of a wider work program. Many questions are left unanswered.

Some of them are experimental. There is essentially no information on the spanwise structure of these large scales. We lack experimental data, and the Reynolds numbers of the numerical simulations are too low to draw scaling conclusions. The data on the streamwise scales is better but partially contradictory. Most of the available high Reynolds number experiments either lack spectral information, have too few y-stations, or have data records which are too short to capture the largest scales. The situation is specially bad for the spanwise velocity component w and for the cospectrum, for which contradictory interpretations exist.

Except with the use of massive probe rakes it is unlikely that experiments would give geometrical information about the structure of these eddies. Numerical simulations should help, but the twin requirements of very long boxes and high Reynolds numbers make direct simulations difficult. It should be possible, however, to attempt large eddy simulations of a few cases to clarify both the scaling an the geometry.

On the theoretical side, the linear model outlined above is clearly only a first approximation. Nonlinearity has to be taken into account although, hopefully, only as a secular perturbation. In free shear flows it appears in the form of Reynolds

stresses that modify the mean profile responsible for the instability. This is probably the root of the 'marginal instability principle' used by Lessen (1978) and co-workers to explain some of their properties. This nonlinear mechanism does not work in wall flows because the mean profile does not feed back into the transverse velocities of the Squire's modes. Weakly nonlinear models of the near-wall streaks have been proposed by Waleffe (1997) and others, and they could perhaps be adapted to the present case. A cycle for the generation of large streamwise structures in a turbulent profile was proposed by Townsend (1976).

Two especially troublesome aspects of the experiments are related to the question of nonlinearity. The first is the difference of about a factor of 2 between the observed spanwise wavelengths of v and of the other two velocity component (see Figs. 1 and 2). It is difficult to explain it as a linear property. The second is the apparent $y^{1/2}$ scaling of the longitudinal scales in Fig. 5 and the corresponding finite range of wavelengths associated with the k^{-1} range, which is supported by the cospectral measurements of Saddoughi and Veeravalli (1994) at higher Reynolds numbers. The square-root scaling suggests a mechanism which is more global than strict self-similarity based on local conditions, but the finite extent of the k^{-1} range suggest the opposite. More experimental results are needed in both cases.

The pay-off of this work should come in various ways. By far the most interesting would be the already discussed possibility of unifying the understanding of the large turbulent scales, which are at present considered non-universal and usually treated in separate 'botanical' ways. Some practical applications may also follow. Since these structures contain energy and Reynolds stresses, they are of practical importance, but their large size makes them expensive to compute. A quasi-linear model would open the way for their 'super-grid' modeling (S. Lele, personal communication). We have already mentioned that they probably control the low frequency noise from boundary layers.

This research has been supported in part by the Center for Turbulence Research and by AFOSR grant #F49620-97-1-0210. Partial support was also provided by the Spanish CICYT under contract PB95-0159, and by the European Commission program E980130118. I am indebted to P. Bradshaw, J. C. R. Hunt, A. E. Perry and V. Zakharov for illuminating discussions, and to J. Kim, R. D. Moser and S. Saddoughi for providing either unpublished or electronic versions of their data. A. A. Wray reviewed a early version of this manuscript and provided thoughtful comments.

REFERENCES

BETCHOV, R. & CRIMINALE, W. O. 1967 *Stability of parallel flows*, Academic Press.

BULLOCK, K. J., COOPER, R. E. & ABERNATHY, F. H. 1978 Structural similarity in radial correlations and spectra of longitudinal velocity fluctuations in pipe flow. *J. Fluid Mech.* **88**, 585-608.

CIMBALA, J. M. NAGIB, H. M. & ROSHKO, A. 1988 Large structure in the far wake of two-dimensional bluff bodies. *J. Fluid Mech.* **190,** 265-298.

CLARK, J. A. & MARKLAND, E. 1971 Flow visualization in turbulent boundary layers. *Proc. Am. Soc. Civil Eng., J. Hydraulics Div.*. **97,** 1635-1664.

CHOI, H. & MOIN, P. 1990 On the space-time characteristics of wall-pressure fluctuations. *Phys. Fluids A.* **2,** 1450-1460.

FARABEE, T. M. & CASARELLA, M. J. 1991 Spectral features of wall pressure fluctuations beneath turbulent boundary layers. *Phys. Fluids A.* **3,** 2410-2420.

GASTER, M., KIT, E. & WYGNANSKI, I. 1985 Large-scale structures in a forced turbulent mixing layer. *J. Fluid Mech.* **150,** 23-39.

HITES, M. H. 1997 Scaling of high-Reynolds number turbulent boundary layers in the National Diagnostic Facility. *Ph. D. Thesis,* Illinois Inst. of Technology.

HUNT, J. C. R. 1984 Turbulence structure in thermal convection and shear-free boundary layers. *J. Fluid Mech.* **138,** 161-184.

JEONG, J., HUSSAIN, F., SCHOPPA, W. & KIM, J. 1997 Coherent structures near the wall in a turbulent channel flow. *J. Fluid Mech.* **332,** 185-214.

JIMÉNEZ, J. & MOIN, P. 1991 The minimal flow unit in near wall turbulence. *J. Fluid Mech.* **225,** 221-240.

JIMÉNEZ, J. & PINELLI, A. 1998 The autonomous cycle of near-wall turbulence. Submitted, *J. Fluid Mech.*

KIM, J., MOIN, P. & MOSER, R. D. 1987 Turbulence statistics in fully developed channel flow at low Reynolds number. *J. Fluid Mech.* **177,** 133-166.

KOMMINAHO, J., LUNDBLADH, A. & JOHANSSON, A. V. 1996 Very large structures in plane turbulent Couette flow. *J. Fluid Mech.* **320,** 259-285.

KROGSTAD, P-A., ANTONIA, R. A. & BROWNE, L. W. B. 1992 Comparison between rough- and smooth-wall turbulent boundary layers. *J. Fluid Mech.* **245,** 599-617.

LAWN, C. J. 1971 The determination of the rate of dissipation in turbulent pipe flow. *J. Fluid Mech.* **48,** 477-505.

LESSEN, M. 1978 On the power laws for turbulent jets, wakes and shearing layers and their relationship to the principle of marginal instability. *J. Fluid Mech.* **88,** 535-540.

MANSOUR, N. N., MOSER, R. D. & KIM, J. 1996 Reynolds number effects in low Reynolds number turbulent channels, Case PCH10 in *AGARD* **AR-345**, 5-8

NAGIB, H. & HITES, M. H. 1995 High Reynolds number boundary-layer measurements in the NDF. *AIAA Paper.* **95-0786**

ORLANDI, P. & JIMÉNEZ, J. 1994 On the generation of turbulent wall friction. *Phys. Fluids A.* **6,** 634-641.

PERRY, A. E. & ABELL, C. J. 1977 Asymptotic similarity of turbulence structures in smooth- and rough-walled pipes. *J. Fluid Mech.* **79,** 785-799.

PERRY, A. E. & CHONG, M. S. 1982 On the mechanism of wall turbulence. *J. Fluid Mech.* **119,** 173-217.

PERRY, A. E., HENBEST, S. & CHONG, M. S. 1986 A theoretical and experimental study of wall turbulence. *J. Fluid Mech.* **165,** 163-199.

PERRY, A. E., LIM, K. L. & HENBEST, S. M. 1987 An experimental study of the turbulence structure in smooth- and rough-wall boundary layers. *J. Fluid Mech.* **177,** 437-466.

PRIYMAK, V. G. & MIYAZAKI, T. 1994 Long-wave motions in turbulent shear flow. *Phys. Fluids.* **6,** 3454-3464.

SANKARAN, R., SOKOLOV, M. & ANTONIA, R. A. 1988 Substructures in a turbulent spot. *J. Fluid Mech.* **197,** 389-414.

SADDOUGHI, S. G. 1997 Local isotropy in complex turbulent boundary layers at high Reynolds number. *J. Fluid Mech.* **348,** 201-245.

SADDOUGHI, S. G. & VEERAVALLI, S. V. 1994 Local isotropy in turbulent boundary layers at high Reynolds number. *J. Fluid Mech.* **268,** 333-372.

TOWNSEND, A. A. 1976 *The structure of turbulent shear flows*, second ed., Cambridge U. Press.

WALEFFE, F. 1997 On a self-sustaining process in shear flows. *Phys. Fluids.* **9,** 883-900.

WUMAN, J. & WINSLOW, J. 1998 Intense sub-kilometer-scale boundary layer rolls observed in hurricane Fran. *Science.* **280,** 555-557.

The instability of streaks in near-wall turbulence

By G. Kawahara, J. Jiménez, M. Uhlmann[1] AND A. Pinelli[1]

1. Motivation and objectives

Several aspects of the self-sustaining mechanism of near-wall turbulence have been studied recently (see Jiménez & Moin 1991; Hamilton, Kim & Waleffe 1995; Waleffe 1997; Schoppa & Hussain 1997; Jiménez & Pinelli 1998). It is well-known that there are two key structures, streamwise vortices and streaks, in the near-wall region. Streamwise vortices generate streaks through the deformation of the mean flow by their induced cross-flow advection. The streaks, which are nearly uniform in the streamwise direction, become unstable, bending along the streamwise direction and leading to the production of streamwise vorticity. Finally, the produced streamwise vorticity evolves nonlinearly into streamwise vortices. In this manner streamwise vortices and streaks generate each other sequentially to sustain near-wall turbulence.

The instability of streaks, to be discussed in this report, is expected to be a crucial ingredient in the self-sustaining cycle. If the streaks were not unstable, then the streamwise vortices should decay under the action of viscosity and so also should the streaks. This decay would mean a termination of the regeneration cycle. Therefore, controlling the streak instability could reduce drag or enhance heat and momentum transfer in near-wall turbulent flows. The control of streaks seems to be easier than that of streamwise vortices since streaks have much larger length scale in the streamwise direction compared to that of streamwise vortices. Because streaky flows over a wall depend on the spanwise direction as well as the wall-normal direction, we cannot apply Squire's transformation to the streak instability, and thus we must consider the three-dimensional mechanism for the instability.

Waleffe (1995, 1997) and Waleffe & Kim (1997) examined numerically the linear stability of streaks in a plane Couette flow at a low Reynolds number. They employed the streamwise velocity field deformed by assumed streamwise rolls as a base flow to demonstrate that sinuous modes, which have often been observed experimentally and numerically, actually grow via the instability mechanism. They stated that the instability originates from inflection points, i.e. wake-like instability, in the spanwise variation of streaky flows. Reddy *et al.* (1998) investigated the same instability systematically in plane Poiseuille flow as well as in plane Couette flow to study subcritical transition. For a turbulent channel flow, on the other hand, Schoppa & Hussain (1997, 1998) examined the time-evolution of small disturbances embedded in a model flow for streaks (on only one wall) by using direct numerical simulations. They found an exponential growth of sinuous modes and discussed the mechanism of the instability. They remarked that the streak instability is not the

1 The School of Aeronautics, U. Politécnica Madrid

same as the wake-like instability; rather, it is similar to the oblique instability of a shear layer. However, at least in the initial linear phase, the structure of growing disturbances which Schoppa & Hussain (1998) observed in their turbulent channel flow is similar to that in a plane Couette flow where the streak instability has been considered to be the same as the wake-like instability, as mentioned above. Much effort has been devoted to investigating the streak instability, but we must admit that our knowledge is still poor concerning the mechanism and the structure of the instability.

The main objectives of our present work are to elucidate the conditions for the streak instability in a turbulent channel flow and to demonstrate the generation mechanism of the streamwise vorticity through the streak instability. We expect that the understanding of the conditions and the streamwise vorticity generation in the streak instability could provide useful information for turbulence control in near-wall flows. In order to accomplish these objectives, we have performed numerically the linear stability analysis of a turbulent-channel-type base flow with a periodic undulation in the spanwise direction.

2. Accomplishments

2.1 Base flow

In the following linear stability analysis, x, y, and z are used to represent the streamwise, the wall-normal, and the spanwise coordinates, respectively. Friction velocity u_τ and channel half-width h (and a resulting time scale h/u_τ) are taken as reference velocity and length (and reference time) for non-dimensionalization.

The base flow to be considered here is a unidirectional flow and has only the x-component of dimensionless velocity, U. U is dependent on both y- and z-coordinates as

$$U(y,z) = U_0(y) + U_1(y)\cos(\gamma z), \tag{1}$$

where $U_0(y)$ stands for a typical mean velocity profile of a turbulent channel flow and is given by numerical integration of (see Reynolds & Tiederman 1967)

$$\frac{\mathrm{d}U}{\mathrm{d}y} = -\frac{Re_\tau(y-1)}{1+\nu_t(y-1)} \quad (0<y<2). \tag{2}$$

The function $\nu_t(\xi)$ is expressed as

$$\nu_t(\xi) = \frac{1}{2}\left\{1+\left[\frac{KRe_\tau}{3}(1-\xi^2)(1+2\xi^2)\left(1-\exp\left(-\frac{Re_\tau(1-|\xi|)}{A}\right)\right)\right]^2\right\}^{\frac{1}{2}} - \frac{1}{2}. \tag{3}$$

Here

$$Re_\tau = \frac{u_\tau h}{\nu} \tag{4}$$

is a Reynolds number, and ν is the kinematic viscosity of the fluid. In this work we restrict ourselves to a low-Reynolds-number turbulent channel flow by setting

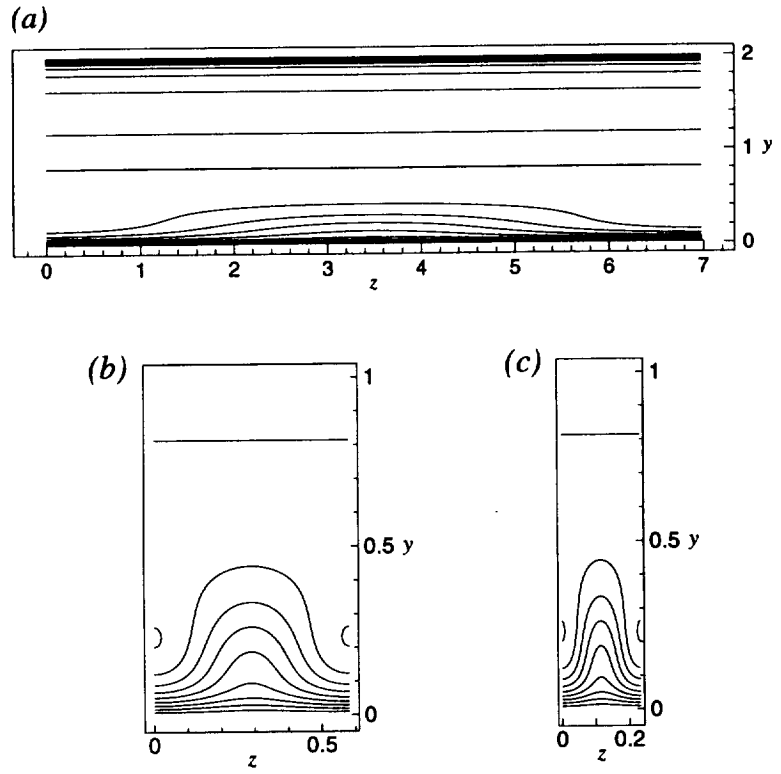

FIGURE 1. Contour plot on (y, z)-plane of the streamwise velocity of the base flow (1) for (a) $\Delta U = 3.0$, $\gamma = 0.9$; (b) $\Delta U = 4.0$, $\gamma = 10.8$; and (c) $\Delta U = 4.0$, $\gamma = 27.0$. Contour increment is 2. Only half the height of the channel is shown in (b) and (c). Modes I, II and III in Fig. 4 have been obtained respectively for the base flows (a), (b), and (c).

$Re_\tau = 180$. In this case the value of the Reynolds number based on the channel centerline velocity is 3300. We have set the values of the adjustable parameters in (3) as $K = 0.525$, $A = 37$ so that the velocity profile $U_0(y)$ can fit a realistic profile for $Re_\tau = 180$ (Waleffe, Kim & Hamilton 1991). On the right-hand side of (1) the second term represents low- and high-speed streaks alternating in the spanwise direction with dimensionless wavenumber γ. $U_1(y)$ is the dimensionless amplitude of the spanwise variation given by

$$U_1(y) = \Delta U \frac{\sqrt{\sigma} y \exp(-\sigma y^2)}{\exp(-1/2)/\sqrt{2}}, \tag{5}$$

which has a maximum ΔU at $y = (2\sigma)^{-1/2}$ and is localized on the lower wall $y = 0$. Here, we set $\sigma = 18$ so that the maximum streak velocity (and so the maximum wall-normal vorticity $\gamma \Delta U$) may be located at $y = \frac{1}{6}$, i.e. 30 wall units. Figure 1

shows the contour plot on (y, z)-plane of the streamwise velocity for the three typical base flows to be discussed in §§2.4 and 2.5.

We confirmed that the y-dependence (5) of streaky flows approximately represents that of real streaks in comparison to the streamwise velocity fluctuation in direct numerical simulations. A similar type of streaks to (5) was also used in Schoppa & Hussain (1997, 1998).

We should note that the base flow (1) is not an exact solution to the Navier-Stokes equation and the actually observed streaky flows have weak time- and x-dependence. However, we believe that the base flow (1) is valid as the first step of the analysis because real near-wall streaks have much larger time and streamwise length scales than those of typical turbulence structures, e.g. streamwise vortices. Another possibility is to obtain fully nonlinear equilibrium solutions, which correspond to streaky flows, in some moving reference frame. But this lies outside the scope of the present work. As is well known, the turbulent-channel-type base flow $U_0(y)$ alone does not possess any unstable eigenmodes of the linearized Navier-Stokes equation.

2.2 Linear stability analysis

When we consider the linear stability problem for the base flow (1), we cannot use Squire's transformation, and thus we must consider three-dimensional disturbances. If wall-normal disturbance velocity v and vorticity η are taken as dependent variables, the time-evolution of an infinitesimal disturbance may be described by the extended Orr-Sommerfeld equation

$$\left(\partial_t + U\partial_x - \frac{1}{Re_\tau}\nabla^2\right)\nabla^2 v - \left[\left(\partial_y^2 - \partial_z^2\right)U\right]\partial_x v$$
$$-2\left(\partial_z U\right)\partial_x\left(\partial_y w - \partial_z v\right) - 2\left(\partial_y\partial_z U\right)\partial_x w = 0, \qquad (6)$$

and by the extended Squire equation

$$\left(\partial_t + U\partial_x - \frac{1}{Re_\tau}\nabla^2\right)\eta - \left(\partial_z U\right)\partial_y v + \left(\partial_y U\right)\partial_z v + \left(\partial_y\partial_z U\right)v + \left(\partial_z^2 U\right)w = 0 \qquad (7)$$

(see Waleffe 1995), where spanwise disturbance velocity w is related to v and η as

$$\left(\partial_x^2 + \partial_z^2\right)w = -\partial_y\partial_z v - \partial_x\eta. \qquad (8)$$

We have used the continuity equation $\partial_x u + \partial_y v + \partial_z w = 0$ and the definition of the wall-normal vorticity $\eta = \partial_z u - \partial_x w$ to have (8), where u is the streamwise disturbance velocity. Equations (6) and (7) are supplemented by boundary conditions

$$v = \partial_y v = 0, \quad \eta = 0$$

at $y = 0, 2$.

In the following, we shall seek solutions to a system of equations (6), (7), and (8) in the normal-mode form

$$v = \mathrm{Re}\left[\hat{v}(y, z)\,\mathrm{e}^{\mathrm{i}\alpha(x - ct)}\right], \qquad (9)$$

$$\eta = \mathrm{Re}\left[\hat{\eta}(y,z)\,\mathrm{e}^{\mathrm{i}\alpha(x-ct)}\right], \tag{10}$$

$$w = \mathrm{Re}\left[\hat{w}(y,z)\,\mathrm{e}^{\mathrm{i}\alpha(x-ct)}\right], \tag{11}$$

where α stands for the streamwise wavenumber and c the complex phase velocity. The growth rate of the disturbance is given by $\alpha\mathrm{Im}(c)$.

We anticipate periodic solutions in the spanwise direction (Floquet theory). Two fundamental modes are considered, i.e. the sinuous mode

$$\hat{v} = \sum_{n=1}^{\infty} \hat{v}_n(y)\,\sin(n\gamma z), \quad \hat{\eta} = \sum_{n=0}^{\infty} \hat{\eta}_n(y)\,\cos(n\gamma z), \quad \hat{w} = \sum_{n=0}^{\infty} \hat{w}_n(y)\,\cos(n\gamma z), \tag{12}$$

and the varicose mode

$$\hat{v} = \sum_{n=0}^{\infty} \hat{v}_n(y)\,\cos(n\gamma z), \quad \hat{\eta} = \sum_{n=1}^{\infty} \hat{\eta}_n(y)\,\sin(n\gamma z), \quad \hat{w} = \sum_{n=1}^{\infty} \hat{w}_n(y)\,\sin(n\gamma z), \tag{13}$$

which are treated separately except for the case where both modes have the same eigenvalue c, since the anti-symmetric and the symmetric modes can be decoupled in (6), (7), and (8).

In the numerical solution of the eigenvalue problem, the infinite series in (12) and (13) are replaced by truncated series up to $n = N_z$ in the spanwise direction z. We then apply a Galerkin method to Eqs. (6) and (7) by using N_s b-splines of order 6 as expansion functions in the wall-normal direction y. We set $N_z = 10$ and $N_s = 40$ to have convergence under 0.2% difference for N_z and under 4% difference for N_s. More details about the discretization can be found in Jiménez *et al.* (1998). The evaluation of the involved integrals leads to a large, coupled system of algebraic equations, $\boldsymbol{A}\hat{\boldsymbol{x}} = c\boldsymbol{B}\hat{\boldsymbol{x}}$, which is of order $N_s \times (2N_z + 1)$, where $\hat{\boldsymbol{x}}$ is the solution vector in spline space and contains the coefficients of the wall-normal velocity and vorticity for each spanwise mode and each discrete wall-normal location. The algebraic eigenvalue problem was solved by using standard library routines (e.g. LAPACK or EISPACK). We have removed spurious eigenvalues that might be caused by the boundary treatment through the tau method before seeking the most unstable (or least stable) eigenvalue and eigenvector.

2.3 Neutral curves

Figure 2 shows the projection on $(\gamma, \Delta U)$-plane of the lower bound of the neutral surface in $(\gamma, \Delta U, \alpha)$-space. Open and closed circles represent the sinuous and the varicose modes, respectively. The streaky flow should be unstable above the neutral curve around the critical streamwise wavenumber α_c. Note that the corresponding spanwise wavenumber of 100 wall units is located at $\gamma/Re_\tau = 0.06$ in this figure. The critical streak amplitude ΔU_c seems to have a finite value (≈ 1.7) as $\gamma \to 0$ both for the sinuous modes and for the varicose modes.

In the case of the sinuous modes, ΔU_c increases abruptly at $\gamma/Re_\tau < 0.01$ and takes a maximum around $\gamma/Re_\tau = 0.03$. From there ΔU_c decreases with increasing

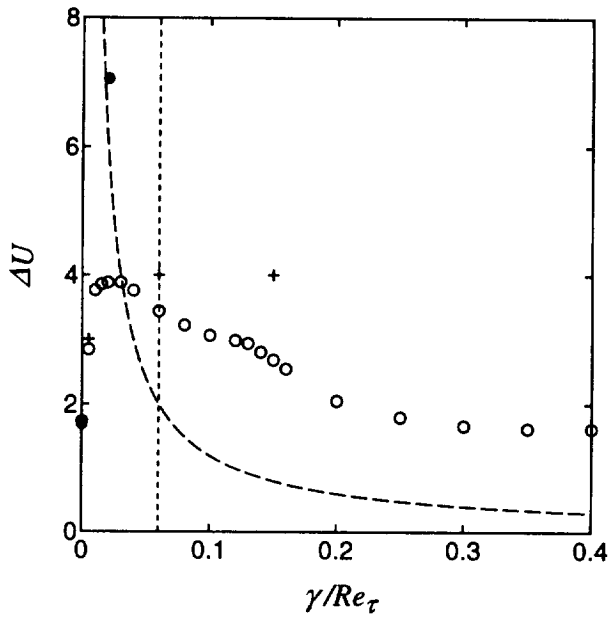

FIGURE 2. Trace of the neutral curve on $(\gamma, \Delta U)$-plane. Open circles represent the sinuous mode and closed circles represent the varicose mode. The dotted vertical line indicates $\gamma/Re_\tau = 0.06$, on which the wall-normal shear and the spanwise shear due to streaks are comparable. The dashed curve denotes the contour of a constant amplitude $\gamma\Delta U/Re_\tau = 0.12$ of the wall-normal vorticity, on which the mean shear at $y = \frac{1}{6}$ is comparable to the spanwise shear of streaks. Three crosses represent modes I, II, and III in Fig. 4.

γ. In general, the actual value of the growth rate $\alpha \mathrm{Im}(c)$ (not shown here) is increased when γ as well as ΔU are increased because they are related to the intensity of the shear layer generated by the streaks. For large γ, however, the effect of viscosity progressively stabilizes the flow. In the case of a two-dimensional wake, the critical Reynolds number is given by $Re_c \approx 5$, and in our case it is estimated as $Re_c = 2\pi Re_\tau(\Delta U/\gamma)$ (≈ 5). This estimate tells us that the stabilization due to the viscosity becomes important only for relatively large γ $(\gamma/Re_\tau \approx 1.3\Delta U)$.

At $\gamma/Re_\tau = 0.06$, i.e. 100 wall-unit wavelength, the instability requires that $\Delta U > 3.44$ for the streamwise velocity and so $\gamma\Delta U/Re_\tau = 0.20$ for the wall-normal vorticity. If we take into consideration that the RMS value of the streamwise fluctuation velocity (and the wall-normal vorticity) attains the maximum of about $2.7u_\tau$ (and $0.2u_\tau^2/\nu$) in the near-wall region, then the above requirements for the instability are expected to be satisfied in a turbulent channel flow.

In the case of the varicose modes, on the other hand, ΔU_c increases abruptly with increasing γ so that a stable region is extended to almost all the parameter plane in Fig. 2.

This significant difference of the instability between the sinuous (bending) and the varicose modes could explain, at least for low Re_τ, the fact that the actually

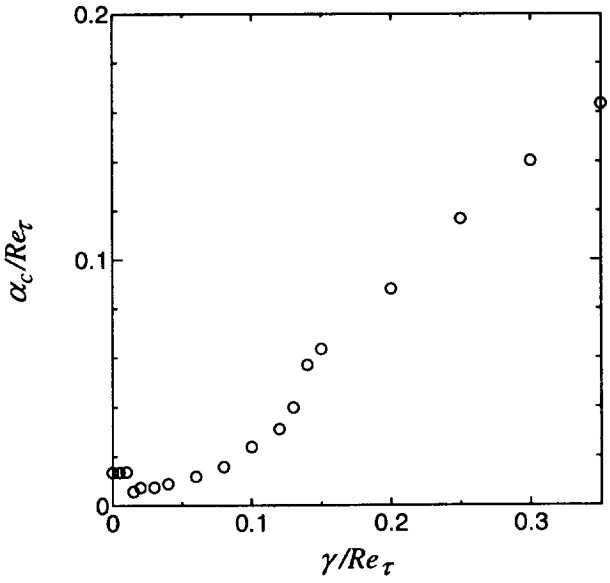

FIGURE 3. Plot of the critical streamwise wavenumber α_c against γ.

observed streak instability involves the bending motion of streaks in the spanwise direction (see Hamilton, Kim & Waleffe 1995; Schoppa & Hussain 1997; Jiménez & Pinelli 1998).

Figure 3 shows the critical streamwise wavenumber α_c against the spanwise wavenumber γ for the sinuous modes. For $\gamma/Re_\tau < 0.01$, α_c is independent of γ, taking a constant value of $\alpha_c/Re_\tau = 0.013$. At $\gamma/Re_\tau > 0.01$, α_c jumps down and gradually increases with increasing γ. For $\gamma/Re_\tau = 0.06$, i.e. 100 wall-unit wavelength, the streamwise wavenumber has a value of $\alpha_c/Re_\tau = 0.012$, which corresponds to 500 wall-unit wavelength. This wavelength is consistent with that of the streak bending often observed in a turbulent channel flow. α_c kinks at $\gamma/Re_\tau \approx 0.12$, and then α_c increases nearly linearly with γ. This jump and kink of α_c implies that there are different instability mechanisms in three ranges: $\gamma/Re_\tau < 0.01$, $0.01 < \gamma/Re_\tau < 0.12$, and $\gamma/Re_\tau > 0.12$. We can now see the corresponding dependence of ΔU_c on γ in each range of γ in Fig. 2.

In the present configuration, streaks (the second term in (1)) have the width $2\pi h/\gamma$ and the height $0.6h$ within which the (dimensionless) streak velocity exceeds $0.01\Delta U$. If $\gamma/Re_\tau = 0.06$, then the width is comparable to the height. Two time scales based on shearing motion of streaks across the spanwise and the wall-normal directions are also comparable at $\gamma/Re_\tau = 0.06$ since they should be estimated as each length scale divided by $\Delta U u_\tau$. On the other hand, the mean flow part $U_0(y)$ in (1) has the velocity gradient of $0.12Re_\tau u_\tau/h$ at $y = \frac{1}{6}$, i.e. 30 wall units, where the streak velocity and vorticity attain a maximum. Thus, at least in the vicinity of this maximum, the time scale of shearing motion of streaks across the spanwise direction is comparable to that of the mean shear if $\gamma\Delta U/Re_\tau = 0.12$.

In Fig. 2, we have shown these relations, $\gamma/Re_\tau = 0.06$ and $\gamma\Delta U/Re_\tau = 0.12$,

respectively by the dotted line and the dashed curve. It turns out that in the case of the instability at $\gamma/Re_\tau < 0.01$, the width of streaks is larger than the height and also the spanwise shear of streaks is weaker than the wall-normal shear and the mean shear. Because α_c is independent of γ for $\gamma/Re_\tau < 0.01$ as shown in Fig. 3, the spanwise shear actually does not affect the instability. In the case of the instability at $\gamma/Re_\tau > 0.12$, on the other hand, the height of streaks is larger than the width, and also the spanwise shear of streaks is stronger than the wall-normal shear and the mean shear. At $0.01 < \gamma/Re_\tau < 0.12$, where the typical streak spacing $\gamma/Re_\tau = 0.06$, i.e. 100 wall units, is located, the streak width and height as well as the streak wall-normal and spanwise shear and the mean shear are nearly comparable.

Reddy *et al.* (1998) examined numerically streak instability in the simplified model for a plane Couette flow and showed that mean shear has the stabilizing effect on the instability (see also Waleffe 1997). Baggett (1996) argued that the spanwise shear by streaks exceeds mean shear leading to the instability of streaks.

2.4 Eigenmodes

In this subsection, we shall discuss the structures of the unstable sinuous eigenmodes near the neutral surface in order to distinguish the effects of the above-mentioned different shear components on the instability.

Figure 4 shows the iso-surface of the streamwise disturbance vorticity of three unstable eigenmodes for (a) $\Delta U = 3.0$, $\gamma/Re_\tau = 0.005$, $\alpha/Re_\tau = 0.013$; (b) $\Delta U = 4.0$, $\gamma/Re_\tau = 0.06$, $\alpha/Re_\tau = 0.012$; and (c) $\Delta U = 4.0$, $\gamma/Re_\tau = 0.15$, $\alpha/Re_\tau = 0.063$ (see Fig. 1 for contour plots of the corresponding base flows). The value of the iso-surfaces is $\pm 4\omega'$, where ω' denotes the RMS value of the disturbance vorticity vector. The light gray and the dark gray iso-surfaces indicate the positive and the negative vorticity, respectively. Hereafter, the eigenmodes (a), (b), and (c) in Fig. 4 are referred to as mode I, mode II, and mode III, respectively. Modes I, II, and III have growth rates of $\alpha \mathrm{Im}(c) = 0.027$, 0.60, and 5.2 and propagate in the streamwise direction at phase velocities of $\mathrm{Re}(c) = 17.4$, 13.6, and 14.2, respectively. For all modes I, II, and III, the magnitude of the wall-normal vorticity is quite small compared to that of the other components. For mode I, the streamwise and the spanwise vorticity are comparable, while for modes II and III, the streamwise vorticity is dominant. The trace of critical points (thin curves), at which the base flow velocity is equal to $\mathrm{Re}(c)$, and of inflection points (thick curves) is shown for modes I, II, and III in Fig. 5. In this figure inflection points are defined as a point at which $\partial_n^2 U = 0$, where n is taken to be normal to iso-velocity lines (see Fig. 1) of the base flow on (y, z)-plane.

In Fig. 4, it can be seen that the three eigenmodes have strikingly different structures. In the case of mode I, the streamwise vorticity is highly localized above the high-speed streak (along the edge of the periodic box). It can be found in Fig. 5a that the critical points nearly coincide with the (upper) inflection points only above the high-speed streak. In this case the spanwise shear of the base flow is weak and inactive (see §2.3 and Fig. 2). Therefore, the instability should be characterized by the three-dimensional instability of a roughly two-dimensional wall jet.

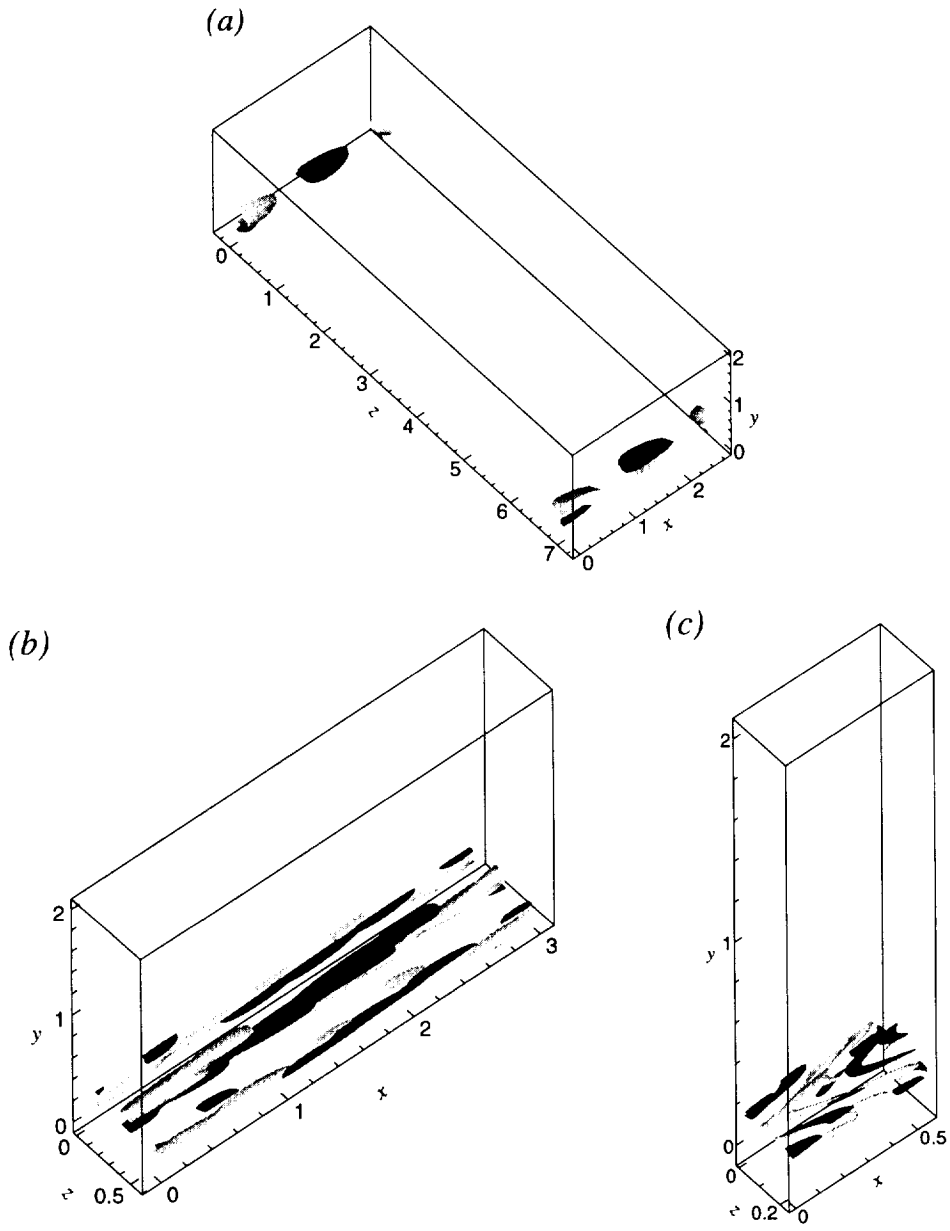

FIGURE 4. Iso-surface of the streamwise disturbance vorticity for unstable sinuous eigenmodes. (a) $\Delta U = 3.0$, $\gamma = 0.9$, $\alpha = 2.4$ (mode I); (b) $\Delta U = 4.0$, $\gamma = 10.8$, $\alpha = 2.1$ (mode II); and (c) $\Delta U = 4.0$, $\gamma = 27.0$, $\alpha = 11.4$ (mode III). The value of iso-surfaces is $\pm 4\omega'$, where ω' denotes the RMS value of the vorticity vector. The light and dark gray surfaces represent the positive and the negative vorticity. The flow is from the lower left to the upper right, and the low-speed (high-speed) streak is located along the center (edge) of the periodic box. See Fig. 1 for the corresponding base flows.

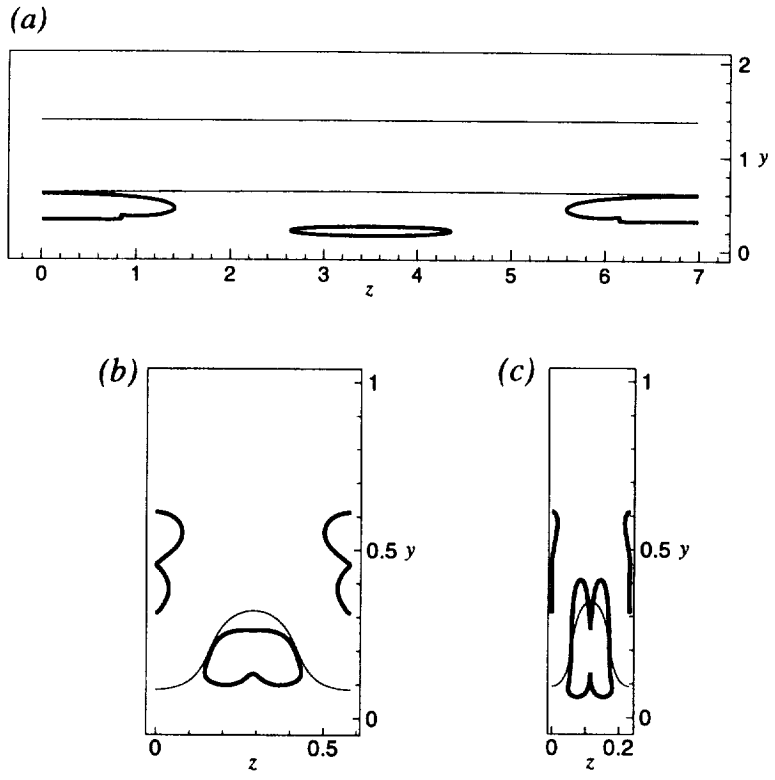

FIGURE 5. Trace of critical points and of inflection points on (y, z)-plane. (a) $\Delta U = 3.0$, $\gamma = 0.9$ (mode I); (b) $\Delta U = 4.0$, $\gamma = 10.8$ (mode II); and (c) $\Delta U = 4.0$, $\gamma = 27.0$ (mode III). The thin curves represent a critical point. The phase velocity of disturbances is $\mathrm{Re}(c) = 17.4$ for (a), $\mathrm{Re}(c) = 13.6$ for (b), and $\mathrm{Re}(c) = 14.2$ for (c). The thick curves represent a inflection point of the base flows (a), (b), and (c) in Fig. 1. Only half the height of the channel is shown in (b) and (c).

In the case of mode II, the streamwise vorticity takes an elongated ribbon-like form in the streamwise direction (Fig. 4b). The ribbon-like structures are located on both the high-speed streak and the low-speed streak (along the center of the periodic box). They are inclined in the streamwise direction from the wall-normal direction. In the case of mode III, on the other hand, the structures of the streamwise vorticity are inclined in the streamwise direction from the spanwise direction rather than from the wall-normal direction (Fig 4c). Structures of the same sign above the low- and high-speed streaks are linked via the thin 'arms' such that they appear v-shaped. This difference in the inclination direction between modes II and III could be related to the difference in the effective shear. In the case of mode III, the spanwise shear of streaks is strongest (see §2.3 and Fig. 2), so that the shearing motion across the spanwise direction could tilt eigenstructures towards the streamwise direction

from the spanwise direction. In the case of mode II, the shearing motion across the wall-normal direction is considered to be effective.

Since for both modes II and III the critical points nearly coincide with the inflection points on the flanks of the low-speed streak (Fig. 5b and c), the origin of the instability for both modes is considered to be similar to a wake instability as pointed out by Waleffe (1995, 1997) and Waleffe & Kim (1997).

In the next subsection, we examine the production of the streamwise vorticity in order to further understand the difference between modes II and III.

2.5 Production of streamwise vorticity

First, we consider the equation for the unstable modal streamwise vorticity as

$$(U-c)\hat{\omega}_x = -\hat{w}\,\partial_y U + \hat{v}\,\partial_z U, \tag{14}$$

or equivalently

$$\hat{\omega}_x + \mathrm{i}\frac{(U-\mathrm{Re}(c))}{\mathrm{Im}(c)}\hat{\omega}_x = -\mathrm{i}\frac{\hat{w}}{\mathrm{Im}(c)}\partial_y U + \mathrm{i}\frac{\hat{v}}{\mathrm{Im}(c)}\partial_z U, \tag{15}$$

where $\hat{\omega}_x(y,z)$ is related to the streamwise vorticity ω_x by $\omega_x = \mathrm{Re}\left[\hat{\omega}_x \mathrm{e}^{\mathrm{i}\alpha(x-ct)}\right]$, and we have neglected the viscous term. The right-hand side of (14) (or (15)) is responsible for the production of the streamwise vorticity through the vortex tilting. The first term in (14) (or (15)) comes from the tilting of the wall-normal disturbance vorticity by the wall-normal shear of the base flow while the second is related to the tilting of the spanwise disturbance vorticity by the spanwise shear. Note that the tilting effects of the base flow vorticity by the disturbance have disappeared from (14) (and so (15)) due to cancellation. If we estimate the order of the first and second terms for mode II and mode III, then we find that in the case of mode II the first term is significant while in the case of mode III the second is significant. The contour plots of $\hat{\omega}_x$ and of the significant production term are shown for mode II and mode III in Figs. 6 and 7, respectively (only the real parts are shown). In these figures, the flow condition of (a) corresponds to (b) in Fig. 4, and that of (b) corresponds to (c) in Fig. 4. In Fig. 7a the first term in (15) is shown, while in Fig. 7b the second term in (15) is shown.

As described in §2.4, in the case of mode II the ribbon-like structures of the positive and negative streamwise vorticity are inclined in the streamwise direction so that the positive and the negative structures are stacked alternately on top of low- and high-speed streaks (see Fig. 6a). This typical distribution of the positive and negative vorticity coincides well with that of the significant production term (Fig. 7a). In their direct numerical simulation, Sendstad & Moin (1992) found that the same production term, $-(\partial_x w)(\partial_y u)$, is dominant for the generation of the streamwise vorticity in near-wall turbulence.

For mode II, if we estimate the order of each component of the disturbance velocity, it turns out that the spanwise disturbance velocity is much larger than the wall-normal one, especially on the low- and high-speed streaks (the streamwise component is very small). The strong spanwise velocity could be induced by spanwise

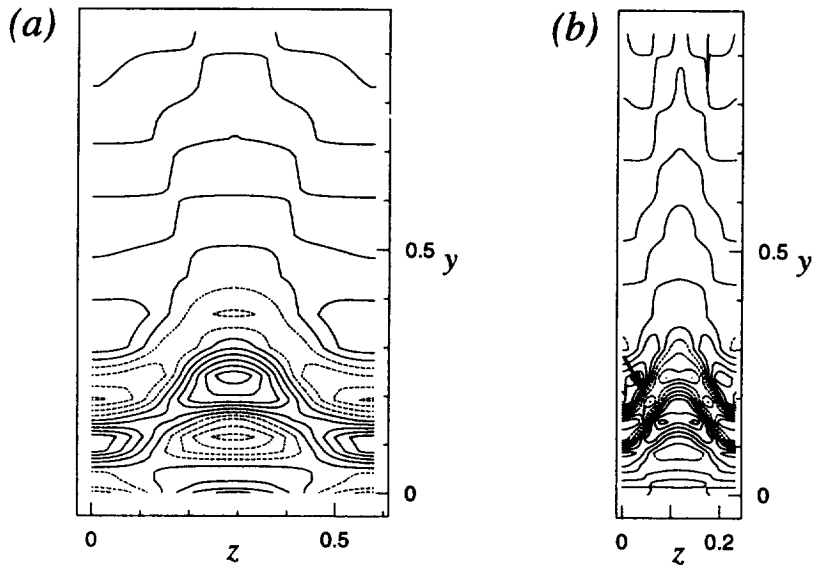

FIGURE 6. Eigenmode $\hat{\omega}_x$ for the streamwise vorticity. (a) $\Delta U = 4.0$, $\gamma = 10.8$, $\alpha = 2.1$ (mode II); and (b) $\Delta U = 4.0$, $\gamma = 27.0$, $\alpha = 11.4$ (mode III). Contour increment is ω'. Negative contours are dotted. Only the real parts of $\hat{\omega}_x$ are shown. In (b) one of the minima, which correspond to the 'arms' in Fig. 4c, is indicated by the arrow.

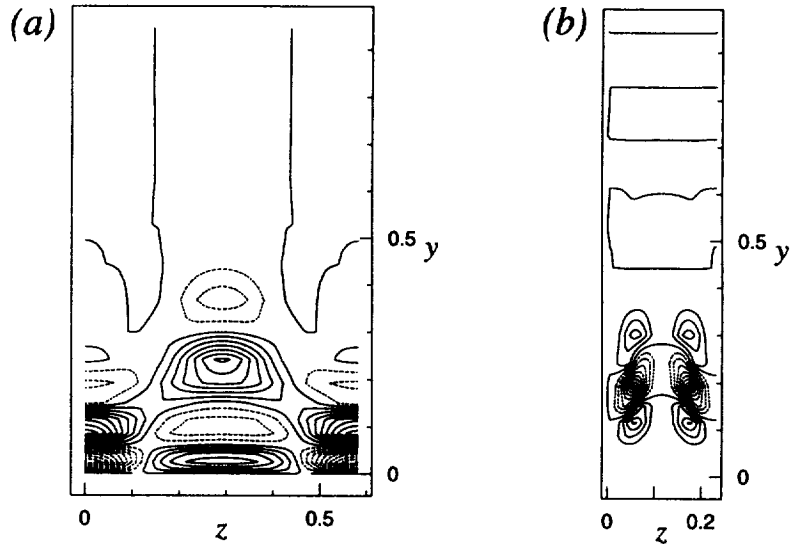

FIGURE 7. Significant production terms for the streamwise vorticity. (a) $-\mathrm{i}\hat{w}(\partial_y U)/\mathrm{Im}(c)$ is shown for $\Delta U = 4.0$, $\gamma = 10.8$, $\alpha = 2.1$ (mode II). (b) $\mathrm{i}\hat{v}(\partial_z U)/\mathrm{Im}(c)$ is shown for $\Delta U = 4.0$, $\gamma = 27.0$, $\alpha = 11.4$ (mode III). Contour increment is $3\omega'$, and negative contours are dotted. Only the real parts are shown.

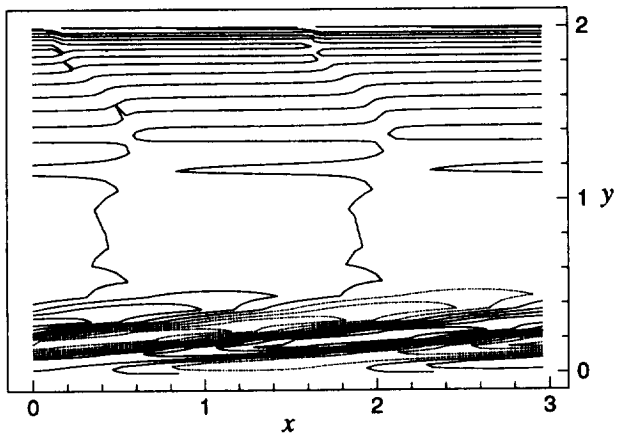

FIGURE 8. Contour plot of the spanwise disturbance velocity on (x, y)-plane for mode II. The slice plane is located at $z = 0.29$, i.e. the centerline of the low-speed streak. Contour increment is v', where v' denotes the RMS value of the velocity vector. Negative contours are dotted.

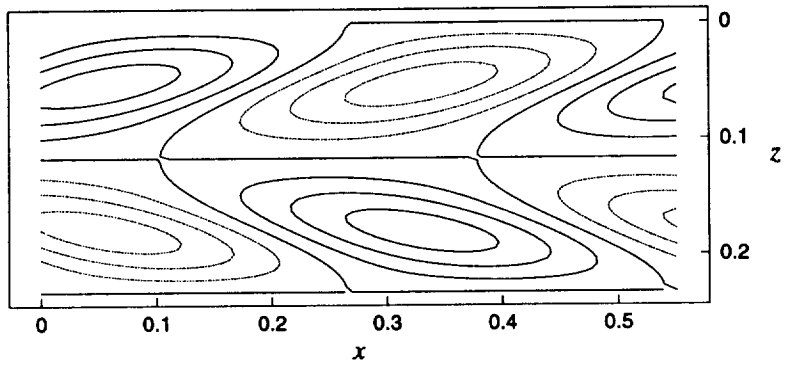

FIGURE 9. Contour plot of the wall-normal disturbance velocity on (x, z)-plane for mode III. The slice plane is located at $y = \frac{1}{6}$, i.e. 30 wall units, where the streak velocity and vorticity attain a maximum. Contour increment is v', where v' denotes the RMS value of the velocity vector. Negative contours are dotted.

bending instability of the streaks similar to a wake-like instability. The eigenmode for the spanwise velocity is inclined from the wall-normal direction towards the streamwise direction under the action of the shearing motion across the wall-normal direction (Fig. 8). The inclined eigenmode for the spanwise velocity directly induces streamwise vorticity as well as wall normal vorticity (see Fig. 10a). The induced

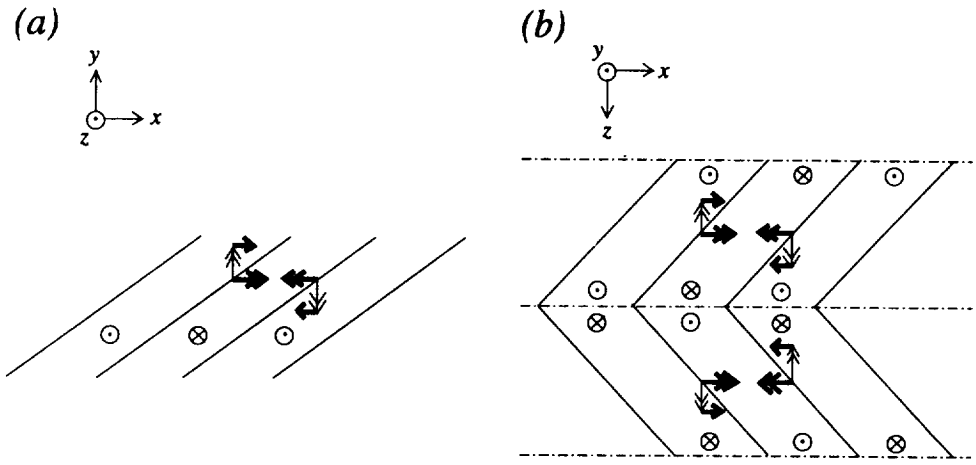

FIGURE 10. Proposed mechanisms of the streamwise vorticity generation for (a) mode II and (b) mode III. Solid lines conceptually show null contours of the disturbance velocity normal to the figure planes, and symbols ⊙ and ⊗ indicate the signs of the velocity component, i.e. coming out of and going in the planes. Thick double arrows denote the induced streamwise vorticity. Thin double arrows denote the induced wall-normal (or spanwise) vorticity in (a) (or in (b)). Thick arrows represent the production of the streamwise vorticity by the vorticity tilting towards the streamwise direction. The dotted-dashed lines in (b) are the centerlines of the low- and high-speed streaks.

wall-normal vorticity is tilted towards the streamwise direction, which then leads to new production of streamwise vorticity. The generated streamwise vorticity, in turn, enhances the spanwise bending of streaks, i.e. the spanwise velocity.

In the case of mode III, on the other hand, one can identify strong localized minima (one of which is indicated by the arrow) of streamwise vorticity situated in between the low- and high-speed streaks in Fig. 6b, which correspond to the 'arms' visible in Fig. 4c. The high vorticity of these minima is apparently produced by the second production term in (15) as the location of the strong minima of production coincides with that of the 'arms' (compare Figs. 7b and 6b).

For mode III, the shearing motion across the spanwise direction is dominant especially between the low- and high-speed streaks. If we examine the order of the disturbance velocity, then we find that the wall-normal velocity much exceeds the spanwise one between the low- and high-speed streaks (the streamwise component is again very small). The eigenmode for the wall-normal velocity is inclined towards the streamwise direction from the spanwise direction by the action of the shear between the low- and high-speed streaks (Fig. 9). The inclined eigenmode for the wall-normal velocity directly induces streamwise vorticity and secondarily produces it through vortex tilting in a manner similar to that found in the case of mode II but with the production taking place essentially in planes parallel to the wall (see

Fig. 10b).

3. Summary and future plans

In this report, we have presented three different instability modes in the base flow composed of a turbulent-channel-type mean flow andsuperimposedstreaks at $Re_\tau = 180$. For $\gamma/Re_\tau < 0.01$, a wall-jet-like instability occurs, and the critical velocity amplitude of streaks is around $\Delta U_c = 1.7$. In the range $0.01 < \gamma/Re_\tau < 0.12$, into which falls the wavelength of 100 wall-units, the critical amplitude is around $\Delta U_c = 3$. In this case, unstable eigenmodes take a form that is inclined towards the streamwise direction from the wall-normal direction, and they directly induce streamwise vorticity. In addition, the streamwise vorticity is secondarily produced on low- and high-speed streaks principally through tilting of the wall-normal disturbance vorticity by the base flow shear across the wall-normal direction. For $\gamma/Re_\tau > 0.12$, on the other hand, the shearing motion between low- and high-speed streaks is dominant so that eigenmodes are oriented in the spanwise direction (with an inclination towards the streamwise direction) rather than in the wall-normal direction. In this case, therefore, the streamwise vorticity is produced between low- and high-speed streaks principally through tilting of the spanwise disturbance vorticity by the base flow shear across the spanwise direction in addition to the direct induction of the streamwise vorticity by inclined eigenmodes. In these latter two cases, the instability is considered to be similar to a wake instability. In these cases, however, the streamwise vorticity is dominant, and it is induced directly through the instability. No two-dimensional instability mechanism can be applied to these two unstable modes. The underlying three-dimensional mechanism is expected to be interpreted directly in terms of the streamwise vorticity.

We are now pursuing an analytical approach to explain the mechanism of the streak instability and the generation of the streamwise vorticity. We are also planning to investigate the effects of a change of boundary conditions on the streak instability in order to get useful information for possible control strategies of near-wall turbulence.

Acknowledgments

The authors are grateful to Dr. Jeffrey Baggett for reviewing the preliminary version of this manuscript. G. K. is supported by the Japanese Ministry of Education, Science and Culture.

REFERENCES

BAGGETT, J. S. 1996 Non-normal dynamics and applications in hydrodynamic stability. PhD Thesis, Cornell Univ.

HAMILTON, J. M., KIM, J. & WALEFFE, F. 1995 Regeneration mechanisms of near-wall turbulence structures. *J. Fluid Mech.* **287,** 317-348.

JIMÉNEZ, J., KAWAHARA, G., PINELLI, A. & UHLMANN, M. 1998 Linear stability analysis of turbulent channel flow including porous walls. Tech. Note ETSIA MF-9811, School of Aeronautics, U. Politécnica Madrid, Spain.

JIMÉNEZ, J. & MOIN, P. 1991 The minimal flow unit in near-wall turbulence. *J. Fluid Mech.* **225,** 213-240.

JIMÉNEZ, J. & PINELLI, A. 1998 The autonomous cycle of near-wall turbulence. Submitted to *J. Fluid Mech.*

REDDY, S. C., SCHMID, P. J., BAGGETT, J. S. & HENNINGSON, D. S. 1998 On stability of streamwise streaks and transition thresholds in plane channel flows. *J. Fluid Mech.* **365,** 269-303.

REYNOLDS, W. C. & TIEDERMAN, W. G. 1967 Stability of turbulent channel, with application to Malkus's theory. *J.Fluid Mech.* **27,** 253-272.

SCHOPPA, W. & HUSSAIN, F. 1997 Genesis and dynamics of coherent structures in near-wall turbulence: A new look. In *Self-sustaining Mechanisms of Near-Wall Turbulence,* Computational Mechanics Publications, 385-422.

SCHOPPA, W. & HUSSAIN, F. 1998 Formation of near-wall streamwise vortices by streak instability. *AIAA 98-3000.*

SENDSTAD, O. & MOIN, P. 1992 The near-wall mechanics of three-dimensional boundary layers. *Rep. TF-57,* Thermosciences Division, Dept. Mechanical Engineering, Stanford Univ., Stanford, CA.

WALEFFE, F. 1995 Hydrodynamic stability and turbulence: Beyond transients to a self-sustaining process. *Stud. Appl. Math.* **95,** 319-343.

WALEFFE, F. 1997 On a self-sustaining process in shear flows. *Phys. Fluids.* **9,** 883-900.

WALEFFE, F. & KIM, J. 1997 How streamwise rolls and streaks self-sustain in a shear flow. In *Self-sustaining Mechanisms of Near-Wall Turbulence,* Computational Mechanics Publications, 309-332.

WALEFFE, F., KIM, J. & HAMILTON, J. M. 1991 On the origin of streaks in turbulent boundary layers. In *Turbulent Shear Flows 8,* Springer, 37-49.

An implementation of the v^2-f model with application to transonic flows

By Georgi Kalitzin

1. Motivation and objectives

This report describes the implementation of the v^2-f model in CFL3D, a code which solves the time-dependent 3-D compressible Reynolds-averaged Navier-Stokes equations using multi-block structured grids.

The turbulence transport equations are solved implicitly with an implicit treatment of the boundary conditions. The large amount of computer memory required for inversion of the matrices resulting from the implicit operator with, for example, GMRES is still a major constraint for computations of 3-D flow around complex geometries. A three-factored Approximate Factorization scheme, which factorizes the 3-D matrix into three 1-D matrices, minimizes the memory required. The stiffness of the ϵ and f boundary conditions require that the source terms and boundary conditions are treated implicitly in the factorized matrix for grid lines normal to the wall. This, however, leads to severe difficulties in the computation of, for example, wing-body junctions, where grid lines of two coordinate directions may be normal to the walls.

A two-factored Approximate Factorization scheme, which factorizes the 3-D matrix into a 2-D and a 1-D matrix, improves the robustness and applicability of the model. The factorization errors scale with Δt^2 in this scheme in contrast to Δt^3 in the three-factored scheme for 3-D flows. GMRES is used for the inversion of the 2-D matrix, and a direct solver is used for the inversion of the 1-D matrix.

The correctness of the implementation of the v^2-f model in CFL3D has been tested on several cases: flow over a flat plate, channel flow, and by-pass transition. Results for the channel flow have been included in this report.

The performance of each numerical scheme has been tested on the computation of transonic flow around the ONERA M6 wing. This 3-D single block test case presented no major numerical problems with any of these schemes, and it allows a quick evaluation of the CPU time and memory requirements of the different numerical methods. The pressure distributions computed on selected wing cuts are compared with experimental data. Comparisons to computations with the Spalart-Allmaras model provide an overall view on the relative cost of computation for the v^2-f model.

2. Accomplishments

2.1 Basic numerical method

CFL3D, a code developed at NASA (Krist *et al.* 1997), solves the time-dependent thin-layer Reynolds-averaged Navier Stokes equations using multi-block structured

grids. A semi-discrete finite-volume approach is used for the spatial discretization. The convective and diffusion terms are discretized with a third-order upwind and a central difference stencil, respectively. The code uses flux-difference splitting based on the Roe-scheme with a smooth flux limiter. Time advancement is implicit. A three-factored Approximate Factorization scheme (Beam and Warming 1978) is used to invert the matrices, resulting from the implicit operator. The steady-state computations have been performed by marching in time from an initial guess. To accelerate convergence, local timestepping is used for all variables both mean flow and turbulence, while multigrid is used only for the mean flow. This code is a state-of-the art flow solver which is widely used at NASA for research and in industry for design purposes.

2.2 Durbin's v^2-f turbulence model

A short description of the model's equations is given to facilitate the description of its implementation in CFL3D. While new versions of the model (Lien *et al.* 1996, 1998) have been developed to overcome some of the numerical problems mainly connected with the f-boundary condition, we consider in this report only the original version of the model. For high Reynolds number flows in particular the original version predicts consistently better skin friction distributions.

In essence the v^2-f model introduced by Durbin (1995) extends the standard k-ϵ model to low-Reynolds number flow regions. This is realized by modifying the eddy-viscosity formulation and solving two additional partial differential equations: an equation describing the transport of the turbulent intensity normal to the streamlines $\overline{v^2}$ and an elliptic relaxation equation for f. The latter models the effect of the pressure-strain term.

Consistent with the non-dimensionalization used in the code

$$k=\frac{\tilde{k}}{\tilde{a}_\infty^2},\ \epsilon=\frac{\tilde{\epsilon}\tilde{\nu}_\infty}{\tilde{a}_\infty^4},\ \overline{v^2}=\frac{\tilde{\overline{v^2}}}{\tilde{a}_\infty^2},\ f=\frac{\tilde{f}\tilde{\nu}_\infty}{\tilde{a}_\infty^2},\ \mu=\frac{\tilde{\mu}}{\tilde{\mu}_\infty},\ \rho=\frac{\tilde{\rho}}{\tilde{\rho}_\infty},\ U=\frac{\tilde{U}}{\tilde{a}_\infty},\ x=\frac{\tilde{x}}{\tilde{L}_R},\ t=\frac{\tilde{t}\tilde{a}_\infty}{\tilde{L}_R}$$

the model's equations for compressible flow are:

$$\partial_t k=\left(\frac{M_\infty}{Re}\right)\frac{1}{\rho}\nabla\cdot\left[(\mu+\frac{\mu_t}{\sigma_k})\nabla k\right]-U\cdot\nabla k+\left(\frac{M_\infty}{Re}\right)P_k-\left(\frac{Re}{M_\infty}\right)\epsilon \quad (1)$$

$$\partial_t \epsilon=\left(\frac{M_\infty}{Re}\right)\frac{1}{\rho}\nabla\cdot\left[(\mu+\frac{\mu_t}{\sigma_\epsilon})\nabla\epsilon\right]-U\cdot\nabla\epsilon+\left(\frac{M_\infty}{Re}\right)\frac{C_{\epsilon 1}P_k}{T}-\left(\frac{Re}{M_\infty}\right)\frac{C_{\epsilon 2}\epsilon}{T} \quad (2)$$

$$\partial_t \overline{v^2}=\left(\frac{M_\infty}{Re}\right)\frac{1}{\rho}\nabla\cdot\left[(\mu+\frac{\mu_t}{\sigma_k})\nabla\overline{v^2}\right]-U\cdot\nabla\overline{v^2}+\left(\frac{Re}{M_\infty}\right)kf-\left(\frac{Re}{M_\infty}\right)\frac{\epsilon}{k}\overline{v^2} \quad (3)$$

$$0=\left(\frac{M_\infty}{Re}\right)^2 L^2\nabla^2 f-f+\frac{C_1}{T}\left[\frac{2}{3}-\frac{\overline{v^2}}{k}\right]+\left(\frac{M_\infty}{Re}\right)^2 C_2\frac{P_k}{k} \quad (4)$$

The time and length scales are computed as

$$T'=\max\left[\frac{k}{\epsilon},6\sqrt{\frac{\nu}{\epsilon}}\right]\ ,\ T=\min\left(T',\left(\frac{Re}{M_\infty}\right)\frac{\alpha k}{\sqrt{3}C_\mu\overline{v^2}\sqrt{2S_{ij}S_{ij}}}\right)$$

$$L' = \min\left(\frac{k^{3/2}}{\epsilon}, \left(\frac{Re}{M_\infty}\right)\frac{k^{3/2}}{\sqrt{3}C_\mu\overline{v^2}\sqrt{2S_{ij}S_{ij}}}\right), \quad L = C_L \max\left[L', C_\eta(\frac{\nu^3}{\epsilon})^{1/4}\right]$$

where $S_{ij} = 0.5(\partial u_i/\partial x_j + \partial u_j/\partial x_i)$ represents the strain tensor. The upper bound for the time and length scales is derived from realizability constraints (Durbin 1996). The eddy-viscosity is given by

$$\mu_t = C_\mu \overline{v^2} T,$$

and the model constants are:

$$C_\mu = 0.19,\ \sigma_k = 1,\ \sigma_\epsilon = 1.3,\ C_{\epsilon 1} = 1.4(1 + 0.045\sqrt{k/\overline{v^2}}),\ C_{\epsilon 2} = 1.9,$$

$$C_1 = 1.4,\ C_2 = 0.3,\ C_L = 0.3,\ C_\eta = 70,\ \alpha = 0.6.$$

The wall boundary conditions for ϵ and f are derived from the near wall asymptotic behavior of the k and $\overline{v^2}$ equations forcing $k \sim y^2$ and $\overline{v^2} \sim y^4$,respectively, as $y \to 0$.

$$k_w = 0,\ \overline{v_w^2} = 0,\ \epsilon_w = \left(\frac{M_\infty}{Re}\right)^2 \frac{2\nu k_1}{y_1^2},\ f_w = -\left(\frac{M_\infty}{Re}\right)^4 \frac{20\nu^2\overline{v_1^2}}{\epsilon_w y_1^4} \tag{5}$$

The indices w and 1 denote respectively the wall and first point above the wall.

2.3 Numerical solution of the turbulence equations

CFL3D uses a segregated approach for the solution of the mean flow and turbulence equations. This facilitates the implementation of the v^2-f model such that the turbulence model can be solved in a single subroutine. Only the boundary conditions are set up elsewhere.

The k, ϵ and $\overline{v^2}$, f equations are solved in a pairwise coupled manor similarly to the implementation in INS2D (Durbin 1995). An equation-by-equation approach used, for example, in STREAM (Lien *et al.* 1996) does not allow an implicit coupled treatment of the boundary conditions. This has been observed to cause convergence problems and may require the use of smaller time steps. In this report we consider only the implementation of the $\overline{v^2}$ and f equations. The k and ϵ equations are discretized and solved in a similar fashion. Equations (3) and (4) written for an implicit scheme in delta form are:

$$\left(I(\frac{1}{\Delta t} + \left(\frac{Re}{M_\infty}\right)\frac{\epsilon}{k}) + \delta_\eta A_\eta + \delta_\xi A_\xi + \delta_\zeta A_\zeta\right)\Delta\overline{v^2} - \left(\frac{Re}{M_\infty}\right)k\Delta f = R \tag{6}$$

with

$$R = -(\delta_\eta A_\eta + \delta_\xi A_\xi + \delta_\zeta A_\zeta)\overline{v^2}^n + \left(\frac{Re}{M_\infty}\right)kf^n - \left(\frac{Re}{M_\infty}\right)\frac{\epsilon}{k}\overline{v^2}^n$$

and

$$(I + \delta_\eta B_\eta + \delta_\xi B_\xi + \delta_\zeta B_\zeta)\Delta f = Q \tag{7}$$

with

$$Q = -L^2(\delta_\eta B_\eta + \delta_\xi B_\xi + \delta_\zeta B_\zeta)f^n - f^n + \frac{C_1}{T}\left[\frac{2}{3} - \frac{\overline{v^2}^n}{k}\right] + \left(\frac{M_\infty}{Re}\right)^2 C_2 \frac{P_k}{k}$$

Here $\delta_\xi A_\xi$ and $\delta_\xi B_\xi$ (in analogy η and ζ) define the expressions

$$\delta_\xi A_\xi = \delta_\xi U_\xi - \left(\frac{M_\infty}{Re}\right)\frac{1}{\rho}\delta_\xi[(\mu + \frac{\mu_t}{\sigma_k})\delta_\xi] \ , \ \delta_\xi B_\xi = -\left(\frac{M_\infty}{Re}\right)^2 \delta_\xi^2$$

The variables $k, \epsilon, \mu_t, L, T, \rho$, and U are set at their previously computed values and thus treated as constant in time. The time update is defined as

$$\Delta\overline{v^2} = \overline{v^2}^{n+1} - \overline{v^2}^n \ , \ \Delta f = f^{n+1} - f^n$$

As mentioned, the wall boundary conditions are treated implicitly. As usual in a cell centered scheme, two rows of halo, or ghost, cells are added to the computational domain. The values in the first row of halo cells are denoted by subscript 0. The values at wall boundaries are linearly extrapolated from the interior. In delta form the equations are:

$$\Delta k_0 = -\Delta k_1, \ \Delta\overline{v_0^2} = -\Delta\overline{v_1^2}, \ \Delta\epsilon_0 = 2\Delta\epsilon_w r - \Delta\epsilon_1, \ \Delta f_0 = 2\Delta f_w r - \Delta f_1 \qquad (8)$$

It has been found that particularly at the beginning of a calculation very small time steps are required to prevent k and $\overline{v^2}$ from becoming negative, which often leads to divergence of the solution. Particularly the value of ϵ at the wall is initially very large due to the factor $1/y^2$ in the boundary condition. The wall distance of the first cell center above the wall y_1 is usually of the order of 10^{-6} times the airfoils cord. Keeping the dissipation of the turbulent kinetic energy ϵ small at the wall during the first iterations ensures a rapid growth of the turbulent kinetic energy and thus of the turbulent boundary layer. One way to relax the ϵ and f boundary conditions can be achieved by multiplying their wall values by a factor which is dependent on the iteration counter n

$$r = \frac{\min(n, n_a)}{n_a}$$

Here n_a is the iteration number up to which the boundary condition is modified. For most applications it has been set to 100.

The convective terms in the k, ϵ, and $\overline{v^2}$ transport equations have been discretized as first-order upwind differences. This increases robustness, and usually this is sufficiently accurate for the turbulence equations since the source terms mainly balance the diffusion terms in wall bounded flows.

The time and length scales require an upper bound only in fully turbulent calculations with stagnation regions to suppress the spurious production of eddy-viscosity (Durbin 1996). However, the strain magnitude S is particularly large close to the wall at the initial iterations. This oversuppresses the value of the eddy-viscosity, hindering the development of a turbulent boundary layer. Therefore fully turbulent flow has been computed without an upper limit on the time and length scales for the first 100 or so iterations.

2.4 Transition modeling

Particularly for high lift computations it can be very important to model transition. Transition is modeled in a crude way by switching off the production source terms in the laminar part of the flow upstream of an a priorly fixed transition line. It has been found that solely switching off the terms which include P_k upstream of transition leads often to numerical difficulties. Large residuals caused by negative values of the turbulent variables prevent convergence in this region. Limiting the lower value of the turbulent variables with the free-stream values and additionally setting f to 0 at the walls upstream of transition seems to eliminate this problem.

The stagnation point anomaly usually does not appear for airfoil computations with a priorly fixed transition. No upper bounds on the time and length scales are therefore needed.

2.5 Approximate Factorization

In the 2-D flow solver INS2D, the matrices on the left-hand side in (6) and (7) are ILU-preconditioned and subsequently solved with the Generalized Minimum Residual (GMRES) (Saad 1986) algorithm. For 3-D computations the non-zero band width in the sparse matrices increases significantly with the third dimension. The inversion of these matrices with GMRES is not practical in the computation of industrial flows due to the large amount of memory required.

A three-factored Approximate Factorization scheme, as used for the mean flow, factorizes our system of Eqs. (6) and (7) into three 1-D problems:

$$\left(I(1+\left(\frac{Re}{M_\infty}\right)\frac{\epsilon}{k}\Delta t)+\delta_\eta A_\eta \Delta t\right)\Delta\overline{v^2}' - \left(\frac{Re}{M_\infty}\right)k\Delta t\Delta f' = R\Delta t \tag{9}$$

$$(I+\delta_\eta B_\eta \alpha)\Delta f' = Q\alpha$$

along η grid lines,

$$(I+\delta_\xi A_\xi \Delta t)\Delta\overline{v^2}'' = \Delta\overline{v^2}' \tag{10}$$

$$(I+\delta_\xi B_\xi \alpha)\Delta f'' = \Delta f'$$

along ξ grid lines, and

$$(I+\delta_\zeta A_\zeta \Delta t)\Delta\overline{v^2}''' = \Delta\overline{v^2}'' \tag{11}$$

$$(I+\delta_\zeta B_\zeta \alpha)\Delta f''' = \Delta f''$$

along ζ grid lines. A modification of the elliptic relaxation equation is required to factorize the matrices. Here the term Δf on the left-hand side in (7) has been substituted with an unsteady like term $\Delta f/\alpha$.

The error of this scheme can be estimated by substituting $\Delta\overline{v^2}''$, $\Delta\overline{v^2}'$, $\Delta f''$ and $\Delta f'$ with the expressions (10) and (11):

$$\left(I(1+\left(\frac{Re}{M_\infty}\right)\frac{\epsilon}{k}\Delta t)+(\delta_\eta A_\eta+\delta_\xi A_\xi+\delta_\zeta A_\zeta)\Delta t\right)\Delta\overline{v^2}''' - \left(\frac{Re}{M_\infty}\right)k\Delta t\Delta f'''$$

$$+\underline{\left(I\left(\frac{Re}{M_\infty}\right)\frac{\epsilon}{k}(\delta_\xi A_\xi+\delta_\zeta A_\zeta)+\delta_\eta A_\eta\delta_\xi A_\xi+\delta_\eta A_\eta\delta_\zeta A_\zeta+\delta_\xi A_\xi\delta_\zeta A_\zeta\right)\Delta t^2\Delta\overline{v^2}'''}$$

$$-\underline{\left(\frac{Re}{M_\infty}\right)k(\delta_\xi B_\xi+\delta_\zeta B_\zeta)\Delta t\alpha\Delta f'''+\left(I\left(\frac{Re}{M_\infty}\right)\frac{\epsilon}{k}+\delta_\eta A_\eta\right)\delta_\xi A_\xi\delta_\zeta A_\zeta\Delta t^3\Delta\overline{v^2}'''}$$

$$-\underline{\left(\frac{Re}{M_\infty}\right)k\delta_\xi B_\xi\delta_\zeta B_\zeta\Delta t\alpha^2\Delta f'''}=R\Delta t \tag{12}$$

$$(I+(\delta_\eta B_\eta+\delta_\xi B_\xi+\delta_\zeta B_\zeta)\alpha)\,\Delta f'''+\underline{(\delta_\eta B_\eta\delta_\xi B_\xi+\delta_\eta B_\eta\delta_\zeta B_\zeta+\delta_\xi B_\xi\delta_\zeta B_\zeta)\,\alpha^2\Delta f'''}$$

$$+\underline{\delta_\eta B_\eta\delta_\xi B_\xi\delta_\zeta B_\zeta\alpha^3\Delta f'''}=Q\alpha \tag{13}$$

The terms underlined are error terms which modify the original Eqs. (6) and (7). They are, however, scaled by powers of the time step Δt and the variable α. Small values of α and Δt minimize the influence of these error terms. On the other hand, a small α modifies the f equation significantly, which is represented exactly in the non-underlined part of Eq. (13), setting $\alpha = 1$. A local time step is used for steady state computations. The time step Δt for transonic flow around the RAE 2822 airfoil (Cook *et al.* 1979) is, for example, of the order of 10^{-5} near the wall, 0.1 at the edge of the boundary layer, and 10 in the free-stream. A constant value of α between 0.1 and 0.01 has been found to work quite well. Note that at convergence Eq. (13) becomes

$$Q = 0$$

and the exact f-equation is solved, irrespective of α.

The matrices on the left-hand side of (9), (10), and (11) are tridiagonal 2×2 block matrices. A direct solver taken from a 1-D channel code is used to invert these matrices. Sub-iterations for the turbulence model could be used to correct the approximation errors (Steinthorsen *et al.* 1993). However, the test cases run so far have been computed without the use of sub-iterations.

It should be noted that the source terms are treated implicitly only with the first factorized matrix (cf. Eq. (9)). The $''$ and $'''$ time updates in the first cell above the wall do not 'see' the wall and are treated in the same way as in the internal cells. The boundary condition is thus applied only to the first update $'$ and not to the final update $'''$. This allows only certain grid lines, here the η-lines, to be normal to a wall, severely limiting the usability of the three-factored scheme. Nevertheless, several airfoil computations and the 3-D ONERA M6 wing computation described later in this report have been successfully carried out with this approach.

Furthermore, it should be noted that only a 1-D array with twice the largest grid dimension ('twice' since two equations are solved simultaneously) is required for the factorization procedure described. However, consistent with other turbulence models implemented in CFL3D, 2-D arrays have been employed, improving the vectorization of the direct solver and reducing the number of operations. These 2-D arrays are first filled in the $\xi - \eta$ plane with the 1-D operator in η direction, then with the 1-D operator in ξ direction, and finally in the $\xi - \zeta$ plane with the 1-D operator in ζ direction.

A two-factored Approximate Factorization scheme overcomes some of the difficulties described. Instead of factorizing the original 3-D system of equations into three 1-D system of equations, the two-factored scheme solves a 2-D and 1-D set of equations:

$$\left(I(1+\left(\frac{Re}{M_\infty}\right)\frac{\epsilon}{k}\Delta t)+\delta_\eta A_\eta \Delta t+\delta_\xi A_\xi \Delta t\right)\Delta\overline{v^2}'-\left(\frac{Re}{M_\infty}\right)k\Delta t\Delta f'=R\Delta t \quad (14)$$

$$(I+\delta_\eta B_\eta \alpha+\delta_\xi B_\xi \alpha)\Delta f'=Q\alpha$$

in the $\xi-\eta$ plane and

$$(I+\delta_\zeta A_\zeta \Delta t)\Delta\overline{v^2}''=\Delta\overline{v^2}' \quad (15)$$

$$(I+\delta_\zeta B_\zeta \alpha)\Delta f''=\Delta f'$$

along ζ grid lines. Practically only the diagonals of the operators $\delta_\eta A_\eta$, $\delta_\xi A_\xi$ and $\delta_\eta B_\eta$, $\delta_\xi B_\xi$ have to be added, allowing the use of the same 2-D arrays. Solving the resulting 2-D matrix with GMRES the implicit source terms are included in the η direction as well as in the ξ direction. These can now be normal to the walls.

The approximation errors of this scheme follow by substituting $\Delta\overline{v^2}'$ and f' with the expressions of (15)

$$\left(I(1+\left(\frac{Re}{M_\infty}\right)\frac{\epsilon}{k}\Delta t)+(\delta_\eta A_\eta+\delta_\xi A_\xi+\delta_\zeta A_\zeta)\Delta t\right)\Delta\overline{v^2}''-\left(\frac{Re}{M_\infty}\right)k\Delta t\Delta f'' \quad (16)$$

$$\underline{+(I\left(\frac{Re}{M_\infty}\right)\frac{\epsilon}{k}+\delta_\eta A_\eta+\delta_\xi A_\xi)\delta_\zeta A_\zeta \Delta t^2\Delta\overline{v^2}''-\left(\frac{Re}{M_\infty}\right)k\delta_\zeta B_\zeta \Delta t\alpha\Delta f''}=R\Delta t$$

$$(I+\delta_\eta B_\eta \alpha+\delta_\xi B_\xi \alpha+\delta_\zeta B_\zeta \alpha)\Delta f''+\underline{(\delta_\eta B_\eta+\delta_\xi B_\xi)\delta_\zeta B_\zeta \Delta f''\alpha^2}=Q\alpha \quad (17)$$

Again we have underlined the error terms. The number of these terms is substantially smaller than when using the three-factored scheme. Additionally, these terms scale with Δt^2 (or with α^2) as opposed to the three-factored scheme, the error of which scale with Δt^3 (or α^3). Often larger time steps can be used. For some flows such as the transonic flow around the RAE 2822 airfoil under the flow conditions of test case 10 (Lien *et al.* 1998), the computation with the v^2-f model and the three-factored scheme did not converge. It had to be computed using GMRES.

The memory requirements for the three-factored and two-factored scheme described are almost the same in CFL3D. They are far smaller than for a procedure in which the original 3-D system of equations is inverted with GMRES.

Currently, all memory additionally required for GMRES is provided locally. Some of the computer operations could be optimized by reordering the coding. The scaling of the f equation with Re/M_∞ affects the eigenvalues of the implicit matrices. This influences the number of GMRES sub-iterations required as well as the convergence tolerance used. 10 GMRES subiterations with a convergence tolerance of 10^{-8} is currently used and may still be optimized in future research.

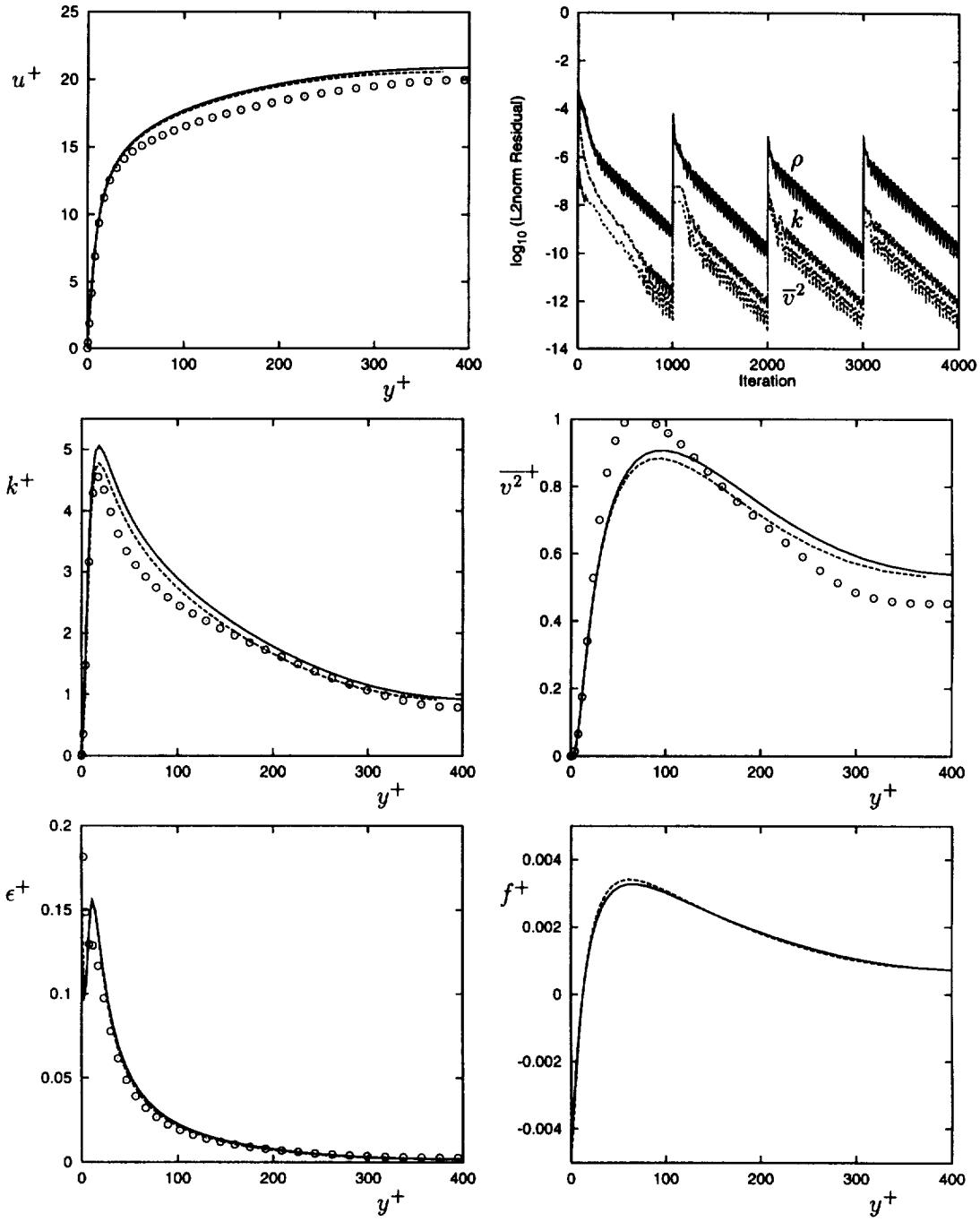

FIGURE 1. Profiles for channel flow, $Re_{u_\tau} = 395$; ——— : v^2-f model and CFL3D, ---- :v^2-f model and 1-D channel code, o : DNS.

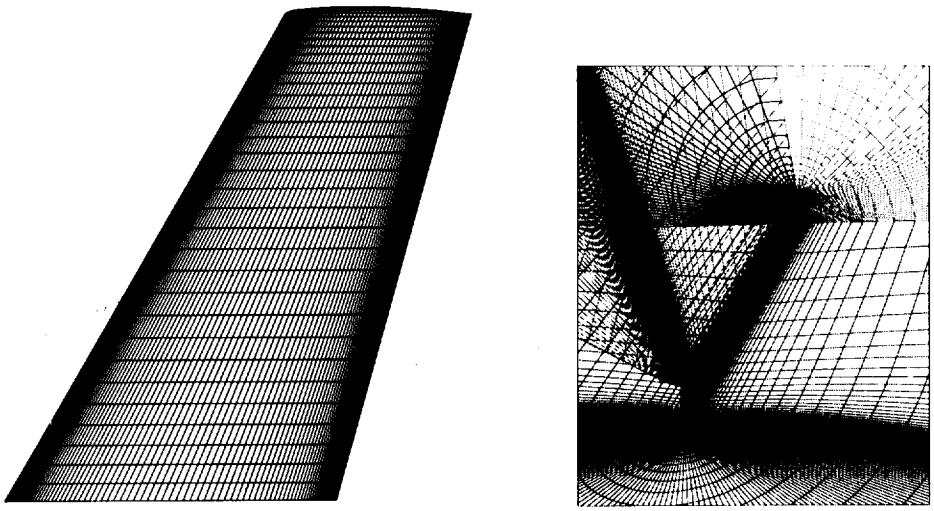

FIGURE 2. Surface mesh and C-O mesh structure for ONERA M6 wing.

2.6 Channel flow

Channel flow has been computed to validate the correctness of the v^2-f implementation in CFL3D. DNS data exists for incompressible flow for $Re_{u_\tau} = 395$ based on the wall shear velocity u_τ and the channel half-width h. A Mach number of $M = 0.2$ has been specified for the computation with CFL3D.

Periodic boundary conditions as for incompressible channel flow can not be specified since the friction at the wall leads to an entropy production which increases the flow temperature. A very long channel $h = 1m, l = 50m$ (32×96 cells) has therefore been computed, avoiding code modifications. The height of the first cell above the wall is 5×10^{-3}, corresponding to a cell-centered value of $y^+ = 1$.

The pressure is extrapolated and the other flow parameters are specified at the inflow of the channel. The pressure at the outflow is obtained over the total enthalpy, which remains constant in the flow for adiabatic walls. The outflow data is then copied to the inflow after achieving convergence. This procedure is repeated until periodicity is obtained with a good approximation, indicating fully developed channel flow. A Reynolds number of about $Re = 7500$, based on the mean flow velocity and the channel half-width h, has been found iteratively to correspond to the correct wall shear velocity.

The convergence plots are given in Fig. 1, which shows the restarted solutions. In the same figure profiles of the velocity and turbulent quantities are plotted against the wall distance y^+. The data computed with CFL3D corresponds quite well with data computed with an incompressible 1-D channel code.

2.7 ONERA M6 wing.

Flow over the ONERA M6 wing (Schmidt *et al.* 1970) has been computed for the flow conditions: Mach number $M = 0.8395$, Reynolds number $Re_c = 11.72 \times 10^6$

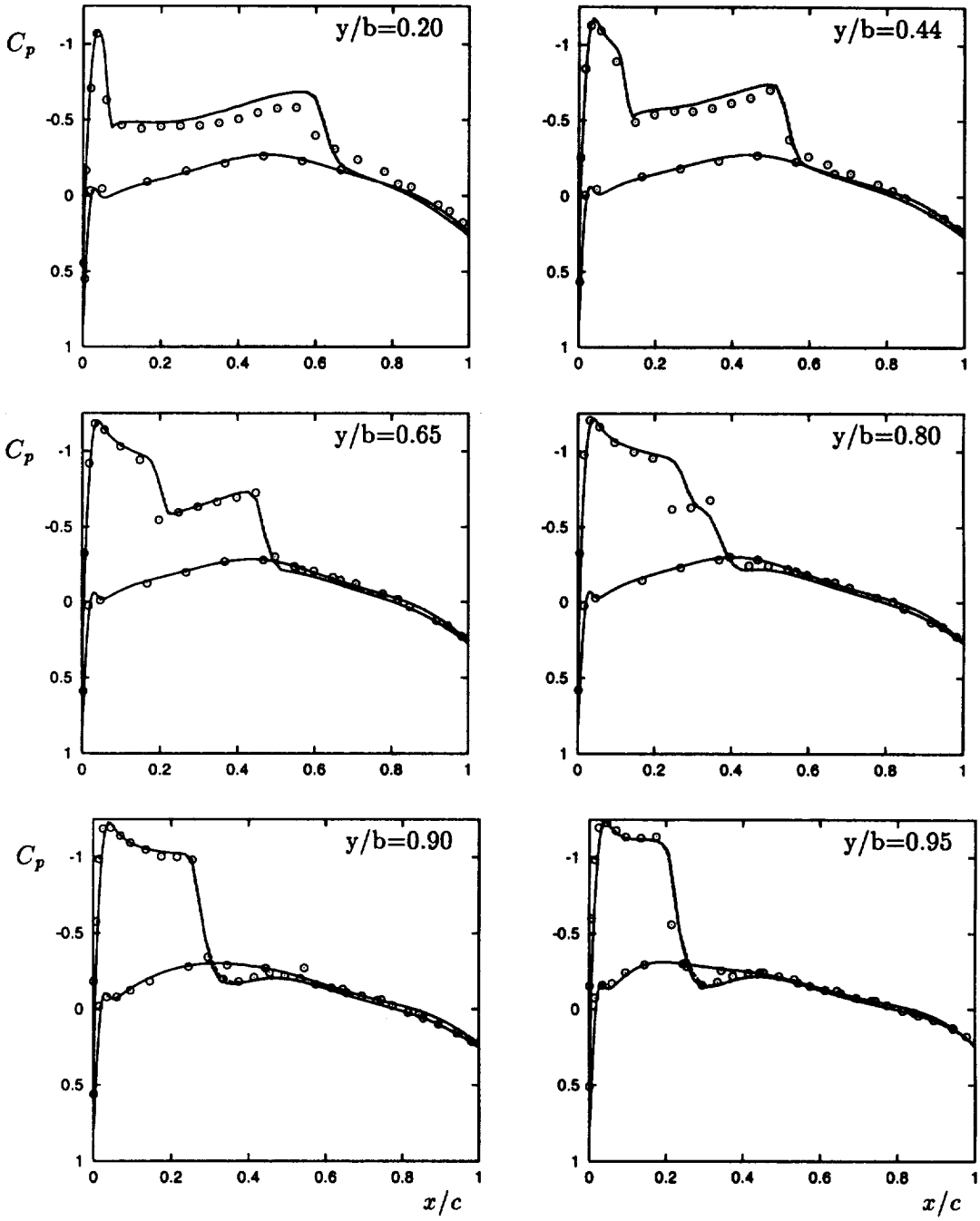

FIGURE 3. Pressure coefficient at cuts for ONERA M6 wing; ——— : v^2-f model, ---- : Spalart-Allmaras, o : Experiment.

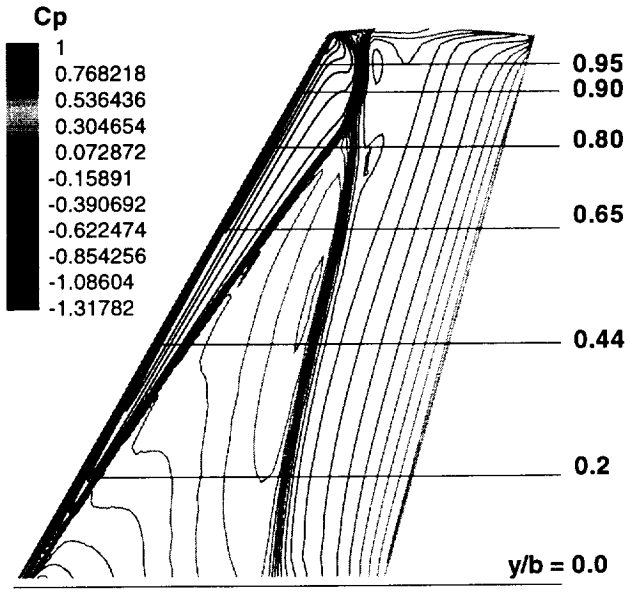

FIGURE 4. Pressure coefficient distribution on ONERA M6 wing (cell-centered data), v^2-f model.

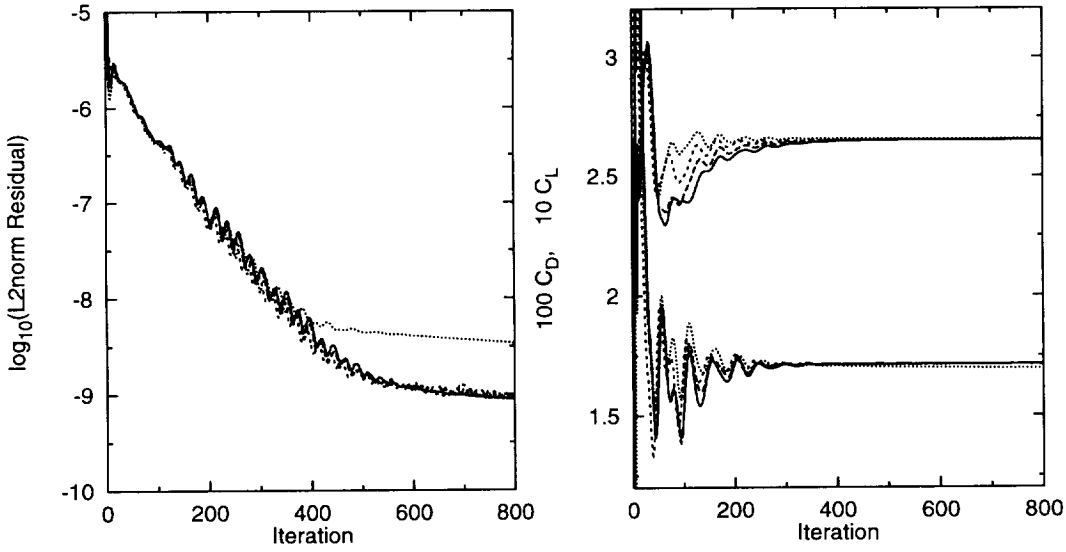

FIGURE 5. Lift, drag and density convergence for ONERA M6 wing; ——— : v^2-f and three-factored AF, – – – : v^2-f and two-factored AF/GMRES, - - - - : v^2-f and GMRES, ····· : Spalart-Allmaras.

based on the mean chord of $c = 0.64607$ and incidence $\alpha = 3.06^o$. This is a swept wing with a root chord of about $c_{root} = 0.8m$ and a span of about $b = 1.2m$. The airfoil profile is symmetric.

The computational grid has been generated with the HYPGEN software package provided by P. Buning (see Chan *et al.* 1993). The single block C-O mesh consists of 665 856 cells (696 969 nodes) with 272 cells in the streamwise direction, 68 normal to the wall, and 36 in the spanwise direction. The inflow is located about 15 chord lengths into the far field. The surface mesh on the wing is 100×36 cells on both the upper and lower surfaces. A plan view of the surface mesh is shown together with the general C-O mesh structure in Fig. 2.

A comparison of pressure distributions computed with the v^2-f and Spalart-Allmaras model with experimental data at selected wing cuts is shown in Fig. 3. The corresponding pressure distribution on the upper wing surface and the location of the cuts are shown in Fig. 4. Although a generally good agreement of the computed and the experimental data can be observed, the pressure distribution at station $y/b = 0.80$ shows both branches of the shock merging prematurely. The pressure distribution on the wing depends more on the particular numerical scheme (i.e. the flux limiter chosen) than the turbulence model used.

The plots in Fig. 5 show a similar convergence history for both models. All three numerical schemes work well for the v^2-f model for this test case. The computations have been carried out with local time steps corresponding to a CFL number of 5.

The computational cost for 800 iterations on a CRAY C90 with the v^2-f model is about 3.1 CPU hours using 42.3 Mword memory with the three-factored scheme and 4.9 hours using 43.6 Mword with the two-factored scheme, in which GMRES has been used in a plane containing the wall normal and streamwise direction. For the solution of the original 3-D problem with GMRES, the CPU time is 12.0 hours using 126.0 Mword memory. For the Spalart-Allmaras model 2.3 CPU hours are required with 38.2 Mword memory.

3. Summary and future plans

The present report describes the current implementation of the v^2-f model in the compressible 3-D flow solver CFL3D. Both an Approximate Factorization scheme and the Generalized Minimum Residual algorithm are implemented for the solution of the turbulence equations. The stiff boundary condition for ϵ and f require that both the source terms and the boundary conditions are treated implicitly in the wall normal direction. This restricts the very fast and memory efficient three-factored Approximate Factorization scheme to computations in which grid lines of the same coordinate, for example η, are normal to the wall. The two-factored scheme allows grid lines of two coordinate directions to be normal to the wall using the same memory requirements. This increases the applicability of the v^2-f model in large flow computations around complex geometries. While less efficient regarding the CPU time needed per iteration, it often permits the use of larger time steps.

The report provides a comparison of a three-factored, a two-factored, and a GMRES solution of the original 3-D turbulence equations. The efficiency of each scheme is demonstrated on the computation of transonic flow around the ONERA M6 wing.

Although all three schemes perform similarly for this test case in terms of convergence per iteration, they require different CPU time and computer memory. The two-factored scheme requires 1.6 times the CPU time of the three factored scheme, using about the same computer memory. The full GMRES solution requires about 2.9 times the amount of memory of both other schemes and 3.9 times the CPU time of the three-factored scheme. However, as mentioned, the implementation of the GMRES routines may not be optimal and can be improved further through future work.

The Spalart-Allmaras model, which consists of one transport equation as opposed to the v^2-f's four partial differential equations, requires 0.74 times the CPU time and 0.90 times the computer memory of the v^2-f computation with the three-factored scheme.

An unsteady term has been added to the f-equation in order to use the Approximate Factorization scheme. Subiterations may be needed to minimize the influence of this term in unsteady computations.

Computation of high-lift test cases are underway which depend significantly on the turbulence model used. Here we concentrate on the computation of flow around the three element trapezoidal wing-body currently investigated experimentally in the wind tunnel at NASA Langley. A patched mesh consisting of about 8 million grid points has been provided by the Subsonic Aerodynamics Branch at Langley (Jones *et al.* 1998).

Computations of the two element NLR7301 airfoil (Van den Berg 1979) and the McDonnell-Douglas slat-wing-flap airfoil (Valarezo *et al.* 1991), previously computed with the INS2D code (Kalitzin 1997), with use of patched and chimera grids is planned. In addition boundary conditions for the ϵ and f equations in flow regions such as the blunt trailing edge of an airfoil may require modifications.

As reported in the CTR Summer Program (Lien, *et al.* 1998), some of the airfoil computations required the use of constant time steps for the integration of the turbulence equations. Small unsteady oscillations in $\overline{v^2}$ and f prevented the solutions from converging using local time steps. This is another aspect for future research.

It is also planned to have a closer look at the shock-boundary layer interaction region, for example for the RAE 2822 test cases. The sonic line parallel to the wall lies deep inside the boundary layer. As pointed out by Bradshaw (1998), the true domain of dependence of a point just upstream of the shock wave is the upstream Mach cone, which blends into the sonic line, plus the subsonic region near the wall. The integration of the f-equation over the whole domain, including shock and the region behind it, introduces errors in comparison to an integration of the f-equation over the upstream-and-subsonic domain only. This research should estimate the significance of this error.

REFERENCES

VAN DEN BERG, B. 1979 Boundary layer measurements on a two-dimensional wing with flap. *NLR TR 79009 U.*

BEAM R. M., & WARMING R. F. 1978 An implicit factored scheme for the compressible Navier-Stokes equations. *AIAA J.* **16,** 393-402.

BRADSHAW, P. 1998 private communications.

CHAN, M. W., CHIU I.-T. & BUNING, P. G. 1993 User's manual for the HYPGEN hyperbolic grid generator and the HGUI graphical user interface. *NASA TM 108791.*

COOK, P. H., MCDONALD, M. A. & FIRMIN, M. C. P. 1979 Aerofoil 2822 - Pressure Distributions, Boundary Layer and Wake Measurements. *AGARD AR 138.*

DURBIN, P. 1995 Separated flow computations with the $k-\epsilon-\overline{v^2}$ model. *AIAA J.* **33,** 659-664.

DURBIN, P. 1996 On the k-ϵ stagnation point anomaly. *Int. J. Heat and Fluid Flow.* **17,** 89-90.

JONES, K. & COMPTON, W. B. 1998 private communications.

KALITZIN, G. 1997 Application of turbulence models to high-lift airfoils. *CTR Annual Research Briefs.* Center for Turbulence Research, NASA Ames/Stanford Univ., 165-177.

KRIST, S., BIEDRON, R. & RUMSEY, C. 1998 CFL3D User's Manual (Version 5.0). *NASA/TM-1998-208444.*

LIEN F. S. & DURBIN P. A. 1996 Non-linear $k-\epsilon-v^2$ modeling with application to high-lift. *CTR Summer Program Proceedings.* Center for Turbulence Research, NASA Ames/Stanford Univ., 5-22.

LIEN F. S., KALITZIN G. & DURBIN P. A. 1998 RANS modeling for compressible and transitional flows. *CTR Summer Program Proceedings.* Center for Turbulence Research, NASA Ames/Stanford Univ., 267-286.

SAAD, Y. & SCHULTZ M. H. 1986 GMRES: a generalized minimal residual algorithm for solving nonsymmetric linear systems. *SIAM J. Sci. Stat. Comp.* **7,** 856-869.

SCHMITT, V. & CHARPIN F. 1970 Pressure distribution on the ONERA M6 wing at Transonic Mach Numbers. *AGARD AR138: Experimental Database for computer program assessment.*

SPALART, P. R. & ALLMARAS, S. R. 1992 A one-equation turbulence model for aerodynamic flows. *AIAA 92-439.*

STEINTHORSEN, E. & SHIH, T.I-P. 1993 Methods for Reducing Approximate-Factorization Errors in Two- and Three-Factored Schemes. *SIAM J. Sci. Comput.* **14-3,** 1214-1236.

VALAREZO, W. O., DOMINIK, C. J., MCGHEE, R. J., GOODMAN, W. L. & PASCHAL, K. B. 1991 Multi-Element Airfoil Optimization for Maximum Lift at High Reynolds Numbers. *AIAA 91-3332.*

Heat transfer predictions in cavities

By A. Ooi, G. Iaccarino AND M. Behnia[1]

1. Motivations & objectives

Artificial roughness elements (ribs) introduced in flow passages is a popular method of enhancing heat transfer in the cooling passage of turbine blades, heat exchangers etc. It is essential to accurately predict the enhancement of heat transfer generated by the roughness elements to ensure good design decisions. Experimental studies have been carried out by various investigators e.g. Han *et al.* (1978), Han (1984), Han *et al.* (1985), Han (1988), Chyu & Wu (1989), Korotky & Taslim (1998), and Rau *et al.* (1998). It has been found that the conventional $k-\epsilon$ turbulence models with wall functions do not accurately predict the data (Simoneau 1992) for this geometrical configuration. This is mainly because the flow field has both separation and reattachment points, and it is well known that the $k-\epsilon$ model with wall functions leads to erroneous predictions for this situation. In order to obtain better predictions, Liou *et al.* (1993) performed two-dimensional numerical simulations using a $k-\epsilon-A$ algebraic stress and heat flux model. Good agreement with experimental data were obtained, but extension of the method to three dimensions is computationally expensive and could lead to equations that are numerically stiff (Gatski & Speziale 1993 and Speziale 1997).

Stephens & Shih (1995) used the $k-\omega$ model to compute three-dimensional ribbed channel with heat transfer and compared their results with experimental data of Chyu & Wu (1989). They achieved good qualitative but not quantitative agreement. More recently, Iacovides (1998) showed that two layer $k-\epsilon$ with the Wolfshtein (1969) one-equation near-wall model for k transport gives unsatisfactory heat transfer predictions in rotating ribbed passages. Better results were obtained by employing a low-Re version of a differential stress model. However, this model is computationally expensive and only achieved marginal improvement in heat transfer predictions.

The v^2-f turbulence model was introduced by Durbin (1991) and has been successfully used to predict heat transfer in attached boundary layers and channel flows (Durbin 1993). This model was later used by Behnia *et al.* (1997) to predict heat transfer in an axisymmetric impinging jet. The impinging jet is a very challenging test case because the applications of traditional turbulence models to this flow configuration have been shown to result in poor agreement with available experimental data. Computations using the v^2-f model give better heat transfer predictions in this axisymmetric two-dimensional environment. Here, the v^2-f

1 Current address: Dept. of Mechanical and Manufacturing Engr., University of New South Wales, NSW 3052, Australia

turbulence model will be used in a three-dimensional domain to test its ability to predict heat transfer in ribbed passages. We will compare results of the current simulation with the experimental data of Rau *et al.* (1998).

Also of interest is the prediction of heat transfer in a geometry resembling the clearance gap between the tip of an axial turbine blade tip and the adjacent stationary shroud. This problem is of great interest in the engineering community because heat transfer at the blade tip can give rise to large temperature gradients, which in turn causes durability problems. Booth *et al.* (1982) and Wadia & Booth (1982) have investigated the aerodynamic characteristics of this narrow flow passage between the pressure and suction sides of the blade. Metzger *et al.* (1989) have provided experimental heat transfer data for this configuration, and we will compare the $v^2 - f$ heat transfer predictions with this data.

2. Accomplishments

2.1 Turbulence models

Most of the results presented below are obtained using the $v^2 - f$ turbulence model. It is computationally more expensive than the conventional $k - \epsilon$ model but is relatively inexpensive compared to algebraic stress and full second moment closure models. The equations for this model can be found in various publications (Behnia 1997, Lien & Durbin 1996) and will not be repeated here. The temperature field is obtained by assuming a constant turbulent Prandtl number, $Pr_t = 0.9$, relating the eddy diffusivities of heat and momentum; i.e. the turbulent heat flux is simply approximated as

$$\langle u_i \theta \rangle = -\frac{\nu_t}{Pr_t} \frac{\partial \Theta}{\partial x_i},$$

where ν_t is the eddy viscosity and Θ is the mean temperature. As will be discussed later, this approximation is only valid for forced convection problems. More complicated models for $\langle u_i \theta \rangle$ are needed where buoyancy effects are significant.

To highlight the advantages of $v^2 - f$ over the more commonly used $k - \epsilon$ model, similar numerical computations were also performed with a $k - \epsilon$ model. For these simulations, the conventional $k-\epsilon$ model matched to the low-Re $k-l$ model proposed by Wolfshtein (1969) is used. This wall-treatment is chosen because it is the default 2 layer model used in many commercial CFD packages.

2.2 Computational domain, parameters, and boundary conditions

Two different sets of computations will be considered in this paper. The first set is the ribbed channel; the corresponding computational domain is shown in Fig. 1. To minimize the number of grid points, symmetry of the mean flow is assumed at the mid-channel. Numerical simulations were carried out with the ribs placed on one wall (1s) or on two opposite walls (2s). For the 2s simulations, symmetric boundary conditions were used on the top of the computational domain, and for the 1s simulations, the no-slip condition is used. The flow is assumed to be fully developed, hence the velocity field is periodic in the streamwise direction. For these

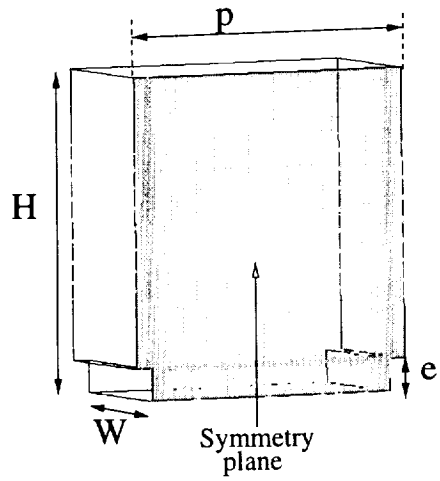

FIGURE 1. Three-dimensional computational domain for ribbed passage simulations.

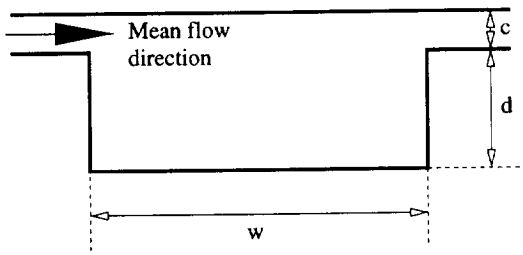

FIGURE 2. Two-dimensional computational domain for blade tip simulations.

simulations the rib height-to-channel hydraulic diameter ratio is fixed at $e/D_h = 0.1$, where the hydraulic diameter, D_h, is defined to be

$$D_h = \frac{2WH}{W+H}.$$

Channel width-to-height ratio (W/H) is unity. Simulations were carried out with different pitch to rib-height ratios of

$$p/e = 6, 9, 12.$$

All Nusselt number distributions for the ribbed channel calculations presented here are normalized with respect to the level obtained in a smooth circular tube (i.e. Dittus-Boelter correlation)

$$Nu_0 = 0.023 Re^{0.8} Pr^{0.4}.$$

The Reynolds number is

$$Re = \frac{U_{bulk} D_h \rho}{\mu} = 30,000$$

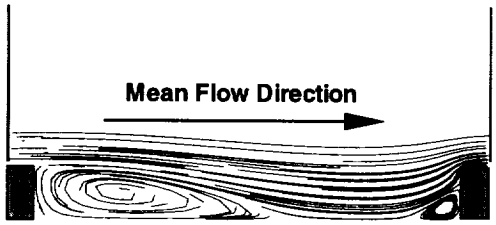

FIGURE 3. Flow pattern on the symmetry plane of the computational domain.

where the bulk velocity, U_{bulk}, is defined as

$$U_{bulk} = \frac{\dot{m}}{\rho A_c}.$$

A_c is the cross-sectional area of the passage. The molecular Prandtl number, $Pr = 0.71$, is kept constant for all simulations. For heat transfer calculations, a constant heat flux is applied at the walls.

All results presented here are from simulations with $81(x) \times 65(y) \times 31(z)$ grid points. To ensure that the results are independent of the grid, all simulations were repeated with twice the number of grid points in each spatial direction. No noticeable difference in the solutions were observed, hence the solutions presented here are assumed to be grid independent.

The other problem considered is a model for the grooved turbine blade tip cross section. This configuration is shown in Fig. 2. The mean flow field in the experiments by Metzger *et al.* (1989) is essentially two-dimensional at Reynolds number

$$Re = \frac{\rho U_{bulk} C}{\mu} = 1.5 \times 10^4.$$

The ratio of clearance height to cavity width, c/w, was fixed at 0.1 and two different

$$d/w = 0.1, 0.2$$

ratios were considered. Constant temperature boundary conditions are used for all walls and the Prandtl number, Pr, is kept constant at 0.71. Nusselt number distribution on the cavity floor will be compared with the experimental data of Metzger *et al.* (1989).

2.3 Results and discussion (ribs)

Figure 3 shows the flow pattern on the symmetry plane of the computational domain. The flow separates after going over the upstream rib creating a low pressure region behind the rib. Further downstream, the flow reattaches and forms a short recovery region downstream of the reattachment point. This flow then impinges on the next rib, forming a small recirculating region in front of the downstream rib. The flow pattern just described is difficult to model mainly because it contains

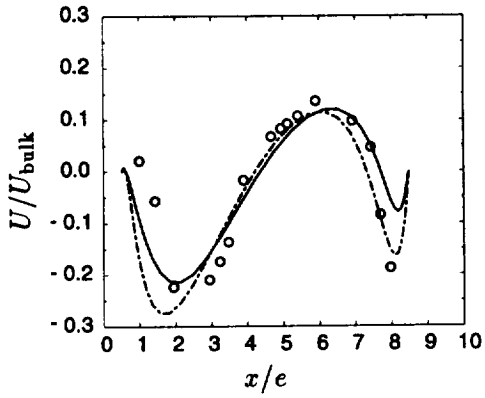

FIGURE 4. Comparison of the streamwise velocity component, U, at $y/e = 0.1$ on the symmetry plane of the computational domain. This figure shows data from a 1s simulation with $p/e = 9$. —— $v^2 - f$ turbulence model, —·— $k - \epsilon$ 2 layer model, o experimental data of Rau *et al.* (1998).

both separation and reattachment points. Parneix & Durbin (1996) have used the $v^2 - f$ model to accurately predict the reattachment point and the downstream recovery region of a backstep flow. Analysis of the data here will determine if $v^2 - f$ can predict the short recovery region and the subsequent separation point before the downstream rib. Figure 4 shows the streamwise velocity distribution close to the floor (10% of the rib height) between the two ribs on the symmetry plane. As can be seen, both the $k - \epsilon$ and $v^2 - f$ models accurately predict the separation and reattachment points. The velocity maximum and minimum in the recovery and reverse flow region are more accurately predicted by the $v^2 - f$. The $k - \epsilon$ model predicts a more accurate minimum streamwise component of velocity in the recirculating bubble just before the downstream rib.

Heat transfer predictions from the $v^2 - f$ and $k - \epsilon$ models are shown in Fig. 5. The comparisons are for the 2s simulations with $p/e = 9$. As can be seen, heat transfer predicted by the $k - \epsilon$ model is roughly half the heat transfer measured in the experiment. Calculations by Iacovides (1998) utilizing the same $k - \epsilon$ low Re number model and using a different p/e and e/D_h ratio also shows that the $k - \epsilon$ model predicts a Nusselt number distribution of about half the actual experimental data. Since his calculations were computed for a rotating channel with different geometrical ratios, using a different numerical method and different types of grids, there can be no numerical issues in the discrepancies between the $k - \epsilon$ predictions and experimental data.

In addition, Iacovides (1998) also calculated the flow using a Reynolds stress model which is computationally more expensive than $v^2 - f$. The Nusselt number predicted by the Reynolds stress model was better than the $k - \epsilon$ calculations. Figure 5 indicates that the $v^2 - f$ model yields very good agreement with experimental values.

In Fig. 6, heat transfer predictions using $v^2 - f$ for different geometrical ratios

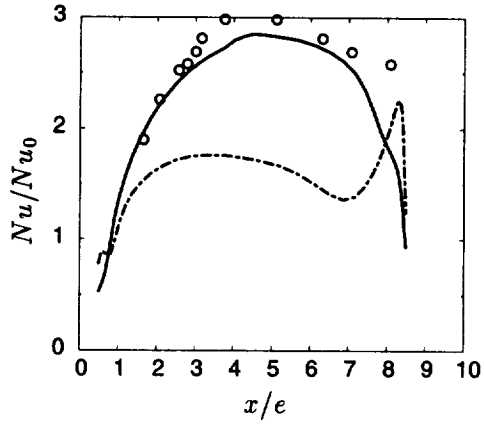

FIGURE 5. Comparison of the Nusselt number distribution for the 2-sided ribbed channel with $p/e = 9$ on the symmetry plane of the computational domain. —— $v^2 - f$ turbulence model, —·— $k - \epsilon$ 2 layer model, o experimental data of Rau *et al.* (1998).

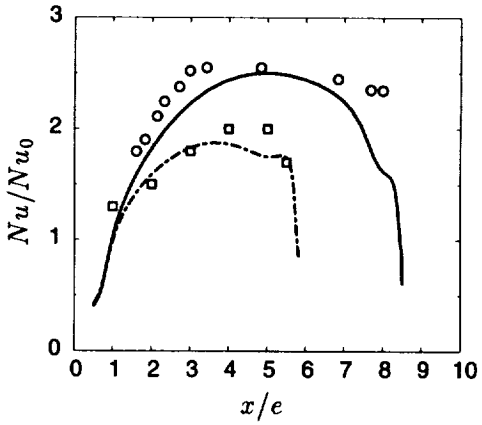

FIGURE 6. Nusselt number distribution on the floor of the symmetry plane. —— $v^2 - f$ with 1s $p/e = 9$, o corresponding experimental data from Rau *et al.* (1998), —·— $v^2 - f$ with $p/e = 6$, □ corresponding experimental data from Rau *et al.* (1998).

are compared with the corresponding data from Rau *et al.* (1998). Experimental data show that the heat transfer rate decreases with p/e ratio. The $v^2 - f$ model accurately reproduces this observation, both qualitatively and quantitatively. The $k - \epsilon$ calculations are not shown in this figure, but the predictions are about half the values obtained from the experiments. This is illustrated in Fig. 7, which shows the average Nusselt number on the floor between the two ribs for different p/e ratios computed here. The results show that the $k - \epsilon$ model consistently underpredicts the heat transfer on the floor between the two ribs. The $v^2 - f$ results are better but still lower than the experimental data.

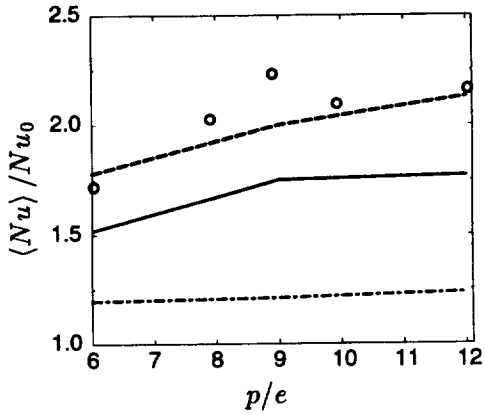

FIGURE 7. Average Nusselt number on the floor of the computational domain. —— $v^2 - f$, ---- $v^2 - f$ for "reduced" domain, —·— $k - \epsilon$, o experimental data from Rau *et al.* (1998).

It must be pointed out that the $v^2 - f$ results shown by the solid line in Fig. 7 are the Nusselt numbers averaged over the whole area between the two ribs. Careful observation of the experimental data shown in Figs. 5 and 6 indicates the first and last experimental data points are approximately $0.5e$ away from the upstream and downstream ribs respectively. The Nusselt number is quite low in the region close to the ribs, and this brings down the average. Thus, a more accurate comparison with experimental data would be to average Nu only in areas where experimental data exist. We are currently in the process of obtaining these experimental data from the group at Von Karman Institute where the experiment was carried out. However, if the Nu was calculated using only an area which is $0.5e$ away from the ribs and $1.0e$ away from the side walls, there is very good agreement between the $v^2 - f$ results and the experimental data. This is shown by the dashed line in Fig. 7.

Figure 8 shows the local Nusselt number distribution for both models on the side wall. The maximum Nusselt number on the side wall is located at the first corner of the downstream rib. The highest contour level for Nu/Nu_0 using the $k - \epsilon$ model is 2.2 and for the $v^2 - f$ model is 2.0. Experimental data shows that the maximum contour level is 2.24. This initial observation might lead one to believe that the $k - \epsilon$ model gives better prediction on the side wall. A better way of determining the performance of the models will be to compare the average Nusselt numbers on the side wall. These data are shown in Fig. 9, and the $v^2 - f$ prediction is closer to the experimental data. However, it is clear that the side wall predictions are not as good as the predictions for the wall between the ribs. Future studies will attempt to find the source of this discrepancy. Similar to the data on the wall between the ribs, there can be better agreement with experimental data if one averages only within the area away from the corners of the computational domain. This is not done for the side wall because it is unclear from the paper by Rau *et al.* (1998) how close to the corners the experimental data on the side wall were taken. We are currently in the process of obtaining this information.

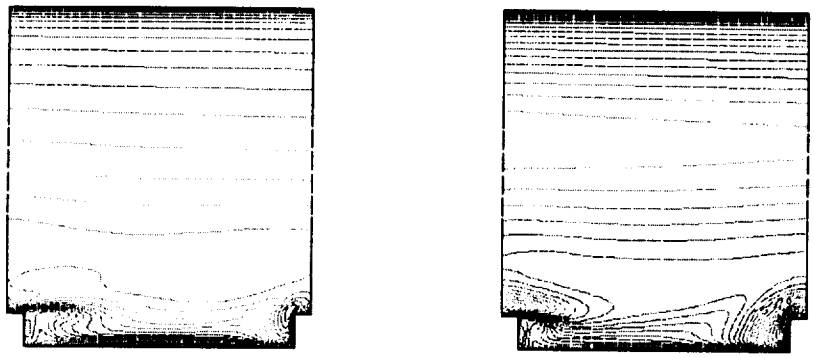

FIGURE 8. Nusselt number contours on the smooth side wall of the computational domain computed using $v^2 - f$ turbulence model (contour level is 0.3–2.0) (left) and $k - \epsilon$ turbulence model (contour level is 0.3–2.2) (right).

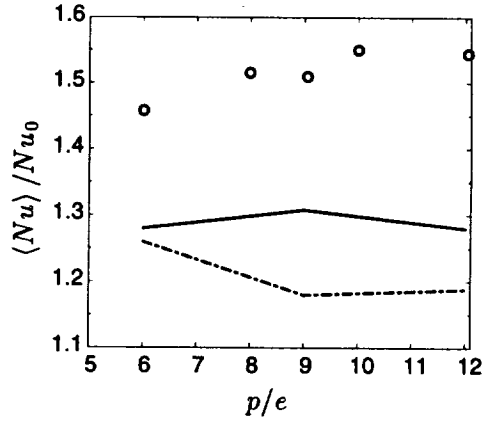

FIGURE 9. Average Nusselt number on the smooth side wall of the computational domain. —— $v^2 - f$, —·— $k - \epsilon$, o experimental data from Rau *et al.* (1998).

2.4 Results and discussion (blade tip)

The second set of simulations were performed to investigate the ability of the $v^2 - f$ model to predict heat transfer at the tip of a turbine blade. The resulting flow fields for $d/w = 0.1$ and $d/w = 0.2$ are shown in Fig. 10. For $d/w = 0.1$, the flow pattern is very similar to the one shown in Fig. 3. The flow separates at wall A and reattaches on the floor. In the case of $d/w = 0.2$, the flow pattern changes and the flow separates as it leaves wall A and reattaches, not on the floor, but on the side of wall B. There is a slow mean recirculating region between walls A and B similar to the driven cavity flow.

The heat transfer predictions on the floor between the two walls are shown in Fig. 11. Similar to the case of the ribbed channel, the Nusselt number distribution predicted by the $k - \epsilon$ model is too low. On the other hand, $v^2 - f$ gives good agreement with experimental data. The agreement with experimental data is better

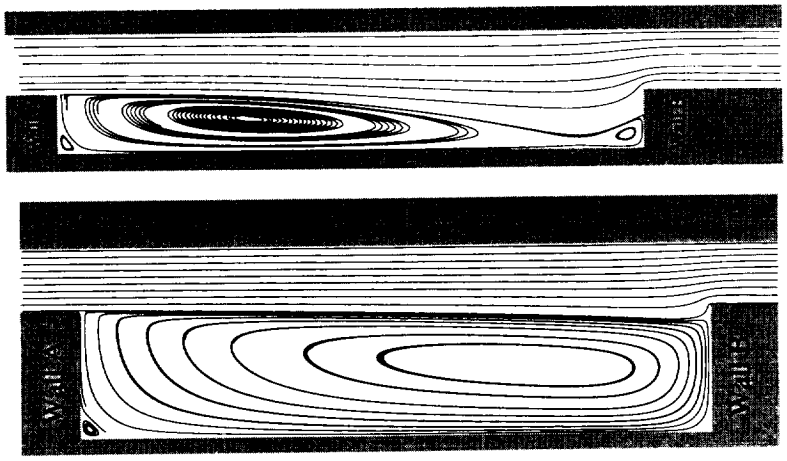

FIGURE 10. Flow pattern for blade tip flow simulation using the $v^2 - f$ turbulence model. The figure on the top is for $d/w = 0.1$ and the figure on the bottom is for $d/w = 0.2$.

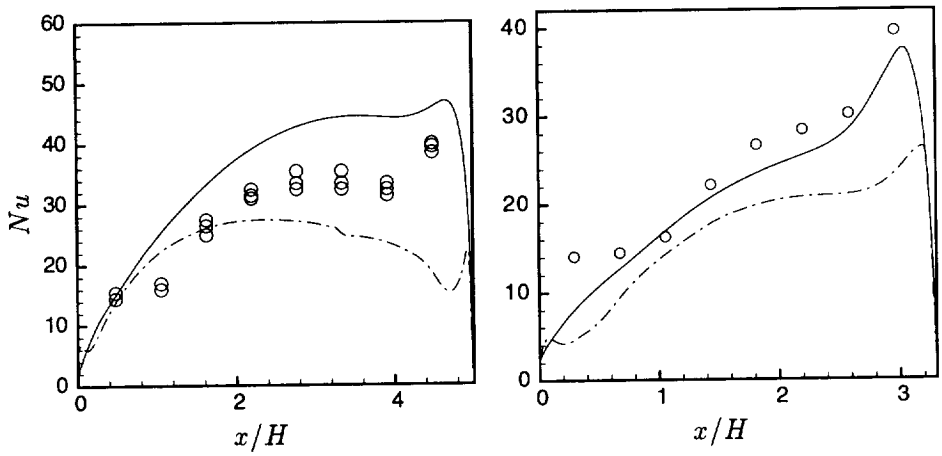

FIGURE 11. Nusselt number distribution on the floor for $d/w = 0.1$ (left) and $d/w = 0.2$ (right). —— $v^2 - f$, —·— $k - \epsilon$, o experimental data of Metzger *et al.* (1989). The experiment was repeated with three different inlet temperatures and all measured data sets are shown in this figure.

for the flow with $d/w = 0.2$ than $d/w = 0.1$. It is interesting to note that the experimental data with $d/w = 0.1$ shows a peak in the Nusselt number close to wall B. The $v^2 - f$ model reproduces this peak whereas data using the $k - \epsilon$ model shows a dip in the heat transfer.

Calculations were also carried out to assess the accuracy of using wall functions with the $k - \epsilon$ model. The computations were done using a similar mesh to the previous calculations. As wall functions are really only valid for approximately $y^+ > 30$, the grid needs to be coarsened so that wall functions can be used. Grid

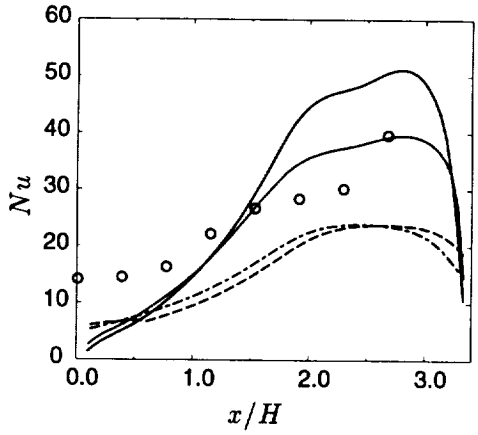

FIGURE 12. Nusselt number distribution on the floor for $d/w = 0.2$. Calculations performed with $k-\epsilon$ model with standard wall functions.—— $y^+ \simeq 3$, ····· $y^+ \simeq 5$,—— y^+---- 30, —·— $y^+ \simeq 50$, o experimental data of Metzger *et al.* (1989).

lines closest to the floor were removed to ensure the distance from the first grid line to the wall is increased. Four meshes were generated corresponding to average y^+ along the cavity floor ranging from approximately 3 to about 50. Results from these calculations are shown in Fig. 12 and compared with the experimental data. As expected, the results are grid dependent for $y^+ < 30$, but surprisingly, the calculations agree quite well with experimental data when $y^+ \approx 3$ or 5. When $y^+ \approx 30$ or 50, the Nusselt number is underpredicted. In this case, the wall function is a bit worse than the two layer model. This is despite the fact that there is a slow recirculation region, and it is questionable whether a log law exists close to the wall of the cavity.

3. Future plans

The results above and computations by Durbin (1993) and Behnia *et al.* (1997) show that the heat transfer predictions by the $v^2 - f$ turbulence model agree very well with experimental data. To this end, the model has only been tested in a forced convection environment, and it has been shown that the simple gradient diffusion hypothesis with a constant turbulent Prandtl number is sufficient to obtain good agreement with experimental data. However, buoyancy effects are not included in the current model, hence $v^2 - f$ cannot be expected to give good predictions in situations where buoyancy plays an important role. Assuming that the Boussinesq approximation holds, the source term due to gravity in the Reynolds stress transport equation becomes

$$-\beta g_i \langle u_j \theta \rangle - \beta g_j \langle u_i \theta \rangle .$$

Thus, to accurately model buoyancy effects, a good model for the turbulence heat flux, $\langle u_i \theta \rangle$, is needed. Future work will explore the feasibility of incorporating buoyancy effects into $v^2 - f$ by extending the algebraic heat flux analysis of Shabany & Durbin (1997).

REFERENCES

BEHNIA, M., PARNEIX, S. & DURBIN, P. 1997 Accurate modeling of impinging jet heat transfer". *CTR Annual Research Briefs,* NASA Ames/Stanford Univ., 149-164.

BOOTH, T. C., DODGE, P. R. & HEPWORTH, H. K. 1982 Rotor-Tip Leakage:Part I-Basic Methodology. *ASME J. Engr. for Power.* **104,** 154-161.

CHYU, M. K. & WU, L. X. 1989 Combined effects of rib angle-of-attack and pitch-to-height ratio on mass transfer from a surface with transverse ribs. *Exp. Heat Transfer.* **2,** 291-308.

DURBIN, P. A. 1991 Near-Wall Turbulence Closure Modeling Without "Damping Functions". *Theor. and Comp. Fluid Dynamics.* **3,** 1-13.

DURBIN, P. A. 1993 Application of a near-wall turbulence model to boundary layers and heat transfer. *Int. J. Heat and Fluid Flow.* **14**(4), 316-323.

GATSKI, T. B. & SPEZIALE, C. G. 1993 On explicit algebraic stress models for complex turbulent flows. *J. Fluid Mech.* **254,** 59-78.

HAN, J. C., GLICKSMAN, L. R. & ROHSENOW W. M. 1978 An investigation of heat transfer and friction for rib-roughened surfaces. *Int. J. Heat Mass Transfer.* **21,** 1143-1156.

HAN, J. C. 1984 Heat Transfer and Friction in Channels With Two Opposite Rib-Roughened Walls. *J. Heat Transfer.* **106,** 774-781.

HAN, J. C., PARK, J. S. & LEI, C. K. 1985 Heat Transfer Enhancement in Channels With Turbulence Promoters. *J. of Engr. for Gas Turbines and Power.* **107,** 628-635.

HAN, J. C. 1988 Heat Transfer and Friction Characteristics in Rectangular Channels with Rib Turbulators. *J. Heat Transfer.* **110,** 321-328.

IACAVIDES, H. 1998 Computation of flow and heat transfer through rotating ribbed passages. *Int. J. Heat and Fluid Flow.* **19,** 393-400.

KOROTKY, G. J. & TASLIM, M. E. 1998 Rib Heat Transfer Coefficient Measurements in a Rib-Roughened Square Passage. *J. Turbomachinery.* **120,** 376-385.

LIEN, F. S.& DURBIN, P. A. 1996 Non-linear $k-\epsilon-v^2$ modeling with application to high-lift. *Proceedings of the 1996 Summer Program.* Center for Turbulence Research NASA Ames/Stanford University, 5-22.

LIOU, T. M., HWANG, J. J. & CHEN, S. H. 1993 Simulation and measurement of enhanced turbulent heat transfer in a channel with periodic ribs on one principal wall. *Int. J. Heat Mass Transfer.* **36**(2), 507-517.

METZGER, D. E., BUNKER, R. S. & CHYU, R. K. 1989 Cavity Heat Transfer on a Transverse Grooved Wall in a Narrow Flow Channel. *J. Heat Transfer.* **111,** 73-79.

RAU, G., CAKAN, M., MOELLER, D. & ARTS, T. 1998 The Effect of Periodic Ribs on the Local Aerodynamic and Heat Transfer Performance of a Straight Cooling Channel. *J. Turbomachinery.* **120,** 368-375.

SHABANY, Y. & DURBIN, P. A. 1997 On Explicit Algebraic Scalar Flux Approximation. *AIAA J.* **35**(6), 985-989.

SIMONEAU, R. J. & SIMON, F. F. 1992 Progress towards understanding and predicting heat transfer in the turbine gas path. *Int. J. Heat and Fluid Flow.* **14**(2), 106-128.

SPEZIALE, C. 1997 Comparison of Explicit and Traditional Algebraic Stress Models of Turbulence. *AIAA J.* **35**(9), 1506-1509.

STEPHENS, M. A. 1995 Computation of Flow and Heat Transfer in a Rectangular Channel with Ribs. *AIAA Paper 95-0180.*

WADIA, A. R. & BOOTH, T. C. 1982 Rotor-Tip Leakage:Part II-Design Optimization Through Viscous Analysis and Experiment. *ASME J. Engr. for Power.* **104,** 162-169.

WOLFSHTEIN, M. 1969 The Velocity and Temperature Distribution of One-Dimensional Flow with Turbulence Augmentation and Pressure Gradient. *Int. J. Heat Mass Transfer.* **12,** 301-318.

A structure-based model with stropholysis effects

By S. C. Kassinos AND W. C. Reynolds

1. Motivation and objectives

The performance of Reynolds Stress Transport (RST) models is limited by the lack of information about two dynamically important effects: the role of energy-containing turbulence structure (dimensionality) and the breaking of reflectional symmetry (stropholysis) due to strong mean or frame rotation. Both effects are fundamentally nonlocal in nature and this explains why it has been difficult to include them in *one-point* closures such as RST models. Information about the energy-containing structure is necessary if turbulence models are to reflect differences in dynamic behavior associated with structures of different dimensionality (nearly isotropic turbulence *vs.* turbulence with strongly organized two-dimensional structures). Information about the breaking of reflectional symmetry is important whenever mean rotation is dynamically important (flow through axisymmetric diffuser or nozzle with swirl, flow through turbomachinery, etc.).

Engineering flows that must now be computed to advance technology require that dimensionality and stropholysis effects be properly captured in one-point closures. The information needed in order to address these issues is carried by new one-point tensors whose definitions and transport equations were obtained in earlier work (Kassinos and Reynolds 1994). Two of these tensors, the dimensionality D_{ij} and circulicity F_{ij}, characterize the energy-containing structure. Another tensor, the third-rank fully symmetric stropholysis Q^*_{ijk}, parameterizes the breaking of reflectional symmetry in the spectrum of turbulence. Reflectional symmetry breaking is not properly captured in second-rank tensors such as the Reynolds stresses R_{ij} or even D_{ij} and F_{ij}.

In our ongoing effort to construct one-point structure-based models for engineering use, we have in the past formulated a simplified nonlocal theory for the deformation of homogeneous turbulence, the Interacting Particle Representation Model or IPRM (see Kassinos and Reynolds 1996). The IPRM gives excellent results for general deformations of homogeneous turbulence and has been helping us formulate one-point models. A one-point model (the *R-D* model described in Kassinos and Reynolds 1997) was formulated using the IPRM ideas and produces excellent results for both rapid and slow *irrotational* deformation of homogeneous turbulence. The *R-D* model cannot be applied to flows with strong mean or frame rotation because it lacks important physics related to stropholysis $\mathbf{Q}^*$.

In the past year, we have formulated a new one-point model, the Q-model, which is based on our understanding of the stropholysis effects and which uses the effective gradients model from the IPRM (see Kassinos & Reynolds 1996) for the modeling of nonlinear effects. For irrotational deformations the Q-model is equivalent to the previously formulated *R-D* model (see Kassinos & Reynolds 1997) and produces

good results for both rapid and slow mean deformations. The Q-model overcomes the restriction to irrotational deformation that applied to the previous model and produces good results even for flows with combinations of strong mean rotation and strain.

The development of the Q-model is an ongoing effort, and we expect that some aspects of the model will eventually be modified, but this preliminary note sketches the basic ideas.

2. Accomplishments

2.1 Why stropholysis-based models?

One-point models based directly on stropholysis transport have certain important advantages. The stropholysis tensor contains information stemming from the breaking of reflectional symmetry in the spectrum of turbulence that has undergone mean rotation. This information is not contained in second-rank tensors such as the Reynolds stress tensor or even the dimensionality D_{ij} and circulicity F_{ij}. This means that models based on these second-rank tensors, including standard Reynolds Stress Transport (RST) models, must be supplemented with ad-hoc phenomenological models in order to emulate even the leading order effects of stropholysis. The use of ad-hoc models for stropholysis in these lower-rank models eliminates any hope of achieving good realizability properties under non-equilibrium conditions. The added computational cost for carrying a third-rank equation might be a reasonable price to pay if stropholysis-based models can capture subtle rotational effects while maintaining good realizability properties. The model described here is a first attempt at exploring these ideas.

2.2 Definitions and constitutive equations

We introduce the turbulent stream function Ψ'_i, defined by

$$u'_i = \epsilon_{its}\Psi'_{s,t} \qquad \Psi'_{i,i} = 0 \qquad \Psi'_{i,nn} = -\omega'_i\,, \tag{1}$$

where u'_i and ω'_i are the fluctuating velocity and vorticity components. The Reynolds stress tensor and the associated nondimensional and anisotropy tensors are defined by

$$R_{ij} = \overline{u'_i u'_j} = \epsilon_{ipq}\epsilon_{jts}\overline{\Psi'_{q,p}\Psi'_{s,t}}\,, \qquad r_{ij} = R_{ij}/q^2, \qquad \tilde{r}_{ij} = r_{ij} - \tfrac{1}{3}\delta_{ij}\,. \tag{2}$$

Here $q^2 = 2k = R_{kk}$. Introducing the isotropic tensor identity (Mahoney 1985)

$$\epsilon_{ipq}\epsilon_{jts} = \delta_{ij}\delta_{pt}\delta_{qs} + \delta_{it}\delta_{ps}\delta_{qj} + \delta_{is}\delta_{pj}\delta_{qt} - \delta_{ij}\delta_{ps}\delta_{qt} - \delta_{it}\delta_{pj}\delta_{qs} - \delta_{is}\delta_{pt}\delta_{qj} \tag{3}$$

one finds

$$R_{ij} + \underbrace{\overline{\Psi'_{k,i}\Psi'_{k,j}}}_{D_{ij}} + \underbrace{\overline{\Psi'_{i,k}\Psi'_{j,k}}}_{F_{ij}} - \underbrace{\overline{\Psi'_{i,k}\Psi'_{k,j}} + \overline{\Psi'_{j,k}\Psi'_{k,i}}}_{C_{ij}+C_{ji}} = \delta_{ij}q^2\,. \tag{4}$$

The constitutive Eq. (4) shows that one-point correlations of stream function gradients, such as the Reynolds stresses, are dominated by the energy-containing scales. These correlations contain independent information that is important for the proper characterization of non-equilibrium turbulence.

For homogeneous turbulence $C_{ij} = C_{ji} = 0$, and the remaining tensors in (4) have equivalent representations in terms of the velocity spectrum tensor $E_{ij}(\mathbf{k})$ and vorticity spectrum tensor $W_{ij}(\mathbf{k})$. These are as follows:

• Structure *dimensionality* tensor

$$D_{ij} = \int \frac{k_i k_j}{k^2} E_{nn}(\mathbf{k})\, d^3\mathbf{k} \qquad d_{ij} = D_{ij}/q^2 \qquad \tilde{d}_{ij} = d_{ij} - \tfrac{1}{3}\delta_{ij} \tag{5}$$

• Structure *circulicity* tensor

$$F_{ij} = \int \mathcal{F}_{ij}(\mathbf{k})\, d^3\mathbf{k} \qquad f_{ij} = F_{ij}/q^2 \qquad \tilde{f}_{ij} = f_{ij} - \tfrac{1}{3}\delta_{ij}\,. \tag{6}$$

Here $\mathcal{F}_{ij}(\mathbf{k})$ is the circulicity spectrum tensor, which is related to the vorticity spectrum tensor $W_{ij}(\mathbf{k}) = \overline{\hat{\omega}_i \hat{\omega}_j^*}$ through the relation

$$\mathcal{F}_{ij}(\mathbf{k}) = \frac{W_{ij}(\mathbf{k})}{k^2}.$$

The familiar rapid pressure–strain-rate term is given by

$$T_{ij} = 2G_{ts}(M_{istj} + M_{jsti}) \tag{7}$$

where the fourth-rank tensor $\mathbf{M}$ is

$$M_{ijpq} = \int \frac{k_p k_q}{k^2} E_{ij}(\mathbf{k})\, d^3\mathbf{k}\,. \tag{8}$$

We define the third rank tensor

$$Q_{ijk} = -\overline{u_j' \Psi_{i,k}'}\,. \tag{9}$$

For homogeneous turbulence, Q_{ijk} has the equivalent definition

$$Q_{ijk} = \epsilon_{ipq} M_{jqpk} \tag{10}$$

where M_{ijpq} is as in (8). The general definition of the third-rank fully symmetric *stropholysis* tensor is given by

$$Q^*_{ijk} = \frac{1}{6}(Q_{ijk} + Q_{jki} + Q_{kij} + Q_{ikj} + Q_{jik} + Q_{kji})\,. \tag{11}$$

In the case of homogeneous turbulence both Q_{ijk} and Q^*_{ijk} are bi-trace free

$$Q_{iik} = Q_{iki} = Q_{kii} = 0 \qquad Q^*_{iik} = 0\,. \tag{12}$$

A decomposition based on group theory shows that Q_{ijk} and Q^*_{ijk} are related to each other and lower-rank tensors,

$$Q_{ijk} = \tfrac{1}{6}q^2\epsilon_{ijk} + \tfrac{1}{3}\epsilon_{ikm}R_{mj} + \tfrac{1}{3}\epsilon_{jim}D_{mk} + \tfrac{1}{3}\epsilon_{kjm}F_{mi} + Q^*_{ijk}\,, \tag{13}$$

and

$$R_{ij} = \epsilon_{imp}Q_{mjp} \quad D_{ij} = \epsilon_{imp}Q_{pmj} \quad F_{ij} = \epsilon_{imp}Q_{jpm}\,. \tag{14}$$

2.1 IPRM formulation

Kassinos & Reynolds (1994, 1996) formulated a simplified nonlocal theory (Particle Representation Model or PRM) for the RDT of homogeneous turbulence. The original idea was to represent the turbulence by an ensemble of fictitious particles. A number of key properties and their evolution equations are assigned to each particle. Ensemble averaging produces a representation of the one-point statistics of the turbulent field, which is exactly correct for the case of RDT of homogeneous turbulence. In essence, this approach represents the simplest theory beyond one-point methods that provides closure for the RDT equations without modeling.

The Interacting Particle Representation Model (IPRM) is the more recent extension of the PRM formulation that includes the effects of the nonlinear eddy-eddy interactions, important when the mean deformations are slow. Unlike standard models, which use return-to-isotropy terms, the IPRM incorporates nonlinear effects through the use of effective gradients. The effective gradients idea postulates that the background nonlinear particle-particle interactions provide a gradient acting on each particle in addition to the actual mean velocity gradient. An advantage of this formulation is the preservation of the RDT structure of the governing equations even for slow deformations of homogeneous turbulence. A detailed account of these ideas is given in Kassinos & Reynolds (1996, 1997) and will not be repeated here. To a large extent, the one-point Q-model is based on the IPRM formulation.

The governing equations for the conditional (cluster averaged) IPRM formulation are (see Kassinos & Reynolds 1996)

$$\dot{n}_i = -G^n_{ki}n_k + G^n_{kr}n_kn_rn_i \tag{15}$$

$$\begin{aligned}\dot{R}^{|n}_{ij} = {} & -G^v_{ik}R^{|n}_{kj} - G^v_{jk}R^{|n}_{ki} + [G^n_{km} + G^v_{km}](R^{|n}_{im}n_kn_j + R^{|n}_{jm}n_kn_i) \\ & - [2C_1R^{|n}_{ij} - C_2^2R^{|n}_{kk}(\delta_{ij} - n_in_j)]\,.\end{aligned} \tag{16}$$

Here $n_i(t)$ is the unit gradient vector and $R^{|n}_{ij}$ is the conditional Reynolds stress tensor corresponding to a cluster of particles with a common $n_i(t)$. The effective gradients are

$$G^n_{ij} = G_{ij} + \frac{C^n}{\tau}r_{ik}d_{kj} \qquad G^v_{ij} = G_{ij} + \frac{C^v}{\tau}r_{ik}d_{kj}\,. \tag{17}$$

where G_{ij} is the mean velocity gradient. The constants C^v and C^n are taken to be $C^n = 2.2C^v = 2.2$. The different values for these two constants account for the different rates of return to isotropy of D_{ij} and R_{ij}.

The turbulent time scale τ is chosen so as to produce the proper dissipation rate. The rate of dissipation of the turbulent kinetic energy $k = \frac{1}{2}q^2$ that is produced by the IPRM Eq. (16) is given by

$$\epsilon^{\text{PRM}} = q^2 \frac{C^v}{\tau} r_{ik} d_{km} r_{mi} \,. \tag{18}$$

To complete the IPRM we use the standard model equation for the dissipation rate (ϵ) with a rotational modification to account for the suppression of ϵ due to mean rotation,

$$\dot{\epsilon} = -C_0(\epsilon^2/q^2) - C_s S_{pq} r_{pq} \epsilon - C_\Omega \sqrt{\Omega_n \Omega_m d_{nm}}\, \epsilon \,. \tag{19}$$

Here Ω_i is the mean vorticity vector, and the constants are taken to be

$$C_0 = 3.6 \qquad C_s = 3.0 \qquad \text{and} \qquad C_\Omega = 0.01 \,.$$

We choose the time scale τ so that $\epsilon^{\text{PRM}} = \epsilon$. This requires that

$$\tau = (\frac{q^2}{\epsilon}) C^v r_{ik} d_{km} r_{mi} \,. \tag{20}$$

The last term in (16) accounts for rotational randomization due to eddy-eddy interactions. We require that the rotational randomization model leaves the conditional energy unmodified. This requires that $C_1 = C_2^2$, and hence using dimensional considerations we take

$$C_r = C_1 = C_2^2 = \frac{8.5}{\tau} \Omega^* f_{pq} n_p n_q \qquad \Omega^* = \sqrt{\Omega_k^* \Omega_k^*} \qquad \Omega_i^* = \epsilon_{ipq} r_{qk} d_{kp} \,. \tag{20}$$

2.3 The stropholysis equation

The most convenient method for deriving the slow $\mathbf{Q}$ equation is to use the conditional (cluster averaged) IPRM formulation to obtain the evolution equation for $\mathbf{M}$ and then contract the $\mathbf{M}$ equation with the alternating tensor ϵ_{ijk} to extract the $\mathbf{Q}$ equation†. The PRM representation for $\mathbf{Q}$ and $\mathbf{M}$ is

$$Q_{ijk} = -\langle V^2 v_j s_i n_k \rangle \qquad M_{ijpq} = \langle V^2 v_i v_j n_p n_q \rangle \tag{21}$$

where s_i is the unit stream function vector. Hence using (15) and (16) and the definitions (10) and (21) , one obtains

† To be precise, stropholysis is the fully symmetric subtensor $\mathbf{Q}^*$. Here we refer to the $\mathbf{Q}$ equation as the stropholysis information since $\mathbf{Q}$ contains the (stropholysis) information found in $\mathbf{Q}^*$.

$$\frac{dQ_{ijk}}{dt} = -G^v_{jm}Q_{imk} - G^n_{mk}Q_{ijm} - G^v_{sm}\epsilon_{its}M_{jmtk} - G^n_{mt}\epsilon_{its}M_{jsmk} + [G^n_{wq} + G^v_{wq}]Q_{iqwjk} + 2G^n_{qr}Q_{ijkqr} - \frac{8.5}{\tau}\Omega^* f_{rs}[Q_{ijkrs} + Q_{jikrs}]. \tag{22}$$

2.3 Closure of the stropholysis equation

Closure of (22) requires a model for the tensor Q_{ijkpq} in terms of Q_{ijk}. Once such a model has been specified, it effectively provides a model for M_{ijpq} in terms of Q_{ijk} since $\mathbf{M}$ can be obtained from Q_{ijkpq} by a contraction with ϵ_{ijk}. For small anisotropies, one can write an exact representation of Q_{ijkpq} in terms of Q_{ijk} that is linear in Q_{ijk}. Other tensors such as R_{ij}, D_{ij}, and F_{ij} can be expressed in terms of Q_{ijk} [see (14)] and need not be included explicitly in the model. Definitions (contractions and continuity) determine all the numerical coefficients in the linear model. Thus the linear model contains no adjustable parameters.

In the presence of mean rotation, *rotational randomization* is an important dynamical effect that must be accounted for in the model. Rotational randomization is a strictly nonlocal effect that is lost in the averaging procedure that generates one-point statistics. Rotational randomization is caused by the differential action of mean rotation on particle velocity vectors (Fourier modes) according to the alignment of the corresponding gradient (wavenumber) vectors with the axis of mean rotation. The main impact of Fourier randomization on one-point statistics is the damping of rotation-induced adjustments; here this effect is added explicitly through a simple model,

$$\frac{DQ_{ijk}}{Dt} = \ldots - \gamma_1(Q_{ijk} - Q^{rf}_{ijk}) - \gamma_2\,\epsilon_{ijm}(R_{mk} - D_{mk}) - \gamma_3\,\epsilon_{ikm}(F_{mj} - D_{mj})\,. \tag{23}$$

The first term accounts for the rotational randomization effects in rotation dominated flows while the remaining two terms account for the modification of these effects due to the combined action of mean strain and rotation. Here γ_1, γ_2 and γ_3 are scalar functions of the invariants of the mean strain and rotation and are determined from simple test cases. A detailed discussion of these models will appear separately.

2.4 Representative results for homogeneous turbulence

Examples of the performance of the new, one-point Q-model for irrotational mean deformation are shown in Figs. 1 and 2. A particularly interesting test case is that of homogeneous turbulence deformed by *slow* axisymmetric expansion (axisymmetric impingement). The mean velocity gradient tensor in this case is

$$S_{ij} = \frac{2}{\sqrt{3}}S\begin{pmatrix} -1 & 0 & 0 \\ 0 & \frac{1}{2} & 0 \\ 0 & 0 & \frac{1}{2} \end{pmatrix}, \qquad S = \sqrt{S_{ij}S_{ij}/2}\,. \tag{24}$$

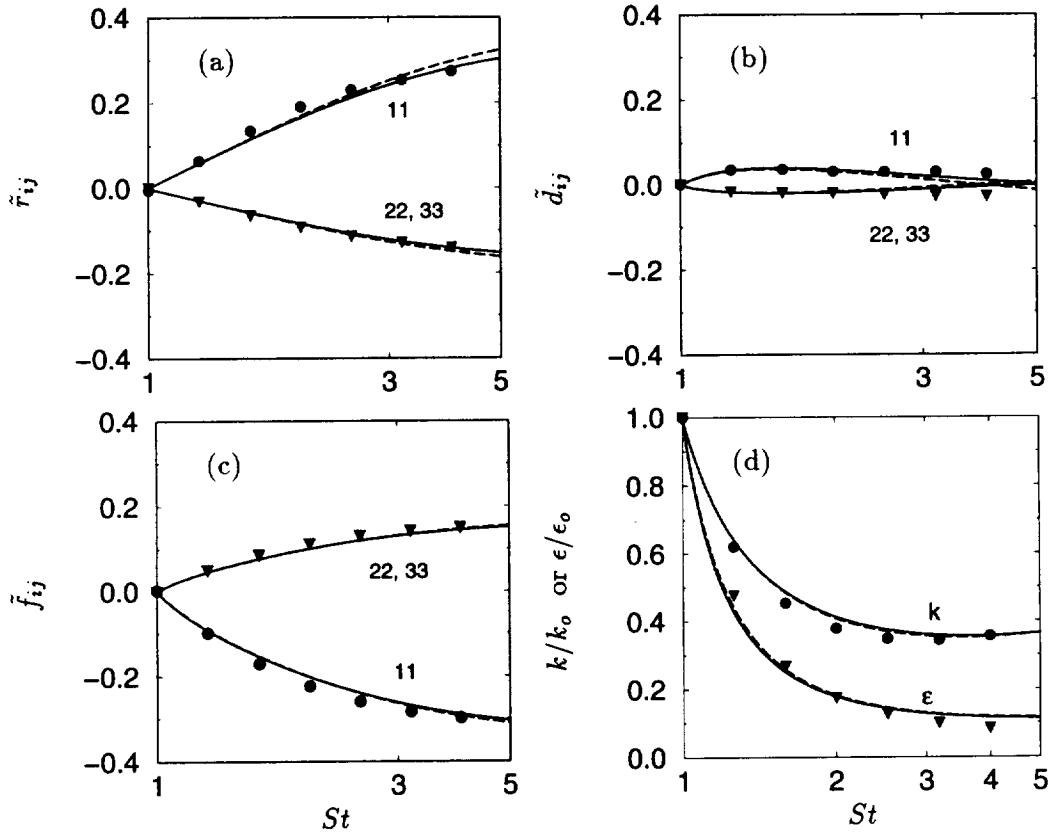

FIGURE 1. Comparison of the one-point Q-model predictions (----) with the IPRM results (———) and the 1985 DNS of Lee & Reynolds (symbols) for the axisymmetric expansion case EXO ($Sq_0^2/\epsilon_0 = 0.82$). (a)-(c) evolution of the Reynolds stress, dimensionality, and circulicity anisotropies; 11 component (•), 22 and 33 components (▾). (d) evolution of the normalized turbulent kinetic energy (•) and dissipation rate (▾).

As was discussed in Kassinos & Reynolds (1996, 1997), the axisymmetric expansion flows exhibit a paradoxical behavior where a slower mean deformation rate produces a stress anisotropy that exceeds the one produced under RDT for the same total mean strain. This effect is triggered by the different rates of return to isotropy in the $\tilde{\mathbf{r}}$ and $\tilde{\mathbf{d}}$ equations, but it is dynamically controlled by the rapid terms. The net effect is a growth of $\tilde{\mathbf{r}}$ in expense of $\tilde{\mathbf{d}}$, which is strongly suppressed. The one-point model (see Fig. 1) is able to capture these effects well and also predicts the correct decay rates for the normalized turbulent kinetic energy k/k_0 and dissipation rate ϵ/ϵ_0. The predictions of the one-point Q-model are comparable to those of the nonlocal IPRM.

The case of homogeneous turbulence deformed by slow plane strain ($Sq_0^2/\epsilon_0 = 1.0$) is shown in Fig. 2. In this case the mean strain tensor is

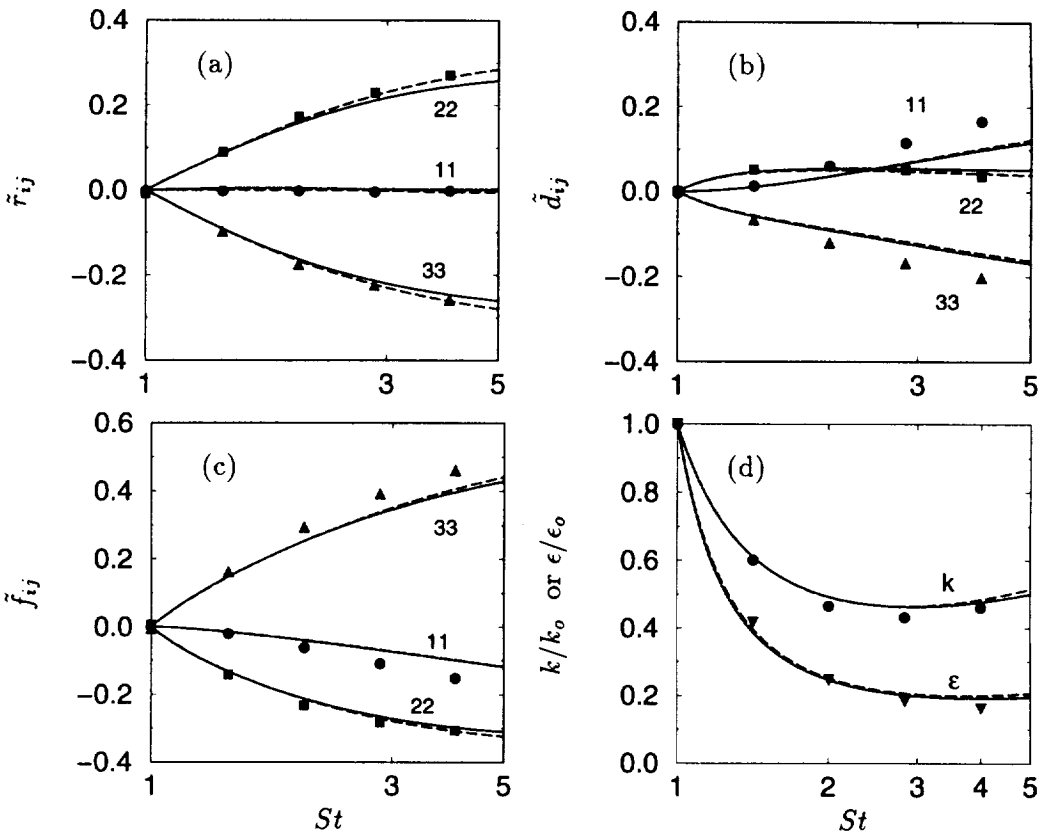

FIGURE 2. Comparison of the one-point Q-model predictions (----) with the IPRM results (———) and the 1985 DNS of Lee & Reynolds (symbols) for the plane strain case PXA ($Sq_0^2/\epsilon_0 = 1.0$). (a)-(c) evolution of the Reynolds stress, dimensionality, and circulicity anisotropies; 11 component (•), 22 component (■), 33 component (▲). (d) evolution of the normalized turbulent kinetic energy (•) and dissipation rate (▼).

$$S_{ij} = S \begin{pmatrix} 0 & 0 & 0 \\ 0 & -1 & 0 \\ 0 & 0 & +1 \end{pmatrix} . \tag{25}$$

Again the performance of the one-point model is comparable to that of the IPRM, and its predictions compare favorably with the DNS results of Lee & Reynolds (1985). The details in the evolution histories of $\tilde{r}_{ij}$, $\tilde{d}_{ij}$ and $\tilde{f}_{ij}$ are captured, and the correct rates are predicted for the decay of the (normalized) turbulent kinetic energy k/k_0 and dissipation rate ϵ/ϵ_0.

The predictions of the one-point Q-model for the case of homogeneous shear are shown in Fig. 3. Comparison is made to the DNS results of Rogers & Moin (1987).

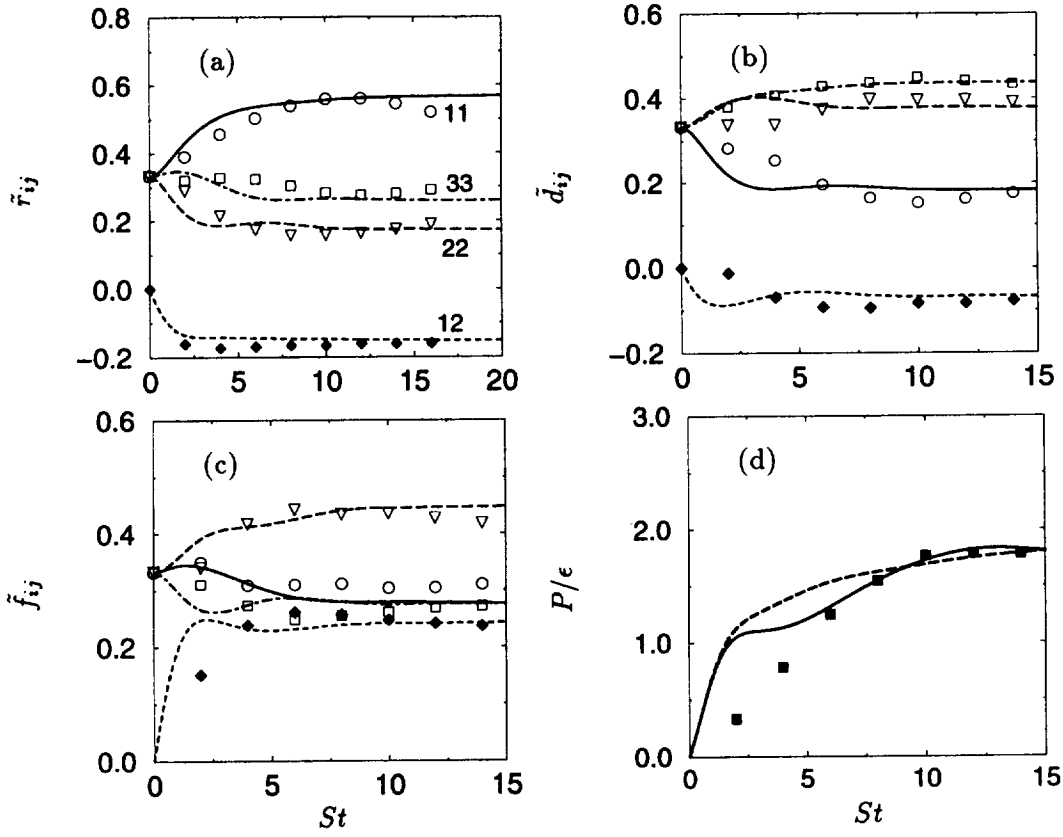

FIGURE 3. Comparison of the one-point Q-model predictions (lines) and the 1986 DNS of Rogers & Moin (symbols). (a)-(c) evolution of the Reynolds stress, dimensionality, and circulicity components in homogeneous shear with $Sq_0^2/\epsilon_0 = 2.36$: 11 component, (——— , o); 22 component, (- - - - , ▽); 33 component, (—·— □); 12 component, (- - - - ,, ♦). (d) evolution of production over dissipation rate (P/ϵ): model, (- - - -); IPRM, (———); DNS (■).

Note that the model produces satisfactory predictions for the components of $r_{ij} = R_{ij}/q^2$, $d_{ij} = D_{ij}/q^2$, $f_{ij} = F_{ij}/q^2$. A fully-developed stage was reached in the simulations for $10 \leq St \leq 15$, and in this range both the Q-model and the IPRM predict the correct level for the dimensionless ratio of production over dissipation, P/ϵ.

A difficult challenge for one-point models is provided by the elliptic streamlines flows (see Fig. 4),

$$G_{ij} = \begin{pmatrix} 0 & 0 & -\gamma - e \\ 0 & 0 & 0 \\ \gamma - e & 0 & 0 \end{pmatrix} \qquad 0 < |e| < |\gamma| \tag{26}$$

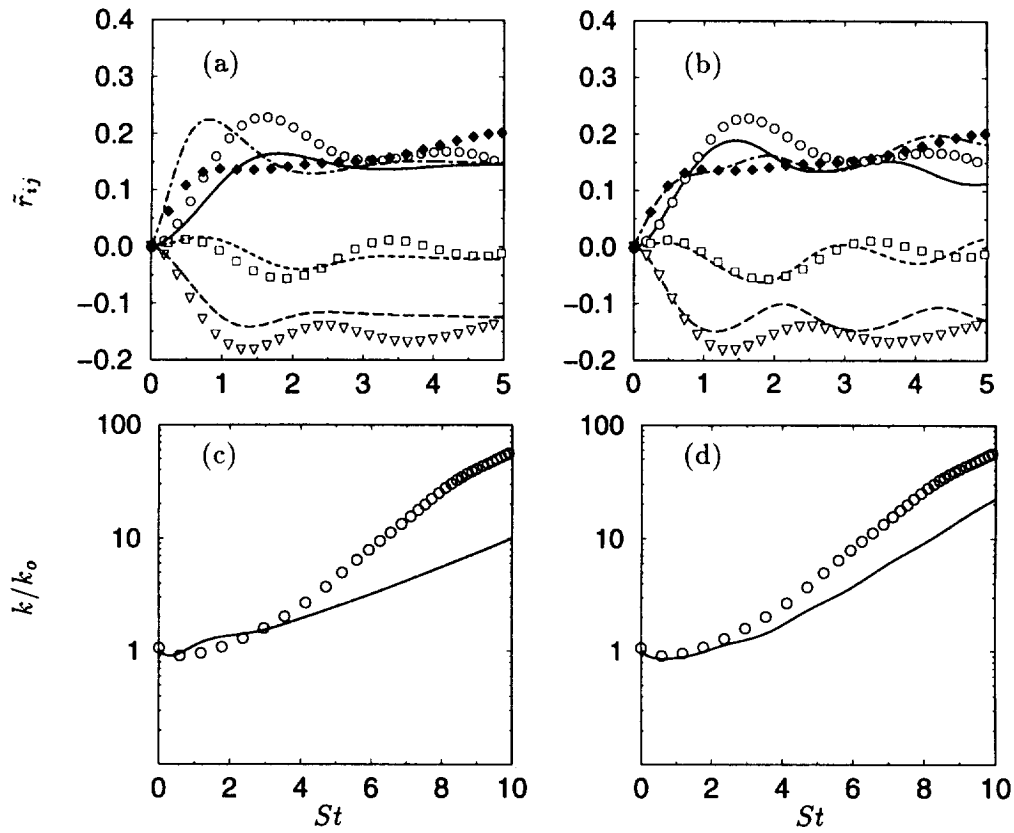

FIGURE 4. Comparison of model predictions (lines) for the evolution of the Reynolds anisotropy in elliptic streamline flow (E=2.0) with the 1996 DNS of Blaisdell (symbols). (a) one-point Q-model vs DNS, (b) IPRM vs DNS: 11 component, (——— , o); 22 component, (---- , ▽); 33 component, (---- , □); 13 component, (—·— , ♦). Growth of the normalized turbulent kinetic energy: (c) one-point Q-model (line) vs DNS (symbols), (d) IPRM (line) vs DNS (symbols).

which combine the effects of mean rotation and plane strain and emulate conditions encountered in turbomachinery. (Note that the case $e = 0$ corresponds to pure rotation while the case $|e| = |\gamma|$ corresponds to homogeneous shear).

Direct numerical simulations (Blaisdell & Shariff 1996) show exponential growth of the turbulent kinetic energy in elliptic streamline flows, which analysis shows is associated with instabilities in narrow wavenumber bands in wavenumber space. Standard k-ϵ models as well as most RST models instead predict decay of the turbulence.

As shown in Fig. 4, both the one-point Q-model and the IPRM predict exponential growth of k. The rate of growth of k predicted by the one-point model is lower than those predicted by the IPRM and DNS but probably satisfactory for most purposes. In addition, the one-point model predicts the details of the evolution of

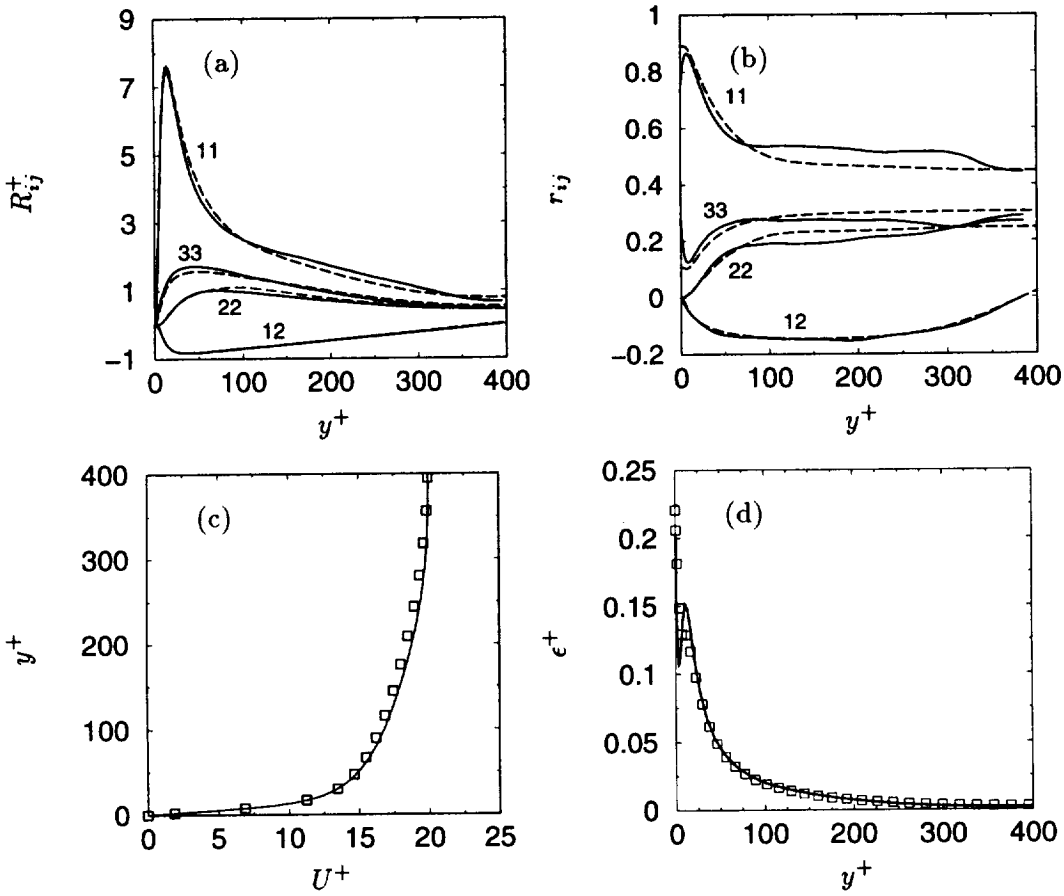

FIGURE 5. Comparison of model predictions with DNS (Mansour, 1998) for fully developed channel flow at $Re_\tau = 395$. (a) components of the Reynolds stress tensor, (b) components of the Reynolds stress tensor normalized by its trace: model, (———); DNS (----). (c) mean velocity profile, (d) dissipation rate profile: model, (———); DNS, (□).

the Reynolds stress anisotropy components with a level of accuracy comparable to the IPRM, which again seems adequate for many engineering purposes, especially since none of the currently available k-ϵ and RST models can predict the elliptic streamlines flows at this level of accuracy and detail.

2.5 Extensions to inhomogeneous flows

The Q-model has been implemented in a 1D code and is currently being tested for fully developed channel flow. Inhomogeneous effects are accounted for through the addition of standard gradient diffusion models in the Q_{ijk} and ϵ equations. In other words in the evolution equations for the turbulent statistics, we allow for turbulent transport in a diffusion-like manner

$$\frac{DQ_{ijk}}{Dt} = \ldots + \frac{\partial}{\partial x_r}([\nu\delta_{rs} + \frac{C_\nu}{\sigma_Q}R_{rs}\tau]\frac{\partial Q_{ijk}}{\partial x_s}) \tag{25}$$

$$\frac{D\epsilon}{Dt} = \ldots + \frac{\partial}{\partial x_r}([\nu\delta_{rs} + \frac{C_\nu}{\sigma_\epsilon}R_{rs}\tau]\frac{\partial \epsilon}{\partial x_s}) . \tag{26}$$

The turbulent kinetic energy is obtained from $k = \epsilon_{ikj}Q_{ijk}/2$.

Wall proximity effects and boundary conditions are treated through an elliptic relaxation scheme based on the ideas of Durbin (1993). Terms in the transport equation for Q_{ijk} which are assumed to represent nonlocal effects are lumped together into a term $\wp_{ijk}$, which is then replaced by a new tensor, $q^2 f_{ijk}/2$, obtained through an elliptic relaxation scheme

$$L^2\nabla^2 f_{ijk} - f_{ijk} = -2\wp_{ijk}/q^2 . \tag{27}$$

The elliptic relaxation scheme allows the imposition of boundary conditions that produce the correct near-wall behavior for various components of Q_{ijk}. Away from the wall (27) allows one to recover the homogeneous model. This is in analogy to the elliptic relaxation scheme applied to RST models by Durbin.

Representative results for fully developed channel flow

Preliminary results obtained with the Q-model for fully developed channel flow are encouraging. The model was implemented in a 1D-code using elliptic relaxation as outlined above and with no wall-function treatment. A comparison of the Q-model predictions with DNS data (Mansour 1998) for fully developed channel flow at $Re_\tau = 395$ is shown in Fig. 5.

The Reynolds stress components (nondimensionalized with the wall shear velocity u_τ) are shown in Fig. 5a. The agreement between the model predictions (dashed lines) and the DNS (solid lines) is satisfactory. The model slightly overpredicts the peak in the streamwise component R_{11}^+ that occurs at about $y^+ \approx 15$. The components of the normalized Reynolds stress tensor $r_{ij} = R_{ij}/q^2$ are shown in Fig. 5b. The agreement between the model predictions and the DNS results is again reasonable. The agreement in the case of the shear stress r_{12} is noteworthy.

The mean velocity profile is shown Fig. 5c. The model prediction is in good agreement with the DNS profile, the most notable difference being in the value of the mean velocity in the log region.

Finally, the model profile of the dissipation rate ϵ is shown in Fig. 5d. The model is again in good agreement with the DNS but has a larger wiggle near the wall than the data show. This difference depends on the model transport equation for ϵ, and we are currently exploring alternative formulations that aim at taking full advantage of the structure information carried in the new model.

Future plans

The performance of standard RST models in flows with strong rotation is often compromised by their incomplete treatment of key physics in rotated turbulence. The new Q-model is based on a more rigorous treatment of rotational effects and offers the possibility to improve our predictive capabilities in strongly rotated turbulence. Hence, our immediate plans include the implementation and testing of the model in rotating wall-bounded flows, including rotating channel flow (with rotation either about the spanwise or streamwise direction) and axially rotating pipe flow. These cases will provide the first real test of the new model in flows where it is expected to perform better than standard closures.

REFERENCES

BLAISDELL, G. A. & SHARIFF, K. 1996 Simulation and modeling of the elliptic streamline flow. *Proceedings of the 1996 Summer Program*, Center for Turbulence Research, NASA Ames/Stanford Univ., 433-446.

DURBIN, P. 1993 A Reynolds-stress model for near-wall turbulence. *J. Fluid Mech.* **249,** 465-498.

MAHONEY, J. F. 1985 Tensor and Isotropic Tensor Identities. *The Matrix and Tensor Quarterly.* **34(5),** 85-91.

KASSINOS, S. C. & REYNOLDS, W. C. 1997 Advances in structure-based modeling. *Annual Research Briefs 1997*, Center for Turbulence Research, NASA Ames/Stanford Univ., 179-193.

KASSINOS, S. C. & REYNOLDS, W. C. 1996 An Interacting Particle Representation Model for the Deformation of Homogeneous Turbulence. *Annual Research Briefs 1996*, Center for Turbulence Research, NASA Ames/Stanford Univ., 31-51.

KASSINOS, S. C. & REYNOLDS, W. C. 1994 *A structure-based model for the rapid distortion of homogeneous turbulence.* Report TF-61, Thermosciences Division, Department of Mechanical Engineering, Stanford University.

LEE, M. J. & REYNOLDS, W. C. 1985 *Numerical experiments on the structure of homogeneous turbulence.* Report TF-24, Thermosciences Division, Department of Mechanical Engineering, Stanford University.

MANSOUR, N. N. 1998 Private communication.

ROGERS, M. M. & MOIN, P. 1987 The structure of the vorticity field in homogeneous turbulent flows. *J. Fluid Mech.* **176,** 33-66.

Modeling a confined swirling coaxial jet

By C. A. Lin

1. Motivation and objectives

Swirling motion is often employed as a mechanism to further promote or control mixing between the fuel spray jet and the adjacent air and, in some occasions, to stabilize the combustion zone due to the presence of the swirl-induced central recirculation region. Since the central recirculation zone induced by the decay of swirl has profound effects on flame stabilization and mixing in combustion systems, a prior knowledge of the flow characteristics is beneficial during the design process.

To investigate the interaction of the air and fuel jet within a combustor, Johnson and Bennett (1981) conducted experiments of a non-reacting confined co-axial jet. Detailed measurements of the velocity and scalar fields were available to determine the turbulent transport processes within the flow. To examine the effects of swirling motion on the mixing characteristic, Roback and Johnson (1983) extended the previous non-swirling experiments to swirling co-axial jets. The results indicated that the peak momentum turbulent transport rates were approximately the same as those for the non-swirling flow condition. One distinct feature of the swirling case was the presence of the central recirculation zone, and the results indicated that the mixing for swirling flow was completed in one-third the length required for non-swirling flow.

In contrast to the traditional Reynolds averaged simulations, Akselvoll and Moin (1996) adopted a large eddy simulation technique to compute Johnson and Bennett's (1981) non-swirling co-axial jet case. Pierce and Moin (1998a,b) further extended the large eddy simulation to the swirling flow and validated their results with the experiments of Roback and Johnson (1983). Both the predicted velocity and scalar fields agreed well with the measurements. The Roback and Johnson case was also investigated by Brankovic *et al.* (1998), but within the Reynolds averaged equation framework. The results indicated that, although the velocity results compared favorably with the measurements, the scalar field was not reproduced correctly. The predicted results by Brankovic *et al.* showed an excessive level of mixing of the scalar field at the region bordering the central recirculation zone. It was indicated that unsteady effects, notably large-scale, low-frequency structures, may be responsible for the discrepancy in the predictions and measurements at this location.

The discrepancy of the predicted results between Pierce and Moin (1998a,b) and Brankovic *et al.* (1998) has motivated the present study to revisit the experimental study of Roback and Johnson computationally. The present computational framework is based on the Reynolds averaged equation approach, and the eddy-viscosity type turbulence models are adopted. Therefore, the objectives of the present study are to identify the causes of the discrepancies and to investigate the influences of grid density and turbulence modeling on the predicted results.

2. The computational model

2.1 The governing equations

The behavior of the flow is in general governed by the fundamental principles of classical mechanics expressing the conservation of mass, momentum, and passive scalar. The time-averaged equations for high-Reynolds-number flow may be described by the equations (in Cartesian tensor):

$$\frac{\partial(\rho U_i)}{\partial x_i} = 0$$

$$\frac{\partial(\rho U_i U_j)}{\partial x_j} = -\frac{\partial P}{\partial x_i} + \frac{\partial}{\partial x_j}[\mu_l(\frac{\partial U_i}{\partial x_j} + \frac{\partial U_j}{\partial x_i}) - \rho\overline{u_i u_j}]$$

$$\frac{\partial \rho U_j \Phi}{\partial x_j} = \frac{\partial}{\partial x_j}[\frac{\mu_l}{\sigma}\frac{\partial \Phi}{\partial x_j} - \rho\overline{u_j\phi}]$$

where $\overline{u_i u_j}$ and $\overline{u_j\phi}$ are the turbulent fluxes arising from the time-averaging process. μ_l and σ are the viscosity and Prandtl number, respectively. The tensorial form of the momentum equation represents the U, V, and rW momentum solved.

Within the framework of eddy-viscosity and adopting the Boussinesq approximation, the Reynolds stress and scalar flux are approximated as:

$$-\rho\overline{u_i u_j} = \mu_t(\frac{\partial U_i}{\partial x_j} + \frac{\partial U_j}{\partial x_i}) - \frac{2}{3}\delta_{ij}\rho k$$

$$-\rho\overline{u_j\phi} = \frac{\mu_t}{\sigma_t}\frac{\partial \Phi}{\partial x_j}$$

where μ_t and σ_t are turbulent viscosity and Prandtl number, respectively. The turbulent Prandtl number is assumed to be 0.9.

2.2 Turbulence models

In the present application, turbulence is described by the high-Reynolds-number $k-\epsilon$ eddy-viscosity model (Jones & Launder, 1972) and $k-\epsilon-v^2-f$ model (Durbin, 1995).

The $k-\epsilon$ model can be summarized as,

$$\mu_t = 0.09\rho\frac{k^2}{\epsilon}$$

$$\frac{\partial \rho U_j k}{\partial x_j} = \frac{\partial}{\partial x_j}(\mu_t\frac{\partial k}{\partial x_j}) - \rho\overline{u_i u_j}\frac{\partial U_i}{\partial x_j} - \rho\epsilon$$

$$\frac{\partial \rho U_j \epsilon}{\partial x_j} = \frac{\partial}{\partial x_j}(\frac{\mu_t}{1.3}\frac{\partial \epsilon}{\partial x_j}) + \frac{\epsilon}{k}(-1.44\rho\overline{u_i u_j}\frac{\partial U_i}{\partial x_j} - 1.92\rho\epsilon)$$

The $k-\epsilon-v^2-f$ model incorporates two additional equations f and $\overline{v^2}$ and is expressed as,

$$\mu_t = 0.19\rho\overline{v^2}T$$

$$\frac{\partial \rho U_j k}{\partial x_j} = \frac{\partial}{\partial x_j}(\mu_t \frac{\partial k}{\partial x_j}) - \rho\overline{u_i u_j}\frac{\partial U_i}{\partial x_j} - \rho\epsilon$$

$$\frac{\partial \rho U_j \epsilon}{\partial x_j} = \frac{\partial}{\partial x_j}(\frac{\mu_t}{1.3}\frac{\partial \epsilon}{\partial x_j}) + \frac{1}{T}(-C_{\epsilon 1}\rho\overline{u_i u_j}\frac{\partial U_i}{\partial x_j} - 1.9\rho\epsilon)$$

$$\frac{\partial \rho U_j \overline{v^2}}{\partial x_j} = \frac{\partial}{\partial x_j}(\mu_t \frac{\partial \overline{v^2}}{\partial x_j}) + \rho k f - \rho\frac{\overline{v^2}}{k}\epsilon$$

$$f = L^2\frac{\partial^2 f}{\partial x_j^2} - 0.3\frac{\overline{u_i u_j}}{k}\frac{\partial U_i}{\partial x_j} - (1-1.4)\frac{1}{T}(\frac{2}{3} - \frac{\overline{v^2}}{k})$$

$$C_{\epsilon 1} = 1.3 + \frac{0.25}{(1+(y/2\ell)^2)^4}$$

where y is the distance to the closest wall and,

$$T = max\left[\frac{k}{\epsilon}, 6(\frac{\nu}{\epsilon})^{1/2}\right], \quad L = 0.3\ell, \quad \ell = max\left[\frac{k^{3/2}}{\epsilon}, 70(\frac{\nu^3}{\epsilon})^{1/4}\right]$$

2.3 Numerical algorithm

This scheme solves discretized versions of all equations on a staggered finite-volume arrangement. The principle of mass-flux continuity is imposed indirectly via the solution of pressure-correction equations according to the SIMPLE algorithm (Patankar, 1980). The flow-property values at the volume faces contained in the convective fluxes which arise from the finite-volume integration process are approximated by the quadratic upstream-weighted interpolation scheme QUICK (Leonard, 1979).

The solution process consists of a sequential algorithm in which each of the sets of equations, in linearized form, is solved separately by application of an alternate-direction tri- or penta-diagonal line-implicit solver. Convergence was judged by monitoring the magnitude of the absolute residual sources of mass and momentum, normalized by the respective inlet fluxes. The solution was taken as having converged when all above residuals fell below 0.01%.

3. Geometry and boundary conditions

The geometry of the model combustor (Roback & Johnson, 1983) consists of an annular duct and a smaller center tube. Passive scalar is supplied through the center tube and the swirling flow is imposed on the annular duct. The two streams meet after a sudden expansion. The inlet Reynolds number based on the overall mass flow rate and the jet diameter is 80,300 and the swirl number is 0.41.

The inlet section of the computational domain is located before the expansion. Because no measured data were available, a fully developed profile was adopted. However, the prescription of inlet swirl profile for the annular duct was needed.

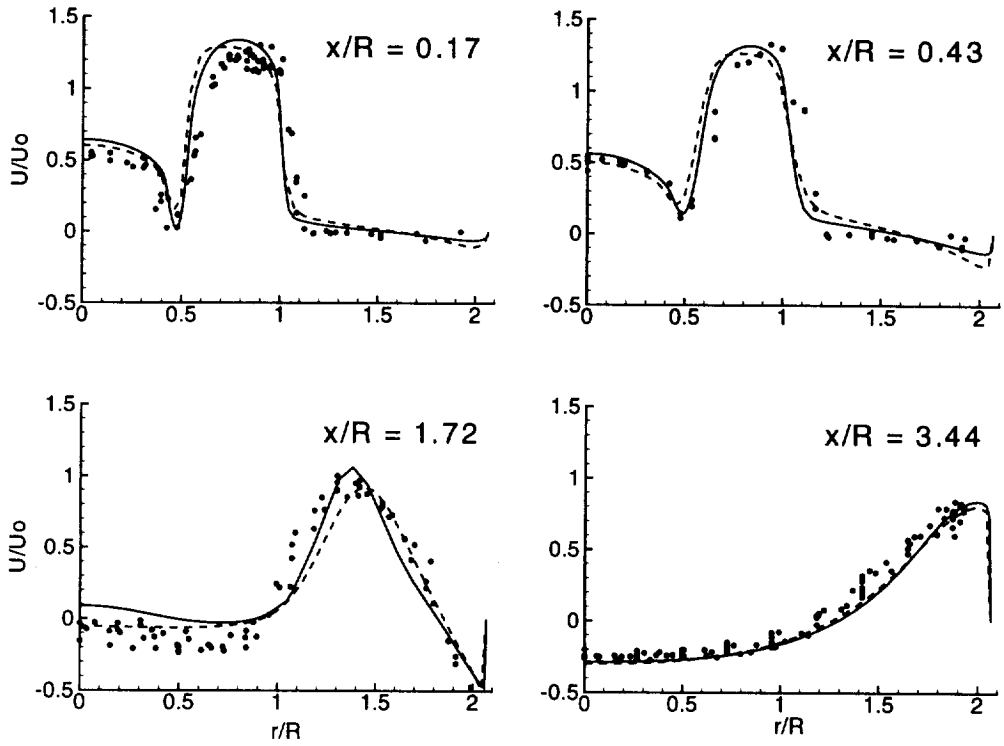

FIGURE 1. Effect of grid density on axial velocity distributions. Symbols: • , exp; ——— , k-ϵ 126x65; ---- , k-ϵ 70x40.

The inlet swirl profile was obtained by applying a constant forcing function in the tangential momentum equation to generate the desired swirl level, a technique developed by Pierce and Moin (1998b).

The treatment at the axis of symmetry simply involved the prescription of zero-gradient conditions for all quantities except radial velocity, which was set to zero. Zero-streamwise-gradient conditions were prescribed along the computational outlet plane.

At the wall, the tangential velocity component U was assumed to vary logarithmically between the semi-viscous sub-layer, at $y_v^+ = 11.2$, and the first computational node lying in the region $30 < y^+ < 100$. The linear variation of the turbulent length scale, $L = \kappa y/C_\mu^{3/4}$, in the log-law region, together with $\epsilon = k^{3/2}/L$, and the invariant value $\epsilon = 2\mu_l k_v/(\rho y_v^2)$ in the viscous sub-layer, allowed the volume-averaged dissipation rate to be determined. This same L-variation was also used to prescribe explicitly the dissipation rate at the near-wall computational node, serving as the boundary condition for inner-field cells.

4. Results and discussions

The case computed was investigated experimentally by Roback and Johnson

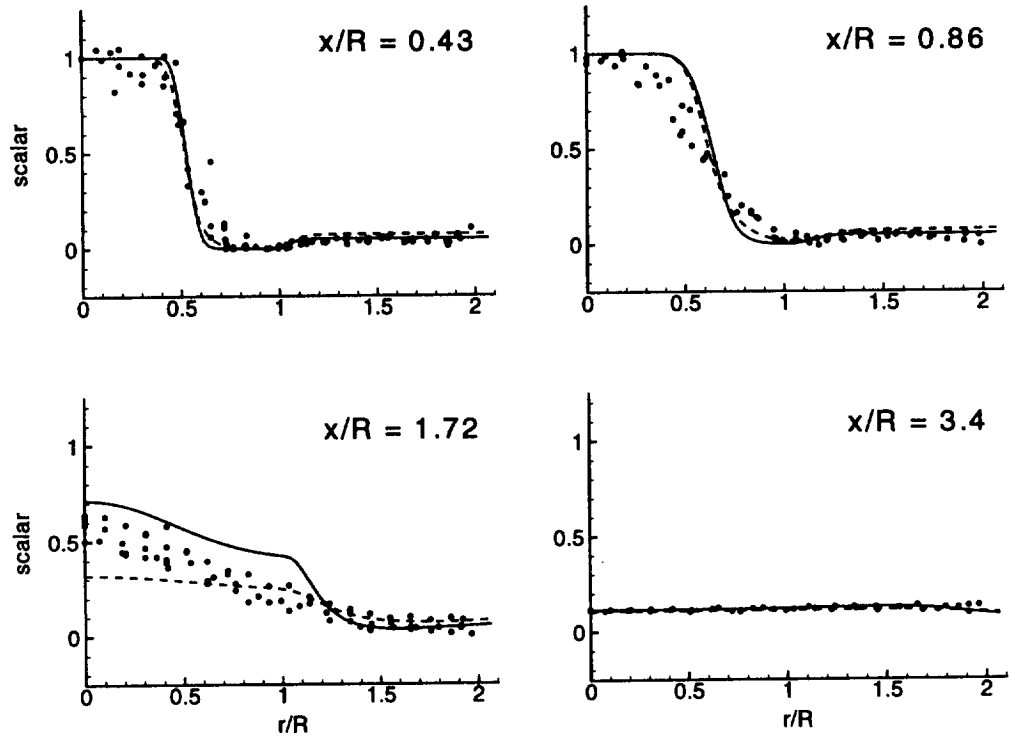

FIGURE 2. Effect of grid density on temperature distributions. Symbols: • , exp; ——— , k-ϵ 126x65; ---- , k-ϵ 70x40.

(1983), where the swirl number and Reynolds number based on the inlet jet velocity are 0.41 and 80,300, respectively. This case was also investigated numerically using large eddy simulation (Pierce & Moin, 1998a); therefore, the predicted results will be contrasted with both measurements and LES results. Under highly swirling conditions it was generally recognized that the eddy-viscosity is not able to capture the strong swirl and turbulence interaction, and the Reynolds stress model is better in this situation (Lin *et al.*, 1996, Chen & Lin, 1998). However, for engineering computations the Reynolds stress transport models are expensive. In the present case, the swirl level is modest; therefore, it would be desirable to investigate the performance of the eddy viscosity models in this complex environment. The inclusion of the $k-\epsilon-\overline{v^2}f$ (v^2f) is motivated by the fact that it performed well in highly separated flow; however, few applications of the model were directed to swirling flows.

4.1 Effects of grid density

Before proceeding to the discussion of the predicted results, it will be beneficial to focus first on the effects of the grid density on the solutions. In the present computations, two meshes of sizes 70x40 and 126x65, which are nonuniform both in the x and y directions, were adopted to compute the flow. Initial tests on the

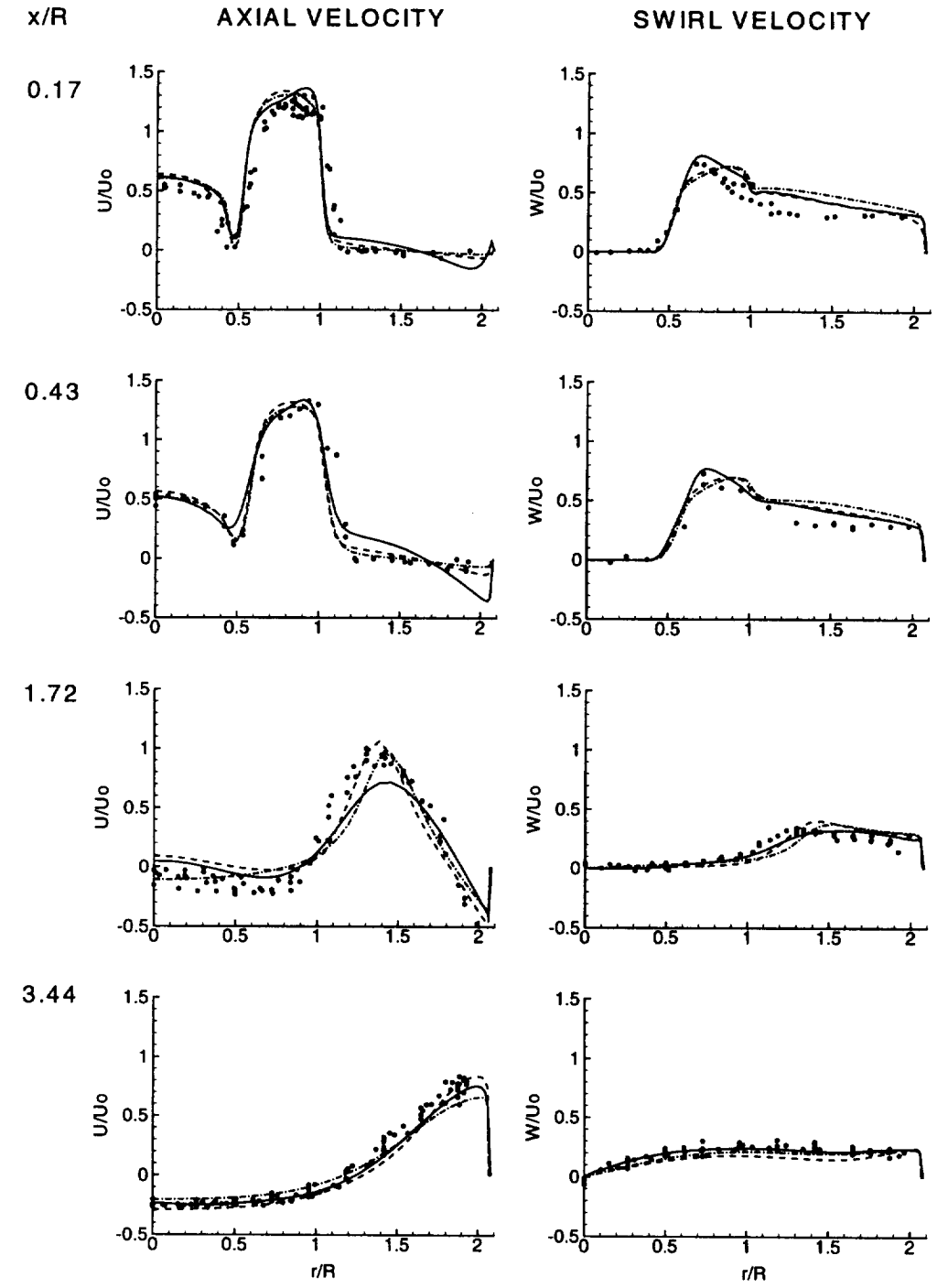

FIGURE 3. Predicted axial and tangential velocity profiles. Symbols: • , exp; ——— , LES; - - - - , k-ϵ; —·— , v^2f.

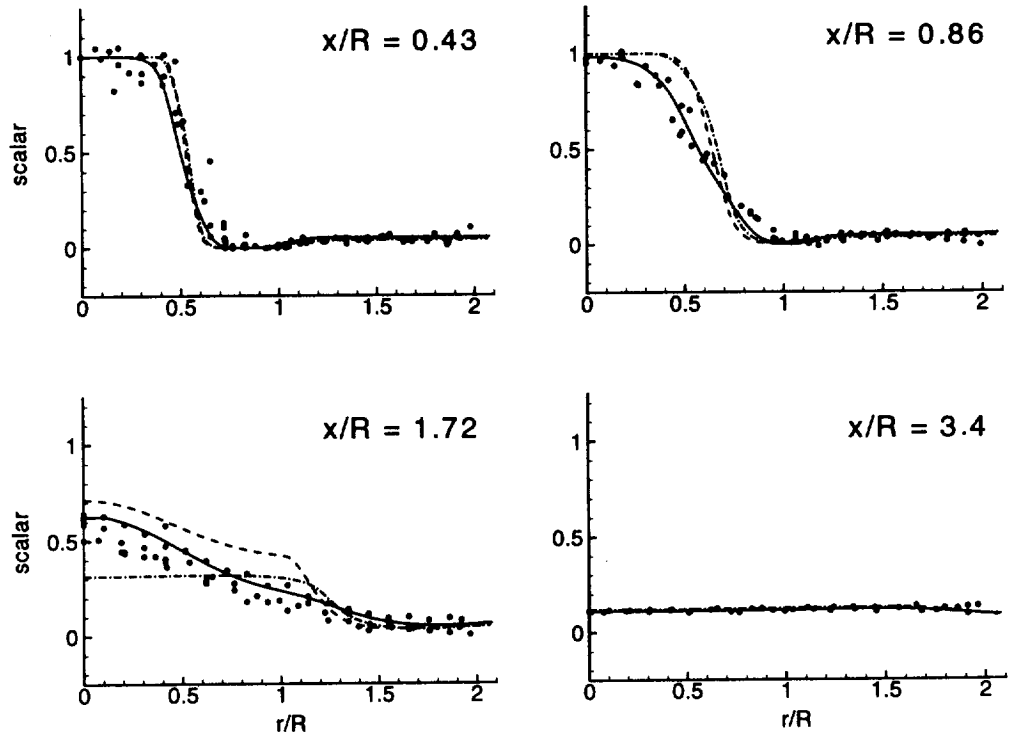

FIGURE 4. Predicted scalar field profiles. Symbols: • , exp; ——— , LES; ---- , k-ϵ; —·— , v^2f.

influences of the convection schemes on the 126x65 grid revealed that the differences between the second order QUICK and the first order hybrid scheme were small.

The dominant features of the flow are the annular recirculation zone after the expansion and the extensive central recirculation zone due to the effect of the swirling co-axial jet. The presence of the center and corner recirculation zones is crucial to the stabilization of the combustion zone within the combustor. It is expected that the mixing within the recirculation is intense, resulting in an expectedly uniform scalar field.

The predicted axial velocity and scalar field at four selected locations are shown in Figs. 1 and 2. The fine grid produces a better resolution of the shear layer, as can be seen from Fig. 1. The coarse grid result, on the other hand, is shown to produce a higher level of diffusive transport, which causes the central jet to decay faster than the fine grid result. This is evidenced by reference to the axial velocity profile at $X/R = 1.72$, a location near the edge of the central recirculation zone. Although the differences of the predicted profiles at $X/R = 1.72$ is small, this small variation has profound influences on the predicted scalar field. This is because the coarse grid result shows the presence of the recirculation zone at this location, $X/R = 1.72$, where a more uniform scalar field is expected due to the elevated level of mixing.

By reference to Fig. 2, the difference of the two results can be seen to be marginal except at location $X/R = 1.72$. At this location, the coarse grid produces a uniform scalar field near the center line region while the fine grid shows a slightly steep variation of the passive scalar. As indicated earlier, this is related to the predicted strength of the central jet. For the fine grid result which shows a positive axial velocity at this location, a higher level of scalar field is transported downstream. For the coarse grid result which shows a negative axial velocity at this location, a lower level and uniform field of passive scalar is expected. It should be pointed out that the forward edge of the central recirculation zone is near the location $X/R = 1.72$. Therefore, the strength of the central jet has profound influences on the transport of the scalar field in this region. The non-physical diffusion tends to accelerate the decay of the central jet, and hence an earlier occurrence of the central recirculation zone. This results in a more uniform scalar field in this region. This argument is partly supported by the scalar field at $X/R = 3.4$. By reference to Fig. 1 at $X/R = 3.4$, it can be observed that the recirculation zone extends accross much of the width of the combustor. Therefore, a uniform scalar field is expected, and this is shown in Fig. 2 at $X/R = 3.4$.

Based on the above observation, the excessive level of mixing of the scalar field at the region bordering the central recirculation zone predicted by Brankovic *et al.* may be due to the insufficient grid density adopted in the solution domain.

4.2 Effects of turbulence modeling

Next, attention is focused on the effects of turbulence modeling on the predicted velocity and scalar fields. Figure 3 shows the predicted axial and tangential velocity profiles at four different axial locations. It can be seen that both the $k-\epsilon$ and v^2f models predict well the development of the mixing layer near r/R=0.5 before the central recirculation bubble, i.e. $X/R < 1.72$. It is interesting to see that the LES results show a slightly higher level of diffusive transport in the near field of the mixing layer.

The location of the central recirculation zone depends on the penetration strength of the central jet, and this can be clearly seen from the predicted axial velocity profiles at $X/R = 1.72$, shown in Fig. 3. The strength of the central jet predicted by the $k-\epsilon$ model is the strongest, and this is followed by the LES simulations. The v^2f prediction, on the other hand, is slightly diffusive, and hence a reverse flow is present along the centerline at this location, $X/R = 1.72$. The measurements indicate that part of the region near the centerline at $X/R = 1.72$ is within the central recirculation zone, and this seems to suggest that the v^2f model is correct. However, by reference to the scalar field at the same location, shown in Fig. 4, the v^2f model prediction is wrong. In contrast, the LES agrees well with measurements. The uniform scalar field predicted by the v^2f model is expected because the velocity field predicted indicates that this region is within the central recirculation zone where the mixing is good. This result is similar to the previous coarse grid $k-\epsilon$ predictions, and the predicted velocity field at this location is also similar as shown in Figs. 1 and 3 at $X/R = 1.72$. Therefore, the difference of the predicted scalar field at $X/R = 1.72$ is due to the predicted level of central jet penetration along the centerline.

Overall, the scalar field predicted by LES is better than the $k-\epsilon$ predictions even though the velocity field predicted by the latter model compares favorably with measurements. In strong contrast, the $k-\epsilon$ predictions show a reduced level of scalar mixing compared to the measured data. The cause of this is not clear, but it might be related to the defect of the constant Prandtl number approach adopted in the models. For example, by observing the predicted results at $X/R = 0.43$ and 0.86 in Fig. 4, it can be clearly seen that the adopted value of turbulent Prandtl number, 0.9, is too high. Other unsteady large scale motions, which are not accounted for by the present steady simulations, might have contributed to the enhanced mixing of the scalar field. The reduced level of mixing predicted by the $k-\epsilon$ model also causes the steep variation of the scalar profile around $r/R = 1.2$ at $X/R = 1.72$, as shown in Fig. 4.

REFERENCES

AKSELVOLL, K. & MOIN, P. 1996 Large Eddy Simulation of Turbulent Confined Co-annular Jet. *J. Fluid Mech.* **315,** 387-411.

BRANKOVIC, A., RYDER, JR., R. C. & SYED, S. A. 1998 Mixing and Combustion Modeling for Gas Turbine Combustor using Unstructured CFD Technology. *AIAA-98-3854.*

CHEN, J. C. & LIN, C. A. 1998 Modeling Strongly Swirling Flows with Second Moment Closure. *Int. J. Num. Methods in Fluids.* In press.

DURBIN, P. A. 1995 Separated Flow Computations with the $k-\epsilon-v^2$ Model. *AIAA J.* **33,** 659-664.

JOHNSON, B. V. & BENNETT J. C. 1981 Mass and Momentum Turbulent Transport Experiments with Confined Coaxial Jets. *NASA CR-165574.*

JONES, W. P. & LAUNDER, B. E. 1972 The Prediction of Laminarization with a Two-Equation Model of Turbulence. *Int. J. Heat Mass Transfer.* **15,** 301-314.

LEONARD, B. P. 1979 A Stable and Accurate Convective Modeling procedure Based on Quadratic Upstream Interpolation. *Comp. Meth. Appl. Mech. Eng.* **19,** 59-98.

LIN, C. H., LIN, C. A. & CHEN, J. C. 1996 Modeling Influences of Inlet Swirl Profiles on Dump Combustor Flows. *AIAA J.* **34,** 2630-2632.

PATANKAR, S. V. 1980 *Numerical Heat Transfer and Fluid Flow.* Hemisphere Publishing Corporation.

PIERCE, C. D. & MOIN, P. 1998a Large Eddy Simulation of a Confined Coaxial Jet with Swirl and Heat Release. *AIAA 98-2892.* 29th AIAA Fluid Dynamics Conference, June 15-18, Albuquerque, NM.

PIERCE, C. D. & MOIN, P. 1998b Method for Generating Equilibrium Swirling Inflow Conditions. *AIAA J.* **36,** 1325-1327.

ROBACK, R. & JOHNSON, B. V. 1983 Mass and Momentum Turbulent Transport Experiments with Confined Swirling Coaxial Jets. *NASA CR-168252.*

Subgrid-scale models based on incremental unknowns for large eddy simulations

By T. Dubois AND F. Bouchon[1]

1. Introduction

Turbulence modeling in the context of large eddy simulation (LES) is based on a decomposition of all flow variables into large (energy-containing) eddies and small scales carrying a small percentage of the total kinetic energy. The scale separation is achieved by applying a filter operation in physical space, based on a filter function, to flow fields. The net effect of the filter is to remove or at least to reduce the energy contained in scales of length smaller than the filter width Δ_f. The equation of motion of the large scales $\bar{u}_i$ are derived by applying the filter operation to the Navier-Stokes equations. The effect of the subgrid scales (SGS) on the dynamics of the large ones appears through a nonlinear interaction term, the SGS stress tensor $\tau_{ij} = \overline{u_i u_j} - \bar{u}_i \bar{u}_j$. This stress corresponds to two mechanical effects, i.e. an energy transfer from large to smaller scales, inducing a dissipative effect on the large scales, and an energy flux from the SGS to the resolved scales, called backscatter.

Among the most commonly used SGS models in LES are the eddy-viscosity models and their dynamic versions. The Smagorinsky model (Smagorinsky, 1963) is based on the assumption that the the SGS stress tensor is proportional to the strain-rate tensor S_{ij}. The traceless part of τ_{ij} is represented as

$$\tau_{ij} - \frac{1}{3}\tau_{kk}\delta_{ij} \equiv -2\nu_T \bar{S}_{ij},$$

where $\nu_T = (C\Delta_f)^2(2\bar{S}_{ij}\bar{S}_{ij})^{1/2}$, C is a non-dimensional constant. Lilly (1967) provided an estimate of C ($\simeq 0.18$) for homogeneous turbulent flows. However, an adjustment is necessary for wall-bounded flows, *viz.*, $C \simeq 0.1$ is more suited in this case. Major advances in eddy-viscosity models were accomplished by the introduction of dynamic modeling ideas (Germano *et al.* 1991, Lilly 1992, and Ghosal *et al.* 1995). Dynamic models provide an expression of the constant C in terms of resolved scales and is then computed as function of time (and space). They have been applied successfully to different kinds of flows, improving results obtained with other models in most cases.

Eddy viscosity models are able to properly predict the amount of SGS dissipation. As they are purely dissipative models, they are unable to account for backscatter effects which are of importance in some flows as transitional or non-equilibrium ones. Moreover, *a priori* analyses of DNS or experimental data (Clark *et al.* 1979,

1 Laboratoire de Mathématiques Appliquées, Université Blaise Pascal, 63177 Aubière, France, and CNRS (UMR 6620).

Kerr *et al.* 1996, and O'Neil and Meneveau 1997) have shown that the exact stress tensor correlates very poorly with the strain-rate tensor. Therefore, eddy viscosity models very poorly represent the local effects of the SGS scales on the resolved ones.

Scale similarity models (Bardina, Ferziger & Reynolds, 1983) provide a better physical representation of the SGS stresses. They assume that most of the SGS stress can be estimated from the smallest resolved scales. The stress tensor is expressed as $\tau_{ij} \equiv \overline{\bar{u}_i \bar{u}_i} - \bar{\bar{u}}_i \bar{\bar{u}}_j$. Similarity models underpredict the net SGS dissipation (Bardina, Ferziger & Reynolds 1983, Liu, Meneveau & Katz 1994, and Scotti & Meneveau 1998) and cannot be used to predict first order statistics of turbulent flows in actual LES. Mixed models (Bardina, Ferziger & Reynolds 1983, Zang, Street & Koseff 1993, and Sarghini & Piomelli 1998) combine the dissipative property of eddy viscosity models and the good representation of the SGS stress by a scale similarity expression.

In both eddy viscosity and similarity approaches, the SGS stress is parameterized in terms of the resolved scales. Recently, Domaradzki and collaborators (Domaradzki & Saiki 1997, and Domaradzki & Loh 1998) proposed a subgrid-scale estimation procedure. The aim of this model is to estimate from the resolved scales a range of smaller (SGS) scales of length $\Delta_f/2$. Schematically, the procedure consists of recovering the large scales by applying a deconvolution operation to the resolved (filtered) scales. Then, smaller scales are generated by nonlinear interactions among large scales. The estimated field, containing scales of length up to $\Delta_f/2$, is then used to evaluate the SGS stress tensor. Hence, the estimation model provides an approximation of the full velocity field as $u_i \simeq \bar{u}_i + \tilde{u}_i$, so that the spectral support of $\bar{u}_i + \tilde{u}_i$ is about two times larger than the support of the resolved scales. The increment $\tilde{u}_i$ is expressed in terms of the resolved scales,

$$\tilde{u}_i = \phi(\bar{u}_i).$$

Note that a similar point of view has been developed by Foias, Manley & Temam (1988) in the context of dynamical system approach of the Navier-Stokes equations.

The estimation models have been motivated by *a priori* analyses of energy transfer among different band of scales of DNS or experimental data (Kerr, Domaradzki & Barbier 1996, and Liu, Meneveau & Katz 1994). They have shown that energy transfers among resolved and SGS scales are dominated by local interactions, i.e. with modes within one octave of the cut-off wave number.

In the estimation procedure, the incremental components $\tilde{u}_i$ are generated by one nonlinear interaction. However, as pointed out in Domaradzki & Loh (1998), in turbulence the generation of small scales is much more complicated, involving nonlinear, viscous, and incompressibility effects among at least one eddy-turnover time. In this report, based on previous works (Dubois, Jauberteau & Temam (1998) and the references therein), we attempt to derive a more detailed procedure. The incremental unknowns (IU) $\tilde{u}_i$ are obtained by solving an approximated version of the SGS governing equations. Computing $\tilde{u}_i$ at each time iteration of the LES in such a way will require too much computational effort and will give results qualitatively similar to a coarse DNS on the grid $\Delta_f/2$. The increment components are evaluated

every q ($q > 1$) iterations of the LES and are, therefore, frozen over time intervals of length $q\Delta t$. Then, the SGS stress dependent upon $\tilde{u}_i$ should be corrected during this period of time in order to preserve its dissipative properties. Two different corrections procedure are proposed leading to purely dissipative models. The IU models are implemented and evaluated for LES of incompressible forced and decaying homogeneous turbulent flows. The results are compared with filtered DNS data and with results obtained with dynamic eddy viscosity models.

2. Mathematical formulation

2.1 The large eddy simulation equations

In large eddy simulation (LES) of turbulent flows, the large and small scales are separated by applying a filter operation to the Navier-Stokes equations. For any flow variable ψ, we define its resolved part as

$$\bar{\psi}(\boldsymbol{x}) = \int_{\Omega} \psi(\boldsymbol{x}')G(\boldsymbol{x},\boldsymbol{x}')\, d\boldsymbol{x}', \tag{1}$$

where Ω is the entire domain filled by the fluid and G is the filter (kernel) function. The net effect of the filtering operation (1) is to damp (or remove) the fluctuations with a characteristic length shorter than the filter width Δ_f.

By applying the filtering operation (Eq. 1) to the Navier-Stokes equations, we obtain the LES equations for incompressible flows

$$\begin{aligned} &\frac{\partial \bar{u}_i}{\partial t} - \nu \frac{\partial^2 \bar{u}_i}{\partial x_j \partial x_j} + \frac{\partial}{\partial x_j}(\bar{u}_i\bar{u}_j + \bar{p}\delta_{ij}) = -\frac{\partial \tau_{ij}}{\partial x_j}, \\ &\frac{\partial \bar{u}_i}{\partial x_i} = 0, \end{aligned} \tag{2}$$

where ν is the kinematic viscosity and p is the pressure. The subgrid-scale (SGS) stress

$$\tau_{ij} = \overline{u_i u_j} - \bar{u}_i\bar{u}_j, \tag{3}$$

represents the effect of the small scales on the resolved ones. This term must be modeled in terms of the resolved quantities in order to close the equations of motion (2).

The filtering operation (Eq. 1) induces a decomposition of the velocity field into large and small-scale components

$$\boldsymbol{u}(\boldsymbol{x}) = \bar{\boldsymbol{u}}(\boldsymbol{x}) + \boldsymbol{u}'(\boldsymbol{x}), \tag{4}$$

where $\boldsymbol{u}'(\boldsymbol{x})$ is the SGS velocity. By considering a filtering operation at scales $\Delta_f/2$, denoted by an overhat, the SGS velocity $\boldsymbol{u}'$ can be decomposed into

$$\boldsymbol{u}'(\boldsymbol{x}) = \tilde{\boldsymbol{u}}(\boldsymbol{x}) + \boldsymbol{u}''(\boldsymbol{x}),$$

where $\tilde{\boldsymbol{u}}(\boldsymbol{x}) = \hat{\boldsymbol{u}}(\boldsymbol{x}) - \bar{\boldsymbol{u}}(\boldsymbol{x})$. Obviously, the filtered velocity field $\hat{\boldsymbol{u}}(\boldsymbol{x})$ satisfies an equation similar to Eq. (2). Therefore, the equation of motion for the velocity component $\tilde{\boldsymbol{u}}(\boldsymbol{x})$ can be easily shown to be

$$\begin{aligned} &\frac{\partial \tilde{u}_i}{\partial t} - \nu \frac{\partial^2 \tilde{u}_i}{\partial x_j \partial x_j} + \frac{\partial}{\partial x_j}\left(\widetilde{\hat{u}_i \hat{u}_j} + \tilde{p}\delta_{ij}\right) = -\frac{\partial \tilde{T}_{ij}}{\partial x_j}, \\ &\frac{\partial \tilde{u}_i}{\partial x_i} = 0, \end{aligned} \tag{5}$$

where $T_{ij} = u_i u_j - \hat{u}_i \hat{u}_j$.

In Domaradzki *et al.* (1993), analysis of DNS data at low Reynolds number has shown that most of the energy transfers from large to small scales are dominated by local interactions, i.e. interactions of the resolved scales with wave numbers $k \in [k_f, 2k_f]$, with k_f being the cut-off wave number. A similar behavior has been noted by Liu, Meneveau & Katz (1994) by analyzing interactions among several separated bands of the fluctuating velocity. Based on these observations, Domaradzki and Saiki (1994) proposed to approximate the SGS stress tensor as follows:

$$\tau_{ij} \simeq \overline{\hat{u}_i \hat{u}_j} - \bar{\hat{u}}_i \bar{\hat{u}}_j. \tag{6}$$

With such an expression for the SGS tensor, the closure problem for Eq. (2) now consists in deriving an approximation of the incremental unknowns $\tilde{u}_i$. In Domaradzki and Saiki (1994), an SGS estimation procedure is proposed. Schematically, the filtered velocity $\hat{u}_i$ is determined solely in terms of the resolved velocity at larger scales $\bar{u}_i$. This is achieved in two steps. The first (kinematic) step consists in a deconvolution of $\bar{u}_i$. The second (dynamic) step generates scales of size two times smaller by nonlinear effects. Only this second step uses information from the Navier-Stokes equations. The unfiltered velocity obtained with this approach satisfies neither the incompressibility constraint nor the equation of motions (2 and 5). The procedure described in this report proposes a different approach. Our aim is to estimate the velocity increments $\tilde{u}_i$ as solutions of an approximation of the equation of motion (Eq. 5).

2.2 A multilevel scheme as a subgrid-scale estimation procedure

The aim of the proposed model is not to accurately evaluate the increment $\tilde{u}_i$, but to estimate a range of scales smaller than the resolved ones in order to obtain an approximation of the SGS stress tensor. Hence, as a first approximation, in Eq. (5) we neglect the nonlinear interactions with smaller scales, setting $T_{ij} \equiv 0$. We then rewrite Eq. (5) as follows:

$$\begin{aligned} &\frac{\partial \tilde{u}_i}{\partial t} - \nu \frac{\partial^2 \tilde{u}_i}{\partial x_j \partial x_j} + \frac{\partial}{\partial x_j}\left(\widetilde{\bar{u}_i \bar{u}_j} + \tilde{p}\delta_{ij}\right) = -\frac{\partial \tilde{T}_{ij}}{\partial x_j}, \\ &\frac{\partial \tilde{u}_i}{\partial x_i} = 0, \end{aligned} \tag{7}$$

where $T_{ij} = \bar{u}_i\tilde{u}_j + \tilde{u}_i\bar{u}_j + \tilde{u}_i\tilde{u}_j$ represents the interactions among resolved and incremental scales. As previously mentioned, the computation at each time iteration of $\tilde{u}_i$ solving a time discretized version of Eq. (7) will require too much computational effort. Moreover, such results will be qualitatively similar to a coarse DNS on grid of mesh size $\Delta_f/2$. In Dubois *et al.* (1998a, 1998b), multilevel schemes have been developed and used to estimate the small scales of homogeneous turbulent flows. They have been applied in the context of DNS to scales with wave number $k \geq k_\eta/4$, with k_η the Kolmogorov wave number. The statistical properties, such as high-order moments of the velocity derivatives, are well reproduced by these procedures. They are based on a quasi-static (QS) approximation of the small scales, i.e. they are frozen over a few time iterations while the large scales are time advanced. Similarly, we apply a QS approximation to the velocity increments, i.e. $\tilde{u}_i$ are kept constant during q iterations. Therefore, we obtain a two-level scheme that can be summarized in the following two steps:

Step $nq+k$, $k \in [1,q]$**:** the resolved scale equation (2) is advanced according to the following time semi-discretized equations

$$\begin{aligned} \frac{\bar{u}_i^{nq+k} - \bar{u}_i^{nq+k-1}}{\Delta t} - \nu\frac{\partial^2 \bar{u}_i^{nq+k}}{\partial x_j \partial x_j} + \frac{\partial}{\partial x_i}\bar{p}^{nq+k} \\ = -\frac{\partial}{\partial x_j}(\bar{u}_i\bar{u}_j)^{nq+k-1} - \frac{\partial}{\partial x_j}\tau_{ij}^{nq+k-1}, \\ \frac{\partial}{\partial x_i}\bar{u}_i^{nq+k} = 0, \end{aligned} \tag{8}$$

where we have set

$$\tau_{ij}^{nq+l} = \overline{\bar{u}_i^{nq+l}\tilde{u}_j^m} + \overline{\tilde{u}_i^m\bar{u}_j^{nq+l}} + \overline{\tilde{u}_i^m\tilde{u}_j^m}, \; m = nq, \; l \in [0, q-1].$$

Step $m+1 = (n+1)q$**:** the incremental unknowns $\tilde{u}_i^{m+1}$ are computed according to

$$\begin{aligned} \frac{\tilde{u}_i^{m+1} - \tilde{u}_i^m}{\Delta t} - \nu\frac{\partial^2 \tilde{u}_i^{m+1}}{\partial x_j \partial x_j} + \frac{\partial}{\partial x_i}\tilde{p}^{m+1} = -\frac{\partial}{\partial x_j}\widetilde{\bar{u}_i\bar{u}_j}^{m+1} - \frac{\partial T_{ij}^m}{\partial x_j}, \\ \frac{\partial}{\partial x_i}\tilde{u}_i^{m+1} = 0, \end{aligned} \tag{9}$$

where

$$T_{ij}^m = \bar{u}_i^{m+1}\tilde{u}_j^m + \tilde{u}_i^m\bar{u}_j^{m+1} + \tilde{u}_i^m\tilde{u}_j^m.$$

Note that the SGS stress $\mathcal{T}_{ij}$, representing the interactions between the velocity component $\hat{u}_i$ and u_i'' in Eq. (5), has been neglected in Eq. (9). The stress tensor T_{ij} corresponds to interactions between the resolved scales and the incremental unknowns $\tilde{u}_i$. Due to Eq. (9) the nonlinear term $\widetilde{\bar{u}_i\bar{u}_j}$ as well as the dissipative one act on the IU components over one time step only during the time interval $[m\Delta t, (m+1)\Delta t]$. The nonlinear term is essentially an energy transfer term, and the balance between dissipation and injection of energy present in the Navier-Stokes

equations cannot be reproduced by Eq. (9). In fact, the net effect of this numerical treatment can be either to reduce or amplify artificially the kinetic energy of the IU scales $\tilde{u}_i$. Therefore, a discontinuity will appear near the cut-off wave number k_f on the distribution of kinetic energy in spectral space. In order to avoid such numerical artifact, the IU scales $\tilde{u}_i^m$ are modified so that the kinetic energy of their largest scales in a band of wave numbers close to k_f is equal to the kinetic energy contained in the smallest scales of $\bar{u}_i^m$. In the spectral space, the Fourier coefficients of $\tilde{u}_i^m$ are modified so that:

$$E_{\tilde{\boldsymbol{u}}^m}(k_f+j) \equiv E_{\tilde{\boldsymbol{u}}^m}(k_f+j)\frac{E_{\bar{\boldsymbol{u}}^m}(k_f)}{E_{\tilde{\boldsymbol{u}}^m}(k_f+1)}, \tag{10}$$

for $j = 1, \ldots, k_f$; $E_{\boldsymbol{\phi}}(k)$ denotes the energy spectrum function of the flow field $\boldsymbol{\phi}(\boldsymbol{x})$. A relation similar to Eq. (10) could be imposed in physical space by using filter functions with local support near k_f in the spectral space.

The above procedure of estimation of the IU components, consisting of Eqs. (9) and (10), does not insure *a priori* that the stress tensor τ_{ij} predicts the right amount of dissipation. In fact, the implementation of this scheme in LES of forced homogeneous turbulence has shown that the stress tensor underpredicts the SGS dissipation in the neighborhood of the cut-off wave number k_f. A more detailed analysis of the behavior of τ_{ij} revealed that the computation of the IU scales via Eqs. (9) and (10) at iteration m provides a stress tensor behaving similarly to the exact one (computed from DNS data) and predicting reasonably well the SGS dissipation. However, a decorrelation between the stress tensor τ_{ij}^{n+l-1} and the resolved scales $\bar{u}_i^{n+l}$ appears for $l > 1$. The SGS dissipation near k_f reduces from iteration to iteration, resulting in an increase of the kinetic energy of the smallest scales of $\bar{u}_i$. As a remedy we define hereafter two procedures to insure that the stress tensor has a dissipative effect on the resolved scales equations. In both cases, the spectral representation of the velocity field is used. Let us denote by $\hat{\boldsymbol{\phi}}(\boldsymbol{k})$ the Fourier coefficients of the flow variable $\boldsymbol{\phi}(\boldsymbol{x})$. The SGS force in the spectral form of Eq. (8) reads

$$\widehat{NL}_l(\boldsymbol{k}) \equiv ik_j\hat{\tau}_{lj}(\boldsymbol{k}),$$

so that in the energy equation we have $\widehat{NL}_i(\boldsymbol{k})\cdot\hat{\bar{u}}_i(\boldsymbol{k})$ as a source term. Once the IU components have been computed according to Eq. (9), we define a complex number of modulus equal to unity by

$$e^{i\theta^m(\boldsymbol{k})} = \frac{\widehat{NL}_i^m(\boldsymbol{k})\cdot\hat{\tilde{u}}_i^m(-\boldsymbol{k})}{|\,\widehat{NL}_i^m(\boldsymbol{k})\cdot\hat{\tilde{u}}_i^m(-\boldsymbol{k})\,|}.$$

The phase $\theta^m(\boldsymbol{k}) \in [-\pi, \pi]$ clearly represents the phase difference between $\widehat{NL}_i^m(\boldsymbol{k})$ and $\hat{\tilde{u}}_i^m(\boldsymbol{k})$. The time decorrelation between the SGS force and the resolved scales can be avoided by keeping constant the phase $\theta^m(\boldsymbol{k})$ on the time interval $[m\Delta t, (m+1)\Delta t]$. However, such a procedure does not bring enough dissipation into the resolved scale equation.

The first procedure consists in modifying $\theta^m(\boldsymbol{k})$ as follows:

$$\tilde{\theta}^m(\boldsymbol{k}) \equiv \frac{\pi}{2} \quad \text{if} \quad \widehat{NL}_i^m(\boldsymbol{k}) \cdot \hat{\bar{u}}_i^m(-\boldsymbol{k}) < 0. \tag{11}$$

The net effect of Eq. (11) is to "turn off" the stress for wave numbers contributing to backscatter of energy. The phases of the SGS force in Eq. (8) are kept constant and set equal to the phase $\tilde{\theta}^m(\boldsymbol{k})$. Then, the SGS force is modified according to:

$$\widehat{NL}_i^{n+l}(\boldsymbol{k}) \equiv \mid \widehat{NL}_i^{n+l}(\boldsymbol{k}) \mid \frac{\hat{\bar{u}}_i^{n+l}(\boldsymbol{k})}{\mid \hat{\bar{u}}_i^{n+l}(\boldsymbol{k}) \mid} e^{i\tilde{\theta}^m(\boldsymbol{k})}, \tag{12}$$

for $l = 1, \ldots, q$. The model consisting of Eqs. (8-11) is, therefore, a dissipative SGS model and is denoted by IU_1 in the following section. Note that Liu, Meneveau & Katz (1994) proposed to modify in a similar way the stress tensor derived from scale similarity models.

Another version, denoted hereafter by IU_2, consists in modifying the phases of the SGS force in Eq. (8) at the temporal iteration $n + l$, according to:

$$\widehat{NL}_i^{n+l}(\boldsymbol{k}) \equiv \mid \widehat{NL}_i^{n+l}(\boldsymbol{k}) \mid \frac{\hat{\bar{u}}_i^{n+l}(\boldsymbol{k})}{\mid \hat{\bar{u}}_i^{n+l}(\boldsymbol{k}) \mid} e^{i\alpha\theta^m(\boldsymbol{k})}, \tag{13}$$

where α is a constant in the range $[0, 1]$. Hence, a dissipative LES model is obtained for values of $\alpha \leq 1/2$. For $\alpha = 0$, the dissipation induced by Eq. (13) is maximum. The use of this value in LES runs has shown that the smallest scales of the resolved field are excessively damped by an overprediction of the SGS dissipation. We have retained the value $\alpha = 1/2$ in the LES runs described in the following section.

3. Numerical implementation

3.1 Large eddy simulation of forced isotropic turbulence

The flow is forced in such a way that the energy injection rate $\langle \boldsymbol{f} \cdot \boldsymbol{u} \rangle$ is constant in time and equal to a given parameter ε. The Reynolds number is taken to be infinite so that $\nu = 0$. In the absence of a model for the SGS stress term, the energy spectrum function tends to reach an k^2 equipartition equilibrium and the total kinetic energy will grow constantly. In an idealistic situation, the model should provide the correct amount of net SGS dissipation at each scale so that the flow reaches a statistically steady state, with an energy spectrum of the form: $E(k) = C_K\ \varepsilon^{2/3}\ k^{-5/3}$, C_K being the Kolmogorov constant. The initial condition has an energy spectrum function of this form with C_K set to 1.6; the phases of the Fourier coefficients are randomly generated. The spectral coefficients $\hat{\boldsymbol{f}}(\boldsymbol{k})$ are nonzero only for wave numbers $|\boldsymbol{k}| \leq k_0$. Hence, by defining $N = \mathrm{Card}\{\boldsymbol{k} \in \mathcal{Z}^3; \mid \boldsymbol{k} \mid \leq k_0\}$ and $\theta(\boldsymbol{k})$ to be the phase of $\hat{\boldsymbol{u}}(\boldsymbol{k})$, $\hat{\boldsymbol{f}}(\boldsymbol{k})$ is given by

$$\hat{\boldsymbol{f}}(\boldsymbol{k}) = \frac{\varepsilon}{N} \frac{e^{i\theta(\boldsymbol{k})}}{\mid \hat{\boldsymbol{u}}(\boldsymbol{k}) \mid}.$$

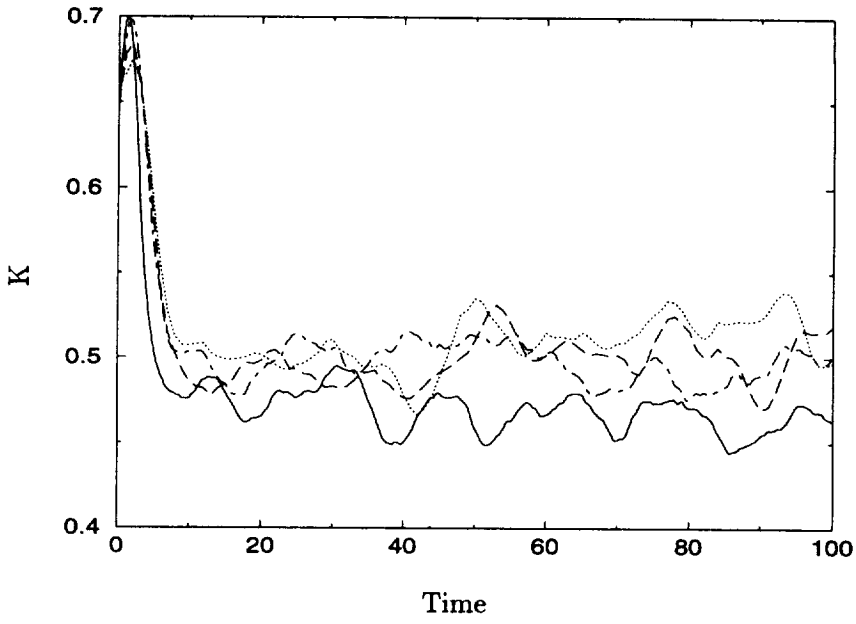

FIGURE 1. Time evolution of the kinetic energy $K = \frac{1}{2}\langle \bar{u}_i \bar{u}_i \rangle$. ——— : IU_1; -·-·-·- : IU_2; - - - - - : DM_1; ····· : DM_2.

In the simulations described hereafter, we have chosen $\epsilon = 0.1$ and $k_0 = 2$. The same problem has been studied in Ghosal *et al.* (1995).

In order to compare results obtained with the IU models described in the previous section, runs with the same parameters and initial conditions have been performed with the dynamic model. Two versions are considered: DM_1 corresponding to the original form derived in Germano *et al.* (1991) and DM_2 the modified version of Lilly (1992). The LES runs are performed here on a 32^3 grid; the computation of the nonlinear terms are dealiased with the 3/2−rule. The parameter q defining the frequency for the estimation of the IU scales was chosen equal to 5 for the simulations presented in this report. It was found that the results were weakly dependent of the value of q for $q \in [5, 20]$; larger values of q have not been tested.

The net SGS dissipation, well predicted by eddy-viscosity models, is known to be a quantity difficult to estimate accurately for other models, as scale similarity ones, in actual LES. For the considered problem, the prediction of

$$\epsilon_{SGS} = \langle \tau_{ij} \bar{S}_{ij} \rangle ,$$

where $\langle - \rangle$ denotes volume average, determines the stability of the system. Indeed, if ϵ_{SGS} is underpredicted, the system will have a tendency to accumulate kinetic energy injected by the external force as no other dissipation than the SGS one is present in the equations of motion of the resolved scales. The resolved scales kinetic energy $K = 1/2 \langle \bar{u}_i \bar{u}_i \rangle$, represented as functions of time in Fig. 1, oscillates near a value in the range $[0.45, 0.5]$ for the IU and DM solutions. Therefore, the IU

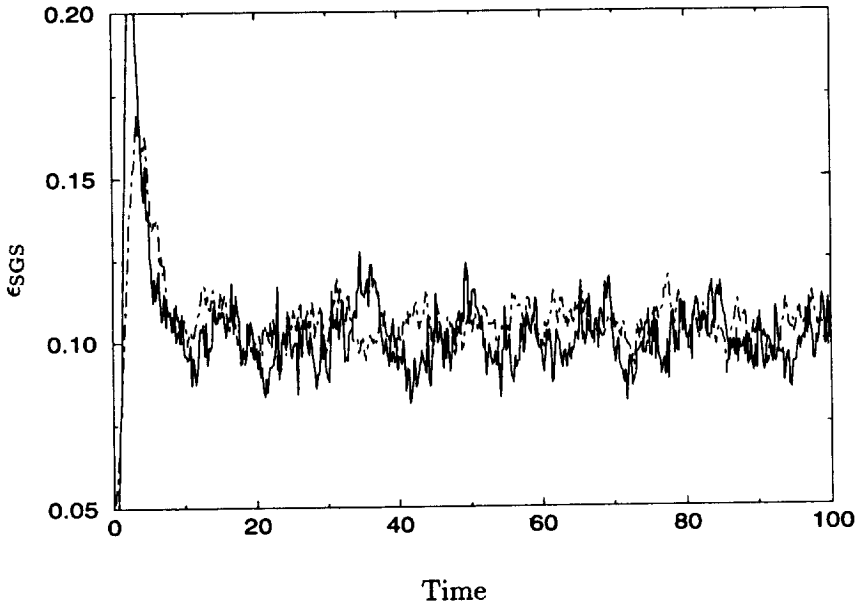

FIGURE 2. Time evolution of the SGS dissipation rate $\epsilon_{SGS} = \langle \tau_{ij} \bar{S}_{ij} \rangle$. ——— : IU_1; - - - - - : IU_2.

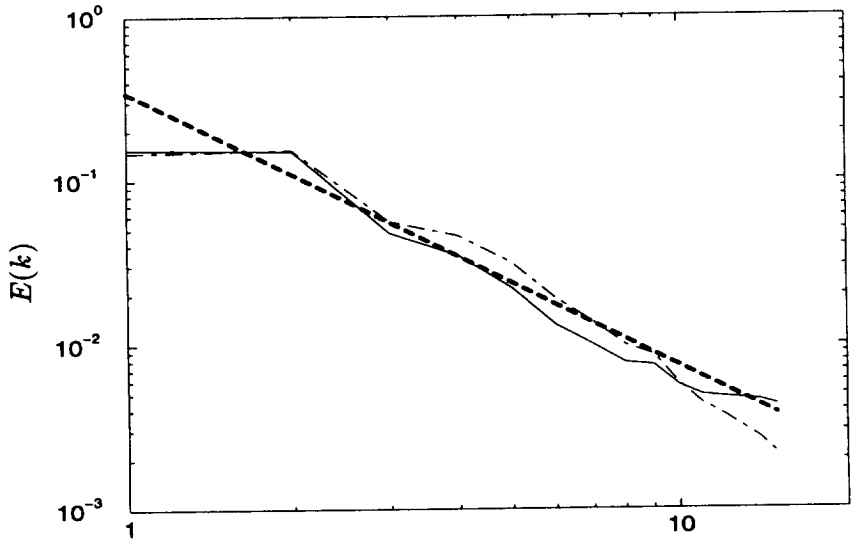

FIGURE 3. Time averaged energy spectrum functions $E(k)$. - - - - - - : $C_K \epsilon^{2/3} k^{-5/3}$; ——— : IU_1; - · - · - · - : IU_2.

models are stable and predict the right amount of global SGS dissipation. This is confirmed by Fig. 2 showing that ϵ_{SGS} obtained by the IU runs oscillate near the energy injection rate, i.e. $\varepsilon = 0.1$; IU_1 and IU_2 models, after the transient period, predict the same amount of global dissipation.

A requirement for LES models is the prediction of the SGS dissipation. Moreover, the spectral distribution of this quantity is of importance for an accurate representation of the distribution of kinetic energy in the spectral space, i.e. the energy spectrum function. For the considered problem, the models should ideally predict a $-5/3$ inertial range. Fig. 3 shows that IU_1 model recovers a spectrum close to the Kolmogorov's 5/3 law; the IU_2 seems to give a steeper decaying spectrum $E(k) \simeq k^{-2}$, very close to the DM_1 spectrum. Compensated spectra $k^{5/3}\varepsilon^{-2/3}E(k)$, represented in Fig. 5, show a plateau for the IU_1 and DM_2 models with Kolmogorov constant $C_K \simeq 1.4$ for IU_1 and $C_K \simeq 1.9$ for DM_2. Values of this constant obtained by measurement of experiments are in the range [1.3, 2.1] (Chasnov (1991)).

The kinetic energy contained in the IU component $K_{SGS} = 1/2\langle\tilde{u}_i\tilde{u}_i\rangle$ is of the order of 0.125 for both IU models. A similar value has been found by Carati, Ghosal & Moin (1995) with a dynamic model carrying an equation for the SGS kinetic energy. Assuming a Kolmogorov law beyond the cut-off wave number k_f, we deduce that

$$K_{SGS} = \frac{3}{2} C_K \left(\frac{\varepsilon}{k_f}\right)^{2/3}.$$

For C_K in the range [1.4, 1.9], we obtain K_{SGS} in the range [0.07, 0.1]. This tends to show that the QS approximation is an efficient way to estimate the incremental scales.

3.2 Large eddy simulation of decaying turbulence

The flow is an incompressible time-decaying flow and is an analog of the grid-turbulence experiments of Comte-Bellot and Corrsin (1971). The reference test is the 512^3 DNS performed by Wray (1998). The initial condition for the LES runs is the 512^3 DNS velocity field at time $t \simeq 0.97$ filtered on a 32^3 grid. The Reynolds number based on the Taylor microscale is of the order of 100. As indicated by Fig. 6 representing energy spectra of DNS at various resolutions, a coarse DNS is unable to follow the decay of the energy spectrum function and, therefore, the decay of the total kinetic energy. Actual LES runs on a 32^3 grid corresponding to the resolved scales have been conducted with the IU_1, IU_2, DM_1 and DM_2 models.

The difficulty of this test is to accurately recover the decay of the kinetic energy $K = 1/2\langle\bar{u}_i\bar{u}_i\rangle$. This again depends on the capacity of the model to predict the net SGS dissipation. Moreover, the model should adjust this prediction as time evolves, as the SGS dissipation decays drastically in the first period of the run, $t \in [1, 2.5]$ (see Fig. 7). In this first period, DM_1 and IU_2 are very close to each other while the two other runs seem to overestimate K. In the second period of the decay, $t > 2.5$, the IU solutions are almost identical and accurately follow the curve corresponding to the filtered DNS. The DM models overpredict the kinetic energy by approximately 20% for $t > 2.5$.

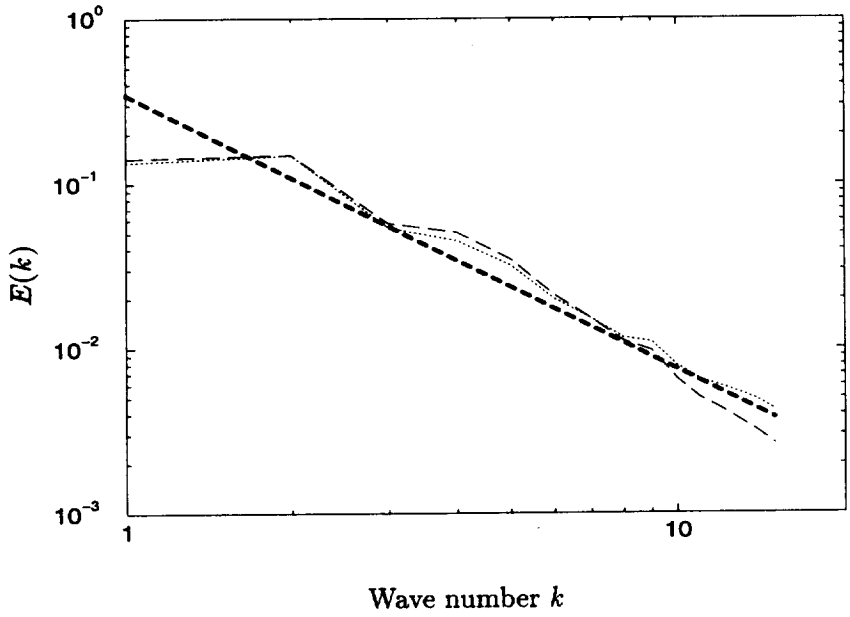

FIGURE 4. Time averaged energy spectrum functions $E(k)$. ------ : $C_K\epsilon^{2/3}k^{-5/3}$; ----- : DM_1; ····· : DM_2.

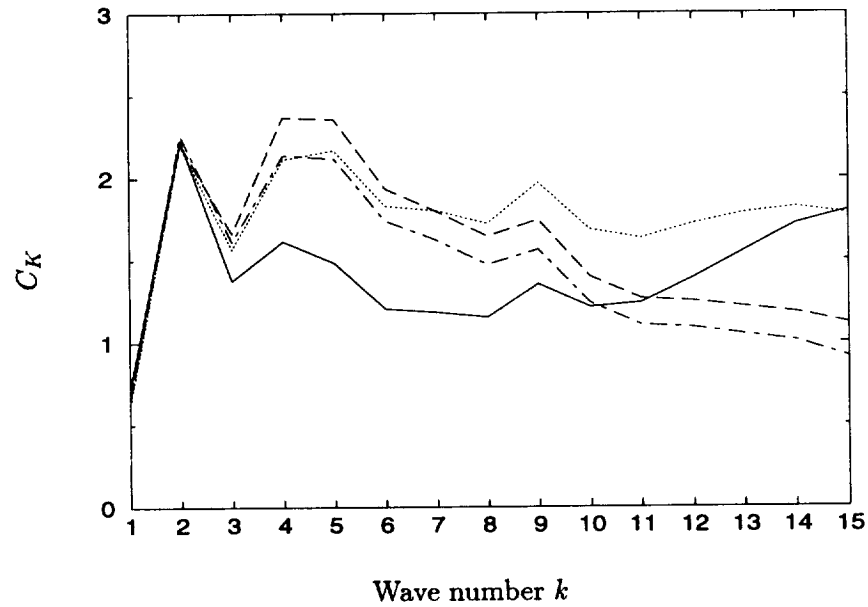

FIGURE 5. Prediction of the Kolmogorov constant $C_K = k^{5/3}\epsilon^{-2/3}E(k)$. ——— : IU_1; -·-·-·- : IU_2; ----- : DM_1; ····· : DM_2.

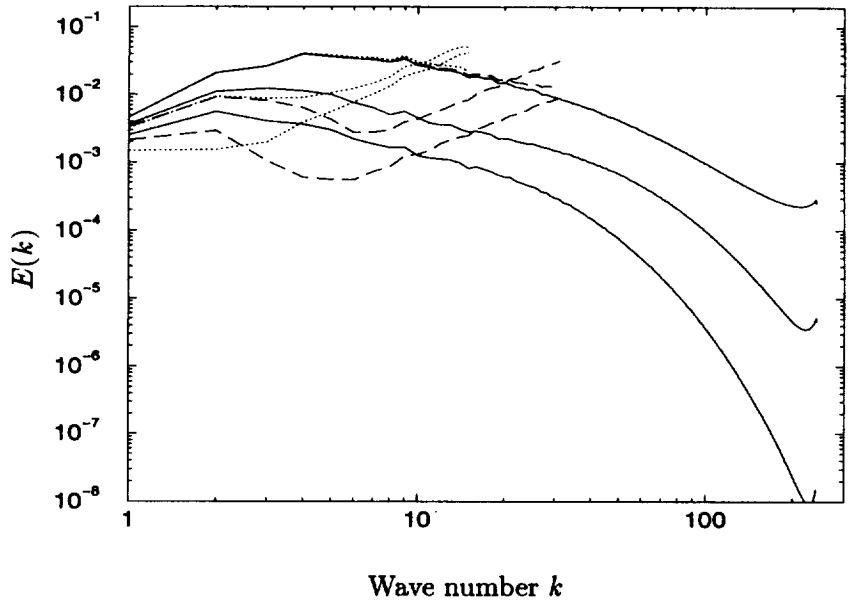

FIGURE 6. Energy spectrum functions at $t = 1.28$, 2.45 and $t = 5.47$. ——— : 256^3 DNS; ····· : 32^3 DNS; ------ 64^3 DNS.

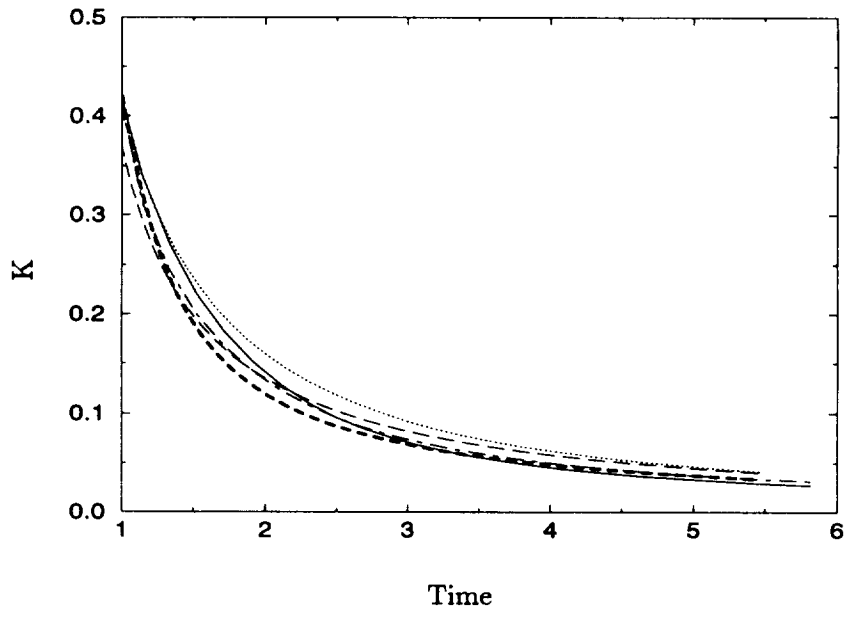

FIGURE 7. Decay of the kinetic energy $K = \frac{1}{2}\langle \bar{u}_i \bar{u}_i \rangle$. ▬▬▬ : filtered DNS; ——— : IU_1; -·-·-·- : IU_2; ----- : DM_1; ····· : DM_2.

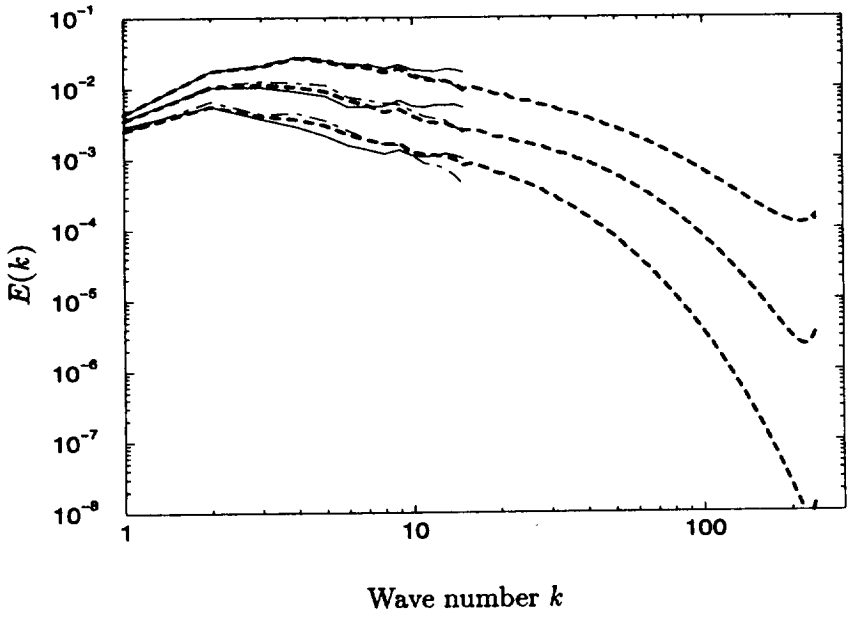

FIGURE 8. Energy spectrum functions at $t = 1.28$, 2.45 and $t = 5.47$. ------ : filtered DNS; —— : IU_1; -·-·-·- : IU_2.

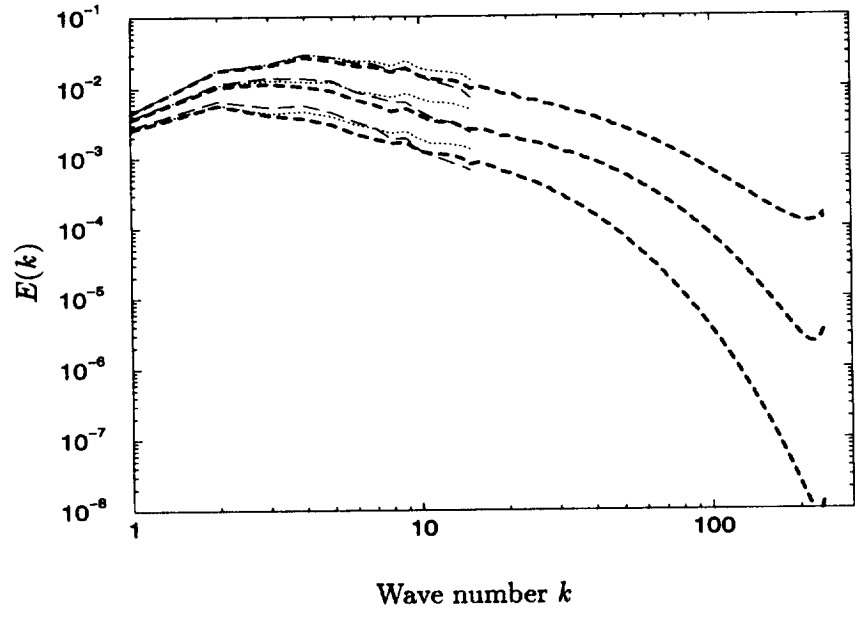

FIGURE 9. Energy spectrum functions at $t = 1.28$, 2.45 and $t = 5.47$. ------ : filtered DNS; - - - - - : DM_1; ····· : DM_2.

The best fit of the DNS energy spectrum is obtained with the IU_2 model on the overall time of decay of the simulation as shown on Fig. 8. The IU_1 model has a tendency to slightly overestimate the last modes near the cut-off wave number at the intermediate time $t = 2.45$. The energy spectrum obtained with the DM models (Fig. 9) have a shape similar to the DNS spectrum but with slightly larger values. This test demonstrates the good dynamic property of the IU models proposed in Section 2.

4. Conclusion

Subgrid-scale modeling based on the concept of incremental unknowns (IU) has been introduced. The incremental velocity components correspond to scales beyond the cut-off wave number defining the resolved scales in LES. Schematically, the IU component have length scales two times smaller than the resolved ones. Therefore, IU modeling is similar to the estimation procedure recently introduced by Domaradzki and coworkers (1997, 1998). However, these approaches differ in the computation of the subgrid scales. The equations of motion are used to advance in time the IU components. The computation of IU components at each time iteration would very poorly resolve the SGS scales as in a coarse DNS. Rather, a quasi-static (QS) approximation is applied to the IU scales, i.e. they are not evaluated at each time iteration of the LES. With the QS approximation we attempt to mimic the dynamic of the subgrid scales. The aim is to develop a more detailed procedure than the estimation one, which generates small scales by only one nonlinear interaction. The QS approximation has been shown to generate small scales, providing SGS stresses with dissipative properties as expected. However, on the time period during which the IU scales are frozen, a decorrelation between IU and resolved scales occurs. This time decorrelation induces an underprediction of the net SGS dissipation. Therefore, the QS approximation cannot be used itself for SGS modeling, but it must be coupled with correction procedures of either the SGS stress tensor or the IU components. We have focused here on the development of phase correction procedures for the SGS tensor. Two procedures have been proposed and implemented in actual LES of forced and decaying homogeneous turbulence. The IU models obtained are fully dissipative ones. The LES runs have shown that both IU models provide the right amount of SGS dissipation. In the case of decaying turbulence, the dynamic property of the flow is well reproduced by the IU solutions, i.e. the decay of the kinetic energy of the resolved scales follows accurately the decay of the filtered DNS. In this test case, IU models perform better than the dynamic model. In the case of forced turbulence at infinite Reynolds number, IU models are able to predict an energy spectrum close to a $k^{-5/3}$ Kolmogorov inertial range. Therefore, we have proved that the IU approach can be used to derive efficient SGS model for LES of turbulent flows. However, the aim of these approaches, based on the evaluation of a range of subgrid scales, is to develop fully nonlinear models accurately representing the SGS stress tensor and its properties, i.e. dissipation and backscatter of energy. At this point, correction procedures have been used to insure such behavior of the SGS stresses. In the future, we should, therefore, concentrate our efforts on the development of models which are able to adjust the IU

components instead of the SGS force. Moreover, IU modeling has been tested here on homogeneous turbulence. It should be applied to wall-bounded flows and even more complicated ones requiring the extension of the approach presented here to implementation in finite difference codes.

REFERENCES

BARDINA, J. & FERZIGER, J. H. & REYNOLDS, W. C. 1983 Improved turbulence models based on large eddy simulation of homogeneous incompressible turbulence. *Report TF-19.* Stanford University.

CARATI, D. & GHOSAL, S. & MOIN, P. 1995 On the representation of backscatter in dynamic localization models. *Phys. Fluids.* **7,** 107.

CHASNOV, J. R. 1991 Simulation of the Kolmogorov inertial subrange using an improved subgrid-scale model. *Phys. Fluids A.* **3,** 188-200.

CLARK, R. A. & FERZIGER, J. H. & REYNOLDS, W. C. 1979 Evaluation of subgrid-scale models using an accurately simulated turbulent flow. *J. Fluid Mech.* **91,** 1.

COMTE-BELLOT, G. & CORRSIN, S. 1971 Simple Eulerian time correlations of full and narrow-band velocity signals in grid-generated isotropic turbulence. *J. Fluid Mech.* **48,** 273-337.

DOMARADZKI, J. A. & LIU, W. & BRACHET, M. E. 1993 An analysis of subgrid-scale interactions in numerically simulated isotropic turbulence. *Phys. Fluids A 5.* **1747.**

DOMARADZKI, J. A. & SAIKI, E. M. 1997 A subgrid-scale model based on the estimation of unresolved scales of turbulence. *Phys. Fluids.* **9**(7), 2148-2164.

DOMARADZKI, J. A. & LOH, K. 1998 The subgrid-scale estimation model in the physical space representation. To appear in *Phys. Fluids.*

DUBOIS, T. & JAUBERTEAU, F. & TEMAM, R. 1998 Incremental unknowns, multilevel methods and the numerical simulation of turbulence. *Comput. Methods Appl. Mech. Engrg.* **159,** 123-189.

DUBOIS, T. & JAUBERTEAU, F. 1998 A dynamic multilevel model for the simulation of the small structures in homogeneous isotropic turbulence. *J. Sci. Comput.* **13**(3), 323-367.

FOIAS, C. & MANLEY, O. P. & TEMAM R. 1988 Modelling of the interaction of small and large eddies in two-dimensional turbulent flows. *Math. Mod. and Num. Anal. (M2AN).* **22**(1), 93-114.

GERMANO, M. & PIOMELLI, U. & MOIN, P. & CABOT, W. H. 1991 A dynamic subgrid-scale eddy viscosity model. *Phys. Fluids A.* **3**(7), 1760-1765.

GHOSAL, S. & LUND, T. S. & MOIN, P. & AKSELVOLL, K. 1995 A dynamic localization model for large-eddy simulation of turbulent flows. *J. Fluid Mech.* **286,** 229-255.

KERR, R. M. & DOMARADZKI, J. A. & BARBIER, G. 1996 Small-scale properties of nonlinear interactions and subgrid-scale energy transfer in isotropic turbulence. *Phys. Fluids.* **8**, 197.

LILLY, D. K. 1967 Proc. IBM Scientific Computing Symposium on Environmental Sciences. Yorktown Heights, N.Y., 195.

LILLY, D. K. 1992 A proposed modification of the Germano subgrid-scale closure method. *Phys. Fluids A.* 4(3), 633-635.

LIU, S. & MENEVEAU, C. & KATZ, J. 1994 On the properties of similarity subgrid-scale models as deduced form measurements in a turbulent jet. *J. Fluid Mech.* **275**, 83.

O'NEIL, J. & MENEVEAU, C. 1997 Subgrid-scale stresses and their modeling in a turbulent wake. *J. Fluid Mech.* **349**, 253.

SARGHINI, F. & PIOMELLI, U. 1998 Scale-similar models for large-eddy simulations. *AIAA 98-0538.*

SCOTTI, A. & MENEVEAU, C. 1998 A fractal model for large-eddy simulation of turbulent flow. To appear in *Physica D.*

SMAGORINSKY, J. 1963 General circulation experiments with the primitive equations. *Mon. Weath. Rev.* **93**, 99.

WRAY, A. A. 1998 in A selection of test cases for the evaluation of large-eddy simulations of turbulent flows. *AGARD Advisory report.* **345**, 63.

ZANG, Y. & STREET, R. L. & KOSEFF, J. R. 1993 A dynamic mixed subgrid-scale model and its applications to turbulent recirculating flows. *Phys. Fluids A.* **5**, 318.

Subgrid scale modeling taking the numerical error into consideration

By Youhei Morinishi[1] AND Oleg V. Vasilyev[2]

1. Motivation and objectives

Large eddy simulation (LES) is regarded as one of the most promising numerical methods to predict unsteady turbulent flows at high Reynolds number. In LES the flow field is decomposed into grid and subgrid scales. The grid scale (GS) flow field is computed numerically using discrete filtered Navier-Stokes equation with a model for the subgrid scale (SGS) stress. Therefore, the reliability of the computed flow field is strongly affected by both the reliability of the SGS model and the accuracy of the numerical method (Ghosal 1996), particularly in the approximation of the convective term. This means that even if we use the exact SGS stress, the computed flow field will be contaminated by the numerical error. This connection between SGS modeling and numerical error was mostly overlooked. As a result all of the existing SGS models have been developed independently from the numerical methods.

One of the objectives of this study is to develop a dynamic subgrid scale model, for which computational results will not depend on the accuracy of the numerical method. The most commonly used SGS model is based on the Smagorinsky eddy viscosity model (Smagorinsky, 1963) with the model coefficient computed dynamically through the *tensor level* identity by Germano *et al.* (1991), hereafter denoted by DSM. However, the tensor level identity does not explicitly include the effect of the numerical error, and thus the computational results strongly depend on the numerical method, especially in simulations with poor resolution. In this report we will present a new dynamic procedure with the *vector level* identity, which takes the numerical error into consideration. We will test the dynamic Smagorinsky SGS model with the vector level identity, hereafter referred as VDSM model.

The second objective of this study is to present a modification to the dynamic two-parameter mixed model. It is well known that the correlation between the Smagorinsky model and the SGS stress is low (for example see Horiuti 1989) while the model based on the scale similarity assumption by Bardina *et al.* (1983) has considerably higher correlation. However, the scale similarity model has a defect: it is not dissipative enough. Therefore, the model is usually used together with the Smagorinsky model. Model coefficients are commonly computed using the dynamic procedure (Zang *et al.* 1993; Vreman *et al.* 1994; Salvetti & Banerjee 1995; Horiuti

1 Nagoya Institute of Technology, Japan

2 Present address: Department of Mechanical and Aerospace Engineering, University of Missouri, Columbia, MO 65211

1997). Nevertheless, the two-parameter mixed model is still not dissipative enough, and the defect of the scale similarity model is not cured by the dynamic procedure. Recently Morinishi (1997) recommended a modification to the two-parameter dynamic procedure which removes that defect. In this study, we will apply the modification to the dynamic two-parameter mixed model (DTM) of Salvetti and Banerjee (1995) since the model seems to be the standard dynamic two-parameter mixed model. The revised model will be named DTMR.

In this study, all computational tests will be done in the turbulent channel flow, and the Reynolds number based on the channel half width and wall friction velocity is 395. To remove the ambiguity regarding the accuracy of the finite difference scheme, we use the higher (up to 12th) order accurate fully conservative finite difference schemes in a staggered grid system proposed by Morinishi *et al.* (1998).

The present report is organized as follows. In section 2.1 numerical method for the channel flow is outlined and the computational results for channel flow without SGS model is presented as a reference. In section 2.2 the dynamic procedure with the vector level identity is proposed and the computational result of VDSM is compared with those of DSM. In section 2.3 a recommended modification to the dynamic two-parameter mixed model is presented and the the computational result of DTMR is compared with those of DTM.

2. Accomplishments

2.1 Numerical method and no SGS model simulation

The basic LES equations for incompressible flows are the filtered Navier-Stokes and continuity equations given by

$$\frac{\partial \bar{u}_i}{\partial t} + \overline{\frac{\partial u_i u_j}{\partial x_j}} = -\frac{\partial \bar{p}}{\partial x_i} + \nu \frac{\partial^2 \bar{u}_i}{\partial x_j \partial x_j}, \tag{1}$$

$$\frac{\partial \bar{u}_i}{\partial x_i} = 0. \tag{2}$$

Here u_i is the velocity component in x_i direction ($i = 1, 2, 3$), p is the pressure divided by the density, ν is the kinematic viscosity, and t is time. The overbar $\overline{\cdot}$ means filtering operator. The commutability between the differentiation and filtering operations is usually assumed, and the filtered convective term is treated as

$$\overline{\frac{\partial u_i u_j}{\partial x_j}} = \frac{\partial \bar{u}_i \bar{u}_j}{\partial x_j} + \frac{\partial \tau_{ij}}{\partial x_j}, \tag{3}$$

where $\tau_{ij} = \overline{u_i u_j} - \bar{u}_i \bar{u}_j$ is the SGS stress which should be modeled.

In this study the numerical tests of several SGS models, described in the subsequent sections, are performed using fully developed plane channel flow. The flow field is assumed to be periodic in the streamwise (x_1) and spanwise (x_3) directions. The Reynolds number ($Re_\tau = u_\tau h/\nu$) based on the channel half width h and the wall friction velocity u_τ is 395. The treatment of the convective term (the

first term in the right-hand side of Eq. (3)) is important for unsteady turbulent numerical simulations at high Reynolds number. Fully conservative higher (2nd, 4th, 8th and 12th) order accurate finite difference schemes proposed by Morinishi *et al.* (1998) are used for the convective term in the periodic directions. The second order accurate scheme in the wall normal direction (x_2) is combined properly and used in order to remove the ambiguity regarding both the conservation properties of the non-uniform meshes and the wall boundary treatment. A semi-implicit time marching method is used. The diffusion term in the wall normal direction is treated implicitly with the Crank-Nicolson method, and a third order Runge-Kutta (RK3) method of Spalart *et al.* (1991) is used for all other terms. The splitting method by Dukowicz and Dvinsky (1992) is used to enforce the solenoidal condition. The resulting discrete Poisson equation for the pressure is solved using a discrete Fourier transform in the periodic directions and a tri-diagonal direct matrix solver in the wall normal direction. The computational box is $2\pi h \times 2h \times 2\pi h/3$ and $32 \times 64 \times 32$ mesh points are used. The grid spacings in the periodic directions are uniform. In this case, the grid spacings in wall units are $\Delta^+_{x_1} = 77.6$ and $\Delta^+_{x_3} = 25.9$. The wall normal grid is stretched using a hyperbolic-tangent function

$$\frac{x_2(j)}{h} = \frac{\tanh[\gamma(2j/N_2 - 1)]}{\tanh[\gamma]}, \qquad j = 0, \ldots, N_2,$$

where $x_2(j)$ is the wall normal grid point for u_2 in the staggered grid system and $x_2(0)$ and $x_2(64) = x_2(N_2)$ correspond to the lower and upper walls respectively. The stretching parameter, γ, is taken to be 2.75. Time increment is $\Delta t = 2.5 \times 10^{-3}$, and it satisfies the stability condition for RK3. The filtering operations in the dynamic SGS models are done in the periodic directions. The test filtering with the filter width $\hat{\Delta}_1 = 2\Delta_{x_1}$ and the grid filtering with the filter width $\bar{\Delta}_1 = \Delta_{x_1}$ in x_1 direction are done respectively as follows:

$$\hat{f}(x_1) = \frac{1}{6}[f(x_1 - \Delta_{x_1}) + 4f(x_1) + f(x_1 + \Delta_{x_1})],$$
$$\bar{f}(x_1) = \frac{1}{24}[f(x_1 - \Delta_{x_1}) + 22f(x_1) + f(x_1 + \Delta_{x_1})].$$

Figures 1 and 2 show the profiles of mean streamwise velocity and velocity fluctuations respectively by the higher order schemes without SGS model at Re_τ=395. In these figures the DNS data by Mansour *et al.* (1996) (see also (Rodi & Mansour 1993)), are also plotted. Note that with the increase of the order of accuracy, the results of finite difference calculations converge. The error of the second order scheme acts as an effective SGS stress, and the mean velocity profile by the second order scheme looks the best on Fig. 1. However, the profile of the velocity fluctuations of the second order scheme is the worst. The differences between the no SGS model simulations and DNS results should be piked up by the SGS model. The amount of required SGS stress depends on the accuracy of the numerical method and the grid resolution.

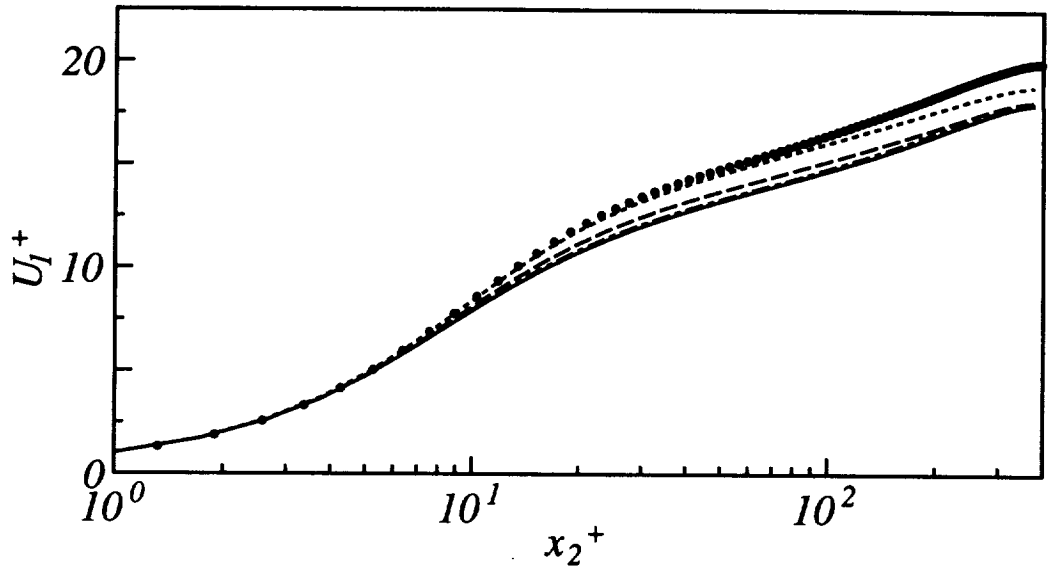

FIGURE 1. Mean streamwise velocity of the channel flow at $Re_\tau = 395$ using no SGS model with the 2nd (·····), 4th (----), 8th (— —) and 12th (———) order schemes. DNS (•) data are also plotted.

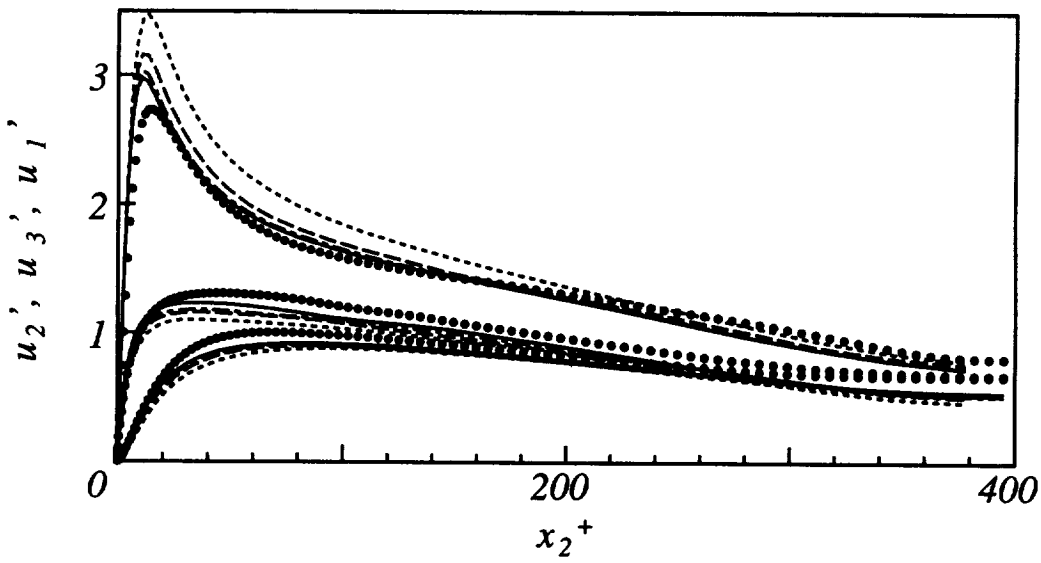

FIGURE 2. Velocity fluctuations of the channel flow at $Re_\tau = 395$ using no SGS model. For symbols see Fig. 1.

2.2 Tensor and vector level identities for the dynamic SGS model

In the dynamic SGS model, the tensor level identity of Germano *et al.* (1991) between the grid and test fields is used to determine the parameter in the SGS model

$$\mathcal{L}_{ij} = T_{ij} - \hat{\tau}_{ij}, \tag{4}$$

where the subtest stress T_{ij} is defined as $T_{ij} = \widehat{\bar{u}_i\bar{u}_j} - \hat{\bar{u}}_i\hat{\bar{u}}_j$, and the resolved stress $\mathcal{L}_{ij}$ is defined as

$$\mathcal{L}_{ij} = \widehat{\bar{u}_i\bar{u}_j} - \hat{\bar{u}}_i\hat{\bar{u}}_j. \tag{5}$$

The Smagorinsky eddy viscosity model is assumed for both the subgrid and subtest stresses in the standard dynamic SGS model.

$$\tau^*_{ij} = -2(C_S\bar{\Delta})^2|\bar{S}|\bar{S}_{ij}, \qquad \bar{S}_{ij} = \frac{1}{2}\Big(\frac{\partial\bar{u}_i}{\partial x_j} + \frac{\partial\bar{u}_j}{\partial x_i}\Big), \qquad |\bar{S}| = \big(2\bar{S}_{ij}\bar{S}_{ij}\big)^{1/2} \tag{6}$$

$$T^*_{ij} = -2(C_S\hat{\bar{\Delta}})^2|\hat{\bar{S}}|\hat{\bar{S}}_{ij}, \qquad \hat{\bar{S}}_{ij} = \frac{1}{2}\Big(\frac{\partial\hat{\bar{u}}_i}{\partial x_j} + \frac{\partial\hat{\bar{u}}_j}{\partial x_i}\Big), \qquad |\hat{\bar{S}}| = \big(2\hat{\bar{S}}_{ij}\hat{\bar{S}}_{ij}\big)^{1/2} \tag{7}$$

The superscript "*" denotes the trace free operator ($\tau^*_{ij} \equiv \tau_{ij} - \frac{1}{3}\delta_{ij}\tau_{kk}$). The model parameter C_S is computed by minimizing the the square of the error $Q = E_{ij}E_{ij}$ (Lilly, 1992), where the error E_{ij} is given by

$$\begin{aligned} E_{ij} &= \mathcal{L}^*_{ij} + 2(C_S\bar{\Delta})^2 M_{ij}, \\ M_{ij} &= \alpha^2|\hat{\bar{S}}|\hat{\bar{S}}_{ij} - \widehat{|\bar{S}|\bar{S}_{ij}}, \end{aligned} \tag{8}$$

and $\alpha^2 = (\hat{\bar{\Delta}}/\bar{\Delta})^2$ is the square value of the test to grid filter widths ratio. In this study we take $\alpha^2 = 4^{2/3} \sim 2.52$. Assuming C_S is a function of x_2, and taking the average in $x_1 - x_3$ plane (denoted by $\langle\cdot\rangle$), we obtain the following equation for $(C_S\bar{\Delta})^2$:

$$(C_S\bar{\Delta})^2 = -\frac{1}{2}\frac{\langle\mathcal{L}_{ij}M_{ij}\rangle}{\langle M_{ij}M_{ij}\rangle}. \tag{9}$$

In this report the dynamic Smagorinsky model given by Eqs. (6) and (9) is called DSM.

Figures 3, 4, and 5 show the profiles of mean streamwise velocity, velocity fluctuations, and the SGS eddy viscosity respectively using the higher order schemes with DSM at Re_τ=395. The SGS eddy viscosity is defined as $\nu_t = (C_S\bar{\Delta})^2|\bar{S}|$. Note that the mean streamwise velocity profiles of the simulations with DSM are shifted up when compared to the results of the simulations without SGS model. The mean velocity and turbulent intensity profiles of DSM do not depend strongly on the order of the accuracy except for the second order scheme. This means that the effect of the numerical error of the second order scheme is considerably larger than those of the higher order schemes. The implicit effect of the order of the finite difference schemes on the eddy viscosity is shown in Fig. 5. The eddy viscosity

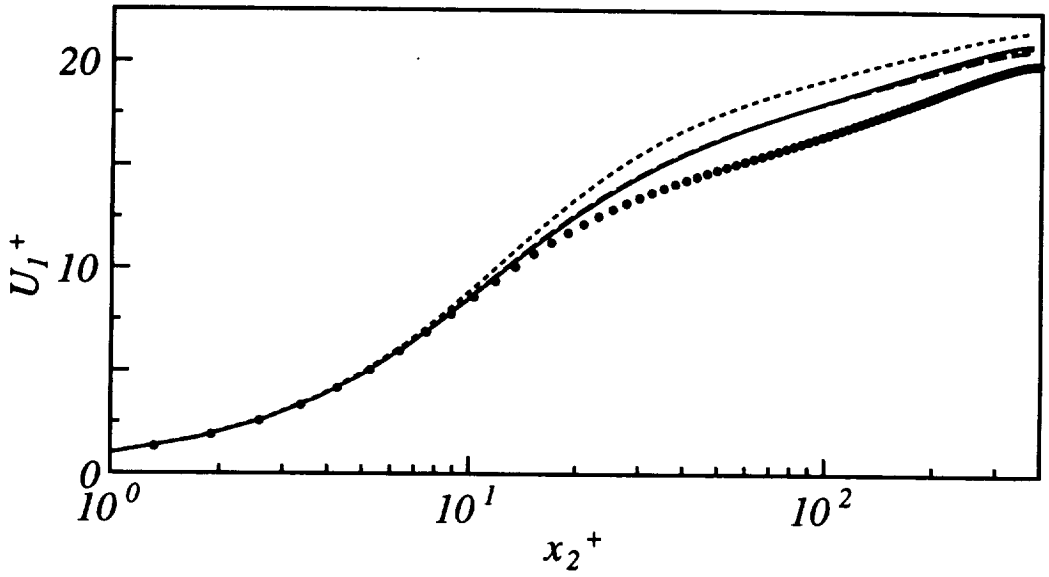

FIGURE 3. Mean streamwise velocity of the channel flow at Re_τ =395 using DSM with the 2nd (·····), 4th (----), 8th (—-—) and 12th (———) order schemes. DNS (•) data are also plotted.

increases gradually with the increase of the order of the scheme. Even for the 12th order scheme, the dynamic procedure with the Smagorinsky model gives excessive SGS eddy viscosity for the chosen resolution, and the mean velocity profile is much higher than the DNS data.

Note that in practical LES applications the finite difference method is usually used, and the first term in the right-hand side of Eq. (3) is approximated by

$$\frac{\partial \bar{u}_i \bar{u}_j}{\partial x_j} = \frac{\delta \bar{u}_i \bar{u}_j}{\delta x_j} + O(h^n), \tag{10}$$

where $\delta u_i u_j / \delta x_j$ is the n-th order accurate finite difference approximation to $\partial u_i u_j / \partial x_j$ and $O(h^n)$ denotes the truncation error. This means that the filtered convective term Eq. (3) suffers from the effect of the numerical error even if we know the exact SGS stress. That is why the development of the higher order accurate finite difference methods has been considered as one of the important areas of LES research.

In this study, we propose an alternate approach to improve the reliability of computational results of LES. The filtered convective term in the grid field is modeled as

$$\overline{\frac{\partial u_i u_j}{\partial x_j}} = \frac{\delta \bar{u}_i \bar{u}_j}{\delta x_j} + \frac{\partial \tau_{ij}}{\partial x_j}, \tag{11}$$

where the numerical error is treated as a part of the SGS stress (exactly, SGS vector) and the rest is modeled with τ_{ij}. The filtered convective term in the test field is

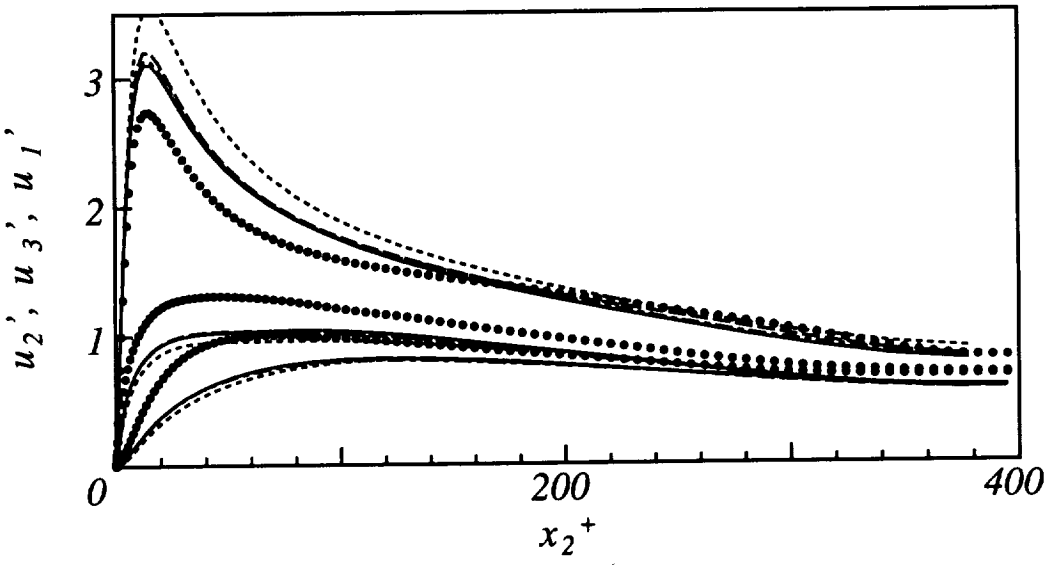

FIGURE 4. Velocity fluctuations of the channel flow at Re_τ =395 using DSM. For symbols see Fig. 3.

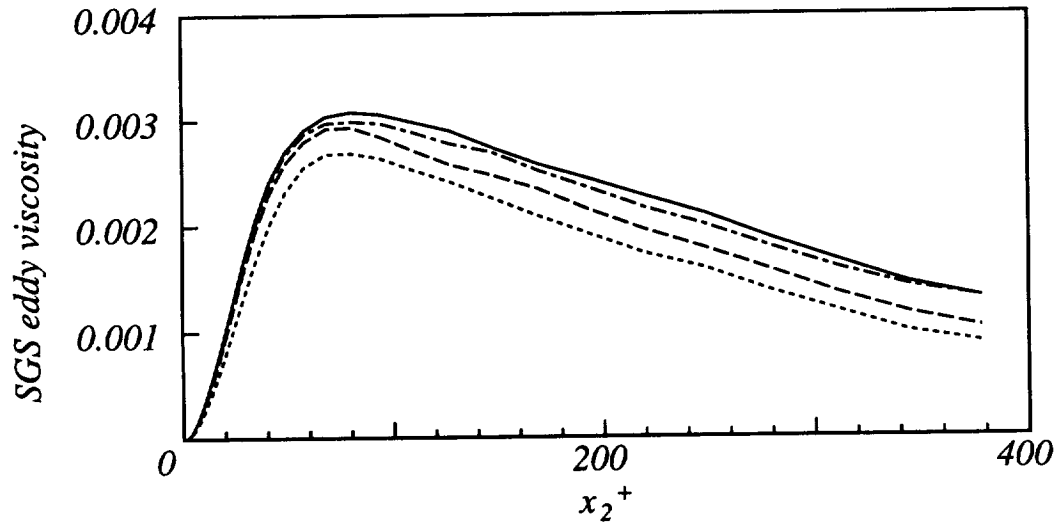

FIGURE 5. SGS eddy viscosity of the channel flow at Re_τ =395 using DSM with the 2nd (·····), 4th (----), 8th (—-—) and 12th (——) order schemes.

assumed as follows.

$$\widehat{\frac{\partial u_i u_j}{\partial x_j}} = \frac{\delta \hat{\bar{u}}_i \hat{\bar{u}}_j}{\delta x_j} + \frac{\partial T_{ij}}{\partial x_j} \tag{12}$$

The model parameter in the dynamic SGS model is determined through the following vector level identity:

$$\mathcal{C}_i = \frac{\partial T_{ij}}{\partial x_j} - \widehat{\frac{\partial \tau_{ij}}{\partial x_j}}, \tag{13}$$

where the resolved convective term $\mathcal{C}_i$ is defined as

$$\mathcal{C}_i = \mathcal{C}_{ij}^j, \qquad \mathcal{C}_{ij}^k = \widehat{\frac{\delta \bar{u}_i \bar{u}_j}{\delta x_k}} - \frac{\delta \hat{\bar{u}}_i \hat{\bar{u}}_j}{\delta x_k}. \tag{14}$$

If the parameter in the dynamic SGS model is estimated through the vector level identity given by Eq. (13), then the numerical error explicitly affect the model parameter. Substituting Eqs. (6) and (7) into Eq. (13), we obtain the following error E_i:

$$E_i = \left(\mathcal{C}_i - \frac{1}{3}\delta_{ij}\mathcal{C}_{kk}^j\right) + 2M_i(C_S\bar{\Delta})^2 + 2M_{ij}\frac{\partial (C_S\bar{\Delta})^2}{\partial x_j}, \tag{15}$$

where

$$M_i = \frac{\partial M_{ij}}{\partial x_j}.$$

The least square minimization of Lilly (1992) is not applicable in this case due to the presence of third term on the right-hand side of Eq. (15). In this study, $(C_S\bar{\Delta})^2$ is estimated by minimizing the following weighted integral:

$$\int\int\int w(x_2)Q(x_1, x_2, x_3)dx_1 dx_2 dx_3, \tag{16}$$

where $w(x_2)$ is a weight function and $Q = E_i E_i$. Assuming that C_S is a function of x_2 and taking the average in the periodic directions, the $(C_S\bar{\Delta})^2$ value, which minimizes the integral (16), is obtained through the variational principal, which leads to the following differential equation:

$$\begin{aligned} &w(x_2)\left[\langle \mathcal{C}_i M_i\rangle + 2\langle M_i M_i\rangle (C_S\bar{\Delta})^2 + \langle M_{i2} M_i\rangle \frac{d(C_S\bar{\Delta})^2}{dx_2}\right] \\ &- \frac{d}{dx_2}\left[w(x_2)\left(\langle \mathcal{C}_i M_{i2}\rangle + 2\langle M_i M_{i2}\rangle (C_S\bar{\Delta})^2 + \langle M_{i2} M_{i2}\rangle \frac{d(C_S\bar{\Delta})^2}{dx_2}\right)\right] = 0. \end{aligned} \tag{17}$$

Equation (17) is discretized using the second order finite difference method and is solved using the direct tri-diagonal solver. In this study the weight is selected as $w(x_2) = 1/\Delta_{x_2}(x_2)$, where $\Delta_{x_2}(x_2)$ is the grid spacing in x_2. The dynamic Smagorinsky model given by Eq. (6) with $(C_S\bar{\Delta})^2$ determined by Eq. (17) is called VDSM.

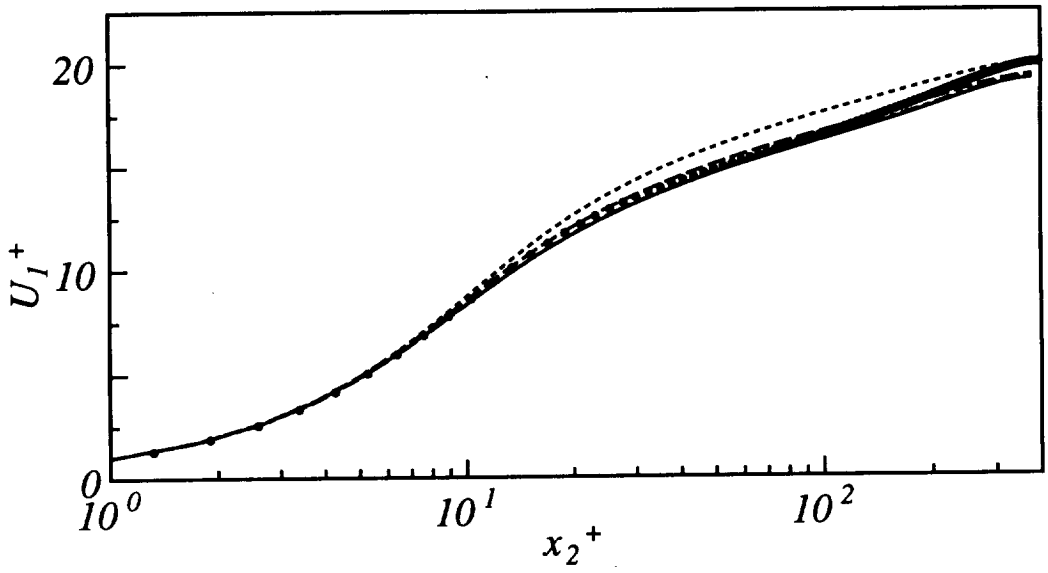

FIGURE 6. Mean streamwise velocity of the channel flow at Re_τ =395 using VDSM with the 2nd (·····), 4th (----), 8th (—·—) and 12th (——) order schemes. DNS (•) data are also plotted.

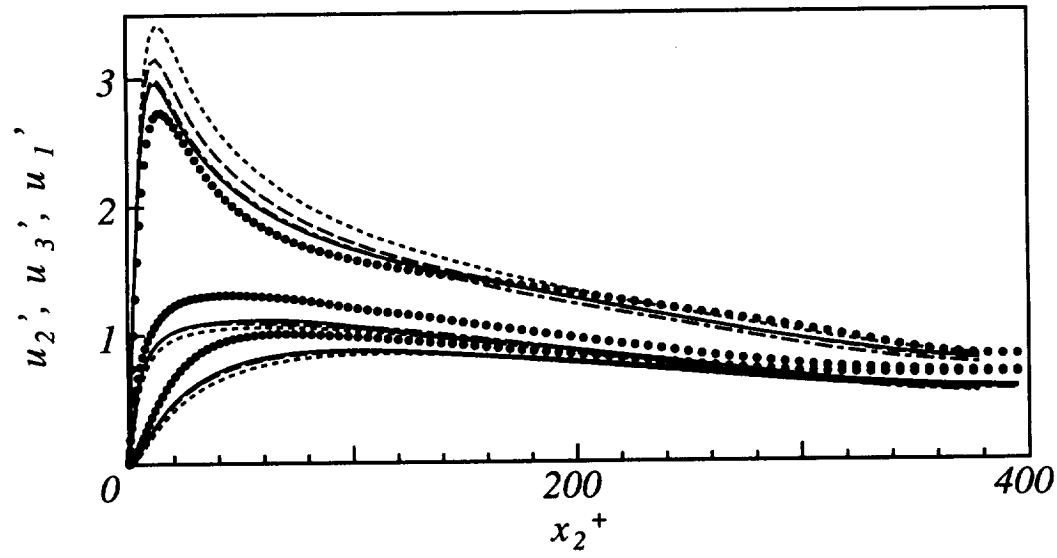

FIGURE 7. Velocity fluctuations of the channel flow at Re_τ =395 using VDSM. For symbols see Fig. 6.

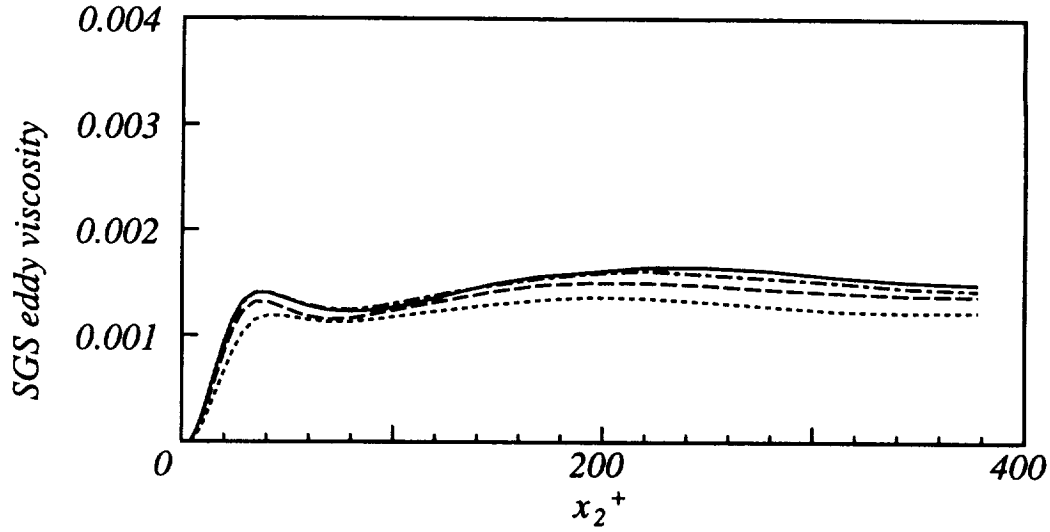

FIGURE 8. SGS eddy viscosity of the channel flow at Re_τ =395 using VDSM with the 2nd (·····), 4th (----), 8th (— —) and 12th (——) order schemes.

Figures 6, 7, and 8 show the profiles of mean streamwise velocity, velocity fluctuations, and SGS eddy viscosity respectively using the higher order schemes with VDSM at Re_τ=395. Although the mean velocity profile for the second order scheme is still higher than the DNS data, the great improvement is accomplished by using the vector level identity. It is noteworthy that the mean velocity profile in the core region is qualitatively represented by VDSM with the higher order schemes while it is not done by DSM.

Figure 9 shows the profiles of the model parameter C_S using the fourth order scheme with DSM and VDSM at Re_τ = 395. The traditional C_S value with the Van Driest (1956) type wall dumping function, $C_S = 0.1 \times [1 - \exp(-x_2^+/25)]$, is also plotted. Near the wall the C_S profile for VDSM qualitatively coincides with the one for DSM although there exists a slight negative region very near the wall in the profile of VDSM. The peak value of the negative region of C_S is about -0.005, and it has practically no effect on the results of computations. The C_S profile by VDSM differs qualitatively from that by DSM in the region away from the wall, and this is the important difference between the tensor and vector level identities. It appears that the profile of C_S away from the wall is affected strongly by the numerical error. It is interesting that the C_S profile by VDSM is closer to the traditional profile than that by DSM in the buffer region.

2.3 Recommended modification to the dynamic two-parameter mixed model

The dynamic two-parameter mixed model of Salvetti & Banerjee (1995) is based on the scale similarity model of Bardina *et al.* (1983) and the Smagorinsky eddy viscosity model.

$$\tau_{ij}^* = C_L\left(\overline{\bar{u}_i\bar{u}_j} - \bar{u}_i\bar{u}_j\right)^* - 2(C_S\bar{\Delta})^2|\bar{S}|\bar{S}_{ij} \tag{18}$$

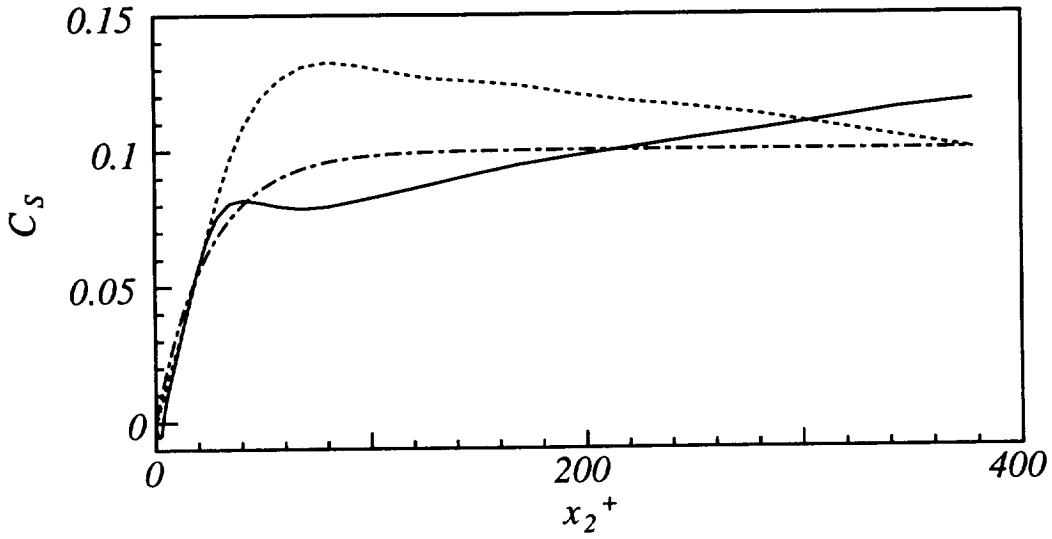

FIGURE 9. The profiles of C_S of the channel flow at Re_τ =395 using DSM (·····) and VDSM (———) with the fourth order scheme. The traditional profile (—·—·), $C_S = 0.1 \times [1 - \exp(-\frac{x_2^+}{25})]$, is also plotted.

The scale similarity model by itself is not dissipative enough, and the Smagorinsky eddy viscosity model is usually added to recover the defect. Following the standard procedure for the plane channel flow, the two parameters, C_S and C_L, are computed simultaneously using the tensor level identity of Germano *et al.* (1991) with the least square minimization. The resulting equations for C_S and C_L are given by

$$(C_S\bar{\Delta})^2 = -\frac{1}{2}\frac{\langle \mathcal{L}_{ij}M_{ij}\rangle\langle \mathcal{H}^*_{ij}\mathcal{H}^*_{ij}\rangle - \langle \mathcal{L}_{ij}\mathcal{H}^*_{ij}\rangle\langle \mathcal{H}^*_{ij}M_{ij}\rangle}{\langle M_{ij}M_{ij}\rangle\langle \mathcal{H}^*_{ij}\mathcal{H}^*_{ij}\rangle - \langle \mathcal{H}^*_{ij}M_{ij}\rangle^2}, \tag{19}$$

$$C_L = \frac{\langle \mathcal{L}_{ij}\mathcal{H}^*_{ij}\rangle\langle M_{ij}M_{ij}\rangle - \langle \mathcal{L}_{ij}M_{ij}\rangle\langle \mathcal{H}^*_{ij}M_{ij}\rangle}{\langle M_{ij}M_{ij}\rangle\langle \mathcal{H}^*_{ij}\mathcal{H}^*_{ij}\rangle - \langle \mathcal{H}^*_{ij}M_{ij}\rangle^2}, \tag{20}$$

where

$$\mathcal{H}_{ij} = \left(\widehat{\hat{\bar{u}}_i\hat{\bar{u}}_j} - \hat{\bar{u}}_i\hat{\bar{u}}_j\right) - \left(\widehat{\bar{u}_i\bar{u}_j} - \bar{u}_i\bar{u}_j\right).$$

In this study, the dynamic mixed model given by Eq. (18) with Eqs. (19) and (20) is called DTM.

Figures 10, 11, and 12 show the profiles of mean streamwise velocity, velocity fluctuations, and SGS eddy viscosity respectively using the higher order schemes with DTM at Re_τ=395. The profile of streamwise velocity fluctuation for DTM is better than the one for DSM (compare Fig. 11 with Fig. 4). However DTM has a defect in that the mean velocity profile is lower than that of DNS when it is used with the higher order schemes. Although the mean velocity profile of DTM

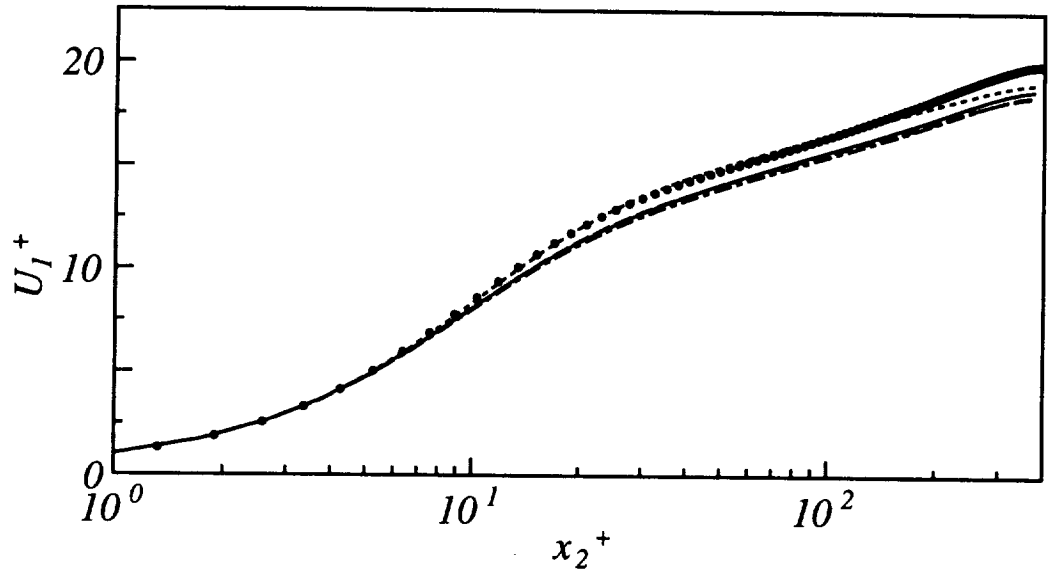

FIGURE 10. Mean streamwise velocity of the channel flow at Re_τ =395 using DTM with the 2nd (·····), 4th (----), 8th (—·—) and 12th (——) order schemes. DNS (•) data are also plotted.

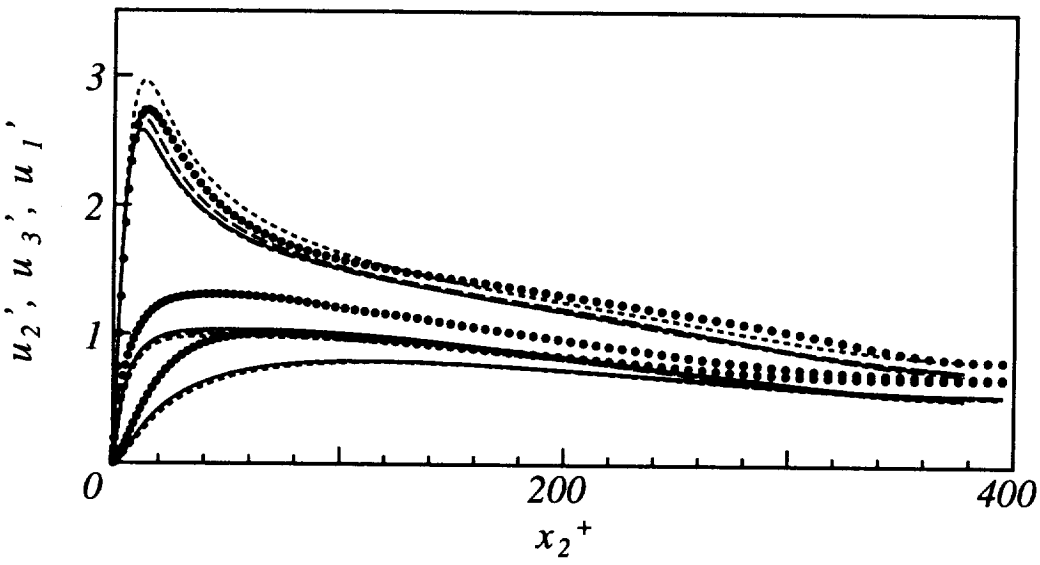

FIGURE 11. Velocity fluctuations of the channel flow at Re_τ =395 using DTM. For symbols see Fig. 10.

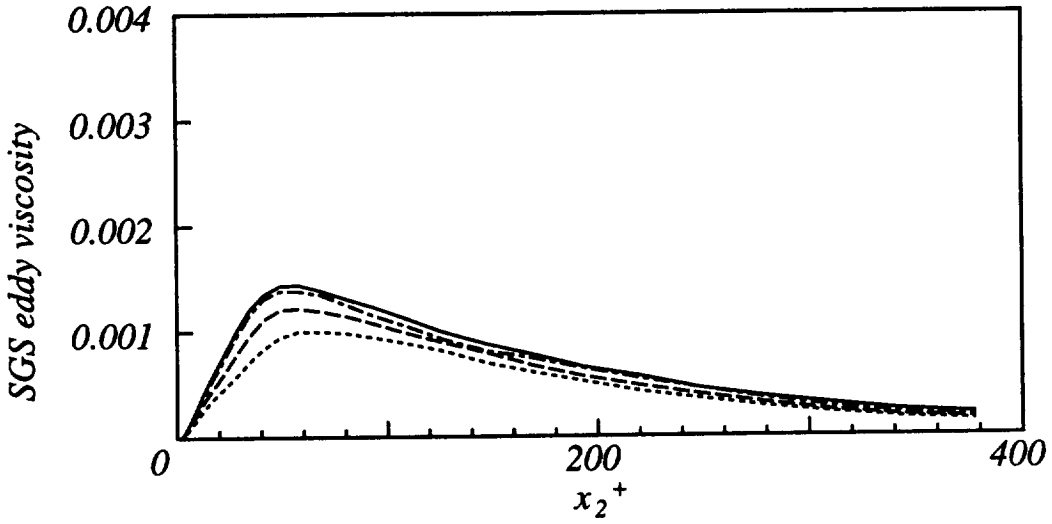

FIGURE 12. SGS eddy viscosity of the channel flow at Re_τ =395 using DTM with the 2nd (·····), 4th (----), 8th (—-—) and 12th (———) order schemes.

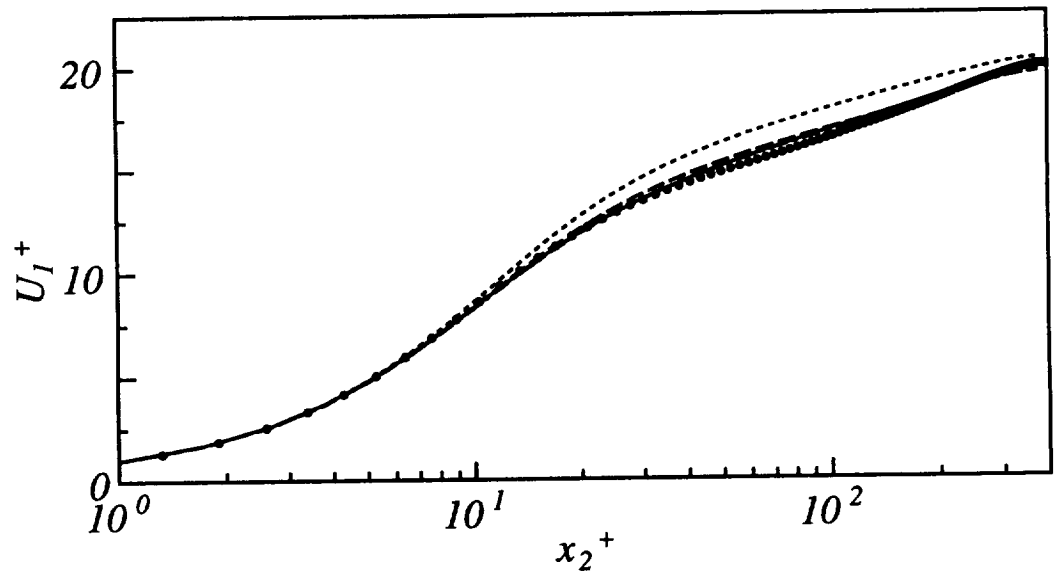

FIGURE 13. Mean streamwise velocity of the channel flow at Re_τ =395 using DTMR with the 2nd (·····), 4th (----), 8th (—-—) and 12th (———) order schemes. DNS (•) data are also plotted.

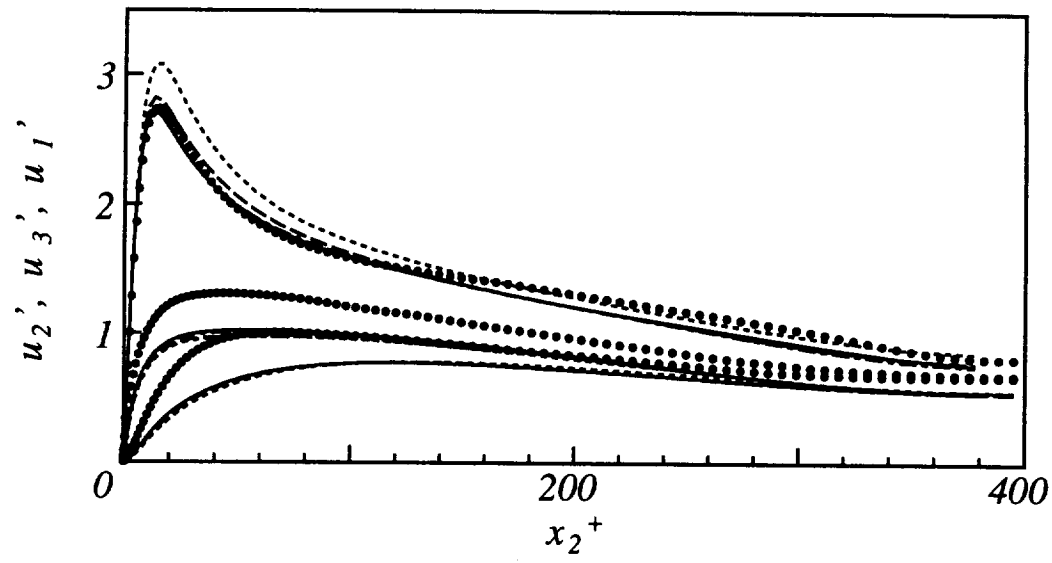

FIGURE 14. Velocity fluctuations of the channel flow at Re_τ =395 using DTMR. For symbols see Fig. 13.

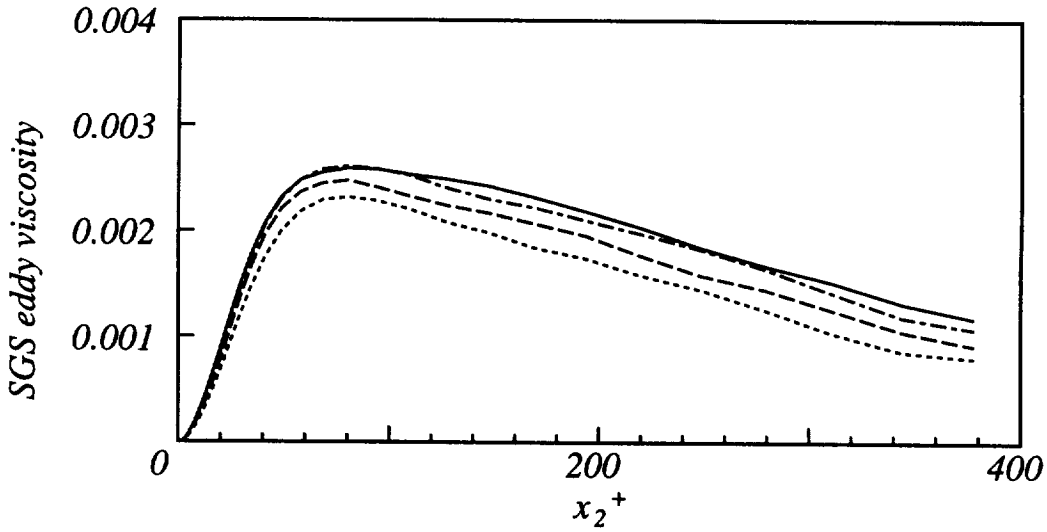

FIGURE 15. SGS eddy viscosity of the channel flow at Re_τ =395 using DTMR with the 2nd (·····), 4th (----), 8th (—·—) and 12th (——) order schemes.

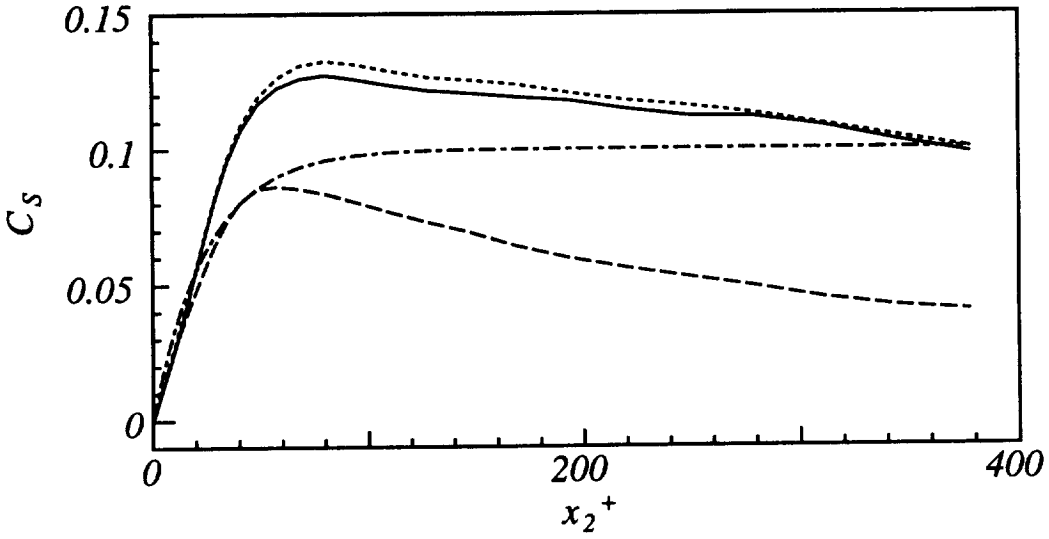

FIGURE 16. The profiles of C_S of the channel flow at Re_τ =395 using DSM (·····), DTM (----) and DTMR (——) with the fourth order scheme. The traditional profile (—·—), $C_S = 0.1 \times [1 - \exp(-\frac{x_2^+}{25})]$, is also plotted.

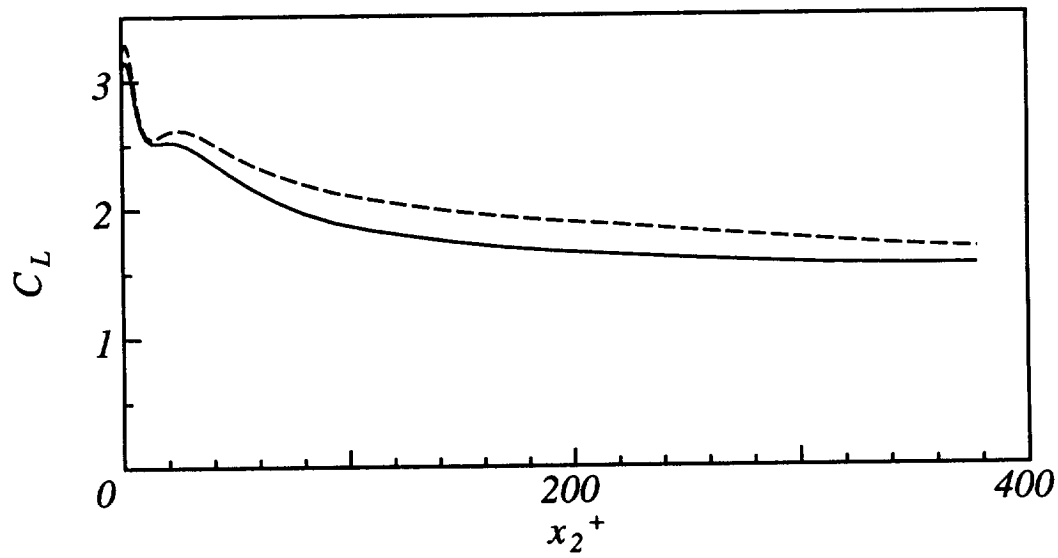

FIGURE 17. The profiles of C_L of the channel flow at Re_τ =395 using DTM (----) and DTMR (——) with the fourth order scheme.

with the second order finite difference method accidentally agrees well with the DNS data, it is caused by the numerical error explained in Fig. 1. In this stage, the model parameters in DTM are estimated through the tensor level identity, and the numerical error is not taken into consideration. Remember that the scale similarity model itself has less dissipation, and therefore the model is used together with the Smagorinsky model as the mixed model to remove the defect. However the profiles of the SGS eddy viscosity in Fig. 12 are much smaller than those in Fig. 5. This indicates that the defect of the scale similarity model is not cured if the model parameters are estimated through the dynamic procedure with the tensor level identity. The reason why the defect is not cured is that the correlation of the Smagorinsky model to the SGS stress is much lower than that of the scale similarity model (for example see Horiuti 1989). This imbalance makes C_S smaller if the two parameters are solved simultaneously.

To remove the problem, Morinishi (1997) proposed a modification to a dynamic two-parameter mixed model. First, the Smagorinsky parameter C_S is computed exactly the same way as in DSM (using Eq. (9)). This ensures that the mixed model has enough dissipation. Secondly, the other parameter is computed dynamically as C_S is known. In this study, we adopt the following modification to the mixed model (18):

$$C_L = \frac{\langle [\mathcal{F}_{ij} + 2(C_S\bar{\Delta})^2 M_{ij}]\mathcal{H}^*_{ij} \rangle}{\langle \mathcal{H}^*_{ij}\mathcal{H}^*_{ij} \rangle}. \tag{21}$$

This revised dynamic two-parameter mixed model is called DTMR.

Figures 13, 14, and 15 show the profiles of mean streamwise velocity, velocity fluctuations, and SGS eddy viscosity respectively using the higher order schemes with DTMR at Re_τ=395. The profiles of the mean velocity and velocity fluctuation using the higher order schemes with DTMR coincide well with the DNS data. Comparing Fig. 15 with Fig. 12, it is apparent that the defect of DTM is recovered by the revised model. Figures 16 and 17 show the profiles of the parameters C_S and C_L respectively by the fourth order scheme with DTM and DTMR (and DSM in Fig. 16). The traditional C_S value with the wall dumping function is also plotted in Fig. 16. The C_S profile of DTMR is almost the same as that of DSM, and the merit of DSM is kept in DTMR. The C_S value of DTM is much lower than those of DSM, DTMR, and the traditional value, and this makes DTM less dissipative. The C_L profile of DTMR is almost the same as that of DTM, and the merit of DTM is kept in DTMR.

3. Future plans

The proposed SGS models will be tested in high Reynolds number channel flow to see if they work well in LES for practical problems. In addition, the vector level identity will be extended to the revised two-parameter mixed model.

REFERENCES

BARDINA, J., FERZIGER, J. H. & REYNOLDS, W. C. 1983 Improved turbulence models based on large eddy simulation of homogeneous, incompressible, turbulent flows, Stanford University Tech. Rep. TF-19.

DUKOWICZ, J. K. & DVINSKY, A. S. 1992 Approximation as a higher order splitting for the implicit incompressible flow equations. *J. Comput. Phys.* **102,** 336-347.

GERMANO, M., PIOMELLI, U., MOIN, P. & CABOT, W.H. 1991 A dynamic subgrid-scale eddy viscosity model. *Phys. Fluids A.* **3,** 1760-1765.

GHOSAL, S. 1996 An analysis of numerical error in large-eddy simulation of turbulence. *J. Comput. Phys.* **125,** 187-206.

HORIUTI, K. 1989 The role of the Bardina model in large eddy simulation of turbulent channel flow. *Phys. Fluids A.* **1,** 426-428.

HORIUTI, K. 1997 A new dynamic two-parameter mixed model for large-eddy simulation. *Phys. Fluids A.* **9,** 3443-3464.

MANSOUR, N. N., MOSER, R. D. & KIM, J. 1996 Reynolds number effects in low Reynolds number turbulent channels. (In preparation, data in AGARD database.)

MORINISHI, Y. 1997 Large eddy simulation of plane channel turbulence using dynamic two-coefficient mixed subgrid-scale models. *Trans. JSME.* **63-606B,** 529-536 (*in Japanese*).

MORINISHI, Y., LUND, T.S., VASILYEV, O. V. & MOIN, P. 1998 Fully conservative higher order finite difference schemes for incompressible flow. *J. Comput. Phys.* **143,** 90-124.

RODI, W. & MANSOUR, N. N. 1993 Low-Reynolds-number $\kappa - \epsilon$ modeling with the aid of direct simulation data. *J. Fluid Mech.* **250,** 509-529.

SALVETTI, M. & BANERJEE, S. 1995 A priori tests of a new dynamic subgrid-scale model for finite-difference large-eddy simulations. *Phys. Fluids A.* **7,** 2831-2847.

SMAGORINSKY, J. 1963 General circulation experiments with the primitive equations. I. The basic experiment. *Mon. Weather Rev.* **91,** 99-165.

SPALART, P., MOSER, R. & ROGERS, M. 1991 Spectral methods for the Navier-Stokes equations with one infinite and two periodic direction. *J. Comput. Phys..* **96,** 297-324.

VAN DRIEST, E.R., H. 1956 On turbulent flow near a wall. *J. Aero. Sci.* **23,** 1007-1011,1036.

VREMAN, B., GEURTS, B. & KUERTEN, H. 1994 On the formulation of the dynamic mixed subgrid-scale model. *Phys. Fluids A.* **6,** 4057-4059.

ZANG, Y., STREET, R. L. & KOSEFF, J. R. 1993 A dynamic subgrid-scale model and its application to turbulent recirculating flows. *Phys. Fluids A.* **5,** 3186-3196.

Towards a near-wall model for LES of a separated diffuser flow

By Hans-J. Kaltenbach[1]

1. Motivation and objectives

Recently it was shown that LES is capable of predicting incipient separation in an asymmetric diffuser (Fatica *et al.*, 1997; Kaltenbach *et al.*, 1998). Despite the low Reynolds number of the flow ($Re_\tau = u_\tau\delta/\nu = 500$ in the inlet duct of height 2δ, $Re_b = U_{bulk}\delta/\nu = 9000$) the computational effort required to obtain good quantitative agreement with measurements is considerable due to the wide range of spatial and temporal scales encountered which necessitate the use of fine meshes as well as lengthy integration times. Proper prediction of the mean velocity profile and turbulence statistics of the incoming developed turbulent channel flow turned out to be challenging using LES in which the near-wall region was resolved. It is desirable to reduce the cost of the simulation both for the diffuser and for the time series of inlet planes by circumventing the need to resolve the fine scale turbulence in the near wall region.

The goal of the present study is to investigate the diffuser flow to see if the wall-model based LES method (Cabot 1995, 1996, 1997 and related contributions in this volume) can be applied. The statistics from a well resolved LES of the diffuser flow are used to study the near-wall zone in order to see (i) what are the relevant terms in the mean momentum balance and (ii) whether the turbulent shear stress in the near-wall layer can be predicted by an algebraic eddy-viscosity model. Based on the outcome of these *a priori* tests, we discuss a model formulation which treats the near wall region primarily in the RANS spirit with emphasis on accurate specification of the mean turbulent stresses.

2. Accomplishments

2.1 Near-wall momentum balance

Following Cabot (1996, 1997) we use data from a well resolved diffuser LES to identify important terms in the tangential-to-the-wall momentum balance. Here we focus on the mean flow statistics as defined through RANS and *not* on statistics for a control volume of typical size used in wall model LES as in Cabot (1995). The streamwise momentum balance in coordinates locally tangential and normal to the walls is integrated from $y = 0$ to y_0, yielding

$$\underbrace{\int_0^{y_0} \frac{\partial \overline{U}^2}{\partial x} dy}_{Adv_x} + \underbrace{\int_0^{y_0} \frac{\partial \overline{u'}^2}{\partial x} dy}_{adv_x} + \underbrace{\overline{U}\,\overline{V}|_{y_0}}_{Adv_y} + \underbrace{\overline{u'v'}|_{y_0}}_{adv_y} + \underbrace{\int_0^{y_0} \frac{\partial p}{\partial x} dy}_{PG} \underbrace{-\tau_{SGS}|_{y_0} - \nu \frac{\partial U}{\partial y}|_{y_0} + \tau_w}_{Visc} = 0 .$$

1 Hermann-Föttinger-Institut, Technische Universität Berlin, 10623 Berlin, Germany

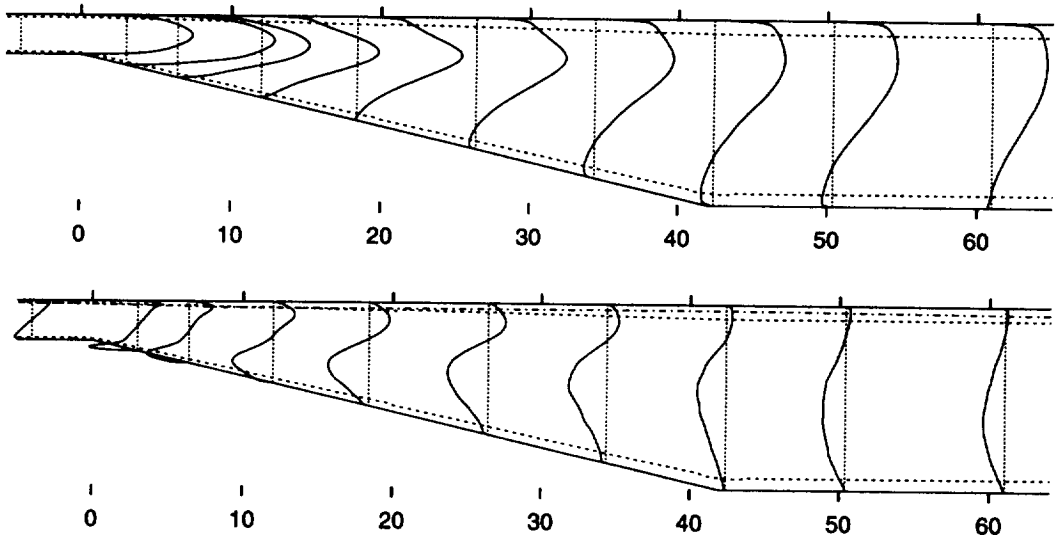

FIGURE 1. Profiles of mean streamwise velocity component (*top*) and shear stress $\overline{uv}$ (*bottom*) at stations $x/\delta = -4, 3, 6.4, 12, 18.4, 26.4, 34.4, 42.4, 50.4, 61$. The dashed lines mark the border of the near wall zone defined to be 7% of the local duct height, whereas the dash-dotted line corresponds to a distance of 70 wall units.

The choice of a meaningful wall distance y_0, which defines the zone in which the horizontal grid resolution is too coarse for LES to yield correct turbulent stresses, is not obvious in the present case. For the inlet duct a definition of y_0 in terms of a characteristic distance based on wall units is appropriate. As the flow separates along the inclined wall, this definition is no longer valid, and we have to find an alternate characteristic length scale.

Inside the inlet duct we define the near-wall zone as the wall-parallel layer in a distance of 70 wall units. For a developed turbulent channel flow, the peak values of the turbulence intensities and turbulent production lie inside this zone.

Figure 1 reveals that the flow inside the expansion is asymmetric with separation occurring on the inclined wall. Since the flow remains attached along the flat wall, the distance of the near wall zone could in principle be chosen based on the local value of u_τ and a thickness of 70 wall units. However, it would be wrong to conclude that this zone is of equal importance all along the flat wall. This can be seen from the position of maximum shear stress $|\overline{uv}|_{max}$, which moves out of the near wall zone into the core flow as the flow decelerates inside of the expansion (see Fig. 1).

Since a u_τ-based definition of a near-wall zone is ill-posed along the inclined wall, we use an alternate definition which simply states that y_0 corresponds to 7% of the local duct height. This definition is equivalent to a distance of 70 wall units along a considerable part of the flat wall (see Fig. 1). A significant part of the duct area lies inside of the near-wall zones, which now account for 14% of the total cross-section. This is a rather atypical property of the present flow, being entirely due to the low Reynolds number. However, for the purpose of meaningful testing of

the wall-model LES approach, it is essential that the zone where the flow is being modeled is thick enough to allow significant reduction of horizontal spacings. As a guideline one can use the following rule: since the horizontal spacing defines the size of the smallest turbulent scales to be resolved, the thickness of the near-wall zone should correspond roughly to the average horizontal spacing.

Because of its atypical thickness, the near-wall zone carries considerable parts of the total mass and momentum fluxes. For this reason we consider it useful to separate the issue of defining the near-wall zone thickness y_0 from the question of adequate numerical approximation of the flow inside this zone. The momentum balance reveals that, unlike turbulent channel flow where wall models have principally been investigated, particularly strong contributions are provided by the mean flow advection terms Adv_x and Adv_y (see Fig. 2). This means that the wall-normal spacing of the mesh has to be reasonably fine to allow meaningful representation of mean flow profiles $\overline{U}(y)$ and $\overline{V}(y)$ for $y < y_0$. In case the near-wall solution is computed on a separate grid, representation of the mean flow inside this zone is essentially a 2D-problem. Note that this is different from the approach of Cabot (1997) where *each* grid cell in the x, z-plane has a locally refined mesh in the wall-normal direction for computing instantaneous values of $u(y)$ and $v(y)$ in the near-wall layer.

For the flow under investigation, no drastic computational savings are achieved by coarsening the mesh in the y-direction. Designing a mesh with the first off-wall line at $y^+ = 10$ is a fair compromise between mesh coarsening and proper representation of the mean flow solution near the wall. This mesh design has consequences for the model approach as outlined in section 2.2.

Figure 2 reveals the important role of mean flow advection for the near wall momentum balance. Turbulent shear stress and viscous stress roughly balance each other in the inlet duct. Near the rounded corner of the diffuser entrance, the magnitude of mean flow advection terms and of the pressure gradient term is substantially larger than in the rest of the domain, emphasizing the need for proper wall-normal resolution in order to represent $\overline{U}$ and $\overline{V}$. Along both walls, the term related to the streamwise turbulence intensity, adv_x, is of little significance except for a small region near the inlet. In the diffuser rear section, along the flat wall both mean momentum flux Adv_y and turbulent shear stress adv_y are equally important whereas along the inclined wall Adv_y has little significance. Our conclusion from this evaluation is the following: in certain regions of the diffuser flow, the near wall momentum balance depends not only on proper prediction (modeling) of the turbulent shear stress $\overline{uv}$, but also on accurate representation of the mean flow and the associated vertical flux of horizontal momentum, $\overline{U}\,\overline{V}|_{y_0}$.

2.2 Model prediction for shear stress in the near-wall region

A widely used model for the near-wall zone consists of prescribing values for instantaneous wall stresses $\tau_{w,xy}$ and $\tau_{w,zy}$ based on information from the interior and assuming that the logarithmic law of the wall is valid for the mean flow across the mesh cell adjacent to the wall. This approach works under the assumption that the last grid cell extends well into the logarithmic region, the first off-wall grid line y_N then being near $y_N^+ \approx 70$. In the control volume adjacent to the wall, the wall

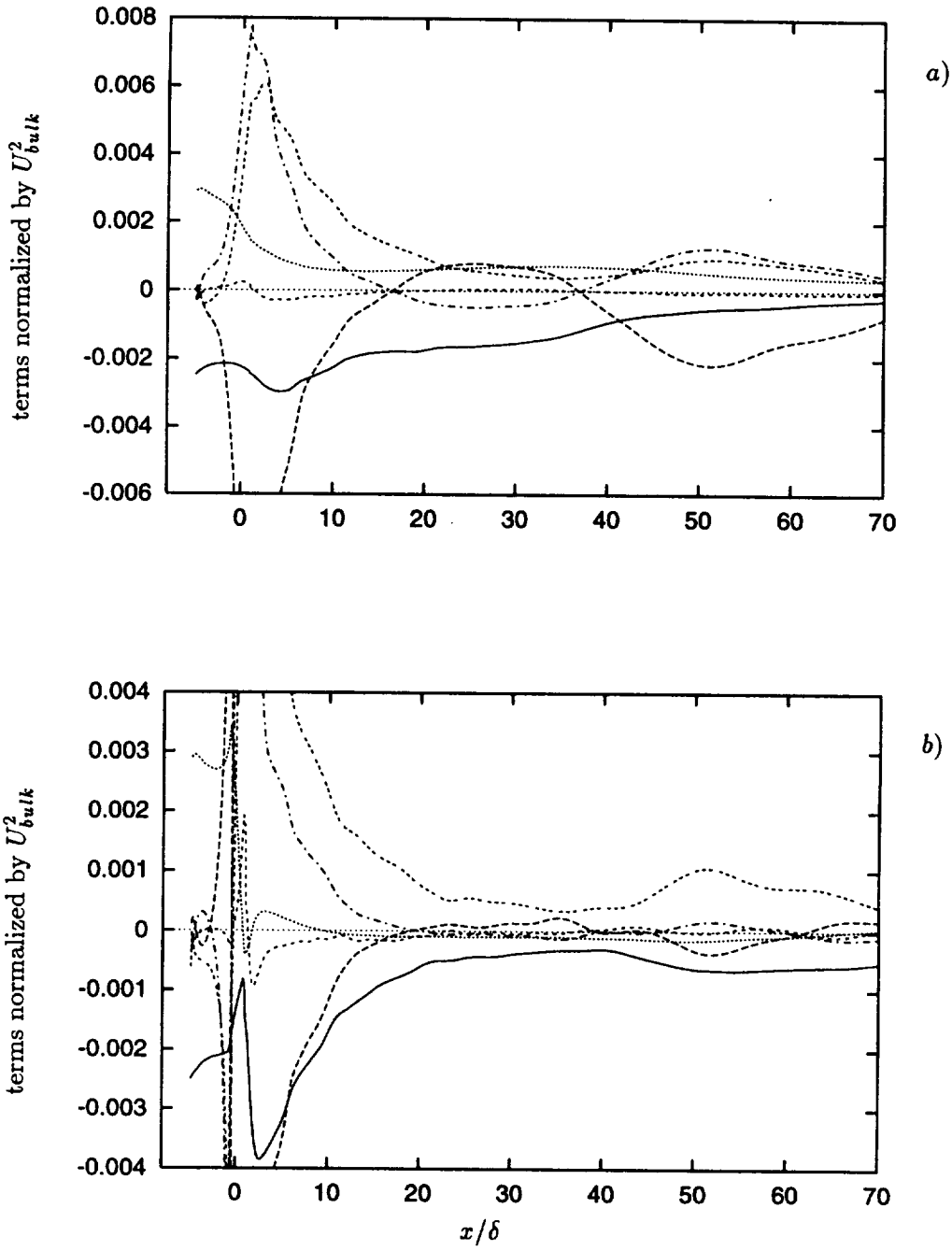

FIGURE 2. Terms of the near wall momentum balance evaluated along flat wall (a) and inclined wall (b) of the diffuser. Line code: Adv_x ---- , adv_x ---- , Adv_y —·— , adv_y —— , PG --- --- , $Visc$ ····· .

normal derivative of the shear stress reduces to

$$\frac{\partial \tau_{xy}}{\partial y} \approx \frac{\tau_{xy}|_N - \tau_{xy}|_s}{\Delta_y} = \frac{-uv|_N + \nu dU/dy|_N + \tau_{SGS}|_N - \tau_{w,xy}}{\Delta_y} \quad ,$$

where the subscript N refers to the location of the first off-wall grid line. The prediction of the resulting force in the streamwise momentum balance depends on the ability of the simulation to capture the correct stresses $\tau_{xy}|_N$.

In cases where the wall-normal grid-spacing is much finer than the distance y_0 — for reasons outlined in the previous section — specification of τ_w only is likely to fail because the grid-scale turbulence (together with SGS stresses) cannot provide the correct stress τ_{xy} at the first off-wall grid line. (An example for this type of failure is given in section 2.3.) Adapting a near-wall model to this specific situation requires that additional "supporting shear stresses" are supplied inside the cells belonging to the near-wall zone. Inside this region the wall-parallel spacings Δx and Δz will be too coarse to support the correct near-wall turbulence structure, and as a result the resolved stresses $\overline{uv}$ will be too low, or the near-wall turbulence structures will be artificially amplified and distorted to provide the correct resolved stresses (Baggett, this volume). There is evidence (Baggett *et al.* 1997, Jiménez & Moser, 1998) that simple SGS models are *not* able to cope with this problem by supplying the missing part to the total shear stress. This has to do with the fact that inside the near-wall region the SGS model would have to carry the *major* part of the shear stress — a situation for which commonly used models are not designed.

Spalart *et al.* (1998) have proposed to modify the subgrid-scale eddy-viscosity in such a way that the missing shear stress (in the mean sense) is supplied by adding a RANS-type contribution to the SGS eddy viscosity inside the near-wall zone; see also Baggett (this volume). Another way of achieving this goal is to add a body force (possibly restricted to the wall-normal direction) to stimulate resolved-scale motion inside the near-wall zone in order to achieve the desired distribution of mean shear stress. This type of scheme has recently been applied successfully in numerical experiments related to delaying boundary layer separation (Driller, 1998).

We see two advantages for the proposed treatment of the near-wall zone for the flow under investigation: (i) a fine wall-normal resolution is desirable for accurate representation of the mean flow and the associated momentum flux $\overline{U}\,\overline{V}$ as outlined in the previous section; (ii) the formulation avoids a sharp interface between near-wall zone and "core" flow, thereby possibly improving the prediction for the core flow since the "supporting stresses" can gradually fade out with increasing distance from the wall.

A central question in this context is whether a good prediction of the near-wall mean shear stress $\overline{\tau}_{xy}$ is possible using a RANS formulation inside the near wall-layer which uses the running time-average of the core flow from the LES solution (cf. Lund *et al.*, 1998) as a boundary condition away from the wall. For this purpose we have started to compare the near-wall stress distribution from the fine-grid diffuser LES with model predictions. As a preliminary step in this direction, we compared the Johnson-King eddy viscosity model (abbreviated as JK model) since it is known

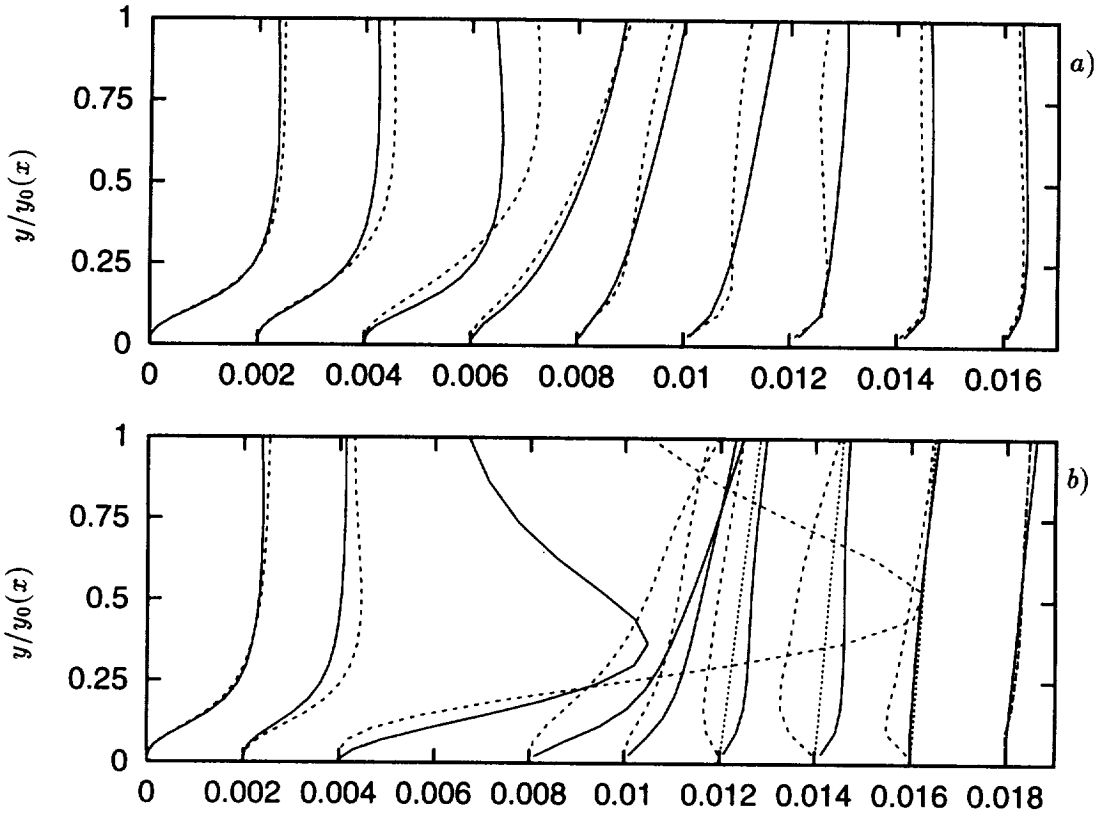

FIGURE 3. Comparison of turbulent shear stress $|\overline{uv} + \tau_{SGS}|$ from fine-grid LES —— with prediction from the Johnson-King model $\nu_t dU/dy$ ---- and a linear extrapolation $\overline{uv}_{max} y/y_{max}$ ····· at stations $x/\delta = -4.1$, -1.0, 1.0, 6.3, 14.2, 26.4, 38.1, 45.6, 65.8 along flat (a) and inclined wall (b). The distance from the wall has been normalized with the thickness y_0 of the near-wall zone.

to perform well in "mildly" separated flows. We use the formulation of Johnson & Coakley (1990) as outlined in Cabot (1995). The essential idea of this model is to use a blend of u_τ and $u_m = \sqrt{-\overline{uv}_{max}}$ as the velocity scale for the eddy viscosity. For the comparison we use the model constants $A = 19$ and $\kappa = 0.4$. Figure 1 shows that downstream of the inlet duct the peak of $\overline{uv}$-profiles lies outside of the near-wall region, thus u_m could in principle be determined from the running time-average of the core flow.

Figure 3 reveals that the JK model gives a satisfactory prediction of shear stresses in a considerable fraction of the diffuser domain. The model performs well along the entire flat wall where the flow remains attached. However, along the inclined wall we find serious deficiencies of the model as soon as the flow enters the expansion. A striking feature of the flow along the inclined wall is the drastic increase in turbulent shear stress close to $x/\delta = 1$. There, the JK model gives the right trend but overpredicts maximum stresses by a factor of two. Ahead of the location of mean

separation and early into the separated flow region, the JK model underpredicts the stresses. It fails completely in the region where backflow occurs because of the inability of an eddy-viscosity approach to cope with "countergradient" momentum transfer, which occurs close to the wall inside of the separated flow region. There, a simple linear extrapolation of the $\overline{uv}$-profile from the location y_m of maximum turbulent stress down to the wall is superior but can only be regarded as a rough estimate for the shear stress in the near-wall region. Note that the near-wall stresses are of less importance in the separated region since their magnitude is small when compared to the maximum shear stress in the core flow.

This evaluation shows that the JK model has some potential for use in predicting the near-wall shear stresses. Still, certain regions of the diffuser exhibit stress distributions near the wall which require a more advanced RANS model. However, before other models should be tested, it is desirable to find out whether specification of the proper mean shear stress distribution near the wall is sufficient for the core flow to behave as in the fine grid LES.

2.3 Inflow boundary conditions

One of the main findings of the original LES of the diffuser flow with resolved near-wall regions is that proper prediction of the flow inside the expansion depends crucially on the quality of the flow in the inlet duct. There exist two methods for creating unsteady Dirichlet boundary conditions to be specified at the inlet plane of a wall-model based LES of the diffuser: (i) extracting planes from an independent channel simulation, which by itself uses a near-wall model and therefore matches the diffuser grid at the inlet; (ii) interpolate available inflow from a fine-grid channel flow database onto a coarser mesh.

Here we focus on the second approach primarily because we want to be as close as possible to the conditions of the fine-grid LES which are in good agreement with experiments. The underlying idea of this method is that, by using data from a finer resolved case, the structure of the incoming "turbulence" is preserved over a considerable distance downstream of the inlet plane since the flow does not immediately feel the adverse effect of having a coarsened mesh.

To test how well this strategy would work in the diffuser, we interpolated the available time series of instantaneous u, v, w-slices onto a mesh which was considerably coarser in the y- and z-directions. The mean flow profile is well preserved, but we find that omitting half the number of modes in the spanwise direction causes a significant drop in the peak values of the turbulence intensity and shear stress profiles. Ideally, the SGS-model should make up for the missing stresses, but *a posteriori* tests show that it cannot do so.

We have used the filtered inflow database to simulate a short stretch of the inlet duct using $64 \times 40 \times 64$ cells. The streamwise spacing was either $\Delta x = 0.06\delta$ ($\Delta x^+ = 30$) as in the original fine grid LES or $\Delta x = 0.2\delta$ ($\Delta x^+ = 100$). We present results from four cases, two for each grid consisting of a run without a wall-model and a simulation with an instantaneous wall-stress boundary condition which guarantees that the mean flow experiences the correct wall-stress corresponding to the pressure drop of the fine-grid channel flow LES. In the latter cases, the instantaneous wall

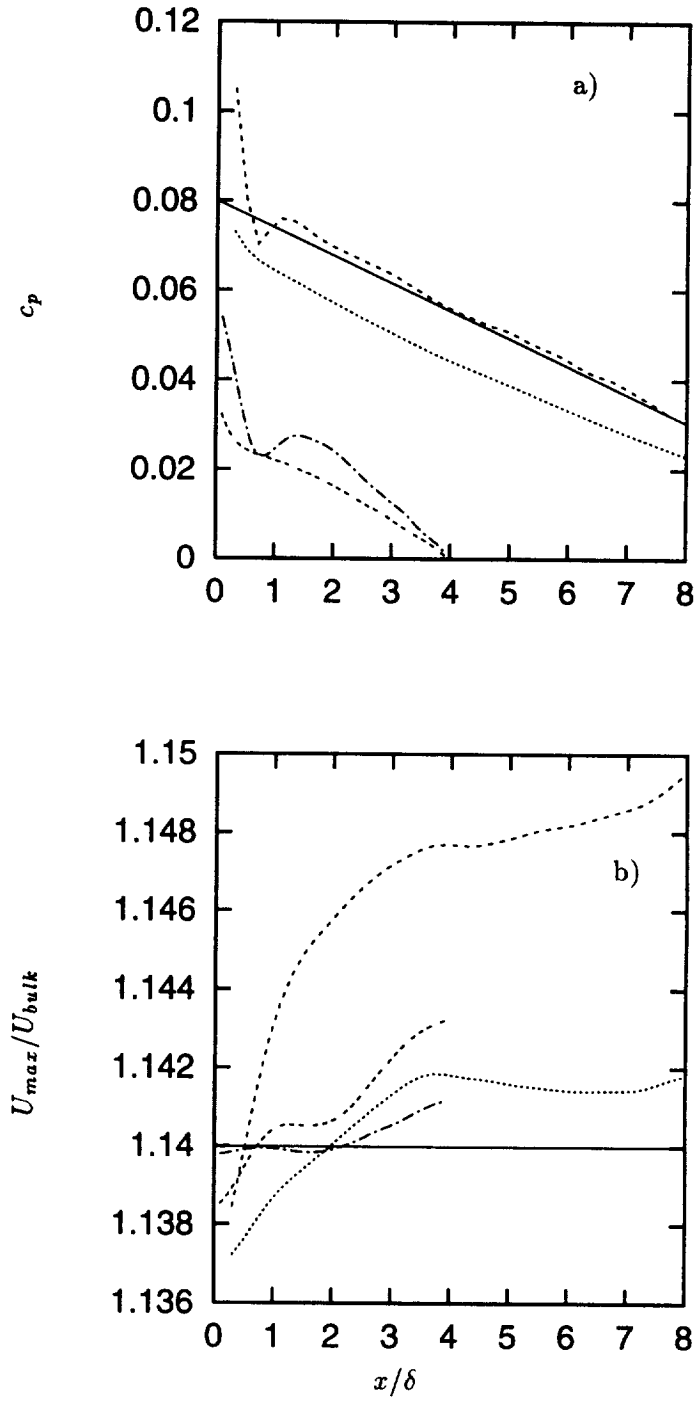

FIGURE 4. Streamwise development of pressure drop (a) and velocity ratio (b) in channel flow using filtered inflow data. Line coding: fine grid LES (target) ——— , CNM ····· , CWM - - - - , FNM - - - - - , FWM —·— .

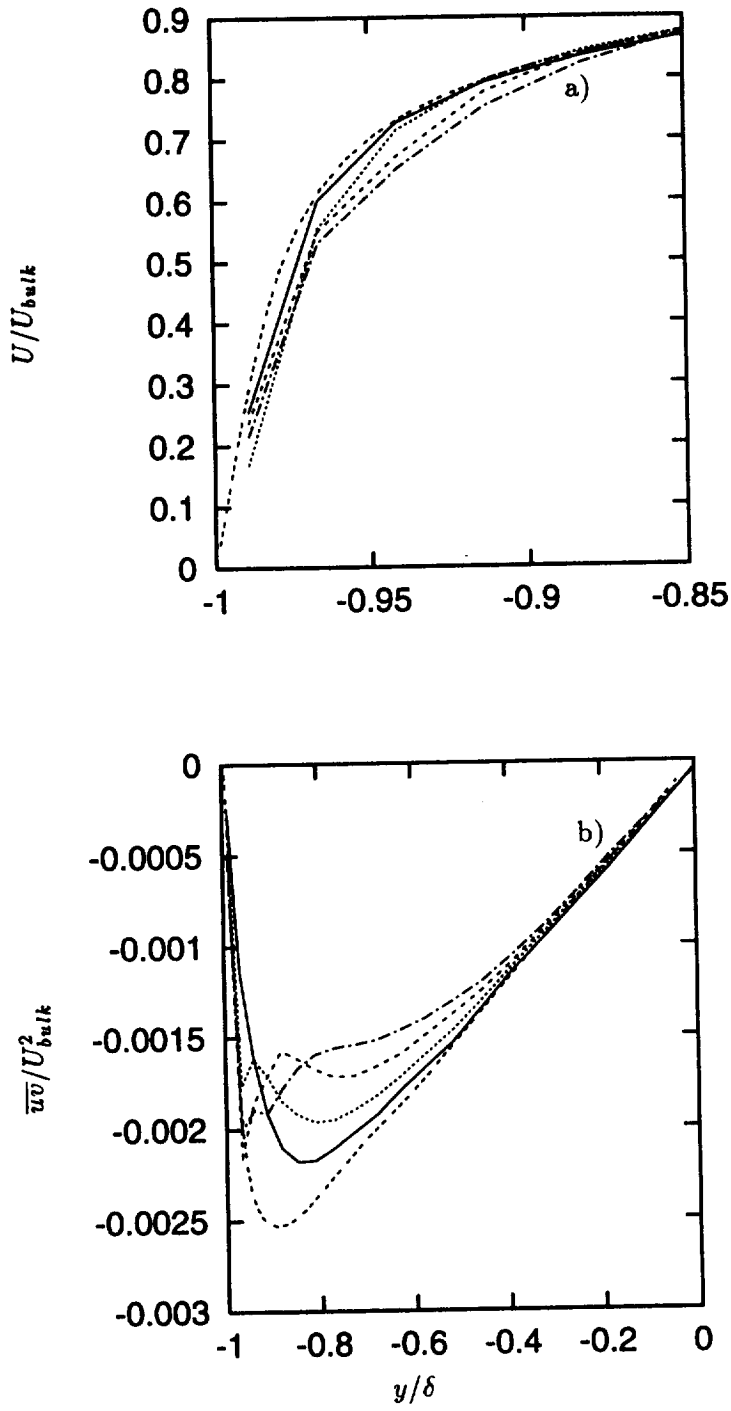

FIGURE 5. Profiles of $\overline{U}(y)$ (a) and $\overline{uv}$ (b) from case FWM at distances $x/\delta = 0.2$ ——— , 0.8 ····· , 2. - - - - , 3.4 —·— . Profiles from the fine-grid LES are marked as --- --- .

stress was constructed using the instantaneous horizontal velocity at the first off-wall position (cf. Wu & Squires, 1998). The four cases are denoted CNM, CWM, FNM, FWM with C, F denoting *coarse* and *fine* grids, respectively, and with NM, WM denoting *no model* or *wall model*, respectively.

Figure 4 compares c_p curves and the development of the mean flow profile shape. All the simulations experienced an unnatural pressure drop close to the inflow plane, which we contribute to changes in the mean profile shape and the associated momentum fluxes. Surprisingly, cases with the correct average wall stress experience the largest drop for which we do not yet have an explanation. Case CWM is the only one which — after considerable readjustments — reaches the correct pressure drop corresponding to the prescribed wall stress. As a result of underprediction of the wall-stress in case CNM, the pressure gradient is lower than the target value. Because the mean flow decelerates near the wall (which is caused by a deficit of shear stress inside the near-wall layer), the core flow speeds up, leading to an increase of the centerline to bulk velocity ratio. Figure 5 shows the corresponding profile changes for case FWM. Coarse grid cases CWM and CNM show larger profile shape deficits than cases FWM and FNM. The coarse (C) cases experience an additional problem which has to do with the staggered variable configuration at the inlet plane: since the inflow database was created with u extracted half of a fine-grid mesh cell downstream of v and w, it is incorrect to feed these data into a domain which has considerably coarser streamwise spacing. It should be investigated whether this problem can be alleviated by invoking Taylor's hypothesis to shift u-slices to a position which is consistent with the coarse mesh staggered variable configuration.

Our conclusion from this test is that for the present configuration supplying the correct wall-stress is not sufficient in order to predict the mean flow profile with the required accuracy. Additional modifications are required to guarantee that the flow experiences the correct total turbulent shear stress inside the near-wall zone in order to reproduce the correct flow inside the inlet duct. It is useless to attempt a full diffuser simulation with a wall-model before this problem is solved.

3. Future plans

At this stage it is desirable to know whether the proposed model concept, i.e. guaranteeing that the flow in the near-wall zone experiences the correct turbulent shear stress in the time-averaged sense, is sufficient for the core flow to render the correct results. For this purpose we plan a simulation where the exact average stresses from the fine-grid diffuser LES are used as target values for the near-wall zone of a coarse LES. Some details about the best way to prescribe or excite the "supporting stresses" have to be sorted out first. If the outcome of this test is satisfactory, we will proceed by coupling the LES with a RANS-based prediction method for the near-wall shear stress distribution.

REFERENCES

BAGGETT, J. S., JIMÉNEZ, J., & KRAVCHENKO, A. G. 1997 Resolution requirements in large-eddy simulations of shear flows. *Annual Research Briefs 1997*,

Center for Turbulence Research, NASA Ames/Stanford Univ., 51-66.

CABOT, W. 1995 Large-eddy simulation with wall models. *Annual Research Briefs 1995*, Center for Turbulence Research, NASA Ames/Stanford Univ., 41-49.

CABOT, W. 1996 Near-wall models in large eddy simulation of flow behind a backward-facing step. *Annual Research Briefs 1996*, Center for Turbulence Research, NASA Ames/Stanford Univ., 199-210.

CABOT, W. 1997 Wall models in large eddy simulation of separated flow. *Annual Research Briefs 1997*, Center for Turbulence Research, NASA Ames/Stanford Univ., 97-106.

DRILLER, D. 1998 Numerical experiments in selective manipulation of a separating turbulent boundary layer. *Diploma thesis,* TU Berlin, Dept. of Mathematics (in German). Available from library of Hermann-Foettinger-Institut, Sekr. HF 1, Strasse des 17. Juni 135, 10623 Berlin, Germany.

FATICA, M., KALTENBACH, H.-J., & MITTAL, R. 1997 Validation of large-eddy simulation in a plain asymmetric diffuser. *Annual Research Briefs 1997*, Center for Turbulence Research, NASA Ames/Stanford Univ., 23-36.

JIMÉNEZ, J., & MOSER, R. 1998 LES: Where are we and what can we expect? *AIAA 98-2891.*

JOHNSON, D. A., & COAKLEY, T. J. 1990 Improvements to a nonequilibrium algebraic turbulence model. *AIAA J.* **28,** 2000-2003.

KALTENBACH, H.-J., FATICA, M., MITTAL, R., LUND, T. S., & MOIN, P. 1998 Study of flow in a planar asymmetric diffuser using large eddy simulation. *Submitted to J. Fluid Mech.*

LUND, T. S., WU, X., & SQUIRES, K. D. 1998 Generation of turbulent inflow data for spatially-developing boundary layer simulations. *J. Comp. Phys.* **140,** 233-258.

WU, X., & SQUIRES, K. D. 1998 Prediction of the three-dimensional turbulent boundary layer over a swept bump. *AIAA J.* **36,** 505-514.

On the feasibility of merging LES with RANS for the near-wall region of attached turbulent flows

By Jeffrey S. Baggett

1. Motivation and objectives

The large number of grid points required in the near-wall region of attached turbulent boundary layers is the chief obstacle to applying large eddy simulation (LES) to many flows of engineering interest. Current subgrid scale models do not accurately model the subgrid scale (SGS) Reynolds stresses (Jiménez & Moser 1998). Thus, if the LES is to include the near-wall region, the filter width has to be such that most of the Reynolds stresses are carried by resolved motions. This requires the filter width to scale as a fixed fraction of the local turbulent integral scales which are proportional to the distance from the wall. Baggett, *et al.* (1997) calculated that the number of grid points required for accurate LES of a turbulent boundary layer scales as $N \sim Re_\tau^2$.

Several approaches have been proposed to alleviate these near-wall resolution requirements, and nearly all of them fall into one of two categories. The first, and most common, approach is to replace the no-slip boundary condition with an approximate boundary condition. Usually, the wall stresses are modeled and the transpiration velocity is set to zero. This approach was introduced by Schumann, who assumed the streamwise wall stress was in phase with the streamwise velocity at the first off-wall grid point (1975). Improvements to the basic idea of Schumann, that the wall stress is a simple deterministic function of the velocity at the first wall point, have been made (Grötzbach 1987, Piomelli *et al.* 1989, Hoffmann & Benocci 1995). More recently, a two-layer approach has been employed in which the three-dimensional unsteady boundary layer equations are integrated on an embedded near-wall grid to estimate the wall stresses (Balaras *et al.* 1996, Cabot 1995, 1996, 1997). There have also been recent attempts to provide boundary conditions which specify the velocities on some plane parallel to the wall, but these have met with limited success (Baggett 1997, Jiménez & Vasco 1998, Nicoud *et al.* 1998).

In the second approach to wall modeling, which we explore in this report, the no-slip boundary condition is applied at the wall, requiring the wall-normal filter width to be refined near the wall. However, the filter width in the directions parallel to the wall is not refined so that the near-wall structures which carry the Reynolds stresses must be accounted for by the SGS model. A simple approach is to supplement the SGS model with a RANS eddy viscosity model in the vicinity of the wall. This idea was originally proposed by Schumann (1975) who used a mixing length eddy viscosity to supplement the Smagorinsky eddy viscosity in the near-wall region. Moin & Kim (1982) and Sullivan *et al.* (1994) have explored similar approaches. More recently, Spalart *et al.* (1998) have advocated the use of the one-equation Spalart-Allmaras eddy viscosity model as an SGS model. The length scale

in the destruction term is modified so that the eddy viscosity crosses over from the usual Spalart-Allmaras RANS eddy viscosity near the wall to a proposed LES eddy viscosity, similar to that of Smagorinsky, away from the wall. Spalart, *et al.* call this approach "Detached-Eddy Simulation" (DES) since it is intended to be used in regions, such as separated regions, in which only eddies that are detached from the surface must be resolved for accurate LES of the flow away from the wall.

In this report, we explore the feasibility of using RANS eddy viscosity models to supplement the SGS model in the near-wall region. This exploration is motivated by Durbin's development of the $v2f$ eddy viscosity RANS model which has been shown to give good near-wall predictions in a variety of flows (Durbin 1991, 1995). Unfortunately, as we shall see below, a direct crossover to RANS in the near-wall region is unlikely to be successful in attached turbulent boundary layers. In the next section our numerical experiments in turbulent channel flow are described. In §2.1 two different techniques for adding a RANS eddy viscosity model to a conventional LES eddy viscosity model in the near-wall region are described. In §2.2 we argue that the failure of such models is due to the formation of an artificial near-wall turbulent cycle with streamwise streaks and vortices occurring at scales dictated by the grid resolution and not by near-wall physics. The artificial cycle is worth investigating because it appears to explain the overly large streamwise velocity fluctuations in the near-wall region as well as the overly large additive logarithmic law constants frequently observed in large eddy simulations of turbulent boundary layers and channel flows. Finally, in §2.3 we mention some other wall modeling approaches being explored at CTR and end with some concluding remarks in §3.

2. Accomplishments

Turbulent channel flow simulations are a good test bed for studying crossovers between LES and RANS since the near-wall dynamics are similar to those in many flows of engineering interest. The Navier-Stokes equations are discretized with second order finite differences in the spatial dimensions and third order Runge-Kutta/Crank Nicolson in time. The subgrid scale model is the Smagorinsky model with the coefficient determined by the plane-averaged dynamic procedure (Germano *et al.* 1991). Unless otherwise stated, all quantities are nondimensionalized by the friction velocity, u_τ, and channel half-height, h, with the usual skin-friction Reynolds number being defined as $Re_\tau = u_\tau h/\nu$.

The computational domain used for all simulations is $[0, 2\pi] \times [-1, 1] \times [0, 2\pi/3]$ with the coordinates representing the streamwise, wall-normal, and spanwise directions, respectively (denoted by x, y, and z below). The spanwise width of the domain is probably inadequate to correctly capture the large eddies which shape the wake region near the channel center, but this is of little consequence for the present study since we are primarily interested in the near-wall region. The grid used has 32 uniformly spaced points in each of the periodic horizontal directions and anywhere from 69 to 101 points in a hyperbolic tangent stretched mesh for the wall-normal direction. The stretching is determined so that the first wall-normal grid point is located within 2 wall units (ν/u_τ) of the wall. In all cases, the mean streamwise pressure gradient is equal to the wall stress, that is, $-\partial P/\partial x = \tau_w = 1$.

2.1 Blending SGS and RANS eddy viscosity models

Two different approaches for incorporating a RANS eddy viscosity in the near-wall region are tested here, the first is designated **Model 1**:

$$\tau_{ij} - \frac{1}{3}\tau_{kk}\delta_{ij} = -\nu_t[\bar{S}_{ij} - (1 - f(y))\langle\bar{S}_{ij}\rangle] - f(y)\nu_R\langle\bar{S}_{ij}\rangle \tag{1}$$

and, **Model 2**:

$$\tau_{ij} - \frac{1}{3}\tau_{kk}\delta_{ij} = -[(1 - f(y))\nu_t + f(y)\nu_R]\bar{S}_{ij}, \tag{2}$$

where τ_{ij} is the usual SGS stress tensor, ν_t is the dynamic Smagorinsky eddy viscosity, and ν_R is the eddy viscosity furnished by an external RANS simulation, which in this case was Durbin's $v2f$ model. The $\langle\cdot\rangle$ denotes a plane average. The "blending" function $f(y)$ facilitates merging the RANS and LES descriptions of the flow. In the case of the second model, $f = 0$ corresponds to the original LES model and $f = 1$ corresponds to a fully RANS model. Generally speaking, f should be a function of the resolution which might be parameterized by the ratio Δ/L_ϵ, where Δ is a measure of the filter width and L_ϵ is an estimate of the turbulent integral dissipation length. However, in the numerical experiments conducted here, f was estimated *a priori* from a mean-flow momentum balance as will be discussed further below.

Model 1 is essentially the model of Schumann (1975) in which the near-wall mixing length eddy viscosity has been replaced with a more general eddy viscosity calculated by the $v2f$ model. The RANS eddy viscosity, ν_R, appears only with the plane averaged resolved strain rate and affects only the mean flow directly. Model 2 is similar to the DES approach (Spalart *et al.* 1998) in which the eddy viscosity parameterizes SGS turbulence away from the wall and all turbulence near the wall. Although, in the DES approach the blending between the RANS and LES regions is accomplished by modifying the dissipation length scale in the transport equation for the eddy viscosity instead of using an explicit blending function f.

Both models were tested in LES of turbulent channel flow at $Re_\tau = 1000$ on a $32 \times 69 \times 32$ mesh. The blending function was estimated through a mean momentum balance using Eqs. (1) and (2) for the subgrid scale models, the resolved stress distribution from an LES simulation with no RANS correction, and the target mean velocity profile from a separate $v2f$ RANS calculation. The profiles of f are shown in Fig. 1. Both models produced somewhat improved mean flow results in the sense that the additive constant in the log-law was approximately correct (instead of being over-estimated by nearly a factor of two without any RANS correction). However, other details of the flow were completely wrong. Model 1 yielded near-wall streamwise velocity fluctuations that were much too high. Model 2 did a better job of estimating the magnitude of the near-wall fluctuating velocities, but the peaks were too far from the wall, and in general the viscous and buffer regions were much too thick. For Model 2 the blending function f peaked at a value of approximately 0.25 in the buffer region. Higher values of f (closer to $f = 1$ corresponding to all

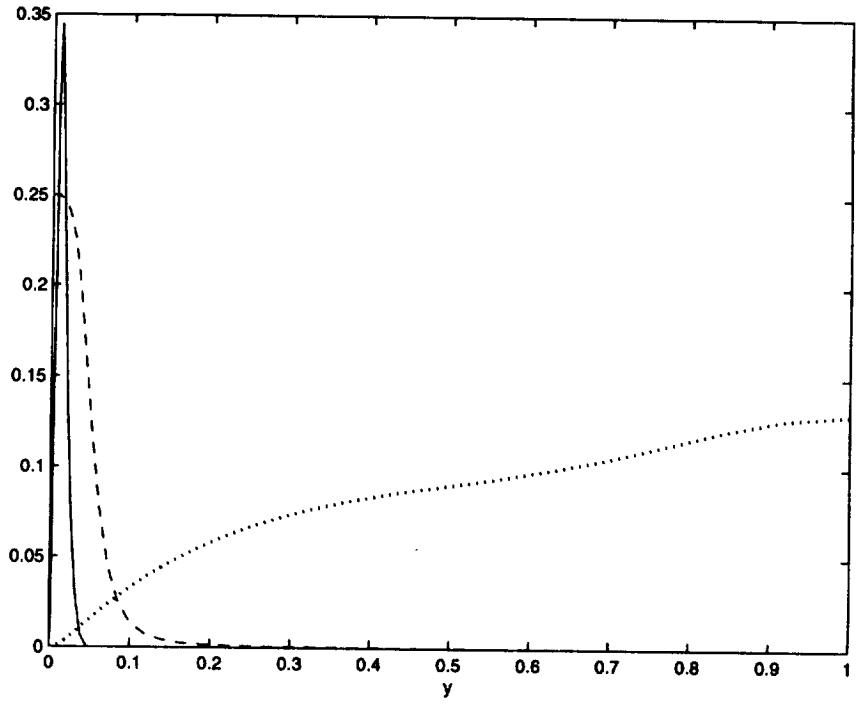

FIGURE 1. Profiles of the blending functions f used for Model 1 (solid line) and Model 2 (dashed line) at $Re_\tau = 1000$. The $v2f$ eddy viscosity is shown as the dotted line.

RANS eddy viscosity) lowered the additive constant in the logarithmic region and further thickened the buffer region.

Closer inspection of the results showed that in both cases the near-wall region contained streamwise vortices and streaks whose horizontal dimensions were much too large. For instance, the streamwise streaks were observed to have a mean spanwise spacing of nearly 260 wall units instead of the physical spacing of 100 wall units. The persistence of this artificial near-wall turbulent cycle makes it unlikely that simple crossovers from LES to RANS models in the near-wall region can be used for LES of turbulent boundary layers as will be discussed in the next section.

2.2 Artificial near-wall turbulence

The near-wall turbulence cannot be completely parameterized by a RANS model because the near-wall region would be effectively laminar and there would be no fluctuating velocities to provide boundary conditions to the turbulent logarithmic region of the outer LES. If the strength of the near-wall RANS contribution is reduced, then only resolved Reynolds stress or viscous stress can balance the difference between the pressure gradient and the contribution from the RANS eddy viscosity. Of course, instabilities ensure the existence of turbulent motions unless the effective Reynolds number, due to the addition of RANS eddy viscosity, is very low. However, as we shall see below, the turbulent motions supported by the simulation are

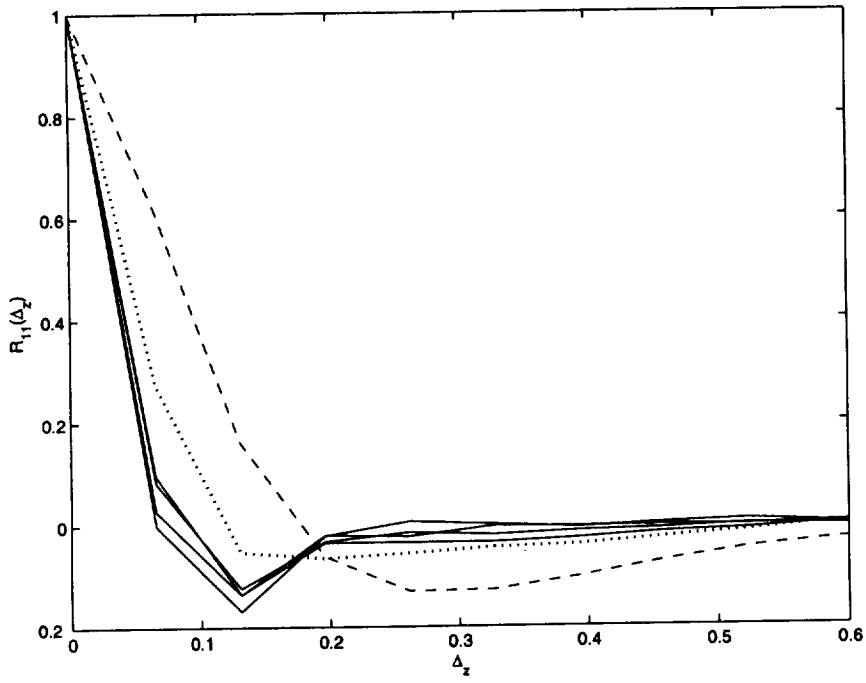

FIGURE 2. Spanwise correlation of streamwise velocity at $y^+ = 10$. There a 4 solid curves corresponding to $Re_\tau = 1000, 2000, 4000$ and $Re_\tau = 1000$ with Model 1 in §2.1. The dotted line corresponds to $Re_\tau = 1000$ with Model 2 in §2.2. Note the slightly larger streak spacing. The dashed line is $Re_\tau = 200$ and the streak spacing is $\Delta_z^+ \approx 105$.

artificial.

The no-slip boundary condition produces a near-wall viscous region in which the mean pressure gradient is balanced only by mean viscous stress so that $\partial\langle U\rangle/\partial y = Re_\tau$ at the wall. The core flow is fully turbulent outside the buffer region so that mean shear scales approximately like $1/y$. In the intermediate buffer region the mean shear has to be reduced by wall-normal streamwise momentum transport, i.e. mean Reynolds stress, to couple the core flow to the wall. In the absence of an SGS model that carries a significant amount of the Reynolds stresses, only resolved motions can contribute the necessary Reynolds stresses. In simulations with a no-slip boundary condition and coarse horizontal resolution, with or without a RANS model contribution, the near-wall region develops an artificial self-sustaining turbulent process consisting of streamwise vortices and streaks with horizontal dimensions dictated by the discretization (the effective horizontal filter width) to carry the necessary Reynolds stresses.

The existence of the overly large streamwise streaks and vortices was confirmed by flow visualizations. Further evidence is offered in Fig. 1 where the spanwise correlation of the streamwise velocity is plotted for several different simulations at

$y^+ = 10$. The location of the first minimum in the spanwise correlation is a measure of the mean distance between the centers of adjacent high and low speed streaks. For Reynolds numbers greater than at least $Re_\tau = 1000$, without the addition of a near-wall RANS model, the streak spacing is independent of the Reynolds number. Visualizations of the near-wall streamwise vorticity showed that the near-wall streamwise vortices had the smallest possible spanwise extent that could be supported on the grid; that is, they were essentially always two grid points wide. When Model 1 was used to blend in a near-wall RANS model, the near-wall turbulent cycle was essentially the same as with no RANS model, only slightly weaker since the wall-normal shear is slightly reduced by the additional mean forcing term. The dotted line in Fig. 1 shows the effect of Model 2 on the spanwise streak spacing. The net effect of Model 2 is to increase the overall viscosity in the neighborhood of the wall, thus decreasing the effective Reynolds number of the artificial near-wall turbulence, leading to larger streaks and a mean-flow profile corresponding to a lower Reynolds number simulation.

As the Reynolds number increases, the viscous stress contribution decreases and the combined SGS and resolved Reynolds stresses must peak closer to the wall. However, since the near-wall streamwise vortices and streaks are constrained to have horizontal dimensions dictated by the grid, their wall-normal to horizontal aspect ratio must increase as the whole process moves closer to the wall. The resulting artificial near-wall turbulence is less effective at providing wall-normal momentum transport as is demonstrated in Fig. 2 where the correlation coefficient of the streamwise and wall-normal velocity fluctuations is plotted for several Reynolds numbers. Since the correlation between u' and v' is decreasing as the Reynolds number increases, the mean shear increases to increase the viscous stress. Some of this mean shear is rotated towards the wall by the streamwise vortices, resulting in the overly large peak in u' and an increased value of the mean Reynolds stress $-\langle u'v' \rangle$. The correlation curves in Fig. 2 also show that the correlation increases adjacent to the wall for all but the $Re_\tau = 200$ simulation, which serves as another indication of the incorrect physics. Moreover, the correlation curve (the dotted line in Fig. 2) for the simulation at $Re_\tau = 1000$ with Model 2 shows higher correlation indicating a lower effective Reynolds number.

Adding in a RANS eddy viscosity through an SGS model like Model 1 can only help the situation slightly. Since the RANS eddy viscosity only affects the mean flow, the near-wall region will still have the artificial near-wall turbulence, which remains effectively unaltered. While it may be possible to find a blending function f which produces a reasonable mean-flow profile with Model 1 in spite of the artificial near-wall turbulence, it seems unlikely that f could be found *a priori* to produce a predictive representation of the near-wall region. In the other approach to blending in a RANS eddy viscosity, as in Model 2 the effect is to lower the effective Reynolds number of the artificial near-wall turbulence resulting in *larger* streamwise vortices and streaks and mean flow profiles corresponding to lower Reynolds numbers. Again, it might be possible to choose a blending function f which produces a mean flow profile with the right gross characteristics, but it seems unlikely that this

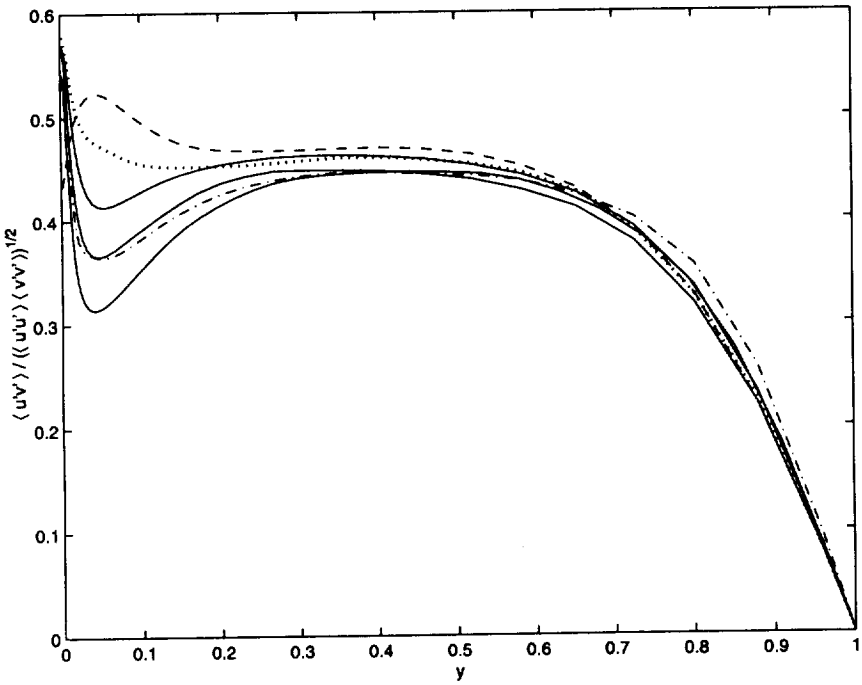

FIGURE 3. Correlation coefficient of the wall-normal and streamwise velocity fluctuations. The three solid lines, in order of decreasing correlation, correspond to LES with no near-wall RANS model at $Re_\tau = 1000, 2000, 4000$, respectively. The dashed line is $Re_\tau = 200$. The dash-dotted line and the dotted line are at $Re_\tau = 1000$ with Models 1 and 2,respectively.

can be done in an *a priori* manner. The overall trend of increasing near-wall eddy viscosity is to increase the dimensions of the near-wall turbulent cycle which should be accounted for entirely by the subgrid scale motions at high Reynolds numbers. The only other alternative is to increase the near-wall RANS eddy viscosity until the flow is effectively "laminar" there, but this will result in an artificial transition region between the laminar-like near-wall flow and the turbulent core flow.

The persistence of this artificial near-wall turbulence explains some common problems encountered in LES of attached turbulent boundary layers. The overly large peak in u' and the overly high value of the additive constant in the logarithmic region are both determined by the inefficient wall-normal transport of streamwise momentum by the distorted near-wall turbulence. Interestingly, without any RANS correction near the wall, the value of additive constant in the logarithmic region increases linearly with the Reynolds number; see Fig. 4. Increasing the near-wall eddy viscosity only compounds the problem.

2.3 Other wall modeling work at CTR

Unless vastly improved, fully anisotropic SGS models are found for the near-wall region, attempts to enforce the no-slip boundary condition are likely to fail

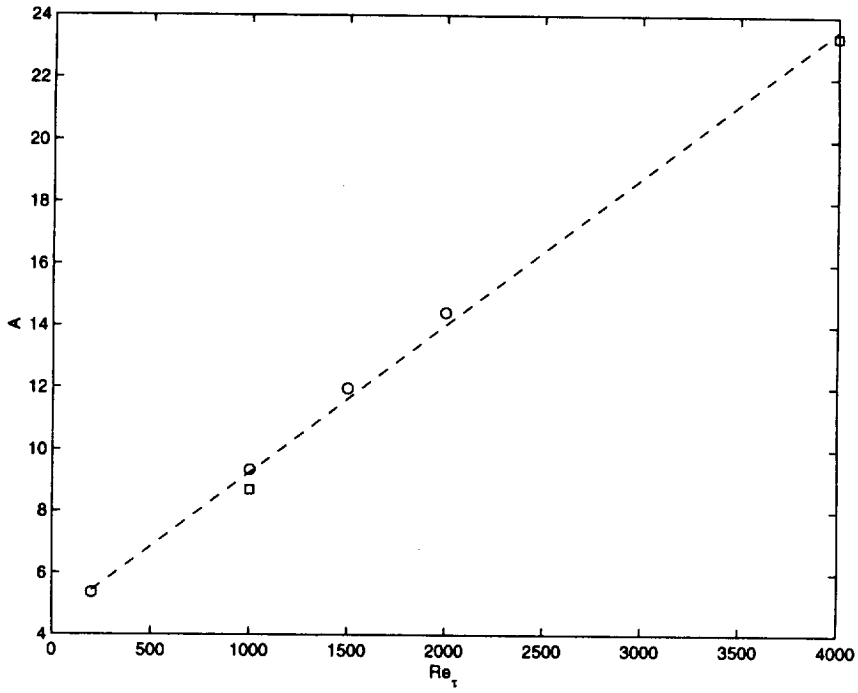

FIGURE 4. Value of the log-region intercept (determined from the mean velocity at 150 wall units) A in $U = \log(y^+)/\kappa + A$ as a function of Reynolds number for LES simulations without any near-wall RANS corrections. The squares indicate simulations with 101 wall-normal points and the circles correspond to 69 wall-normal points. The dashed line is the least squares fit of the data. For $Re_\tau = 200$, we have $A \approx 5.4$.

unless the LES has resolution similar to that of a direct numerical simulation in the near-wall region. This is because the outer flow is coupled to the wall through the buffer region which develops an artificial near-wall turbulent cycle to exchange streamwise momentum with the wall. The source of the problem is the no-slip boundary condition which can only be "seen" by a properly resolved inner flow. Usually this is addressed by providing approximate wall stress boundary conditions (with zero transpiration velocity).

Most of the current wall stress models assume that the first off-wall grid point of the LES is in the logarithmic region. Thus the first grid point has to be located at some minimum distance from the wall which depends on the Reynolds number. This problem can be removed, thus allowing near-wall grid refinement without a no-slip boundary condition, by neglecting the viscosity in the outer LES equations and integrating them down to and even on the wall. The horizontal velocities are allowed to slip on the wall and the zero transpiration condition is maintained so that the turbulent length scales are set by the blocking effect of the wall. The inviscid LES equations at the wall require the surface values of the SGS stress tensor,

which are provided by an auxiliary model that must incorporate the effects of the unresolved near-wall turbulence (and hence, the effects of viscosity). The inviscid approximation is only expected to be valid at high Reynolds numbers where the wall-normal extent of the viscous and buffer regions is very small compared to the LES region of interest. In separated regions, where the local Reynolds numbers are relatively low, it may be necessary to include viscous terms so that the no-slip boundary condition can be applied. The issue of changing the boundary conditions in this zonal manner still must be addressed.

We are currently developing this framework in LES of turbulent channel flow and in the separated boundary layer computations reported by Cabot elsewhere in this volume. The surface values of the SGS stress tensor are given by integrating the three-dimensional unsteady boundary layer equations, with a mixing length eddy viscosity, which are driven by the wall slip velocities as in the two-layer wall-modeling approach mentioned in the introduction. Efforts are also underway to replace the wall-damped mixing length eddy viscosity in the boundary layer equations with a model similar to Durbin's $v2f$ model.

3. Future plans

The results presented in this report indicate that a direct blending of RANS and LES eddy viscosities as a way of merging RANS and LES regions is unlikely to work in near-wall regions where it is important to have good boundary conditions for not only the mean flow, but also the fluctuating velocities. This is because the outer flow is coupled to the wall through a physically incorrect buffer region. However, merging LES and RANS may certainly be possible in flows where the details of the near-wall fluctuations are not important for the LES of the outer flow as is envisioned by Spalart *et al.* (1998) in their DES approach. However, there is still the issue of generating high Reynolds number turbulent inflow conditions at the entrance to the separated region for which no satisfactory solution is presently available.

It seems that the no-slip boundary condition must be abandoned for high Reynolds number LES. Instead, as mentioned in §2.3, we are currently testing the inviscid LES core flow approximation with estimates of the surface SGS stresses coming from the integration of separate three-dimensional unsteady boundary layer equations that represent the near-wall region.

Two other directions with regards to the near-wall sublayer equations are also being explored. The first direction is to replace the wall-damped mixing length eddy viscosity in the three-dimensional near-wall boundary layer equations with the more general eddy viscosity generated by a coupled $v2f$ RANS simulation (Durbin 1991). In the second direction under investigation, the three-dimensional boundary layer equations are reduced to a simplified set of one-dimensional ordinary differential equations in the wall-normal direction at each location where a wall-stress estimate is required (W. C. Reynolds, private communication, 1998).

REFERENCES

AKSELVOLL, K. & MOIN, P. 1995 Large eddy simulation of turbulent confined coannular jets and turbulent flow over a backward facing step. *Dept. of Mech. Eng. Tech. Rep.* **TF-63,** Stanford Univ.

BAGGETT, J. S. 1997 Some modeling requirements for wall models in large eddy simulation. *Annual Research Briefs 1997*, Center for Turbulence Research, NASA Ames/Stanford Univ., 123-134.

BAGGETT, J. S., JIMÉNEZ, J., & KRAVCHENKO, A. G. 1997 Resolution requirements in large-eddy simulations of shear flows. *Annual Research Briefs 1997*, Center for Turbulence Research, NASA Ames/Stanford Univ., 51-66.

BALARAS, E., BENOCCI, C. & PIOMELLI, U. 1996 Two-layer approximate boundary conditions for large-eddy simulations. *AIAA J.* **34,** 1111-1119

CABOT, W. 1995 Large-eddy simulations with wall models.*Annual Research Briefs 1995*, Center for Turbulence Research, NASA Ames/Stanford Univ., 41-50.

CABOT, W. 1996 Near-wall models in large eddy simulations of flow behind a backward-facing step. *Annual Research Briefs 1996*, Center for Turbulence Research, NASA Ames/Stanford Univ., 199-210.

CABOT, W. 1997 Wall models in large eddy simulation of separated flow. *Annual Research Briefs 1997*, Center for Turbulence Research, NASA Ames/Stanford Univ., 97-106.

DURBIN, P. A. 1991 Near wall turbulence closure modeling without "damping functions". *Theor. Comput. Fluid Dyn.* **3,** 1-13.

DURBIN, P. A. 1995 Separated flow computations with the $\kappa-\epsilon-\nu^2$ model. *AIAA J.* **33,** 659-664.

GERMANO, M., PIOMELLI, U., MOIN, P., & CABOT, W. H. 1991 A dynamic subgrid-scale eddy viscosity model. *Phys. Fluids A* **3**, 1760-1765. Erratum: *Phys. Fluids A* **3**, 3128

GRÖTZBACH, G. 1987 Direct numerical and large eddy simulation of turbulent channel flows. *Encyclopedia of fluid mechanics.* Gulf Publications.

JIMÉNEZ, J., & MOSER, R. 1998 LES: Where are we and what can we expect? *AIAA 98-2891.*

JIMÉNEZ, J., & VASCO, C., 1998 Approximate lateral boundary conditions for turbulent simulations. *Proceedings of the 1998 Summer Program*, Center for Turbulence Research, NASA Ames/Stanford Univ., 399-412.

MOIN, P. & KIM, J. 1982 Numerical investigations of turbulent channel flow. *J. Fluid Mech.* **118,** 341-378.

NICOUD, F., WINCKELMANS, G., CARATI, D., BAGGETT, J., & CABOT, W. 1998 Boundary conditions for LES away from the wall. *Proceedings of the 1998 Summer Program*, Center for Turbulence Research, NASA Ames/Stanford Univ., 413-422.

SCHUMANN, U. 1975 Subgrid scale model for finite difference simulations in plane channels and annuli. *J. Comp. Phys.* **18**, 376-404

SPALART, P.R., JOU, W.-H., STRELETS, M. & ALLMARAS, S.R. 1998 Comments on the feasibility of LES for wings, and on a hybrid RANS/LES approach. *Advances in DNS/LES*. Greyden Press.

SULLIVAN, P.P., MCWILLIAMS, J.C. & MOENG, C.-H. 1994 A subgrid-scale model for large-eddy simulation of planetary boundary-layer flows. *Boundary-Layer Met.* **71**, 247-276

Large-eddy simulation of a separated boundary layer

By W. Cabot

1. Motivation and objectives

In tests of wall models on a very coarse grid in the flow behind a backward-facing step (Cabot 1996), simple models in which wall stresses were modeled by assuming a local log law gave good results in attached regions but underpredicted the magnitude of the negative skin friction in the primary separated region, compared with well resolved large-eddy simulation (LES) results. More complicated thin boundary layer equations were able to give better overall results, but the negative skin friction predicted by this model was observed to be somewhat too large in magnitude. Because of the very coarse resolution, no model was able (or really expected) to capture secondary recirculation features in the corner. Subsequent tests (Cabot 1996, 1997) were ambiguous as to cause of this behavior, noting that the near-wall eddy viscosity model (a mixing length prescription with a wall damping function) was ill suited for separated flow and that the standard subgrid-scale (SGS) model used was inaccurate for coarsely gridded near-wall meshes. The severe corner geometry was also thought to be complicating the interpretation of the results. To provide a clearer test case for wall modeling in complex, separated flow without such geometrical complications, a new test case was chosen featuring mild separation on a flat plate due to an induced adverse pressure gradient, for which Na & Moin (1998) had performed a direct numerical simulation (DNS) at a low Reynolds number. The goal of recent work has been to perform a less expensive LES of this flow with a well resolved wall for use as a test case for evaluating the performance of wall models with coarsely resolved walls (Cabot 1997). Initially, the same low Reynolds number case as the DNS was to be simulated to validate the LES with well resolved walls and then used to perform tests of LES with coarsely resolved walls using wall models. Further, with the general shift to parallel supercomputing architectures and the diminishing availability of serial time, the separated boundary layer codes needed to be converted to a portable parallel framework (MPI) and validated with results from the extant serial vector code.

The status of the separated boundary layer simulations is given in §2 and the directions for future simulations and wall model tests therein are given in §3.

2. Accomplishments

The flow configuration for the separated boundary layer simulation is described in detail by Na & Moin (1998): A flow field from Spalart's (1988) DNS boundary layer simulation is perturbed and interpolated onto the inflow plane of flow over a flat plate. Strong sucking is introduced along the top zero-vorticity boundary followed by strong blowing, which induces a strong adverse pressure gradient in the

middle of the computational domain. The flow undergoes mild separation along the bottom wall, then partially recovers before it exits the domain using convective outflow boundary conditions. The Reynolds number at the inflow plane is about 300 based on momentum thickness and 500 based on displacement thickness δ^*. The computational domain is $357 \times 64 \times 50$ in units of δ^* in the streamwise, wall-normal, and spanwise directions, respectively. The grid is uniform in the streamwise and spanwise directions and stretched with hyperbolic tangent profiles in the wall-normal direction.

2.1 Codes

Serial Code. The second-order staggered central finite difference serial code used by Na & Moin (1998) was modified to include the dynamic SGS model, both in its standard form (Germano *et al.* 1991, Lilly 1992) and in a "mixed" form (Zang *et al.* 1993, Vreman *et al.* 1994). In the former, the trace-free (*) part of residual stress is modeled as a purely dissipative term:

$$(\overline{\boldsymbol{u}\boldsymbol{u}} - \overline{\boldsymbol{u}}\,\overline{\boldsymbol{u}})^* \sim -2\nu_t \overline{\boldsymbol{S}}\,, \tag{1}$$

where $(\bar{})$ denotes the filter, ν_t is the eddy viscosity, and $\boldsymbol{S}$ is the strain tensor; in the latter, the model also includes a self-similar part:

$$(\overline{\boldsymbol{u}\boldsymbol{u}} - \overline{\boldsymbol{u}}\,\overline{\boldsymbol{u}})^* \sim (\overline{\overline{\boldsymbol{u}}\,\overline{\boldsymbol{u}}} - \overline{\overline{\boldsymbol{u}}}\,\overline{\overline{\boldsymbol{u}}})^* - 2\nu_t \overline{\boldsymbol{S}}\,. \tag{2}$$

Further, the option to use two forms of the eddy viscosity was implemented: either a "Smagorinsky" (1963) form,

$$\nu_t = C\overline{\Delta}^2 (2\overline{\boldsymbol{S}} : \overline{\boldsymbol{S}})^{1/2}\,, \tag{3}$$

where $\overline{\Delta}$ is the effective filter width, or a "Kolmogorov" form (Carati *et al.* 1995),

$$\nu_t = C\overline{\Delta}^{4/3} \varepsilon^{1/3}\,, \tag{4}$$

where the dissipation rate ε is assumed to be constant with filter width. In most runs the Kolmogorov form was used since it is less expensive to use with the dynamic procedure and gives very similar results compared with the Smagorinsky form; the Kolmogorov form was used for all of the results reported later in this section.

The serial LES code originally used second-order test filters and, in the case of the mixed model, second-order grid filters as well; these are of the form

$$\widehat{u} = u + (h^2/6)\delta^2 u\,, \tag{5}$$

where h is the filter half-width and δ^2 is the discrete second derivative. Second-order filters used with the standard dynamic procedure were found to generate large, spurious eddy viscosities in the regions below the vigorous top-wall transpiration, which often led to unstable growth of a spurious velocity signal there. This occurs because

the second-order filter produces residuals for low-order, large-scale variations in the mean flow that have nothing to do with turbulence. For example, if u in Eq. (5) has a linear variation in x, then $\widehat{uu} - \widehat{u}\widehat{u} = (h^2/6)(du/dx)^2$. The mixed model does not suffer as much from this defect, because residuals up to fourth order are treated by the self-similar term in the model, removing them from the dissipative term in the dynamic procedure. For tests with the standard dynamic procedure, it was necessary to implement fourth-order test filters (Vasilyev *et al.* 1998) of the form

$$\widehat{u} = u - (h^4/16)\delta^4 u \,, \tag{6}$$

which also greatly reduces spurious eddy viscosity generation although it is not necessarily consistent for use in second-order codes.

Parallel Code 1. The previous serial LES code was ported to a MPI version (with M. Fatica), which allows it to run on a variety of parallel machines with little modification. Along the way, the solver was updated to enforce continuity at each substep in the time advancement scheme rather than at the end of the full time step only, which increases the accuracy of the solver. Further, a bug was found (and corrected) in the original serial code's inflow interpolation scheme that was adding spurious noise to the inflow signal. The computational domain is chunked only in the wall-normal direction into planar slabs, which allows plane filtering to be performed in the standard dynamic procedure without any additional processor communication. The dynamic mixed SGS model has not been implemented in this version of the code. This parallel LES code has been run on a SGI Origin 2000 and Cray T3Es, and it has been validated by a detailed comparison with results from the serial code.

Parallel Code 2. A newer, faster LES boundary layer code has been supplied to us by C. Pierce (personal communication), which was written from the ground up in Fortran 90 and MPI, also using second-order finite differencing and a standard implementation of the dynamic procedure for the SGS model. One significant structural difference from the previous code is that the domain is chunked both in the wall-normal and streamwise directions for greater efficiency in communication. The appropriate boundary conditions for the separated boundary layer case have been implemented, as well as fourth-order test filtering for the dynamic procedure. The inflow conditions in this code are interpolated in a different way than in Na & Moin's (1998) code, which leads to some differences in the results; the issue of setting up consistent inflow conditions will be discussed later in more detail. This code is currently being tested on an Origin 2000 and will be ported to a T3E as well. Because Pierce's code is cleaner and appears to be appreciably faster than the parallel version based on Na & Moin's code, it will probably be used as the primary simulation code in future work.

2.2 Preliminary results

The LES test cases use the same domain size and boundary conditions as Na & Moin's (1998) DNS case except that inflow conditions are interpolated onto a coarser grid. Two LES grids were chosen: *Grid 1* resolves the viscous region along

the lower wall, using the same stretching as Na & Moin in the wall-normal direction with half as many grid points; *Grid 2* does not resolve the wall, using an even coarser, nearly uniform grid. (The grid cannot be coarsened very much near the top boundary without developing numerical instabilities in the laminar blowing region.) Grid 1 uses 7 times fewer computational cells than the DNS: $256 \times 108 \times 64$ computational cells in the streamwise, wall-normal, and spanwise directions, respectively, as compared to $512 \times 192 \times 128$ used in the DNS. The time step based on the CFL criterion is about 4 times greater for this LES case compared to the DNS. Grid 2 uses $160 \times 80 \times 48$ computational cells, or about 20 times fewer grid points than the DNS with time steps about 25 times greater. Near the inlet Grid 1 has about 10 points in the viscous sublayer ($y^+ < 10$) and 45 points in the whole boundary layer, while Grid 2 has about 10 points in the boundary layer with the viscous sublayer completely unresolved. Simulations were performed on these grids with and without the SGS model active to assess its effect. No wall model was used in these initial tests with Grid 2, such that the wall stress was generally much too low.

Grid 1. When no SGS model is active, the turbulence in the inlet section is more intense than in the DNS. Separation occurs later than in the DNS, and the near-wall pressure is too high in the separated region, as seen in Fig. 1 for the wall stress and pressure coefficient. When the SGS model is active, the major effect is a dramatic drop in the wall-normal and spanwise turbulence intensities in the inlet section, as illustrated in Fig. 2 for the wall-normal rms velocity at a height of about half of the inlet boundary thickness. The boundary layer thickens too rapidly upstream of separation, and separation tends to occur early, especially in the case using the dynamic mixed SGS model. The skin friction is seen to drop much too rapidly in the whole inlet section in Fig. 1. Visualizations confirm that the flow in fact undergoes partial relaminarization, then undergoes a transition of sorts back to a turbulent state just in front of the separated region. Reverse flow along the wall appears to travel quite far up the laminar patches ahead of the main separation bubble. This occurs for all SGS models, even though in the mean separation point for the standard dynamic SGS model case appears to be in good agreement with the DNS position.

Grid 2. The relaminarization of the inflow turbulence is less severe in the case with the unresolved wall although it still occurs to some extent. In Fig. 3 the near-wall streamwise velocity is shown in lieu of the wall stress, which cannot be determined reliably on the coarse wall-normal grid. Results for the standard dynamic SGS model are shown using Parallel Codes 1 and 2. Differences in results are seen in the inlet region due to different interpolation schemes of the inflow data (the former using spatial interpolation, the latter using spatial and temporal interpolation). The near-wall velocity stays in fair agreement with the DNS in the inlet region with Code 1 slightly slower and Code 2 showing some excess acceleration. At the outlet, the flow is much faster than in the DNS, which is expected, since the coarse grid cannot predict enough drag on the wall. The fair agreement of the near-wall flow speed in the inlet region is somewhat fortuitous, arising from a balance of

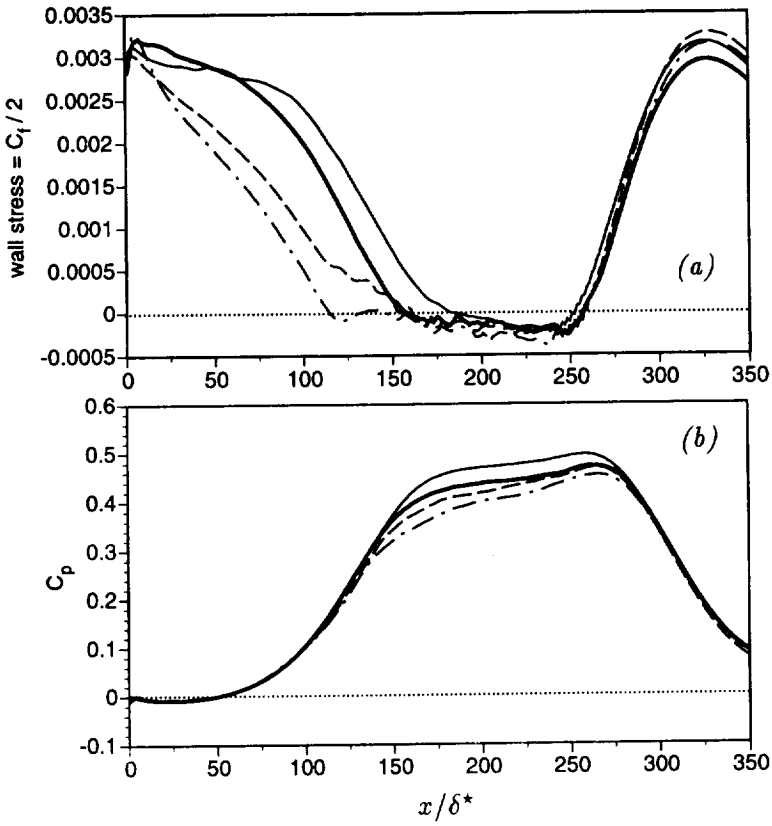

FIGURE 1. (a) The wall stress and (b) the pressure coefficient from the DNS and LES with a well resolved wall (Grid 1): —— Na & Moin's (1998) DNS (serial code); —— Grid 1 with no SGS model (serial code); ---- LES with standard dynamic SGS model (parallel code 1); —·— LES with dynamic mixed SGS model (parallel code 2). The pressure coefficient is set relative to the pressure at $x/\delta^* = 50$.

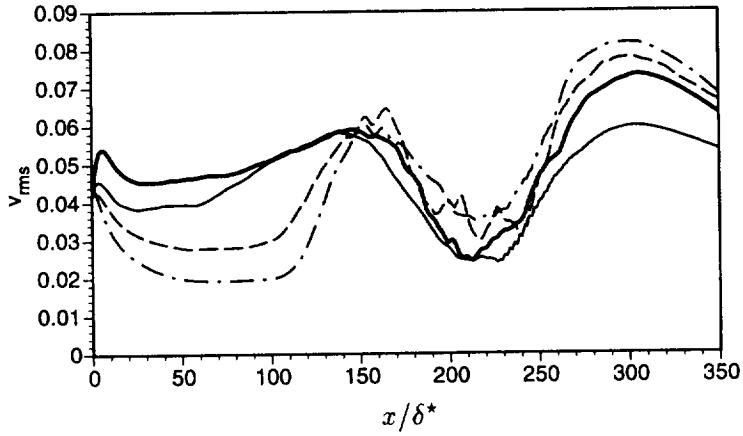

FIGURE 2. The wall-normal rms velocity from the DNS and LES with a well resolved wall (Grid 1) at a height $y = 2.9\delta^*$: same symbols as in Fig. 1.

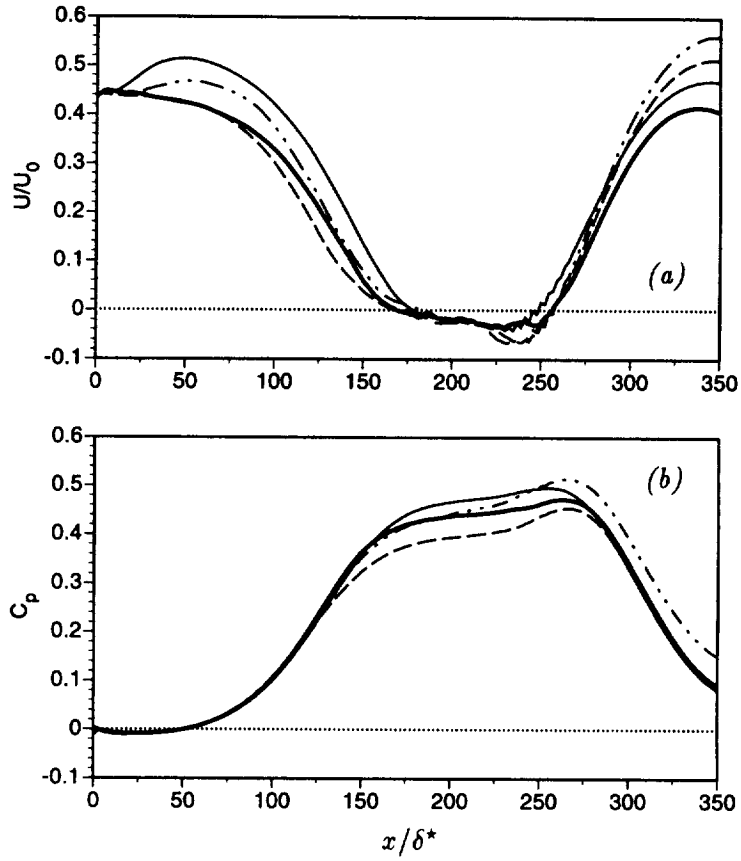

FIGURE 3. (a) The wall stress and (b) the pressure coefficient from the DNS and LES with an unresolved wall (Grid 2): —— Na & Moin's (1998) DNS (serial code); —— Grid 2 with no SGS model (parallel code 1); LES with standard dynamic SGS model using ---- parallel code 1 and —··— parallel code 2. The pressure coefficient is set relative to the pressure at $x/\delta^* = 50$.

too low drag with the opposing effect seen on Grid 1 due to the relaminarization of the inflow turbulence.

The reattachment point appears to be rather insensitive to the SGS model and grid, being set for the most part by the strong blowing peak from the top boundary. When no model is active, the reattachment occurs slightly early, while it occurs at the same location as in DNS when the SGS model is active. While mean flow quantities are not very sensitive to the SGS model downstream of reattachment, the turbulence intensities are much more sensitive, probably reflecting the very different upstream conditions that develop in the inlet region. With no SGS model, the turbulence intensities, that were comparable or higher than DNS values in the inlet region, are lower in the exit region. The reverse is true when an SGS model is active (cf. Fig. 2). Obviously more consistent inflow conditions need to be set up in the different cases to facilitate meaningful comparisons of overall flow statistics.

Calculated flow fields exhibit numerical oscillations for all grids, especially in the wall-normal velocity component near the reattachment point. These oscillations are especially pronounced in Grid 2, which may require some refinement in this region in future simulations to reduce this effect. It is not known if these oscillations are responsible for the pronounced peak near the reattachment point in near-wall velocity and pressure seen in Fig. 3 or if this is due to other factors such as the underprediction of wall stress or shear layer stress. Simulations with wall models will help answer this question.

3. Future plans

3.1 LES

The inflow generation technique described by Lund *et al.* (1998) will be used to provide consistent conditions at the inlet for the different separated boundary layer cases. In this scheme, the same numerical scheme, grid, time step, SGS model, and wall model to be used in the separated boundary layer simulation are used in a zero pressure gradient flat plate simulation in which the inflow data is generated by rescaling a plane in the flow near the outlet (but far enough away from the outlet not to be seriously contaminated by the convective outflow condition). After the inflow simulation has reached a statistical steady state, a history of the flow field at a plane in the middle of the numerical domain with the desired momentum thickness will be recorded and be used as the inlet boundary condition in the separated boundary layer simulation. Initial tests with this scheme successfully remove the strong transients in the inlet section evident with the old scheme. Because these new inflow conditions will necessarily differ to some extent from the original DNS by Na & Moin (1998), it may still be difficult to get a very quantitative comparison between LES and DNS.

In the first series of simulations with the new inflow conditions, the same Reynolds number as in the DNS will be used, mostly to validate the performance of the LES. The dynamic mixed SGS model will also be implemented in the parallel codes for comparison. Later it may prove useful to perform LES of the separated boundary layer with and without wall models at much higher Reynolds numbers, where both the SGS and the wall modeling are expected to perform better.

Wall models will be used to supply wall stresses to the LES with unresolved walls. The first set of tests will involve an approach like that used in simulations of flow over a backward-facing step (Cabot 1996). Solutions of simple ODEs or more expensive PDEs based on thin boundary layer equations are computed on a separate, refined near-wall grid and used to predict the wall stress when matched to outer LES flow conditions; the latter approach has been found to give reasonable mean values of wall stress even in separated regions where the equations are known to be invalid. We then intend to implement the more sophisticated v^2f RANS model (Durbin 1991) in the refined near-wall region. Ultimately we will blend it smoothly into the LES's SGS model throughout the near-wall region using a single grid refined in the wall-normal direction (Shur *et al.* 1998; also see discussion by Baggett in this volume). Also note that because the inflow generation calculations

must use the same wall models as the main calculation, this will also provide an additional test of wall modeling in a zero pressure gradient boundary layer.

3.2 Wall modeling issues

A number of outstanding issues concerning the proper way(s) of simulating near-wall regions remain to be resolved, and we will attempt to address many of these issues in future work.

As demonstrated by Baggett *et al.* (1997), a proper LES must resolve all the large energy-containing scales in the flow, which, however, become very small relative to outer scales near walls both in the wall-normal and tangential directions. An example of a proper (but more expensive) LES is that by Kravchenko & Moin (1998), which used a zonal mesh refined in all directions near the wall. It is more usual in LES of wall-bounded flow to use fine resolution only in the wall-normal direction near walls in conjunction with SGS model based on isotropy and self-similarity in the inertial range (usually modified with a wall damping function or the dynamic procedure to get the right asymptotic behavior); such models are not well suited for the near-wall region because the flow is highly anisotropic and the energy-containing scales in the horizontal directions are not resolved. The flow may be better described by a RANS solution near the walls, which is motivating the search for ways to meld RANS and LES descriptions in the near-wall region (cf. Baggett in this volume). Most RANS models still require special near-wall treatment in the form of wall damping functions. The wall's blocking effect is handled more physically in Durbin's (1991) $v^2 f$ model without the aid of damping functions, but the model is more complex, and it will be a challenge to incorporate it in LES. Another problem with most RANS models and thin boundary layer equations is that they rely on an eddy viscosity parameterization of the Reynolds stress, which is not valid in separated regions where turbulence and Reynolds stress is, to a large extent, convected rather than produced (Le *et al.* 1997). While this suggests that transport equations for Reynolds stresses are required, these are currently felt to be prohibitively expensive. Other options may prove to be more economical, e.g., resolving separated regions (since structures there are largely laminar, albeit small in scale), or applying special scaling or modeling relations in separated regions based on local flow criteria.

Although one can attempt to avoid simulating the near-wall region altogether by placing the numerical boundaries at off-wall locations, it is has proven very difficult to specify accurate enough boundary conditions to avoid generating spurious off-wall boundary layers and large pressure fluctuations (cf. Baggett 1997; Jiménez & Vasco 1998; Nicoud *et al.* 1998), and this approach will probably not be pursued in this flow.

On meshes (or more correctly, *for filters*) that are very coarse in the wall-normal direction near the wall, the issue of defining meaningful filters normal to the wall and consistent wall boundary conditions remains unsettled. This issue is skirted in LES with well resolved walls in which the filter is assumed to be comparable to the grid spacing, since filtering in the wall-normal direction near the wall has little effect. It would be worthwhile to consider performing LES and *a priori* DNS tests on

refined grids but with very broad near-wall filters in order to better understand the effects of near-wall filtering, in particular whether supplemental stresses need to be supplied only at the wall or, as we expect, throughout the boundary layer. Another closely related problem is defining consistent boundary conditions for the outer flow. Because there is no specific spatial information within a given filter width near the wall, one has virtually no wall information for filters much coarser than the viscous sublayer or the buffer region in a boundary layer, and hence both slip conditions and locally permeable conditions are admissible — and perhaps necessary for an accurate description.

Acknowledgments

Some of the simulations were performed on a Cray T3E at the University of Texas under a NPACI grant.

REFERENCES

BAGGETT, J. S. 1997 Some modeling requirements for wall models in large eddy simulation. *Annual Research Briefs 1997*, Center for Turbulence Research, NASA Ames/Stanford Univ., 123-134.

BAGGETT, J. S., JIMÉNEZ, J., & KRAVCHENKO, A. G. 1997 Resolution requirements in large-eddy simulations of shear flows. *Annual Research Briefs 1997*, Center for Turbulence Research, NASA Ames/Stanford Univ., 51-66.

CABOT, W. 1996 Near-wall models in large eddy simulations of flow behind a backward-facing step. *Annual Research Briefs 1996*, Center for Turbulence Research, NASA Ames/Stanford Univ., 199-210.

CABOT, W. 1997 Wall models in large eddy simulation of separated flow. *Annual Research Briefs 1997*, Center for Turbulence Research, NASA Ames/Stanford Univ., 97-106.

CARATI, D., JANSEN, K., & LUND, T. 1995 A family of dynamic models for large-eddy simulation. *Annual Research Briefs 1995*, Center for Turbulence Research, NASA Ames/Stanford Univ., 35-40.

DURBIN, P. A. 1991 Near wall turbulence closure modeling without "damping functions". *Theor. Comput. Fluid Dyn.* **3**, 1-13.

GERMANO, M., PIOMELLI, U., MOIN, P., & CABOT, W. H. 1991 A dynamic subgrid-scale eddy viscosity model. *Phys. Fluids A* **3**, 1760-1765. Erratum: *Phys. Fluids A* **3**, 3128.

JIMÉNEZ, J., & VASCO, C. 1998 Approximate lateral boundary conditions for turbulent simulations. *Proceedings of the 1998 Summer Program*, Center for Turbulence Research, NASA Ames/Stanford Univ., 399-412.

KRAVCHENKO, A., & MOIN, P. 1998 B-spline methods and zonal grids for numerical simulations of turbulent flows. Dept. Mech. Eng. Rep. **TF-73**, Stanford Univ.

LE, H., MOIN, P., & KIM, J. 1997 Direct numerical simulation of turbulent flow over a backward-facing step. *J. Fluid Mech.* **330,** 349-374.

LILLY, D. 1992 A proposed modification of the Germano subgrid-scale closure method. *Phys. Fluids A* **4**, 633-635.

LUND, T. S., WU, X., & SQUIRES, K. D. 1998 Generation of turbulent inflow data for spatially-developing boundary layer simulations. *J. Comp. Phys.* **140,** 233-258.

NA, Y., & MOIN, P. 1998 Direct numerical simulation of a separated turbulent boundary layer. *J. Fluid Mech.* **374,** 379-405.

NICOUD, F., WINCKELMANS, G., CARATI, D., BAGGETT, J., & CABOT, W. 1998 Boundary conditions for LES away from the wall. *Proceedings of the 1998 Summer Program*, Center for Turbulence Research, NASA Ames/Stanford Univ., 413-422.

SHUR, M., SPALART, P. R., STRELETS, M., & TRAVIN, A. 1998 Detached-eddy simulation of an airfoil at high angle of attack. Preprint.

SMAGORINKSY, J. 1963 General circulation experiments with the primitive equations. I. The basic experiment. *Mon. Weather Rev.* **91,** 99-164.

SPALART, P. R. 1988 Direct numerical simulation of a turbulent boundary layer up to $Re_\theta = 1400$. *J. Fluid Mech.* **187,** 61-98.

VASILYEV, O. V., LUND, T. S., & MOIN, P. 1998 A general class of commutative filters for LES in complex geometries. *J. Comp. Phys.* **146,** 82-104.

VREMAN, B., GEURTS, B., & KUERTEN, H. 1994 On the formulation of the dynamic mixed subgrid-scale model. *Phys. Fluids* **6**, 4057-4059.

ZANG., Y., STREET, R. L., & KOSEFF, J. R. 1993 A dynamic mixed subgrid-scale model and its application to turbulent recirculating flows. *Phys. Fluids A* **5**, 3186-3196.

Numerical study of a channel flow with variable properties

By F. C. Nicoud

1. Motivation and objectives

In many industrial devices such as heat exchangers, piston engines, or propulsion systems strong temperature gradients arise in the near wall region even if the characteristic Mach number is close to zero. A strong coupling exists between momentum and energy equations caused by variations in the fluid properties, and the classical wall models for incompressible flows are not appropriate.

In the 1950's through the mid 1960's, many experimental studies focused on the assessment of global quantities at the wall (friction coefficient, Nusselt number) for laminar/turbulent flows with variable properties. Some empirical correlations of engineering interest were derived. More recent studies also deal with velocity and temperature profiles, and it has now reached the point that the supersonic compressible turbulent boundary layer with or without heat transfer is now well documented (see Bradshaw (1977), Fernholz & Finley (1980) and Spina *et al.* (1994) for reviews). The Strong Reynolds Analogy was introduced by Morkovin (1961) in the context of adiabatic boundary layers and has often been used in turbulence modeling. An extension was proposed by Gaviglio (1987) and subsequently Huang *et al.* (1995) for use in the presence of heat transfer. Some experimental data support these analogies in the case of a supersonic boundary layer over a cooled or heated wall and low speed flow on a slightly heated wall. Dimensional analysis of the inner layer shows that the law of the wall can be described in terms of two non-dimensional wall parameters, the friction Mach number $M_\tau = \frac{u_\tau}{c_w}$ and the heat flux parameter $B_q = \frac{q_w}{\rho_w C_p u_\tau T_w}$, where u_τ is the friction velocity $\sqrt{\frac{\tau_w}{\rho_w}}$, c_w the speed of sound, q_w the heat flux, C_p the constant-pressure specific heat, and T_w the temperature at the wall. Two cases, (M_τ, B_q)=(0.08,−0.05) and (0.12,−0.14), were considered in the DNS study of a supersonic channel flow performed by Coleman *et al.* (1995). These data were found in Huang & Coleman (1994) to support the validity of the Van Driest (1951) transformation

$$U_{VD}^+ = \int_o^{u^+} \left(\frac{\rho}{\rho_w}\right)^{1/2} du^+ = \frac{1}{\kappa} ln y^+ + C$$

and suggest that the additive constant C is a function of both M_τ and B_q.

The case with large heat transfer and small Mach number has received very minor attention (W. Kays, private communication). The usefulness of the Van Driest transformation to retrieve the classical logarithmic law of the wall is not fully accepted in this case (Cheng & Ng (1982), Wardana *et al.* (1994), Wang & Pletcher (1996)) although some of the results in the latter reference appear to be erroneous

(P. Bradshaw, private communication). An LES of subsonic turbulent channel flow with constant heat flux performed by Dailey & Pletcher (1998) suggests that when the Mach number is close to 0 the constant C depends slightly on heat transfer. In the latter study, a Smagorinsky subgrid-scale model with Van-Driest damping at the wall was used to account for the subgrid scale effects. Since the value of C is expected to depend on conditions in the viscous and buffer layers (i.e. where the empirical Van Driest damping function is active), these LES data are questionable. In their experiments, Wardana *et al.* (1992, 1994) study the effect of strong wall heating on turbulence statistics of a channel flow. They provide high-order correlations for the velocity components and conclude that near the wall the ejection of low-speed fluid is intensified. They suppose that the local thermal expansion close to the heated wall is the driving force of the intensification. Since they do not use the Van Driest transformation to represent their mean velocity profiles, it is difficult to use their data to study the dependence of the additive constant on the heat transfer parameter B_q. Their experiments correspond to $B_q \approx$ 0, 0.073, 0.11, 0.13, and 0.17.

The objective of the present work is to study the case where the thermo-physical properties vary significantly in the absence of compressibility effects ($M = M_\tau = 0$). We perform a DNS of a *low speed* flow with a *large temperature gradient* in order to generate high-fidelity data which is not presently available. The configuration is a plane channel flow between two isothermal walls with temperatures T_1 and T_2 (see Fig. 1). Regarding the turbulence modeling, the objective is to provide more reliable information about the variation of the constant of integration C as a function of B_q. Other questions of interest relate to how good the Gaviglio's analogy is in the zero Mach number limit and the exact role of the fluid-property variations. A recent analytical study performed by Eames & Hunt (1997) shows how a lump of fluid experiences a lift force when it moves perpendicularly to a density gradient. A fundamental question that can be addressed using DNS is how this inviscid effect can modify the near wall streaks. Is it related to the intensification of the ejection events observed by Wardana *et al.* (1992, 1994)? The low Mach number approximation and the numerical method are discussed in Sections 2 and 3. The first DNS results are given in Section 4.

2. Low Mach number approximation

To avoid contamination of the solution by the non-physical acoustic modes reported in Coleman *et al.* (1995), a low Mach number approximation is first applied to the 3D compressible Navier-Stokes equations. In doing so, the density is decoupled from the pressure so that no acoustics are present in the computation. This also eliminates the acoustic CFL restriction on time step size.

To derive the low Mach number equations, one expands the dependent variables as a power series in $\epsilon = \gamma M^2$, which is a small parameter (see Paolucci (1982) for a complete discussion). Substituting these expansions into the Navier-Stokes equations and collecting the lowest order terms in ϵ yields:

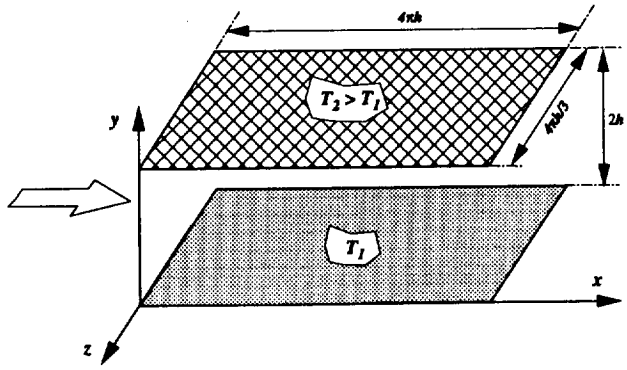

FIGURE 1. Computational domain.

$$\frac{\partial \rho}{\partial t} + \frac{\partial \rho u_j}{\partial x_j} = 0 \tag{1}$$

$$\rho \frac{\partial u_i}{\partial t} + \rho u_j \frac{\partial u_i}{\partial x_j} = -\frac{\partial P}{\partial x_i} + \frac{1}{R_e} \frac{\partial \tau_{ij}}{\partial x_j} \tag{2}$$

$$\rho C_p \frac{\partial T}{\partial t} + \rho C_p u_j \frac{\partial T}{\partial x_j} = \frac{1}{R_e P_r} \frac{\partial q_j}{\partial x_j} + \frac{\gamma - 1}{\gamma} \frac{dP_o}{dt} \tag{3}$$

In these equations, all the variables are normalized using the reference state ρ^{ref}, u^{ref}, $T^{\text{ref}} = P_o^{\text{ref}}/\rho^{\text{ref}}$, $C_p^{\text{ref}} = C_p^*(T^{\text{ref}})$, $\mu^{\text{ref}} = \mu^*(T^{\text{ref}})$, and $k^{\text{ref}} = k^*(T^{\text{ref}})$ where the superscript * represent dimensional quantities. Also $R_e = \rho^{\text{ref}} u^{\text{ref}} L^{\text{ref}}/\mu^{\text{ref}}$ and $P_r = \mu^{\text{ref}} C_p^{\text{ref}}/k^{\text{ref}}$ are the Reynolds and the Prandtl number while γ is the ratio of specific heats at the reference state. u_i, ρ, T, and C_p stand for the non-dimensionalized velocity vector, density, temperature, and specific heat. $\tau_{ij} = \mu\left(\frac{\partial u_i}{\partial x_j} + \frac{\partial u_j}{\partial x_i} - \frac{2}{3}\delta_{ij}\frac{\partial u_k}{\partial x_k}\right)$ and $q_j = k\frac{\partial T}{\partial x_j}$ are the viscous stress tensor and the heat flux vector respectively. Moreover, P may be interpreted as the hydrodynamic pressure. In the low-Mach number approximation, the thermodynamic pressure P_o only depends on time and must be computed if it is not constant. The equation of state is simply:

$$P_o = \rho T \tag{4}$$

Since density is uniquely determined by the temperature (and the thermodynamic pressure which is constant in space), the energy equation acts as a constraint which is enforced by the hydrodynamic pressure. This constraint is:

$$\frac{\partial u_i}{\partial x_i} = \frac{1}{P_o(t) C_p} \left[\frac{1}{R_e P_r} \frac{\partial}{\partial x_j} \left(k \frac{\partial T}{\partial x_j} \right) + \left(\frac{\gamma - 1}{\gamma} - C_p \right) \frac{dP_o}{dt} \right]$$

Integrating over the flow domain V leads to the following ODE for the thermodynamic pressure in a closed system:

$$\frac{dP_o}{dt} = \frac{1}{\int_V \left(\frac{\gamma-1}{\gamma} - C_p\right) dV} \left[\frac{1}{R_e P_r} \int_V \frac{\partial}{\partial x_j} \left(k \frac{\partial T}{\partial x_j} \right) dV + P_o(t) \int_V u_i \frac{\partial C_p}{\partial x_i} dV \right] \tag{5}$$

Since $\int_V \frac{\partial}{\partial x_j}\left(k\frac{\partial T}{\partial x_j}\right)dV = \int_S k\frac{\partial T}{\partial x_j}dS_j$, this relation expresses how the rate of change of the mean pressure is affected by the heat flux through the surface S of the domain V and the gradients of heat capacity of the gas. In many practical applications the fluid may be considered as a calorifically perfect gas so that $C_P = 1$ and the time derivative of P_o is simply:

$$\frac{dP_o}{dt} = \frac{\gamma}{V}\frac{1}{R_e P_r}\int_V \frac{\partial}{\partial x_j}\left(k\frac{\partial T}{\partial x_j}\right)dV = \frac{1}{V}\frac{1}{R_e P_r}\int_S k\frac{\partial T}{\partial x_j}dS_j \tag{6}$$

Thus the constraint on the velocity field becomes:

$$\frac{\partial u_i}{\partial x_i} = \frac{1}{P_o(t)R_e P_r}\left[\frac{\partial}{\partial x_j}\left(k\frac{\partial T}{\partial x_j}\right) - \frac{1}{V}\int_V \frac{\partial}{\partial x_j}\left(k\frac{\partial T}{\partial x_j}\right)dV\right] \tag{7}$$

If the system considered is open, then the thermodynamic pressure is set by atmospheric conditions. If it is closed, then the amount of mass in it, M_0, is constant over time so that by integrating the equation of state over the whole domain one obtains the following expression for the thermodynamic pressure:

$$P_o(t) = \frac{M_0}{\int_V \frac{1}{T}dV} \tag{8}$$

Note that, in the limit of an inviscid flow of a calorifically perfect gas, the thermodynamic pressure remains constant over time (from Eq. (6)) and the velocity field is divergence-free (from Eq. (7)). The solution (ρ, u_i, T, P, P_o) is completely described by Eqs. (1)-(5). The constraint (7) should also be satisfied since it is a linear combination of Eqs. (1), (3), and (4).

3. Numerical method

The numerical method chosen for solving the variable density momentum and temperature equations is a generalization of a fully conservative fourth order spatial scheme developed for incompressible flows on staggered grids by Morinishi *et al.* (1998). A scheme to solve the momentum equations in non-conservative form is described in the following subsection. After that, a scheme with 'good' conservative properties is discussed.

3.1 Scheme in non-conservative form

For a uniform mesh, the advective term in the momentum equation (2) is discretized as:

$$\rho u_j \frac{\partial u_i}{\partial x_j} \equiv \frac{\overline{\frac{9}{8}\left(\frac{9}{8}\overline{\rho^{(4j)}u_j}^{1x_i} - \frac{1}{8}\overline{\rho^{(4j)}u_j}^{3x_i}\right)\frac{\delta_1 u_i}{\delta_1 x_j}}^{1x_j}}{-\overline{\frac{1}{8}\left(\frac{9}{8}\overline{\rho^{(4j)}u_j}^{1x_i} - \frac{1}{8}\overline{\rho^{(4j)}u_j}^{3x_i}\right)\frac{\delta_3 u_i}{\delta_3 x_j}}^{3x_j}} \tag{9}$$

where the finite-difference operator with stencil n acting on ϕ with respect to x_i is defined as

$$\frac{\delta_n \phi}{\delta_n x_i} = \frac{\phi(x_i + nh_i/2) - \phi(x_i - nh_i/2)}{nh_i}$$

and the interpolation operator with stencil n acting on ϕ in the x_i direction is

$$\overline{\phi}^{nx_i} = \frac{\phi(x_i + nh_i/2) + \phi(x_i - nh_i/2)}{2}.$$

$\rho^{(4j)} = \frac{9}{8}\overline{\rho}^{1x_j} - \frac{1}{8}\overline{\rho}^{3x_j}$ is a fourth order interpolation of ρ in the x_j direction. When the density is constant, Eq. (9) reduces to the advective form (Adv.-S4) in Morinishi *et al.* (1998). The pressure term in Eq. (2) in discretized by:

$$\frac{\partial P}{\partial x_i} \equiv (Pres.)_i = (\nabla_d P)_i = \frac{9}{8}\frac{\delta_1 P}{\delta_1 x_i} - \frac{1}{8}\frac{\delta_3 P}{\delta_3 x_i} \tag{10}$$

and the discrete divergence operator is defined consistently: $\frac{\partial u_i}{\partial x_i} \equiv \nabla_d \cdot (u_i) = \frac{9}{8}\frac{\delta_1 u_i}{\delta_1 x_i} - \frac{1}{8}\frac{\delta_3 u_i}{\delta_3 x_i}$. The viscous terms in Eq. (2) are written using the generic form:

$$\begin{aligned} \frac{\partial}{\partial x_j}\left(\mu \frac{\partial u_i}{\partial x_j}\right) \equiv\ & \frac{9}{8}\frac{\delta_1}{\delta_1 x_j}\left[\mu^{(4i),(4j)}\left(\frac{9}{8}\frac{\delta_1 u_i}{\delta_1 x_j} - \frac{1}{8}\frac{\delta_3 u_i}{\delta_3 x_j}\right)\right] \\ & -\frac{1}{8}\frac{\delta_3}{\delta_3 x_j}\left[\mu^{(4i),(4j)}\left(\frac{9}{8}\frac{\delta_1 u_i}{\delta_1 x_j} - \frac{1}{8}\frac{\delta_3 u_i}{\delta_3 x_j}\right)\right] \end{aligned} \tag{11}$$

The advective term for the temperature is discretized as:

$$\rho u_j \frac{\partial T}{\partial x_j} \equiv \frac{9}{8}\overline{\rho^{(4j)} u_j \frac{\delta_1 T}{\delta_1 x_j}}^{1x_j} - \frac{1}{8}\overline{\rho^{(4j)} u_j \frac{\delta_3 T}{\delta_3 x_j}}^{3x_j} \tag{12}$$

A semi-implicit time marching algorithm is used in which the diffusion terms in the wall normal direction are treated implicitly with a Crank-Nicolson scheme while a third order Runge-Kutta scheme is used for all other terms. The temperature equation is advanced first so that ρ^{n+1} is known via the state equation $\rho = P_o/T$, where P_o is first assessed using Eq. (8) written at time $n+1$. Then a fractional step method is used to solve the momentum equation.

$$\begin{aligned} \rho^{(4i),n+1}\frac{u_i^{n+1} - u_i^n}{\Delta t} &= \rho^{(4i),n+1}\frac{u_i^{n+1} - \hat{u}_i}{\Delta t} + \rho^{(4i),n+1}\frac{\hat{u}_i - u_i^n}{\Delta t} \\ &= \frac{\beta_k}{2}\left(I^{n+1} + I^n\right) + \gamma_k E^n + \zeta_k E^{n-1} - 2\beta_k \nabla_d P^n - 2\beta_k \nabla_d \delta P^{n+1} \end{aligned} \tag{13}$$

where I and E represent all the spatial implicit and explicit terms except for the pressure at n and the pressure update $\delta P^{n+1} = P^{n+1} - P^n$. The parameters β_k, γ_k, and ζ_k ($k = 1, 3$) are chosen so that the mixed Runge-Kutta/Crank-Nicolson time stepping is recovered after the third substep (Spalart, 1987). Equation (13)

is then split into a decoupled set which is a second-order approximation in time to the original equation:

$$\rho^{(4i),n+1}\frac{\hat{u}_i - u_i^n}{\Delta t} = \frac{\beta_k}{2}\left(I^{n+1} + I^n\right) + \gamma_k E^n + \zeta_k E^{n-1} - 2\beta_k \nabla_d P^n \quad (14)$$

$$\rho^{(4i),n+1}\frac{u_i^{n+1} - \hat{u}_i}{\Delta t} = -2\beta_k \nabla_d \delta P^{n+1} \quad (15)$$

Equation (14) is solved for $\hat{u}_i$ by using the discretizations (9), (10), and (11). Then (15) is divided by $\rho^{(4i),n+1}$ before its discrete divergence is taken to obtain:

$$\nabla_d \cdot \left(\frac{1}{\rho^{(4i),n+1}}\nabla_d \delta P\right) = \frac{1}{2\beta_k \Delta t}\left(\nabla_d \cdot \hat{u}_i - \nabla_d \cdot u_i^{n+1}\right) = S \quad (16)$$

A similar Poisson equation with variable coefficients was solved in Bell & Marcus (1992) to impose the divergence-free constraint for variable-density flows.

Since the transport equation for T has been advanced prior to the momentum equation, the last term in the equation for the pressure variation is known from Eq. (7), written at time $n+1$. The non-linear Poisson equation (16) for the pressure is solved using the iterative procedure:

$$\nabla_d \cdot \left(\frac{1}{\left\langle \rho^{(4i),n+1}\right\rangle}\nabla_d \delta P^{k+1}\right) = \frac{1}{2\beta_k \Delta t}\left(S + \nabla_d \cdot \left(\left[\frac{1}{\left\langle \rho^{(4i),n+1}\right\rangle} - \frac{1}{\rho^{(4i),n+1}}\right]\nabla_d \delta P^k\right)\right) \quad (17)$$

where $<>$ denote a plane averaging in the two homogeneous directions x and z. Each sub-iteration is solved exactly using a Fast Poisson Solver. The advantage of solving Eq. (16) to update the pressure is that the divergence-free constraint is recovered in the inviscid limit, as it has to be from Eq. (7). This is not the case when a backward approximation of $\frac{\partial \rho}{\partial t}$ is used to compute the source term of a linear Poisson equation for δP as proposed by McMurthry *et al.* (1986), Cook & Riley (1996). The other advantage is that the pressure terms remain energy conserving in the inviscid limit as discussed in the following subsection. Several basic test cases have been computed to validate the above procedure (see Subsection 3.3).

3.2 Toward a fully conservative scheme

Although the previous scheme was found to be accurate, it only conserves momentum and kinetic energy to its own order of accuracy. Experience has shown that the latter quantity must be conserved exactly if a robust and dissipation-free numerical method is sought. Morinishi *et al.* (1998) developed a set of fully conservative (mass, momentum, and kinetic energy) high order schemes for incompressible flow. In the general case of the Navier-Stokes equations without body force, the transport equation for the kinetic energy per unit volume ρk reads:

$$\frac{\partial \rho k}{\partial t} + \frac{\partial \rho u_j k}{\partial x_j} = P S_{jj} - \frac{\partial P u_j}{\partial x_j} + \frac{\partial \tau_{ij} u_i}{\partial x_j} - \tau_{ij} S_{ij} \quad (18)$$

Let us consider a periodic (or infinite) domain so that, after Eq. (18) is integrated over the domain, the flux terms $\frac{\partial \rho u_j k}{\partial x_j}$ and $\frac{\partial P u_j}{\partial x_j}$ make no contribution. Due to the dissipation term $\tau_{ij} S_{ij}$, the question of conservation of the kinetic energy is only relevant in the inviscid limit where $\tau_{ij} = 0$. We know from Eq. (7) that in this limit the velocity field is divergence-free, that is $S_{jj} = 0$. Thus global conservation of kinetic energy is a common feature of incompressible and low Mach number flows. The purpose of this section is to investigate how this property can be extended in discrete space. Let us define the following discrete approximations of the possible forms for the non-linear term in the momentum equation:

$$\begin{aligned}(Adv.)_i \;=\; & \overline{\tfrac{9}{8}\left(\tfrac{9}{8}\overline{\rho^{(4j)}u_j}^{1x_i} - \tfrac{1}{8}\overline{\rho^{(4j)}u_j}^{3x_i}\right)\tfrac{\delta_1 u_i}{\delta_1 x_j}}^{1x_j} \\ & \overline{-\tfrac{1}{8}\left(\tfrac{9}{8}\overline{\rho^{(4j)}u_j}^{1x_i} - \tfrac{1}{8}\overline{\rho^{(4j)}u_j}^{3x_i}\right)\tfrac{\delta_3 u_i}{\delta_3 x_j}}^{3x_j}\end{aligned} \tag{19}$$

$$\begin{aligned}(Div.)_i \;=\; & \tfrac{9}{8}\tfrac{\delta_1}{\delta_1 x_j}\left[\left(\tfrac{9}{8}\overline{\rho^{(4j)}u_j}^{1x_i} - \tfrac{1}{8}\overline{\rho^{(4j)}u_j}^{3x_i}\right)\overline{u_i}^{1x_j}\right] \\ & - \tfrac{1}{8}\tfrac{\delta_3}{\delta_3 x_j}\left[\left(\tfrac{9}{8}\overline{\rho^{(4j)}u_j}^{1x_i} - \tfrac{1}{8}\overline{\rho^{(4j)}u_j}^{3x_i}\right)\overline{u_i}^{3x_j}\right]\end{aligned} \tag{20}$$

$$(Skew.)_i = \frac{1}{2}\left((Adv.)_i + (Div.)_i\right) \tag{21}$$

The forms $(Adv.)$, $(Div.)$, and $(Skew.)$ are the discrete equivalent to the advective $\rho u_j \frac{\partial u_i}{\partial x_j}$, conservative $\frac{\partial \rho u_i u_j}{\partial x_j}$, and skew-symmetric $\frac{1}{2}\left(\rho u_j \frac{\partial u_i}{\partial x_j} + \frac{\partial \rho u_i u_j}{\partial x_j}\right)$ form of the convective term. The following relations hold between these three discrete forms:

$$(Div.)_i = (Adv.)_i + u_i\left(\frac{9}{8}\overline{(Cont.)}^{1x_i} - \frac{1}{8}\overline{(Cont.)}^{3x_i}\right) \tag{22}$$

$$(Skew.)_i = (Adv.)_i + \frac{1}{2}u_i\left(\frac{9}{8}\overline{(Cont.)}^{1x_i} - \frac{1}{8}\overline{(Cont.)}^{3x_i}\right) \tag{23}$$

$$(Skew.)_i = (Div.)_i - \frac{1}{2}u_i\left(\frac{9}{8}\overline{(Cont.)}^{1x_i} - \frac{1}{8}\overline{(Cont.)}^{3x_i}\right) \tag{24}$$

where $(Cont.) = \frac{9}{8}\frac{\delta_1 \rho^{(4j)}u_j}{\delta_1 x_j} - \frac{1}{8}\frac{\delta_3 \rho^{(4j)}u_j}{\delta_3 x_j}$ is the discrete form of the divergence of ρu_j.

A key assumption in the semi-discrete analysis proposed in Morinishi *et al.* (1998) for incompressible flow is that the operator $(Cont.)$ is identically zero so that the three forms $(Div.)_i$, $(Adv.)_i$, and $(Skew.)_i$ are equivalent. Since $(Div.)_i$ is conservative ***a priori*** for the momentum equation and $(Skew.)_i$ is conservative ***a priori*** in the kinetic energy equation, a fully conservative scheme is obtained as soon as the velocity constraint $\frac{\partial u_j}{\partial x_j} = 0$ is imposed properly through the pressure correction step. In the present case where the density is not constant, the velocity constraint $\frac{\partial u_j}{\partial x_j} = 0$ (in the inviscid limit) does not imply that $\frac{\partial \rho u_j}{\partial x_j}$ is zero. Thus the discrete operators $(Div.)_i$, $(Adv.)_i$, and $(Skew.)_i$ are not equivalent in the low Mach number case, meaning that a fully discrete analysis (including the time discretization) must be conducted to achieve conservation of kinetic energy.

A conservative scheme for the momentum can be derived by solving the divergence form of Eq. (2). The first guess for the velocity is obtained by:

$$\frac{\hat{\rho}^{(4i)}\hat{u}_i - \rho^{(4i),n}u_i^n}{\Delta t} = -\gamma_k(Div.)_i^n - \zeta_k(Div.)_i^{n-1} - 2\beta_k(Pres.)_i^n \tag{25}$$

where $\hat{\rho}$ can be either any intermediate value. Then the projection step is:

$$u_i^{n+1} = \frac{\hat{\rho}^{(4i)}}{\rho^{(4i),n+1}}\hat{u}_i - 2\beta_k\frac{1}{\rho^{(4i),n+1}}\nabla_d\delta P\Delta t \tag{26}$$

where the Poisson equation for δP must be:

$$\nabla_d\cdot\left(\frac{1}{\rho^{(4i),n+1}}\nabla_d\delta P\right) = \frac{1}{2\beta_k\Delta t}\left(\nabla_d\cdot\left(\frac{\hat{\rho}^{(4i)}}{\rho^{(4i),n+1}}\hat{u}_i\right) - \nabla_d\cdot u_i^{n+1}\right) \tag{27}$$

Obviously, Eqs. (25), (26), and (27) constitute a scheme which is momentum conserving. To investigate whether it also conserves kinetic energy, let us multiply Eq. (25) by $\hat{u}_i + u_i^n$ and integrate over the whole domain. The overall contribution of the first pressure term in the kinetic energy equation reads as:

$$\int_V u_i^n(Pres.)_i^n dV = \int_V\left(\frac{9}{8}u_i^n\overline{\frac{\delta_1 P}{\delta_1 x_i}}^{1x_i} - \frac{1}{8}u_i^n\overline{\frac{\delta_3 P}{\delta_3 x_i}}^{3x_i}\right)dV \tag{28}$$

where

$$\frac{9}{8}\overline{u_i^n\frac{\delta_1 P}{\delta_1 x_i}}^{1x_i} - \frac{1}{8}\overline{u_i^n\frac{\delta_3 P}{\delta_3 x_i}}^{3x_i} = \frac{9}{8}\frac{\delta_1 u_i^n\overline{P}^{1x_i}}{\delta_1 x_i} - \frac{1}{8}\frac{\delta_3 u_i^n\overline{P}^{3x_i}}{\delta_3 x_i} - P\left(\frac{9}{8}\frac{\delta_1 u_i^n}{\delta_1 x_i} - \frac{1}{8}\frac{\delta_3 u_i^n}{\delta_3 x_i}\right) \tag{29}$$

The first two terms do not contribute because they are in divergence form; the last two are identically zero because the non-linear Poisson equation (27) is solved with $\nabla_d\cdot u_i^{n+1} = \frac{9}{8}\frac{\delta_1 u_i^n}{\delta_1 x_i} - \frac{1}{8}\frac{\delta_3 u_i^n}{\delta_3 x_i} = 0$ imposed in the source term. The contribution of the term $\hat{u}_i(Pres.)_i^n$ is of order Δt because $\hat{u}_i = u_i^n + O(\Delta t)$. Using Eq. (24), the overall contribution of the RHS of Eq. (25) may be written as

$$\begin{aligned} &\int_V(\hat{u}_i + u_i^n)\left(-\gamma_k(Skew.)_i^n - \zeta_k(Skew.)_i^{n-1}\right)dV \\ -\ &\gamma_k\int_V\frac{\hat{u}_i+u_i^n}{2}u_i^n\left(\tfrac{9}{8}\overline{(Cont.)^n}^{1x_i} - \tfrac{1}{8}\overline{(Cont.)^n}^{3x_i}\right)dV \\ -\ &\zeta_k\int_V\frac{\hat{u}_i+u_i^n}{2}u_i^{n-1}\left(\tfrac{9}{8}\overline{(Cont.)^{n-1}}^{1x_i} - \tfrac{1}{8}\overline{(Cont.)^{n-1}}^{3x_i}\right)dV \\ +\ &O(\Delta t) \end{aligned} \tag{30}$$

The first integral in (30) contributes to the order Δt because $(Skew.)_i$ is kinetic energy conserving in nature and because $\hat{u}_i$, u_i^n, and u_i^{n-1} are equal to the order Δt. On the other hand, the contribution of the LHS of (25) may be written:

$$\int_V\frac{\hat{\rho}^{(4i)}(\hat{u}_i)^2 - \rho^{(4i),n}(u_i^n)^2}{\Delta t}dV + \int_V u_i^n\hat{u}_i\frac{\hat{\rho}^{(4i)} - \rho^{(4i),n}}{\Delta t}dV \tag{31}$$

Comparing Eqs. (30) and (31) it appears that the discrete rate of change of the kinetic energy (the first integral in Eq. (31)) is at most of order Δt if one defines the intermediate density as:

$$\frac{\hat{\rho}-\rho^n}{\Delta t} = -\gamma_k(Cont.)^n - \zeta_k(Cont.)^{n-1} \tag{32}$$

In the context of second order scheme, the same definition of $\hat{\rho}$ was adopted (C. Pierce, private communication) to achieve approximate conservation of kinetic energy. Multiplying the projection step Eq. (26) by $\hat{u}_i + u_i^{n+1}$ and integrating over the whole domain, the following expression can be derived:

$$\int_V \frac{\rho^{(4i),n+1}\left(u_i^{n+1}\right)^2 - \hat{\rho}^{(4i)}\left(\hat{u}_i\right)^2}{\Delta t} dV = \int_V \hat{u}_i u_i^{n+1} \frac{\hat{\rho}^{(4i)} - \rho^{(4i),n+1}}{\Delta t} dV + O(\Delta t) \tag{33}$$

This shows that the global rate of change of the kinetic energy is of order Δt only if $\hat{\rho}^{(4i)} - \rho^{(4i),n+1} = O(\Delta t^n)$, $n \geq 2$. Unfortunately, n is only 1 in the most general case. A conservative scheme is obtained if one accepts that the state equation (4) is verified to the order Δt only, viz:

$$\rho^{n+1} = \hat{\rho} = \frac{P_o}{T^{n+1}} + O(\Delta t) \tag{34}$$

In this case, the error in the kinetic energy conservation is at most of order Δt.

3.3 Basic test cases

The following test cases were designed to check the accuracy of the numerical method. In what follows, AdvSC and DivSC stand for the schemes discussed in Sections 3.1 and 3.2 respectively. Except as otherwise stated (Section 3.3.2), the state equation (4) is enforced exactly.

3.3.1 1D Euler convection

If the Peclet number is infinite, the velocity field must be divergence-free; that is, u must be constant in 1D. Also, the pressure should remain constant. To test the ability of the two formulations to reproduce this feature of Eqs. (1)-(3), consider the domain $0 \leq x \leq 1$, periodic in x. The initial condition is $u = u_0 = 1$, $P = 0$, and $T = 1 + A\exp\left[-\left(\frac{x-x_0}{a}\right)^2\right]$ with $A = 1$, $x_0 = 0.5$, and $a = 0.05$. When the grid contains $N_x = 24$ points, only 6 points are used to describe a Gaussian perturbation. Figure 2 shows $P_{\text{rms}}/\rho_0 u_0^2$ as a function of the grid spacing, where three grid levels were considered: 24, 48, and 96 points in x. The rms of pressure is assessed for the time $t = 20a/u_0$. The CFL number is of order 0.5 in all cases. Both schemes are fourth-order accurate in space, but AdvSC is exact for this particular test case. The divergence is zero in both cases because it is explicitly enforced through the Poisson equations (27) for DivSC and (16) for AdvSC.

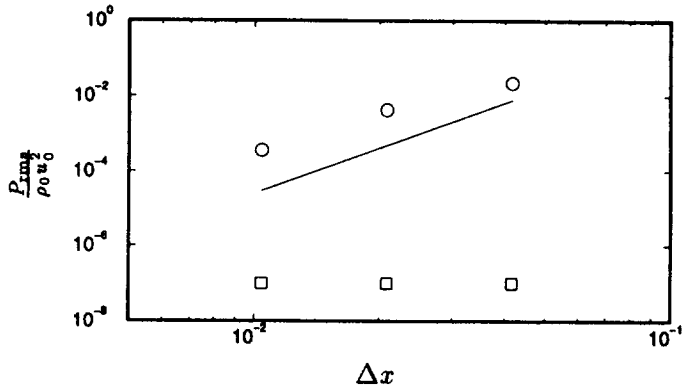

FIGURE 2. Root-mean-square of pressure as a function of the grid spacing at time $t = 20a/u_0$. ——— : $P_{\text{rms}} \propto \Delta x^4$; o : DivSC; □ : AdvSC.

3.3.2 Small 1D perturbations

In the case where the Reynolds number is finite but where the perturbation in temperature is small ($A << 1$), the analytical resolution of Eqs. (1)-(3) can be conducted and the structure of the perturbation which propagates is given by:

$$\rho' = -\frac{\rho_0}{T_0} T' \tag{35}$$

$$u' = \frac{1}{R_e P_r} \frac{\partial T'}{\partial x} \tag{36}$$

$$p' = \frac{4}{3 R_e^2 P_r^2} \frac{\partial^2 T'}{\partial x^2} \left(P_r - \frac{3}{4} \right) \tag{37}$$

An interesting feature is that the pressure fluctuation should vanish in the limit $P_r = \frac{3}{4}$. Figure 3 shows the error in Eq. (37) in the case $N_x = 24$, $a = 0.05$, $A = 0.01$, and $R_e = 50$. The initial condition is uniform for u and P and the physical time simulated is large enough ($t \approx 160a/u_0$) so that the values reported in the figure are asymptotic values. For this poor resolution, the remaining error for DivSC is much greater than for AdvSC.

3.3.3 2D Random perturbations

To validate the results of Section 3.2 with numerical tests, inviscid flow simulations were performed on a 2D periodic domain. The analytical solution dictates that the total momentum in each direction $\langle \rho u_i \rangle$ and total kinetic energy $\langle K \rangle = \frac{1}{2} \langle \rho u_i^2 \rangle$ should be conserved in time. The domain is $0 \leq x \leq L$, $0 \leq y \leq L$, and a 24x24 mesh is used. Solenoidal velocity fields are used as the initial condition together with random temperature fluctuations. The initial mean kinetic energy is of order 1.5 while $T_{\text{rms}} \approx 0.15 < T >$ at $t = 0$. Figure 4 shows the relative error for the total kinetic energy $\frac{\langle K_0 - K \rangle}{\langle K_0 \rangle}$ after an integration time of $t = 0.125 L / \sqrt{\langle K_0 \rangle}$. As expected from Section 3.2, the error for the scheme DivSC is not a function of the time step only, but also of space the space discretization. On the other hand, it appears that

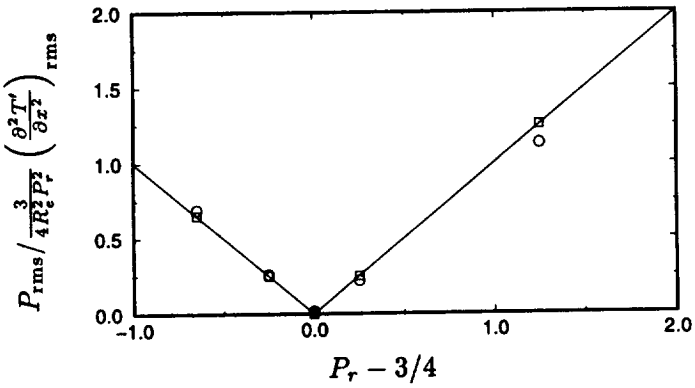

FIGURE 3. Root-mean-square of pressure as a function of the Prandtl number. $P_{\rm rms}$ is non-dimensionalized by its theoretical value as a function of T'. ——— : exact solution Eq. (37); o : DivSC; □ : AdvSC.

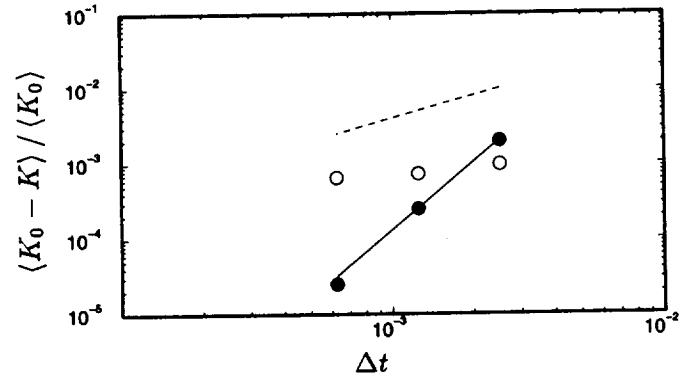

FIGURE 4. Kinetic energy conservation error as a function of the time step. ——— : Δt^3 behavior; ---- : Δt behavior; o : DivSC; • : DivSC with approximate equation of state, Eq. (34).

the same scheme with the approximate equation of state, Eq. (34), produces no violation in the conservation of kinetic energy due to the spatial scheme. The measured error behaves like Δt^3 instead of Δt as predicted in 3.2 . Indeed, a single substep of the time integration was considered in the analysis so that the cancellation of error in the full third-order Runge-Kutta procedure was not accounted for.

3.3.4 Linear stability in a channel

To check the accuracy of the code in the case where the physical properties vary in space and time through the temperature, the evolution of low amplitude eigenmodes in laminar channel flow is simulated. The linear stability problem in a channel flow between two isothermal walls with temperature $T_1 = 1 - \frac{\delta T}{2}$ and $T_2 = 1 + \frac{\delta T}{2}$ was studied by Suslov & Paolucci (1995) under the low Mach number assumption. They found that the critical Reynolds number increases with the parameter $\frac{\delta T}{2}$. It

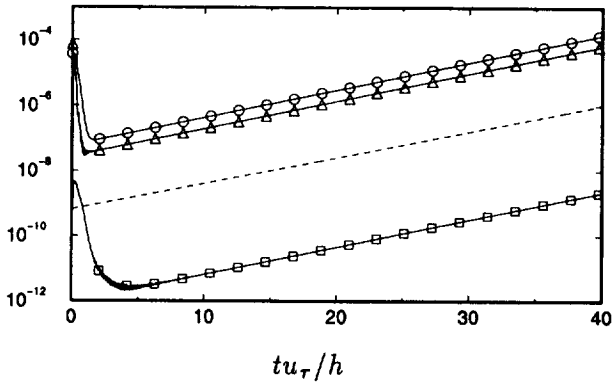

FIGURE 5. Time evolution of the global energy of the fluctuations in the computational domain. ---- : linear stability theory (Suslov & Paolucci (1995)); —o— : $< u'^2 >$; —△— : $< v'^2 >$; —□— : $< T'^2 >$.

is of order 40000 for $\frac{\delta T}{2} = 0.4$, compared to 5772 in the isothermal case ($\delta T = 0$). In their analysis the dimensionless thermal conductivity and dynamic viscosity are given by Sutherland's law:

$$k(T) = T^{3/2}\frac{1+S_k}{T+S_k} \qquad \mu(T) = T^{3/2}\frac{1+S_\mu}{T+S_\mu} \tag{38}$$

where $S_k = 0.648$ and $S_\mu = 0.368$ for air at $T_{\text{ref}} = 300K$ and normal pressure. The molecular Prandtl number is 0.76. In the computation, the length of the periodic domain in x is $L = 2\pi/\alpha$, where α is the wave number of the mode of interest. The initial condition consists of a small amplitude (0.01%) random noise on u, v superimposed to the laminar solution of the problem (Suslov & Paolucci (1995)). A stretched grid is used in the normal direction in order to capture the eigenvector accurately near the walls. The wall normal velocity points are distributed according to a hyperbolic tangent function ($j = 0, 1, 2, ..., N$):

$$y_v(j) = y_{j+\frac{1}{2}} = \frac{\tanh(\gamma\,(\frac{2j}{N}-1))}{\tanh(\gamma)} \tag{39}$$

A typical result is shown in Fig. 5. In this case the resolution is 24x100 with $\gamma = 2$ for the stretching parameter. The CFL number is fixed at 1. The length of the domain is $L = 2.4\pi h$ ($\alpha = \frac{5}{6}\frac{1}{h}$) and the Reynolds number is 45000, based on the maximum velocity and the channel half-height h. The temperature ratio is $\frac{T_2}{T_1} = 2.33$, i.e. $\frac{\delta T}{2} = 0.4$. For these conditions, the flow is linearly unstable (see Suslov & Paolucci (1995)). The code predicts a reasonable growth rate for this eigenmode. Note that a fairly long time ($10h/u_\tau$) is needed for the mode to settle in. Once the transition phase is finished, the temperature and the two velocity components develop with exactly the same rate, as dictated by the linear stability theory. DivSC and AdvSC give similar results (AdvSC shown).

4. Results

Two DNS's of a channel flow are performed to study the effect of the temperature gradient on the flow. Details of the test cases adopted are given in Table I.

Case	T_2/T_1	$R_{\tau 1}$	$R_{\tau 2}$	R_{ec}	Δx^+	Δy^+	Δz^+
A	1.01	180	180	3300	18.8	$0.25-10$	6.28
B	2	200	82	2700	$8.4-21.5$	$0.25-9$	$2.8-7.2$

Table I: Numerical parameters of the two computations performed.

In each case the domain size is $(4\pi h, 2h, 4\pi/3h)$ and the grid contains 120x100x120 cells. The statistics shown for Case B were obtained over a time period of order $5.7h/\overline{u_\tau}$, where $\overline{u_\tau} = \frac{u_{\tau 1}+u_{\tau 2}}{2}$ is the mean friction velocity. The wall normal velocity points are distributed according to Eq. (39) with $\gamma = 2.5$ for Case A. For Case B, the Reynolds number near the hot wall is expected to be smaller than near the cold wall and the following non-symmetric distribution is used:

$$y_v(j) = 2\frac{\hat{y}_v(j)+1}{\hat{y}_v(N)+1} - 1 \tag{40}$$

with

$$\hat{y}_v(j) = \frac{\tanh(\gamma\,(\frac{2\alpha j}{N} - 1))}{\tanh(\gamma)} \tag{41}$$

and $\gamma = 2.5$ and $\alpha = 0.9$. Buoyancy effects are neglected and the dimensionless thermal conductivity and dynamic viscosity are given by Sutherland's law (see Section 3.3.4). The molecular Prandtl number is 0.76. In Case A the temperature is almost uniform and the results may be compared to previous incompressible DNS performed by Kim & Moin (1987) and Kasagi (1992) as well as semi-empirical correlations derived by Kader (1981) for the passive scalar case. In Case B one expects the temperature (density) variations to be large enough to modify the momentum balance through both viscous and inviscid effects. The analytical work of Eames & Hunt (1997) shows that when a body moves perpendicularly to a density gradient, a lift force, $C_L(U \times \nabla\rho) \times U$, pushes it towards the denser fluid. Thus the order of magnitude of the inviscid lift acting on a turbulent structure in the channel flow is $C_L u_\tau^2 \Delta\rho/h$. Requiring that this inviscid force is of the same order of magnitude as the viscous force, $\tau_w/h = \rho u_\tau^2/h$, one obtains the estimate $\Delta\rho/\rho \simeq 1/C_L$, where C_L is the lift coefficient. With C_L in the range $1/4 - 1/2$, the inviscid lift related to the density gradient may balance the viscous forces for $\Delta\rho/\rho$ in the range $2-4$. Note that one overestimates the required $\Delta\rho/\rho$ by assuming that the density gradient in the near wall region is equal to the mean density gradient $\Delta\rho/h$. Case B corresponds to $T_2/T_1 = 2$, viz. $\Delta T/T = \Delta\rho/\rho = 2/3$ and the density gradient may be strong enough to generate important inviscid effects.

4.1 Mean quantities

Figure 6 shows that Case A is in good agreement with previous incompressible DNS (Kim *et al.*, 1987) for the mean velocity profile. The expected (for

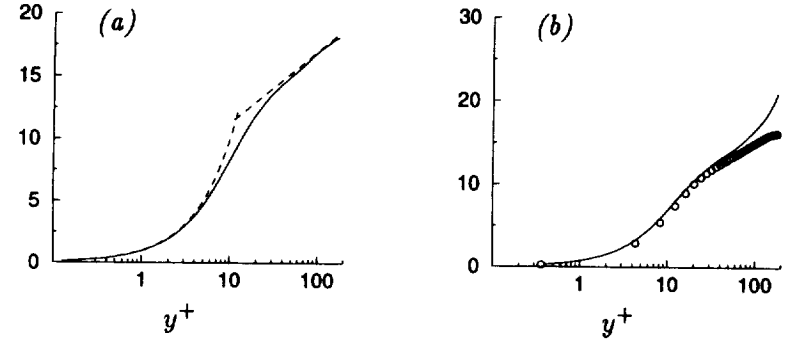

FIGURE 6. Mean profile of velocity (a) and temperature (b) for Case A. Wall units. ---- : Law-of-the-wall; o : Kader's formula ——— : Case A.

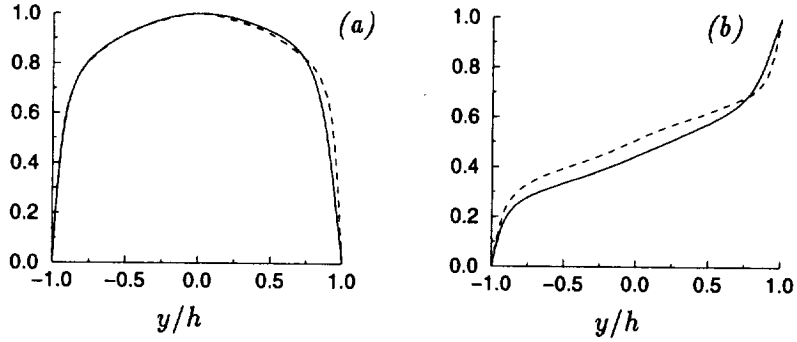

FIGURE 7. Mean profile of velocity (a) and temperature (b) in global coordinates. ---- : Case A; ——— : Case B. Non-dimensionalization is u/u_{max} and $(T - T_1)/(T_2 - T_1)$.

the Reynolds number R_τ considered) law-of-the-wall $u^+ = 2.5ln(y^+) + 5.5$ is obtained, and there is good agreement with Kader's formula for the mean temperature. The non-dimensionalization is such that $T^+ = P_r y^+$ in the limit $y^+ \to 0$, viz. $T^+ = (T_w - T)/(B_q T_w)$ or $T^+ = (T_w - T)\rho_w C_p u_\tau / q_w$. Note that the linear behavior for T near $y^+ = 180$ is related to the inflexion point near the centerline, as shown in Fig. 7. This figure also shows the profiles for Case B. The temperature difference is strong enough to induce a significant asymmetry in the mean quantities. The temperature gradient is smaller near the hot wall so that, with the Sutherland's law Eq. (38), the heat flux is the same in absolute value at both sides. In semi-log plot, the mean velocity profile does not match the classical law-of-the-wall if scaled by the friction velocity. However, once transformed as proposed by Van Driest (1951), a logarithmic behavior is clearly obtained for the two sides of the channel. The slope remains close to its incompressible value whereas the additive constant is (slightly) greater for both the heated and the cooled wall. This puzzling result (there is no physical reason to believe that $C(B_q)$ is even) may be due to a low Reynolds number effect near the hot wall where density is lower and dynamic viscosity is higher. The temperature profiles (see Fig. 9) for Case A and Case B collapse only through

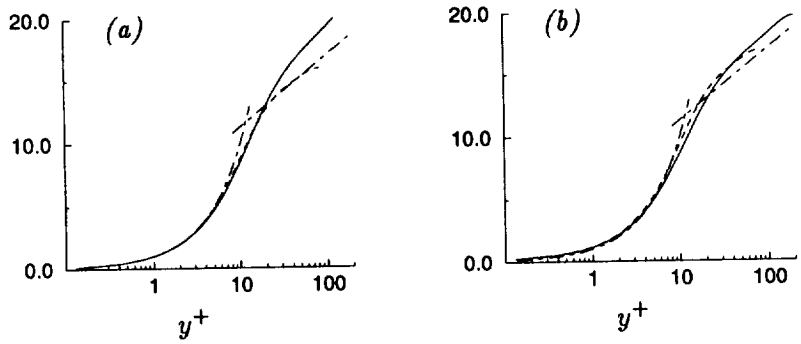

FIGURE 8. Mean profile of velocity in wall units for Case B. (a): non-transformed; (b): Transformed (Van Driest, 1951). ····· : $u^+ = y^+$ and $u^+ = 2.5ln(y^+) + 5.5$; ——— : Case B - Cold wall; ---- : Case B - Hot wall.

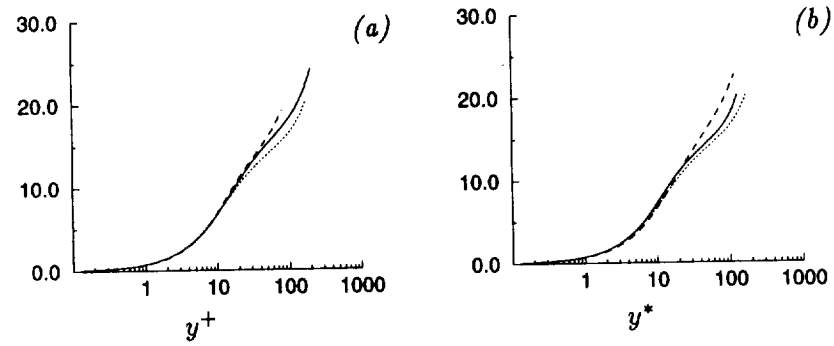

FIGURE 9. Mean profile of temperature in wall units. (a): classic scaling; (b): semi-local scaling. ····· : Case A; ——— : Case B - Cold wall; ---- : Case B - Hot wall.

the beginning of the buffer layer ($y^+ \approx 15$). The Peclet number is so low near the hot wall ($P_e \approx 62$) that the linear behavior due to the inflexion point begins before the logarithmic region ($y^+ \approx 50$). A better collapse between Case A and the cold side of Case B is obtained when a semi-local scaling is used as suggested in Huang *et al.* (1995) (replacing ρ_w with $\rho(y)$, μ_w with $\mu(y)$ and $u_\tau = \sqrt{\tau_w/\rho_w}$ with $u_\tau^*(y) = \sqrt{\tau_w/\rho(y)}$ and then defining T^* and y^* in a similar manner as T^+ and y^+).

From Eq. (7), the mean normal velocity:

$$\overline{v} = \frac{1}{P_o R_e P_r}\left(\overline{k\frac{\partial T}{\partial y}} - \left|\overline{k\frac{\partial T}{\partial y}}\right|_w\right) \tag{42}$$

is not zero although the continuity equation requires that the Favre-averaged normal velocity $\widetilde{v} = \overline{\rho v}/\overline{\rho}$ is zero. However, the negative mean velocity generated by the turbulent heat transfer is only a small fraction ($\approx 1\%$) of the mean friction velocity $\overline{u_\tau}$. From Eq. (42), the total heat flux $q = -\overline{\rho}\widetilde{v''T''} + \overline{k\frac{\partial T}{\partial y}}$ is constant through the channel. Table II gives the principal mean physical characteristics for Case B.

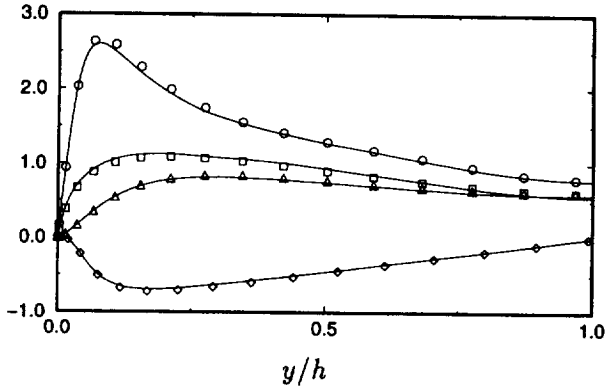

FIGURE 10. Velocity fluctuations for Case A. Wall units. Symbols from Kim *et al.* (1987). ○ : $u^+_{\rm rms}$, △ : $v^+_{\rm rms}$, □ : $w^+_{\rm rms}$, ◇ : $\overline{u'v'}^+$; ——— : Case A.

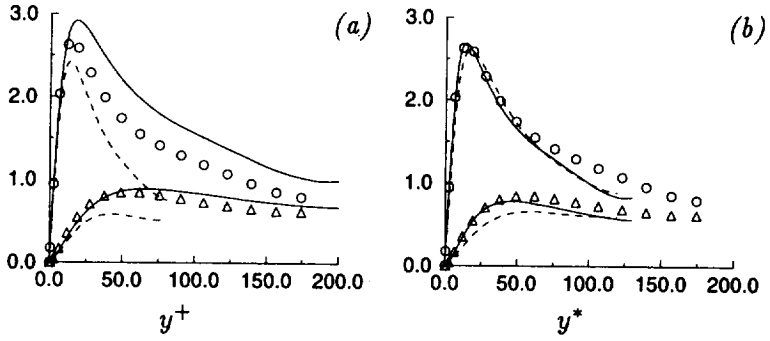

FIGURE 11. Velocity fluctuations in streamwise and normal direction. (a): classic scaling; (b): semi-local scaling. See previous figure for symbols. ——— : Case B - Cold wall; ---- : Case B - Hot wall.

T_2/T_1	$u_{\tau 1}/\overline{u_\tau}$	$u_{\tau 2}/\overline{u_\tau}$	C_{f1}	C_{f2}	B_{q1}	B_{q2}
2	0.87	1.13	2.82×10^{-3}	2.48×10^{-3}	−0.018	0.014

Table II: Physical parameters for Case B.

The friction coefficient is based on the mean density in the channel and the maximum velocity. Due to density and dynamic viscosity variation, the friction velocity is higher at the hot wall but the shear stress is higher at the cold wall. The values obtained for the heat flux parameter B_q are small in absolute value compared to those in the DNS's of Coleman *et al.*, 1995 ($B_q = -0.05$ and -0.14) although the mean channel centerline-to-wall temperature ratios are equivalent (1.5 for Case B, compared to 1.4 and 2.5 for the compressible case). This is because the dissipation term in the internal energy equation is neglected in the low Mach approximation.

4.2 Turbulent fluctuations

For Case A, Fig. 10 shows a good agreement with previous incompressible DNS (Kim *et al.*, 1987) for the three velocity fluctuations and the Reynolds shear stress.

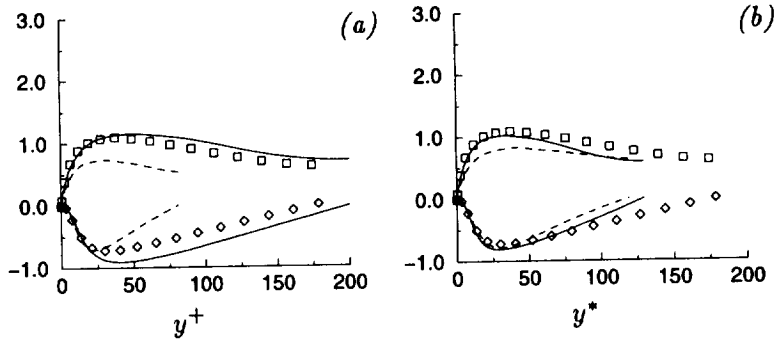

FIGURE 12. Velocity fluctuations in spanwise direction and correlation $\overline{u'v'}$. (a): classic scaling; (b): semi-local scaling. See previous figure for symbols. ——— : Case B - Cold wall; ---- : Case B - Hot wall.

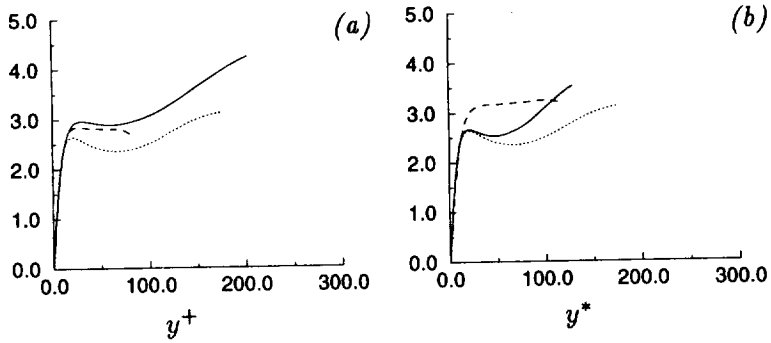

FIGURE 13. Temperature fluctuations. (a): classic scaling; (b): semi-local scaling. ..... : Case A; ——— : Case B - Cold wall; ---- : Case B - Hot wall.

In Case B, these profiles are no longer symmetric and the inner layer appears to be thicker near the hot wall. Large departure from the incompressible case exists if the classic wall scaling is used (see Figs. 11a and 12a). The semi-local scaling allows the profiles to collapse very well. Still, the maximum of $v^*_{\rm rms}$ and $w^*_{\rm rms}$ is smaller in the hot side of Case B. The same trend was observed by Dailey & Pletcher (1998) in their strong heating case (in the supersonic channel flow studied by Coleman *et al.* (1995), both sides correspond to a strong cooling). It suggests that all the differences between the isothermal and heated flow cannot be reduced to a simple mean density effect. It is worth studying this point in more detail. The temperature fluctuations collapse neither for the classic nor for the semi-local scaling (see Fig. 13), except close to the wall and if only Case A and the cooled side of Case B are considered.

Gaviglio (1987) invokes a distinction between large and small scales in turbulence and argues that temperature and velocity fluctuations are highly correlated within large coherent structures. Defining the characteristic length as $l_u = \frac{u_{\rm rms}}{|\partial\overline{u}/\partial y|}$ and

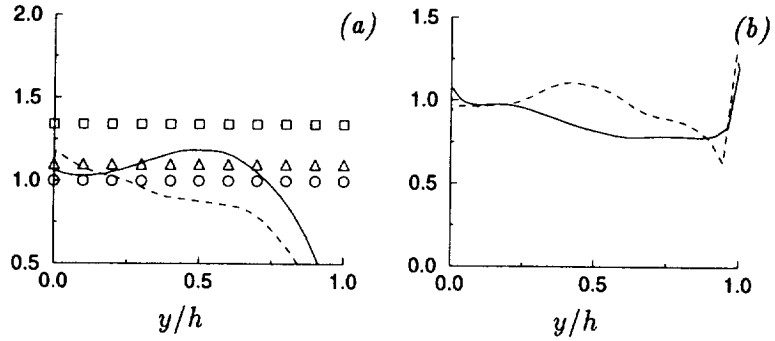

FIGURE 14. (a): $\frac{T_{\rm rms}}{u_{\rm rms}} \frac{|\partial\overline{u}/\partial y|}{|\partial\overline{T}/\partial y|}$ from the DNS Case B. ——— : cold wall; ---- : hot wall; symbols: theoretical ratio from. o : Gaviglio (1987), △ : Huang *et al.* (1995), □ :Rubesin (1990). (b): Turbulent Prandtl number. ····· : Case A; ——— : Case B - Cold wall; ---- : Case B - Hot wall.

$l_T = \frac{T_{\rm rms}}{|\partial\overline{T}/\partial y|}$ and assuming $l_u \propto l_T$, he derives:

$$\frac{T_{\rm rms}}{u_{\rm rms}} \frac{|\partial\overline{u}/\partial y|}{|\partial\overline{T}/\partial y|} = R_0 \tag{43}$$

Gaviglio's formulation imposes $R_0 = 1$ whereas Huang *et al.* (1995) propose $R_0 = 1/Pr_t$ ($Pr_t \approx 0.9$) and Rubesin (1990) chooses $R_0 = 1.34$. These analogies are tested in Fig. 14a and appear to give a reasonable representation of the present results. Figure 14a suggests that $R_0 = 1/Pr_t$ is a good choice. The turbulent Prandtl number is given in Fig. 14b. The cold side of the channel looks like the incompressible Case A with a peak around 1.1 at the wall, a plateau around $y^* \approx 40$, and a constant decrease through the center of the channel where $Pr_t \approx 0.7$. However, at the hot side of the channel, the turbulent Prandtl number is closer to a constant value and $Pr_t \approx 1$ would be a good approximation everywhere. It is not clear yet whether this different behavior is due to differing thermal conditions between the two walls, or whether it simply reflects a low-Reynolds number effect ($R_{\tau 2}$ is half $R_{\tau 1}$). The same question arises in looking at the correlation coefficients for the shear stress and the heat fluxes (Fig. 15). The main differences appear in the hot side of the channel where the Reynolds number is small. The maximum of R_{uv} and R_{vT} is located further from the wall in Case B, but the difference disappears when wall units are adopted. However, the profile of R_{uT} is fuller in the heated case with a larger negative correlation between u and T ($R_{uT} \approx -0.80$ compared to $R_{uT} \approx -0.60$ at $y/h = 0.5$). A scaling argument can hardly explain the difference. Kim & Moin (1987) did not observe that $|R_{uT}|$ increases for lower Peclet numbers.

4.3 Higher-order statistics

The computed skewness and flatness factors for u and v are shown in Figs. 16 and 17. The adequacy of the sample size used to compute the higher-order statistics is only marginal for Case B. However, these quantities are strongly related to the

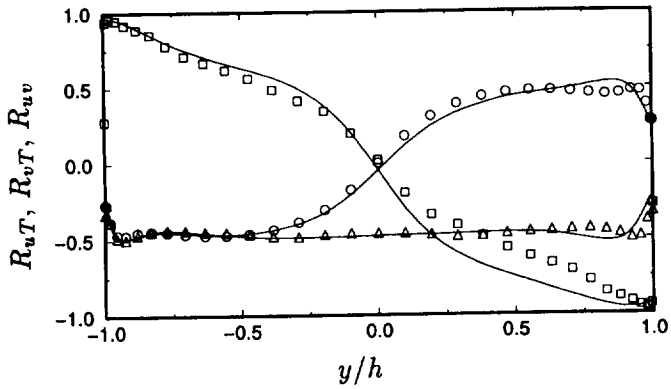

FIGURE 15. Correlation coefficients for Case B. Symbols from Kim *et al.* (1987). ○ : R_{uv}, △ : R_{vT}, □ : R_{uT}; ——— : Case B.

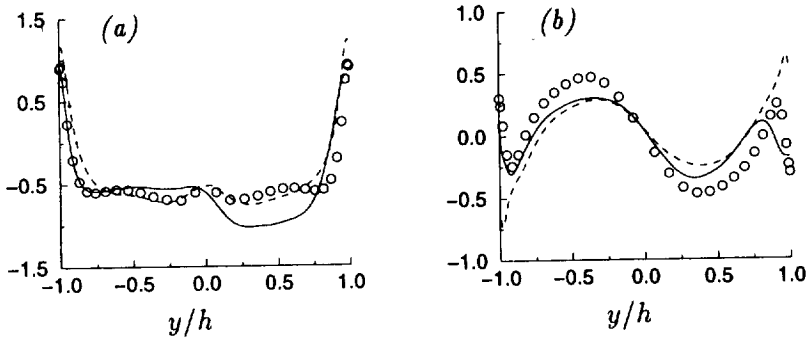

FIGURE 16. Skewness factors of u (a) and v (b). ——— : Case B; ---- : Incompressible DNS, $R_\tau = 110$; ○ : Incompressible, $R_\tau = 180$, from Kim *et al.*

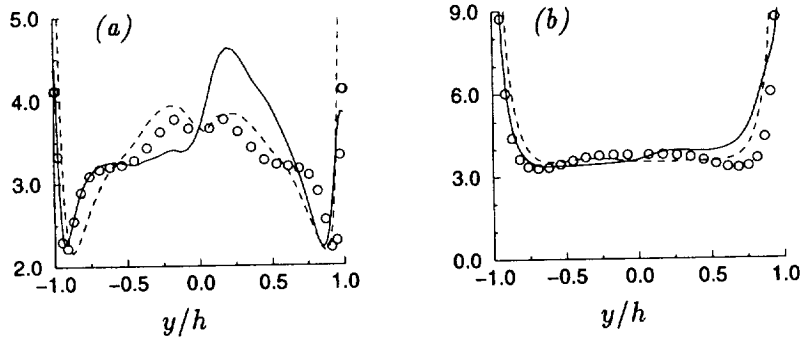

FIGURE 17. Flatness factors of u (a) and v (b). ——— : Case B; ---- : Incompressible DNS, $R_\tau = 110$; ○ : Incompressible, $R_\tau = 180$, from Kim *et al.*

turbulence structure, and it is worth considering how they are modified by a strong heating/cooling. In Figs. 16 and 17, the results for Case B are compared to the incompressible data of Kim *et al.* (1987). To distinguish between the heat transfer

and the Reynolds number effect, a DNS of an incompressible channel flow at very low Reynolds number ($R_\tau = 110$) was performed with the fourth-order accurate code of Morinishi *et al.* (1998). The domain size for this simulation is ($4\pi h$,$2h$,$4\pi/3h$) and the grid contains 72x50x60 cells. Although $R_{\tau 2}$ is only about 80 in Case B, the incompressible simulation with $R_\tau = 110$ is adequately representative of the hot (upper) half of the channel in Case B. Indeed, because of the rapid near-wall variations of mean properties, the Reynolds number $R^*_{\tau 2}$ based on properties evaluated locally is equal to 110 in Case B at the distance $0.4h$ from the hot wall.

The skewness factor of the streamwise velocity u (see Fig. 16a) is roughly -0.5 to -0.6 for $y^+ \approx 50$ for the incompressible DNS's at $R_\tau = 180$ and $R_\tau = 110$. At the same time, the normal velocity (see Fig. 16b) is skewed positively in the lower half-channel and negatively in the upper one. It is known that these features of the skewness factors correspond to large excursions of fluid from the walls to the core region. Figure 16a shows that the skewness factor of u in the heated (upper) half-channel of Case B is approximately twice as large as in the incompressible cases. This strongly suggests that the density gradient enhances the ejection events in this region. The same trend is visible in Fig. 16b, which also suggests that the ejection events are weakened in the cooled (lower) half-plane. These findings would be consistent with the existence of a force that pushes the lumps of fluid from the hot to the cold wall. Wardana *et al.* (1992) supposed that the thermal expansion was responsible for the modifications observed in the turbulence structure. From Eq. (42), the mean dilatation in Case B produces negative mean momentum whose modulus is roughly $\rho|q_w|/P_o$. It acts on turbulent structures with time scale $\alpha h/u_\tau$, where $\alpha < 1$ expresses that the vortices are smaller than the channel half-height ($\alpha \approx 0.1$ at the distance $y = 0.2h$ from the wall). Requiring that the resulting impulsion, $\rho|q_w|u_\tau/(P_o \alpha h)$, is of the same order of magnitude as the viscous force, $\tau_w/h = \rho u_\tau^2/h$, one obtains the estimate $B_q \approx 0.1$ for the heat flux parameter. In Case B, as the modulus of B_q is of order 10^{-2}, it is unclear whether or not thermal expansion is significant. The inviscid force studied by Eames & Hunt (1997) offers an alternative to the mean thermal expansion to explain the modifications in the turbulence structure. It has the right sign (it is oriented from the hot wall to the cold wall) and the relative density variation $\Delta\rho/\rho$ is of order 1 in Case B, so that this force is not negligible (see the beginning of Section 4). Figures 17a and 17b show that the intermittency is higher in the heated side, smaller in the cooled side of the channel. This is consistent with the enhancement/damping of the strong bursting events illustrated above.

5. Discussion and future plans

The analogies developed in the context of supersonic boundary layers work well in the case of a low-speed flow with strong heat transfer. It is not very surprising since these analogies were derived assuming that compressibility effects are negligible except for the mean density gradient. An advantage of the present configuration is that each DNS provides information about both one positive and one negative heat flux parameter B_q. In this respect, the classical Van Driest transformation was tested for both a cooled and a heated wall, and the logarithmic behavior was well

retrieved for the mean velocity. The results suggest that the additive constant C is in both cases greater than its incompressible value. This unexpected result may be due to a low Reynolds number effect. Indeed, the Reynolds number R_τ at the hot wall is half its value at the hot wall and it is known that the additive constant in the law-of-the-wall increases for low Reynolds numbers. Assuming that the Reynolds number ratio $R_\tau^{hot}/R_\tau^{cold}$ behaves roughly like the temperature ratio T_1/T_2, it is clear that a DNS with strong heat transfer and sufficiently high Reynolds number everywhere in the domain would be very expensive. To this end, a 'non-physical' simulation where both the thermal conductivity and dynamic viscosity are inversely proportional to the temperature may serve as a less expensive way to minimize Reynolds number effects. Some differences appeared between the incompressible case and the cooled/heated channel that a re-scaling based on the mean density gradient was unable to eliminate altogether (amplitude of the peak in $v_{\rm rms}$ and $w_{\rm rms}$, shape of the profile of Pr_t, value of R_{uT}). The higher-order statistics reveal large modifications in the turbulence structure when the density gradient is not negligible. It is suggested that these modifications are related to a purely inviscid effect which pushes the turbulent structures towards the denser fluid. A case with a larger temperature ratio would be worth considering to investigate these differences in further detail.

P. Bradshaw and C. Pierce are acknowledged for their helpful comments on an earlier version of this manuscript.

REFERENCES

BELL, J. B. & MARCUS, D. L. 1992 A second-order projection method for variable-density flows. *J. Comp. Phys.* **101,** 334-348.

BRADSHAW, P. 1977 Compressible turbulent shear layers. *Ann. Rev. Fluid Mech.* **9,** 33-54.

BUELL, J. C. 1990 Direct simulations of compressible wall-bounded turbulence. *CTR Annual Research Briefs.* Center for Turbulence Research, NASA Ames/ Stanford Univ., 347-356.

CHENG, R. K. & NG, T. T. 1982 Some aspects of strongly heated turbulent boundary layers flows. *Phys. Fluids.* **25,** 8, 1333-1341.

COLEMAN, G. N., KIM, J., & MOSER, R. D. 1995 A numerical study of turbulent supersonic isothermal-wall channel flow. *J. Fluid Mech.* **305,** 159-183.

COOK, A. & RILEY, J. 1996 Direct numerical simulation of a turbulent reactive plume on a parallel computer. *J. Comp. Phys.* **129,** 263-283.

DAILEY, L. D. & PLETCHER, R. H. 1998 Large eddy simulation of constant heat flux turbulent channel flow with property variations. *AIAA 98-0791.*

EAMES, I. & HUNT, J. C. R. 1997 Inviscid flow around bodies moving in weak density gradients without buoyancy effects. *J. Fluid Mech.* **353,** 331-355.

FERNHOLZ, H. H. & FINLEY, P. J. 1980 A critical commentary on mean flow data for two-dimensional compressible turbulent boundary layers. *AGARD-AG-253.*

GAVIGLIO, J. 1987 Reynolds analogies and experimental study of heat transfer in the supersonic boundary layer. *Int. J. Heat Mass Transfer.* **30,** 5, 911-926.

HUANG, P. G. & COLEMAN G. N. 1994 Van Driest transformation and compressible wall-bounded flows. *AIAA J.* **32,** 10, 2110-2113.

HUANG, P. G., COLEMAN, G. N. & BRADSHAW, P. 1995 Compressible turbulent channel flows: DNS results and modeling. *J. Fluid Mech.* **305,** 185-218.

KADER, B. 1981 Temperature and concentration profiles in fully turbulent boundary layers. *Int. J. Heat Mass Transfer.* **24,** 9, 1541-1544.

KASAGI, N., TOMITA, Y. & KURODA, A. 1992 DNS of the passive scalar field in a turbulent channel flow. *ASME J. Heat Transfer.* **114,** 598-606.

KIM, J., MOIN, P. & MOSER, R. 1987 Turbulence statistics in fully developed channel flow at low Reynolds number. *J. Fluid Mech.* **177,** 133-166.

KIM, J. & MOIN, P. 1987 Transport of passive scalars in a turbulent channel flow. *Turbulent Shear flows.* **6,** 85-96.

MCMURTHRY, P., JOU, W., RILEY, J. & METCALFE, R. 1986 DNS's of a reacting mixing layer with chemical heat release. *AIAA J.* **24,** 6, 962-970.

MORINISHI, Y., LUND, T., VASILYEV, O. & MOIN, P. 1998 Fully Conservative higher order finite difference schemes for incompressible flow. *J. Comp. Phys.* **143,** 1, 90-124.

MORKOVIN, M. V. 1962 *Effects of compressibility on turbulent flows*, Coll. CNRS No. 108, Mécanique de la Turbulence, 367-380.

PAOLUCCI, S. 1982 On the filtering of sound from the Navier-Stokes equations. *SAND82-8253,* Sandia National Laboratories, Livermore.

RUBESIN, M.W. 1990 Extra compressibility terms for Favre-averaged two-equation models of inhomogeneous turbulent flows. *NASA CR-177556.*

SPALART, P. 1987 Hybrid RKW3 + Crank-Nicolson scheme. *Internal Report,* NASA-Ames Research Center, Moffett Field, CA.

SPINA, E. F., SMITS, A. J. & ROBINSON, S. K. 1994 The physics of supersonic turbulent boundary layers. *Ann. Rev. Fluid Mech.* **26,** 287-319.

SUSLOV, S. & PAOLUCCI, S. 1995 Stability of mixed-convection flow in a tall vertical channel under non-Boussinesq conditions. *J. Fluid Mech.* **302,** 91-115.

VAN DRIEST, E. R. 1951 Turbulent boundary layers in compressible fluids. *J. Aero. Sci.* **18,** 3, 145-160.

WANG, W. & PLETCHER, R. 1996 On the large eddy simulation of a turbulent channel flow with significant heat transfer. *Phys. Fluids.* **8,** 12, 3354-3366.

WARDANA, I. N. G., UEDA, T. & MIZOMOTO, M. 1992 Structure of turbulent two-dimensional channel flow with strongly heated wall. *Exp. Fluids.* **13,** 17-25.

WARDANA, I. N. G., UEDA, T. & MIZOMOTO, M. 1994 Effect of strong wall heating on turbulence statistics of a channel flow. *Exp. Fluids.* **18,** 87-94.

On the construction of high order finite difference schemes on non-uniform meshes with good conservation properties

By Oleg V. Vasilyev[1]

1. Motivation and objectives

Numerical simulation of turbulent flows (DNS or LES) requires numerical methods that can accurately represent a wide range of spatial scales. One way to achieve a desired accuracy is to use high order finite difference schemes. However, additional constraints such as discrete conservation of mass, momentum, and kinetic energy should be enforced if one wants to ensure that unsteady flow simulations are both stable and free of numerical dissipation. In addition, both pressure and velocity fields must be physical. These requirements are usually achieved by using a staggered grid and enforcing continuity.

Until recently the standard second order accurate staggered grid finite difference scheme of Harlow and Welch (1965) was the only scheme that simultaneously conserved mass, momentum, and kinetic energy. It was observed by Ghosal (1996) that the accuracy of second order finite difference scheme is low and fine meshes are required to achieve acceptable results. For that reason Morinishi *et al.* (1998) derive the general family of fully conservative higher order accurate finite difference schemes for uniform staggered grids. Both the scheme of Harlow and Welch (1965) and that of Morinishi *et al.* (1998) conserve mass, momentum, and kinetic energy on a uniform mesh. However, generalizing these schemes to non-uniform meshes and preserving the conservation properties is not straightforward. For example, the generalization of the fourth order accurate finite difference scheme, suggested in (Morinishi *et al.*, 1998), does not even conserve momentum. Furthermore, Morinishi *et al.* (1998) mistakenly concluded that in order to construct conservative schemes, one should choose between the accuracy and conservation. One of the reasons why the authors came to this conclusion may be the fact that they tried to generalize the scheme by changing the weights in the difference operators as a function of local grid spacings and preserving the order of local truncation error. As a consequence of this generalization, the resulting scheme does not preserve symmetries of the uniform mesh case. Veldman and Versappen (1998), in their analysis of convective-diffusion equation on non-uniform meshes, showed that in order for the scheme to be conservative, it should preserve symmetries of the underlying operator, *i.e.* the convective derivative should be approximated by skew-symmetric operator.

1 Present address: Department of Mechanical and Aerospace Engineering, University of Missouri, Columbia, MO 65211

This report is an attempt to generalize the high order schemes of Morinishi *et al.* (1998) to non-uniform meshes by preserving the symmetries of the uniform mesh case.

2. Accomplishments

2.1 Analytical requirements

In this section, we briefly outline the analytical requirements for conservation of mass, momentum, and energy for incompressible flow. For further details we refer the reader to (Morinishi *et al.*, 1998).

An equation of the form:

$$\frac{\partial \phi}{\partial t} + {}^1Q(\phi) + {}^2Q(\phi) + {}^3Q(\phi) + \cdots = 0, \tag{1}$$

is said to be written in conservative form if all the terms ${}^kQ(\phi)$ can be written in divergence form:

$${}^kQ(\phi) = \nabla \cdot ({}^k\mathbf{F}(\phi)) = \frac{\partial({}^kF_j(\phi))}{\partial x_j}. \tag{2}$$

In this report we use bold letters to denote a vector function, *e.g.* $\mathbf{F} = (F_1, F_2, F_3)^{\mathrm{T}}$. The requirement (2) follows from Gauss' divergence theorem. In particular, if we integrate Eq. (1) over a volume, we obtain:

$$\frac{\partial}{\partial t}\int\int\int_V \phi \, dV = -\int\int_S ({}^1\mathbf{F}(\phi) + {}^2\mathbf{F}(\phi) + {}^3\mathbf{F}(\phi) + \cdots) \cdot d\mathbf{S}. \tag{3}$$

From this equation it is easy to see that the integral never changes in the periodic case if ${}^kQ(\phi)$ has a conservative form for all k. Following this definition of conservation, it is easy to show that mass, pressure, and viscous terms are conserved *a priori* since these terms appear in divergence form. The convective term is also conservative *a priori* if it is written in divergence form, which is not always the case. There are four commonly used forms of the convective term. These forms are referred to as *divergence*, *advective*, *skew-symmetric*, and *rotational* forms and are defined as follows:

$$(Div.)_i \equiv \frac{\partial u_j u_i}{\partial x_j}, \tag{4a}$$

$$(Adv.)_i \equiv u_j \frac{\partial u_i}{\partial x_j}, \tag{4b}$$

$$(Skew.)_i \equiv \frac{1}{2}\frac{\partial u_j u_i}{\partial x_j} + \frac{1}{2}u_j \frac{\partial u_i}{\partial x_j}, \tag{4c}$$

$$(Rot.)_i \equiv u_j \left(\frac{\partial u_i}{\partial x_j} - \frac{\partial u_j}{\partial x_i}\right) + \frac{1}{2}\frac{\partial u_j u_j}{\partial x_i}. \tag{4d}$$

The four forms are connected with each other through the following analytical relations:

$$(Adv.)_i = (Div.)_i - u_i \cdot (Cont.), \tag{5a}$$

$$(Skew.)_i = \frac{1}{2}(Div.)_i + \frac{1}{2}(Adv.)_i, \tag{5b}$$

$$(Rot.)_i = (Adv.)_i, \tag{5c}$$

where $(Cont.) \equiv \frac{\partial u_i}{\partial x_i}$. Note that the advective, skew-symmetric, and rotational forms are conservative as long as the continuity equation is satisfied.

The transport equation of the square of a velocity component, for instance, ${u_1}^2/2$, can be written as

$$\frac{\partial {u_1}^2/2}{\partial t} + u_1 \cdot (Conv.)_1 + u_1 \cdot (Pres.)_1 + u_1 \cdot (Visc.)_1 = 0, \tag{6}$$

where $(Conv.)_i$ is a generic form of the convective term, and $(Pres.)_i$ and $(Visc.)_i$ are the pressure and viscous terms respectively. The convective term in Eq. (6) can be written for each of the forms as

$$u_1 \cdot (Div.)_1 = \frac{\partial u_j {u_1}^2/2}{\partial x_j} + \frac{1}{2}{u_1}^2 \cdot (Cont.), \tag{7a}$$

$$u_1 \cdot (Adv.)_1 = \frac{\partial u_j {u_1}^2/2}{\partial x_j} - \frac{1}{2}{u_1}^2 \cdot (Cont.), \tag{7b}$$

$$u_1 \cdot (Skew.)_1 = \frac{\partial u_j {u_1}^2/2}{\partial x_j}. \tag{7c}$$

Note that the skew-symmetric form is conservative *a priori* in the velocity square equation. Since the rotational form is equivalent to the advective form, the four convective forms are energy conservative if the continuity equation is satisfied.

The transport equation of the kinetic energy, $K \equiv u_i u_i/2$ can be written as

$$\frac{\partial K}{\partial t} + u_i \cdot (Conv.)_i + u_i \cdot (Pres.)_i + u_i \cdot (Visc.)_i = 0. \tag{8}$$

The conservation property of the convective term can be determined in the same manner as for ${u_1}^2/2$. The terms involving pressure and viscous stress in Eq. (8) can be written as

$$u_i \cdot (Pres.)_i = \frac{\partial p u_i}{\partial x_i} - p \cdot (Cont.), \tag{9a}$$

$$u_i \cdot (Visc.)_i = \frac{\partial \tau_{ij} u_i}{\partial x_j} - \tau_{ij}\frac{\partial u_i}{\partial x_j}. \tag{9b}$$

The pressure term is conservative if the continuity equation is satisfied. The viscous term is not conservative because the second term on the right-hand side of Eq. (9b) is the kinetic energy dissipation.

Morinishi *et al.* (1998) derived a class of high order schemes for a uniform staggered grid which satisfy the conservation properties in a discrete sense. The objective of this work is to generalize the higher order schemes of Morinishi *et al.* (1998) to the non-uniform meshes while preserving discrete conservation as much as possible.

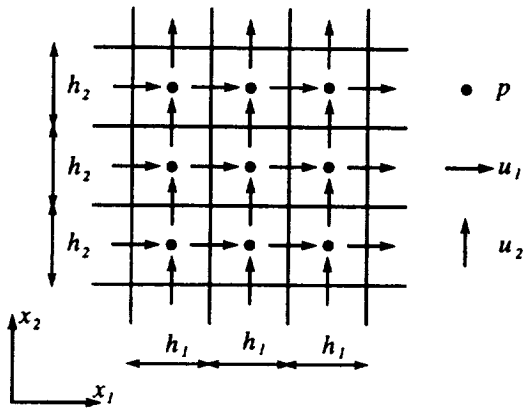

FIGURE 1. Staggered grid arrangement.

2.2 Discrete operators

In order to simplify the analysis, we limit our consideration to the rectangular algebraic non-uniform meshes with non-uniform grid spacing in each x_1, x_2, and x_3 direction. By algebraic grid we imply that the computational grid in physical domain is obtained by mapping a uniform computational grid in the computational domain to physical domain. Let $D = [a_1, b_1] \times [a_2, b_2] \times [a_3, b_3]$ and $\Omega = [\alpha_1, \beta_1] \times [\alpha_2, \beta_2] \times [\alpha_3, \beta_3]$ be respectively the physical and computational domains, $\mathbf{x} = (x_1, x_2, x_3)^{\mathrm{T}}$ and $\boldsymbol{\xi} = (\xi_1, \xi_2, \xi_3)^{\mathrm{T}}$ be coordinates in physical and computational domains, $\boldsymbol{\xi} = \mathbf{f}(\mathbf{x})$ be a nonlinear map of physical domain D into computational domain, and Δ_1, Δ_2, Δ_3 be uniform grid spacings in the respective directions in computational domain Ω. In this report we limit our consideration to the case when mapping $\boldsymbol{\xi} = \mathbf{f}(\mathbf{x})$ can be written in the form

$$\xi_i = f_i(x_i), \qquad i = 1, \ldots, 3. \tag{10}$$

In other words, we consider only uni-directional mappings, and the computational grid in physical space can be constructed as a tensor product of one-dimensional computational grids.

Let us briefly describe the staggered grid arrangement. An example of a uniform staggered grid is shown in Fig. 1. In the case of uniform grid spacings, the choice for location of velocity and pressure points is natural: the velocity components U_i $(i = 1, 2, 3)$ are distributed around the pressure points. The continuity equation is centered at the pressure points while the momentum equations corresponding to each velocity component are centered at the respective velocity points. In the case of a non-uniform staggered grid, the location of pressure and velocity points are ambiguous: these points can be determined as geometrical volume and edge centers either in physical or computational spaces. Morinishi *et al.* (1998) followed the first approach. However, the generalization to non-uniform meshes suggested in (Morinishi *et al.*, 1998) preserves the conservation properties only in the case of the second order scheme. The reason is that for the higher order schemes

(4th order and higher) the resulting discrete operators do not preserve symmetries of the uniform mesh case. Veldman and Rinzema (1992) and Veldman and Versappen (1998) showed that in order for the scheme to be conservative, it should preserve symmetries of the underlying operator. The basic idea behind Veldman and Versappen's generalization is that the differentiation operation is performed in computational space. The derivative in physical space is calculated using the local Jacobian, which can be found numerically using the same stencil and the same order accuracy as finite differencing operator in the computational space. To illustrate this idea let us consider one dimensional case. First, we approximate derivative in computational space

$$\frac{\delta\phi}{\delta\xi} = \frac{\phi_{i+1} - \phi_{i-1}}{2\Delta},$$

where Δ is uniform grid spacing. The derivative in physical space is found as

$$\frac{\delta\phi}{\delta x} = \frac{1}{J}\frac{\delta\phi}{\delta\xi}, \tag{11}$$

where J is the Jacobian of the transformation $x \to \xi$, which can be found numerically by substituting x for ϕ

$$J = \frac{\delta x}{\delta\xi} = \frac{x_{i+1} - x_{i-1}}{2\Delta}.$$

Substitution of this equation into Eq. (11) gives us the following approximation of the derivative in physical space:

$$\frac{\delta\phi}{\delta x} = \frac{\phi_{i+1} - \phi_{i-1}}{x_{i+1} - x_{i-1}},$$

This seemingly simple idea is the key which enables us to generalize the higher order schemes of Morinishi *et al.* (1998) to non-uniform meshes.

Let the finite difference operator in computational domain with stencil n acting on ϕ with respect to ξ_1 be defined as

$$\left.\frac{\delta_n\phi}{\delta_n\xi_1}\right|_{\xi_1,\,\xi_2,\,\xi_3} \equiv \frac{\phi(\xi_1 + n\Delta_1/2,\,\xi_2,\,\xi_3) - \phi(\xi_1 - n\Delta_1/2,\,\xi_2,\,\xi_3)}{n\Delta_1}. \tag{12a}$$

The interpolation operator with stencil n acting on ϕ in the ξ_1 direction is given by

$$\left.\overline{\phi}^{n\xi_1}\right|_{\xi_1,\,\xi_2,\,\xi_3} \equiv \frac{\phi(\xi_1 + n\Delta_1/2,\,\xi_2,\,\xi_3) + \phi(\xi_1 - n\Delta_1/2,\,\xi_2,\,\xi_3)}{2}. \tag{12b}$$

In addition, we define a special interpolation operator with stencil n of the product of ϕ and ψ in the ξ_1 direction,

$$\begin{aligned}\left.\widehat{\phi\psi}^{n\xi_1}\right|_{\xi_1,\,\xi_2,\,\xi_3} \equiv{}& \frac{1}{2}\phi(\xi_1 + n\Delta_1/2,\,\xi_2,\,\xi_3)\,\psi(\xi_1 - n\Delta_1/2,\,\xi_2,\,\xi_3) \\ &+ \frac{1}{2}\psi(\xi_1 + n\Delta_1/2,\,\xi_2,\,\xi_3)\,\phi(\xi_1 - n\Delta_1/2,\,\xi_2,\,\xi_3).\end{aligned} \tag{12c}$$

Discrete operators in the ξ_2 and ξ_3 directions are defined in the same way as for the ξ_1 direction.

The following identities will be needed to derive some relations later in the paper:

$$\frac{\delta_n \widehat{\phi\psi}^{n\xi_j}}{\delta_n \xi_j} = \phi \frac{\delta_{2n}\psi}{\delta_{2n}\xi_j} + \psi \frac{\delta_{2n}\phi}{\delta_{2n}\xi_j}, \tag{13a}$$

$$\widehat{(\phi\psi)\cdot\psi}^{n\xi_j} = \overline{\phi}^{n\xi_j}\widehat{\psi\psi}^{n\xi_j}, \tag{13b}$$

$$\overline{\phi}^{n\xi_j}\overline{\psi}^{n\xi_j} = \frac{1}{2}\overline{\phi\psi}^{n\xi_j} + \frac{1}{2}\widehat{\phi\psi}^{n\xi_j}, \tag{13c}$$

$$\frac{\delta_n \overline{\phi}^{n\xi_j}}{\delta_n \xi_j} = \frac{\delta_{2n}\phi}{\delta_{2n}\xi_j}, \tag{13d}$$

$$\frac{\delta_n \overline{\phi}^{m\xi_i}}{\delta_n \xi_j} = \overline{\frac{\delta_n \phi}{\delta_n \xi_j}}^{m\xi_i}, \tag{13e}$$

$$\overline{\psi\frac{\delta_n\phi}{\delta_n\xi_j}}^{n\xi_j} = \frac{\delta_n\,\psi\cdot\overline{\phi}^{n\xi_j}}{\delta_n\xi_j} - \phi\frac{\delta_n\psi}{\delta_n\xi_j}, \tag{13f}$$

$$\phi\frac{\delta_n\,\psi\cdot\overline{\phi}^{n\xi_j}}{\delta_n\xi_j} = \frac{1}{2}\frac{\delta_n\,\psi\cdot\widehat{\phi\phi}^{n\xi_j}}{\delta_n\xi_j} + \frac{1}{2}\phi\phi\frac{\delta_n\psi}{\delta_n\xi_j}. \tag{13i}$$

Note that ξ_i appearing as a superscript does not follow the summation convention.

For notational convenience let us introduce the discrete finite difference operator in the physical domain:

$$\left.\frac{\delta_n\phi}{\delta_n x_i}\right|_{x_1,\,x_2,\,x_3} \equiv \frac{1}{J(\xi_i)}\left.\frac{\delta_n\phi}{\delta_n\xi_i}\right|_{\xi_1,\,\xi_2,\,\xi_3}, \tag{14a}$$

where $J(\xi_i)$ is local Jacobian of the transformation $x_i \to \xi_i$. Note that the subscript i appearing in $J(\xi_i)$ in Eq. (14a) and all subsequent equations does not follow the summation convention. We emphasize that it is the form of Eq. (14a) which allows the construction of higher order schemes on non-uniform meshes with good conservation properties.

The averaging operators (12b) and (12c) use only functional values at grid points and do not use any information about grid spacing. Consequently, these operations can be performed in both physical and computational spaces. For clarity of the notation, we define the following operators in physical space:

$$\left.\overline{\phi}^{nx_i}\right|_{x_1,\,x_2,\,x_3} \equiv \left.\overline{\phi}^{n\xi_1}\right|_{\xi_1,\,\xi_2,\,\xi_3}, \tag{14b}$$

$$\left.\widehat{\phi\psi}^{nx_i}\right|_{x_1,\,x_2,\,x_3} \equiv \left.\widehat{\phi\psi}^{n\xi_i}\right|_{\xi_1,\,\xi_2,\,\xi_3}. \tag{14c}$$

We define two types of conservative forms in the discrete systems. ${}^kQ(\phi)$ in Eq. (1) is (*locally*) *conservative* if the term can be written as

$$ {}^kQ(\phi) = \frac{\delta_1({}^kF_j^1(\phi))}{\delta_1 x_j} + \frac{\delta_2({}^kF_j^2(\phi))}{\delta_2 x_j} + \frac{\delta_3({}^kF_j^3(\phi))}{\delta_3 x_j} + \cdots. \tag{15} $$

This definition corresponds to the analytical conservative form of Eq. (2).

We call ${}^kQ(\phi)$ to be *globally conservative* if the following relation holds in a periodic field:

$$ \sum_{x_1}\sum_{x_2}\sum_{x_3} {}^kQ(\phi)\,\Delta V(\mathbf{x}) = 0, \tag{16} $$

where the sums that appear in Eq. (16) are taken in the respective directions, $\Delta V(\mathbf{x}) \equiv J(\boldsymbol{\xi})\Delta V(\boldsymbol{\xi})$, $J(\boldsymbol{\xi}) = \prod_{k=1}^3 J(\xi_k)$ is the Jacobian of the transformation $\mathbf{x} \to \boldsymbol{\xi}$, and $\Delta V(\boldsymbol{\xi}) = \prod_{k=1}^3 \Delta_k$ is a constant volume in the computational domain. Note that in the periodic case local conservation (15) also implies global conservation. Also note that the definition (16) is a discrete analogue of Eq. (3).

2.3 Finite difference schemes on a non-uniform staggered grid

2.3.1 Continuity and pressure terms

We define the discrete continuity and pressure terms as

$$ (Cont. - NS2) \equiv \frac{\delta_1 U_i}{\delta_1 x_i} = 0, \tag{17} $$

$$ (Pres. - NS2)_i \equiv \frac{\delta_1 p}{\delta_1 x_i}, \tag{18} $$

where the $NS2$ denotes the second order accurate finite difference scheme on a non-uniform staggered grid. Analogously, fourth order approximations are

$$ (Cont. - NS4) \equiv \frac{9}{8}\frac{\delta_1 U_i}{\delta_1 x_i} - \frac{1}{8}\frac{\delta_3 U_i}{\delta_3 x_i} = 0, \tag{19} $$

$$ (Pres. - NS4)_i \equiv \frac{9}{8}\frac{\delta_1 p}{\delta_1 x_i} - \frac{1}{8}\frac{\delta_3 p}{\delta_3 x_i}. \tag{20} $$

Local kinetic energy is an ambiguous quantity in a staggered grid arrangement since the individual velocity components are defined at different locations in space. Some sort of interpolation must be used in order to obtain the kinetic energy at the same point. The required interpolations for the pressure terms in the K equations are

$$ \frac{1}{J(\xi_i)}\overline{U_i\frac{\delta_1 p}{\delta_1 \xi_i}}^{1\xi_i} = \frac{\delta_1 U_i \overline{p}^{1x_i}}{\delta_1 x_i} - p\cdot(Cont - NS2), \tag{21} $$

$$ \frac{9}{8}\frac{1}{J(\xi_i)}\overline{U_i\frac{\delta_1 p}{\delta_1 \xi_i}}^{1\xi_i} - \frac{1}{8}\frac{1}{J(\xi_i)}\overline{U_i\frac{\delta_3 p}{\delta_3 \xi_i}}^{3\xi_i} = \frac{9}{8}\frac{\delta_1 U_i \overline{p}^{1x_i}}{\delta_1 x_i} - \frac{1}{8}\frac{\delta_3 U_i \overline{p}^{3x_i}}{\delta_3 x_i} - p\cdot(Cont - NS4). \tag{22} $$

Therefore, Eqs. (18) and (20) are globally conservative if the corresponding discrete continuity equations are satisfied.

2.3.2 Second order accurate convective schemes

As we have already mentioned, local kinetic energy $K \equiv U_i U_i/2$ can not be defined uniquely on a staggered grid. Let us assume that a term is (locally) conservative in the transport equation of K if the term is (locally) conservative in the transport equations of ${U_1}^2/2$, ${U_2}^2/2$ and ${U_3}^2/2$. Since the conservation properties of ${U_2}^2/2$ and ${U_3}^2/2$ are estimated in the same manner as for ${U_1}^2/2$, only the conservation properties of the convective schemes in the momentum and ${U_1}^2/2$ equations need to be considered.

Let us define second order accurate convective schemes for non-uniform staggered grids as follows:

$$(Div. - NS2)_i \equiv \frac{\delta_1 \overline{U_j}^{1x_i} \overline{U_i}^{1x_j}}{\delta_1 x_j}, \tag{23}$$

$$(Adv. - NS2)_i \equiv \frac{1}{J(\xi_j)} \overline{\overline{U_j}^{1\xi_i} \frac{\delta_1 U_i}{\delta_1 \xi_j}}^{1\xi_j}, \tag{24}$$

$$(Skew. - NS2)_i \equiv \frac{1}{2}(Div. - NS2)_i + \frac{1}{2}(Adv. - NS2)_i. \tag{25}$$

Using Eqs. (13e), (13f), (14a), and (14b) the advective $(Adv. - NS2)_i$ and divergence $(Div. - NS2)_i$ forms of the convective term are connected via

$$(Adv. - NS2)_i = (Div - NS2)_i - U_i \frac{\delta_1 \overline{U_j}^{1x_i}}{\delta_1 x_j}. \tag{26}$$

Using (13e), Eq. (26) can be further simplified as follows:

$$\begin{aligned}(Adv. - NS2)_i = (Div - NS2)_i - U_i \cdot \overline{(Cont. - NS2)}^{1x_i} \\ + U_i \cdot \left[\overline{\frac{\delta_1 U_i}{\delta_1 x_i}}^{1x_i} - \frac{\delta_1 \overline{U_i}^{1x_i}}{\delta_1 x_i} \right],\end{aligned} \tag{27}$$

where there is no summation over i. Note that the term in square brackets is the commutation error between finite differencing (14a) and averaging (14b) operators and in general is not zero, unless the grid is uniform in x_i direction.

Equations (23) and (27) are the discrete analogs of the Eqs. (4a) and (5a) respectively. Clearly, Eqs. (4a) and (23) have the same structure while Eq. (27) has an additional term in it when compared to Eq. (5a). For that reason the discrete conservation properties for both advective and skew-symmetric forms of the convective term are different from analytical ones. In other words, the divergence $(Div. - NS2)_i$ form of the convective term is conservative *a priori* in the momentum equation while enforcing the discrete continuity is not enough to make both advective $(Adv. - NS2)_i$ and skew-symmetric $(Skew. - NS2)_i$ forms conserve the momentum. This is due to the presence of commutation error term which, in general, is non-zero for non-uniform meshes.

Using Eqs. (13f), (13i), and (14) the product between U_1 and $(Skew.-NS2)_1$ can be rewritten as

$$U_1 \cdot (Skew.-NS2)_1 = \frac{1}{2}\frac{\delta_1 \overline{U_j}^{1x_1}\widehat{U_1 U_1}^{1x_j}/2}{\delta_1 x_j}. \tag{28}$$

Therefore, $(Skew.-NS2)_1$ is conservative *a priori* in the transport equation of ${U_1}^2/2$. Note that in the case of the non-uniform staggered grid, the commutation error term is non-zero and neither divergence $(Div.-NS2)_i$ nor advective $(Adv.-NS2)_i$ forms of the convective term conserve kinetic energy. We also note that in the case of a uniform mesh, the commutation error is zero, and we fully recover the conservation properties described in (Morinishi *et al.*, 1998).

2.3.3 Higher order accurate convective schemes

In this section we will generalize the higher order accurate convective schemes of Morinishi *et al.* (1998) for non-uniform meshes. The fourth order accurate convective schemes on a non-uniform staggered grid are defined as

$$\begin{aligned}(Div.-NS4)_i \equiv & \frac{9}{8}\frac{\delta_1}{\delta_1 x_j}\left\{\left(\frac{9}{8}\overline{U_j}^{1x_i}-\frac{1}{8}\overline{U_j}^{3x_i}\right)\overline{U_i}^{1x_j}\right\} \\ & -\frac{1}{8}\frac{\delta_3}{\delta_3 x_j}\left\{\left(\frac{9}{8}\overline{U_j}^{1x_i}-\frac{1}{8}\overline{U_j}^{3x_i}\right)\overline{U_i}^{3x_j}\right\},\end{aligned} \tag{29}$$

$$\begin{aligned}(Adv.-NS4)_i \equiv & \frac{9}{8}\frac{1}{J(\xi_j)}\overline{\left(\frac{9}{8}\overline{U_j}^{1\xi_i}-\frac{1}{8}\overline{U_j}^{3\xi_i}\right)\frac{\delta_1 U_i}{\delta_1 \xi_j}}^{1\xi_j} \\ & -\frac{1}{8}\frac{1}{J(\xi_j)}\overline{\left(\frac{9}{8}\overline{U_j}^{1\xi_i}-\frac{1}{8}\overline{U_j}^{3\xi_i}\right)\frac{\delta_3 U_i}{\delta_3 \xi_j}}^{3\xi_j},\end{aligned} \tag{30}$$

$$(Skew.-NS4)_i \equiv \frac{1}{2}(Div.-NS4)_i + \frac{1}{2}(Adv.-NS4)_i. \tag{31}$$

Using Eqs. (13e), (13f), (14a), and (14b), the advective $(Adv.-NS4)_i$ and divergence $(Div.-NS4)_i$ forms of the convective term are connected via

$$\begin{aligned}(Adv.-NS4)_i = & (Div.-NS4)_i \\ & -U_i\cdot\left(\frac{9}{8}\overline{(Cont.-NS4)}^{1x_i}-\frac{1}{8}\overline{(Cont.-NS4)}^{3x_i}\right) \\ & +\frac{9}{8}U_i\cdot\left(\frac{9}{8}\left[\overline{\frac{\delta_1 U_i}{\delta_1 x_i}}^{1x_i}-\frac{\delta_1\overline{U_i}^{1x_i}}{\delta_1 x_i}\right]-\frac{1}{8}\left[\overline{\frac{\delta_3 U_i}{\delta_3 x_i}}^{1x_i}-\frac{\delta_3\overline{U_i}^{1x_i}}{\delta_3 x_i}\right]\right) \\ & -\frac{1}{8}U_i\cdot\left(\frac{9}{8}\left[\overline{\frac{\delta_1 U_i}{\delta_1 x_i}}^{3x_i}-\frac{\delta_1\overline{U_i}^{3x_i}}{\delta_1 x_i}\right]-\frac{1}{8}\left[\overline{\frac{\delta_3 U_i}{\delta_3 x_i}}^{3x_i}-\frac{\delta_3\overline{U_i}^{3x_i}}{\delta_3 x_i}\right]\right),\end{aligned} \tag{32}$$

where there is no summation over i. Fourth order convective schemes exhibit the same pattern as second order schemes: only the divergence form $(Div.-NS4)_i$ of

the convective term is conservative *a priori* in the momentum equation. The presence of commutation error in both advective $(Adv. - NS4)_i$ and skew-symmetric $(Skew. - NS4)_i$ forms of the convective term results in non-conservation of momentum on a non-uniform mesh.

The conservation properties for $U_1^2/2$ can be estimated exactly the same way as in previous section. Using Eqs. (13f), (13i), and (14), the following relation can be obtained:

$$\begin{aligned} U_1 \cdot (Skew. - NS4)_1 = \frac{9}{8}\frac{\delta_1}{\delta_1 x_j}\left\{\left(\frac{9}{8}\overline{U_j}^{1x_1} - \frac{1}{8}\overline{U_j}^{3x_1}\right)\widehat{\frac{U_1 U_1}{2}}^{1x_j}\right\} \\ - \frac{1}{8}\frac{\delta_3}{\delta_3 x_j}\left\{\left(\frac{9}{8}\overline{U_j}^{1x_1} - \frac{1}{8}\overline{U_j}^{3x_1}\right)\widehat{\frac{U_1 U_1}{2}}^{3x_j}\right\}. \end{aligned} \tag{33}$$

Thus, $(Skew. - NS4)_i$ is conservative *a priori* in the transport equation of ${U_1}^2/2$ while both the divergence $(Div. - NS4)_i$ and advective $(Adv. - NS4)_i$ forms of the convective term do not conserve kinetic energy when the staggered grid is non-uniform.

Higher order finite difference schemes on non-uniform meshes can be constructed in the same way as for the fourth order schemes. The nth order accurate convective schemes on a non-uniform staggered grid are defined as

$$(Div. - NSn)_i \equiv \sum_{k=1}^{n/2} \alpha_k \frac{\delta_{(2k-1)}}{\delta_{(2k-1)}x_j}\left\{\left(\sum_{l=1}^{n/2}\alpha_l \overline{U_j}^{(2l-1)x_i}\right)\overline{U_i}^{(2k-1)x_j}\right\}, \tag{34}$$

$$(Adv. - NSn)_i \equiv \sum_{k=1}^{n/2} \frac{\alpha_k}{J(\xi_j)}\overline{\left(\sum_{l=1}^{n/2}\alpha_l \overline{U_j}^{(2l-1)\xi_i}\right)\frac{\delta_{(2k-1)}U_i}{\delta_{(2k-1)}\xi_j}}^{(2k-1)\xi_j}, \tag{35}$$

where the α_k are the interpolation weights. The continuity and pressure terms involve straightforward applications of the higher order interpolation operators and can be written as

$$(Cont. - NSn) \equiv \sum_{k=1}^{n/2} \alpha_k \frac{\delta_{(2k-1)}U_i}{\delta_{(2k-1)}x_i} = 0, \tag{36}$$

$$(Pres. - NSn)_i \equiv \sum_{k=1}^{n/2} \alpha_k \frac{\delta_{(2k-1)}p}{\delta_{(2k-1)}x_i}. \tag{37}$$

As an example, the sixth order accurate finite difference schemes on a staggered non-uniform grid are given by

$$(Cont. - NS6) \equiv \frac{150}{128}\frac{\delta_1 U_i}{\delta_1 x_i} - \frac{25}{128}\frac{\delta_3 U_i}{\delta_3 x_i} + \frac{3}{128}\frac{\delta_5 U_i}{\delta_5 x_i} = 0, \tag{38}$$

$$(Pres. - NS6)_i \equiv \frac{150}{128}\frac{\delta_1 p}{\delta_1 x_i} - \frac{25}{128}\frac{\delta_3 p}{\delta_3 x_i} + \frac{3}{128}\frac{\delta_5 p}{\delta_5 x_i}, \tag{40}$$

$$\begin{aligned}(Div. - NS6)_i \equiv & \frac{150}{128}\frac{\delta_1}{\delta_1 x_j}\left\{\left(\frac{150}{128}\overline{U_j}^{1x_i} - \frac{25}{128}\overline{U_j}^{3x_i} + \frac{3}{128}\overline{U_j}^{5x_i}\right)\overline{U_i}^{1x_j}\right\} \\ & - \frac{25}{128}\frac{\delta_3}{\delta_3 x_j}\left\{\left(\frac{150}{128}\overline{U_j}^{1x_i} - \frac{25}{128}\overline{U_j}^{3x_i} + \frac{3}{128}\overline{U_j}^{5x_i}\right)\overline{U_i}^{3x_j}\right\} \\ & + \frac{3}{128}\frac{\delta_5}{\delta_5 x_j}\left\{\left(\frac{150}{128}\overline{U_j}^{1x_i} - \frac{25}{128}\overline{U_j}^{3x_i} + \frac{3}{128}\overline{U_j}^{5x_i}\right)\overline{U_i}^{5x_j}\right\},\end{aligned} \tag{41}$$

$$\begin{aligned}(Adv. - NS6)_i \equiv & \frac{150}{128}\frac{1}{J(\xi_j)}\overline{\left(\frac{150}{128}\overline{U_j}^{1\xi_i} - \frac{25}{128}\overline{U_j}^{3\xi_i} + \frac{3}{128}\overline{U_j}^{5\xi_i}\right)\frac{\delta_1 U_i}{\delta_1 \xi_j}}^{1\xi_j} \\ & - \frac{25}{128}\frac{1}{J(\xi_j)}\overline{\left(\frac{150}{128}\overline{U_j}^{1\xi_i} - \frac{25}{128}\overline{U_j}^{3\xi_i} + \frac{3}{128}\overline{U_j}^{5\xi_i}\right)\frac{\delta_3 U_i}{\delta_3 \xi_j}}^{3\xi_j} \\ & + \frac{3}{128}\frac{1}{J(\xi_j)}\overline{\left(\frac{150}{128}\overline{U_j}^{1\xi_i} - \frac{25}{128}\overline{U_j}^{3\xi_i} + \frac{3}{128}\overline{U_j}^{5\xi_i}\right)\frac{\delta_5 U_i}{\delta_5 \xi_j}}^{5\xi_j},\end{aligned} \tag{42}$$

$$(Skew. - NS6)_i \equiv \frac{1}{2}(Div. - NS6)_i + \frac{1}{2}(Adv. - NS6)_i. \tag{43}$$

2.4 Periodic inviscid flow simulations

To confirm the results of the previous sections numerically, three-dimensional inviscid channel flow simulations are performed. The flow field is assumed to be periodic in the streamwise (x_1) and spanwise (x_3) directions. The fourth order accurate finite difference scheme is used for the convective term. The zero-normal velocity boundary conditions are assumed along the walls. Solenoidal initial velocity fields are generated using homogeneous random numbers. A third order Runge-Kutta (RK3) method of Spalart *et al.* (1991) is used for time integration. The splitting method by Dukowicz and Dvinsky (1992) is used to enforce the solenoidal condition. The resulting discrete Poisson's equation for the pressure is solved using a discrete Fourier transform in the periodic directions and a penta-diagonal direct matrix solver in the wall normal direction. The computational box is $2\pi \times 2 \times 2\pi$ and $16 \times 16 \times 16$ mesh points are used. The grid spacings in the periodic directions are uniform. The wall normal grid is stretched using a hyperbolic-tangent function

$$x_2(j) = \frac{\tanh(\gamma(2j/N_2 - 1))}{\tanh(\gamma)}, \qquad j = 0, \ldots, N_2. \tag{44}$$

Numerical tests are performed for $\gamma = 3$.

The analytical conservation requirements dictate that the total momentum, $\langle u_i \rangle$, and total kinetic energy, $\langle K \rangle \equiv \frac{1}{2}\langle {u_1}^2 + {u_2}^2 + {u_3}^2 \rangle$, should be conserved in time. We normalize the initial velocity field in such a way that $\langle u_1|_{t=0} \rangle = \langle u_3|_{t=0} \rangle = 0$ and $\langle K|_{t=0} \rangle = 1$. Due to the fact that grid spacing is uniform in streamwise and spanwise directions, the convective schemes have much better conservation

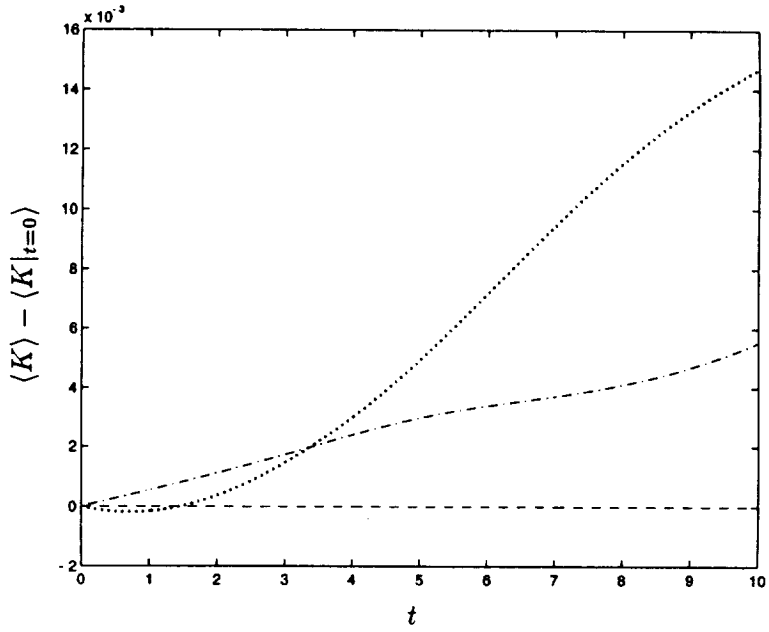

FIGURE 2. Evolution of the kinetic energy conservation error for $(Div. - NS4)$ (·····), $(Adv. - NS4)$ (—·—), and $(Skew. - NS4)$ (----) convective schemes.

properties. Since commutation error in Eq. (32) is zero for $i = 1, 3$, both advective and skew-symmetric forms of the convective term conserve momentum in x_1 and x_3 directions. However, the commutation error between averaging and differencing operators in wall normal direction is not zero. Consequently, the kinetic energy is still conserved only for the skew-symmetric form of the convective term.

The conservation of momentum is confirmed numerically up to machine accuracy. Surprisingly, the momentum is conserved for all three forms of the convective term in all three directions even though the grid in wall normal direction is not uniform. We attribute this to the specific properties of the inviscid flow between parallel plates.

As we have already mentioned, the total kinetic energy is also an ambiguous quantity since it can not be defined uniquely on a staggered grid. In this report we used the following norm for the total kinetic energy:

$$K = \sum_{i=1}^{3} \sum_{x_1} \sum_{x_2} \sum_{x_3} U_i^2(\mathbf{x})\, \Delta V(\mathbf{x}). \tag{45}$$

where the sums that appear in Eq. (45) are taken in the respective directions, $\Delta V(\mathbf{x}) \equiv J(\xi_2)\Delta V_\xi$, $J(\xi_2)$ is the Jacobian of the transformation $x_2 \to \xi_2$, and $\Delta V_\xi = \prod_{k=1}^{3} \Delta_k$ is a constant volume in the computational domain. The energy norm (45) is not conserved for both divergence and advective forms of the convection

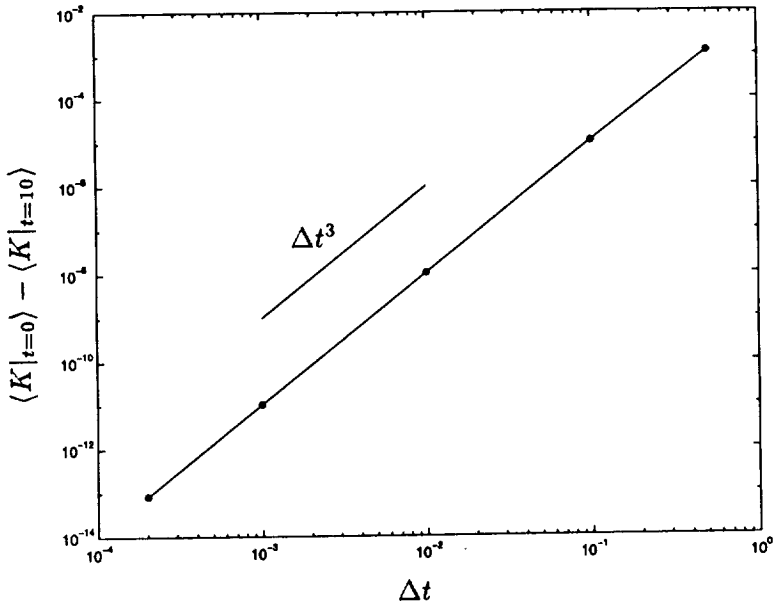

FIGURE 3. Kinetic energy conservation error at $t = 10$ as a function of time step Δt for $(Skew. - NS4)$ convective scheme.

term. However, an alternative energy norm may be conserved. For that reason further investigation is needed to confirm or deny the existence of such a norm.

The time evolution of the total kinetic energy defined by Eq. (45) is shown in Fig. 2. It can be easily seen that for both divergence and advective forms of the convective term the energy is not conserved. Also it should be noticed that the sign of the conservation energy is not defined since the conservation error is given by the nonlinear term, which can be either positive or negative.

The conservation of the kinetic energy for the skew-symmetric form is confirmed in Fig. 3. Kinetic energy is not conserved exactly since the third order Runge-Kutta time stepping method introduces a slight dissipative error. To demonstrate that the skew-symmetric scheme is conservative, the time step is decreased and the error is compared against the time step. As expected, the time stepping error decreases with the cube of Δt (see Fig. 3), and we observe no violation of kinetic energy conservation due to the spatial scheme.

2.4 Conclusions

The class of high order staggered grid finite difference schemes proposed by Morinishi *et al.* (1998) is generalized to non-uniform meshes. The proposed schemes do not simultaneously conserve mass, momentum, and kinetic energy. However, depending on the form of the convective term, conservation of either momentum or energy in addition to mass can be achieved. Furthermore, the non-conservation is weak; it is a function of the commutation error, which is very small for smoothly varying meshes. Certainly, experience has shown that schemes that are fully conservative on uniform meshes perform considerably better on non-uniform meshes when

compared to the schemes which are not fully conservative even on uniform meshes. The results presented in this report are not discouraging at all: the same kind of analysis for the standard generalization to a non-uniform grid of the second order scheme of Harlow and Welch (1965) would lead to similar conclusions. Thus, the generalized schemes developed in this report will enable us to perform numerical simulations with greater accuracy while preserving the conservation properties of the second order scheme of Harlow and Welch.

3. Future plans

The new higher order schemes for non-uniform staggered grids will be tested in high Reynolds number channel flow to demonstrate that they have an advantage over the non-conservative formulation of Morinishi *et al.* (1998). In addition, the issue of conservation of kinetic energy will be investigated further to see whether there exists an alternative kinetic energy norm which would be conserved in divergence form of the convective term.

REFERENCES

DUKOWICZ, J. K. & DVINSKY, A. S. 1992 Approximation as a higher order splitting for the implicit incompressible flow equations. *J. Comp. Phys.* **102,** 336-347.

GHOSAL, S. 1996 An analysis of numerical errors in large-eddy simulations of turbulence. *J. Comp. Phys.* **125,** 187-206.

HARLOW, F. H. & WELCH, J. E. 1965 Numerical calculation of time-dependent viscous Incompressible Flow of Fluid with Free Surface. *Phys. of Fluids.* **8,** 2182-2189.

MORINISHI, Y, LUND, T. S., VASILYEV, O. V., & MOIN, P. 1998 Fully conservative higher order finite difference schemes for incompressible flow. *J. Comp. Phys.* **142,** 1-35.

SPALART, P., MOSER, R., & ROGERS, M. 1991 Spectral methods for the Navier-Stokes equations with one infinite and two periodic direction. *J. Comp. Phys.* **96,** 297-324.

VELDMAN, A. E. P. & RINZEMA, K. 1992 Playing with nonuniform grids. *J. Eng. Mech.* **26,** 119-130.

VELDMAN, A. E. P. & VERSTAPPEN, R. W. C. P. 1998 Symmetry-conserving discretization with application to the simulation of turbulent flow. In *Proceedings of ICFD, Conference on Numerical Methods for Fluid Dynamics*, University of Oxford, March 31-April 3.

Development of immersed boundary methods for complex geometries

By J. Mohd-Yusof

1. Motivation and objectives

For fluid dynamics simulations, the primary issues are accuracy, computational efficiency, and the ability to handle complex geometries. Spectral methods offer the highest accuracy but are limited to relatively simple geometries. In order to accommodate more complex geometries, finite-difference or finite-element methods are generally used. However, these methods suffer from relatively low accuracy, requiring fine meshes to obtain good results. Finite element schemes, while able to handle complex geometries, often require significant computational time for grid generation. Spectral element methods can be used for complex geometries, but the grid stretching inherent in these methods leads to time-step limitations and clustering of grid-points in an inefficient manner.

In general, any computational scheme which requires regridding to accommodate changes in geometry will incur significant penalties in simulating time-varying geometries. For relatively simple motions, it is possible to use grid-stretching techniques (Carlson *et al.*, 1995), but these are still slow. Vortex element methods for moving bodies (Koumoutsakos, 1995) are presently under development but are also rather slow, especially with respect to calculation of spectra.

In Mohd-Yusof (1997) we demonstrated a discrete-time immersed boundary method which allows implementation of complex geometries in existing pseudo-spectral codes. The method does not incur significant additional cost as compared to the base computational scheme and changes in surface geometry simply require modification of the input files without any further modification of the code itself. Although the method appears to work well in this implementation, the actual convergence properties are not well documented. Also, the earlier code did not properly accommodate moving boundaries. Finally there was a term omitted from the derivation of the forcing presented in that report. While that omission does not affect the results from the earlier work, it would invalidate computations in more complex surface geometries.

2. Accomplishments

The accomplishments are presented in three sections. First, the correct form of the forcing function is derived and implemented in the B-spline/Fourier code. This accounts for the divergence of the force which was omitted in the previous derivation. Second, the method is extended to accommodate moving boundaries and coupled to a genetic algorithm. In order to minimize the effect of interpolation required by the moving surface geometry, high order interpolation methods are implemented in the B-spline direction only. No interpolation is performed in the Fourier direction:

i.e. the forcing points are constrained to lie on collocation lines. Preliminary results are presented to demonstrate the degree of drag modification which is possible with moving-bump type actuators. Finally, a study is presented which demonstrates the effect of smoothing the forcing profile on the convergence of the results.

2.1 Immersed boundary concept

We begin with an examination of the continuous (in time and space) Navier-Stokes equations to demonstrate the principle of the immersed boundary technique. We consider incompressible flows governed by the Navier–Stokes equations, including the body force term:

$$\frac{\partial \mathbf{u}}{\partial t} = -\mathbf{H} - \nabla P + \frac{1}{Re}\nabla^2 \mathbf{u} + \mathbf{F} \tag{1}$$

and the continuity equation:

$$\nabla \cdot \mathbf{u} = 0 \tag{2}$$

where Re is the Reynolds number, $\mathbf{u} = (u, v, w)$ is the velocity vector, $\mathbf{H} = \mathbf{u} \times \omega = (H_u, H_v, H_w)$ is the convective term, and $\mathbf{F} = (F_u, F_v, F_w)$ is the forcing vector.

The full Navier-Stokes equations allow the inclusion of an external body force. In incompressible flows, this force is generally assumed to derive from some potential field (e.g. gravity) which is constant and therefore may be neglected. However, the NS equations themselves allow the force to be a function of both time and space. In that event, the divergence of the force may be non-zero and, therefore, must be included in the Poisson equation for pressure if that equation is used to solve the system.

The immersed boundary method involves specifying the body force term in such a way as to simulate the presence of a flow boundary within the computational domain without altering the computational grid. The advantage of this is that bodies of almost arbitrary shape can be added without grid restructuring, a procedure which is often time-consuming. Furthermore, multiple bodies may be simulated, and relative motion of those bodies may be accomplished at reasonable computational cost.

The concept of the immersed boundary technique has been used for pseudo-spectral simulations of flows in complex geometries (Goldstein *et al.* 1995). However, the timestep restriction imposed by their derivation severely limits the applicability of the method to turbulent and other strongly time-dependent flows. This restriction can be removed by the use of a *discrete-time* derivation of the forcing value (Mohd-Yusof 1996). When combined with appropriate choice of internal boundary conditions, this scheme leads to a forcing scheme which does not require any filtering of the forcing field.

A second issue of importance to the immersed boundary method is the ability of the underlying numerical scheme to place a sufficient number of grid-points near the immersed boundary to adequately resolve the flow scales in that region. While the grid geometry may be considerably simplified as compared to a body-fitted grid, there is still a fundamental need to tailor the grid-point distribution to the underlying flow scales. To this end, we employ a B-spline formulation, which allows flexibility of grid-point distribution, zonal embedded grids, and high accuracy

(Kravchenko *et al.* 1996). Coupled with Fourier-pseudo-spectral methods, this yields a numerical scheme which allows simulation of flows in complex geometries on Cartesian grids with high accuracy.

2.1 Numerical method

We now consider the discrete-time Navier-Stokes equations in general form:

$$\frac{\mathbf{u}^{n+1}-\mathbf{u}^n}{\Delta t} = -\mathbf{H} - \nabla P + \frac{1}{Re}\nabla^2\mathbf{u} + \mathbf{F} \tag{3}$$

We wish to drive the velocity, $\mathbf{u}$, on some surface, Ω, to some desired value, $\mathbf{v}(\Omega)$. Rearrangement of the discrete NS equation gives us the velocity update equation which is of the form:

$$\mathbf{u}^{n+1} = \mathbf{u}^n + \Delta t(-\mathbf{H} - \nabla P + \frac{1}{Re}\nabla^2\mathbf{u} + \mathbf{F}) \tag{4}$$

If we know $\mathbf{H}$, ∇P, and $\nabla^2\mathbf{u}$, then the forcing term is simply:

$$\mathbf{F} = \begin{cases} \mathbf{H} + \nabla P - \dfrac{1}{Re}\nabla^2\mathbf{u} + \dfrac{1}{\Delta t}(\mathbf{v}-\mathbf{u}^n), & \text{on } \Omega; \\ 0 & \text{elsewhere.} \end{cases} \tag{5}$$

2.1.1 Velocity-vorticity formulation

Following the same approach as in Kim *et al.* (1991), one can reduce Eqs. (1) and (2) to a fourth-order equation for v and a second-order equation for the normal component of vorticity g:

$$\frac{\partial}{\partial t}\nabla^2 v = h_v + \frac{1}{Re}\nabla^4 v + f_v \tag{6}$$

$$\frac{\partial}{\partial t} g = h_g + \frac{1}{Re}\nabla^2 g + f_g \tag{7}$$

$$p + \frac{\partial v}{\partial y} = 0 \tag{8}$$

where

$$p = \frac{\partial u}{\partial x} + \frac{\partial w}{\partial z}, \quad g = \frac{\partial u}{\partial z} - \frac{\partial w}{\partial x} \quad f_g = \frac{\partial F_u}{\partial z} - \frac{\partial F_w}{\partial x} \tag{9}$$

$$h_v = -\frac{\partial}{\partial y}\left(\frac{\partial H_u}{\partial x} + \frac{\partial H_w}{\partial z}\right) + \left(\frac{\partial^2}{\partial x^2} + \frac{\partial^2}{\partial z^2}\right)H_v \tag{10}$$

$$f_v = -\frac{\partial}{\partial y}\left(\frac{\partial F_u}{\partial x} + \frac{\partial F_w}{\partial z}\right) + \left(\frac{\partial^2}{\partial x^2} + \frac{\partial^2}{\partial z^2}\right)F_v \tag{11}$$

$$h_g = \frac{\partial H_u}{\partial z} - \frac{\partial H_w}{\partial x} \tag{12}$$

Note especially that the force in both the equations is transformed in exactly the same manner as the nonlinear terms. In this formulation the velocity field is assumed divergence-free; however, the force is not in general solenoidal, so the projection of the force onto a solenoidal field must be accomplished in the same manner as with the term h_v in Eq. (10). All further numerical details of the code are unchanged from those presented in Mohd-Yusof (1997) and are omitted for the sake of brevity.

2.2 Turbulent channel simulation

The immersed boundary method allows a wide range of different surface geometries to be simulated with a single code. This flexibility makes it uniquely suited to coupling with optimization schemes for drag reduction in turbulent flows. Once the parameter space is chosen (which is not necessarily obvious) the code can be used to simulate the flow in question. The results of the simulation can then be fed back into a genetic algorithm (e.g, Koumoutsakos, 1997) to determine the optimal geometry for achieving the desired goal. We envision such a combined simulation/optimization tool as not only a diagnostic tool to explore the performance potential of current surface actuators, but also as a way to design surface actuators which may not yet have been built. To this end, the test case we have chosen for the moving boundary simulation is that of a turbulent channel with moving-bump actuators on one wall.

In this case, the optimization parameters could be the bump height, spacing, streamwise and spanwise extent, and the period of bump motion. For our preliminary tests we fix all but the last parameter and measure the surface drag for varying bump periods.

2.2.1 Computational mesh

In order to simulate a turbulent channel using the immersed boundary, it is necessary to use computational mesh which is refined near the location of the immersed boundary. In this instance we use a double-cosine stretched grid as shown in Fig. 1. This grid provides the same near-wall resolution as a traditional cosine stretched grid in a conventional calculation. The computational domain extends from -1 to 1. The mean location of the immersed boundary wall is fixed at -0.8 for all simulations.

For simplicity, the forcing function for the moving bumps is computed on an embedded auxiliary mesh which is refined in the wall normal direction near the location of the bumpy wall, $y = -0.8$. The resulting force is interpolated, using b-splines, to the solution mesh. The spacing of the mesh is identical to the base mesh in the two Fourier directions. In the wall-normal direction, the mesh spacing is approximately equal to the finest spacing on the cosine stretched grid.

2.2.2 Results

Figure 2 shows the drag on the bumpy wall, as a function of time, from the simulation compared with the flat wall case. In all cases the bumpy wall was of the type shown in Fig. 1; four bumps operating in two sets with opposite phase. The bump shape is given by $h(r) = 1 + cos(2\pi r/r_{max})$ for $r < r_{max}$. The height of the bumps varies sinusoidally in time with period t_{bump} (all times are nondimensionalized by the friction velocity and the channel half height). For the cases shown the simulations are started using identical fully developed turbulent channel flow data obtained by running the code with a flat wall immersed boundary. For all the bump frequencies tested, the mean wall drag is slightly reduced by the introduction of the bumps. However, the duration of the simulations performed to date is too short to provide a meaningful result.

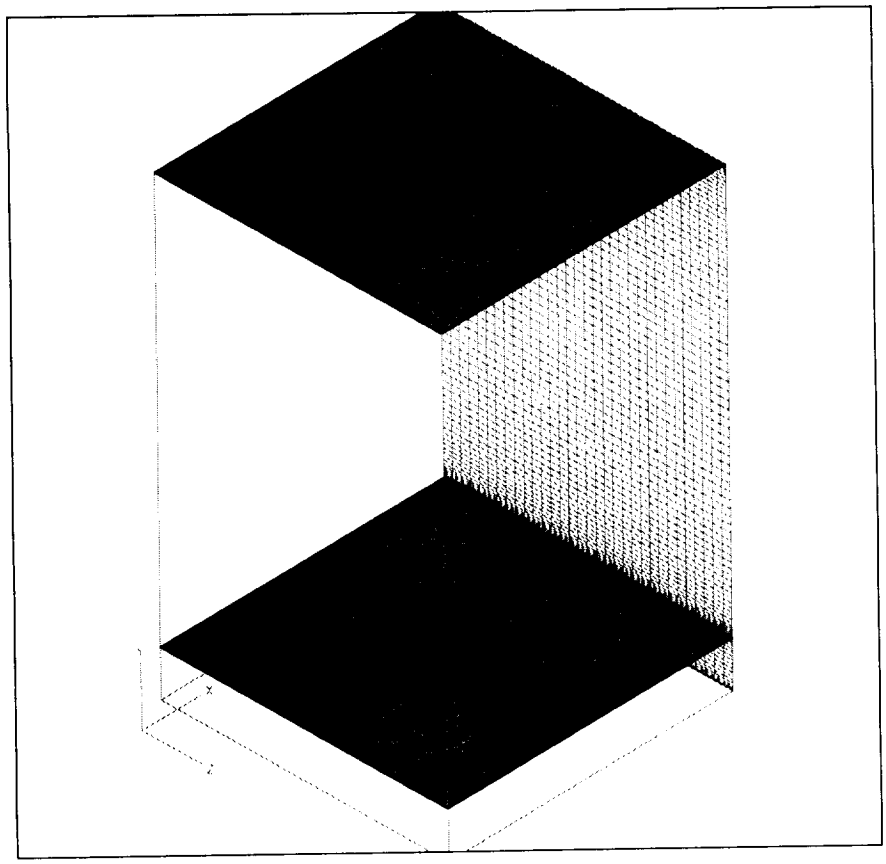

FIGURE 1. Representative sketch of the computational domain. The stretched solution grid is shown, and a representative isosurface showing the location of the immersed boundary.

Flow visualizations of the bumpy-wall results indicates the presence of large low-speed structures which span the entire streamwise extent of the computational domain. These structures seem to be present in all the cases tested, and the structures are centered over the bumps themselves. Note that since the bump pairs are out of phase, the structures extend over one bump and the accompanying dip. The persistence of the structures over long times may also be an artifact of the periodic computational domain.

2.3 Convergence properties and smoothing

There have been, to the author's knowledge, no rigorous proofs of the convergence properties of immersed boundary methods. Evidence suggests that the method of Goldstein *et al.* converges very slowly, if at all. The likely cause of this is the fact that the forcing is applied as a series of point forces at the collocation points. Thus, the force is effectively implemented as a series of δ-functions with commensurately poor convergence properties. Goldstein *et al.* attempt to smooth the forcing by

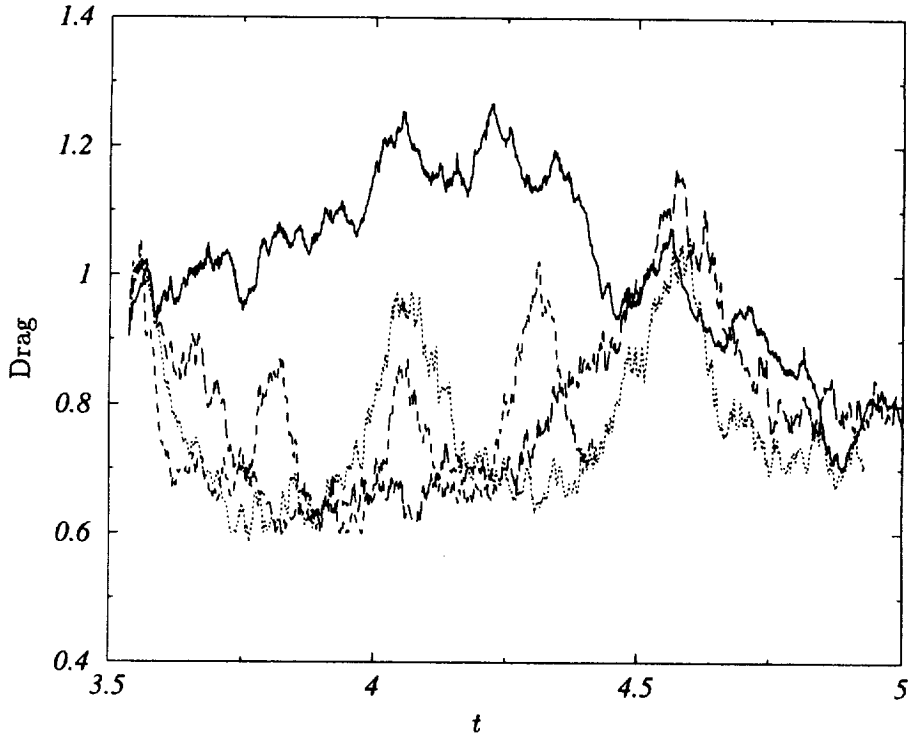

FIGURE 2. Drag traces for varying bump oscillation periods and the flat wall case. ——— flat wall case; ····· $t_{bump} = 1$; ——— $t_{bump} = 2$; ---- $t_{bump} = 0.5$. All times are nondimensionalized by friction velocity and channel half height.

spreading the force as a Gaussian: this still converges slowly and furthermore allows the force to be non-zero in the solution region of interest.

In contrast, the current method attempts to smooth the force by utilizing an internal boundary layer, confined to the region of the solution which is not part of the flow itself. In this section we will examine the effect of modifying the specification in the force within this internal layer in order to improve the convergence properties of the global solution. Intuitively, the rate at which the solution converges will depend on our ability to enforce the boundary condition with a forcing function which has as narrow a spectrum as possible, confined to the lowest practical wavenumbers. This will be the opposite of the delta function, which has equal energy at all resolved wavenumbers.

It is instructive to first examine the behavior of the body force in a simple test case, in the absence of any smoothing or interpolation error. The test case used here will be a simple Couette flow, simulated on a periodic domain. That is, we wish to enforce no-slip conditions on two walls, at $x = \pi/2$ and $x = 3\pi/2$, moving with velocity 1 and -1, respectively. The 'correct' solution in this case will be a linear velocity profile in the region $\pi/2 < x < 3\pi/2$, and the flow in the remainder of the domain is extraneous.

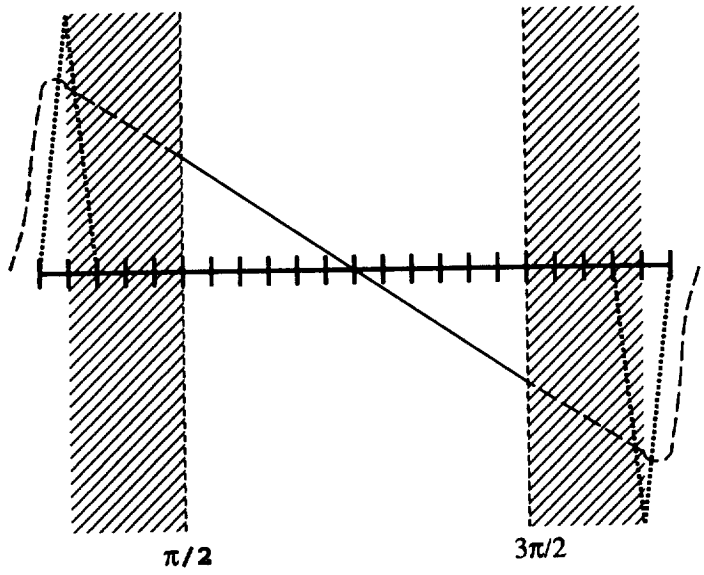

FIGURE 3. Representative sketch of the test case considered showing a sample solution grid. The hatched areas represent the internal boundary layers where the flow reversal is applied. —— desired solution, ---- extraneous solution, ····· the required force distribution on this grid, without smoothing.

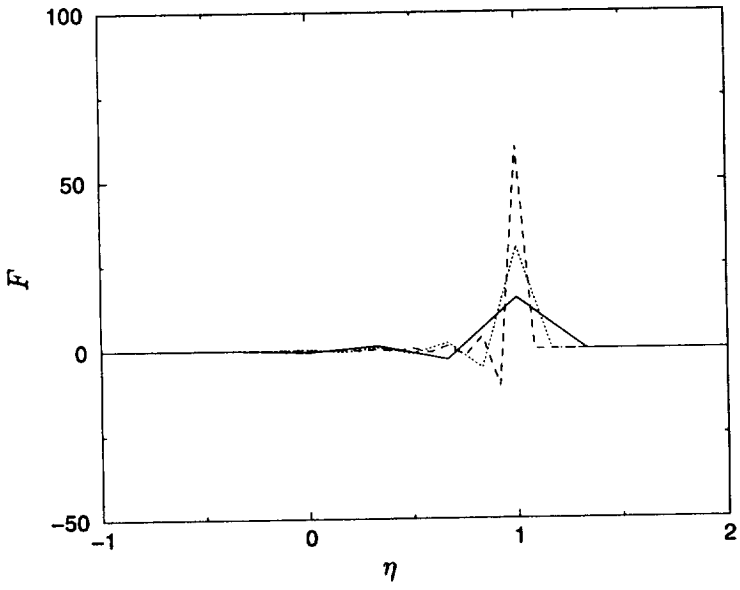

FIGURE 4. Distribution of the force without any smoothing for simulations using —— 48, ····· 96 and ---- 192 points.

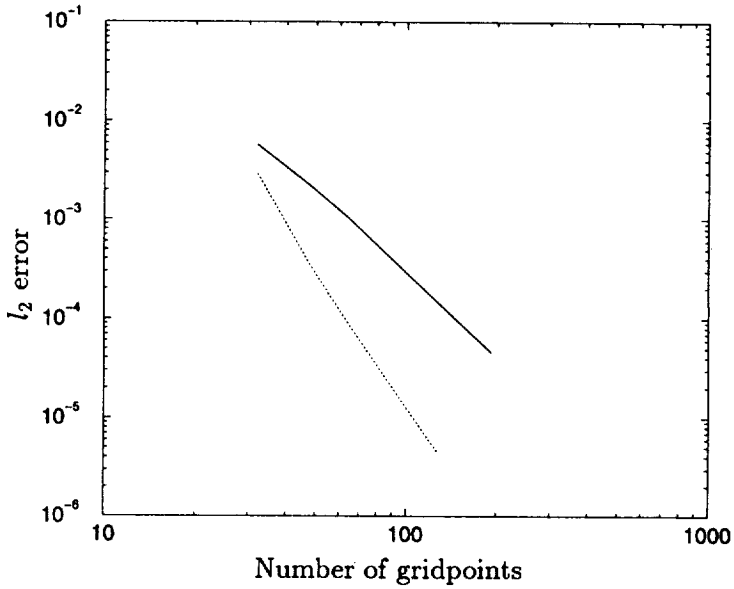

FIGURE 5. Comparison of the convergence rates for the smoothing functions —— $S(\eta) = 1 - \eta$ and ---- $S(\eta) = (1 + cos(\eta))/2$, which yield 3rd and 5th order convergence, respectively. Since the choice of error norm does not change the slope, only the l_2 data is shown for each case.

Since our forcing scheme requires an internal boundary layer to be formed in the body, we require at a minimum 3 points in this extraneous region to accommodate these two boundary layers (which will have opposite velocities as sketched in Fig. 3). The force distribution required to achieve the desired solution in this case is essentially a pair of δ-functions located at the single collocation point at the edge of the internal BL; the body force applied at the surface is near zero. The vanishing force at the surface is an expected result upon examination of the force specification equation; once the velocity at the surface is small, all the terms vanish except the viscous term, which is driven to zero by the presence of the boundary layer.

If we fix the geometric thickness of this internal boundary layer and perform the simulation on progressively refined grids, then in the absence of any smoothing, the force distribution essentially remains a pair of δ-functions, with increasingly compact support, located at the edge of the internal BL (Fig. 4). As will be shown later, the force is uniformly distributed in spectral space, and thus the convergence of the scheme is poor.

The goal of the smoothing function, it would then appear, is to distribute the force within this internal boundary layer in such a way as to minimize the spectral bandwidth of the final forcing distribution while at the same time not compromising the local character and simplicity of the scheme.

We choose therefore to apply the force in the internal boundary layer in the following way: the force applied to any collocation point within the internal BL, located a distance η from the desired wall location, will be the force required to

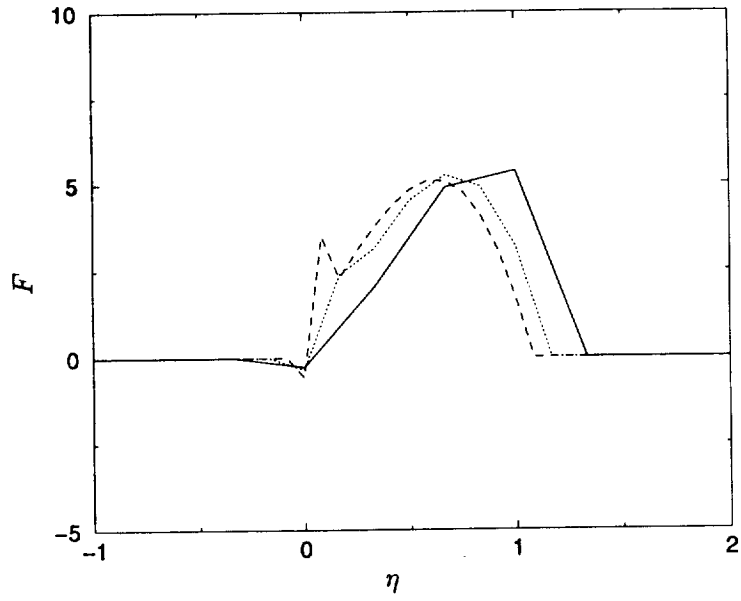

FIGURE 6. Distribution of the force with $S(\eta) = 1 - \eta$, for simulations using —— 48, ····· 96 and ---- 192 points.

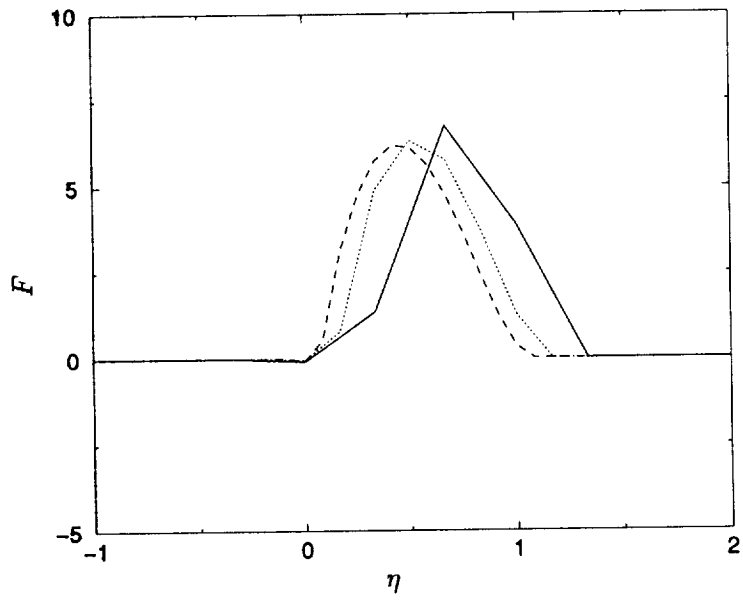

FIGURE 7. Distribution of the force with $S(\eta) = (1 + cos(\eta))/2$ for simulations using —— 48, ····· 96 and ---- 192 points.

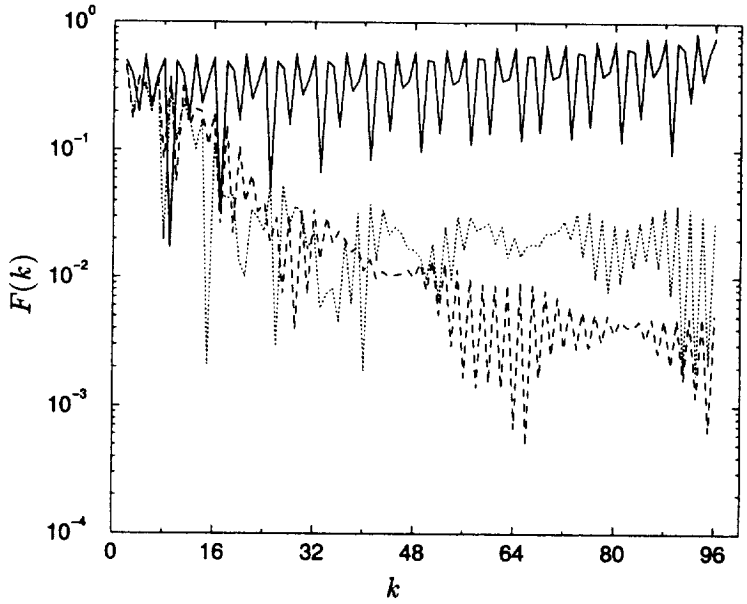

FIGURE 8. Spectra of the force distribution with various smoothing functions used: —— unsmoothed, ····· , $S(\eta) = 1 - \eta$, ---- $S(\eta) = (1 + cos(\eta))/2$. For clarity, only the spectra for 192-point simulations are shown.

reverse the velocity at the corresponding mirror-image point in the solution flow, $-\eta$, scaled by some smoothing function $S(\eta)$. In this case we scale η such that $\eta = 0$ at the surface and $\eta = 1$ is the thickness of the internal boundary layer. For each case, we track the l_1,l_2, and l_{inf} norms of the error in the 'true' solution region.

We examine some simple test cases for the force smoothing function $S(\eta)$. Figure 5 shows the convergence rate of the global error (within the domain of interest) for the smoothing functions $S(\eta) = 1 - \eta$, and $S(\eta) = (1 + cos(\eta))/2$. We choose to show only the curves for the l_2 error since the choice of norm does not change the slope. The convergence rates for the two smoothing functions are 3rd and 5th order, respectively.

Figures 6 and 7 show the force distributions for the choices of smoothing function $S(\eta) = 1 - \eta$ and $S(\eta) = (1 + cos(\eta))/2$, respectively. Note that in both cases the magnitude of the force has been reduced by an order of magnitude compared to the unsmoothed case.

Our supposition that the reduced spectral bandwidth of the resultant force distribution is responsible for the improved convergence is demonstrated in Fig. 8. The marked reduction in spectral bandwidth of the various smoothed forcing distributions can clearly be seen. Note that the magnitude of the even-numbered wavenumbers is reduced due to the odd symmetry of the problem chosen.

There are several important points to note in these simplified tests. First, the Couette flow case does not require the forcing function to impose no-penetration at the solid surface, only no-slip. The imposition of no-penetration may considerably

alter the convergence properties of the method. Secondly, the convergence properties of the steady state solution may not translate into similar properties for the time-dependent solution. Thirdly, the 'optimal' smoothing function, if one exists, is that which results in the narrowest spectral bandwidth of the forcing field, which is itself a function of the boundary layer profile in the 'external' flow. Thus, the optimal solution for a Couette flow may be different than that for a channel flow, for example. Since we would prefer the forcing scheme to be independent of the flow geometry, further refinement of the smoothing function may be of dubious benefit.

3. Future plans

The primary obstacle to obtaining useful results from the combined optimization/simulation scheme is the slow turnaround time for the simulations themselves. The code is being rewritten to improve the computational efficiency, primarily via the implementation of collocation methods for the quadratic terms. An interim solution has been to implement the immersed boundary method in the finite difference code (Lund *et al.*, 1995), which is considerably faster although formally less accurate. The fact that this implementation required less than one day of work underscores the flexibility of the immersed boundary method itself and the ease with which it can be incorporated into existing flow solvers. This method has also been implemented in finite difference LES codes and has proved to be very efficient (Verzicco *et al.*, 1998).

The question of the convergence of the forcing scheme will also be investigated further. There has been, to the author's knowledge, no formal proof of the convergence properties of such schemes in general. For our purposes, it should suffice to continue numerical experiments to attempt to improve on the 5th order convergence of the smoothing demonstrated in this report.

REFERENCES

CARLSON, H. A., BERKOOZ G. & LUMLEY J. L. 1995 Direct numerical simulation of flow in a channel with complex, time-dependent wall geometries: A pseudospectral method. *J. Comp. Phys.* **121,** 155-175.

GOLDSTEIN, D., HANDLER R. & SIROVICH L. 1993 Modeling a no-slip flow boundary with an external force field. *J. Comp. Phys.* **105,** 354-366.

KOUMOUTSAKOS, P. 1995 Fast multipole methods for three-dimensional N-body problems. *Annual Research Briefs 1995*, Center for Turbulence Research, NASA Ames/Stanford Univ., 377-390.

KOUMOUTSAKOS, P. 1997 Active Control of Vortex-Wall Interactions. *Phys. of Fluids A.* **9,** 3808-3816.

KRAVCHENKO, A. G., MOIN, P. & MOSER, R. 1996 Zonal embedded grids for numerical simulations of wall-bounded turbulent flows. *J. Comp. Phys.* **127,** 412-423.

LUND, T.S. & KALTENBACH, H.-J. 1995 Experiments with explicit filtering for LES using a finite difference method. *Annual Research Briefs 1995*, Center for Turbulence Research, NASA Ames/Stanford Univ., 91-105.

MOHD-YUSOF, J. 1996 Interaction of massive particles with turbulence. *PhD thesis*, Cornell University.

MOHD-YUSOF, J. 1997 Combined immersed-boundary/B-spline methods for simulations of flow in complex geometries. *CTR Annual Research Briefs*, Center for Turbulence Research, NASA Ames/Stanford Univ., 317-327.

VERZICCO, R., MOHD-YUSOF, J., ORLANDI, P. & HAWORTH, D. 1998 LES in complex geometries using boundary body forces. *Proceedings of the Summer Program 1998*, Center for Turbulence Research, NASA Ames/Stanford Univ., 171-186.

Particle methods for micro and macroscale flow simulations

By P. Koumoutsakos

1. Introduction

Particle methods are powerful computational techniques to simulate phenomena ranging from protein formation to stellar cluster formation. In fluid dynamics, particle methods have been implemented for simulations of flows inside micro and nanotubes (via *molecular dynamics* simulations) as well as for flows around aerodynamic shapes (via *vortex methods*). The underlying principle of particle methods is the use of computational elements that automatically adapt to resolve the flow field.

In molecular dynamics simulations, the computational elements carry information about the material properties of the fluid while elements in vortex methods represent macroscale quantities such as the vorticity of the flow field. The method of molecular dynamics has been extensively developed in the last decade, and the reader is referred to the review article by Koplik and Banavar (1998) and references therein for an extensive survey of computational issues in flow simulations using this technique.

Vortex methods are based on the discretization of the vorticity field and the Lagrangian description of the governing equations, which when solved determine the evolution of the computational elements. In addition to automatically adapting to the solution, classical vortex methods enjoy advantages such as the use of computational elements only where the vorticity field is nonzero and the rigorous treatment of boundary conditions at infinity. Until recently, disadvantages such as the computational cost and the inability to treat accurately viscous effects had limited their application to modeling the evolution of the vorticity field of unsteady high Reynolds number flows using a few tens to a few thousands computational elements. These difficulties have been overcome with the advent of fast summation algorithms (multipole and particle-grid techniques) that have optimized the computational cost. Moreover, recent developments in numerical analysis allow for the accurate treatment of viscous effects. Vortex methods have today reached a level of maturity, offering an interesting alternative to finite difference and spectral methods for high resolution numerical solutions of the Navier-Stokes equations. In the last three decades research in numerical analysis aspects of vortex methods has provided a solid mathematical background for understanding the accuracy and stability of the method (see Cottet and Koumoutsakos 1999 - referred to as *CK99* from here on). At the same time vortex methods retain their appealing physical character that, we believe, was the motivation for their introduction.

In this article, we report some recent developments on the formulation of boundary conditions and the implementation of spatially varying smoothing functions for

vortex methods (*CK99*). These developments have been implemented in Cloud In Cell and Fast Multipole algorithms for simulations of vortex ring-wall interactions and cylinders in rotational oscillations, revealing a drastic modification of the wake structure and significant drag reduction.

In the present line of work we exploit the common features of various particle methods in order to construct computational tools for flow simulations over a large range of scales. Hence the tree data structure that has been developed for the efficient velocity evaluation in vortex methods is being used to identify near neighbors for Lennard-Jones type interaction in Molecular Dynamics Simulations. Using this algorithm we conduct simulations of droplet evaporation and coalescence.

Our goal is a hybrid particle algorithm suitable for simulations of macroscale flows involving micro and nano devices. In such an algorithm molecular dynamics could be implemented for the microscale component simulations, thus providing us with boundary condition for the simulations of the macroscale flows, using vortex methods.

2. Vortex methods

The computationally intensive part of vortex methods is the evaluation of the velocity field on the computational elements (particles) from the vorticity field. As particles carry vorticity the straightforward implementation amounts to pairwise interactions of the computational elements. For N particles this is the classical N-body problem whose computational cost scales as $\mathcal{O}(N^2)$. Fast velocity evaluations can be realized either by employing Particle-Mesh (Cloud in Cell - CIC) techniques or by using multipole methods and efficient tree data structures. While the latter algorithms are the methods of preference as they do not require explicit far field conditions or any regularity of the domain, CIC algorithms are the method of choice for flows in regular and/or periodic domains due to the efficiency and speed of existing Fast Poisson solvers.

2.1 Cloud In Cell (CIC)

An excellent account of particle mesh techniques such as CIC can be found in the classic book by Hockney and Eastwood (1988). At each time step the mesh vorticity is constructed from the particle strength using higher order assignment/interpolation functions. A vector Poisson equation, $\nabla^2 \boldsymbol{\Psi} = -\boldsymbol{\omega}$ is solved for the stream function $\boldsymbol{\Psi}$ subject to Dirichlet or Neumann boundary conditions. The particle velocity is subsequently interpolated from the mesh velocity $\mathbf{u} = \nabla \times \boldsymbol{\Psi}$ using the same interpolation procedures. We implement 4th order interpolation/assignment schemes that conserve up to the third moment of the vorticity flowfield invariants of the flow.

Simulations of vortex ring reconnection using a CIC code are currently being conducted in parallel computer architectures. Typical simulations use 60000 particles for the initial configuration and approximately 500000 particles during the reconnection phase. The calculations were performed on a Sun Ultra 2 workstation and on a NEC SX4. The CPU time per time step for 500000 particles and a 140^3 mesh

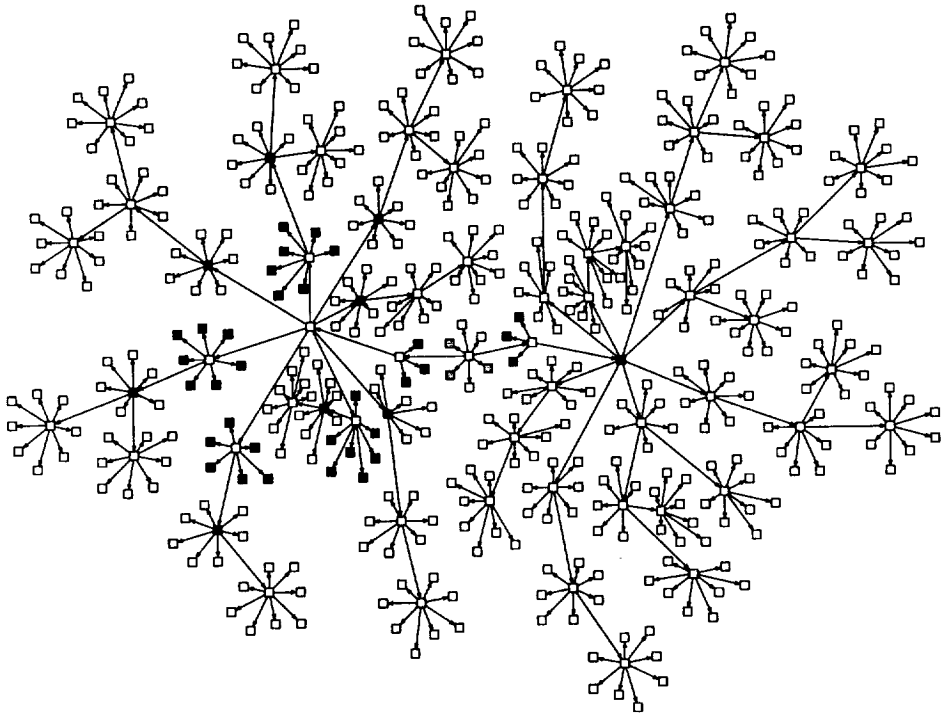

FIGURE 1. Tree data structure for two normally distributed group of particles.

is approximate 140 seconds for the Sun and 4.7 seconds for the SX4. The sustained performance on the SX4 is 1.0 GFlop, approximately 50% of peak performance.

2.2 Fast multipole methods

The CIC method is ideally suited to vortical flows in simple geometries, for which fast Poisson solvers are efficient. For complex geometries, the velocity field can be derived from the vorticity field using the Biot-Savart integral, enforcing at the same time the far field boundary conditions. However, when this integral is discretized using as quadrature points the locations of the vortex particles, the nominal cost of the method is proportional to the square of the computational elements, making it prohibitively expensive. A remedy to this situation, which unlike the CIC avoids the implementation of a grid, while maintaining the accurate treatment of the far field boundary condition is the Fast Multipole Method (FMM) first proposed by Greengard and Rohklin (1987) (see also a more recent review article by Greengard, 1997). It is based on the observation that the influence of a cluster of particles at a certain distance may be approximated by a finite series expansion. In order to exploit this observation, clusters of particles are spatially decomposed into a hierarchy of clusters formally represented by a tree data structure.

The tree is constructed by initially defining its root as the cubic box enclosing

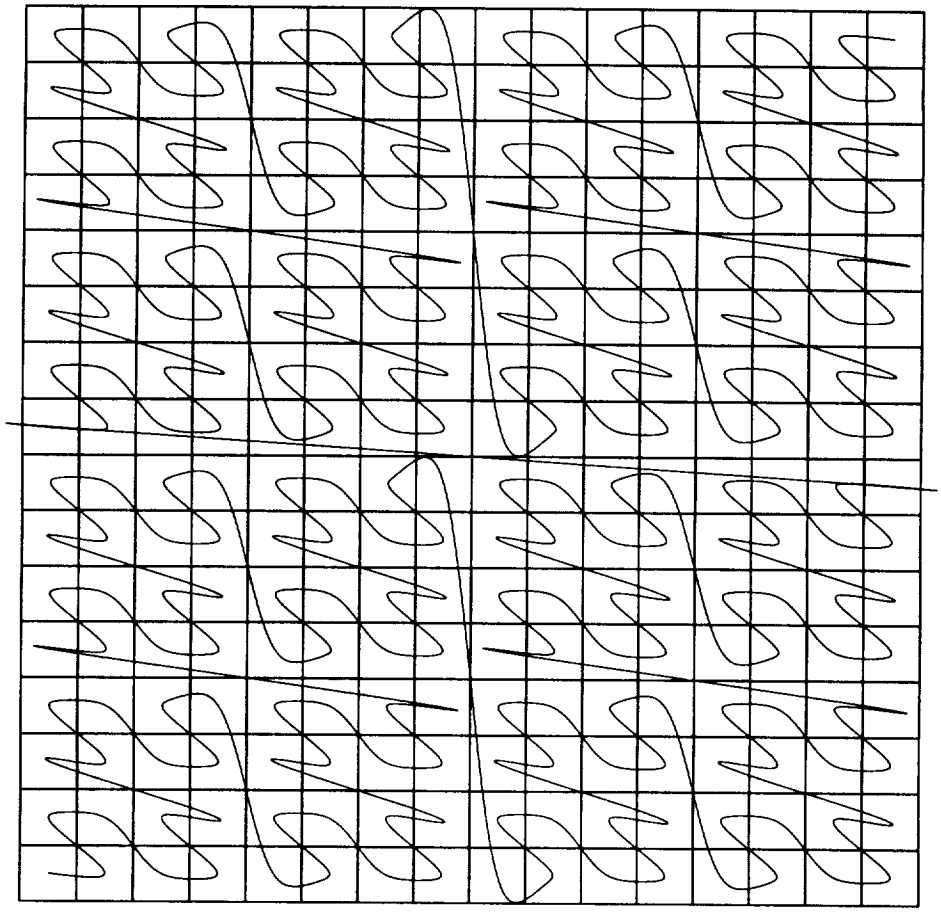

FIGURE 2. The particles sorted in Morton order to allow efficient parallel/vector processing.

all the computational elements. The root and its descendants are recursively subdivided into eight identical boxes until each of the boxes contains only a certain maximum number of particles or the maximum allowable levels of subdivisions has been reached. A genealogical list of parent child relations and four interaction lists of each box in the tree effectively determine the validity of the expansions.

Figure 1 shows an example of an imploded adaptive oct-tree for two normal distributed groups of particles. The tree consists of 430 boxes in 6 levels.

The contribution of a cluster of particles to the potential of a given particle can be computed to desired accuracy if the particle is sufficiently far from the cluster in proportion to the size of the cluster and a sufficiently large number of terms in the multipole expansions is taken. Since the creation of the p-term expansions requires $\mathcal{O}(Np^2)$ operations for each of the $\log_8 N$ levels of the tree, the total amount of

work scales as $\mathcal{O}(\mathcal{N}\log\mathcal{N})$.

Further improvements are possible if well separated boxes are allowed to interact. These interactions are in the form of shifting the expansions of a certain cluster with the desired accuracy to the center of another cluster. Then these expansions are used to determine the velocities of the particles in the second cluster. The cost associated with the translation of a p-term multipole expansion is $\mathcal{O}(p^4)$ or $\mathcal{O}(p^2)$ if the multipole expansions are converted into exponential expansions (Greengard, 1997). The box-box interaction minimizes the tree traversal for the individual particles, making the algorithm formally $\mathcal{O}(N)$. A parallel version of the FMM is currently being developed using the exponential expansions. Other techniques for promoting vectorization and parallelization (data locality) is to sort the particles according to their position in the tree using Morton ordering. Particles in the same childless box are mapped consecutively in memory, securing an efficient stride im memory (Fig. 2). The spatial relations described by the tree are further utilized during load balancing of the particles and the boxes.

The tree data structure is used to identify clusters of particles and to identify for a certain particle its near-neighbor list and the clusters for which far-field expansions will be implemented. Naturally this property is exploited for other types of particle simulations such as the molecular dynamics presented in the following section.

2.3 Boundary conditions for 3d viscous vortex methods

The formulation of vorticity boundary conditions in terms of integral equations linking boundary terms and vorticity in the flow is presented in *CK99*. Following this work, we report here the implementation of boundary conditions in a three-dimensional viscous splitting algorithm.

Vorticity boundary conditions for three-dimensional viscous flows have, compared to the two-dimensional case, two additional difficulties. First, since vorticity is a vector, one needs 3 instead of 1 boundary condition. Secondly, vorticity created at the boundary must be divergence-free, and this constraint must enter the boundary conditions. To simplify the exposition, we will assume that the boundary is a flat plate located at $x_3 = 0$. The general case follows by using local coordinate axis parallel and orthogonal to the wall. We will also assume a velocity vanishing at the wall.

One vorticity boundary condition immediately follows from the no-slip condition: the wall-normal component of the vorticity vanishes at the wall:

$$\omega_3 = 0$$

It is worthwhile to notice that a consequence of this condition is that, at the wall, $(\mathbf{u}\cdot\nabla)\omega_3 = (\boldsymbol{\omega}\cdot\nabla)u_3 = 0$. Hence the normal component of the vorticity equation written at the wall yields

$$\frac{\partial^2\omega_3}{\partial x_3^2} = 0$$

Let us now turn to the tangential components of the vorticity. A natural extension of the two-dimensional vorticity flux boundary conditions is to enforce no-slip for

the components u_1 and u_2 of the velocity by creation of vorticity for the components ω_2 and ω_1 respectively

This leads to the following three-dimensional version of the algorithm:

I. solve the convection diffusion for the three components of the vorticity, with homogeneous Dirichlet boundary condition for the normal component and homogeneous Neumann boundary conditions for the tangential components:

$$\omega_3 = \frac{\partial \omega_1}{\partial x_3} = \frac{\partial \omega_2}{\partial x_3} = 0$$

II. compute the slip (u_1, u_2) at the boundary

III. repeat sub-step 1 for the tangential components, with the new Neumann boundary conditions

$$\frac{\partial \omega_1}{\partial x_3} = -\frac{u_2}{\Delta t}, \quad \frac{\partial \omega_2}{\partial x_3} = \frac{u_1}{\Delta t}$$

It is easy to check (see *CK99*) that this procedure guarantees that the vorticity remains divergence-free for all times. Figure 3 shows the viscous interaction of a vortex ring impinging at an angle on a solid wall using the high order CIC method. The Reynolds number based on the circulation of the ring is 800. The ring is resolved using 500000 particles and a 140^3 mesh (*CK99*). These simulations were performed on a cluster of DEC-Alpha workstations with a performance of about 5000 particles per CPU second per processor.

2.4 Variable size vortex methods

In order to account for diffusion in vortex methods simulations, we employ the scheme of Particle Strength Exchange (PSE). As it is discussed in *CK99*, the PSE has enough flexibility in dealing with viscous effects to allow the treatment of variable viscous scales in the vorticity redistribution scheme. As we wish to use fewer particles and thus reduce the computational cost, in flow regions with relatively small vorticity gradients (such as a cylinder far wake), we are interested in developing diffusion and convection formulas for vortex methods with spatially varying blob sizes (ϵ). This can be done through merging of nearby vortices, or, more generally, by periodically remeshing the particle distribution on a variable size mesh.

A consistent treatment of the diffusion requires the overlapping of the particles on a scale given by the kernel used in the PSE formula. As a result, a locally coarser particle resolution must go with an increasing diffusion range ϵ. In the case of the Biot-Savart integral the incorporation of variable blobs consists of replacing ϵ by $\epsilon(\mathbf{y})$ in the otherwise unchanged quadrature formulas. However, this technique would not be consistent in the case of the integrals that are used to replace the Laplacian operator in the PSE formulation (see *CK99* for details). The correct way to implement a variable blob size in a PSE scheme is through a change of variables which maps the variable particle grid to a uniform one.

For simplicity let us focus on the one-dimensional case. We will denote locations in the physical space with variable grid size by x, y and locations in the mapped

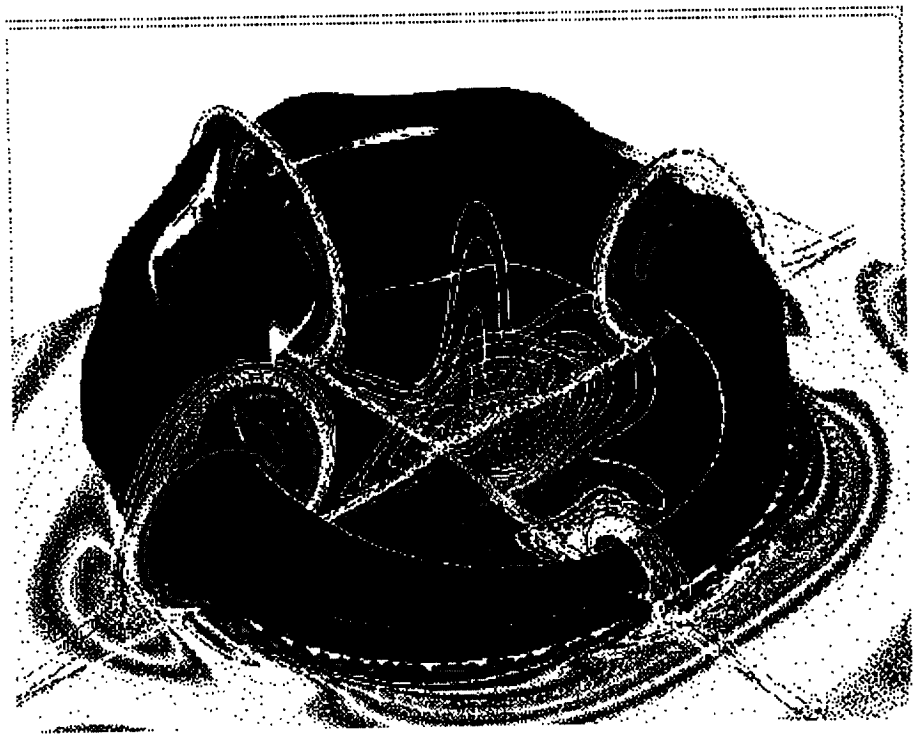

FIGURE 3. Isosurfaces and vorticity contours for a vortex ring impinging at an angle on a flat wall (*CK99*).

coordinates where the grid-size is uniform by $\hat{x}, \hat{y}$. We will assume that the mapping is given by the formulas

$$x = f(\hat{x}), \hat{x} = g(x), \omega(x) = \hat{\omega}(\hat{x}).$$

Writing derivatives in the mapped coordinates yields:

$$\frac{d^2\omega}{dx^2} = h(\hat{x})\frac{d}{d\hat{x}}\left[h(\hat{x})\frac{d\hat{\omega}}{d\hat{x}}\right]$$

where $h(\hat{x}) = g'(x)$. Next, we use the following integral approximation (see *CK99* for a proof):

$$\frac{d}{d\hat{x}}\left[h(\hat{x})\frac{d\hat{\omega}}{d\hat{x}}\right] \simeq \epsilon^{-3}\int \frac{h(\hat{x}) + h(\hat{y})}{2}[\hat{\omega}(\hat{x}) - \hat{\omega}(\hat{y})]\eta(\frac{\hat{x} - \hat{y}}{\epsilon})\, d\hat{y}.$$

In the above formula, the kernel η satisfies the necessary moment properties and ϵ is a *constant* blob size. This leads to the following PSE scheme for the heat equation in one dimension with $\nu = 1$

$$\frac{d\omega_p}{dt} = \epsilon^{-3}h(\hat{x}_p)\sum_q \hat{v}_q \frac{h(\hat{x}_p) + h(\hat{x}_q)}{2}[\omega_q - \omega_p]\eta(\frac{\hat{x}_p - \hat{x}_q}{\epsilon})$$

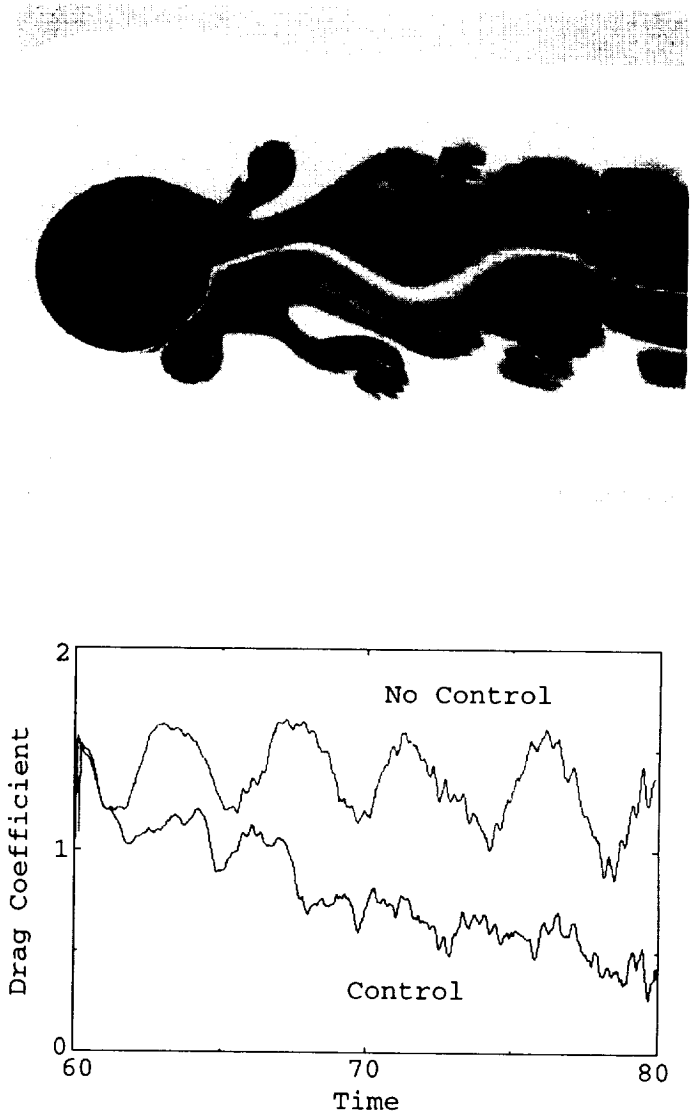

FIGURE 4. Vorticity contours and drag coefficient curves for two-dimensional flow past a circular cylinder performing rotary oscillations at $Re = 2000$.

where $\hat{v}_q$ denotes the volumes of the mapped particles. Notice that the volumes of the physical and mapped particles are related through the Jacobian of the mapping:

$$\hat{v}_q = v_q h(\hat{x}_q)$$

which establishes that the scheme is indeed conservative. To extend this approach to two or three-dimensional flows, one must handle integral approximations of differential terms involving diffusion tensors.

In convection-diffusion problems, the use of variable blob sizes must be combined with regridding techniques to ensure that the particle discretization is everywhere consistent with the local blob sizes and that particles maintain an adequate overlap.

The vortex method is ideally suited to simulations of external flows because it allows an exact treatment of the far field conditions, and their computational effort is restricted to vortical zones of the flow. They can be made even more efficient if one can take advantage of the decay of vorticity gradients in the wake to save computational elements. In the case of a wake behind a cylinder, the blob size is proportional to the distance to the center of the obstacle. Particles are mapped to a uniform mesh through a logarithmic mapping. In the mapped coordinates the diffusion operators allow the use of simple PSE formulas. The particle distributions in the wake of an impulsively started cylinder at $Re = 200$, using the uniform particle distribution and the the variable blob sizes according to the logarithmic mapping, were compared. The evolution of the drag coefficient obtained for the two simulations is identical while the variable blob simulation requires an order of magnitude less particles (about 5000), which translates to respective savings in the computational times.

Using these new vortex methods, we conducted two-dimensional simulations at $Re = 1000$, for a cylinder undergoing rotary oscillations. The motivation for these simulations was to investigate the experimental findings of Tokumaru and Dimotakis (1992), which have shown that at $Re = 15000$ rotary cylinder oscillations may result in up to 80% drag reduction. In the present simulations a similar drag reduction was observed (Fig. 4), and it is attributed to the destruction of the Karman wake and the formation and ejection of vortex dipoles from the surface of the body. Clearly one does not expect the flow to be purely two-dimensional at these Re numbers, and the results of the simulations should not be considered as direct numerical simulations (DNS). However the similar drag reduction between computations and experiments and the mechanism of dipole ejection from the cylinder surface merit further investigation as effective control mechanisms via three-dimensional DNS.

3. Molecular dynamics

Molecular Dynamics (MD) is the method of choice for the study of flow phenomena in micro and nanoscale flows. In the context of particle methods, MD algorithms may be easily constructed from tools already developed for vortex methods. The tree data structures developed for the identification of near-neighbors in vortex methods is implemented in MD simulations using the Lennard-Jones potential.

We present here results from the implementation of a molecular dynamics algorithm to the simulation of microdroplet evaporation and coalescence (see Walther and Koumoutsakos (1999) for further details).

3.1 Droplet evaporation

To study the evaporation of nano-droplets, the tree code was adapted for molecular dynamics (MD) simulation. The short range potential of the 12-6 Lennard-Jones system ($U(r) = 4\epsilon[(\sigma/r)^{12} - (\sigma/r)^6]$) allows a simple truncation of the potential at $r/\sigma = 2.5 - 10$. Hence, the tree effectively serves to identify neighboring particles.

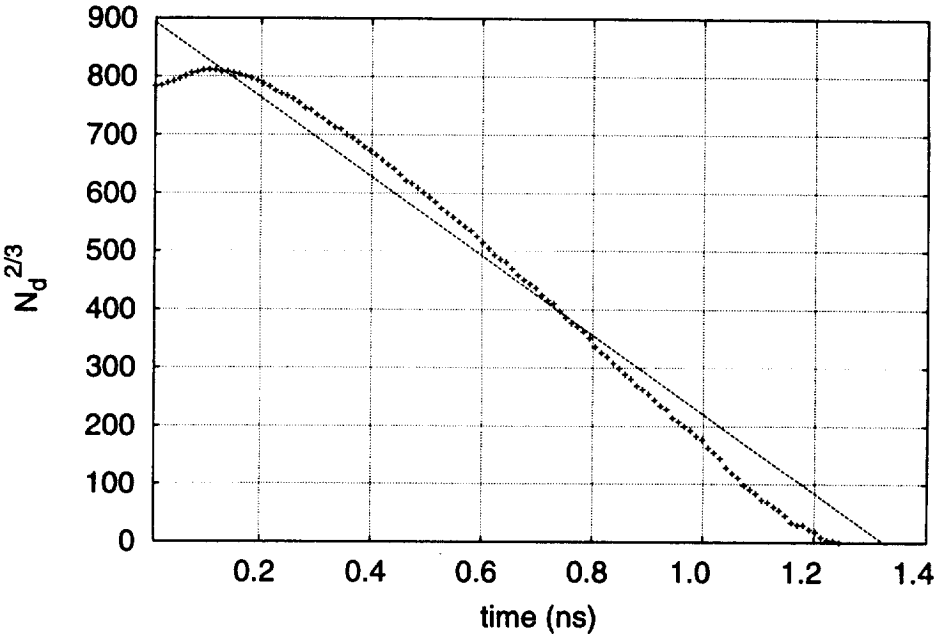

FIGURE 5. Evaporation curve for a 22360 molecule droplet. +++: MD simulation; ---- : D^2 evaporation law.

Standard leapfrog integration is used to advance the molecules in time subject to periodic boundary condition using a ghost-layer technique.

Simulation of the evaporation of an Argon droplet into Argon vapor has been conducted for systems involving 20000 - 150000 molecules. The far-field temperature boundary condition is enforced by heating the molecules in the far-field at regular intervals.

Initially the molecules are places on a face-centered-cubic (f.c.c.) lattice with the desired temperature. The system is then relaxed during 5000 to 10000 time steps, heating the complete system to the equilibrium temperature of $T^* = Tk_B/\epsilon = 0.83$. After the relaxation the temperature of the vapor is increased to $T^* = 2.50$, and as the droplet reaches the saturation temperature ($T^* \approx 1.0$), evaporation commences/begins/starts. The simulations were performed on Sun Ultra 2, allowing approximately 20000 particles per CPU seconds per time step.

Figure 5 compares the predicted evaporation coefficient, β_v, with the D^2 evaporation laws (Kuo, 1986) in terms of the enumeration of molecules in the droplet (N_d). The predicted value is within 10-20% of the D^2-law, which is considered to be a good agreement considering the approximations of the simulation.

3.2 Droplet coalescence

Another study currently being conducted involves the coalescence and breakup of nano droplets. The governing physical parameters are the Weber number, $We = \rho 2RU^2/\gamma$, Reynolds number $Re = \rho 2RU/\mu$, and the impact parameter $B = \chi/2R$,

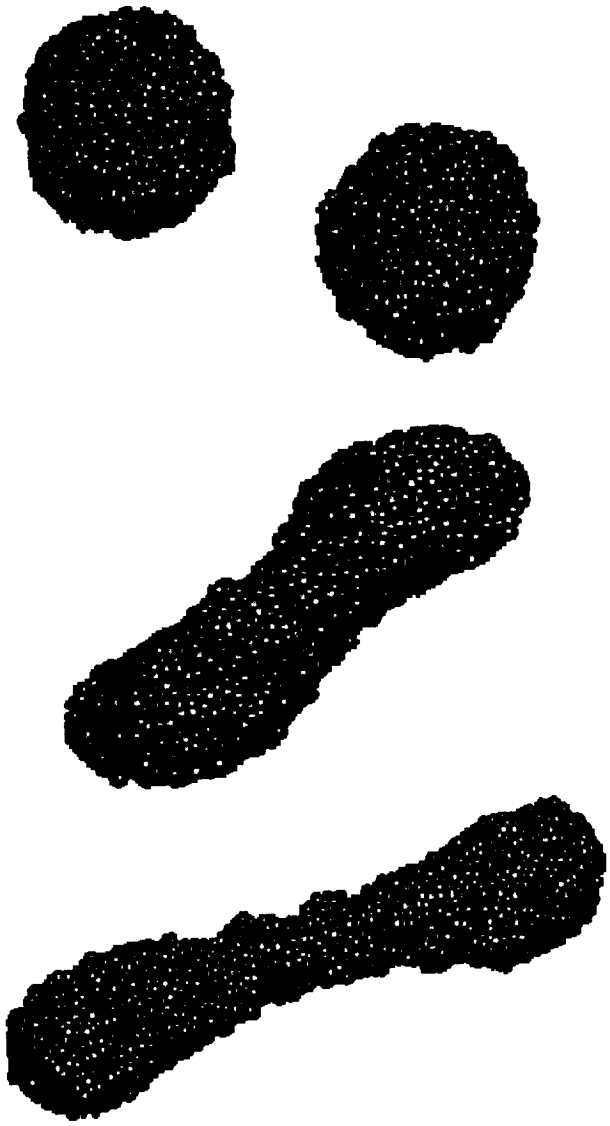

FIGURE 6. Snapshots of droplet molecules during coalescence.

where U is the relative velocity, γ the surface tension, and χ is the projection of the separation distance between the droplet centers in the direction normal to that of U.

The system consists of 2×5576 and 16556 molecules for the droplet and gas phase, respectively. Assuming a Lennard-Jones potential and a cutoff of 6.5σ, the

simulations require 5 CPU seconds per time step on a Sun Ultra 2.

Figure 6 shows snapshots of the droplet molecules during coalescence and breakup for the parameters $(We, Re, B) = (210, 570, 0.5)$.

5. Summary and conclusions

We have presented some results from our ongoing investigations on particle methods (vortex methods and molecular dynamics). Having resolved in the last decade several issues concerning the accuracy and numerical capabilities of vortex methods, the key issue is the use of efficient computational techniques for the solution of the associated N-body problem. Particle-Mesh techniques and multipole summation algorithms coupled with efficient tree-data structures have being implemented, allowing for large scale simulations using millions of computational elements in two and three dimensions.

Looking ahead, particle methods are envisioned as a computational technique that could help bridge the gap in simulations of incompressible flows in micro and macroscales. The coupling may be achieved by using molecular dynamics algorithms to simulate the microscale phenomena and provide boundary conditions for macroscale simulations using vortex methods. This hybrid procedure may be further extended to other schemes, coupling particle and grid based methods in a formulation that takes advantage of the complementary advantages of each method. Such numerical algorithms may offer an accurate and viable alternative to existing multiblock schemes while offering the capability of extending simulations to the level of nano and microscale flow phenomena. Portability and efficiency of the numerical codes and the exploitation of emerging large scale parallel computer architectures will be crucial in these developments.

Acknowledgments

I am grateful for the collaboration of Georges-Henri Cottet and Jens Walther throughout the course of this work.

REFERENCES

COTTET, G.-H. AND KOUMOUTSAKOS, P. 1999 *Vortex methods: theory and applications.* Cambridge University Press.

GREENGARD, L. AND ROKHLIN V. 1987 A fast algorithm for particle simulation. *J. Comp. Phys.* **73,** 325.

GREENGARD, L. AND ROKHLIN, V. 1997 A new version of the fast multipole method for the Laplace equation in three dimensions. *Acta Numerica.* **7,** 229-269.

HOCKNEY R. W. AND EASTWOOD, J. W. 1988 *Computer simulation using particles.* IOP Publishing.

KOLPIK J. AND BANAVAR J. R. 1998 Physics of Fluids at Low reynolds Numbers-A molecular Approach. *Comput. Phys.* **12,** 424-431.

KUO, K. K.-Y. 1986 *Principles of combustion.* John Wiley & Sons.

TOKUMARU, P. AND DIMOTAKIS, P. 1991 Rotary Oscillation control of a cylinder wake. *J. Fluid Mech.* **224,** 77-90.

WALTHER, J. AND KOUMOUTSAKOS, P. 1999 Large scale molecular dynamics simulations of droplet coalescence and evaporation. *(Submitted J. Chem. Phys.)*

Appendix
ROSTER

NAME/TERM		AREA OF RESEARCH
POSTDOCTORAL FELLOWS		
BAGGET, Dr. Jeffrey 9/96-present	(Ph.D. Mathematics, 1996, Cornell)	Large-eddy simulation
BOERSMA, Dr. Bendiks Jan 9/97-present	(Ph.D. Engineering 1997, Univ. of Twente)	Direct simulation, Turbulent combustion, Aeroacoustics
BOTELLA, Dr. Olivier 9/98-present	(Ph.D. Engineering, 1997, University of Nice-Sophia Antipolis	Numerical methods
BUSHE, Dr. W. Kendal 9/96-present	(Ph.D. Engineering, 1996, University of Cambridge)	Turbulent combustion
CAI, Dr. Xiaodan 12/98-8/98	(Ph.D. Mechanical Engineering, 1997, SUNY Stony Brook)	Compressible turbulence
DUBOIS, Dr. Thierry 9/97-8/98	(Ph.D. Mathematics, 1989, University of Paris - Sud)	Incremental unknowns for large eddy simulation
FERNANDEZ, Dr. Eduardo 12/98-present	(Ph.D. Physics, Univ. Wisconsin-Madison, 1997)	Plasma simulations in Hall thrusters
KALITZIN, Dr. Georgi 1/97-present	(Ph.D. Mechanical Engr., 1991, Technical University, Magdeburg)	Turbulence modeling
KIM, Dr. ChongAm 9/97-2/98	(Ph.D. Mechanical & Aerospace Engr., 1997, Princeton)	Numerical methods
LOUCH, Dr. Derek S. 9/98-present	(Ph.D. Engineering, 1998, University of Cambridge)	Turbulent combustion

MOHD. YUSOF, Dr. Jamaludin 9/96-8/98	(Ph.D. Aerospace Engr., 1996, Cornell)	Numerical methods for complex flows
NICOUD, Dr. Franck 1/98-present	(Ph.D. Fluid Mechanics 1993, Institut Nationale Polytechnique Toulouse)	Turbulent flows with variable properties
OOI, Dr. Andrew S. H. 2/98-present	(Ph.D. Engineering, 1997, University of Melbourne)	Turbulence modeling
REIF, Dr. Bjorn A. P. 9/98-present	(Ph.D. Mechanical Engr., 1997, Norwegian University of Science and Technology)	Turbulence modeling
SU, Dr. Lester 9/97-present	(Ph.D. Aerospace Engineering, 1995, University of Michigan)	Turbulent combustion
UMURHAN, Dr. Matt 9/98-present	(Ph.D. Astronomy, 1998, Columbia Univ.)	Acoustics and combustion
VASILYEV, Dr. Oleg V. 9/96-8/98	(Ph.D. Aerospace & Mechanical Engr., 1996, Notre Dame Univ.)	Large-eddy simulation and numerical methods
ZIANE, Dr. Mohammed 6/97-5/98	(Ph.D. Mathematics, 1997, Indiana Univ., Ph.D. Applied Analysis, 1995, Univ. Paris, Sud)	Optimal control theory
SR. RESEARCH ASSOC.		
CABOT, Dr. William H. 3/88-present	(Ph.D. Physics, 1983, Univ. of Rochester)	Large-eddy simulation and convection
WANG, Dr. Meng 9/92-present	(Ph.D. Mechanical Engr., 1989, University of Colorado)	Aerodynamic noise
RESEARCH ASSOCIATES		
FATICA, Dr. Massimiliano 10/95-present	(Ph.D. Fluid Mechanics, 1995, Univ. of Rome)	Parallel computing
KASSINOS, Dr. Stavros 1/95-present	(Ph.D. Mechanical Engr., 1994, Stanford)	Turbulence modeling

KOUMOUTSAKOS, Dr. Petros 8/94-present	(Ph.D. Aeronautics & Applied Mathematics, 1992, California Institute of Technology)	Turbulence physics Active control
MAHESH, Dr. Krishnan 6/96-present	(Ph.D., Mechanical Engr., 1996, Stanford)	Numerical methods
RUETSCH, Dr. Gregory 9/93-present	(Ph.D. Applied Mathematics, 1991, Brown University)	Turbulent combustion and parallel computing
RESEARCH ENGINEER		
IACCARINO, Gianluca 4/98-present	University of Naples	Turbulence modeling
SR. VISITING FELLOWS		
BEHNIA, Prof. Masud 2/98, 7/98	University of New South Wales	Turbulence modeling and heat transfer
BIESENGER, Dr. Thomas 9/98	University of Cambridge	Turbulence modeling
BILGER, Prof. Robert W. 4/98	University of Sydney	Turbulent combustion
BISSETT, Dr. David 8/98-present	University of Newcastle	Numerical methods
CAMBON, Dr. Claude 6/98	Ecole Centrale Lyon	Turbulence modeling
HUNT, Julian C. R. 6/98, 8/98-9/98	University of Cambridge	Turbulence physics and transition
KALTENBACH, Dr. Hans-Jakob 8/98	TU-Berlin	Large eddy simulation
KAWAHARA, Prof. Genta 8/98-present	Ehime University, Japan	Turbulent boundary layers
KLEIN, Prof. Rupert 9/98	Freie Universitaet Berlin, Germany	Turbulent combustion

LIN, Prof. Chao-An 10/98	National Tsing Hua University, Taiwan	Turbulence modeling
MASLOWE, Prof. Sherwin 7/98-8/98	McGill University, Canada	Hydrodynamic stability
MORINISHI, Dr. Youhei 8/98	Nagoya Institute of Technology, Japan	Large eddy simulation
PROSSER, Dr. Robert 8/98	University of Cambridge	Turbulent combustion
STEINER, Dr. Helfried 1/97-present	Technical University –Graz, Austria	Turbulent combustion
VAN WIJNGAARDEN, Prof. Leendert 10/97-3/98	University of Twente, The Netherlands	Two phase flows

SR. RESEARCH FELLOWS

BROADWELL, Dr. James E. 1/94-12/98		Turbulent combustion
JIMENEZ, Prof. Javier 1987-present		Boundary conditions for large-eddy simulation
YAGLOM, Prof. Akiva 7/95-present		Writing of 2nd edition, "Statistical Fluid Mechanics"

GRADUATE STUDENTS

DAY, Mark 4/98-6/98		Compressible reacting mixing layer
HAMMOND, Edward 10-97-6/98		Non-dissipative numerical methods in plasma studies

1998 ADVISORY COMMITTEE

Dr. David E. Crow
United Technologies Pratt & Whitney

Prof. Steven Crow
Starcar Development Company

Mr. Robert H. Kelly-Wickemeyer
Boeing Commercial Airplane Group

Prof. Brian Launder
University of Manchester

Dr. Spiro Lekoudis
Office of Naval Research

Prof. John L. Lumley
Cornell University

Dr. Mark Glauser
Air Force Office of Scientific Research

Prof. Norbert Peters
RWTH - Aachen

Dr. Dennis M. Bushnell (Ex-officio)
NASA Langley Research Center

Dr. Marvin E. Goldstein (Ex-officio)
NASA Lewis Resesarch Center

Dr. Jack Hansen (Ex-officio)
NASA Ames Research Center

1998 STEERING COMMITTEE

Prof. Paul A. Durbin
Professor, Mechanical Engineering,
Stanford

Prof. Javier Jiménez
Senior Research Fellow, Center for
Turbulence Research, and
Professor, University of Madrid

Prof. Sanjiva K. Lele
Professor, Aeronautics and Astronautics,
Stanford University

Dr. Nagi N. Mansour
Sr. Staff Scientist
NASA Ames Research Center

Prof. Parviz Moin
Director, Center for Turbulence Research
Professor, Mechanical Engineering and
Aeronautics & Astronautics, Stanford
Sr. Staff Scientist, NASA Ames Research
Center

Prof. William C. Reynolds
Program Coordinator, Center for
Turbulence Research
Professor, Mechanical Engineering and
Aeronautics & Astronautics, Stanford
Sr. Staff Scientist, NASA Ames
Research Center

Dr. Charles A. Smith
Acting Chief
AeronauticalTechnologies Division
NASA Ames Research Center

Prof. Leen Van Wijngaarden
Senior Visiting Fellow, Center for
Turbulence Research, and Professor,
U. Twente, the Netherlands